UiO : Universitetet i Oslo

Md Jamilur Rahman

Seal and overburden rock characterization of potential CO_2 storage sites in the northern North Sea

Thesis submitted for the degree of Philosophiae Doctor

Department of Geosciences

Faculty of Mathematics and Natural Sciences

2022

Series of dissertations submitted to the
Faculty of Mathematics and Natural Sciences, University of Oslo
No. 2517

ISSN 1501-7710

Cover: Hanne Baadsgaard Utigard.
Print production: Graphics Center, University of Oslo.

… *essentially, all models are wrong, but some are useful***…**

George E.P. Box (1919-2013)

Preface

This dissertation has been submitted to the Department of Geosciences, Faculty of Mathematics and Natural Sciences at the University of Oslo in accordance with the requirements for the degree of Philosophiae Doctor (Ph.D.). The study was conducted under the project OASIS – Overburden Analysis and Seal Integrity Study for CO_2 sequestration in the North Sea, which is part of ”The CLIMIT programme’’ that provides financial support for developing carbon capture and storage (CCS) technology with collaboration between Gassnova SF and the Research Council of Norway. Moreover, under the OASIS project, UiO has a partnership with international universities (Curtin University, Australia and Colorado School of Mines, USA), national and international research institutes (Norwegian Geotechnical Institute, Norway, Norwegian Computing Center, Norway, and National Oceanography Center, UK) and industries (Equinor and TotalEnergies). The principal supervisor of this work was Prof. Nazmul Haque Mondol (UiO & NGI), and co-supervisors were Prof. Jens Jahren (UiO), Dr. Jung Chan Choi (NGI), and Dr. Manzar Fawad (UiO).

The main objective of this study was to evaluate the top seal (faults, cap, and overburden rocks) integrity in potential subsurface CO_2 storage sites by integrating petrography, petrophysics, rock physics, seismic inversion, and stochastic analytical and numerical modeling. The injection sites from the Horda Platform, northern North Sea, had been selected as the study area. The dissertation is divided into three sections.

- **Section-1 (Overview of the Ph.D. dissertation):** This section consists of the research objectives, background, theoretical framework, database, methodologies, and key findings.
- **Section-2 (Journal papers):** This section includes four peer-reviewed papers published in different journals where I am the first author.
- **Section-3 (Appendices)**: This section includes four additional peer-reviewed papers (**Appendix-1**) and four conference proceedings (**Appendix-2**) relevant to this Ph.D. research where I am the first/second author.

Md Jamilur Rahman, Oslo, June 2022

Acknowledgments

Firstly, I would like to express my sincere gratitude to my primary supervisor, Professor Nazmul Haque Mondol, for the continuous guidance, support, and motivation over the last years. Thank you for always making time for our discussion in Bengali, inspiring, and helping me build my confidence as an independent researcher.

I am deeply thankful to my supervisor Dr. Jung Chan Choi, for his in-depth discussion and suggestions in geomechanics. I learned a lot from our inclusive conversation. I am also grateful to my supervisor Professor Jens Jahren for valuable discussions and input to my work, along with the jokes in Norwegian. I want to express my greatest appreciation to my supervisor, Dr. Manzar Fawad. He is always there for me when needed and has made my Ph.D. life easier.

I also would like to express my gratitude to the department of geoscience, the University of Oslo, the Research Council of Norway, and industry partners for the financial support of this Ph.D. fellowship. Furthermore, I acknowledge the technical and academic support and assistance from Thanusha Naidoo, Salahalldin Akhavan, Siri Simonsen, Mufak Said Naoroz, Michel Heeremans, Kjetil Bakke, Catherine Braathen, Anne Cathrine Modahl, Anne Gunhild Innes and Thor Axel Thorsen at the Department of Geosciences, UiO.

Over my years at the University of Oslo, one of my outstanding achievements is to meet many good souls as fellow students, colleagues, and office mates. I am very thankful for the companionship, support, and motivation from you guys over the past years; Tesfa, Sajjad, Sigurd, Vemund, Henrik, James, Hassan, John, Jørgen, Noora, Anna, Mark, Lina, Val, Camilla, Miquel, Uli, Aurora, Jonny, Sian, Nora, Feng, Khoir, Bayene, Ali, Ibrahim and Abishek.

Finally, I want to thank my parents and my wife, Afroza, for their encouragement, never-ending support, and always being there for me.

Summary

It is generally accepted that the main reason for human-induced global warming is the emission of greenhouse gases, mainly carbon dioxide (CO_2) and methane (CH_4). The impact of global warming may trigger the critical thresholds called tipping points if warming increases to equal or greater than 1.5^0C. Despite the pledges made under the 2015 Paris agreement, global warming will still reach about 2.8^0C by the end of the century unless emissions are cut by half by 2030, and net-zero emissions are achieved by 2050. Carbon capture and storage (CCS) is one of the solutions that cut emissions with the lowest possible cost. CO_2 will be captured from the point sources, transported, and permanently stored in suitable subsurface geological formations. Although the practicalities of CCS are being demonstrated by several pilot projects globally, subsurface injections of CO_2 may have several mechanical consequences including fault reactivation, top seal fracturing and/or failure, surface heave, leakage along the legacy wells, and porosity-permeability changes due to reservoir expansion, etc. A detailed analysis of such factors is required for safe and permanent subsurface CO_2 storage.

The primary focus of this Ph.D. research is to improve a methodology to evaluate the top seal and overburden geomechanical risks by integrating petrography, petrophysics, rock physics, seismic inversion, and modeling approaches. The Smeaheia and Aurora injection sites from the Horda Platform area have been the major focal point for this study. Work is divided into three parts. The first part explores the depositional and diagenetic effect on the evolution of rock properties in fine-grained clastic sediments. The second part consists of an analytical method where the top seal, including faults and caprock shale, reliability has been assessed based on probabilistic structural failure analysis. Although the structural reliability analysis is widely used on surface structures, this research has introduced the approach for the first time for subsurface reliability as a means of understanding the leakage potential of CO_2 storage sites. In addition, a field-scale numerical model is followed by an analytical model where a robust geomechanical modeling workflow has been proposed to evaluate field-scale rock mechanical failure and deformation. Finally, a combined site-specific top seal evaluation function and probabilistic risks ranking template have been developed.

Although this study focuses on the Horda Platform area, the proposed methods are applicable globally to characterize subsurface CO_2 storage sites. Apart from CCS projects, the outcome of this Ph.D. research can be beneficial for other subsurface injection projects such as water injection for reservoir management, wastewater injection for disposal, unconventional hydraulic fracking, etc.

List of papers, conference proceedings, and invited talks

Section-2 (Journal papers)

This dissertation includes the following peer-reviewed journal papers:

Paper-1: Organic-Rich Shale Caprock Properties of Potential CO_2 Storage Sites in the Northern North Sea, Offshore Norway
Rahman, Md Jamilur; Fawad, Manzar & Mondol, Nazmul Haque
Marine and Petroleum Geology, 2020, **122,** p.104665
https://doi.org/10.1016/j.marpetgeo.2020.104665

Paper-2: Probabilistic Analysis of Vette Fault Stability in Potential CO_2 Storage Site Smeaheia, Offshore Norway
Rahman, Md Jamilur; Choi, Jung Chan; Fawad, Manzar & Mondol, Nazmul Haque
International Journal of Greenhouse Gas Control, 2021, **108,** p.103315
https://doi.org/10.1016/j.ijggc.2021.103315

Paper-3: Effect of overburden spatial variability on field-scale geomechanical modeling of potential CO_2 storage site Smeaheia, offshore Norway
Rahman, Md Jamilur; Fawad, Manzar; Choi, Jung Chan & Mondol, Nazmul Haque
Journal of Natural Gas Science and Engineering, 2022, **99**, p.104453
https://doi.org/10.1016/j.jngse.2022.104453

Paper-4: 3D field-scale geomechanical modeling of potential CO_2 storage site Smeaheia, offshore Norway
Rahman, Md Jamilur; Fawad, Manzar & Mondol, Nazmul Haque
energies, 2022, **15(4)**, p.1407
https://doi.org/10.3390/en15041407

Section-3 (Appendix-1)

The relevant papers (RP) have been added to the Appendix-1:

RP-1: Rahman, Md Jamilur; Fawad, Manzar & Mondol, Nazmul Haque (**2021**). Reservoir Fluid Effect on Caprock Properties in the Horda Platform Area, Northern North Sea. Proceedings of the 15th Greenhouse Gas Control Technologies Conference 15-18 March 2021. *http://dx.doi.org/10.2139/ssrn.3812432*

RP-2: Fawad, Manzar; **Rahman, Md Jamilur** & Mondol, Nazmul Haque (**2021**). Seismic Reservoir Characterization of Potential CO_2 Storage Reservoir Sandstones in Smeaheia Area, Northern North Sea. Journal of Petroleum Science and Engineering, 205, p. 108812. *https://doi.org/10.1016/j.petrol.2021.108812*

RP-3: Rahman, Md Jamilur; Choi, Jung Chan; Fawad, Manzar & Mondol, Nazmul Haque (**2021**). Probabilistic Analysis of Draupne Shale Caprock Reliability of the Alpha Prospect-A Potential CO_2 Storage Site in the Smeaheia Area, Northern North Sea. SINTEF Academic Press (SINTEF Proceeding), 2021. Trondheim, Norway. Short Papers from the 11th International Trondheim CCS Conference (TCCS-11). *https://hdl.handle.net/11250/2780683*

RP-4: Fawad, Manzar; **Rahman, Md Jamilur** & Mondol, Nazmul Haque (**2021**). Seismic-derived geomechanical properties of potential CO_2 storage reservoir and cap rock in Smeaheia area, northern North Sea. The leading Edge, 40(4): 254. *https://doi.org/10.1190/tle40040254.1*

Section-3 (Appendix-2)

The conferences proceedings (CP) have been added to the Appendix-2:

CP-1: Rahman, Md Jamilur; Fawad, Manzar & Mondol, Nazmul Haque (**2021**). Mineralogy Based Geomechanical Behavior of Draupne Caprock Shales in the Northern North Sea, Offshore Norway. EAGE 82nd annual conference and exhibition, 18-21 October 2021. *https://doi.org/10.3997/2214-4609.202011458*

CP-2: Rahman, Md Jamilur; Fawad, Manzar & Mondol, Nazmul Haque (**2020**). Depositional Processes and Shallow Diagenesis Effect on Caprock Elastic Properties in Horda Platform Area, Northern North Sea. GeoConvention, 21-23 September 2020.
https://geoconvention.com/wp-content/uploads/abstracts/2020/57281-depositional-processes-and-shallow-diagenesis-effe.pdf

CP-3: Fawad, Manzar; **Rahman, Md Jamilur** & Mondol, Nazmul Haque (**2020**). "Mineralogy Analysis of Jurassic Reservoir Sandstones Using Wireline Log Data in the Northern North Sea." In GeoConvention 2020.
https://geoconvention.com/wp-content/uploads/abstracts/2020/57739-mineralogy-analysis-of-jurassic-reservoir-sandston-01.pdf

CP-4: Rahman, Md Jamilur; Lebedev, Maxim & Mondol, Nazmul Haque (**2021**). Nanoscale mechanical properties of organic-rich Draupne shale caprock, offshore Norway. SEG annual meeting (IMAGE) 26 September – 1 October 2021. *https://doi.org/10.1190/segam2021-3581994.1*

Invited talks

1. **Rahman, Md Jamilur**; Mondol, Nazmul Haque; Jahren, Jens; Choi, Jung Chan & Fawad, Manzar (**2021**). Caprock/fault and overburden characterization of potential CO_2 storage sites in the northern North Sea. OASIS (Overburden Analysis and Seal Integrity Study for CO_2 Sequestration in the North Sea) project annual update meeting, 8 December 2021. Oslo, Norway.

2. **Rahman, Md Jamilur**; Fawad, Manzar & Mondol, Nazmul Haque (**2021**). Importance of overburden rock characterization for potential CO_2 storage site Aurora, northern North Sea. 4th SEG Virtual Student Conference presentation.

3. **Rahman, Md Jamilur**; Mondol, Nazmul Haque; Jahren, Jens; Choi, Jung Chan & Fawad, Manzar (**2020**). Reservoir, caprock/fault, and overburden characterization of potential CO_2 storage sites in the northern North Sea. OASIS (Overburden Analysis and Seal Integrity Study for CO_2 Sequestration in the North Sea) project annual update meeting, 11 December 2020. Oslo, Norway.

4. **Rahman, Md Jamilur**; Choi, Jung Chan; Fawad, Manzar & Mondol, Nazmul Haque (**2020**). Probabilistic Analysis of Vette Fault Stability. NCCS Task-10 Workshop, 21 October 2020. Oslo, Norway.

5. **Rahman, Md Jamilur**; Choi, Jung Chan; Fawad, Manzar & Mondol, Nazmul Haque (**2020**). Probabilistic Analysis of Vette Fault Stability. Norwegian Geotechnical Institute (NGI)-University of Oslo Research Workshop, 15 September 2020. Oslo, Norway.

6. **Rahman, Md Jamilur** (**2020**). Evaluating the risks during anthropogenic CO_2 injection into the saline aquifer. DEEP Communication, 18 June 2020. Oslo, Norway.

7. **Rahman, Md Jamilur**; Fawad, Manzar; Mondol, Nazmul Haque; Jahren, Jens & Choi, Jung Chan (**2019**). Geomechanical properties of caprock shales (Draupne and Heather Formations) of CO_2 storage site in northern North Sea. Norwegian Geotechnical Institute (NGI)-University of Oslo Research Workshop, 10 December 2019. Oslo, Norway.

8. **Rahman, Md Jamilur** & Mondol, Nazmul Haque (**2019**). Rock compositional effect on geomechanical properties of Heather and Draupne caprock shales in the North Sea. Prometheus project bi-annual meeting, 29 November 2019. Oslo, Norway.

Table of Contents

SECTION-1

(OVERVIEW OF THE Ph.D. DISSERTATION)

1. Introduction

1.1 Motivation, background, and research objectives

Top seal integrity is a critical part of any subsurface fluid injection project, including water injection for reservoir management, wastewater injection for disposal, hydraulic fracturing for unconventional, and subsurface CO_2 injection for sequestration (CCS). For a saline aquifer, trapping mechanism of the top seal is quite uncertain but a crucial component of containment issues. Hence, accurate assessment of top seal integrity is one of the critical parameters in any injection project. Seal rock strength is one of the important parameters that affect the integrity of cap and overburden rocks, which can trap low-density fluid plumes. If the reservoir pressure-induced effective stress exceeds the seal's tensile or shear strength, leakage can be triggered in caprocks and faults (Fig. 1.1). A rapid increase of reservoir pressure can also lead to membrane seal failure (advection and diffusion through caprock) or hydraulically dilated faults and fractures (shear or tensile failure of caprock and existing faults reactivation). There have been many natural and geological evidence of leakages caused by pressure-build up. Gas leakage (gas chimney) through the top seal is a common phenomenon in hydrocarbon fields, which are easily detectable in seismic sections as a columnar disturbance with lower reflection continuity and amplitudes than the surrounding areas (Sales, 1997; Heggland, 1997; Foschi and Cartwright, 2020; Hansen et al., 2020; Rahman et al., 2022). Depending on the overburden lithology, migrated fluids might be trapped within the overburden section or might also have migrated up to the seabed (offshore site) or atmosphere (onshore site). Seafloor pockmarks might be an indication of fluid escaping, and have been observed in basins all over the world (Foschi and Cartwright, 2020). Studies of the hydrocarbon fields give us an excellent analogue for injection related activity. Unlike hydrocarbon fields, injection projects need to characterize containment risks beforehand to achieve leakage free permanent storage. Nevertheless, seal integrity is a complex process and depends on many factors such as mineralogy, pressure, temperature, and mechanical properties. Due to the complex nature of factors affecting the top seal integrity, it is hard to quantify, and it requires an integrated assessment approach for better reliability.

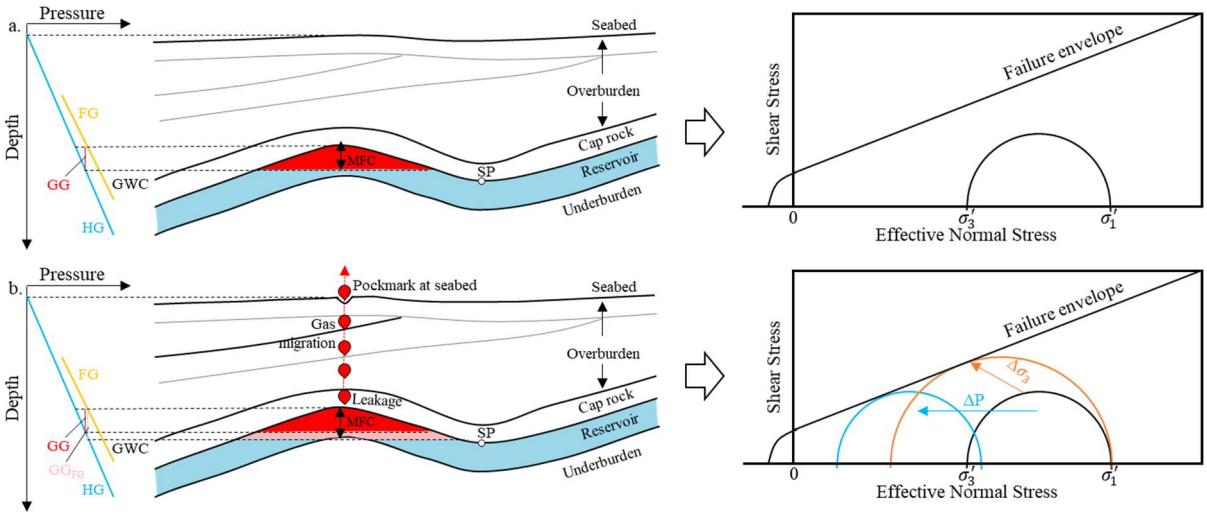

Fig. 1.1: Graphical illustration of pressure-depth plot based on a structural trap with a thick fluid column (modified after Foschi and Cartwright, 2020). A representative Mohr-Coulomb failure diagram is presented for no gas leakage scenario (a) and gas leakage through caprock and overburden by diffusion and/or rock failure due to overpressure or horizontal stress perturbation (b). *HG – hydrostatic gradient; FG – fracture gradient; GG – gas gradient; GG_{FG} – gas gradient during caprock fracture; GWC – gas*

water contact; SP – spill point; MFC – maximum fluid column; σ_1' - effective vertical stress; σ_3' - effective horizontal stress.

One of the well-known injection-related seal integrity issues is a membrane seal failure. Due to the importance of proper seal integrity assessment for hydrocarbon exploration, the study of top seal risk assessment was started in the 1970s and 1980s where the theoretical foundation was established in a series of published papers (Berg, 1975; Schowalter, 1979; Rouchet, 1981; Downey, 1984; England et al., 1987; Watts, 1987; Sales, 1997). These initial studies emphasized buoyancy pressure dependent seal capacity where the membrane seal failure occurs when buoyancy force exceeds the capillary entry pressure of the top seal (Schowalter, 1979; Foschi and Cartwright, 2020) The same diffusion concept was studied in fluid migration from the source rock. Since this study deals with clastic rocks with high organic matter content, the analog to fluid migration from source rocks is valid. When the fluid volume increases within a trap similar to matured organic shales, hydrocarbon molecules can diffuse into the overlying rock and escape (Leythaeuser et al., 1984, 1982; Sales, 1997; Abay, 2017). The same concept is also applicable in the crestal trap between the reservoir and the caprock interval. Although the diffusion process might initiate fluid leakage, many studies have suggested that the process in a water-filled pore system is extremely slow (Smith et al., 1971). The process may become faster if caprock shale has microfractures induced by overpressure due to petroleum generation within shales (Tissot and Welte, 1984; Bjørlykke, 2015), or through kerogen networks (Stainforth and Reinders, 1990; Johnson et al., 2022b). However, flow through the networks is dependent on several factors such as the caprock shale's kerogen quantity (percentage), quality (types), and the degree of thermal maturation (Abay, 2017; Johnson et al., 2022b). In addition, thickness of the caprock shale plays a vital role during diffusion-related fluid escape (Karlsen et al., 2004; Johnson et al., 2022).

Another critical aspect of injection-related geomechanical risk is an induced seismicity. Artificial injection of fluids into the Earth's crust can induce seismicity. Injected fluids not only perturb stress and create new fractures/faults, but it also potentially causes slip in pre-existing fault zones (Jimenez and Chalaturnyk, 2002; Rutqvist and Tsang, 2002; Nordbotten et al., 2004; Streit and Hillis, 2004; Hawkes et al., 2005; Rutqvist et al., 2007, 2008; Soltanzadeh and Hawkes, 2008; Herwanger and Koutsabeloulis, 2011; Davies et al., 2013). Additionally, there might be the possibility of ground deformation in the vicinity of the injection/production area. Deep water injection has been practiced by the oil industry for over 100 years for oil displacement and over 70 years for wastewater disposal (Dusseault, 2011). The record of induced seismicity is routinely documented and monitored. Globally, increased rates of seismic activity are reported in the vicinity of injection wells and attributed to fluid injection (Horton, 2012; Keranen et al., 2013; Kim, 2013; Ellsworth, 2013; Schultz et al., 2014, 2020; Fan et al., 2016; Levandowski et al., 2018). However, natural seismicity (earthquake) is also common and requires monitoring near injection sites (Rubinstein and Mahani, 2015).

The aforementioned risks of the seal failure and the induced seismicity are significantly affected by the behavior of pore fluid under the drainage condition and associated stress paths within the reservoirs and surroundings (Segall, 1989; Grasso, 1992; Addis, 1997; Hillis, 2001). Additional processes such as hydraulic aperture evolution, hydrological property changes, effective stress induction, and mechanical strength degradation can also influence the effective stress of cap and overburden rock deformations. These geomechanical processes can lead to top seal failure. The failed top seal may act as a leakage pathway for injected fluids to migrate upward into the overburden and potentially into the atmosphere. These events will trigger the environmental challenges that are associated with this technique (Cambell et al., 2020; Schultz et al., 2020). To avoid this, one must assess the potential top seal (caprock and fault)

geomechanical failure risks using the available database, where an integrated analysis approach should be carried out.

The major challenges in the geomechanical assessment are: accurate delineation of in-situ physical properties and conditions (i.e., temperature, in-situ stresses, and pressure), and predicting accurate injection-induced mechanical behaviors, including subsidence/heave. For instance, 8m seafloor subsidence in the Ekofisk field was indicative of a failure to predict subsidence during the development phase. Geomechanical model need to deal mainly with coupled problems requiring simultaneous consideration of changes in temperature, pressure, stress and chemical processes (THMC). However, the lack of relevant subsurface material information has been one of the difficulties in geomechanical simulation. Especially, the sensitive phase behavior of CO_2 will complicate the modeling process further in CCS projects. For instance, supercritical CO_2 is in liquid form but behaves like a gas. The buoyancy pressure and solubility rate of CO_2 are also faster and different than hydrocarbon fluids. Furthermore, due to the sensitivity of local in-situ stress conditions (influenced by induced seismicity), a site-specific characterization and associated geomechanical analysis is suggested (Fan et al., 2016).

The above discussion explains the importance and necessity of subsurface geomechanical characterization in any fluid injection project. This study addressed injection-related issues by focusing on characterizing the containment risks in the Horda Platform, northern North Sea potential CCS injection sites. Although most of the North Sea fault-related discoveries indicated either no or minor fault-related leakage (i.e., sealed faults), some critically stressed faults in the North Sea lead to a Mohr-Coulomb failure condition (Grollimund and Zoback, 2003). Due to a lack of core data in cap and overburden sections, most geomechanical studies may need simplification in the elastic moduli and Mohr-Coulomb parameters (Grollimund and Zoback, 2003). The simplified input may result in overlooking the possible geomechanical risks. In addition, geological history can also result in another uncertain factor. For instance, Cenozoic uplift and erosion in the study area result in uncertainties in the magnitude and orientation of the principal stresses. The caprock shear failure or fault reactivation (top seal integrity) is also influenced by the in-situ stress magnitude and orientation in any sedimentary basins (Bjørlykke et al., 2005). This observation suggests that a better understanding of geological history and accurate geomechanical characterization should be considered for the injection-induced stability of faults in the case of CO_2 injection into saline aquifers, especially, when the site lacks information about the in-situ stresses and mechanical properties.

To obtain a better containment risk assessment, an integrated approach is needed, including all the available data (wireline logs, seismic, wellbore samples, etc.) analyses, accompanied by geomechanical modeling and investigation (Rodriguez-Herrera et al., 2014). However, most of the efforts usually focus on reservoir and caprock, while very few studies have been focused on the whole subsurface, including both reservoir and caprock in practical and research areas (Sengupta et al., 2011). This is because good data coverage is usually acquired only within reservoir sections; however, the caprock and overburden sections are usually ignored while acquiring cores, wireline logs, and pressure readings. In order to compensate for this lack of data, seismic data can be used as input to extract geomechanical properties of cap and overburden rocks since seismic data especially 3D cube has full coverage from the surface to horizons much deeper than the reservoir rocks.

Quantification of effects of overburden variability is also essential for the integrated approach. Usually, the overburden rock has natural variability due to heterogenous characteristics. In-situ stress condition in the overburden is determined not only by its depositional geomechanical characteristics (i.e., Poisson's ratio) but also by geological history (i.e., tectonic stress, heaving,

and subsidence). Therefore, it is not easy to get accurate values from the field (Moos et al., 2003). Natural fractures in caprock shales are also heterogeneous, which may significantly affect the caprock strength and by extension leakage pathways. Therefore, the deterministic evaluation of caprock integrity using limited borehole data can result in poor judgment regarding decision-making. In addition, the overburden leakage can be caused by the interaction of multiple events such as breakage of capillary barriers, geomechanical slip, tensile opening, fluid-driven fracture propagation, etc. Therefore, an integrated approach is required to evaluate the top seal (cap, overburden, and fault) in any CO_2 injection site characterizations.

Considering the abovementioned uncertainties and challenges, this Ph.D. research is focused on improving seal integrity knowledge by building a robust geomechanical model integrating all the available databases. Statistical seismic inverted properties are directly resampling to the model grid as model property input. Extracting rock properties directly from 3D seismic can cover volumes from the surface down to a depth below the potential reservoir. Seismic inverted properties such as acoustic impedance, Vp/Vs ratio, density, Young's modulus, and Poisson's ratio can be used for rock characterization (Rasmussen et al., 2004; Johnson, 2017; Yenwongfai et al., 2017). This study used seismic inverted property cubes to simulate 3D field-scale geomechanical models. In addition to geomechanical model, caprock characterization and probabilistic structural reliability assessment studies have been carried out. The overall objectives of this Ph.D. dissertation are:

- Develop a clear understanding of exhumation, paleo-depositional environment, tectonic and structural history, and their effect on rock geomechanical properties. Build an integrated workflow to characterize caprock shale.
- Probabilistic assessment of caprock and fault structural reliability and assess the sensitivity of the input data uncertainties.
- Develop a seismic data-driven field-scale 3D geomechanical modeling workflow focusing on the overburden and cap rocks to evaluate the stress-strain change due to injection-induced pressure alteration.

These objectives are achieved by interdisciplinary research involving laboratory experiments (**CP-4**), petrophysical-geophysical data analysis (**Paper-1; RP-1 & -2; CP-1 to -3;** Rahman et al., 2022), and analytical and numerical model investigation (**Paper-2 to -4; RP-3 & -4**) are shown in figure 1.2. The wireline log-based analysis, mainly the caprock characterization (**Paper-1;** Rahman et al., 2022), has been carried out over the greater Horda Platform area so that it would be easier to evaluate future injection sites surrounding the present sites (i.e., Smeaheia and Aurora). The rest of the journal papers (**Paper-2 to -4**) and additional relevant papers (**RP-1 to -4**), and conference proceedings (**CP-1 to CP-4**) are focused on the specific injection site (i.e., Smeaheia). However, the proposed methods are suitable to characterize any fluid injection projects such as other CO_2 injection sites or exploration and development phases in the oil and gas industry.

This research has improved the knowledge gap related to top seal integrity assessment. To our knowledge, the proposed workflows to characterize caprock, faults, and overburden stress-related risks have novelty. Results from this research are also indicated the effectiveness of these methods and approaches. The uniqueness of these processes are described below:

- Due to the complex nature of fine-grained clastic rock properties, the proposed integrated workflow to characterize depositional and diagenetic influences is necessary and effective in injection sites with the clastic top seal.

- The probabilistic structural reliability method is widely used for surface structure characterization, but the novelty of this approach is that it is the first time introduced for subsurface top seal structural failure analysis.
- The proposed top seal risk ranking template based on brittleness and structural reliability is a unique approach to the qualitative top seal failure risks. Further analysis is required to improve it.
- Seismic property based anisotropic overburden gridded 3D field-scale geomechanical model is a novel approach in stress-stain coupling research.

Although the investigation focuses on CO_2 storage site characterization, the proposed methods can be applied for any subsurface injection site characterization, such as wastewater disposal, unconventional hydraulic fracking, etc.

1.2 Fundamental of subsurface CO_2 storage

Human-induced global warming processes change the climate and have large-scale impacts on weather patterns. Climate change is a natural process that observed in the geological time scale. However, the current change is more rapid than any known events in Earth's history (Allen et al., 2018). It is generally accepted that the main reason for this unprecedented rise in global temperature is the emission of greenhouse gases, mainly carbon dioxide (CO_2) and methane (CH_4). The impact of climate change is already being felt at the current level of warming, which is about 1.2^0C (CLIMA, 2021). According to IPCC (International Panel on Climate Change), the impact might significantly increase if warming reaches 1.5^0C, or above the preindustrial level (IPCC, 2018), which could trigger the critical thresholds called tipping points (Pachauri et al., 2014). Considering the severe irreversible loss and damage to nature and society, the 2015 Paris Agreement was adopted. Nations collectively agreed to keep warming well below 2^0C above the pre-industrial level and pursue efforts to limit the temperature increase to 1.5^0C (Longship-Report, 2020). However, despite pledges made under the agreement, global warming will still reach about 2.8^0C by the end of the century (Climate Action Tracker, 2021) unless emissions are cut by half by 2030, and net-zero emissions are achieved by 2050 (Rogelj et al., 2018).

Several countries, including the EU, have committed to a net-zero target by 2050. Norway specifically targeted reducing greenhouse gas emissions by at least 50% by 2030 compared with the 1990 level (Norwegian Government Climate goal Report, 2020). We are talking about 'net-zero', but what does that actually mean? The net-zero target means that greenhouse gas emissions into the atmosphere must be equivalent to zero by increasing the natural sequestration of CO_2 through processes such as agriculture, forestry, and other land use, or by capturing and permanently storing CO_2 underground (Longship-Report, 2020). Subsurface geological CO_2 storage is considered one of the viable solutions to mitigate global warming. The CCS processes (carbon capture and storage) consist of three parts: capturing CO_2 from the point sources, transporting the captured CO_2 to a storage site, and finally injecting/storing it into the subsurface reservoirs (i.e., saline aquifers or depleted hydrocarbon fields). According to the United Nations, IPCC, and IEA (International Energy Agency), CCS will be necessary to reduce global greenhouse gas emissions at the lowest possible cost. CICERO (Center for International Climate Research Organization) has concluded that CCS is critical in most emission pathways to achieve the temperature reduction goals (Peters and Sognnæs, 2019). CCS is also vital because (i) it may be challenging to reduce the source of emissions to net-zero quickly enough without it, (ii) currently there are no viable alternatives to CCS for certain sectors (i.e., cement, steel, long-distance sea, and air transport, etc.), and (iii) CCS might be the

cheapest and best way of reducing emissions (Longship-Report, 2020). Therefore, it is well understood that we need more CCS projects globally for sustainability.

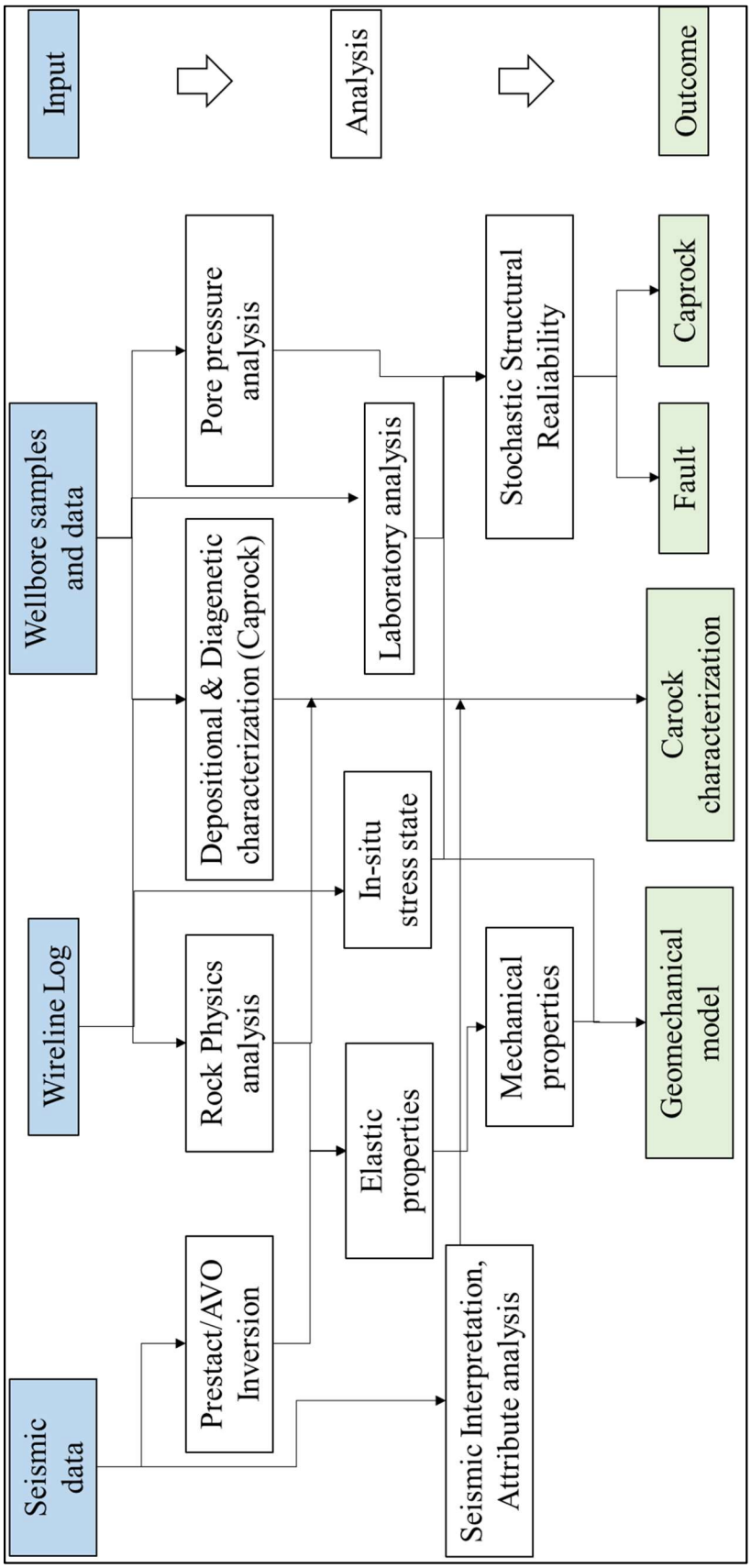

Fig. 1.2: The overall workflow of this Ph.D. dissertation illustrated the input database and the journal papers as output.

Geological storage of CO_2 is not a new concept. It was first utilized during the 1970s in Texas, United States (Hedley, 2014). However, the purpose was not environmental; instead, it was used for enhanced oil recovery (Dicharry et al., 1973). The first CO_2 injection was started for the sole purpose of preventing atmospheric emissions and commenced operation in 1992. Statoil (now Equinor) separated CO_2 from the produced hydrocarbon in the Sleipner field, North Sea, and re-injected it into the brine saturated Utsira Formation (Korbøl and Kaddour, 1995; Baklid et al., 1996). According to the Global CCS Institute database (GCCSI), 58 large-scale CCS projects are in progress worldwide, out of which twenty projects are already in operation. Thirteen (13) of these projects are located in North America, five are distributed between Asia, Australia, and South America, whereas two projects (Sleipner & Snøhvit) are located in Norway, the only country in Europe with projects in the operational phase now.

Norway is able to contribute to the development of carbon capture and storage because the country has over 25 years of planning and implementation experience. There is vast potential for geological storage of CO_2 beneath the seabed on the Norwegian Continental Shelf (NPD CO_2 Atlas, 2014). The Norwegian Government and Northern Lights JV (a joint venture company owned by Equinor, Shell, and TotalEnergies) initiated a full-scale (capture, transport, and storage) CO_2 storage demonstration project named 'Longship' (Fig. 1.3). Northern Lights is the transport and storage component of the Longship project, which includes the capturing of CO_2 from industrial point sources (i.e., cement factory and waste-to-energy plant). The captured CO_2 will be liquefied and transported by ships to an onshore terminal (Øygarden municipality) on the Norwegian west coast. From there, the supercritical CO_2 will be injected and permanently stored into a deep saline aquifer (~2.5 to 3.0 km below the seabed) by ~100 km pipeline in the Horda Platform area, northern North Sea. Phase 1 includes the capacity to transport, inject and store up to 1.5 Mt of CO_2 per year (source: Northern Lights JV). The investment in subsequent phases will be triggered (up to 5 Mt of CO_2 per year) by market demand from large CO_2 emitters across Europe. The Longship project is the first project of its kind; however, many potential geomechanical risks need to be evaluated for a successful, safe and permanent CO_2 storage.

In CCS technology, the injected CO_2 has been compressed into a supercritical phase before injection. In this condition, the density of CO_2 is significantly increased, therefore requiring less space per given volume within the reservoir (Fig. 1.4a). The critical point represents 304.13K and 7.3773 MPa temperature and pressure, respectively. The critical point can be roughly equivalent to around 800 m total vertical subsea depth (TVDSS), considering the standard basin temperature (30-35 deg/km) and pressure (10kPa/m) gradients (Span and Wagner, 1996). Hence, one of the main challenges in CCS is to keep the injected fluids below the threshold depth to stay in the supercritical phase because of the high buoyancy force of CO_2 fluid. Therefore, the major concern in any CCS project is to assess the risk of potential leakage of CO_2 into the overburden and eventually into the atmosphere.

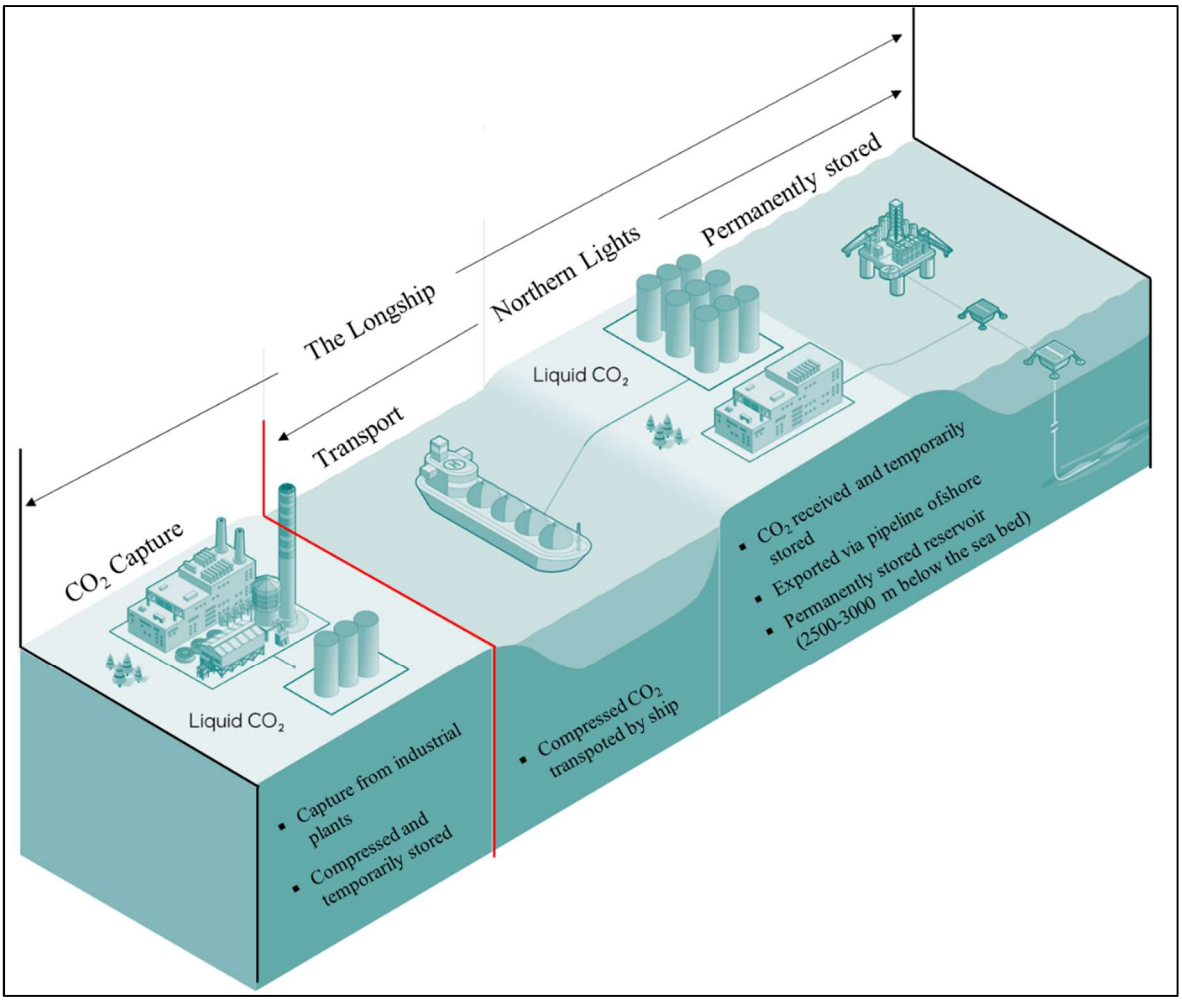

Fig. 1.3: The full chain schematic of proposed large-scale CO_2 sequestration project "Longship" in the northern North Sea (Courtesy: Equinor).

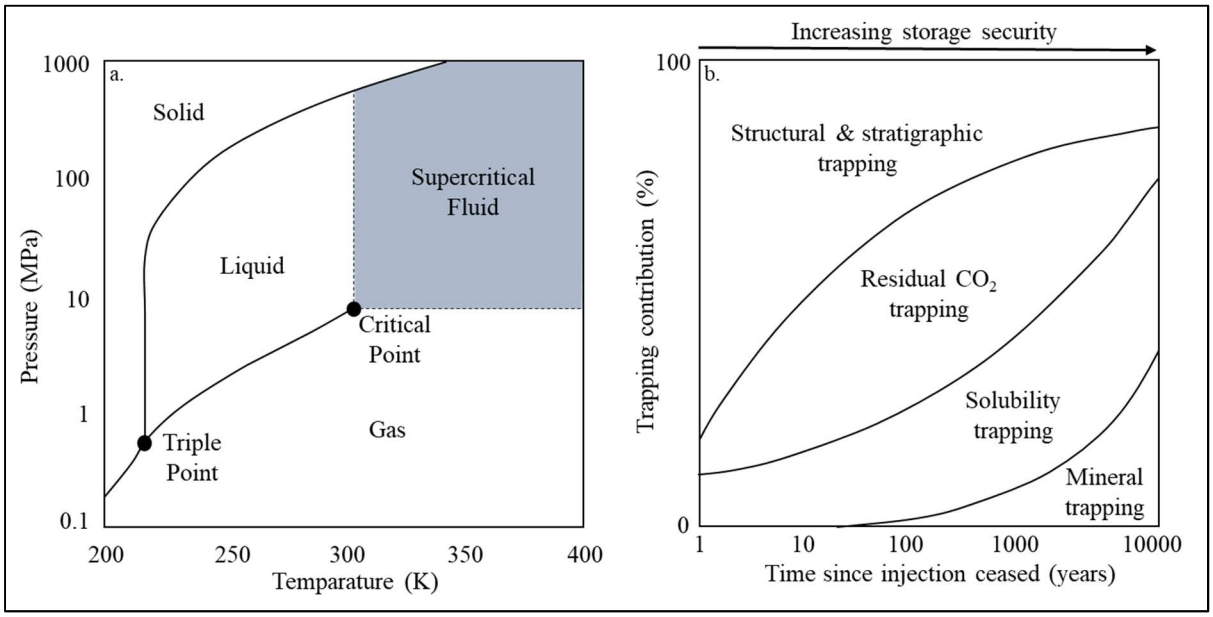

Fig. 1.4: CO_2 Phase diagram illustrating the different phases based on pressure and temperature (a), and the schematic diagram demonstrating the trapping contribution changes over time (b). The storage

security increases over time by changing from physical (structural) to geochemical (mineral precipitation) trapping (modified after IPCC, 2005).

CO_2 can be trapped after injecting into a reservoir (Fig. 1.4b) in four different trapping mechanisms such as structural & stratigraphic, residual, solubility, and mineral precipitation trappings. Storage security increases with time by the change in trapping mechanisms from physical to geochemical processes. In the beginning, the majority of CO_2 (%) will be trapped physically within the structure below the top seals in structural and stratigraphic traps. However, the CO_2 percentage stored this way decreases significantly with time by CO_2 mineral trapping and increased residual trapping mechanisms. These changes will increase storage security, as there is a higher possibility of CO_2 leakage in structural trapping than mineral trapping. However, the time required to shift from structural to chemical storage is relatively long; hence, a reliable top seal characterization has been critical for project decisions.

For reliable and permanent CO_2 storage, the injection processes must consider a long-term CO_2 migration monitoring. The focus should concentrate on scaling efficiency as the trapping mechanisms including solubility and mineral trapping, are not capable of retaining a large amount of gas or taking a very long time to gain a significant storage contribution. Caprock and faults (top seal) must be sealed to prevent the vertical buoyancy-driven CO_2 migration and provide sufficient time for additional trapping mechanisms to contribute to the overall processes (Heinemann, 2013). Failure to uphold any one of these criteria may result in CO_2 migration upwards into the overburden, where it may escape to the surface or possibly be trapped by a secondary seal. Therefore, the overburden rock characterization is also crucial in a CCS project. In the worst-case scenario, it may come back to the atmosphere, thereby failing the overall project objectives. Failure may also result in polluting freshwater aquifers near onshore injection sites. However, this concern is not applicable for offshore facilities such as Sleipner & Snøhvit, as well as for the Longship storage sites (the study area of this Ph.D. research). Instead, offshore CO_2 leaking may pollute sea water and escape to the atmosphere again as a greenhouse gas.

1.3 Geological setting of the study area

1.3.1 Structural framework

The northern North Sea experienced two main rifting events, during the Permo-Triassic and the Late Jurassic to Mid-Cretaceous times (Steel and Ryseth, 1990; Færseth, 1996; Whipp et al., 2014; Fig. 1.5a). A wide basin with deep-rooted faults and thick syn-depositional wedges is centered below the Horda Platform due to the first rifting event (Fig. 1.5b). During the Late Jurassic to Mid Cretaceous event, the major rifting and tilting zones are shifted westward (i.e., Lomre Terrace) (Stewart et al., 1995). It is assumed that weak stretching occurred with the reactivation of major Permo-Triassic faults on the Horda Platform (Steel and Ryseth, 1990; Steel, 1993; Roberts et al., 2019, 1993; Færseth, 1996; Whipp et al., 2014). Significant normal faults with predominant N, NE, and NW orientations controlled the basin formation, resulting in half-grabens (15-50 km in width) which are the fundamental morphological elements in the area (Færseth, 1996). Half-grabens in the North Sea may reach 100 km along-strike length; however, studies suggested that normal faults occur in segments and are generally no longer than 20 km each (Jackson and White, 1989; Roberts and Jackson, 1991). The eastern margin of the Triassic sedimentary basins south of 61^0N are, in general, associated with the Øygarden Fault Complex (ØFC). In this segment, the vertical displacement is generally between 3-5 km across normal faults (Yielding et al., 1992; Færseth et al., 1995). However, north of 61^0N, the structural pattern is controlled by the east-dipping Sogn Graben fault of Permo-Triassic origin, which created a westerly tilted basement with sediment deposits to the east (Færseth, 1996).

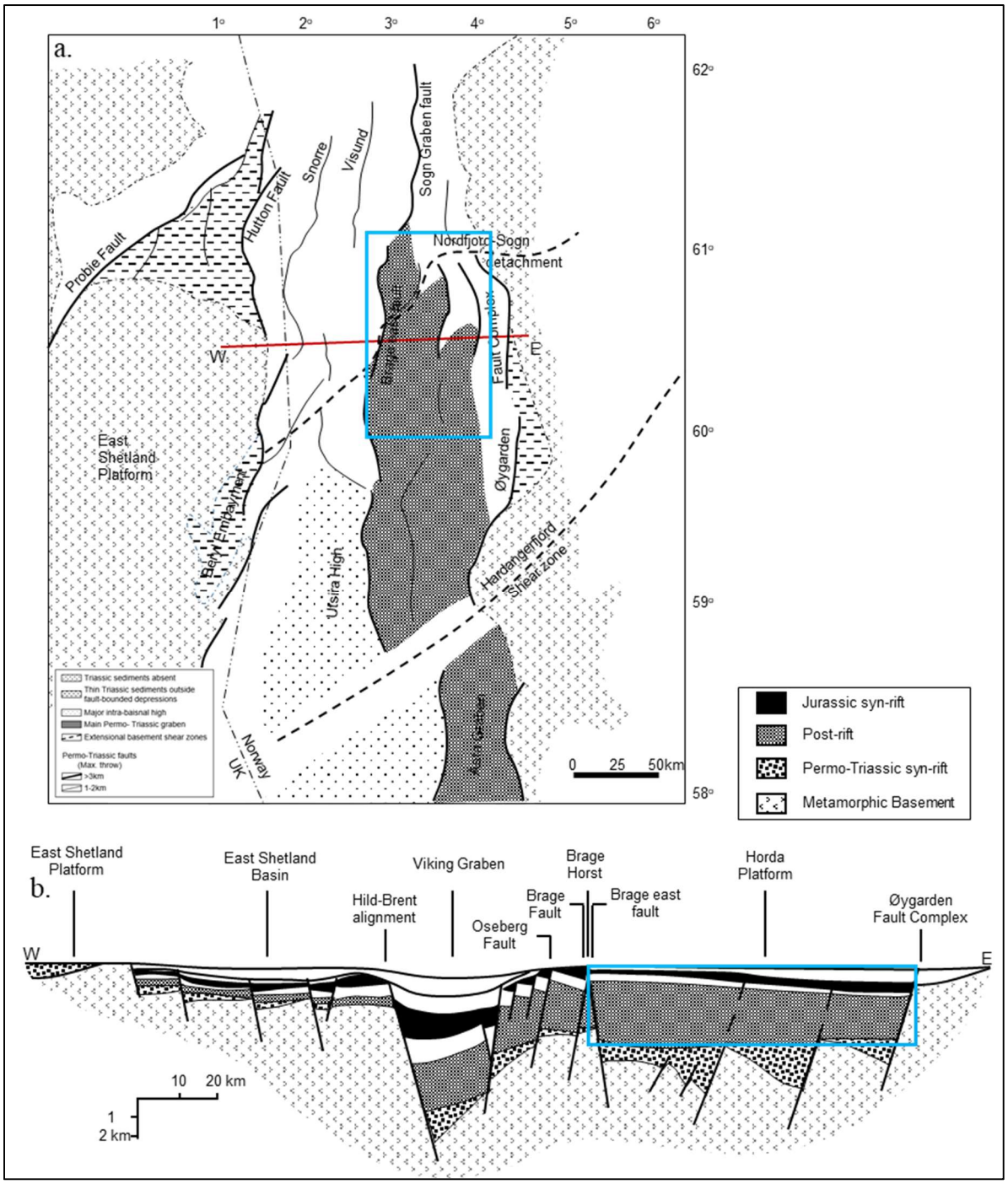

Fig. 1.5: (a) Main structural elements of the northern North Sea, resulting from Permo-Triassic extension, reveal the major faults and Nordfjord-Sogn detachment, (b) An E-W cross-section through the northern North Sea (marked in Fig. 1.5a) showing the sedimentation and major faults during syn- and post-rift times (modified after Færseth, 1996).

The fault polarity change at 61^0N, between the Sogn Graben and the northern Horda Platform, created opposite facing half-grabens, constrained mainly by a pronounced basement shear zone known as the Nordfjord-Sogn detachment (Badley et al., 1988; Færseth et al., 1995; Færseth, 1996) (Fig. 1.5a). This shear zone, interpreted as a Late Devonian extensional feature, separates Caledonian-influenced Precambrian rocks in the footwall to the south and metamorphosed Lower Paleozoic supra-crustals in the hanging wall (Klemperer, 1988; Fichler and Hospers, 1990; Hospers and Ediriweera, 1991). Integrated seismic, gravity, and magnetic data show this

basement feature-oriented NE-SW across the northern North Sea. This feature is at an anomalously high structural level immediately to the southeast (i.e., Horda Platform). The detachment significantly influences the sedimentation between the northern and southern zones (reflected by thickness variations through syn-rift and post-rift time). The major and minor faults created by rifting and subsequent thermal subsidence within the area played an important role in structural deformation and sediment deposition (Jordt et al., 1995; Anell et al., 2009; Faleide et al., 2015).

The study area is located in the Horda Platform, south of 61^0N, and consists of the selected CO_2 storage sites Smeaheia and Aurora. The Øygarden Fault Complex bounds the Smeaheia area to the east and Vette fault to the west, while the Aurora area is located further west, bounded by the Tusse fault to the east and the Svartalv fault to the west (Fig. 1.5). Overall, the study area is significantly influenced by structural events that control the paleodeposition; hence, compositional variations both laterally and vertically.

1.3.2 Lithostratigraphy

In this research, two sets of reservoir-caprock pairs are studied, which belong to Smeaheia and Aurora injection sites. Stratigraphically, the Smeaheia site has a younger cap and reservoir rocks than Aurora, that were deposited in the Upper to Middle Jurassic and Lower Jurassic, respectively. In this thesis, we denoted the Smeaheia caprock and reservoir as pair-1, while the Aurora has been indicated as pair-2. A detailed lithological description of pair-1 and -2 are given below:

Caprock-Reservoir pair – 1

The reservoir and caprock of the Smeaheia injection site are deposited in the Upper to Middle Jurassic time, the same formations where the giant Troll field hydrocarbon accumulations occurred. The primary caprock is the organic-rich Draupne Formation shale, which is part of the Viking Group and deposited in the Upper Jurassic within the East Shetland Basin, the Viking Graben, and over the Horda Platform area (NPD CO_2 Atlas, 2014). The thickness of this unit varies significantly within the Horda Platform area. The formation is deposited in an open marine environment with restricted bottom circulation and often with anaerobic conditions (NPD, 2022). It consists of dark grey-brown to black, usually non-calcareous, carbonaceous, and occasionally fissile claystone. This shale unit is characterized by high gamma-ray values (usually above 100 API) because of high TOC and Uranium content. Interbedded sandstone and siltstone, as well as minor limestone streaks and concretions, are also present. The Draupne Formation generally has a diachronous contact with the underlying Heather Formation (Fig. 1.6). However, on the northern Horda Platform, the Upper Jurassic Sognefjord Formation sandstones mark the base of the Draupne Formation. The upper boundary of the Draupne Formation is usually marked by Cretaceous rock (Cromer Knoll Group), which has a higher velocity and lower gamma-ray response than the over and underlying rocks (NPD, 2022).

The secondary caprock in the Horda Platform area is the Heather Formation shale overlying and inter-fingering with Krossfjord, Fensfjord, and Sognefjord formation sandstones of the Viking Group (Fig. 1.5). Heather Formation is also deposited in an open marine environment but contains comparatively less organic matter than Draupne shale and consists of mainly grey silty claystone with thin streaks of limestone (NPD, 2022). The Heather Formation has significant thickness variations within the study area. Stewart et al. (1995) divided the Horda Platform's Heather Formation into three sub-units (A, B, and C). In this research, we considered only the Heather C unit, which lies between Sognefjord and Draupne formations.

The Upper to Middle Jurassic Sognefjord, Fensfjord, and Krossfjord formation sandstones act as the main reservoir rock with good to moderate reservoir quality (Dreyer et al., 2005; Holgate et al., 2015; Fawad et al., 2021). The reservoirs are deposited in a coastal shallow marine environment while interfingering with Heather Formation (NPD, 2022).

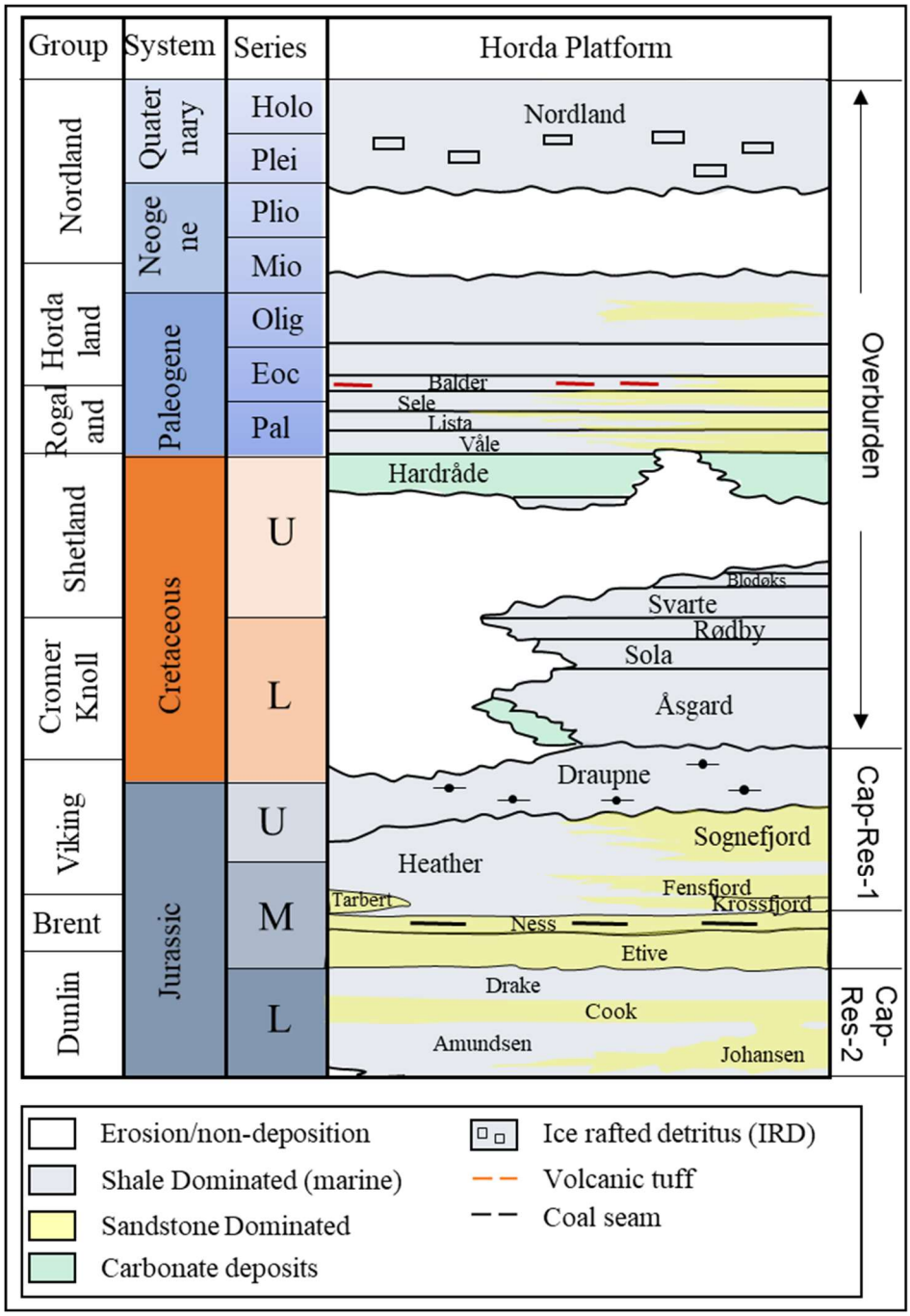

Fig. 1.6: A generalized stratigraphic succession of Horda Platform area covering the section from Lower Jurassic to the Quaternary system (modified after CO_2 Atlas, 2014).

Caprock-Reservoir pair – 2

The target Lower Jurassic sandstone reservoir (i.e., Johansen and Cook formations) for CO_2 injection in the Aurora site is stratigraphically older than that of the Smeaheia site (Fig. 1.6). The Lower Jurassic Drake and Amundsen (also called the Burton Formation) formation shales are the primary caprock. The Drake Formation mainly consists of marine shales (Steel, 1993) within the deeper parts of the sub-basins. Close to the basin margins, sandy deposits are comparatively higher to the deep basin (Vollset and Doré, 1984). In the study area, the formation can be divided into two parts based on the lithological variation. The upper part consists of heterolithic deposits comprising sandstones alternating with siltstones and claystones, while the lower part is clay dominated. Another caprock, the Amundsen shale, consists of light to dark grey, non-calcareous siltstones, and shales, and some parts are carbonaceous and pyritic (Vollset and Doré, 1984). However, the upper part of the Amundsen Formation shale is not laterally continuous in the Horda Platform area and therefore is not considered a formal top seal.

The reservoir rocks, Johansen and Cook formation sandstones, are mainly separated by the upper part of the Amundsen shales and siltstones (Burton Formation). However, the Amundsen Formation has not been deposited in the entire region; hence, Johansen and Cook formations are juxtaposed and treated as one aquifer. The Johansen and Cook formation sandstones have good to moderate reservoir quality, and the aquifer's total capacity depends on the communication between them (Gassnova, 2012; NPD, 2022).

1.4 Thesis organization

This Ph.D. dissertation is divided into three main sections. The first section is referred to as 'OVERVIEW OF THE Ph.D. DISSERTATION', which is divided into six separate headings. The first part introduces the background, motivation, and objectives of the research, followed by the second part, which comprises the theoretical framework used in this study. The database and methods are introduced in the third and fourth parts, respectively. In addition, an overall summary of this study (**Paper- 1 to -4**) is described in the fifth part. Discussion of the major scientific contributions are also presented in the last subsection of the fifth part. Relevant papers (**RP-1 to -4**) and conference proceedings (**CP-1 to -4**) have also been included in the fifth part. Finally, the last part (within section 1) covers the concluding remarks with a few suggestions for future research continuation.

The second section of the dissertation consists of four published articles (**Paper-1 to -4)**, where I am the first author in all the papers. In the third section, appendices are added, which is divided into appendix-1 and appendix-2. In appendix-1, four relevant first and second-author papers have been added (**RP-1 to -4**), while four conference proceedings are included in appendix-2 (**CP-1 to -4**).

2. Theoretical framework

This part describes the fundamental theories for understanding the subsequent results. However, a detailed description of methods and workflows used to achieve the thesis goals are explained in a separate heading (Part 4). Structure of part-2 is followed by a sequence that first describes the effect of deposition and diagenesis on rock properties, which are followed by relevant theories of rock physics templates (**Paper-1, RP-1 & -2, CP-1 to -3**). Seismic inversion is out of scope of this work; however, the theoretical background is presented as the inverted properties are used in the geomechanical modeling workflow (**RP-4**). Basic concepts of the structural reliability analysis are also presented (**Paper-2, RP-3**). Finally, the pore pressure and stress coupling are explained using the poroelasticity theories that are the backbone of the numerical modeling work (**Paper-3 & -4**). Nano-indentation techniques are not described here (**CP-4**), but this method's promising outcomes have been included in the discussion section (Part 5.2.4).

2.1 Evolution of rock properties

Rock properties of clastic rocks are described as the reservoir is sandstone, while the caprock mainly consists of shale. The diagenetic processes started altering the rock shortly after deposition, where the rock's composition plays a crucial role. Primary composition of the sediments is the result of complex processes including the function of provenance (rock erosion), transport, and depositional environments (Bjørlykke, 2015). Therefore, the diagenetic analysis must be linked with the paleo weathering and climate, sediment transport, facies models, and sequence stratigraphy that should be integrated with interdisciplinary basin analysis.

Reservoir sandstones consist primarily of sand grain (>62 μm) with quartz, feldspar, and rock fragments. Sandstones also contain some portions of silt-sized grains (4-62 μm) and clay minerals (<4 μm). The most critical factor in reservoir quality prediction at depth is the primary clastic composition and the depositional environment. The sandstone reservoir quality is described in terms of its composition, textural parameters (i.e., grain size, sorting, and grain shape), total pore space called porosity, and connectivity of the pores termed permeability (Folk, 1980; Wentworth, 1922).

In contrast, the caprock shale or mudstones, which make up 75% of the global sedimentary record (Sayers, 1994; Hornby, 1998; Aplin and Macquaker, 2011), mainly consists of clay and silt size particles. Mudstones differ from other clastic rocks in terms of composition, porosity, permeability, and heterogeneity (Storvoll et al., 2005; Mondol et al., 2011, 2008; Hart et al., 2013). Shale can also deposit in a wide range of environments (i.e., floodplains, lakes, shoreface, prodelta, abyssal plains, etc.); from different origins (i.e., weathering products, biogenic remains), and through a multitude of post-depositional processes (i.e., bioturbation, compaction, cementation, recrystallization, dissolution, organic maturation, etc.). These various processes lead to significant changes in grain size, and mineralogy within shales, which are the main controlling parameters influencing their properties. Furthermore, fabric of clay and non-clay minerals, mineral aggregates, porosity, and organic matter play a significant role in shale anisotropy.

The dominant assembly of clay minerals characterize the shales or mudstones with variable portions of quartz, feldspar, pyrite, and carbonates (dolomite, calcite, and siderite). However, clay minerals (mainly smectite, illite, kaolinite, and Chlorite) are not always the dominant minerals in shale. Other minerals such as quartz, feldspar, pyrite, and carbonates (e.g., dolomite, calcite, and siderite) can be present in variable proportions such as fine-grained detrital or

diagenetic grains. These mineralogical constituents can be sourced from terrigenous material, including clay and silt-sized siliciclastic minerals (e.g., clay minerals, quartz, feldspar, rock fragments, and terrigenous type III organic matter), biogenic components containing calcite, silica/opal, phosphate, and type I and II organic matters and diagenetic products such as pore-filling carbonate cement and concretions, pyrite framboids and crystal, overgrowth/pore-filling silica cement and clay minerals (Hart et al., 2013). The relative proportion of these constituents varies within the shale rocks due to the difference in depositional processes and diagenetic pathways. Initial clay composition is influenced by diagenesis, which is important for determining the properties (i.e., velocity and density) of mudrocks and shales (Mondol et al., 2008, 2007). The organic content within organic-rich shale also influences the properties, usually expressed as volume percent of kerogen (v. %) or as TOC (total organic carbon) in weight percent (wt. %). A source rock can have anywhere from 2-3% to more than 20% by weight TOC (Gautier, 2005). The type, amount, and maturity of kerogen significantly influence the shale properties. Generally, high TOC shales show a high gamma-ray signature with low density and velocity compared with inorganic shales at similar burial depths (assuming similar compaction), indicating that TOC has a substantial effect on velocity and density (Hansen et al., 2020). Moreover, thermal maturation of the organic matter, cracking of kerogen, and generation/expulsion of oil and gas (Tissot and Welte, 1984) might further alter the acoustic properties (Vernik and Nur, 1992; Allan et al., 2016).

Two types of compaction processes (diagenesis) alter the rock after deposition to deep burial. The mechanical compaction (MC) defines rock property changes as a function of effective stress due to the overburden load of sediments and usually occurs at low temperature (less than 60-70^{0}C) corresponding to depths less than 2km (Bjørlykke and Høeg, 1997; Bjørlykke, 2014). When temperature increases, the sediment crosses the transition zone (TZ), and enters into the chemical compaction (CC) domain. This compaction zone is dependent on temperature and time. Compaction trends between caprock shales and reservoir sandstones vary significantly (Fig. 2.1). Sandstone compaction is initially a function of mechanical crushing and reorientation (Chuhan et al., 2002; Fawad et al., 2011) up to a specific temperature (70-80^{0}C) where the chemical precipitation of mineral cement takes over and stiffens the rock (Bjørlykke et al., 1989; Thyberg and Jahren, 2011). A small amount of quartz cement is required to stiffen the rock and inhibit further mechanical compaction (Lander and Walderhaug, 1999; Bjørkum et al., 2001). In mudstone or shale, the initial high porosity rapidly decreases during the initial stage (Mondol et al., 2008, 2007) of burial by rearranging the platy clay minerals (Fig. 2.1). After reaching transition temperature (~70^{0}C), thermodynamically unstable smectite mineral, if present, transforms to illite in the presence of potassium, a process that releases water and precipitates micro quartz cement (Bjørlykke et al., 1989; Bjørlykke, 1998; Thyberg and Jahren, 2011). A similar chemical alteration occurs if unstable kaolinite clay mineral is present, but the transition temperature (~120^{0}C) is much higher than that of smectite alteration. The type of clay minerals within shales are strongly dependent on the provenance, tectonic settings, and erosion and particle transportation rate from sediment source to deposition (Bjørlykke, 2015).

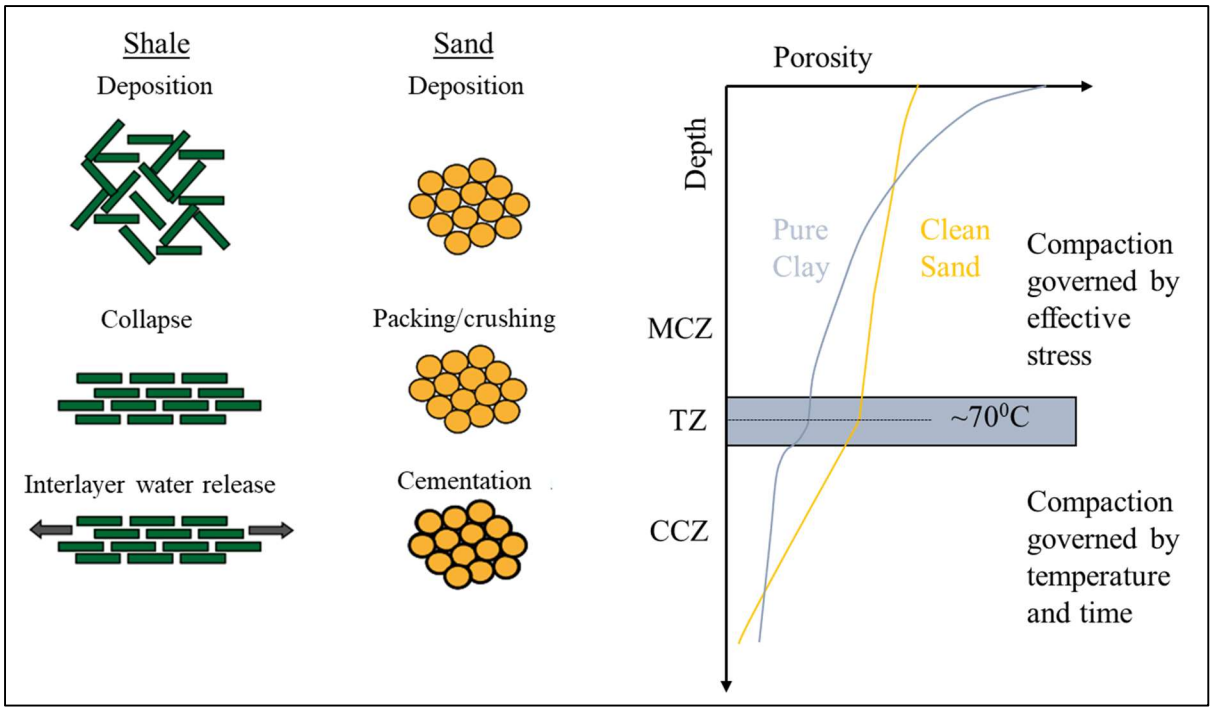

Fig. 2.1: The porosity reduction trends for sand and shale show variations in different compaction zones. The different arrangements of shale and sand grains with depth are also illustrated (modified after Avseth et al., 2010, 2005). MCZ = Mechanical Compaction Zone; TZ = Transition Zone and CCZ = Chemical Compaction Zone.

2.2 Rock Physics model

Rock physics provides a link between rock properties (i.e., porosity, shale volume, sorting, fluid content, organic content, etc.) and seismic properties (i.e., compressional velocity - Vp, shear velocity - Vs, acoustic impedance - AI, shear impedance – SI, etc.). For instance, if the mineralogical and fluid compositions of a rock, the modulus and density of each mineral type, and fluid and texture and pore geometry of the rock are known, we can theoretically estimate the effective velocities and impedance of that rock unit (Mavko et al., 2009). Therefore, the rock physics model is necessary to extract geological information from seismic or vice versa.

An important parameter in the rock physics model is the upper and lower bounds, which can be predicted by assigning values to the two first prerequisites (i.e., volume fractions and elastic properties of each phase) and excluding the geometries. The upper and lower elastic bounds, such as the Voigt (upper), Reuss (lower), or Hashin-Shtrikman (denoted H-S^+ and H-S^-) bounds, are shown in figure 2.2 (Hashin and Shtrikman, 1963), which assume isotropic, linear, and elastic constituents of the rock. The modified Hashin-Shtrikman bound for critical porosity is also useful for practical rock physics applications (Fig. 2.2b). Although the elastic bounds are based on a simple assumption, rock physics analysis must consider these physical bounds in the template.

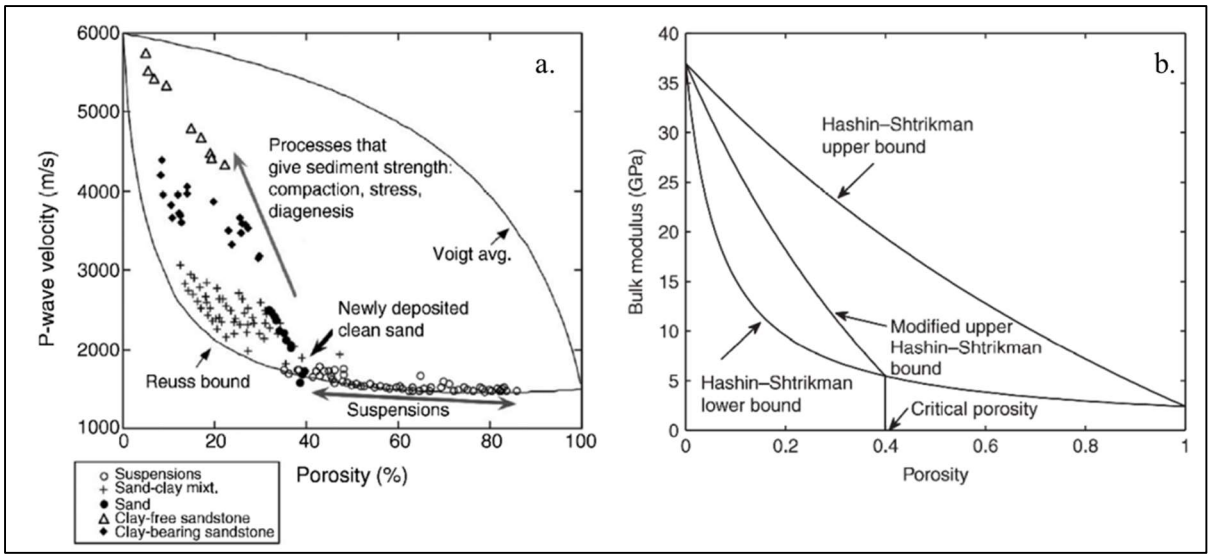

Fig. 2.2: (a) The upper and lower bounds on a velocity versus porosity plot show Voigt and Reuss bounds (adapted from Mavko et al., 2009), and (b) Hashin-Shtrikman bounds on bulk modulus and the modified version for critical porosity (Nur et al., 1998, 1991) for a quartz water system (adapted from Avseth et al., 2010).

Many different models for sandstones exist, where a hybrid cement model is frequently used in Norwegian Continental Shelf. The model includes a combination of the friable sand, constant (Avseth et al., 2000), and contact (Dvorkin et al., 1994; Dvorkin and Nur, 1996) cement models (Fig. 2.3a). These models use modified H-S bounds to describe the sorting and cementation of sands by interpolation between high porosity and low porosity end members. The dry elastic properties at the critical porosity point (high porosity end) are calculated using Hertz-Mindlin (H-M) contact theory (Mindlin, 1949). However, most rock physics models are constrained by local conditions such as depth, temperature, mineralogy, fluid properties, etc. Combining the rock physics models and the above-mentioned theories, a rock physics template can be established (Avseth and Odegaard, 2004) and used to directly interpret seismic inversion data (Fig. 2.3b).

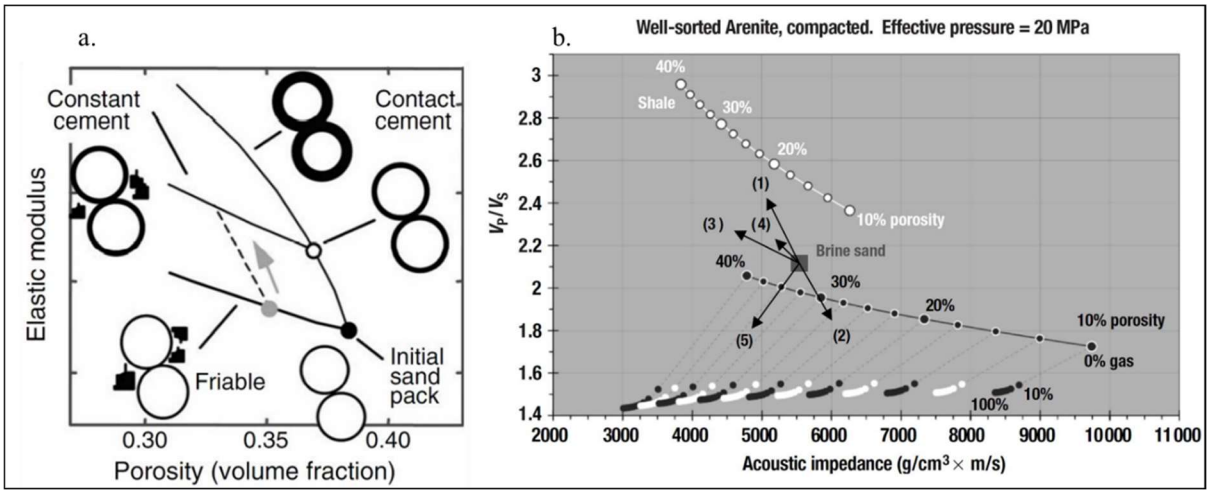

Fig. 2.3: (a) The sandstone models for sorting and cementation in elastic modulus versus porosity plot, (b) Rock physics template in AI-Vp/Vs plot shows the variation due to various lithology, porosity and different gas saturations in sandstones. The arrows indicate the theoretical trends on a given brine saturated sandstone point: (1) increasing clay content, (2) increasing cement volume, (3) increasing

porosity, (4) decreasing effective pressure, and (5) increasing gas saturation (adapted from Avseth et al., 2005).

As discussed earlier, the shales are different from sandstones in many ways. Hence, their rock physics models are also different. A semi-empirical shale compaction model named Dvorkin-Gutierrez silty shale model is described in Avseth et al. (2005), where the saturated elastic moduli of shale are estimated by using the H-S lower bound as a function of clay content, assuming adding silt grains consist of 100% quartz. This model is relatively simple and not very applicable to typical mudstone texture and pore pressure; however, it can be a good predictor of the depth-dependent relationship between the elastic properties of shale (Avseth et al., 2005). Additionally, few shale models have targeted the effect of geomechanical property (such as brittleness) and mineralogy, typically in unconventional exploration settings (Grieser and Bray, 2007; Guo et al., 2012; Perez and Marfurt, 2014; Johson, 2017). A few of these models have been used in this study, which is described under methodology subsections (part 4). However, these models are basin-specific in many cases and need careful attention when attempting to apply them globally. Furthermore, a relatively accurate assumption about mineralogical composition must be made for the models to be accurate (Vernik, 2016); hence, a simple local empirically calibrated model is desired, which in some cases may serve the purpose better (Avseth et al., 2005; Mavko et al., 2009).

2.3 Principle of seismic inversion

P-wave velocity (Vp), S-wave velocity (Vs), and bulk density (ρ) can be used to describe any layer of rock. Considering a simplified earth model (isotropic, elastic and homogeneous), the seismic wave velocities can be defined as:

$$V_p = \sqrt{\frac{K+4/3\mu}{\rho}} \tag{2.1}$$

$$V_s = \sqrt{\frac{\mu}{\rho}} \tag{2.2}$$

where K is the bulk modulus, and μ is the shear modulus. The same can be expressed by combining density with Young's modulus (E) and Poisson's ratio (υ). The reflectivity or reflection coefficient of any interface between two subsurface layers is dependent on the impedance (i.e., density × velocity) of that layers. The reflectivity of a seismic P-wave normal incidence (i.e., zero offset) is:

$$R_p(0) = \frac{AI_2 - AI_1}{AI_2 + AI_1} \tag{2.3}$$

where AI is the P-impedance and subscripts 1 and 2 denote the upper and lower layers, respectively. The effect of offset (incident angle) denoted as AVO (amplitude versus offset) can be resolved using the Zoeppritz equation. Shuey (1985) approximates three-term to the Zoeppritz equation for P-wave (Vp) reflectivity, which is denoted as:

$$R_p(\theta) \approx A + G\sin^2\theta + C(\tan^2\theta - \sin^2\theta) \tag{2.4}$$

where A is the amplitude at normal incident reflectivity $R_p(0)$ also known as intercept, G is called AVO gradient, which describes the amplitude variation at intermediate offsets, and term C represents curvature or behavior at far offsets which is excluded in some approximations and practical applications.

In the acoustic impedance inversion process, we can recover the P-impedance/acoustic impedance (AI) from the recorded seismic signal inversion using the recursive equation proposed by Lindseth (1979):

$$AI_2 = AI_1 \left[\frac{1+R_p(0)}{1-R_p(0)}\right] \tag{2.5}$$

Combining the three-term AVO extraction and impedance inversion into a single step, the inversion equation (Fatti et al., 1994) can be written as:

$$R_p(\theta) \approx (1 + tan^2\theta)\frac{\Delta AI}{2A} - 8\left(\frac{V_s}{V_p}\right)^2 sin^2\theta \frac{\Delta SI}{2SI} \tag{2.6}$$

where SI is shear impedance. Hampson et al. (2005) later modified the equation using a small reflectivity approximation and stated that:

$$T(\theta) = \tilde{c}_1 W(\theta) D ln(AI) + \tilde{c}_2 W(\theta) D \Delta ln(SI) + c_3 W(\theta) D \Delta ln(\rho) \tag{2.7}$$

where T(θ) represents a seismic trace at a given angle θ, while the angle-dependent wavelet matrix and the derivative matrix are denoted as W and D, respectively. Additionally, the deviation from the background linear trends is indicated using the term Δln(SI) and Δln(ρ). The term $\tilde{c}_1$ is modified from the original term ($c_1 = 1 + tan^2\theta$) using the regression coefficients from the background trend, $\tilde{c}_2 = 0.5c_2 = -4\left(\frac{V_s}{V_p}\right)^2 tan^2\theta$, and $c_3 = -0.5tan^2\theta + 2\left(\frac{V_s}{V_p}\right)^2 sin^2\theta$. The term $\tilde{c}_1$ is stated as:

$$\tilde{c}_1 = 0.5c_1 + 0.5kc_2 + mc_3 \tag{2.8}$$

The missing low-frequency information is retrieved iteratively from the low-frequency background model (Yenwongfai et al., 2017).

2.4 Concept of reliability analysis

The reliability of a structure depends on the uncertainties of the applied load (S) and the resistance (R). Considering normal distribution, the failure probability is assessed directly by the safety margin M and denoted as:

$$M = R - S \tag{2.9}$$

and the probability of failure might be assessed through:

$$P_f = \mathrm{P}(\mathrm{R} - \mathrm{S} \leq 0) = \mathrm{P}(\mathrm{M} \leq 0) \tag{2.10}$$

where M is normally distributed with mean $\mu_M = \mu_R - \mu_S$ and standard deviation $\sigma_M = \sqrt{\sigma_R^2 - \sigma_S^2}$. The failure probability can be determined by the use of the standard normal distribution function as:

$$P_f = \phi\left(\frac{0-\mu_M}{\sigma_M}\right) = \phi(-\beta) \tag{2.11}$$

where $\mu_M/\sigma_M = \beta$ is called the reliability index, which is the standard deviation by which the mean value of the safety margin M exceeds zero or most likely exceeds the failure point (Fig. 2.4). However, if several random variables are acting, the safety margin M will be expressed by the function of the same random variables and statistically dependent:

$$M = R - S = f_1(X) - f_2(X) = g(X) \tag{2.12}$$

where X is a vector of basic random variables, and the function g(X) is denoted as the limit state function, which is a boundary between desired (g(X)>0) and undesired (g(X)≤0) performance of any structure (Ditlevsen and Madsen, 2007).

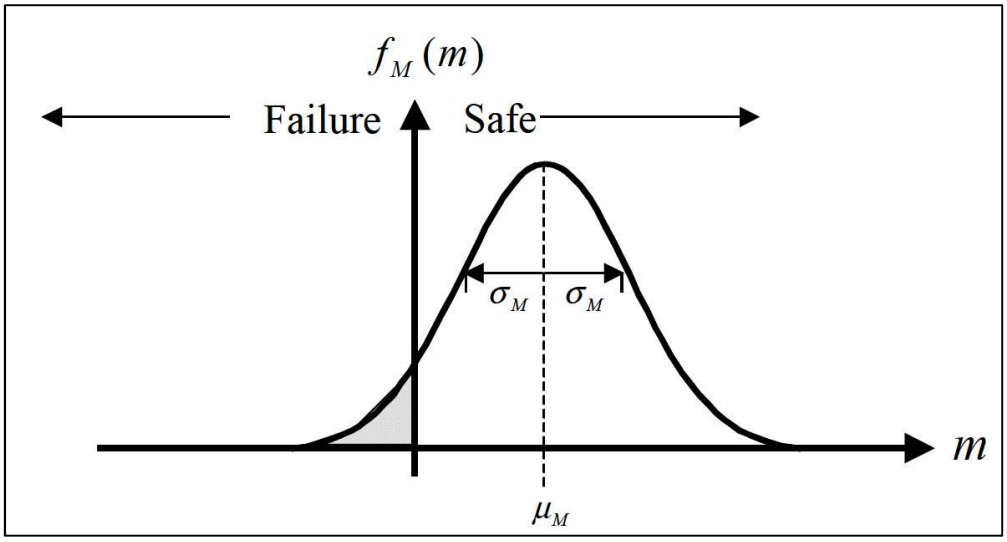

Fig. 2.4: Normally distributed safety margin M showing the boundary between the desire and undesired numbers of events (modified after Faber (2009).

2.5 Pore pressure and stress coupling

Injection of supercritical carbon-di-oxide (CO_2) into the reservoir may increase the pore pressure spatially. In response to that, mechanical stresses within the reservoir change. However, the stress change is transferred far beyond the injected reservoir intervals to the surrounding formations. The biggest changes occur near the wellbore while gradually declining away from the injectors. The spatial deviation of the pore pressure depends on the reservoir quality, such as porosity and permeability. Due to these injection-induced stress changes, the rock deforms with the magnitude depending on the mechanical properties of the rocks. Therefore, the optimal injection fluid volume needs to be estimated so that the stress does not exceed failure strength or weaken the rock, creating new faults and fractures or reactivating the existing faults. If the injection-induced pressure exceeds the threshold, new leakage pathways for CO_2 plumes may be created. Therefore, it is necessary to avoid stress increases beyond the fracture pressure limit, rock strength, or friction along fault/fracture planes (Bjørnarå, 2018).

The total vertical stress (σ_v) is generated from the overburden, which is carried out by the grain framework (solid phase) and the pore pressure (fluid phase) within any subsurface layer (i.e., caprock and reservoirs). In any subsurface interval, the pore pressure always counters the overburden stress; hence, less impact of total stress on the grain framework. Therefore, effective stress is equal to the overburden vertical stress minus the pore pressure. The effective stress is an important input to evaluate the stress influence on rock failure because it is the stress transmitted through the gain contacts (Fig. 2.5). Terzaghi (1943) first introduced this concept,

who stated that the effective stresses are different from either total stress or pore pressure. The concept is used today, where the influence of pore pressure changes the state of stress quantified. However, the differential stress (i.e., maximum minus minimum principal stresses) is always constant in response to pore pressure change because the pore pressure acts equally on all three principal stresses direction and not at all on the shear stresses. The mean effective stress (i.e., the average of principal stresses) changes with pore pressure.

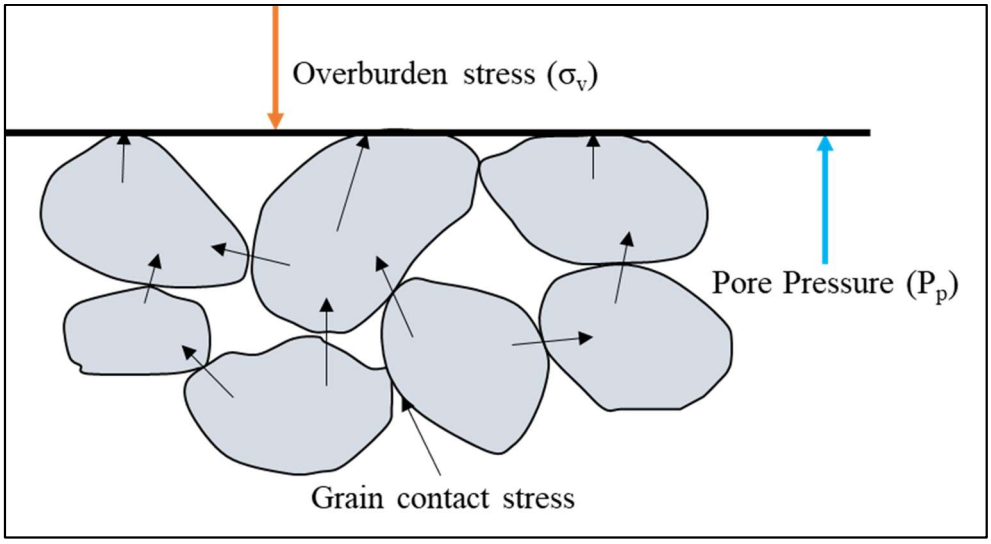

Fig. 2.5: The overburden stress is counteracted by the mineral grain framework and pore pressure (modified after Bjørlykke, 2015).

2.5.1 Poroelasticity

A geomechanical model can describe the interactions between the solid phase of the porous media and the fluid phase in the pore space. Poroelasticity is the constitutive behavior of a fluid-saturated rock, which is a linearized solution, described as the compressibility and other constitutive coefficients. The theory is assumed to be independent of stress because the stress increments are small enough that the consequences can be considered negligible.

The poroelasticity concept is based on the effective stress theory (Terzaghi, 1925), which is the part of the total stress that causes the deformation of the porous media. The previous section gives a detailed description of the effective stress; however, the sign convention is not explained. Negative confining stress (Fig. 2.6a) is used for an extensional stress regime, while a positive sign is used in the compressive regime (Fig. 2.6b). Therefore, the total stress (σ) of a porous media with the incompressible grain is given by:

$$\sigma = \sigma' - p_s \quad \text{[Extensional]} \tag{2.13}$$

$$\sigma = \sigma' + p_s \quad \text{[Compressional]} \tag{2.14}$$

where p_s is the stress the pore fluid exerts on the solid.

For a poroelastic material where the grains are compressible, it can be defined using Biot's theory of linear poroelasticity and denoted as:

$$\sigma = \sigma'' - \alpha p_s \quad \text{[Extensional]} \tag{2.15}$$

$$\sigma = \sigma'' + \alpha p_s \quad \text{[Compressional]} \tag{2.16}$$

where effective stress is denoted as σ'' following Lewis et al. (1998) and α is the Biot's coefficient which is defined as:

$$\alpha = 1 - \frac{K}{K_s} \tag{2.17}$$

where K is the bulk modulus of the rock and K_s is the bulk modulus of the grains (solid constituents of the porous medium). The magnitude of the σ' and σ'' are not equal though used by the same constitutive relations; however, the total stress will be the same regardless of the compressibility of the solid constituents.

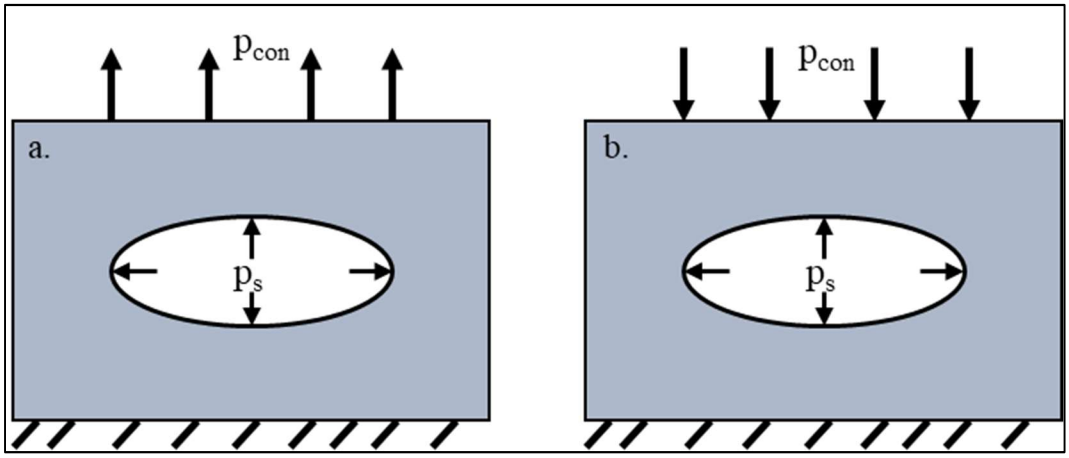

Fig. 2.6: The sketch illustrated a pore space within a solid in an extensional (a) and compressive (b) regimes (modified after Bjørnarå, 2018). Please note that the sign convention of confining pressure varies for the different regimes.

The stress is a critical parameter in rock mechanics, which is coupled with the pore pressure change. If a surface force $\vec{F}_0$ is acting on a surface A in any arbitrary direction, the stress vector $\vec{T}$ can be defined as:

$$\vec{T} = \lim_{\Delta A \to 0} \frac{\Delta \vec{F}_0}{\Delta A} \tag{2.18}$$

$\vec{F}_0$ can be divided into two stress components such as normal stress (σ_n) and shear stress (τ):

$$\sigma_n = \lim_{\Delta A \to 0} \frac{\Delta \vec{F}_n}{\Delta A}, \qquad \tau = \lim_{\Delta A \to 0} \frac{\Delta \vec{F}_s}{\Delta A} \tag{2.19}$$

The state of stress at any infinite volume element (i.e., $\Delta A \longrightarrow 0$) can be described by all the normal and shear stresses acting on it. Mathematically the stress tensor σ_{ij} for a three-dimensional cartesian coordinate system with the axes x, y and z can be stated that:

$$\sigma_{ij} = \begin{pmatrix} \sigma_{xx} & \sigma_{xy} & \sigma_{xz} \\ \sigma_{yx} & \sigma_{yy} & \sigma_{yz} \\ \sigma_{zx} & \sigma_{zy} & \sigma_{zz} \end{pmatrix} \tag{2.20}$$

where the first index i stands for the surface normal to the stress component and j indicates the direction of the stress component acting on the plane. For the normal stress condition $i = j$ while the shear stress specified $i \neq j$. While performing a principal axis transformation, only the three normal stresses are converted and called principal stresses. The maximum principal

stress (σ_1), the intermediate principal stress (σ_2), and the minimum principal stress (σ_3) define the stress tensor, which are σ_{xx}, σ_{yy} and σ_{zz} in a three-dimensional coordinate system.

2.5.2 Tectonic stress regime

The principal stresses are always perpendicular to one another. The surface of the earth is normally considered a stress plane and has two horizontal principal stresses, often termed as σ_H and σ_h. Both stresses are perpendicular to each other, where subscript H and h indicate the magnitude (i.e., $\sigma_H > \sigma_h$). The vertical stress (σ_v), which is approximately the weight of the rock, is considered to be the third principal stress. The magnitude and order of these principal stresses may vary between locations, and the type of faulting is related to the combination of stresses. Anderson (1905) categorized three types of faults based on the magnitude of the principal stresses, which is called Andersonian fault classification (Fig. 2.7). Depending on the magnitude, differences between the principal stresses following three main faults/stress regimes can be defined:

- Normal faulting/extensional stress regime:
  - $\sigma_1 = \sigma_v > \sigma_2 = \sigma_H > \sigma_3 = \sigma_h$
  - Failure on steeply dipping planes at $< 45^0$ to σ_1 (the vertical stress)
- Reverse (thrust) faulting/compressional stress regime:
  - $\sigma_1 = \sigma_H > \sigma_2 = \sigma_h > \sigma_3 = \sigma_v$
  - Failure on shallowly dipping planes at $< 45^0$ to σ_1 (the maximum horizontal stress)
- Strike-slip or wrench faulting/ strike-slip stress regime:
  - $\sigma_1 = \sigma_H > \sigma_2 = \sigma_v > \sigma_3 = \sigma_h$
  - Failure is horizontal on near-vertical planes striking/trending $< 45^0$ to σ_1 (the maximum horizontal stress)

Two intermediate stress regimes also can occur between (1) extensional and strike-slip stress regimes, and (2) between compressional and strike-slip stress regimes. The stress state allows us to identify the fault orientation; however, we must keep in mind that the stress state can change during production/injection, especially when the stress state is close to the various regimes.

Although the pore pressure does not change outside the reservoir, the induced stress (injection/production) will transfer to the overburden, sideburden, and underburden. The pore pressure and deformation changes lead to variations in the differential stress (maximum minus minimum principal stresses) of the system and can reactivate existing faults/fractures. In general, the poro-perm within the reservoir is higher than the caprock and overburden; hence, the direct pressure change observed is inside the reservoir. However, due to the stress transfer from the reservoir to the caprock, the effect should influence the strength of the cap and overburden rocks.

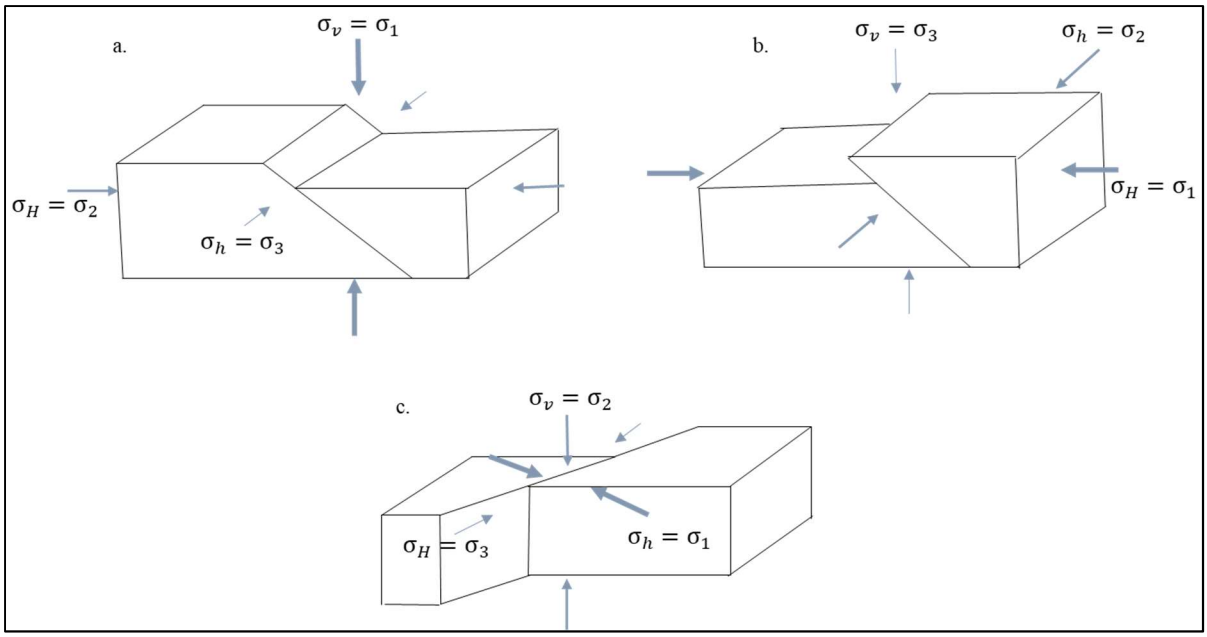

Fig. 2.7: Illustration of the changes of principal stresses direction and intensity in different fault classifications (a) normal faulting, (b) thrust faulting, and (c) strike-slip regimes. (modified after Eisbacher, 1996 cited in Altmann, 2010).

2.5.3 Failure mechanisms

The seal integrity (i.e., caprock and faults) in any CO_2 injection site depends on the function of the stress field and failure criteria; hence, comparative analysis between them is essential. A detailed description of Mohr-Coulomb failure criteria is addressed out of other commonly used failure criteria (i.e., Griffith criterion, Drucker-Prager, Von-Mises, Tresca, etc.) because this criterion is used in failure assessment studies (both analytical and numerical models).

Based on the principal stresses σ_1 and σ_3 acting on an arbitrarily oriented shear fracture plane in a rock sample, Mohr (1882) developed a graphical tool which is called the Mohr circle. When the Mohr circle is displayed in a shear versus normal stress diagram, it is called a Mohr diagram (Fig. 2.8a). The semicircle shape describes all possible shear and normal stress combinations on a potential failure plane oriented between $0^0 \leq \theta \leq 90^0$. The center of the circle is determined by $(\sigma_1 + \sigma_3)/2$, while the radius (maximum shear stress) is given by $(\sigma_1 - \sigma_3)/2$. $(\sigma_1 - \sigma_3)$ is also called differential stress σ_d. The maximum shear stress occurs at $2\theta = 90^0$, which indicates a 45^0 angle between the fracture plane and the principal stresses.

The Coulomb (1776) failure envelope, which is a straight line in a shear versus normal stress diagram, can be stated as:

$$\tau_{crit} = S_0 + \mu^* \sigma_n \tag{2.21}$$

where S_0 is cohesion (a material property) and μ^* is the coefficient of internal friction, and the typical values are $0.5 < \mu^* < 1$ (Sibson, 2000). The frictional coefficient can be expressed by the angle ϕ between the abscissa and the straight line (Fig. 2.8b) and stated that:

$$\mu^* = tan\phi \tag{2.22}$$

Mohr diagrams, together with equation 2.21, can determine the stability of any rock body. The rock is stable as long as the stress state described by Mohr circles lies under the failure envelope.

However, the rock becomes unstable if the failure envelope becomes tangential to or is cut through by the Mohr circle (Fig. 2.8b).

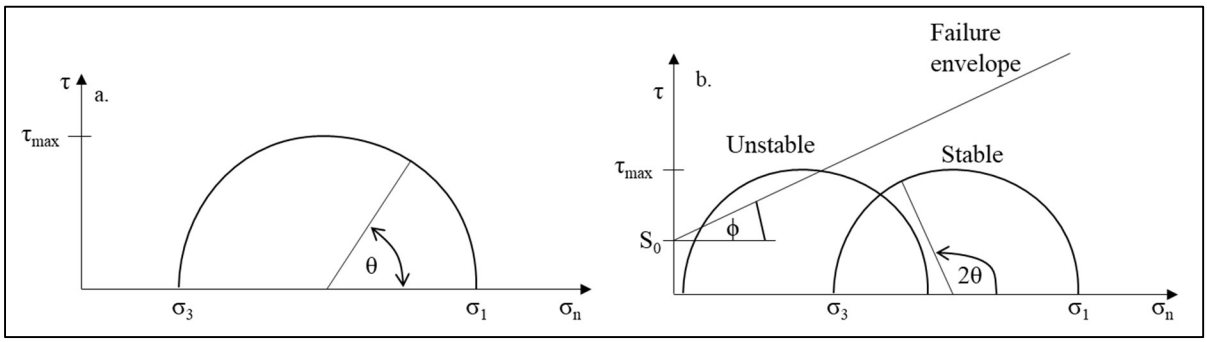

Fig. 2.8: The Mohr circle plotted in normal vs. shear stress illustrated all possible combinations of normal and shear stresses for one state of stress, depending on the orientation (2ϑ) with respect to the principal axes (a). The Mohr-Coulomb failure criteria described stable and unstable stress states based on the mathematically described failure envelope line (b). The failure envelope depends on the cohesion (S_0), the angle of internal friction (μ^*) and the normal stress (σ_n). Note that the red Mohr circle is in an unstable stress state condition (modified after Altmann, 2010).

Based on the Mohr-Coulomb failure criterion, there are two modes of failure generally considered:

- Shear failure of intact rock
- Tensile failure of intact rock

The normal stress σ_n acting on a plane with angle θ can be expressed in terms of principal stress magnitude (Ramsay, 2000; Vidal-Gilbert et al., 2010; Zoback, 2010). In isotropic horizontal conditions, it is expressed as:

$$\sigma_n = \frac{\sigma_1+\sigma_3}{2} + \frac{\sigma_1-\sigma_3}{2} cos2\theta, \tag{2.23}$$

and the shear stress τ is:

$$\tau = \frac{\sigma_1-\sigma_3}{2} sin2\theta \tag{2.24}$$

To define the failure criteria, we have to estimate effective stresses. The effective normal stress is expressed as the difference between the applied stress and the pore pressure inside the samples:

$$\sigma_n' = \sigma_n - p \tag{2.25}$$

where p is the pore pressure, which describes the effective state of stress by reducing the normal stress by the magnitude of the pore pressure. Therefore, if the total stress is assumed to be constant, the higher the pore pressure, the lower the effective stresses, and vice versa. Under the assumption of constant total stresses, pore pressure only influences the effective normal and effective principal stresses but not shear stresses. Therefore, Mohr circles do not change diameter but rather a horizontal position. This explains the higher failure risks during CO_2 injection. Due to increasing pore pressure, the Mohr circle moves to the left towards the failure envelope and becomes unstable.

The reactivation of an existing cohesionless fault or fracture is more likely to occur before the shear failure of intact rock (Fig. 2.9). The friction angle property of rocks also varies between themselves and can intersect such that the likely failure mechanism changes. In addition, the existing fault or fracture zones are structurally complex and not well-understood, despite significant research and publications on the topic (Færseth et al., 2007, 1984; Zieglar, 1992; Jev et al., 1993; Gibson, 1994; Yielding et al., 1997; Kim et al., 2003; Færseth, 2006; Faulkner et al., 2010; Rahman et al., 2021;). Furthermore, most fault zones are beyond seismic resolution and contain several major slip surfaces (Gibson, 1994; Childs et al., 1997; Foxford et al., 1998; Walsh et al., 1998; Doughty, 2003; Færseth et al., 2007;). These uncertainties significantly influence the prediction and quantification of reactivation processes.

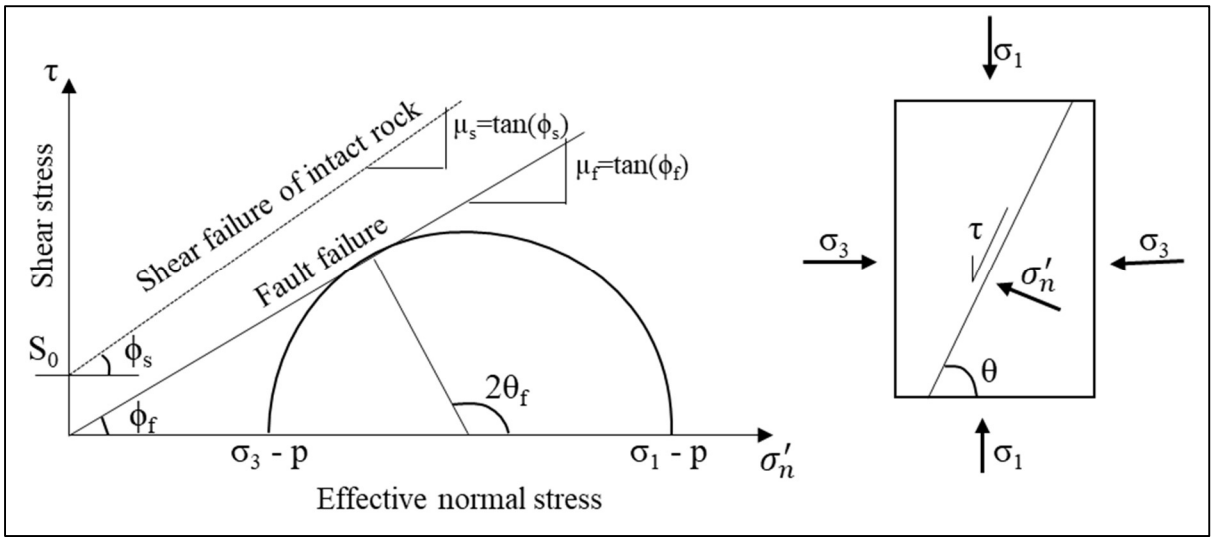

Fig. 2.9: The shear stress versus effective normal stress plot shows the Mohr diagram with various failure modes such as shear failure and fault reactivation (modified after Bjørnarå, 2018; Mathias et al., 2009).

2.5.4 Horizontal stress approximation

The horizontal stress approximation in any sedimentary basin is essential to define the stress state condition, which can be estimated using various techniques. The stress state of horizontal stresses can be determined by k_0 method, which is the ratio between the effective minimum horizontal stress and the effective vertical stress. This method has been widely used to describe the state of stress in any basin (Engelder and Fischer, 1994; Addis, 1997; Hillis, 2003; Tingay et al., 2003) and stated that:

$$k_0 = \frac{\sigma_h - p}{\sigma_v - p} \tag{2.26}$$

The vertical stress σ_v in any subsurface point can be estimated as the total weight of the overlying rocks and fluids. Therefore, we can rearrange equation 2.26 and approximate the horizontal stress:

$$\sigma_h = k_0\sigma_v + (1 - k_0)p \tag{2.27}$$

The compaction-induced changes in the total vertical stress are minimal for laterally extensive reservoirs, assuming equal elastic properties for the reservoir and overburden (Geertsma, 1973). Hettema et al. (2000) show in a numerical solution that the stiffness contrast has a very negligible effect on the vertical total stress change in a laterally extensive reservoir. However,

the horizontal stress path is very sensitive to the pore pressure changes. The explanation is that the ground surface is a free boundary surface while there are constraints in lateral strains (Bjørnarå, 2018).

The change of horizontal stresses by reservoir operations can be expressed using the horizontal stress path or pore pressure-stress coupling coefficients where the change in horizontal stress is proportional to the change in pore pressure and stated as (Hettema et al., 2000):

$$\gamma_h = \frac{\Delta\sigma_h}{\Delta P} = \alpha\left(\frac{1-2\upsilon}{1-\upsilon}\right) \tag{2.28}$$

$$\gamma_H = \frac{\Delta\sigma_H}{\Delta P} = \alpha\left(\frac{1-2\upsilon}{1-\upsilon}\right) \tag{2.29}$$

where ΔP is the pore pressure change, α is Biot's coefficient or effective stress parameter, and υ is the Poisson's ratio. Differentiating equation 2.27 with respect to pore pressure p, we can state:

$$\frac{d\sigma_h}{dp} = (1-k_o)(1-\Delta k_o) \tag{2.30}$$

Considering the Biot's coefficient is equal to 1, equations 2.26 and 2.27 can be seen that:

$$k_0 = \frac{\upsilon}{1-\upsilon} \tag{2.31}$$

Therefore, if we know the Poisson's ratio of the rocks, we can approximate the change of the stress state of any basin using the assumption of elasticity.

How the pore pressure stress coupling affects the state of stress and rock stability in different stress regimes (i.e., normal, reverse, and strike-slip) are illustrated by the Mohr diagram in figure 2.10. In a normal faulting regime, the effective vertical stress is reduced by the amount of pore pressure increase, while the effective horizontal stress is decreased not by pressure but by the strength of the coupling ($\frac{\Delta\sigma_h}{\Delta P}$). Therefore, the effective differential stress decreases due to increasing pore pressure with a smaller Mohr circle (grey) compared to the initial circle (Fig. 2.10a). The resulting effective stresses under consideration of pore pressure stress coupling are expressed by:

$$\sigma_v' = \sigma_v'^0 - \Delta P' \tag{2.32}$$

$$\sigma_h' = \sigma_h'^0 + \frac{\Delta\sigma_h}{\Delta P}.\Delta P' - \Delta P' \tag{2.33}$$

where $\sigma_v'^0$ and $\sigma_h'^0$ represent the initial effective state of stress, $\Delta P'$ is the pore pressure change and σ_v' & σ_h' are the effective state of stress after pore pressure change.

The pore pressure change has the opposite effect in a reverse faulting regime compared to a normal faulting regime. The differential stress increases (larger Mohr circle) due to injection-induced pore pressure increase (pore pressure stress coupling), and the Mohr circle moves to the left towards the failure envelope (Fig. 2.10b). Both maximum and minimum horizontal stresses are equally affected by pore pressure coupling in a strike-slip regime. Therefore, the size of the Mohr circle does not change; however, the circle horizontally shifts during injection or depletion (Fig. 2.10c).

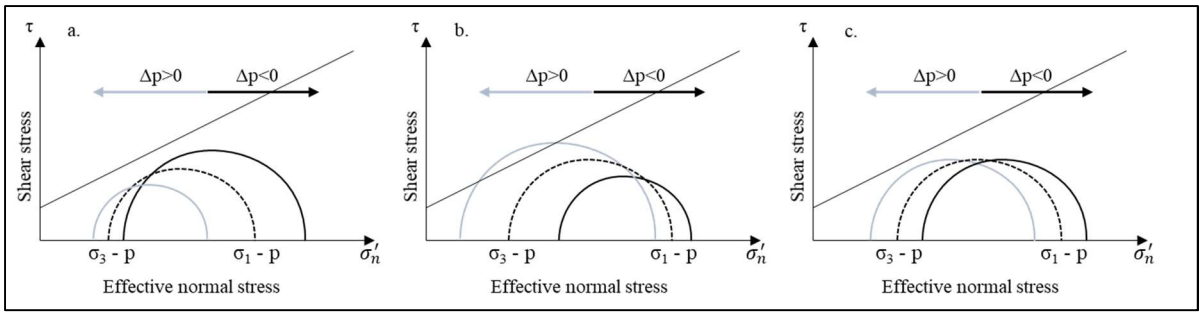

Fig. 2.10: The Mohr-Coulomb diagram for various stress regimes (a) normal faulting, (b) reverse/thrust faulting, and (c) strike-slip faulting. The effect of pore pressure changes on the Mohr circle is also illustrated (modified after Altmann, 2010).

2.5.5 Poromechanical coupling

The study of mechanical deformation of a fluid-saturated porous rock mass is called poromechanics. Fluid flow through the interconnected pores and the geomechanical deformation are coupled processes like the stress and pore pressure change. A fluid-saturated porous medium can deform by changing the external load or internal pore-fluid pressure. An external load (i.e., overburden stress) will compress both the rock framework and the pore volume. The reduced pore volume will compress pore fluid in a rapid load situation, increasing pore-fluid pressure. On the contrary, slow overburden stress allows the fluid to escape with no pressure increase. This phenomenon can be described as the coupling that occurs through deformation and pore-fluid interaction and is called it direct hydro-mechanical (HM) coupling (Kümpel, 2002; Rutqvist and Stephansson, 2003; Fig. 2.11). The criteria stated that:

1. a solid-to-fluid coupling that occurs when a change in applied stress produces a change in fluid pressure or fluid mass;
2. a fluid-to-solid coupling that occurs when a change in fluid pressure or fluid mass produces a change in the volume of the porous medium.

In these cases (i.e., 1 & 2), the cross-sectional area will be reduced due to the reduction of pore volume, which is influenced by the reduction of fluid flow capacity. Due to compression stress, there might be more grain-to-grain contacts, and as a result, the rock might become stiffer. These changes lead to an indirect HM coupling where the mechanical and hydraulic processes affect each other through material property changes. The indirect HM coupling phenomenon's are:

3. a solid-to-fluid coupling that occurs when applied stress produces a change in hydraulic properties;
4. a fluid-to-solid coupling that occurs when a change in fluid pressure produces a change in mechanical properties

All the coupled processes may be fully reversible except for inelastic responses such as yielding, fracturing, or fault slip, which are irreversible in porous and fractured media. The direct HM coupling (no. 1 and 2) is also crucial in relatively soft and low-permeability rocks and soils, while the indirect (no. 3 and 4) coupling tends to be most important in fractured rock as an intact rock with flat intergrain micropores (Rutqvist and Stephansson, 2003).

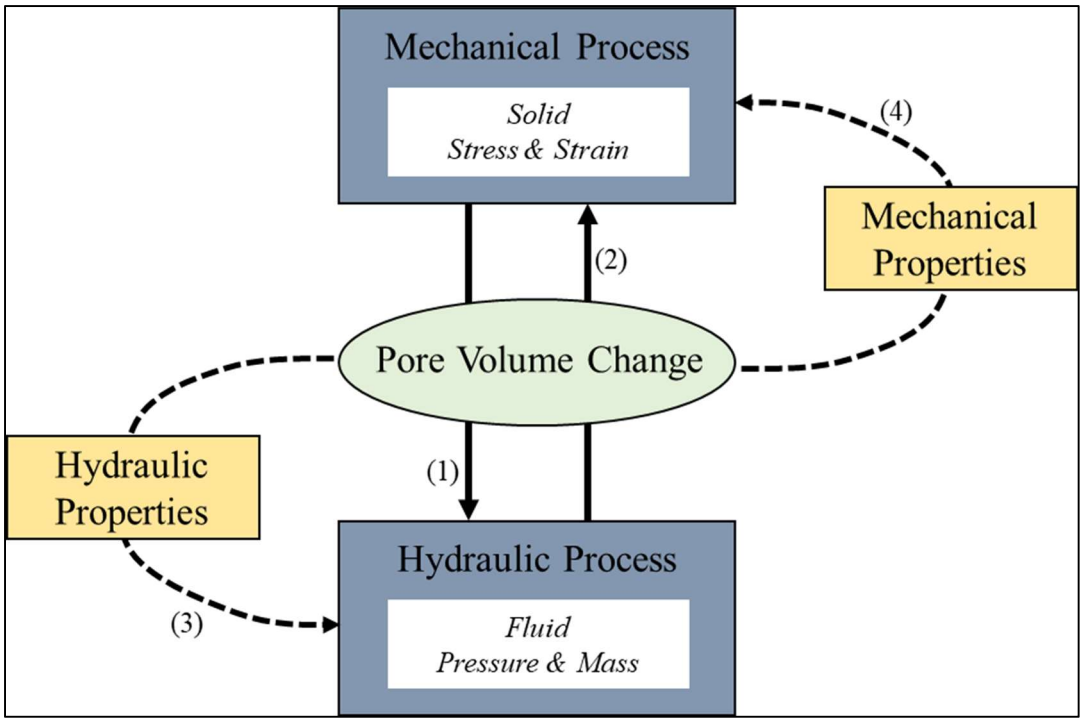

Fig. 2.11: Hydromechanical (HM) coupling in a porous media shows the direct (1&2) coupling through pore volume change and indirect (3&4) coupling through changes in material properties (modified after Rutqvist and Stephansson, 2003).

2.6 Modeling approach

2.6.1 Analytical model

An analytical model is a quantitative analysis of a specific question to answer or make a specific design decision. Different analytical models are required to address different aspects of the system, such as performance, reliability, or mass properties. Furthermore, this model needs to justify sufficient precision, and the model input parameters need to check the reliability. Therefore, the input parameters sensitivity is required to validate the models' accuracy.

2.6.2 Numerical simulation

The numerical solution, such as the finite element method, is used when the mathematical problem is too complex to solve analytically. For instance, a field-scale 3D geomechanical model is complex and has tens of thousands of grids; hence needs a finite element method to solve the model. Each grid consists of nodes at the corners and integration points inside the grid. The simulator (finite element solver) solves the partial differential equations for each grid iteratively and finishes the calculation when the solution is within a certain limit. The accuracy of the solution depends on the grid resolution means the smaller the grids, the better the solution. However, higher resolution often increases the computation time. Therefore, one must compromise between these two factors when solving a numerical model.

3. Database

This part describes the main database used in the Ph.D. research. Different subsets of data have been investigated to achieve the individual paper's objective. However, the overall database is introduced here. A description of the individual paper datasets is given in part four. Although the primary objective of this research is to evaluate the Smeaheia and Aurora CO_2 injection sites, a broader area is considered to evaluate future injection sites (**Paper-1**). According to Longship (2020), the total amount of CO_2 will be increased from 1.2 to 5 GT/year in the future if the EU demands increase. The first phase of infrastructure installation, additional injection sites, and exploration within the studied area will have a higher priority. Therefore, the wireline log-based analysis is carried out regionally, covering the structural elements named by NPD (2021), such as Bjørgvin Arch (BA), Stord Basin (SB), Lomre Terrace (LT), Oseberg Fault Complex (OFC), Brage Horst (BH), Flatfisk Slope (FS), Uer Terrace (UT), Mokkurkalve Fault Complex (MFC), Tjalve Terrace (TT), and Marflo Spur (MS) (Fig. 3.1).

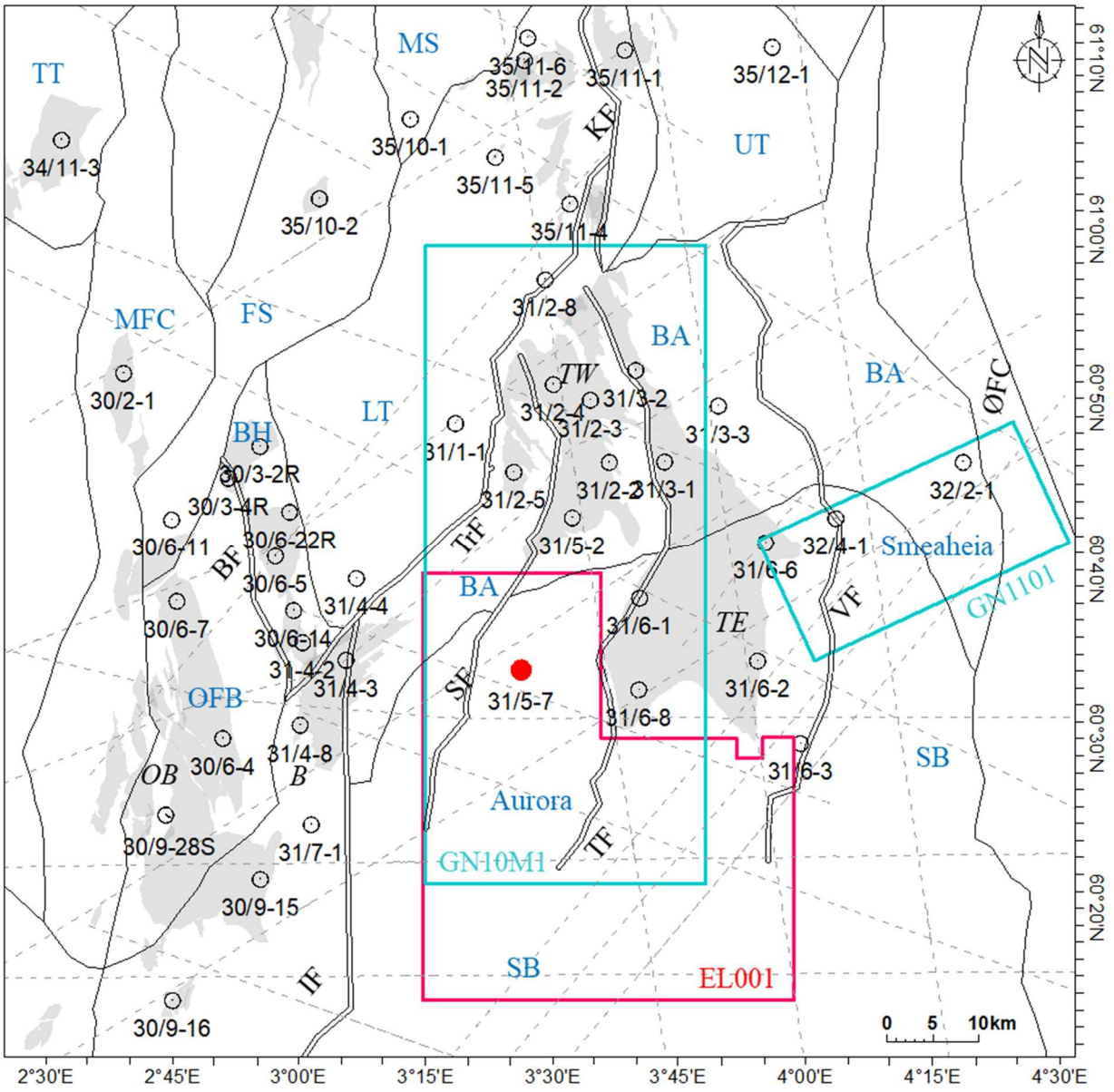

Fig. 3.1: Map of the study area shows wells (black circles), faults and structural elements boundary (black lines e.g., BA = Bjørgvin Arch; BH = Brage Horst; FS = Flatfisk Slope; HP = Horda Platform; LT = Lomre Terrace; MS = Marflo Spur; SB = Stord Basin; TT = Tjalve Terrace; UT = Uer Terrace;

Faults: BF = Brage Fault; IF = Idunn Fault; KF = Kinna Fault; MFC = Mokkurkalve Fault Complex; OFB = Oseberg Fault Block; TF = Tusse Fault; TrF = Troll Fault; ØFC = Øygarden Fault Complex). The grey shaded polygons illustrate the hydrocarbon fields and discoveries (e.g., *B = Brage; OB = Oseberg; TE = Troll East; TW = Troll West*) in the study area. The blue boundaries represent 3D seismic cubes GN10M1 and GN1101. Grey dashed lines indicate the 2D seismic lines. The first CCS license (EL001) in offshore Norway is marked by a violet polygon.

3.1 Exploration wells

A total of 64 exploration well datasets were selected for the interpretation, where the maximum number of wells were from the Bjørgvin Arch, Stord Basin, and Lomre Terrace areas (Table 3.1). Wells from these areas got higher priority as the Smeaheia and Aurora injection sites are located within these same structural elements. Wells have been chosen according to their penetration in the zones of interest, as well as data availability. In addition, wireline log suites (i.e., gamma-ray, density, velocities, deep resistivity) from the same wells are analyzed.

Table 3.1
Total depth and oldest formation penetrated by the studied wells. The structural elements are as suggested by NPD (2022).

Well name	Structural Elements (NPD)	TD (TVD)		Oldest penetration Formation	Well Type/purpose	Field
		Present	Max*			
30/9-15	Bjørgvin Arch	2763.5	2943.5	Statfjord Gp.	Exploration/Wildcat	Oseberg Sør
30/9-16		3549	3714	Statfjord Gp.	Exploration/Wildcat	Oseberg Sør
30/12-1		3640.5	3775.5	Statfjord Gp.	Exploration/Wildcat	Dry
31/2-1		2433	2553	Hegre Gp.	Exploration/Wildcat	Troll West
31/2-2R		2599	2729	Hegre Gp.	Exploration/Apprisal	Troll West
31/2-3		2600	2990	Hegre Gp.	Exploration/Apprisal	Troll West
31/2-4		5035	5295	Hegre Gp.	Exploration/Apprisal	Troll West
31/2-5		2532	2772	Hegre Gp.	Exploration/Apprisal	Troll West
31/2-6		1754	1994	Fensfjord Fm.	Exploration/Apprisal	Troll West
31/2-8		3373	3603	Hegre Gp.	Exploration/Apprisal	Oil show
31/2-15		1677	2067	Fensfjord Fm.	Exploration/Apprisal	Troll West
31/2-18		1711	2081	Fensfjord Fm.	Exploration/Apprisal	Troll West
31/3-1		2374	2754	Hegre Gp.	Exploration/Apprisal	Troll East
31/3-2		2090	2410	Drake Fm.	Exploration/Apprisal	Troll East
31/3-3		2571	3091	Statfjord Gp.	Exploration/Wildcat	Dry
31/3-4		2122	2492	Etive Fm.	Exploration/Wildcat	Dry
31/4-3		4981	5141	Rotliegend Gp.	Exploration/Wildcat	Brage
31/4-6		2447	2697	Drake Fm.	Exploration/Apprisal	Brage
31/4-8		2611	2751	Lunde Fm.	Exploration/Apprisal	Brage
31/4-10		2342	2492	Heather Fm.	Exploration/Apprisal	Brage
31/5-2		2500	2690	Hegre Gp.	Exploration/Apprisal	Troll West
31/5-5		1930	2100	Krossfjord Fm.	Exploration/Apprisal	Troll West
31/5-6		2368	2573	Drake Fm.	Exploration/Wildcat	Oil show
31/7-1		2780	2990	Johansen Fm.	Exploration/Wildcat	Brasse
32/2-1		1300	2100	Lunde Fm.	Exploration/Wildcat	Dry
35/11-7		2895	3090	Statfjord Gp.	Exploration/Wildcat	Fram
31/5-7	Stord Basin	2915	3265	Statfjord Gp.	Exploration/Wildcat-CCS	Aurora Site
31/6-1		4070	4400	Basement	Exploration/Wildcat	Troll East
31/6-2R		2235	2695	Hegre Gp.	Exploration/Apprisal	Troll East
31/6-3		2250	2680	Hegre Gp.	Exploration/Wildcat	Dry
31/6-5		2028	2418	Drake Fm.	Exploration/Apprisal	Troll East
31/6-6		2291	2761	Hegre Gp.	Exploration/Apprisal	Troll East
31/6-8		2138	2468	Cook Fm.	Exploration/Apprisal	Troll East
31/8-1		2629	2829	Krossfjord Fm.	Exploration/Wildcat	Dry
32/4-1		3185	3885	Basement	Exploration/Wildcat	Dry
31/1-1	Lomre Terrace	2920	3120	Statfjord Gp.	Exploration/Wildcat	Dry

31/2-8		3373	3573	Hegre Gp.	Exploration/Wildcat	Oil show
31/2-19S		3669	3669	Statfjord Gp.	Exploration/Wildcat	Dry
31/4-4		3150	3150	Statfjord Gp.	Exploration/Wildcat	Dry
35/11-2		4024	4184	Statfjord Gp.	Exploration/Wildcat	Vega
35/11-4		3125.5	3315.5	Statfjord Gp.	Exploration/Wildcat	Vega
35/11-5		3768	3948	Statfjord Gp.	Exploration/Wildcat	Swisher
35/11-6		3989	4139	Statfjord Gp.	Exploration/Apprisal	Oil show
35/11-9		2828	3048	Heather Fm.	Exploration/Apprisal	Fram
30/3-3	Oseberg Fault Block	3419	3539	Statfjord Gp.	Exploration/Wildcat	Dry
30/3-4R		3287	3412	Statfjord Gp.	Exploration/Apprisal	Veslefrikk
30/6-4		2942	3132	Burton Fm.	Exploration/Apprisal	Oseberg
30/6-7		3236	3356	Statfjord Gp.	Exploration/Apprisal	Oseberg
30/6-19R		3298	3423	Eiriksson Fm.	Exploration/Wildcat	Oseberg Øst
30/9-13S		3964	3964	Statfjord Gp.	Exploration/Wildcat	Oseberg Sør
30/9-28S		3928	3928	Statfjord Gp.	Exploration/Wildcat	Oseberg Sør
30/3-2R	Brage Horst	3566	3696	Hegre Gp.	Exploration/Wildcat	Veslefrikk
30/6-5		3550	3690	Lunde Fm.	Exploration/Wildcat	Oseberg Øst
30/6-14		2900	3055	Statfjord Gp.	Exploration/Wildcat	Oseberg Øst
30/6-22R		3329	3434	Statfjord Gp.	Exploration/Apprisal	Oseberg Øst
31/4-2		2900	3014	Hegre Gp.	Exploration/Wildcat	Brage
35/11-1	Uer Terrace	3360	3690	Hegre Gp.	Exploration/Wildcat	Dry
35/12-1		3018	3498	Amundsen Fm.	Exploration/Wildcat	Oil show
35/12-3		2758	3248	Etive Fm.	Exploration/Wildcat	Dry
30/6-11	Flatfisk Slope	4001	4091	Statfjord Gp.	Exploration/Wildcat	Show
35/10-2		4675	4800	Statfjord Gp.	Exploration/Wildcat	-
30/2-1	Mokkurkalve Fault Complex	4237	4302	Statfjord Gp.	Exploration/Wildcat	Huldra
34/11-3	Tjalve Terrace	4476	4506	Statfjord Gp.	Exploration/Apprisal	Kvitebjørn
35/10-1	Marflo Spur	3982	4122	Statfjord Gp.	Exploration/Wildcat	-

*Exhumation corrected based on Rahman et al., 2020; Baig et al., 2019.

3.2 Core and cutting samples

Twelve (12) shale core and cutting samples are collected from the NPD core store in Stavanger, Norway. The petrographical and laboratory analysis are carried out using these samples. Nanoscale mechanical laboratory analysis is performed using the nano-indentation technique in Curtin University lab in Australia to estimate the mechanical properties of rock, such as hardness and indentation modulus (**CP-4**). The XRD and SEM analyses are also carried out in-house for all the samples (**CP-1**) where 5 related samples out of 12 are presented in **Paper-1** and **CP-2**.

3.3 Seismic data

Both 2D and 3D seismic data are available for this research. Two long offset 2D seismic surveys, such as North Sea Renaissance (NSR) and SG8043 provided the regional coverage of the study area, so they are used for regional horizon interpretation (Fig. 3.1; **Paper-1**). Two site-specific 3D cubes of wide-ranged angle stacks were also available where GN1101 and GN10M1 covered the Smeaheia and Aurora sites, respectively (Fig. 3.1). Both seismic volumes have a combined coverage area of 2581 km^2, where the majority of the area is covered by GN10M1 (2136 km^2). A set of five partial stacks with angles 0-10^0, 10-20^0, 20-30^0, 30-40^0, and 40-50^0 are available for both 3D surveys to carry out seismic inversion analysis (**RP-2 & -4**). The seismic inverted property cubes have been used in the numerical field-scale model grid for simulation (**Paper-3 & -4**).

4. Methods and Workflows

This part describes the methods and workflows used in this research. The fundamental theories behind the methods (i.e., rock physics template, workflows, empirical equations, etc.) are described in part 2 and are not repeated here. The research is divided into three sub-topics: geological & geophysical (G&G) characterization, analytical assessment, and numerical modeling (Fig. 4.1). These research sub-sections have different approaches to characterize the top seal, mainly focusing on the CO_2 injection site from the northern North Sea. For instance, the G&G caprock characterization includes integrated petrography, petrophysics, rock physics, and seismic attributes analysis (**Paper-1; RP-1 & -2, CP-1 to -4**), while in the analytical modeling analysis, the probabilistic structural reliability of the top seal is analyzed (**Paper-2; RP-3**). In addition, numerical modeling based on finite element methods allows us to evaluate the injection-induced mechanical failure risk on a field scale (**Paper-3 & -4; RP-4**). Description of the methods and workflows follow the same chronological order as illustrated in figure 4.1.

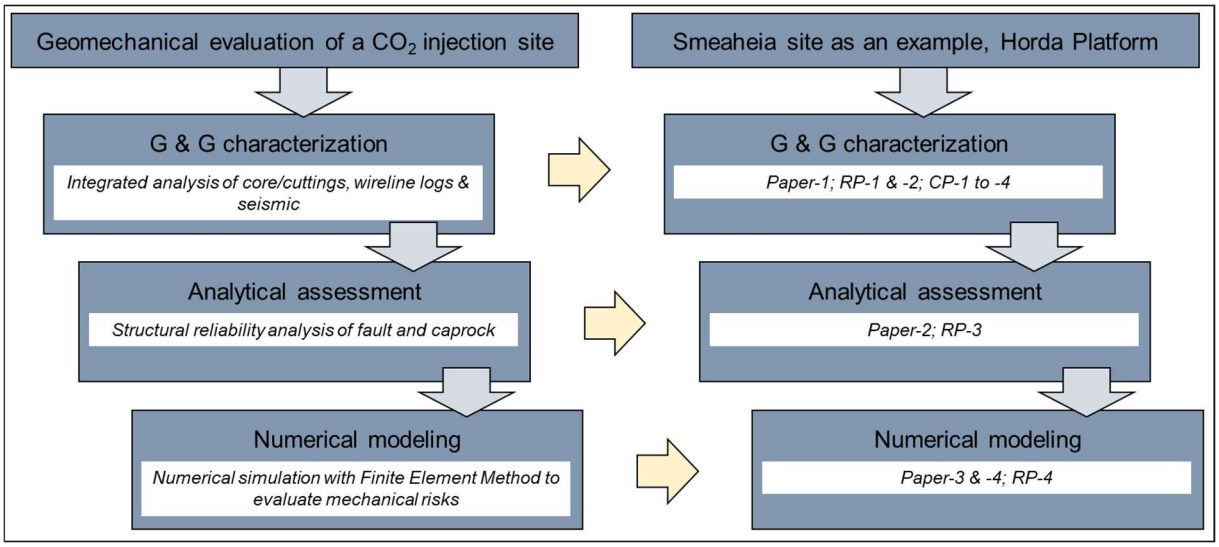

Fig. 4.1: The research sub-topics and the corresponding papers are illustrated the chronological workflow followed in this study.

4.1 Geological & Geophysical characterization

In this sub-class, a detailed analysis has been carried out to characterize the caprock properties. **Paper-1; RP-1 and CP-1, -2 & -4** focused on evaluating the Draupne and Heather formation shales, while **RP-2** and **CP-3** evaluated the Sognefjord, Fensfjord, and Krossfjord sandstones from the Horda Platform, northern North Sea. A similar analysis has been conducted and published for caprock-2 (Drake), which is not included in this dissertation (Rahman et al., 2022). The main objective of G&G characterization is to evaluate top seal integrity. An integrated workflow has been tested, where wireline logs and 2D/3D seismic data from the study area have been used (Fig. 4.2). Vertical and lateral distribution of different properties of caprock are analyzed by combining results from petrophysics, petrographic, rock physics, seismic inversion, and seismic amplitude analyses. The individual method used in each sub-section is described below:

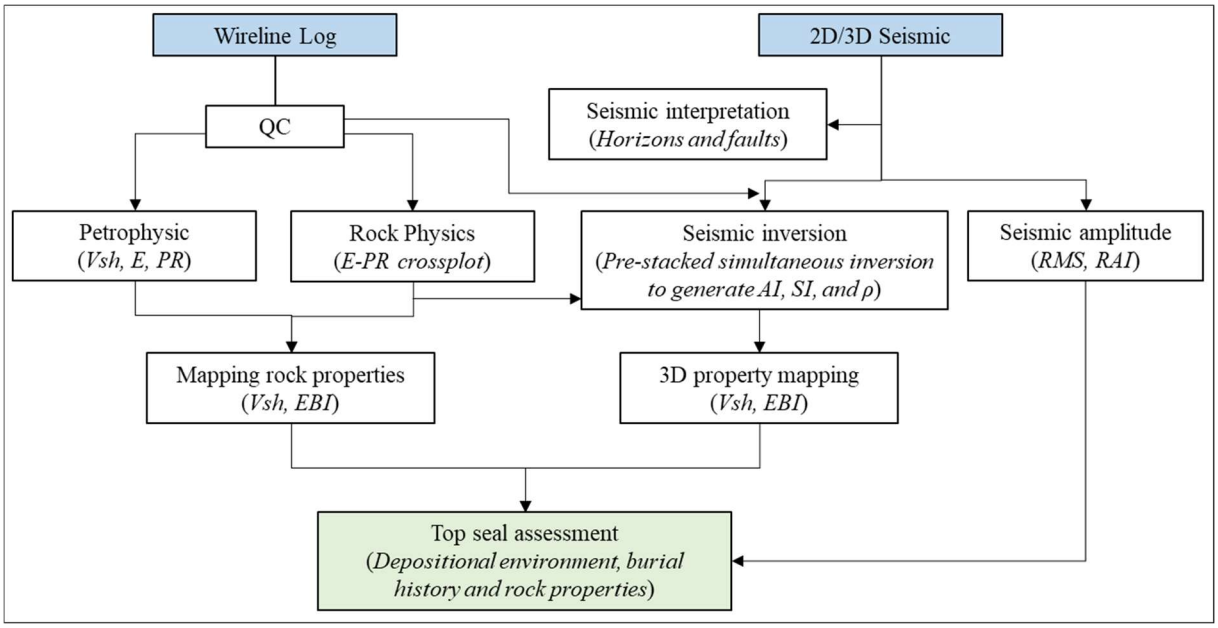

Fig. 4.2: An integrated workflow to characterize top seal properties is illustrated by various processes followed systematically (modified after Rahman et al., 2022).

4.1.1 Petrographic analysis

Bulk mineralogy of the core and cutting samples (mentioned in part 3.2) has been estimated using the X-ray Diffraction (XRD) technique. Additional bulk mineralogy databases are scouted from the published literature (Kalani et al., 2015; Koochak Zadeh et al., 2017; Nooraiepour et al., 2017; Hansen et al., 2020). Scanning Electron Microscope (SEM) images of the same samples are also assessed. The SEM images also revealed the type of minerals and a qualitative assessment of the grain size of the studied samples. This information helped define the mineral assemblages during XRD interpretation to estimate the percentage. The XRD and SEM analysis results are used in paleo-depositional environment study and mineralogy-based brittleness indices estimation (**Paper-1; CP-1 & -2**).

4.1.2 Petrophysical analysis

Wireline logs are extensively used in geological and geophysical characterization investigations. The Shale volume (V_{sh}) is calculated from the gamma-ray log using the Larionov (1969) old (equation 4.1) and young (equation 4.2) rocks equations stated below:

$$V_{sh} = 0.33(2^{2\times I_{GR}} - 1) \tag{4.1}$$

and,

$$V_{sh} = 0.083(2^{3.7\times I_{GR}} - 1) \tag{4.2}$$

where I_{GR} is the gamma-ray index which can be estimated by defining the sand and shale lines and expressed as:

$$I_{GR} = \frac{GR_{logs} - GR_{max}}{GR_{min} - GR_{max}} \tag{4.3}$$

To evaluate the transition zone, which is the boundary between mechanical and chemical compactions, temperature gradient of each well has been estimated using bottom hole temperature (BHT) and total vertical depth (TVD) and denoted as:

$$m = \frac{y-c}{TD} \tag{4.4}$$

where m is the temperature gradient, y is the bottom hole temperature, c is the mean annual temperature at the seafloor (i.e., 5^0C for the North Sea), and TD is the total depth below the seafloor.

Organic material within the shale can significantly influence caprock properties including mechanically. There are several empirical relationships available that estimate total organic carbon from wireline logs. This study tested two petrophysical methods where the total organic carbon (TOC) has been estimated from P-sonic, deep resistivity, and density logs. The first technique is called ΔlogR method, where the P-sonic (Δt) and the deep resistivity (R_d) are used as input (Meyer and Nederlof, 1984; Passey et al., 1990). When the baseline for non-organic fine-grained lithology has been defined, the ΔlogR value can then be estimated at each depth interval as:

$$\Delta logR = log_{10}\left(\frac{R_d}{R_{d_{baseline}}}\right) + 0.02 \times (\Delta t - \Delta t_{baseline}) \tag{4.5}$$

The total organic carbon (TOC) content in wt% is then predicted as:

$$TOC = (\Delta logR) \times 10^{(2.297 - \ .1688 * LOM)} \tag{4.6}$$

where LOM is the level of Organic Metamorphism (LOM) corresponding to the source rock maturity, which can be evaluated based on Rock-Eval or vitrinite reflectance data.

A second method is also a petrophysical approach where TOC is predicted from a bulk density log (Vernik and Landis, 1996; Carcione, 2000) and stated that:

$$TOC = a\frac{\rho_k(\rho_m - \rho_b)}{\rho_b(\rho_m - \rho_k)} \tag{4.7}$$

where subscripts to density (ρ) indicated kerogen (k), matrix (m), and recorded bulk density (b), a is a constant related to the fraction of carbon in the organic matter.

Laboratory estimated TOC within the study area has been scouted from NPD (2020). Afterward, TOC predicted using two separate methods has been calibrated with the estimated TOC percentage. An example from well 35/11-6 is illustrated in figure 4.3. Density-based relationships (equation 4.7) exhibit a better correlation coefficient; hence are utilized for the rest of the wells without lab-based TOC estimates.

Geomechanical properties such as Young's modulus (E) and Poisson's ratio (υ) are proxies of rock stiffness and represent the geomechanical parameters of any rock. The scope of this analysis is to characterize the geomechanical properties of rocks, mainly caprock and overburden using wireline logs. Therefore, wireline log based dynamic properties such as E and υ are calculated using the compressional wave velocity (Vp), shear wave velocity (Vs), and bulk density (ρ) logs using the equations below:

$$E = \frac{\rho V_s^2\left(3V_p^2 - 4V_s^2\right)}{V_p^2 - V_s^2} \tag{4.8}$$

$$\upsilon = \frac{V_p^2 - 2V_s^2}{2(V_p^2 - V_s^2)} \tag{4.9}$$

The Vp and density logs are available for all the studied wells; however, a limited number of wells have measured Vs logs. Therefore, to estimate Vs machine learning-based random forest (RF) algorithms have been used. Several petrophysical logs (i.e., Gamma-ray, caliper, deep-resistivity, neutron porosity, photoelectric, Vp, Vs & Vp/Vs) have been used to train the model. A considerable match between measured and RF Vs has been observed.

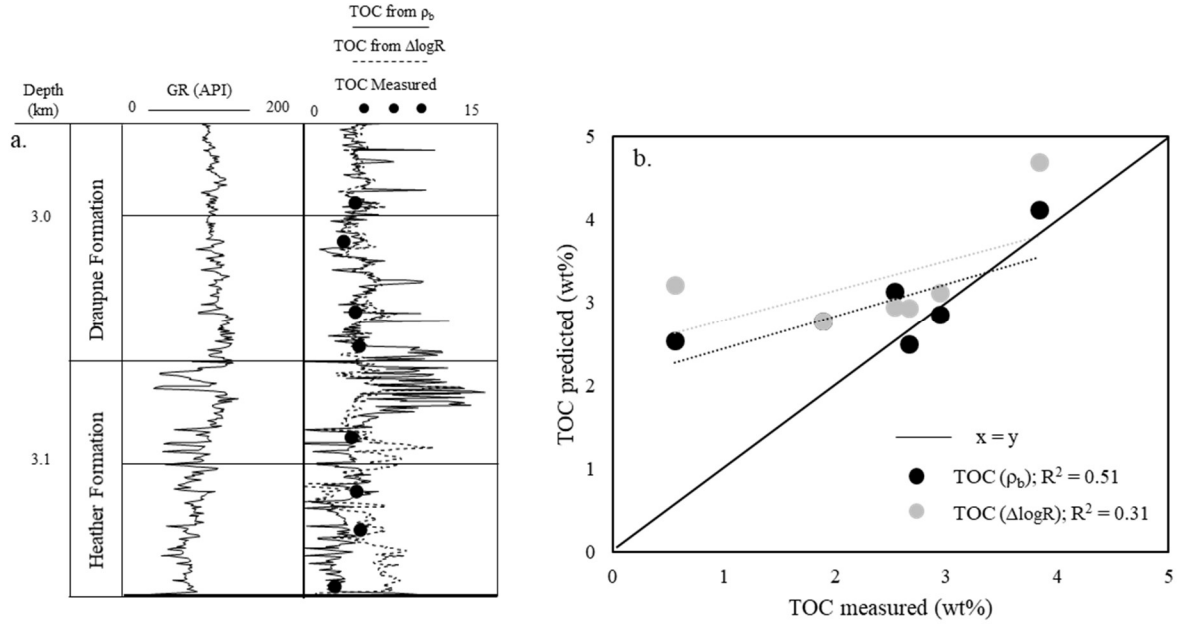

Fig. 4.3: Comparison between predicted TOC and measured TOC (NPD, 2020), estimated within the Draupne and Heather formations intervals from well 35/11-6 (a). The comparative correlation coefficient between the two empirical methods is also illustrated (b).

4.1.3 Brittleness Indices

Brittleness index (BI) is a quantitative measurement of rock behavior, estimated using many available empirical equations. In this thesis, two (2) mineralogy-based BI (MBI) and two (2) elastic properties based BI (EBI) have been analyzed (**Paper-1; RP-1; CP-1 & -2**). Lab based mineralogy data (XRD) has limitations; hence the relationship between MBI and EBI is critical. If there is a better match observed between these two methods, we can use available elastic property based relationships to estimate caprock brittleness. The findings of this comparative analysis have been described in detail in part 5.

The mineral fraction based BI (MBI^1) is first proposed by Jarvie et al. (2007), which is tested in this research. The equation stated that:

$$MBI^1 = \frac{Qtz}{Qtz+Carb+Cly} \tag{4.10}$$

where Qtz is quartz, Carb is carbonate, and Cly is clay fractions. MBI^1 = 1 indicates brittle rock, while = 0 represents the ductile behavior of the rock.

Several authors proposed modified MBI equations by considering dolomite (Wang and Gale, 2009), Carbonate (Glorioso and Rattia, 2012), Feldspar (Jin et al., 2014), and Pyrite (Alzahabi et al., 2015; Rybacki et al., 2016) as stiff minerals while TOC (Wang and Gale, 2009) as the ductile mineral. Considering this, a modified equation (4.11) was proposed and tested in **Paper-1** and **CP-1**. The combined equation is as follows:

$$MBI^2 = \frac{Qtz+Carb+Fsp+}{Qtz+Carb+Fsp+Py+Cly+TOC} \tag{4.11}$$

where Fsp is feldspar, Py is pyrite, and TOC is the total organic carbon.

Similar to MBI, many elastic property-based brittleness indices (EBI) equations are also available (Grieser and Bray, 2007; Rickman et al., 2008; Sharma and Chopra, 2012; Chen* et al., 2014; Jin et al., 2014; Fawad and Mondol, 2021). Out of these, two equations are used in this research where Grieser and Bray (2007) equation is the normalization of Young's modulus (E) and Poisson's ratio (υ), which is expressed as:

$$EBI^1 = \frac{1}{2}\left[\frac{E-E_{min}}{E_{max}-E_{min}} + \frac{\upsilon-\upsilon_{max}}{\upsilon_{min}-\upsilon_{max}}\right] \tag{4.12}$$

where E is the static Young's modulus, E_{max} is 69 GPa, E_{min} is 0 GPa, υ is static Poisson's ratio, υ_{max} is 0.5 and υ_{min} is 0. Also higher the EBI^1 more brittle the rock would be.

The log driven dynamic E (equation 4.8) and υ (equation 4.9) are converted to log-based static values using Mullen et al. (2007) equation:

$$E_{stat} = \left[\frac{E_{dyn}}{3.367}\right]^{2.042} \tag{4.13}$$

and

$$\upsilon_{stat} = \upsilon_{dyn} \tag{4.14}$$

Another empirical equation to directly measure static Young's modulus from Vp has also been implied (Rahman et al., 2022). The equation is proposed by Horsrud (2001) and states that:

$$E_{stat} = 0.076V_p^{3.23} \tag{4.15}$$

The other EBI equation used is proposed by Fawad and Mondol (2021), which is based on acoustic impedance (AI) and deep resistivity (R_d) and is defined as:

$$EBI^2 = \frac{0.00044AI-1.3-\sqrt{0.62\frac{R_w}{R_d}}(0.00019AI+0.25)}{1.35+0.00028AI} \tag{4.16}$$

4.1.4 Rock Physics Templates

The rock physics template is useful for characterizing reservoir and cap rocks. Several rock physics templates have been used in geology and geophysical characterization analysis. The effect of different mineral fractions within shale is evaluated using the Dvorkin-Gutierrez silty shale model (Fig. 4.4a). The important rock behavioral property (brittleness) is assessed using the templates illustrated in figures 4.4b, c & d. Grieser and Gray (2007) proposed by the template for brittle and ductile regions, while the other two templates with further classification are suggested by Perez and Marfurt (2014).

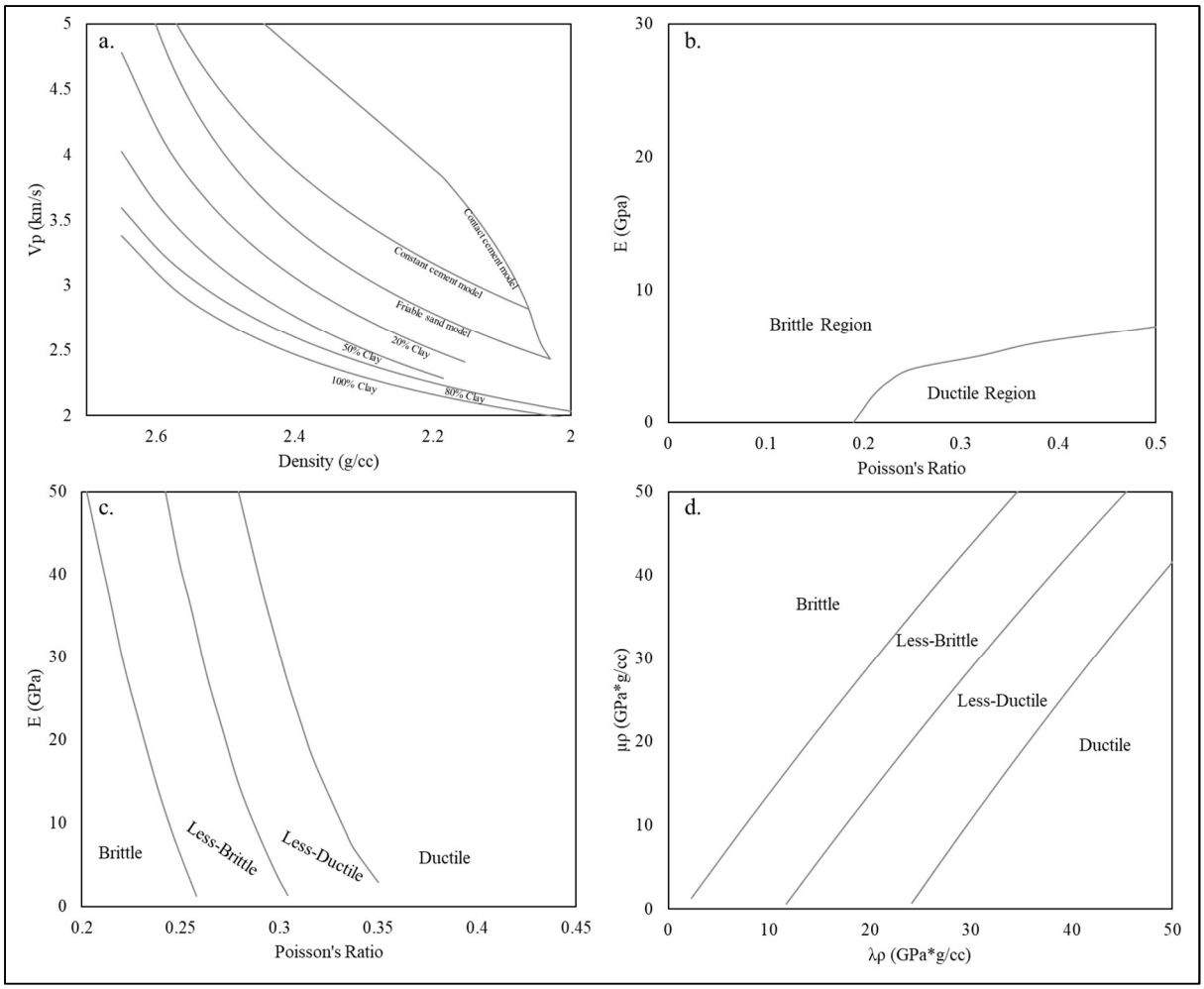

Fig. 4.4: Rock physics templates used in this study; (a) the Dvorkin-Gutierrez silty shale model and cement models in velocity-density plot (modified after Avseth et al., 2005), (b) ductile and brittle region in Young's modulus- Poisson's ratio plot (modified after Grieser and Bray, 2007) and ductile to brittle template in young's modulus- Poisson's ratio plot (c) and MuRho-LambdaRho plot (d) (modified after Perez and Marfurt, 2014).

4.2 Analytical integrity assessment

A deterministic approach to evaluate structural safety is somewhat questionable when the varying degree of uncertainties is present (Duncan, 2000). Instead, a probabilistic method is more suitable in this case (Christian, 2004; Nadim, 2007). A stochastic structural reliability approach is first introduced in this study for subsurface (**Paper-2 & RP-3**), though this method is widely used for surface structures. The proposed workflow is illustrated in figure 4.5, where a Mohr-Coulomb failure criteria-based model is defined based on the rock properties. Monte Carlo and First Order Reliability Method (FORM) have been used to estimate the probabilistic structural reliability. The sensitivity of each parameter is also verified during the analytical modeling.

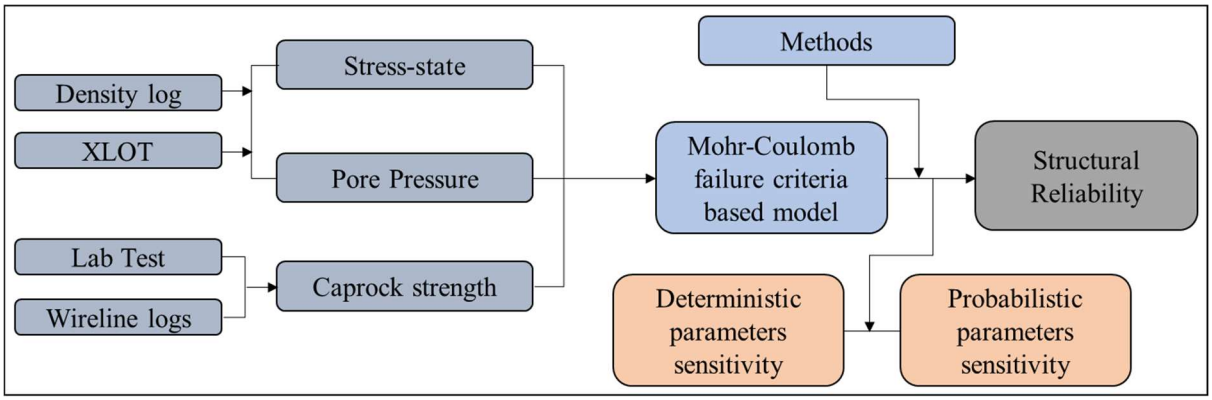

Fig. 4.5: The workflow to estimate probabilistic structural reliability of any subsurface structure such as faults (**Paper-2**) and caprocks (**RP-3**) integrity.

4.2.1 Stability assessment model

The Mohr-Coulomb failure criteria-based limit state function is assigned based on the deterministic factor of safety (FoS) equation. Assuming an isotropic horizontal stress condition within a normal faulting regime, the factor of safety (FoS) for the shear failure of fault (**Paper-2**) and caprock (**RP-3**) is defined as:

$$FoS_{fault} = \frac{S_0 + \sigma_n' tan\emptyset}{\frac{\sigma_1' - \sigma_3'}{2} sin2\theta} \tag{4.17}$$

$$\sigma_n' = \frac{\sigma_1' + \sigma_3'}{2} + \frac{\sigma_1' - \sigma_3'}{2} cos2\theta \tag{4.18}$$

and,

$$FoS_{caprock} = \frac{[\left(\frac{\sigma_1' + \sigma_3'}{2}\right) + \frac{S_0}{tan\phi}] sin\phi}{\frac{\sigma_1' - \sigma_3'}{2}} \tag{4.19}$$

$$\sigma_1' = \sigma_1 - p_p \tag{4.20}$$

$$\sigma_3' = \sigma_3 - p_p \tag{4.21}$$

where, σ_n' is effective normal stress, σ_1' is effective vertical stress, σ_1 is vertical stress, σ_3' is effective horizontal stress, σ_3 is horizontal stress, p_p is pore pressure, S_0 is cohesion, and $\emptyset$ is friction angle, and θ is fault dip.

The state of the structure is safe when the factor of safety is greater than 1 and fails when it is less than 1. Therefore, the limit-state function defines as:

$$g\_shear(x) = FoS - 1 \tag{4.22}$$

where, g(x) is the limit-state function which is the boundary between safe (g(x) >0) and failure (g(x) ≤ 0) state.

4.2.2 Reliability methods

Several well-established reliability methods are available (i.e., First Order Second Moment, First Order Reliability Method/Second-Order Reliability Method, Monte Carlo simulation, etc.). In this research, we tested Monte Carlo Simulation (MCS) and First Order Reliability Method (FORM) for fault failure estimation (**Paper-2**) and only FORM to estimate the caprock structural reliability (**RP-3**). The MCS is a procedure where the limit state function is evaluated by randomly selected samples from the input values to determine whether the configuration is desirable or not. The probability of failure (P_f), however, is estimated by the number of unwanted settings (n_f), with respect to the total number of samples (n).

$$P_f = \frac{n_f}{n} \tag{4.23}$$

It is a powerful technique but sometimes impractical when the probability of failure is small and requires many simulations to obtain a reliable distribution. However, sampling techniques (i.e., Latin Hypercube, Orthogonal, etc.) can optimize the number of simulations required for reliable distribution of the response, which we did not consider in this study.

The FORM method proposed by Hasofer and Lind (1974) is another technique, which is widely used in practical engineering problems (Nadim, 2007; Faber, 2009). Let's assume two random variables with limit state function g(x) stated in physical space where the grey zone represents the failure events while the white zone is the safe region (Figure 4.6a). The FORM method normalized the random variables into normally distributed variables (Z_1 and Z_2) with zero mean and defined the limit state function g(z) = 0. After that, the g(z) surface has been linearized at point z*, which is the shortest distance from the zero mean and is called the design point (Figure 4.6b). The shortest distance is called the reliability index (β), which is an indicator of structural stability. The higher the distance, the safer the structure is. The normal vector direction to the failure surface denotes α and indicates the random variable's relative importance. This relative design factor (α) is often referred to as the probabilistic sensitivity factor, which is useful for the relative ranking of random variables. In FORM analysis, the probabilistic sensitivity value can be achieved by performing several iterations and treating every individual parameter as a deterministic variable in each study (NESUS Theoretical Manual, 2011; Pereira et al., 2014), where a positive value indicates a direct relationship between the variables value and the response, while a negative sensitivity suggests an inverse relation. In addition, the square of each sensitivity factor (α_i^2) can reveal the input parameters' contribution to the failure probability estimation.

Mathematically the reliability index (β) can be expressed as:

$$\beta = \vec{\alpha} z^* \tag{4.24}$$

where the normal vector to the failure surface $\vec{\alpha}$ is denoted as:

$$\vec{\alpha} = \frac{\nabla g(z^*)}{|\nabla g(z^*)|} \tag{4.25}$$

where g(z) is the gradient vector and assumed to exist:

$$\nabla g(z) = \left(\frac{\partial g}{\partial z_1}(z), \dots\dots\dots\dots\dots, \frac{\partial g}{\partial z_n}(z) \right) \tag{4.26}$$

Therefore, an iterative method is used to estimate the reliability index due to the non-linear optimization problem (Thoft-Christensen and Baker, 1982; Madsen et al., 2006).

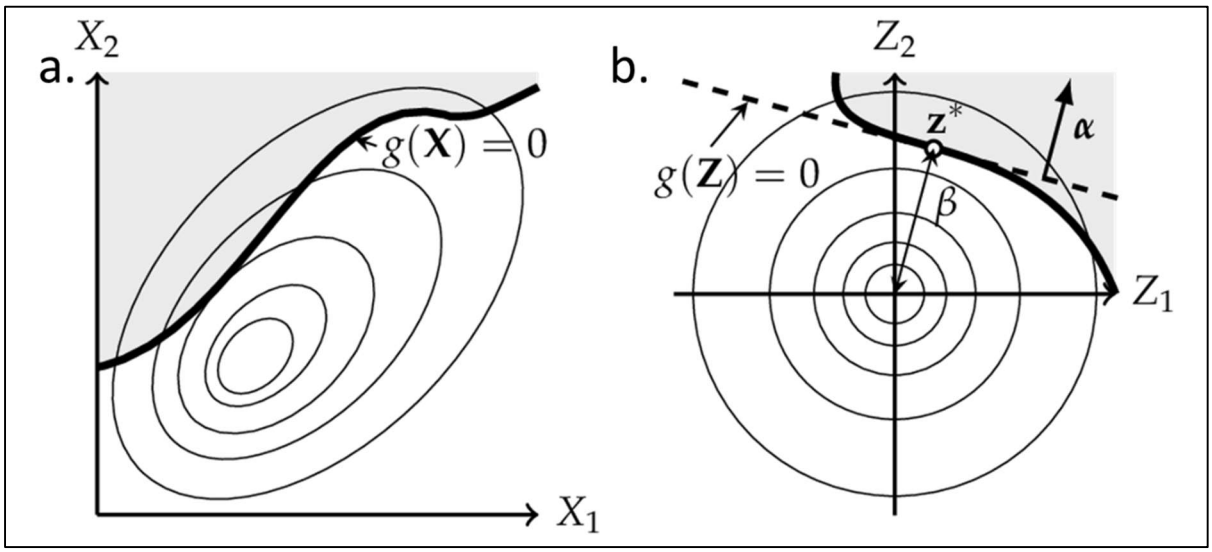

Fig. 4.6: (a) Limit state function g(x) stated in the physical space using two random variables (X1 and X2), (b) after normalization to zero average with the design point z*, reliability index β and the normal vector to the failure surface α (modified after Madsen et al., 2006).

4.3 Numerical simulation

A seismic data-driven field-scale geomechanical modeling is carried out to evaluate the rocks' failure and deformation potential in both static and dynamic conditions. The proposed workflow is illustrated in figure 4.7, which is used in **Paper-3 and -4**. Irrespective of the limitations, this modeling approach is a new method that is introduced in this research. The key processes are described below:

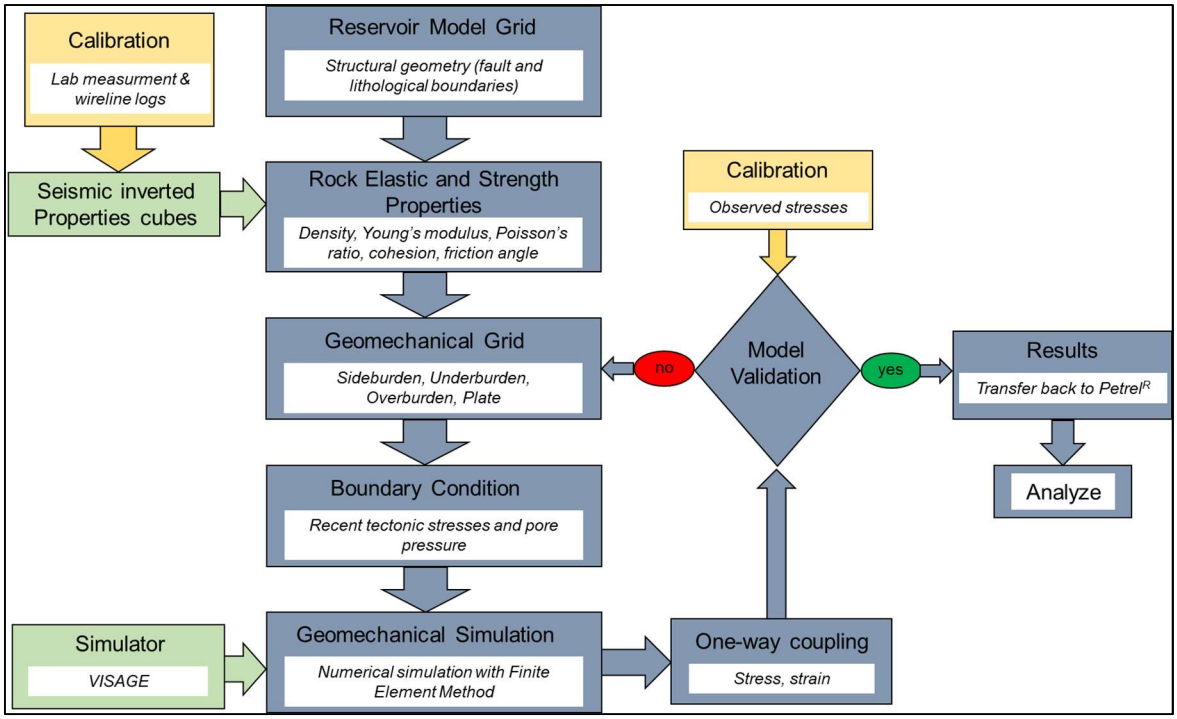

Fig. 4.7: The proposed seismic data-driven geomechanical-modeling workflow used in **Paper-3 & -4.**

4.3.1 Structural framework

The structural geometry of the model is the first step to building a field-scale 3D model grid. The lithological boundaries (i.e., Formation tops) are interpreted from the post-stack seismic volumes and then converted into time surfaces. During the interpretation process, the displacement of the faults (both major & minor) has been considered. The surfaces have considered fault influence. These same surfaces are used to build the reservoir grid.

4.3.2 Rock property cubes

Based on the theory described in section 2.3, the seismic inverted acoustic impedance (AI), P- to S-wave ratio (Vp/Vs), and density (ρ) cubes are obtained. The geomechanical properties such as Young's modulus (E) and Poisson's ratio (υ) cubes have been estimated using equations 4.8 and 4.9 (**RP-4**). The dynamic E later converted into static by using a function, wherein the shallow section $E_{static} \approx 1/5E_{dynamic}$, and deeper interval $E_{static} \approx 1/3E_{dynamic}$ have been implemented (Herwanger and Koutsabeloulis, 2011). Static υ is assumed to be equal to the dynamic υ ($\nu_{static} \approx \nu_{dynamic}$). In addition, the unconfined compressive stress (UCS) is estimated from the P-wave velocity using the equation proposed by Horsrud (2001):

$$UCS = 0.77V_p^{2.93} \tag{4.27}$$

where Vp is in km/s and UCS is in MPa.

Additional properties such as volume of shale (Vsh) and porosity (Phi) cubes are also estimated using the following equations (**RP-2**):

$$V_{sh} = \frac{\left\{\rho_{ma} - \frac{AI}{V_{Pma}} - \left[1 - \left(\frac{V_S}{V_P G\alpha}\right)^{\frac{1}{n}}\right]\left[AI\left(\frac{1}{V_{Pw}} - \frac{1}{V_{Pma}}\right) - (\rho_w - \rho_{ma})\right]\right\}}{\left[(\rho_{sh} - \rho_{ma}) - AI\left(\frac{1}{V_{Ps}} - \frac{1}{V_{Pma}}\right)\right]} \tag{4.28}$$

where AI is in g/cm^3*m/s, Vp and Vs are in m/s. G is the mineralogy/shaliness coefficient, α is Vs/Vp ratio of the mineral/rock matrix, n is stress/cementation coefficient, Vpma, Vpsh, and Vpw are the P-wave velocities (in m/s) of the mineral matrix (i.e., quartz), shale pole and water pole.

$$Phi = 1 - \frac{^{0.001429AI - J}\left[1 - \left(\frac{V_S}{V_P G\alpha}\right)^{\frac{1}{n}}\right]^{[0.00024AI + J - 1]}}{\left[(\rho_{ma} - J) - AI\left(\frac{1}{V_{Pma}} - 0.001429\right)\right]} \tag{4.29}$$

where Phi is porosity in fraction and J is calibration coefficient (with values 1 to 4).

5. Scientific contributions

5.1 Summary of papers

This Ph.D. dissertation comprises four papers (**Paper-1 to -4**), four relevant papers (**RP-1 to -4**), and four conference proceedings (**CP-1 to -5**) from the three sub-group (Fig. 4.1). The **Paper-1, RP-1,** and **CP-1 to -4** represent the G&G characterization of the caprock and reservoir, and **Paper-2** and **RP-2** reveal the probabilistic structural reliability of faults and caprock. The last two papers (**Paper-3 & -4**) and **RP-4** are from the geomechanical modeling sub-group and illustrated a stress-strain one-way coupling method with the seismic inverted properties. However, the additional four relevant papers (**RP-1 to -4**) and four conference proceedings (**CP-1 to -4**) have not been summarized in this subheading (5.1) but only described the journal papers (**Paper-1 to -4**). The finding from the relevant papers and conference proceedings have been considered in the discussion section under the sub-heading *5.2*. The papers presented here used the Smeaheia area as an example, but the proposed methods are applicable in any injection site characterization globally. The papers follow the chronological sequence; hence, the summary follows the same order. The summary of each paper, including motivation and objectives, material and methods, and key findings, is presented following the research sub-groups.

5.1.1 Geological and Geophysical Characterization

Paper-1:
Organic-Rich Shale Caprock Properties of Potential CO_2 Storage Sites in the Northern North Sea, Offshore Norway

Motivation and Objectives

One of the critical factors for CO_2 injection within a saline reservoir is the change in pore pressure, which ultimately changes the state of effective stress (i.e., principal stress minus pore pressure) and controls deformation and failure of reservoir-caprock pairs (Verdon et al., 2013). Additionally, hydrological and geochemical processes influence the effective stress, potentially affecting the geomechanical properties of caprocks (Norton, 1984; Johnson et al., 2005; Shell-Report, 2014). A potential consequence is the shear fracture or failure of caprock when shear stress exceeds the shear strength. This event depends not only on failure criteria but also on the caprock's ductility or brittleness (Nygård et al., 2006). Brittle deformation more likely occurs when a material is stiff and has higher shear strength. Thus, lithified shales are more fragile than young and uncemented mudrocks (Nygård et al., 2006). Rocks with certain mineralogy have less effect on brittleness with increasing pressure and temperature (Wang and Gale, 2009). However, all caprock properties' processes are very complicated and depend on the depositional and diagenetic processes. These complexities of caprock properties motivate us to carry out this research. The main objective is to evaluate the effect of depositional and diagenetic processes on the mechanical properties of caprocks by petrographic, petrophysical, rock physical, and geophysical interpretations.

Material and Methods

The caprock's depositional variations within the sub-basins are established by analyzing the gamma-ray shape and stacking patterns. Due to differences in depositional environments, the effect on the caprock compaction behavior is investigated by integrating petrographical analysis of core and cutting samples from three wells and by rock physical analysis of wireline log data from 27 exploration wells. Three rock physics templates (i.e., Vp versus ρ; E versus υ; $\lambda\rho$ versus

μρ) are used where the wireline log data are interpreted using the published background trends. The effect of kerogen type, maturation level, and deposition environment on caprock properties within the study area are also evaluated. Caprock property, such as brittleness, is estimated using two mineralogy and two elastic property-based, empirical relations. Finally, the seismic inversion method is assessed for the possibility of extracting caprock properties from seismic data.

Key findings

- The high-energy NE-SW trend following the Troll fault zone separates the study area into two paleo-depositional regions where the NW part has high energy silts deposited compared to fine-grained clay-bearing zones in the SE part. However, soft clay content and a higher percentage of organic matter are found in the NW and SW corners of the study area (far from the coastal plain).

- Draupne and Heather formations in the study area showed a wide range of elastic and geomechanical properties. The data clustering, irrespective of diagenetic variation, makes it difficult to assess the properties from seismic data.

- A strong relationship is found between the rock mineralogical composition and caprock properties (i.e., elastic and geomechanical parameters).

- The mechanical properties of the studied caprocks appear to be ductile. However, Heather Formation is comparatively less ductile compared to Draupne Formation. The brittleness increment trend showed a significant difference with the previously published reference curves and increased with increasing AI, E, μρ, and λρ.

- The sparsely distributed (primarily immature) TOC within the study area has an insignificant impact on the geomechanical properties of the studied caprocks. The geomechanical properties of caprocks are complex, and further work is needed to quantify the TOC effect.

5.1.2 Analytical assessment

Paper-2:
Probabilistic Analysis of Vette Fault Stability in Potential CO_2 Storage Site Smeaheia, Offshore Norway

Motivation and Objectives

Fault sealing potential is a critical factor that needs to be evaluated in any CO_2 injection-related activity where the trapping structure is related to the faults. However, the uncertainties in the subsurface associated with fault properties (i.e., fault rock lithologies, strength, and geometry of fault) pose a significant challenge to assessing the fault's stability. Additionally, the operational uncertainties associated with pore pressure change during CO_2 injection into a saline aquifer can be another critical factor. In the case of a supercritical CO_2 (sCO_2) injection, additional processes such as hydraulic aperture evolution, hydrological property changes, effective stress induction, and mechanical strength degradation can influence the effective stresses in fault planes, which can lead to reactivation and failure of faults (Rutqvist et al., 2007; Park et al., 2020). Due to these complexities, it is crucial to assess the fault structural reliability

in any CO2 injection site. The motivation of this work is to evaluate the fault probability of failure, where Vette fault from the Smeaheia area is used as an example.

Material and Methods

This study evaluated the stability of Vette fault probabilistically using the Monte-Carlo simulation (MCS) and the First Order Reliability Method (FORM). The fault stability is evaluated using analytically estimated stress conditions acting on the fault plane and the Mohr-Coulomb failure criteria. The uncertainty of the fault-rock strength properties is handled by interpreting four different fault smearing scenarios and their likelihood based on the study area's geological understanding. The overall VF system reliability is estimated based on the qualitative approximation of all four scenarios using an event tree technique. The likelihood of each fault rock strength scenario and the corresponding probability of failure is embedded in the system failure number, which could be a reasonable estimation for the future project decision. The pore pressure/stress coupling, also known as the reservoir stress path, is incorporated to evaluate the complex poroelastic interaction due to the fluid injection in the horizontal stress field. Finally, the relative importance of different parameters (i.e., vertical and horizontal stresses assumptions, pore pressure, stress path, fault rock strength, etc.) on fault stability is evaluated.

Key findings

- The cohesionless fault scenario has the highest failure probability, while the fault rock properties equivalent to the Rødby Formation case show the lowest value. In addition, the difference between the initial condition and the after-injection scenario is minimal.

- Both deterministic and probabilistic sensitivity analyses revealed that the in-situ stresses (vertical and horizontal) and fault rock strength properties (cohesion and friction angle) are the critical parameters influencing fault stability.

- Integrating the likelihood of possible scenarios using the event tree method can quantify the overall structural failure. The failure value estimated using this approach better represents total failure compared to the case considering only the most likely scenario because the event tree method considered all the possible scenarios. However, caution needs to be taken for the low likelihood scenarios if the low likelihood scenario's failure probability is significantly higher than other likely scenarios.

- The Vette fault system reliability analysis' probabilistic value suggested that the fault seems to be structurally reliable. Hence, it may act as a potential barrier during the injection of CO_2 into the Alpha structure.

5.1.3 Numerical modeling

Paper-3:
Effect of overburden spatial variability on field-scale geomechanical modeling in CO_2 storage site Smeaheia, offshore Norway

Motivation and Objectives

During drilling a well, there has been good coverage of data (i.e., cores, wireline logs, pressure data, etc.) acquired in the reservoir section. The caprock and overburden sections have been

ignored most of the time. This data gap is reflected in most of the geomechanical modeling works (i.e., Grollimund and Zoback, 2003; Vidal-Gilbert et al., 2010; Fokker et al., 2011; Ouellet et al., 2011; Fischer and Henk, 2013; Tenthorey et al., 2013; Olden et al., 2014; Newell et al., 2017; Mandal et al., 2021), where simple assumptions are used for overburden rock property evaluation. The results from a simple modeling approach might hide possible risks. Therefore, a high-resolution spatial gridded overburden section is needed in geomechanical modeling work to assess the realistic overburden rock deformation (i.e., subsidence or heave). This limitation motivated to carry out this study where the sensitivity of spatially gridded seismic driven overburden properties is analyzed. A seismic data-derived properties-based approach has been implemented, which has been used for geomechanical models only for reservoir and caprock intervals but not the whole subsurface (Sengupta et al., 2011). This gap in geomechanical model building workflow motivates us to carry out this research to integrate all the pieces and build a robust model to answer the critical questions regarding associated risks during CO_2 injection into the prospective reservoirs.

Material and Methods

A one-way coupling geomechanical modeling workflow has been proposed (Fig. 4.5). The 3D seismic inverted property cubes, which are calibrated with lab measurement and wireline logs during estimation, are directly used in the 3D structural grid. The seismic resampling function in the Petrel-2019 earth modeling module is used to distribute the properties within the model grids. However, the structural grid is constructed before using the seismic interpreted time surfaces. Afterward, the whole reservoir model (i.e., structural grid and properties) is converted into depth using the Smeaheia average velocity cube. Geomechanical grid is introduced in-depth domain by adding sideburden, underburden, overburden, and plate with the reservoir grid. The boundary conditions (i.e., present tectonic stresses and pore pressure) have been defined. The model is now ready for numerical simulation; hence, the VISAGE simulator is used to run one-way coupling (i.e., changing strain with stress change). After validation, the numerically simulated field-scale 3D model is transferred to the Petrel-2019 software for interpretation.

Key findings

- The effect of overburden properties on sea floor deformation is significant. For instance, the simplified average constant overburden properties doubled the sea floor uplift compared with the model using the seismic inverted spatial properties. In addition, the Mohr-Coulomb failure envelopes of overburden rocks indicated the importance of spatial overburden properties within the geomechanical modeling workflow.

- Vertical rock deformation increases with time in both seafloor and reservoir-caprock interface. However, the vertical rock uplift is slightly higher in the reservoir-caprock interface compared with the sea floor.

- Although the induced pressure increase in each time step used a constant change, the rock deformation spatially varied due to the variation in mechanical properties.

- The simplified assumption of overburden properties in the geomechanical model effect the CO_2 storage project significantly by influencing the capacity and injectivity of any site.

Paper 4:
3D field-scale geomechanical modeling of potential CO_2 storage site Smeaheia, offshore Norway

Motivation and Objectives

Paper-4 is the continuation of **Paper-3** where the same model grid and properties have been used. However, the total pore volume and pore compressibility influence the rock mechanical behavior by changing different injection-induced pore pressure for the same amount of CO_2 injection. This difference in pore pressure along with the spatial variation of the rock properties might influence the rock failure behavior. This is our motivation to carry out this study, where the sensitivity of the pore volume and pore compressibility have been assessed. Furthermore, a comparative analysis between different injection locations in the Smeaheia site has been evaluated.

Material and Methods

This paper also used a similar workflow where seismic inverted property cubes were incorporated directly into the model grid. However, based on the various pore volume and pore compressibility conditions, nine different models have been simulated where the worst-, base- and best-case models are presented in the result section.

Key findings

- The pore volume and pore compressibility significantly influence the mechanical rock failure and deformation. The low pore volume with reference compressibility was estimated ~74 cm vertical upliftment on the reservoir-caprock interval, while the pessimistic compressibility model with base pore volume calculated ~40 cm uplift. Irrespective of considerable vertical upliftment, no caprock failure is observed in any models. However, although there is no reservoir rock failure in in-situ stress state conditions, tensile failure occurred after injection pressure change scenarios.

- The Mohr-Coulomb failure risks varied within the studied locations. The Alpha structure indicated low mobilized shear stress/strength compared to the Beta and Mid-Model locations based on the assessment. However, a fluid simulation model should be implemented to evaluate the plume migration to build confidence.

5.2 Discussion

The main objective of this Ph.D. thesis is to evaluate the geomechanical risks associated with top seal (caprock and fault) and overburden. One of the crucial criteria for reliable CO_2 sequestration is to have an impermeable seal, which means caprock needs to be effectively impermeable. The bounding faults (fault-based closures) must remain sealed before and after injection. In addition, the effect of spatial overburden interval is often overlooked, and therefore needs to be included within the risk assessment. This study integrated different investigations and proposed a site-specific top seal characterization workflow for evaluating geomechanical risks. Another integrated probabilistic top seal assessment template is also proposed to help project decisions in the initial stage.

5.2.1 Caprock characterization

Caprock shale acts as the barrier for vertically migrating CO_2 plumes where the integrity as a top seal is indicative of the ability for the shale to hold the CO_2, up to a certain amount of fluid pressure prior to failure. The quantitative assessment of the integrity of shale depends on the rock's geomechanical properties including brittleness/ductility. The brittleness properties of the rock and the failure criteria often control the injection-induced fracturing within shale (Fig. 5.1). However, the geomechanical properties of rock (brittleness) are complex and depend on many factors including mineral composition, lithology, grain size, thickness, pressure regime, compaction state, temperature, strain rate, fluid composition, TOC type, maturation, and regional stresses, etc. (Rutqvist and Tsang, 2002; Walles, 2004; Bennion and Bachu, 2005; Nygård et al., 2006; Rutqvist et al., 2007; Halland et al., 2011; Halland and Riis, 2014; Nooraiepour et al., 2017). The effect of depth on brittleness is compounded and can work in both directions because pressures, temperature, diagenesis, and TOC maturation are functions of depth (Johnson et al., 2022a). An increase in depth generally increases pressure and temperature, hence the degree of diagenesis, and tends to mature TOC. Walls (2004) pointed out that diagenetic alteration toward silica enrichment due to the smectite to illite transition enhances brittleness, and lower TOC typically increases the brittleness of the shale. However, for a rock sample with a specific composition, increases in pressure and temperature decrease brittleness (Wang and Gale, 2009). Mineralogy and rock fabric within shale changes with increasing depth because of depositional and diagenetic modifications leading to sudden caprock failure/fracturing if brittle and gradual deformation if ductile (Fig. 5.1).

Brittleness scale (i.e., brittle to ductile), while not universal, significantly varies between caprock shales. The transition value from brittle to ductile also varies considerably. For instance, a comparison between the Upper Jurassic Draupne shale with Middle-Lower Jurassic Drake caprock in the study area showed distinct differences where the organic rich Draupne Formation represents comparatively more ductile rock than the Drake Formation (Fig. 5.2). However, a Mohr-Coulomb failure plot of both caprock shales in in-situ stress state conditions indicated Drake caprock failure chances are lower than the Draupne shale (Fig. 5.3). Although the definition of caprock strength properties differs between shales, the findings indicate that site-specific and formation-specific analysis is required for better caprock geomechanical characterization.

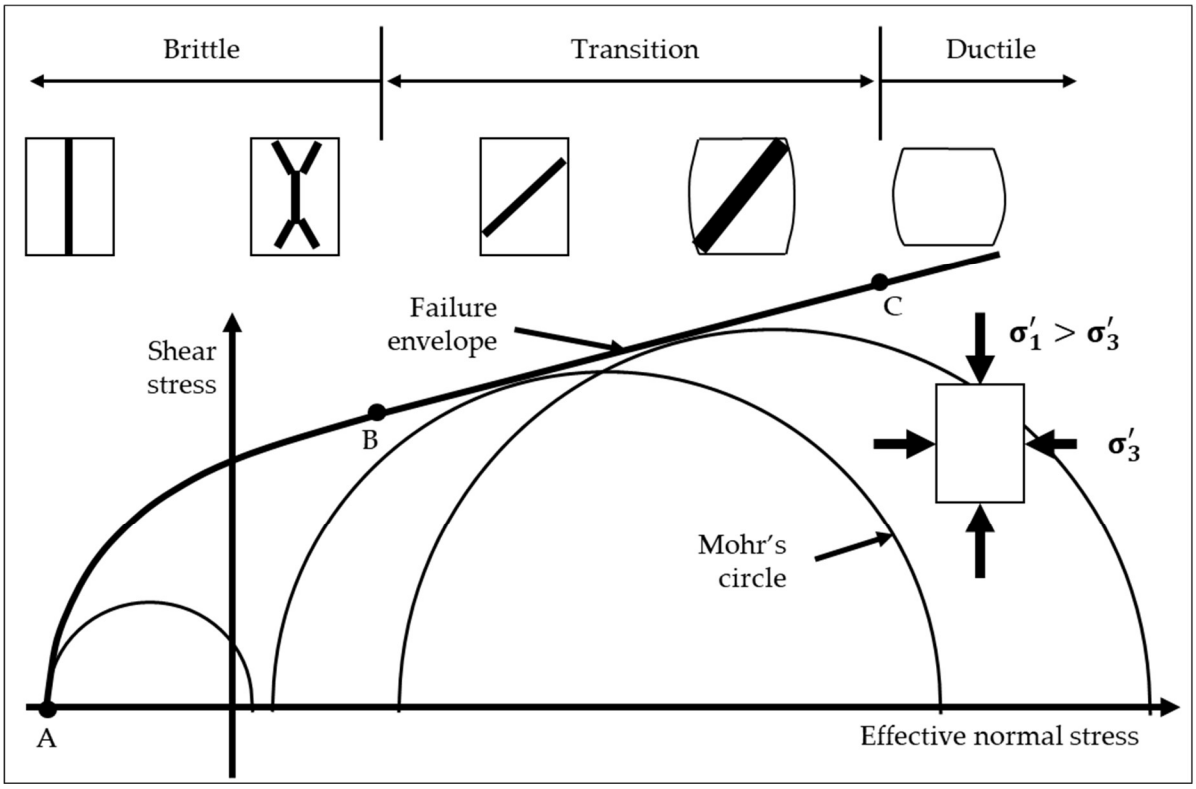

Fig. 5.1: The relation between caprock ductility and failure types are illustrated in the Mohr-Coulomb failure chart (modified from Nygård et al., 2006).

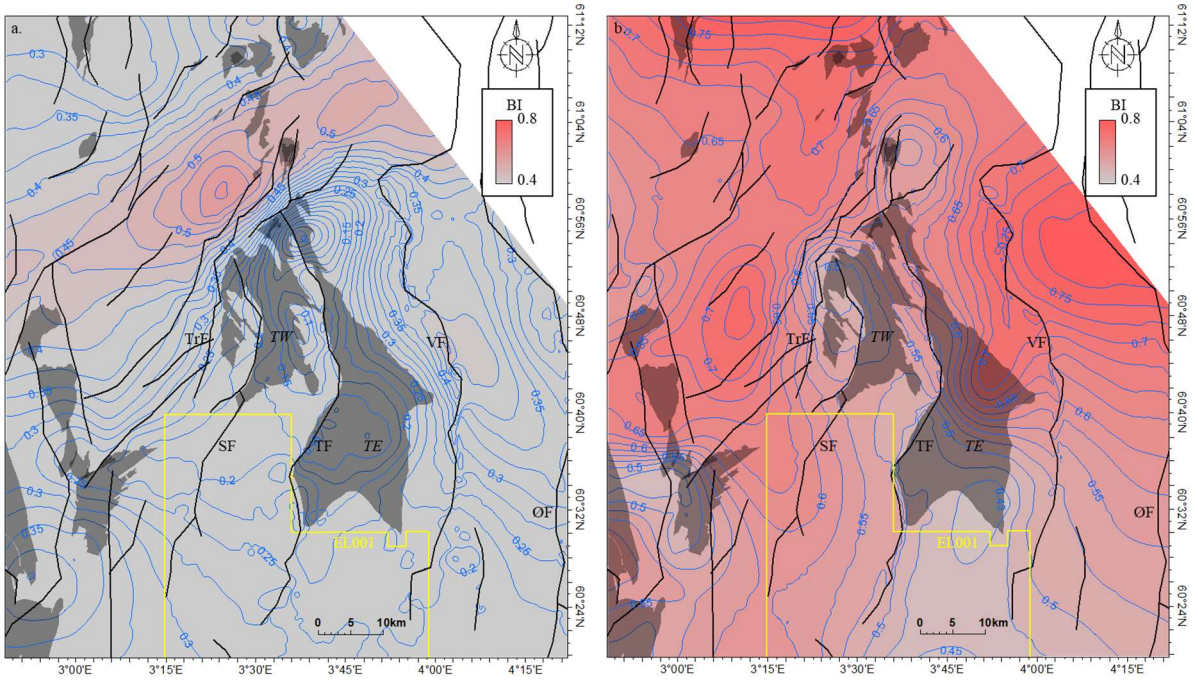

Fig. 5.2: Brittleness Indices maps of Draupne (a) and lower Drake unit (b) estimated using equation 4.16 illustrated lateral variation in the study area. For comparison same color scale has been used. The black lines represent major (TrF – Troll fault; SF – Svartalv fault; TF – Tusse fault; VF – Vette fault; ØF – Øygarden fault) and minor faults while the yellow polygon (EL001) is the first CCS license in Horda Platform area. The grey shaded polygons indicated hydrocarbon fields (*TE – Troll east; TW – Troll west*) and discoveries in the area.

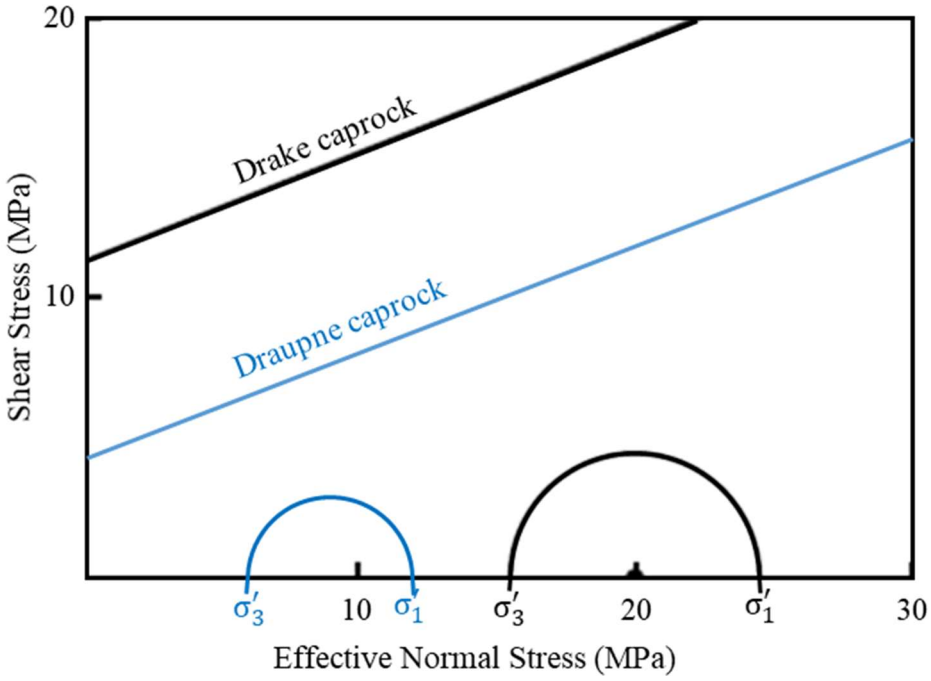

Fig. 5.3: Mohr-Coulomb failure diagram of Draupne and upper Drake caprock shales in in-situ stress state conditions show the difference between the two shales.

Geomechanical behaviour of the Draupne and Heather caprock shale is analyzed based on the depositional and diagenetic processes acting upon them (**Paper-1, RP-1, CP-1 & -2)**. A strong correlation between mineral fractions, brittleness indices, and acoustic properties is observed. This relationship validates the possible extraction of mechanical properties from seismic (**Paper-1**). A complex relationship is observed between the total organic carbon (TOC) and brittleness (i.e., brittleness property changes with the maturation of source rock shales). The maturity of TOC played a crucial role where the immature TOC acts as a ductile mineral-like clay. However, the maturation and expulsion of hydrocarbons are difficult to assess in relationship to the influence it has on the overall shale caprock due to the complexity of the processes. In addition, a thick hydrocarbon column has a considerable effect on the caprock's geomechanical properties (i.e., Young's modulus and Poisson's ratio; **RP-1**). The Draupne and Heather formations in the Horda Platform area show ductile to less-ductile behavior indicating good-quality top seal potential. However, the Draupne shale represents a more ductile formation than the Heather formation as indicated by lower acoustic impedance (AI) and Young's modulus (Fig. 5.4a&b).

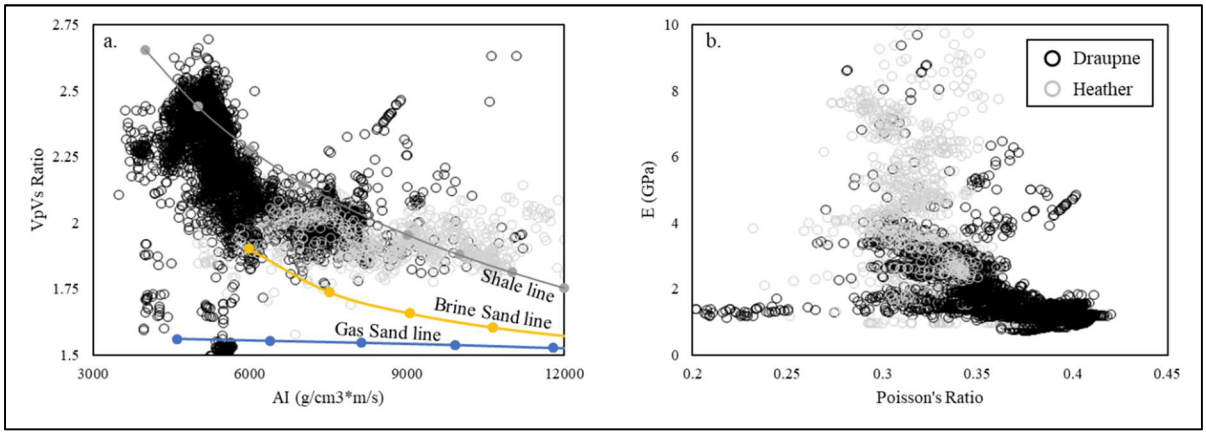

Fig. 5.4: Draupne and Heather formation shales from the studied wells are illustrated in the (a) Vp/Vs ratio versus AI and (b) Young's modulus versus Poisson's ratio plots.

Compared to wireline logs, mineralogical estimation of rocks is limited and mainly available for the reservoir interval. Therefore, the correlation between mineralogical brittleness indices (MBI) and elastic property based brittleness indices (EBI) is critical to assess the brittleness property of any caprock shale. The Upper Jurassic caprock shale data points from the North Sea and the Barents Sea indicates a trend between EBI and MBI, where 0.65 corralation coefficient has been estimated (Fig. 5.5b). EBI also show a strong negative trend with ductile mineral assemblages (Fig. 5.5a). There relationships have increased the confidence of characterizing caprock brittleness from wireline logs and from seismic, where mineralogical estimation is not present.

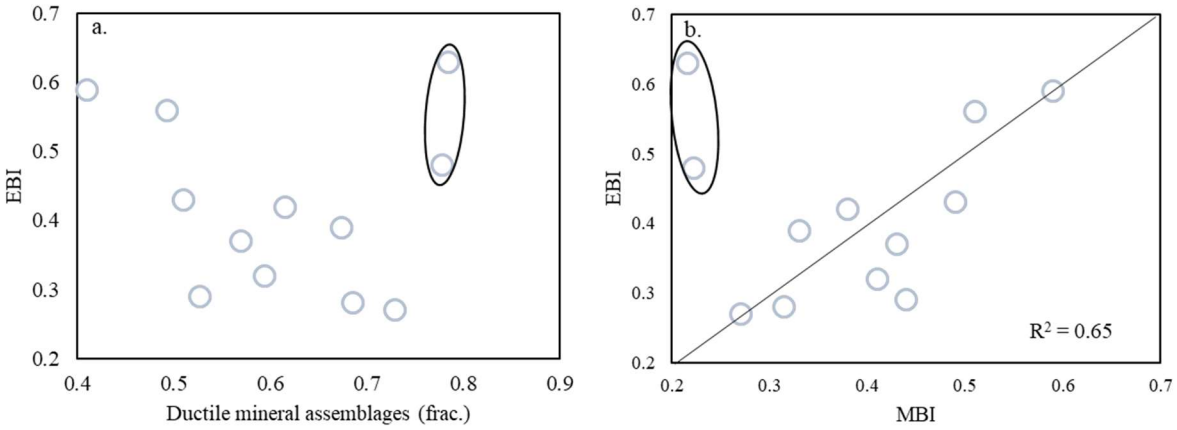

Fig. 5.5: Crossplots show correlation between the elastic property based brittleness indices (EBI) versus ductile mineral assemblages (a) and mineralogy based brittleness indices (MBI) (b). Data points plotted here are represented the Upper Jurassic organic-rich shale from the North Sea and the Barents Sea.

In addition to the geological and geophysical characterization of the caprock, the structural reliability as a top seal is also evaluated. The structural integrity of the Draupne caprock shale is assessed in the Alpha prospect at the Smeaheia location (**RP-3**). Based on the Mohr-Coulomb failure criteria, there are very low chances of caprock shear failure in the Alpha injection site. This result can be validated by the G&G observation with a ductile Draupne top seal.

5.2.2 Fault seal analysis

Fault-related gas leakage is a possible threat for CCS because the potential reservoirs are fault-bounded structures. There may be the possibility of fault reactivation due to injection-related pressure build-up and micro-seismicity. However, the subsurface fault architecture and fault-zone rock strength properties are often highly uncertain because of the seismic resolution (sub-seismic fault zone). Additionally, very few wells penetrated through the fault itself. The scenario-based analysis in **Paper-2** indicated the significance of the probabilistic event tree approach for the fault integrity study. The event tree method allows us to consider the less probable but nonetheless significant cohesionless fault scenario (i.e., case 1 in fig. 5.6). Structural failure of a system (i.e., Vette fault system) will provide guidelines for future investigation. According to the Mohr-Coulomb failure criteria, the probability of Vette fault leakage in the Alpha location is low.

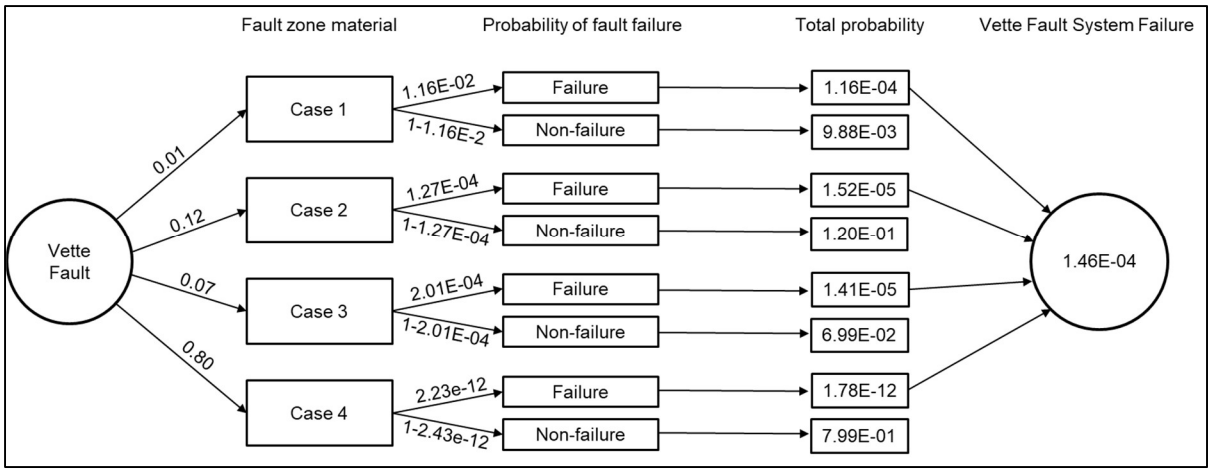

Fig. 5.6: Estimation of Vette fault system failure using the event tree method.

5.2.3 Overburden rock characterization

The major faults present in the study area terminate near the overburden (Fig. 5.7). Significant numbers of small-scale polygonal faults/fractures are present in the overburden section in the Horda Platform area (Fig. 5.7). If fault parallel migration of injected CO_2 takes place, the overburden rock needs to hold said migrated fluids. Therefore, the overburden rock characterization is crucial in the study area. Nevertheless, the polygonal fault assessment study is not included in the Ph.D. dissertation. There is gas leakage observed in the northern part of the Troll west gas field (Fig. 5.7b). Overburden Hordaland clay acted as a secondary caprock where the migrated gas might accumulate. The gas leakage scenario from Troll west added confidence for CO_2 injection in the study area since a secondary seal exists within the overburden interval. Going through this process also highlights the importance of characterizing overburden rock for all injection sites.

Geomechanical properties of the overburden spatially varied (**Paper-3**), which influenced the fracture pattern and intensity within the same rock unit. Geomechanical modeling of the Smeaheia area (**Paper-3 & -4**) reveals that the spatially gridded overburden properties significantly influence the injection-induced rock deformation (i.e., seafloor heave). This observation indicated the importance of the overburden rock properties in numerical simulation and for the overall project.

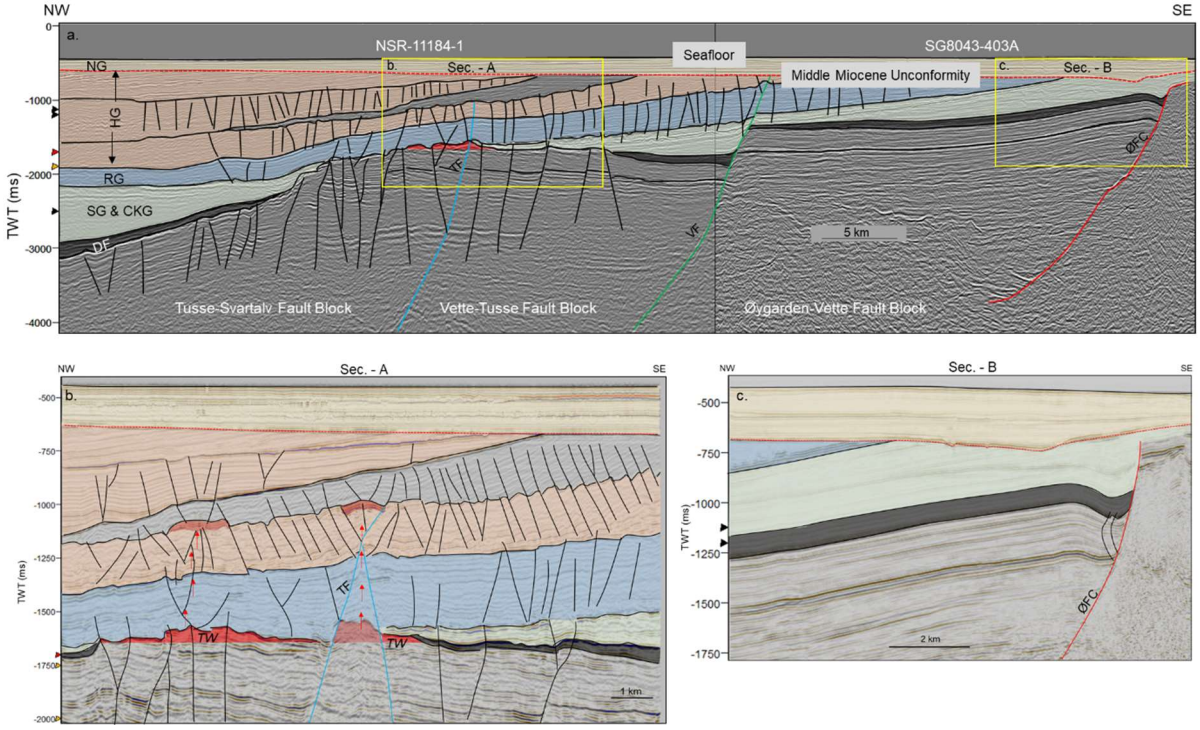

Fig. 5.7: SW-NE 2D seismic (Surveys NSR-11184-1 & SG8043-403A) cross-section shows major faults (TF - Tusse fault; VF – Vette fault; ØFC – Øygarden fault complex) with numerous polygonal faults within the overburden from the northern Horda Platform area (a). 3D cross-sections from Aurora (GN10M1; Sec. - A) and Smeaheia (GN1101; Sec. - B) seismic cubes are also presented in (b) and (c), respectively. Possible gas leakage from Troll west (TW) and trapped within the Hordaland clay is illustrated. The overburden intervals are: NG – Nordland Group; HG – Hordaland Group; RG – Rogaland Group; SG – Shetland Group; CKG – Cromer Knoll Group & DF – Draupne Formation.

5.2.4 Nanoscale caprock mechanical properties

Rocks mechanical property (stress or stiffness) is usually estimated from conventional laboratory experiments using unconfined and confined triaxial compression and shear tests (Lama and Vutukuri, 1978), true triaxial shear tests (Colmenares and Zoback, 2002; Minaeian et al., 2014), and ultrasonic techniques (Wang, 2002). However, these laboratory tests often require relatively large core samples that are sometimes difficult to obtain (Hongyan et al., 2013; Tianshou and Ping, 2014) and often suffer from high inter-sample variability (Du et al., 2020). Nano-indentation techniques proposed by Oliver and Pharr (2004, 1992) use comparatively small cuttings or core samples, and do not have the same failings as these other techniques. The mechanical properties (i.e., H, C, and indentation modulus M) can be determined from the indentation depth which is generated by applying a load to the materials. This might resolve the experimental data limitation issues in caprock and overburden section. Nano-indentation based laboratory mechanical properties showed promising results (**CP-4**). A considerable match has been observed between the nano-indentation and triaxial test dataset. A strong correlation between the nanoscale Young's modulus and clay fraction has been identified (Fig. 5.8), which is also seen in the wireline log-based analysis. This analysis indicated the viability of the nano-indentation method to estimate the laboratory based mechanical properties for intervals where only the cutting samples are available.

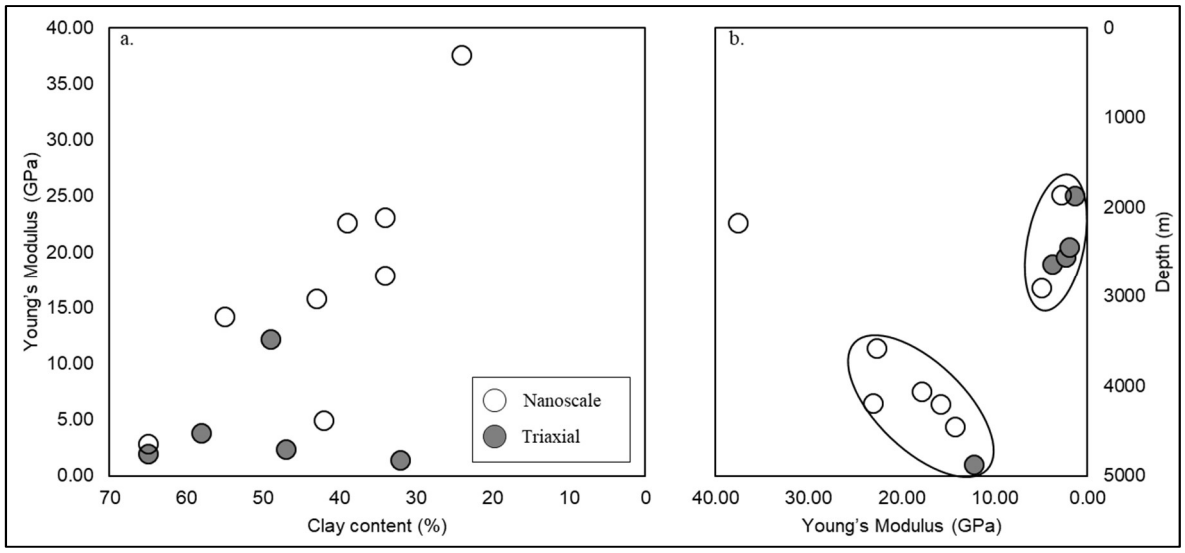

Fig. 5.8: Relation between the nanoscale Young's modulus versus total clay mineral percentage of studied shale samples are illustrated as a strong correlation with a 75% correlation coefficient.

5.2.5 Seismic property driven field-scale 3D model grid

In the conventional 3D model building process, the well data points are interpolated using an algorithm such as kriging, GSG, etc. However, when the number of wells are limited, the uncertainties away from the wells increase significantly. Seismic property driven modeling approaches may resolve this issue by covering the property distributed laterally and vertically. However, the seismic inverted properties need to be validated before using them directly as an input to the model grid. For the Smeaheia injection site characterization, the inverted property cubes have been successfully estimated and calibrated (**RP-2 & -4**). Later the cubes were resampled into the field-scale 3D model grid for 1-way geomechanical simulation (**Paper-3 & -4**). However, seismic data has been used for 3D models before (Sengupta et al., 2011) but only for reservoir and cap rocks and not for the whole subsurface. The inverted property cubes allow us to use the spatial properties for the whole overburden and partial underburden model grids (**Paper-3 & -4**). Our proposed modeling workflow (Fig. 4.7) shows the practicality and possibility of evaluating the field-scale 3D geomechanical assessment.

5.2.6 Top seal assessment integrated workflow

With the fluid injection project, the injection-induced geomechanical consequences such as surface heave, new faults/fractures generation, or existing faults reactivation are addressed in this Ph.D. dissertation. This integrated approach (i.e., petrophysics, petrographic, rock physics, and seismic interpretation) to evaluate the geomechanical risks in any injection project would support the decision-maker with more confidence. Rock failure criteria is a complex process and is controlled by a combination of factors such as in-situ stress condition, pore-throat size, matrix permeability, capillary pressure, the existence of natural fractures, manner of well completion, as well as the rock properties such as elastic moduli and mineralogy (Yang et al., 2013). This study follows a sequence to evaluate caprock integrity, for example, **Paper-1** to **-4** for the Smeaheia area where the geomechanical risks are evaluated at different scales, levels, and dimensions for injection sites. The relevant papers (**RP-1 to -4**) and conference proceedings (**CP-1 to -4**) also illustrated a similar geomechanical risk assessment. While the results presented in this research are focused on the Smeaheia CCS injection site, the proposed caprock and fault-sealing analyses are valid for basin-wide prospect maturation. An integrated workflow

to evaluate site-specific top seal is proposed based on the research carried out for this Ph.D. thesis. The assessment processes are illustrated in figure 5.9.

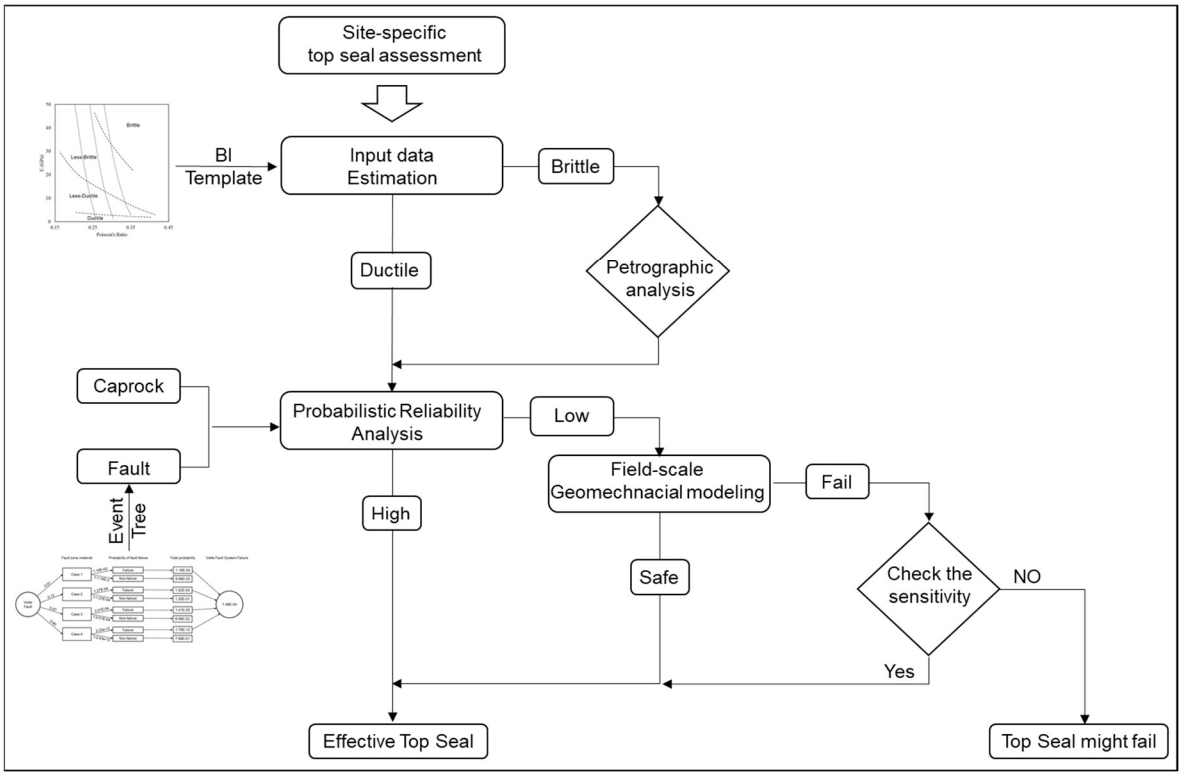

Fig. 5.9: A proposed integrated workflow to evaluate effective top seal in any CO_2 storage site globally.

In any injection site, a rock property characterization study should be carried out to identify the ductility of the top seal (**Paper-1; RP-1; CP-1 & -2**). As supporting material, the brittleness indices template can be used. If the top seal property is ductile, the probabilistic reliability analysis can be done directly. If not, an additional petrographic analysis such as XRD, SEM, and nano-indentation lab tests (**CP-4**) can be done to evaluate the mineral fraction including type, grain size, sorting, and laboratory based strength properties. After which, the analytical probabilistic structural failure analysis should be continued (**Paper-2, RP-3**). Finally, if needed, the numerical simulation can reveal the rock failure potential in 3-dimensions with different pressure change scenarios (**Paper-3 & -4**), where the seismic inverted properties should be utilized (**RP-2 & -4**). This integrated workflow can be used to assess the top seal collectively in any injection site, thereby supporting project decisions at any stage.

5.2.7 Top seal risk assessment template

A probabilistic risk assessment template has been proposed based on the brittleness indices and reliability index (Fig. 5.10). The terms 'Low, Medium, High, and Extreme' indicate the possibility of top seal failure. For instance, low indicates the chances of failure being minimum with a high-reliability index value and low brittleness indices (more ductile). On the contrary, extreme represents a brittle caprock with a low-reliability index, which may fail easily. In the initial stage of any CCS site characterization project, this tool might help assess the top seal integrity, one of the key parameters in CCS storage site characterization (IEAGHG report, 2009). However, we have to keep in mind that there are many other parameters and processes involved in seal integrity, but this template might help us to identify how much analysis we need to characterize top seal effectiveness in any CCS injection site.

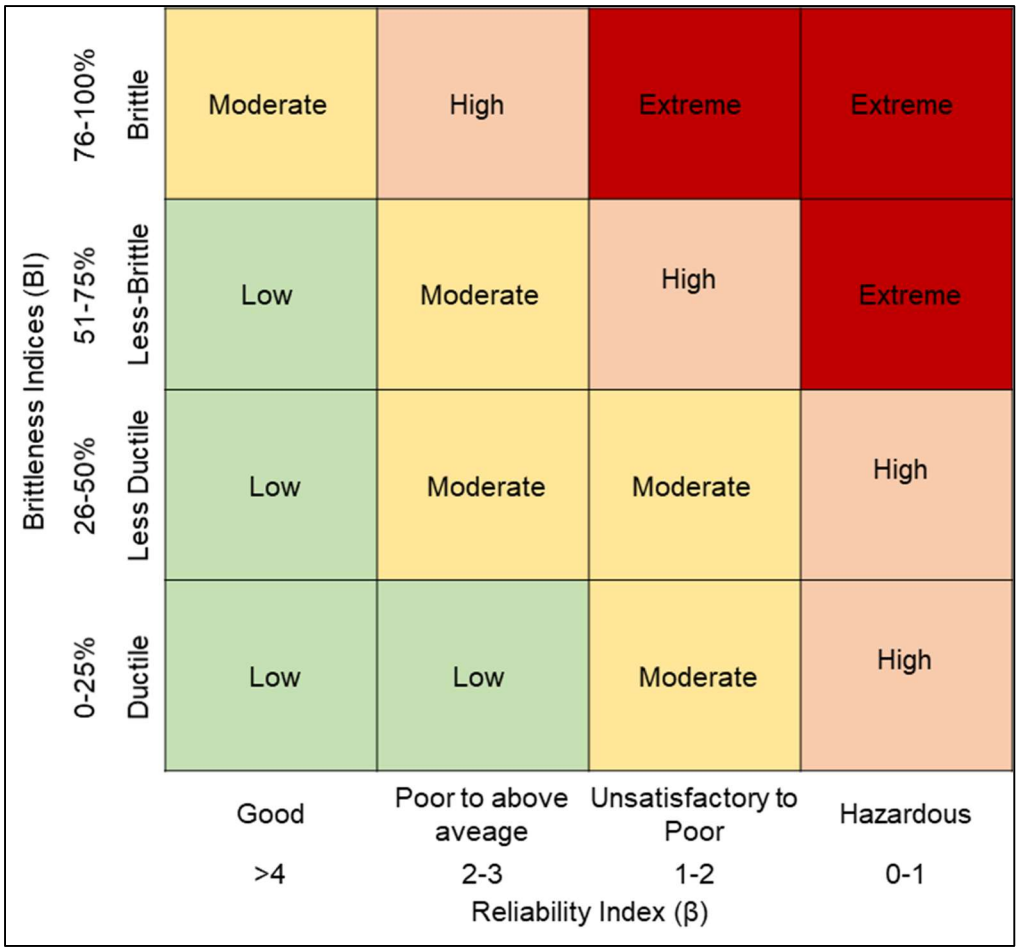

Fig. 5.10: The Brittleness Indices (BI) and reliability Index (β) based template to rank the top seal failure risk represents the intensity of the potential risk for different BI and β values.

6. Concluding remarks

In this Ph.D. dissertation, I have investigated the properties of rocks (i.e., caprocks and overburden) by integrating petrophysics, petrography, rock physics, and seismic inversion analysis. A stochastic analytical model was used to evaluate the caprock shale and fault integrity as a potential seal. Furthermore, a field-scale 3D geomechanical model has been carried out to numerically evaluate the rock failure potential. While only the overall outcome is summarized here, the specifics of the workflow and their results may be referred to in part five or any specific paper in section two.

Overall, this research has improved the understanding of the mechanical behavior of subsurface rocks. Furthermore, the approaches used in this dissertation can help the management for any injection decision. The key outcomes from this study are:

- Depositional and diagenetic effect on rock mechanical behavior is extensively analyzed in caprock shales (i.e., Upper Jurassic Draupne and Heather formations). A strong relation between mineralogy, brittleness, and acoustic properties indicated the possibilities of extracting mechanical properties from seismic.

- The proposed stochastic structural reliability method can estimate the caprock and fault failure probability. A scenario-based event tree method can reduce uncertainty. In addition, the input data sensitivity reveals the influence of relative percentage on total failure, which also allows us to focus on specific future parameters characterization.

- A robust integrated seismic data-driven geomechanical model building workflow has been proposed and tested to resolve the data limitation issues in caprock and overburden sections. In addition, seismic inverted properties directly resampling within the grid improved the spatial distribution of the properties compared to the conventional interpolation method with limited wells data points.

- The spatial overburden properties significantly influence rock deformation compared with simple constant properties.

- The proposed integrated workflow to evaluate the top seal effectiveness might be useful to any site-specific top seal characterization. Furthermore, the probabilistic risk assessment template might be a helpful tool in the CCS site characterization project.

The methods and workflows tested in this thesis have been useful in characterizing any potential fluid injection sites. The integrated workflows are not specific to any particular area; hence, they can be used to evaluate top seals anywhere.

6.1 Outlook

Many new ideas and research questions are encountered during this Ph.D. research. A couple of them are in progress to be submitted to scholarly journals, which are not included in this dissertation. Despite my interest, I do not have time to investigate any further. However, several research directions relating to this study, in my opinion, deserve further consideration:

6.1.1 Geological and geophysical characterization

Caprock geomechanical characterization workflow (**Paper-1**) focusing on the specific injection sites (i.e., Smeaheia) can be further extended to evaluate the whole Norwegian Continental Shelf so that it will not only help to identify other CO_2 injection sites but also evaluate the exploration potential. The proposed basin-specific brittleness template (Fig. 6.1) needs further improvement by including data from other NCS sub-basins, and the effect of the geothermal gradient could benefit from being added.

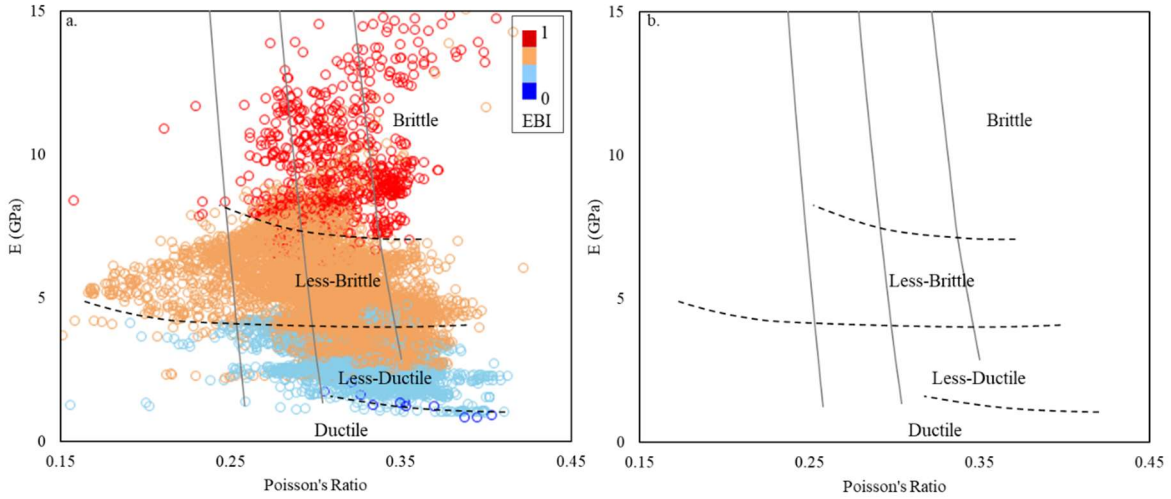

Fig. 6.1: Proposed basin-specific template shows the difference with Perez and Marfurt's (2014) classification scheme (modified after Rahman et al., 2022).

6.1.2 Analytical assessment

The proposed stochastic structural reliability method for subsurface has shown itself to be practical and appears feasible to use for the evaluation of caprock and fault integrity. However, the effect of other parameters such as mineralogy, temperature, and others can be further investigated. Furthermore, the statistical analysis of input data with a machine learning (ML) based solution can be implemented to achieve field-scale evaluation (Ahmadi Goltapeh et al., 2022). In addition, because this method is novel for the subsurface, there is no available failure chart to compare with currently. Therefore there is a future opportunity to develop a failure rank chart for subsurface structural reliability analysis. The expected performance table could improve the reliability index-based probabilistic risk assessment template (Fig. 5.10).

6.1.3 Numerical modeling

Although the proposed one-way geomechanical modeling workflow estimated the mechanical rock failure and deformation, many improvement opportunities are available. Due to the temperature difference between the injected reservoir interval and the cold injected CO_2, there might be a significant influence on mechanical behavior. This indicates a possible addition of temperature within the workflow. Faults should be included within the structural grid and analyzed for potential leakage.

One of the limitations of the proposed workflow is the pore pressure change before, during, and after injection. Integration of a fluid simulation model would reduce the pressure change uncertainty and allow for an estimation of optimal reservoir capacity and injectivity. Evaluating the optimal capacity and injectivity is generally one of the key criteria for site evaluation. A seismic-property-driven fluid flow model will be a future research opportunity where the

injection rate, reservoir capacity, and spatial and vertical injection location sensitivity can be evaluated. This approach will increase the confidence in the leakage-free subsurface injection of excess atmospheric CO_2.

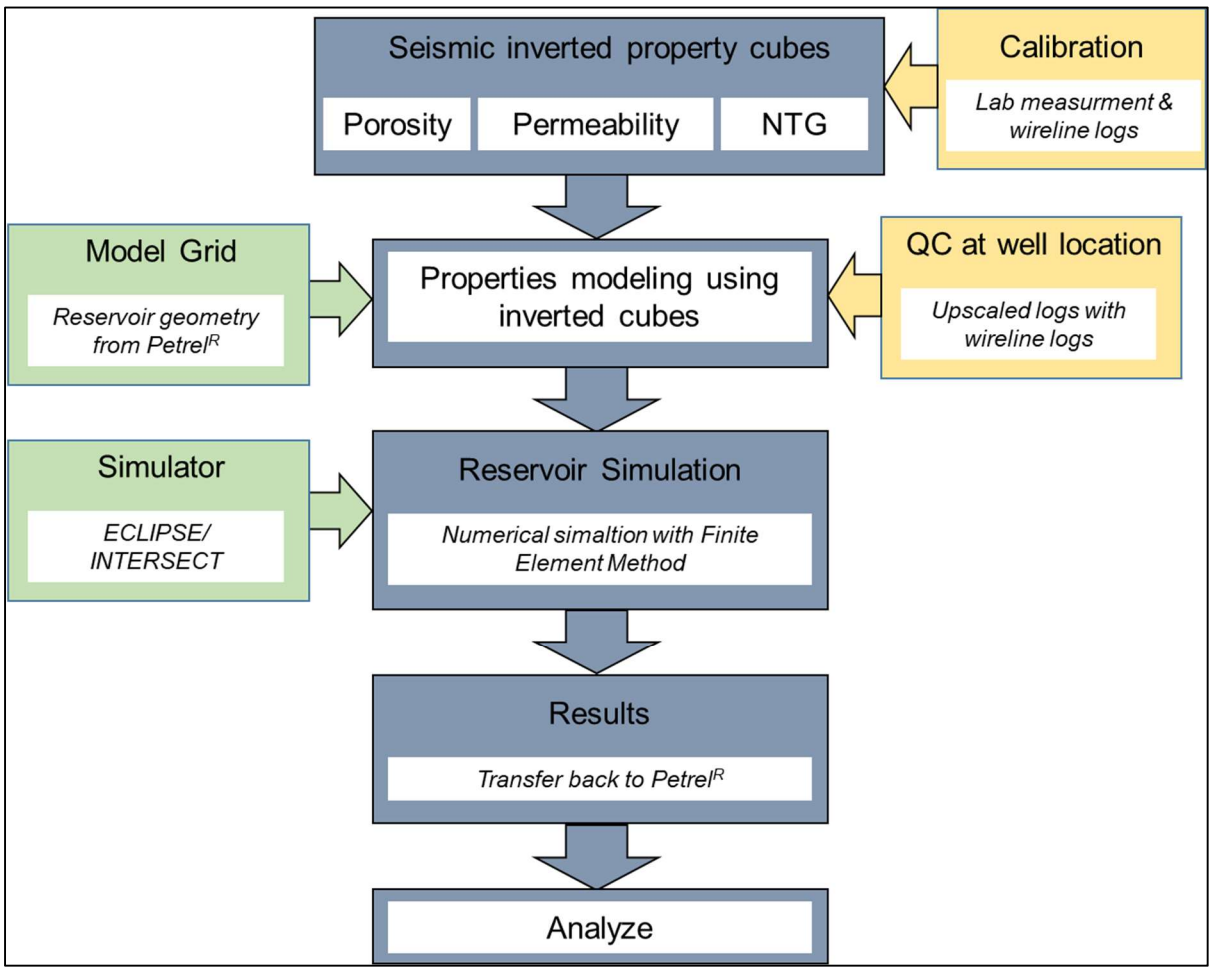

Fig. 6.2: The workflow of seismic property based fluid flow model should implement for optimal capacity and injection rate estimation.

Bibliography

Abay, T.B., 2017. Diversity of Petroleum in terms of Source Rock Properties and Secondary Alteration Processes. A study of source rocks, migrated petroleum, oils and condensates from the Norwegian Continental Shelf.

Addis, M.A., 1997. The stress-depletion response of reservoirs, in: SPE Annual Technical Conference and Exhibition. Society of Petroleum Engineers.

Ahmadi Goltapeh, S., Rahman, M.J., Mondol, N.H., Hellevang, H., 2022. Artificial Neural Network-Based Caprock Structural Reliability Analysis for CO2 Injection Site—An Example from Northern North Sea. Energies 15, 3365.

Allan, A.M., Clark, A.C., Vanorio, T., Kanitpanyacharoen, W., Wenk, H.-R., 2016. On the evolution of the elastic properties of organic-rich shale upon pyrolysis-induced thermal maturation. Geophysics 81, D263–D281.

Allen, M.R., Dube, O.P., Solecki, W., Aragón-Durand, F., Cramer, W., Humphreys, S., Kainuma, M., Kala, J., Mahowald, N., Mulugetta, Y., 2018. Framing and Context in Global Warming of 1.5 C: An IPCC Special Report on the impacts of global warming of 1.5 C above pre-industrial levels and related global greenhouse gas emission pathways, in the context of strengthening the global response to the th. Sustain. Dev. Efforts to Eradicate Poverty'.(Eds V Masson-Delmotte, P Zhai, HO Pörtner, D Roberts, J Skea, PR Shukla, A Pirani, W Moufouma-Okia, C Péan, R Pidcock, S Connors, JBR Matthews, Y Chen, X Zhou, MI Gomis, E Lonnoy, T Maycock, M Ti 41–91.

Altmann, J.B., 2010. Poroelastic effects in reservoir modelling.

Alzahabi, A., AlQahtani, G., Soliman, M.Y., Bateman, R.M., Asquith, G., Vadapalli, R., 2015. Fracturability Index is a Mineralogical Index: A New Approach for Fracturing Decision, in: SPE Saudi Arabia Section Annual Technical Symposium and Exhibition. Society of Petroleum Engineers.

Anderson, E.M., 1905. The dynamics of faulting. Trans. Edinburgh Geol. Soc. 8, 387–402.

Anell, I., Thybo, H., Artemieva, I.M., 2009. Cenozoic uplift and subsidence in the North Atlantic region: Geological evidence revisited. Tectonophysics 474, 78–105.

Aplin, A.C., Macquaker, J.H.S., 2011. Mudstone diversity: Origin and implications for source, seal, and reservoir properties in petroleum systems. Am. Assoc. Pet. Geol. Bull. 95, 2031–2059.

Avseth, P., Dvorkin, J., Mavko, G., Rykkje, J., 2000. Rock physics diagnostic of North Sea sands: Link between microstructure and seismic properties. Geophys. Res. Lett. 27, 2761–2764.

Avseth, P., Mukerji, T., Mavko, G., 2010. Quantitative seismic interpretation: Applying rock physics tools to reduce interpretation risk. Cambridge university press.

Avseth, P., Mukerji, T., Mavko, G., 2005. Quantitative seismic interpretation: Applying rock physics tools to reduce interpretation risk: Cambridge.

Badley, M.E., Price, J.D., Dahl, C.R., Agdestein, T., 1988. The structural evolution of the northern Viking Graben and its bearing upon extensional modes of basin formation. J. Geol. Soc. London. 145, 455–472.

Baklid, A., Korbol, R., Owren, G., 1996. Sleipner Vest CO2 Disposal, CO2 Injection Into A

Shallow Underground Aquifer, in: SPE Annual Technical Conference and Exhibition. Society of Petroleum Engineers. *https://doi.org/10.2118/36600-MS*

Bennion, B., Bachu, S., 2005. Relative permeability characteristics for supercritical CO2 displacing water in a variety of potential sequestration zones, in: SPE Annual Technical Conference and Exhibition. OnePetro.

Berg, R.R., 1975. Capillary pressures in stratigraphic traps. Am. Assoc. Pet. Geol. Bull. 59, 939–956.

Bjørkum, P.A., Walderhaug, O., Nadeau, P.H., 2001. Thermally driven porosity reduction: impact on basin subsidence. Geol. Soc. London, Spec. Publ. 188, 385–392.

Bjørlykke, K., 2015. Petroleum Migration, in: Petroleum Geoscience. Springer, pp. 373–384.

Bjørlykke, K., 2015. Compaction of sedimentary rocks: Shales, sandstones and carbonates, in: Petroleum Geoscience. Springer, pp. 351–360.

Bjørlykke, K., 2014. Relationships between depositional environments, burial history and rock properties. Some principal aspects of diagenetic process in sedimentary basins. Sediment. Geol. 301, 1–14.

Bjørlykke, K., 1998. Clay mineral diagenesis in sedimentary basins—a key to the prediction of rock properties. Examples from the North Sea Basin. Clay Miner. 33, 15–34.

Bjørlykke, K., Høeg, K., 1997. Effects of burial diagenesis on stresses, compaction and fluid flow in sedimentary basins. Mar. Pet. Geol. 14, 267–276.

Bjørlykke, K., Høeg, K., Faleide, J.I., Jahren, J., 2005. When do faults in sedimentary basins leak? Stress and deformation in sedimentary basins; examples from the North Sea and Haltenbanken, offshore Norway. Am. Assoc. Pet. Geol. Bull. 89, 1019–1031.

Bjørlykke, K., Ramm, M., Saigal, G.C., 1989. Sandstone diagenesis and porosity modification during basin evolution. Geol. Rundschau 78, 243–268.

Bjørnarå, T.I., 2018. Model development for efficient simulation of CO2 storage.

Campbell, N.M., Leon-Corwin, M., Ritchie, L.A., Vickery, J., 2020. Human-induced seismicity: Risk perceptions in the state of Oklahoma. Extr. Ind. Soc. 7, 119–126.

Carcione, J.M., 2000. A model for seismic velocity and attenuation in petroleum source rocksAn Acoustic Model for Petroleum Source Rocks. Geophysics 65, 1080–1092.

Chen*, J., Zhang, G., Chen, H., Yin, X., 2014. The construction of shale rock physics effective model and prediction of rock brittleness, in: SEG Technical Program Expanded Abstracts 2014. Society of Exploration Geophysicists, pp. 2861–2865.

Childs, C., Walsh, J.J., Watterson, J., 1997. Complexity in fault zone structure and implications for fault seal prediction, in: Norwegian Petroleum Society Special Publications. Elsevier, pp. 61–72.

Christian, J.T., 2004. Geotechnical engineering reliability: How well do we know what we are doing? J. Geotech. geoenvironmental Eng. 130, 985–1003.

Chuhan, F.A., Kjeldstad, A., Bjørlykke, K., Høeg, K., 2002. Porosity loss in sand by grain crushing—Experimental evidence and relevance to reservoir quality. Mar. Pet. Geol. 19, 39–53.

CLIMA, T., 2021. State of the Global Climate 2020.

Colmenares, L.B., Zoback, M.D., 2002. A statistical evaluation of intact rock failure criteria

constrained by polyaxial test data for five different rocks. Int. J. Rock Mech. Min. Sci. 39, 695–729.

Coulomb, C.A., 1776. Essai sur une application des rèles des maximis et minimis a quelques problems de statique. Mem. Acad. R. des Sci. 7.

Davies, R., Foulger, G., Bindley, A., Styles, P., 2013. Induced seismicity and hydraulic fracturing for the recovery of hydrocarbons. Mar. Pet. Geol. 45, 171–185.

Dicharry, R.M., Perryman, T.L., Ronquille, J.D., 1973. Evaluation and design of a CO2 miscible flood project-SACROC unit, Kelly-Snyder field. J. Pet. Technol. 25, 1309–1318.

Ditlevsen, O., Madsen, H.O., 2007. Structural Reliability Methods, Internet e. ed. John Wiley and Sons.

Doughty, P.T., 2003. Clay smear seals and fault sealing potential of an exhumed growth fault, Rio Grande rift, New Mexico. Am. Assoc. Pet. Geol. Bull. 87, 427–444.

Downey, M.W., 1984. Evaluating seals for hydrocarbon accumulations. Am. Assoc. Pet. Geol. Bull. 68, 1752–1763.

Dreyer, T., Whitaker, M., Dexter, J., Flesche, H., Larsen, E., 2005. From spit system to tide-dominated delta: integrated reservoir model of the Upper Jurassic Sognefjord Formation on the Troll West Field, in: Geological Society, London, Petroleum Geology Conference Series. Geological Society of London, pp. 423–448.

Duncan, J.M., 2000. Factors of safety and reliability in geotechnical engineering. J. Geotech. geoenvironmental Eng. 126, 307–316.

Dusseault, M.B., 2011. Geomechanical challenges in petroleum reservoir exploitation. KSCE J. Civ. Eng. 15, 669–678.

Dvorkin, J., Nur, A., 1996. Elasticity of high-porosity sandstones: Theory for two North Sea data sets. Geophysics 61, 1363–1370.

Dvorkin, J., Nur, A., Yin, H., 1994. Effective properties of cemented granular materials. Mech. Mater. 18, 351–366.

Du, J., Whittle, A.J., Hu, L., Divoux, T., Meegoda, J.N., 2020. Characterization of meso-scale mechanical properties of Longmaxi shale using grid microindentation experiments. J. Rock Mech. Geotech. Eng.

Eisbacher, G.H., 1996. Einführung in die Tektonik. Enke Stuttgart.

Ellsworth, W.L., 2013. Injection-induced earthquakes. Science (80-.). 341, 1225942.

Engelder, T., Fischer, M.P., 1994. Influence of poroelastic behavior on the magnitude of minimum horizontal stress, S h in overpressured parts of sedimentary basins. Geology 22, 949–952.

England, W.A., Mackenzie, A.S., Mann, D.M., Quigley, T.M., 1987. The movement and entrapment of petroleum fluids in the subsurface. J. Geol. Soc. London. 144, 327–347.

Faber, M.H., 2009. Basics of structural reliability. Swiss Fed. Inst. Technol. ETH, Zürich, Switz.

Færseth, R.B., 2006. Shale smear along large faults: continuity of smear and the fault seal capacity. J. Geol. Soc. London. 163, 741–751.

Færseth, R.B., 1996. Interaction of Permo-Triassic and Jurassic extensional fault-blocks during the development of the northern North Sea. J. Geol. Soc. London. 153, 931–944.

Færseth, R.B., Gabrielsen, R.H., Hurich, C.A., 1995. Influence of basement in structuring of the North Sea basin, offshore southwest Norway. Nor. Geol. Tidsskr. 75, 105–119.

Færseth, R.B., Johnsen, E., Sperrevik, S., 2007. Methodology for risking fault seal capacity: Implications of fault zone architecture. Am. Assoc. Pet. Geol. Bull. 91, 1231–1246.

Færseth, R.B., Oppenboen, K.A., Saeboe, A., 1984. Trapping Styles and Associated Hydrocarbon Potential in Norwegian North Sea. Am. Assoc. Pet. Geol. Bull. 68, 1201–1201.

Faleide, J.I., Bjørlykke, K., Gabrielsen, R.H., 2015. Geology of the Norwegian Continental Shelf, in: Petroleum Geosciences: From Sedimentary Environments to Rock Physics. pp. 603–637.

Fan, Z., Eichhubl, P., Gale, J.F.W., 2016. Geomechanical analysis of fluid injection and seismic fault slip for the Mw4. 8 Timpson, Texas, earthquake sequence. J. Geophys. Res. Solid Earth 121, 2798–2812.

Fatti, J.L., Smith, G.C., Vail, P.J., Strauss, P.J., Levitt, P.R., 1994. Detection of gas in sandstone reservoirs using AVO analysis: A 3-D seismic case history using the Geostack technique. Geophysics 59, 1362–1376.

Faulkner, D.R., Jackson, C.A.L., Lunn, R.J., Schlische, R.W., Shipton, Z.K., Wibberley, C.A.J., Withjack, M.O., 2010. A review of recent developments concerning the structure, mechanics and fluid flow properties of fault zones. J. Struct. Geol. 32, 1557–1575.

Fawad, M., Mondol, N.H., 2021. Monitoring geological storage of CO 2: a new approach. Sci. Rep. 11, 1–9.

Fawad, M., Mondol, N.H., Jahren, J., Bjørlykke, K., 2011. Mechanical compaction and ultrasonic velocity of sands with different texture and mineralogical composition. Geophys. Prospect. 59, 697–720.

Fawad, M., Rahman, M.D.J., Mondol, N.H., 2021. Seismic reservoir characterization of potential CO2 storage reservoir sandstones in Smeaheia area, Northern North Sea. J. Pet. Sci. Eng. 205, 108812.

Fichler, C., Hospers, J., 1990. Deep crustal structure of the northern North Sea Viking Graben: results from deep reflection seismic and gravity data. Tectonophysics 178, 241–254.

Fischer, K., Henk, A., 2013. A workflow for building and calibrating 3-D geomechanical models &ndash a case study for a gas reservoir in the North German Basin. Solid Earth 4, 347–355.

Fokker, P.A., Orlic, B., Van der Meer, L.G.H., Geel, C.R., 2011. Geomechanical modeling of surface uplift around well KB-502 at the In Salah CO2 storage site, in: 73rd EAGE Conference and Exhibition Incorporating SPE EUROPEC 2011. European Association of Geoscientists & Engineers, p. cp-238.

Folk, R.L., 1980. Petrology of sedimentary rocks. Hemphill publishing company.

Foschi, M., Cartwright, J.A., 2020. Seal failure assessment of a major gas field via integration of seal properties and leakage phenomena. Am. Assoc. Pet. Geol. Bull. 104, 1627–1648.

Foxford, K.A., Walsh, J.J., Watterson, J., Garden, I.R., Guscott, S.C., Burley, S.D., 1998. Structure and content of the Moab Fault Zone, Utah, USA, and its implications for fault seal prediction. Geol. Soc. London, Spec. Publ. 147, 87–103.

Gassnova, 2012. Geological storage of CO2 from Mongstad. Interim report Johansen

Formation.

Gautier, D.L., 2005. Kimmeridgian shales total petroleum system of the North Sea graben province. US Geological Survey.

GCCSI, n.d. Global CCS Institute [WWW Document]. URL *https://www.globalccsinstitute.com/*

Geertsma, J., 1973. A basic theory of subsidence due to reservoir compaction; the homogeneous case.

Gibson, R.G., 1994. Fault-zone seals in siliciclastic strata of the Columbus Basin, offshore Trinidad. Am. Assoc. Pet. Geol. Bull. 78, 1372–1385.

Glorioso, J.C., Rattia, A., 2012. Unconventional reservoirs: basic petrophysical concepts for shale gas, in: SPE/EAGE European Unconventional Resources Conference & Exhibition-From Potential to Production. European Association of Geoscientists & Engineers, p. cp-285.

Grasso, J.-R., 1992. Mechanics of seismic instabilities induced by the recovery of hydrocarbons. Pure Appl. Geophys. 139, 507–534.

Grieser, W.V., Bray, J.M., 2007. Identification of production potential in unconventional reservoirs, in: Production and Operations Symposium. Society of Petroleum Engineers.

Grollimund, B., Zoback, M.D., 2003. Impact of glacially induced stress changes on fault-seal integrity offshore Norway. Am. Assoc. Pet. Geol. Bull. 87, 493–506.

Guo, Z., Chapman, M., Li, X., 2012. Exploring the effect of fractures and microstructure on brittleness index in the Barnett Shale, in: SEG Technical Program Expanded Abstracts 2012. Society of Exploration Geophysicists, pp. 1–5.

Halland, E.K., Gjeldvik, I.T., Johansen, W.T., Magnus, C., Meling, I.M., Pedersen, S., Riis, F., Solbakk, T., Tappel, I., 2011. CO2 Storage Atlas Norwegian North Sea. Nor. Pet. Dir. PO Box 600.

Halland, E.K., Riis, F., 2014. Evaluation of CO2 storage possibilities on the Norwegian Continental Shelf. Energy Procedia 63, 5192–5199.

Hampson, D.P., Russell, B.H., Bankhead, B., 2005. Simultaneous inversion of pre-stack seismic data, in: SEG Technical Program Expanded Abstracts 2005. Society of Exploration Geophysicists, pp. 1633–1637.

Hansen, J.A., 2020. Quantitative analysis of source, reservoir, and cap rocks on the Norwegian Continental Shelf: An integrated study of geology, geophysics, petrophysics and rock physics.

Hansen, J.A., Mondol, N.H., Tsikalas, F., Faleide, J.I., 2020. Caprock characterization of Upper Jurassic organic-rich shales using acoustic properties, Norwegian Continental Shelf. Mar. Pet. Geol. 121, 104603. https://doi.org/10.1016/j.marpetgeo.2020.104603.

Hart, B.S., Macquaker, J.H.S., Taylor, K.G., 2013. Mudstone ("shale") depositional and diagenetic processes: Implications for seismic analyses of source-rock reservoirs. Interpretation 1, B7–B26.

Hashin, Z., Shtrikman, S., 1963. A variational approach to the theory of the elastic behaviour of multiphase materials. J. Mech. Phys. Solids 11, 127–140.

Hawkes, C.D., McLellan, P.J., Bachu, S., 2005. Geomechanical factors affecting geological storage of CO2 in depleted oil and gas reservoirs. J. Can. Pet. Technol. 44.

Hedley, B., 2014. Feasibility of Geological Carbon Dioxide Storage; From Exploration to Implementation.

Heggland, R., 1997. Detection of gas migration from a deep source by the use of exploration 3D seismic data. Mar. Geol. 137, 41–47.

Heinemann, N., 2013. Physical and chemical effects of CO2 storage in saline aquifers of the southern North Sea.

Herwanger, J., Koutsabeloulis, N., 2011. Seismic geomechanics. How to Build Calibrate Geomech. Model. Using 3D 4D Seism. Data EAGE Publ.

Hettema, M.H.H., Schutjens, P., Verboom, B.J.M., Gussinklo, H.J., 2000. Production-induced compaction of a sandstone reservoir: the strong influence of stress path. SPE Reserv. Eval. Eng. 3, 342–347.

Hillis, R.R., 2003. Pore pressure/stress coupling and its implications for rock failure. Geol. Soc. London, Spec. Publ. 216, 359–368.

Hillis, R.R., 2001. Coupled changes in pore pressure and stress in oil fields and sedimentary basins. Pet. Geosci. 7, 419–425.

Holgate, N.E., Jackson, C.A.L., Hampson, G.J., Dreyer, T., 2015. Seismic stratigraphic analysis of the Middle Jurassic Krossfjord and Fensfjord formations, Troll oil and gas field, northern North Sea. Mar. Pet. Geol. 68, 352–380.

Hongyan, W., Yuzhang, L., Dazhong, D., Qun, Z., Dong, D., 2013. Scientific issues on effective development of marine shale gas in southern China. Pet. Explor. Dev. 40, 615–620.

Hornby, B.E., 1998. Experimental laboratory determination of the dynamic elastic properties of wet, drained shales. J. Geophys. Res. Solid Earth 103, 29945–29964.

Horsrud, P., 2001. Estimating mechanical properties of shale from empirical correlations. SPE Drill. Complet. 16, 68–73.

Horton, S., 2012. Disposal of hydrofracking waste fluid by injection into subsurface aquifers triggers earthquake swarm in central Arkansas with potential for damaging earthquake. Seismol. Res. Lett. 83, 250–260.

Hospers, J., Ediriweera, K.K., 1991. Depth and configuration of the crystalline basement in the Viking Graben area, Northern North Sea. J. Geol. Soc. London. 148, 261–265.

IEAGHG report, 2009. CCS site Characterization Criteria.

IPCC, 2018. Summary for Policymakers.

IPCC, 2005. Carbon dioxide capture and storage.

Jackson, J.A., White, N.J., 1989. Normal faulting in the upper continental crust: observations from regions of active extension. J. Struct. Geol. 11, 15–36.

Jarvie, D.M., Hill, R.J., Ruble, T.E., Pollastro, R.M., 2007. Unconventional shale-gas systems: The Mississippian Barnett Shale of north-central Texas as one model for thermogenic shale-gas assessment. Am. Assoc. Pet. Geol. Bull. 91, 475–499.

Jev, B.. I., Kaars-Sijpesteijn, C.H., Peters, M.P.A.M., Watts, N.L., Wilkie, J.T., 1993. Akaso field, Nigeria: Use of integrated 3-D seismic, fault slicing, clay smearing, and RFT pressure data on fault trapping and dynamic leakage. Am. Assoc. Pet. Geol. Bull. 77, 1389–1404.

Jimenez, J.A., Chalaturnyk, R.J., 2002. Integrity of bounding seals for geological storage of

greenhouse gases, in: SPE/ISRM Rock Mechanics Conference. OnePetro.

Jin, X., Shah, S.N., Roegiers, J.-C., Zhang, B., 2014. Fracability evaluation in shale reservoirs-an integrated petrophysics and geomechanics approach, in: SPE Hydraulic Fracturing Technology Conference. Society of Petroleum Engineers.

Johnson, J.R., 2017. Applications of geostatistical seismic inversion to the Vaca Muerta, Neuquen Basin, Argentina. M.S. thesis. Colorado School of Mines.

Johnson, J.R., Hansen, J.A., Rahman, J., Renard, F., Mondol, N.H., 2022a. Mapping the maturity of organic-rich shale with combined geochemical and geophysical data, Draupne Formation, Norwegian Continental Shelf. Marine and Petroleum Geology, 138, 105525.

Johnson, J.R., Kobchenko, M., Mondol, N.H., Renard, F., 2022b. Multiscale synchrotron microtomography imaging of kerogen lenses in organic-rich shales from the Norwegian Continental Shelf. International Journal of Coal Geology 253, 103954.

Johnson, J.R., Kobchenko, M., Mondol, N.H., Renard, F., 2022c. Experimental modeling of primary migration in a layered, brittle analogue system. Tectonphysics, 4089599.

Johnson, J.W., Nitao, J.J., Morris, J.P., Benson, S., 2005. Reactive transport modeling of cap-rock integrity during natural and engineered CO2 storage. Carbon dioxide capture storage Deep Geol. Form. 2, 787.

Jordt, H., Faleide, J.I., Bjørlykke, K., Ibrahim, M.T., 1995. Cenozoic sequence stratigraphy of the central and northern North Sea Basin: tectonic development, sediment distribution and provenance areas. Mar. Pet. Geol. 12, 845–879.

Kalani, M., Jahren, J., Mondol, N.H., Faleide, J.I., 2015. Petrophysical implications of source rock microfracturing. Int. J. Coal Geol. 143, 43–67. https://doi.org/10.1016/j.coal.2015.03.009.

Karlsen, D.A., Skeie, J.E., Backer-Owe, K., Bjørlykke, K., Olstad, R., Berge, K., Cecchi, M., Vik, E., Schaefer, R.G., 2004. Petroleum migration, faults and overpressure. Part II. Case history: the Haltenbanken Petroleum Province, offshore Norway. Geol. Soc. London, Spec. Publ. 237, 305–372.

Keranen, K.M., Savage, H.M., Abers, G.A., Cochran, E.S., 2013. Potentially induced earthquakes in Oklahoma, USA: Links between wastewater injection and the 2011 Mw 5.7 earthquake sequence. Geology 41, 699–702.

Kim, W., 2013. Induced seismicity associated with fluid injection into a deep well in Youngstown, Ohio. J. Geophys. Res. Solid Earth 118, 3506–3518.

Kim, J., Berg, R.R., Watkins, J.S., Tieh, T.T., 2003. Trapping capacity of faults in the Eocene Yegua Formation, east sour lake field, southeast Texas. Am. Assoc. Pet. Geol. Bull. 87, 415–425.

Klemperer, S.L., 1988. Crustal thinning and nature of extension in the northern North Sea from deep seismic reflection profiling. Tectonics 7, 803–821.

Koochak Zadeh, M., Haque Mondol, N., Jahren, J., 2017. Velocity anisotropy of Upper Jurassic organic-rich shales, Norwegian continental shelf. Geophysics 82, C61–C75.

Korbøl, R., Kaddour, A., 1995. Sleipner vest CO2 disposal-injection of removed CO2 into the Utsira formation. Energy Convers. Manag. 36, 509–512.

Kümpel, H.J., 2002. Theory of Linear Poroelasticity—with Applications to Geomechanics and Hydrogeology Herbert F. Wang, Princeton University Press, 2000, 287 pp, ISBN 0-691-

03746-9, Hardback, $65.00.

Lama, R.D., Vutukuri, V.S., 1978. Handbook on mechanical properties of rocks-testing techniques and results-volume iii.

Lander, R.H., Walderhaug, O., 1999. Predicting porosity through simulating sandstone compaction and quartz cementation. Am. Assoc. Pet. Geol. Bull. 83, 433–449.

Larionov, V. V, 1969. Radiometry of boreholes. Nedra, Moscow 127.

Levandowski, W., Weingarten, M., Walsh III, R., 2018. Geomechanical sensitivities of injection-induced earthquakes. Geophys. Res. Lett. 45, 8958–8965.

Lewis, Roland Wynne, Lewis, Roland W, Schrefler, B.A., 1998. The finite element method in the static and dynamic deformation and consolidation of porous media. John Wiley & Sons.

Leythaeuser, D., Radke, M., Schaefer, R.G., 1984. Efficiency of petroleum expulsion from shale source rocks. Nature 311, 745–748.

Leythaeuser, D., Schaefer, R.G., Yukler, A., 1982. Role of diffusion in primary migration of hydrocarbons. Am. Assoc. Pet. Geol. Bull. 66, 408–429.

Lindseth, R.O., 1979. Synthetic sonic logs—A process for stratigraphic interpretation. Geophysics 44, 3–26.

Longship-Report, 2020. Longship - Carbon capture and storage. *https://www.regjeringen.no/en/dokumenter/meld.-st.-33-20192020/id2765361/*

Madsen, H.O., Krenk, S., Lind, N.C., 2006. Methods of structural safety. Courier Corporation.

Mandal, P.P., Essa, I., Saha, S., Rezaee, R., 2021. Multi-purpose utility of constructing 3D static Geomechanical model in the Ichthys field, Browse Basin. 3rd AEGC Geosci. Sustain. World.

Mathias, S.A., Hardisty, P.E., Trudell, M.R., Zimmerman, R.W., 2009. Screening and selection of sites for CO2 sequestration based on pressure buildup. Int. J. Greenh. gas Control 3, 577–585.

Mavko, G., Mukerji, T., Dvorkin, J., 2009. The Rock Physics Handbook: Tools for Seismic Analysis of Porous Media. Cambridge University Press.

Meyer, B.L., Nederlof, M.H., 1984. Identification of source rocks on wireline logs by density/resistivity and sonic transit time/resistivity crossplots. Am. Assoc. Pet. Geol. Bull. 68, 121–129.

Minaeian, V., Rasouli, V., Dewhurst, D., 2014. A laboratory procedure proposed for mechanical testing of shales. APPEA J. 54, 337–344.

Mindlin, R.D., 1949. Compliance of elastic bodies in contact.

Mohr, O., 1882. Ueber die Darstellung des Spannungszustandes eines Korperelements: Civilingenieure, v. 28.

Mondol, N.H., Bjørlykke, K., Jahren, J., 2008. Experimental compaction of clays: relationship between permeability and petrophysical properties in mudstones. Pet. Geosci. 14, 319–337.

Mondol, N.H., Bjørlykke, K., Jahren, J., Høeg, K., 2007. Experimental mechanical compaction of clay mineral aggregates—Changes in physical properties of mudstones during burial.

Mar. Pet. Geol. 24, 289–311.

Mondol, N.H., Jahren, J., Berre, T., Grande, L., Bjørlykke, K., 2011. Permeability Anisotropy in Synthetic Mudstones− An Experimental Study, in: 73rd EAGE Conference and Exhibition Incorporating SPE EUROPEC 2011. European Association of Geoscientists & Engineers, p. cp-238.

Moos, D., Peska, P., Finkbeiner, T., Zoback, M., 2003. Comprehensive wellbore stability analysis utilizing quantitative risk assessment. J. Pet. Sci. Eng. 38, 97–109.

Mullen, M.J., Roundtree, R., Turk, G.A., 2007. A composite determination of mechanical rock properties for stimulation design (what to do when you don't have a sonic log), in: Rocky Mountain Oil & Gas Technology Symposium. Society of Petroleum Engineers.

Nadim, F., 2007. Tools and strategies for dealing with uncertainty in geotechnics, in: Probabilistic Methods in Geotechnical Engineering. Springer, pp. 71–95.

NESUS Theoretical Manual, 2011. Southwest Research Institute. San Antorio, Texas.

Newell, P., Yoon, H., Martinez, M.J., Bishop, J.E., Bryant, S.L., 2017. Investigation of the influence of geomechanical and hydrogeological properties on surface uplift at In Salah. J. Pet. Sci. Eng. 155, 34–45.

Nooraiepour, M., Mondol, N.H., Hellevang, H., Bjørlykke, K., 2017. Experimental mechanical compaction of reconstituted shale and mudstone aggregates: Investigation of petrophysical and acoustic properties of SW Barents Sea cap rock sequences. Mar. Pet. Geol. 80, 265–292. *https://doi.org/10.1016/j.marpetgeo.2016.12.003*

Nordbotten, J.M., Celia, M.A., Bachu, S., 2004. Analytical solutions for leakage rates through abandoned wells. Water Resour. Res. 40.

Northern Lights [WWW Document], n.d. URL *https://northernlightsccs.com/what-we-do/*

Norton, D.L., 1984. Theory of hydrothermal systems. Annu. Rev. Earth Planet. Sci. 12, 155–177.

NPD, 2022. NPD FactPages [WWW Document]. URL *https://npdfactpages.npd.no/factpages/Default.aspx?culture=en*

NPD CO2 Atlas, 2014. NPD CO2 Atlas Report.

Nur, A., Marion, D., Yin, H., 1991. Wave velocities in sediments, in: Shear Waves in Marine Sediments. Springer, pp. 131–140.

Nur, A., Mavko, G., Dvorkin, J., Galmudi, D., 1998. Critical porosity: A key to relating physical properties to porosity in rocks. Lead. Edge 17, 357–362.

Nygård, R., Gutierrez, M., Bratli, R.K., Høeg, K., 2006. Brittle–ductile transition, shear failure and leakage in shales and mudrocks. Mar. Pet. Geol. 23, 201–212.

Olden, P., Jin, M., Pickup, G., Mackay, E., Hamilton, S., Somerville, J., Todd, A., 2014. Geomechanical modelling of CO2 geological storage with the use of site specific rock mechanics laboratory data. Pet. Geosci. 20, 323–337.

Oliver, W.C., Pharr, G.M., 2004. Measurement of hardness and elastic modulus by instrumented indentation: Advances in understanding and refinements to methodology. J. Mater. Res. 19, 3–20.

Oliver, W.C., Pharr, G.M., 1992. An improved technique for determining hardness and elastic modulus using load and displacement sensing indentation experiments. J. Mater. Res. 7,

1564–1583.

Ouellet, A., Bérard, T., Desroches, J., Frykman, P., Welsh, P., Minton, J., Pamukcu, Y., Hurter, S., Schmidt-Hattenberger, C., 2011. Reservoir geomechanics for assessing containment in CO2 storage: a case study at Ketzin, Germany. Energy Procedia 4, 3298–3305.

Pachauri, R.K., Allen, M.R., Barros, V.R., Broome, J., Cramer, W., Christ, R., Church, J.A., Clarke, L., Dahe, Q., Dasgupta, P., 2014. Climate change 2014: synthesis report. Contribution of Working Groups I, II and III to the fifth assessment report of the Intergovernmental Panel on Climate Change. Ipcc.

Park, J.-W., Guglielmi, Y., Graupner, B., Rutqvist, J., Kim, T., Park, E.-S., Lee, C., 2020. Modeling of fluid injection-induced fault reactivation using coupled fluid flow and mechanical interface model. Int. J. Rock Mech. Min. Sci. 132, 104373.

Passey, Q.R., Creaney, S., Kulla, J.B., Moretti, F.J., Stroud, J.D., 1990. A practical model for organic richness from porosity and resistivity logs. Am. Assoc. Pet. Geol. Bull. 74, 1777–1794.

Pereira, F.L.G., Roehl, D., Laquini, J.P., Oliveira, M.F.F., Costa, A.M., 2014. Fault reactivation case study for probabilistic assessment of carbon dioxide sequestration. Int. J. Rock Mech. Min. Sci. 71, 310–319.

Perez Altamar, R., Marfurt, K., 2014. Mineralogy-based brittleness prediction from surface seismic data: Application to the Barnett Shale. Interpretation 2, T1–T17.

Peters, G., Sognnæs, I., 2019. The role of carbon capture and storage in the mitigation of climate change. CICERO Rep.

Rahman, M.J., Fawad, M., Jahren, J., Mondol, N.H., 2022. Top seal assessment of Drake Formation shales for CO2 storage in the Horda Platform area, offshore Norway. Int. J. Greenh. Gas Control 119, 103700. https://doi.org/10.1016/J.IJGGC.2022.103700.

Rahman, M.J., Choi, J.C., Fawad, M., Mondol, N.H., 2021. Probabilistic analysis of Vette fault stability in potential CO2 storage site Smeaheia, offshore Norway. Int. J. Greenh. Gas Control 108, 103315. https://doi.org/10.1016/j.ijggc.2021.103315

Rahman, M.J., Fawad, M., Mondol, N.H., 2020. Organic-rich shale caprock properties of potential CO2 storage sites in the northern North Sea, offshore Norway. Mar. Pet. Geol. 122, 104665.

Ramsay, J.G., 2000. Modern Structural Geology: Applications of Continuum Mechanics in Structural Geology. Academic Press.

Rasmussen, K.B., Bruun, A., Pedersen, J.M., 2004. Simultaneous seismic inversion, in: 66th EAGE Conference & Exhibition.

Report, 2020. The Norwegian Government, Norway steps up 2030 climate goal to at least 50% towards 55%.

Rickman, R., Mullen, M.J., Petre, J.E., Grieser, W.V., Kundert, D., 2008. A practical use of shale petrophysics for stimulation design optimization: All shale plays are not clones of the Barnett Shale, in: SPE Annual Technical Conference and Exhibition. Society of Petroleum Engineers.

Roberts, A.M., Kusznir, N.J., Yielding, G., Beeley, H., 2019. Mapping the bathymetric evolution of the Northern North Sea: from Jurassic synrift archipelago through Cretaceous–Tertiary post-rift subsidence. Pet. Geosci. 25, 306–321.

Roberts, A.M., Yielding, G., Kusznir, N.J., Walker, I., Dorn-Lopez, D., 1993. Mesozoic extension in the North Sea: constraints from flexural backstripping, forward modelling and fault populations, in: Geological Society, London, Petroleum Geology Conference Series. Geological Society of London, pp. 1123–1136.

Roberts, S., Jackson, J., 1991. Active normal faulting in central Greece: an overview. Geol. Soc. London, Spec. Publ. 56, 125–142.

Rodriguez-Herrera, A., Zdravera, O., Koutsabeloulis, N., 2014. Geomechanical Velocity Model Building, in: 76th EAGE Conference and Exhibition. Amsterdam.

Rogelj, J., Shindell, D., Jiang, K., Fifita, S., Forster, P., Ginzburg, V., Handa, C., Kheshgi, H., Kobayashi, S., Kriegler, E., 2018. Mitigation pathways compatible with 1.5 C in the context of sustainable development, in: Global Warming of 1.5° C. Intergovernmental Panel on Climate Change, pp. 93–174.

Rouchet, J. du, 1981. Stress fields, a key to oil migration. Am. Assoc. Pet. Geol. Bull. 65, 74–85.

Rubinstein, J.L., Mahani, A.B., 2015. Myths and facts on wastewater injection, hydraulic fracturing, enhanced oil recovery, and induced seismicity. Seismol. Res. Lett. 86, 1060–1067.

Rutqvist, J., Birkholzer, J., Cappa, F., Tsang, C.-F., 2007. Estimating maximum sustainable injection pressure during geological sequestration of CO2 using coupled fluid flow and geomechanical fault-slip analysis. Energy Convers. Manag. 48, 1798–1807.

Rutqvist, J., Birkholzer, J.T., Tsang, C.-F., 2008. Coupled reservoir–geomechanical analysis of the potential for tensile and shear failure associated with CO2 injection in multilayered reservoir–caprock systems. Int. J. Rock Mech. Min. Sci. 45, 132–143.

Rutqvist, J., Stephansson, O., 2003. The role of hydromechanical coupling in fractured rock engineering. Hydrogeol. J. 11, 7–40.

Rutqvist, J., Tsang, C.-F., 2002. A study of caprock hydromechanical changes associated with CO 2-injection into a brine formation. Environ. Geol. 42, 296–305.

Rybacki, E., Meier, T., Dresen, G., 2016. What controls the mechanical properties of shale rocks?–Part II: Brittleness. J. Pet. Sci. Eng. 144, 39–58.

Sales, J.K., 1997. AAPG Memoir 67: Seals, Traps, and the Petroleum System. Chapter 5: Seal Strength vs. Trap Closure--A Fundamental Control on the Distribution of Oil and Gas.

Sayers, C.M., 1994. The elastic anisotrophy of shales. J. Geophys. Res. Solid Earth 99, 767–774.

Schowalter, T.T., 1979. Mechanics of secondary hydrocarbon migration and entrapment. Am. Assoc. Pet. Geol. Bull. 63, 723–760.

Schultz, R., Skoumal, R.J., Brudzinski, M.R., Eaton, D., Baptie, B., Ellsworth, W., 2020. Hydraulic fracturing-induced seismicity. Rev. Geophys. 58, e2019RG000695.

Schultz, R., Stern, V., Gu, Y.J., 2014. An investigation of seismicity clustered near the Cordel Field, west central Alberta, and its relation to a nearby disposal well. J. Geophys. Res. Solid Earth 119, 3410–3423.

Segall, P., 1989. Earthquakes triggered by fluid extraction. Geology 17, 942–946.

Sengupta, M., Dai, J., Volterrani, S., Dutta, N., Rao, N.S., Al-Qadeeri, B., Kidambi, V.K., 2011.

Building a seismic-driven 3D geomechanical model in a deep carbonate reservoir, in: SEG Technical Program Expanded Abstracts 2011. Society of Exploration Geophysicists, pp. 2069–2073.

Sharma, R.K., Chopra, S., 2012. New attribute for determination of lithology and brittleness, in: SEG Technical Program Expanded Abstracts 2012. Society of Exploration Geophysicists, pp. 1–5.

Shell-Report, 2014. Limited. 2014. Peterhead CCS Project.

Shuey, R.T., 1985. A simplification of the Zoeppritz equations. Geophysics 50, 609–614.

Sibson, R.H., 2000. Fluid involvement in normal faulting. J. Geodyn. 29, 469–499.

Smith, J.E., Erdman, J.G., Morris, D.A., 1971. Migration, accumulation and retention of petroleum in the earth, in: 8th World Petroleum Congress. OnePetro.

Soltanzadeh, H., Hawkes, C.D., 2008. Semi-analytical models for stress change and fault reactivation induced by reservoir production and injection. J. Pet. Sci. Eng. 60, 71–85.

Span, R., Wagner, W., 1996. A new equation of state for carbon dioxide covering the fluid region from the triple-point temperature to 1100 K at pressures up to 800 MPa. J. Phys. Chem. Ref. data 25, 1509–1596.

Stainforth, J.G., Reinders, J.E.A., 1990. Primary migration of hydrocarbons by diffusion through organic matter networks, and its effect on oil and gas generation. Org. Geochem. 16, 61–74.

Steel, R., Ryseth, A., 1990. The Triassic—Early Jurassic succession in the northern North Sea: megasequence stratigraphy and intra-Triassic tectonics. Geol. Soc. London, Spec. Publ. 55, 139–168.

Steel, R.J., 1993. Triassic–Jurassic megasequence stratigraphy in the Northern North Sea: rift to post-rift evolution, in: Geological Society, London, Petroleum Geology Conference Series. Geological Society of London, pp. 299–315.

Stewart, D.J., Schwander, M., Bolle, L., 1995. Jurassic depositional systems of the Horda Platform, Norwegian North Sea: Practical consequences of applying sequence stratigraphic models. Nor. Pet. Soc. Spec. Publ. 291–323.

Storvoll, V., Bjørlykke, K., Mondol, N.H., 2005. Velocity-depth trends in Mesozoic and Cenozoic sediments from the Norwegian Shelf. Am. Assoc. Pet. Geol. Bull. 89, 359–381.

Streit, J.E., Hillis, R.R., 2004. Estimating fault stability and sustainable fluid pressures for underground storage of CO2 in porous rock. Energy 29, 1445–1456.

Tenthorey, E., Vidal-Gilbert, S., Backe, G., Puspitasari, R., Pallikathekathil, Z.J., Maney, B., Dewhurst, D., 2013. Modelling the geomechanics of gas storage: A case study from the Iona gas field, Australia. Int. J. Greenh. Gas Control 13, 138–148.

Terzaghi, K., 1943. Theoretical soil mechanics. johnwiley & sons. New York 11–15.

Terzaghi, K., 1925. Erdbaumechanik auf bodenphysikalischer Grundlage. F. Deuticke.

Thoft-Christensen, P., Baker, M.J., 1982. Reliability of structural systems, in: Structural Reliability Theory and Its Applications. Springer, Berlin, Heidelberg, pp. 113–127.

Thyberg, B., Jahren, J., 2011. Quartz cementation in mudstones: sheet-like quartz cement from clay mineral reactions during burial. Pet. Geosci. 17, 53–63.

Tianshou, M.A., Ping, C., 2014. Study of meso-damage characteristics of shale hydration based

on CT scanning technology. Pet. Explor. Dev. 41, 249–256.

Tingay, M.R.P., Hillis, R.R., Morley, C.K., Swarbrick, R.E., Okpere, E.C., 2003. Pore pressure/stress coupling in Brunei Darussalam—implications for shale injection. Geol. Soc. London, Spec. Publ. 216, 369–379.

Tracker, C.A., 2021. Warming projections global update. Clim. Anal. New Clim. Institute, May.

Verdon, J.P., Kendall, J.M., Stork, A.L., Chadwick, R.A., White, D.J., Bissell, R.C., 2013. Comparison of geomechanical deformation induced by megatonne-scale CO2 storage at Sleipner,Weyburn, and In Salah. Proc. Natl. Acad. Sci. 110, E2762–E2771.

Vernik, L., 2016. Seismic petrophysics in quantitative interpretation. Society of Exploration Geophysicists.

Vernik, L., Landis, C., 1996. Elastic Anisotropy of Source Rocks: Implications for Hydrocarbon Generation and Primary Migration1. Am. Assoc. Pet. Geol. Bull. 80, 531–544.

Vernik, L., Nur, A., 1992. Ultrasonic velocity and anisotropy of hydrocarbon source rocks. Geophysics 57, 727–735.

Vidal-Gilbert, S., Tenthorey, E., Dewhurst, D., Ennis-King, J., Van Ruth, P., Hillis, R., 2010. Geomechanical analysis of the Naylor Field, Otway Basin, Australia: Implications for CO2 injection and storage. Int. J. Greenh. Gas Control 4, 827–839.

Vollset, J., Doré, A.G., 1984. A revised Triassic and Jurassic lithostratigraphic nomenclature for the Norwegian North Sea. Oljedirektoratet.

Walles, F., 2004. A new method to help identify unconventional targets for exploration and development through integrative analysis of clastic rock property fields.

Walsh, J.J., Watterson, J., Heath, A.E., Childs, C., 1998. Representation and scaling of faults in fluid flow models. Pet. Geosci. 4, 241–251.

Wang, F.P., Gale, J.F.W., 2009. Screening criteria for shale-gas systems.

Wang, Z., 2002. Seismic anisotropy in sedimentary rocks, part 2: Laboratory data. Geophysics 67, 1423–1440.

Watts, N.L., 1987. Theoretical aspects of cap-rock and fault seals for single-and two-phase hydrocarbon columns. Mar. Pet. Geol. 4, 274–307.

Welte, D.H., Tissot, P.B., 1984. Petroleum formation and occurrence. Springer.

Wentworth, C.K., 1922. A scale of grade and class terms for clastic sediments. J. Geol. 30, 377–392.

Whipp, P.S., Jackson, C.L., Gawthorpe, R.L., Dreyer, T., Quinn, D., 2014. Normal fault array evolution above a reactivated rift fabric; a subsurface example from the northern Horda Platform, Norwegian North Sea. Basin Res. 26, 523–549.

Yang, Y., Sone, H., Hows, A., Zoback, M.D., 2013. Comparison of brittleness indices in organic-rich shale formations, in: 47th US Rock Mechanics/Geomechanics Symposium. American Rock Mechanics Association.

Yenwongfai, H.D., Mondol, N.H., Faleide, J.I., Lecomte, I., 2017. Prestack simultaneous inversion to predict lithology and pore fluid in the Realgrunnen Subgroup of the Goliat Field, southwestern Barents Sea. Interpretation 5, SE75–SE96.

Yielding, G., Freeman, B., Needham, D.T., 1997. Quantitative fault seal prediction. Am. Assoc. Pet. Geol. Bull. 81, 897–917.

Yielding, G., Walsh, J., Watterson, J., 1992. The prediction of small-scale faulting in reservoirs. First Break 10.

Zieglar, D.L., 1992. Hydrocarbon columns, buoyancy pressures, and seal efficiency: comparisons of oil and gas accumulations in California and the Rocky Mountain area. Am. Assoc. Pet. Geol. Bull. 76, 501–508.

Zoback, M.D., 2010. Reservoir geomechanics. Cambridge University Press.Case.

SECTION-2

(JOURNAL PAPERS)

Paper-1

Organic-Rich Shale Caprock Properties of Potential CO_2 Storage Sites in the Northern North Sea, Offshore Norway

Md Jamilur Rahman
Manzar Fawad
Nazmul Haque Mondol

Marine and Petroleum Geology, 2020

Marine and Petroleum Geology 122 (2020) 104665

Contents lists available at ScienceDirect

Marine and Petroleum Geology

journal homepage: www.elsevier.com/locate/marpetgeo

Research paper

Organic-rich shale caprock properties of potential CO_2 storage sites in the northern North Sea, offshore Norway

Md Jamilur Rahman [a,*], Manzar Fawad [a], Nazmul Haque Mondol [a,b]

[a] Department of Geosciences, University of Oslo (UiO), Sem Sælands Vei 1, 0371, Oslo, Norway
[b] Norwegian Geotechnical Institute (NGI), Sognsveien 72, 0806, Oslo, Norway

ARTICLE INFO

Keywords:
Organic-rich shale
Caprock properties
Rock brittleness
Compaction
Rock physics analysis
Northern North Sea

ABSTRACT

Assessment of the geomechanical properties of organic-rich shale caprocks is critical for a successful CO_2 storage into a saline aquifer. In this study, we investigated the geochemical properties of the organic-rich shale caprocks of the Draupne and Heather formations, overlying the potential sandstone reservoirs of Sognefjord, Fensfjord, and Krossfjord formations in the northern North Sea, offshore Norway. The caprock's depositional variations within the sub-basins are established by analyzing the gamma-ray shape and stacking patterns. The effect due to differences in depositional environments, on the caprock compaction behavior is investigated by integrating petrographical analysis of core and cutting samples from 3 wells and by rock physical analysis of wireline log data from 27 exploration wells. Three rock physics templates are used where the wireline log data are interpreted using the published background trends. The effect of kerogen type, maturation level, and deposition environment on caprock properties within the study area are also evaluated. Moreover, the caprock property, such as brittleness, is estimated by using four mineralogy and elastic property-based, empirical relations, which is a quantitative measure of caprock property with respect to changes in stress-state. Finally, the seismic inversion method is assessed for the possibility of extracting caprock properties from surface seismic data. Regardless of compaction processes, the results indicate that the Heather Formation is mechanically stronger than the Draupne Formation. However, both formations appear to be ductile in nature. The depositional environments control the mineralogical composition and fabric of the Draupne and Heather formations, which influence the caprock properties significantly. Results also show that the effect of TOC on caprock properties is insignificant in the study area. The brittleness of the organic-rich shale caprocks in the study area follows a different trend compared to the published trends. We also observed an excellent correlation between the log-derived elastic properties and geomechanical parameters. Still, it is difficult to assess the caprock elastic properties from seismic due to the overlap of data clusters. The evaluation of caprock geomechanical behaviors is challenging as these properties are site-specific and also influenced by other factors such as exhumation, in-situ stress conditions, the existence of natural fractures, and their orientations.

1. Introduction

Geological storage of human-generated CO_2 into a saline aquifer is one of the many solutions for reducing CO_2 impact on the atmosphere. Norwegian Government has developed a strategy for large scale CCS (carbon capture and storage) as the necessity of it is already well documented by the UN's climate panel (IPCC) and International Energy Agency (IEA). Partnership with the industries, the government is interested in defining the best possible sites for sequestrating CO_2 into the subsurface in the Norwegian Continental Shelf (NCS). Smeaheia is one of the potential storage sites evaluated by Equinor and Gassonova, which is located in the eastern part of the northern North Sea (Fig. 1). The structures within the Semaheia area are mainly fault-bounded three-way closures with thin organic-rich shale caprocks. Troll Oil/Gas Field located west of Smeaheia, has oil and gas production from the same-targeted reservoirs. There is a possibility of lateral connectivity between Smeaheia, and the Troll Field that has been considered a potential risk. Moreover, this area has experienced several stages of rifting events (Faleide et al., 2015), following the collapse of Caledonian Orogeny in the Devonian time (Fossen and Hurich, 2005; Gabrielsen et al., 2010),

* Corresponding author.
E-mail addresses: m.j.rahman@geo.uio.no (M.J. Rahman), manzar.fawad@geo.uio.no (M. Fawad), nazmulh@geo.uio.no (N.H. Mondol).

https://doi.org/10.1016/j.marpetgeo.2020.104665
Received 7 May 2020; Received in revised form 15 August 2020; Accepted 17 August 2020
Available online 19 August 2020

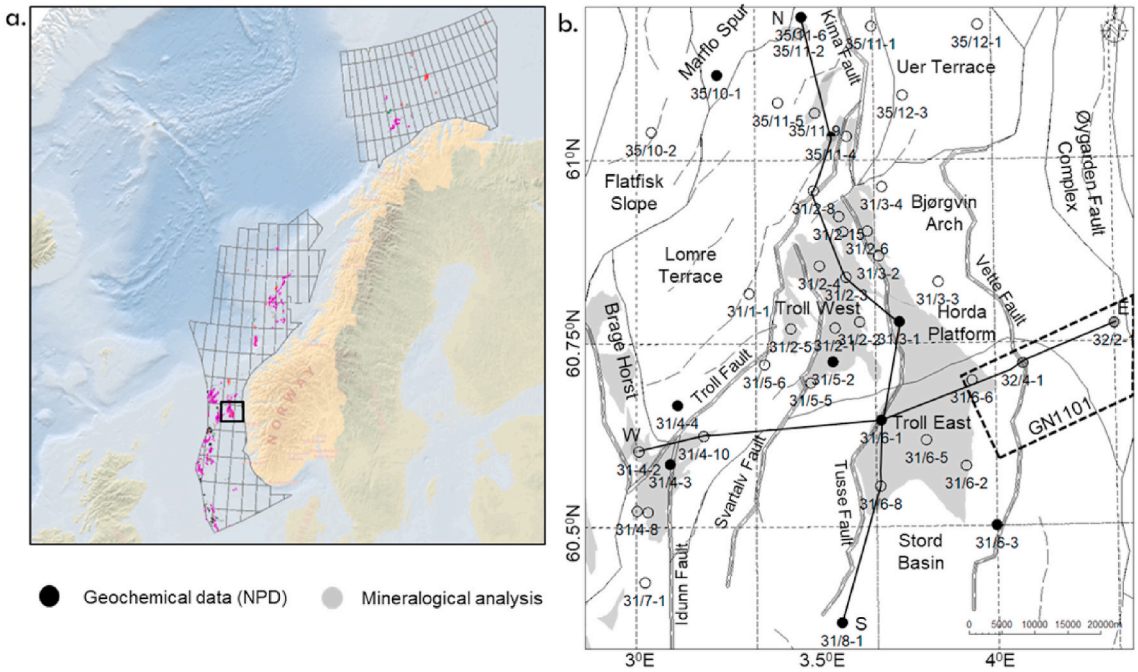

Fig. 1. a) The rectangle shows the study area on the Norwegian Continental Shelf, b) The locations of the studied wells correspond to the structural elements and major faults. The grey shaded areas are the hydrocarbon discoveries within the study area. The GN1101 3D seismic survey is outlined with a stippled rectangle, and the black lines represent the N–S and E-W well correlations presented in Fig. 2.

which leads to forming several large scale faults penetrating through the reservoir and caprocks up to the overburden. Therefore, careful investigations of caprock properties are necessary to prevent any CO_2 leakage risk.

In the study area, the main reservoir sandstones are the Jurassic Sognefjord, Fensfjord and Krossfjord formations, and organic-rich Draupne and Heather formations act as the primary seal. The thickness of caprocks varies significantly. One of the critical factors for CO_2 injection within a saline reservoir is the change in pore pressure, which ultimately changes the state of effective stress (i.e., principal stress minus pore pressure) and controls deformation and failure of reservoir-caprock pairs (Verdon et al., 2013). Additional, hydrological and geochemical processes influence the effective stress, potentially affecting the geomechanical properties of caprocks (Norton, 1984; Johnson et al., 2004; Shell, 2014). A potential consequence is the shear fracture or failure of caprock when shear stress exceeds the shear strength. This event not only depends on failure criteria but also controlled by the ductility or brittleness of the caprock (Nygård et al., 2006). This geomechanical properties (brittleness or ductility) of caprock is a complex function of rock lithology, texture, effective stress, temperature, strength, fluid type (Handin and Hagar, 1957; Davis and Reynolds, 1996; Nygård et al., 2006), diagenesis, TOC maturation, etc. (Walles, 2004). Additionally, natural fractures and planes of weakness can also affect these properties (Gale et al., 2007). Soft clay and organic matter (OM) cause a reduction in velocities and Young's modulus (E) while increasing the Poisson's ratio (PR) whereas stiff minerals (i.e., quartz, feldspar, pyrite, and carbonate) increase velocities and E with decreasing PR (Aoudia et al., 2010). The depth of burial can have both positive and negative effects on rock brittleness. An increase in depth generally increases pressure and temperature; hence the increase in the degree of compaction, along with the alteration of organic matter to enhance the brittleness. Furthermore, the silica enrichment due to clay mineral alteration with depth increase brittleness (Walles, 2004). Brittle deformation more likely occurs when a material is stiff and has higher shear strength. Thus, lithified shales are more fragile than young and uncemented mudrocks (Nygård et al., 2006). Rocks with certain mineralogy have less effect on brittleness with increasing pressure and temperature (Wang and Gale, 2009). However, all processes that govern the caprock properties are very complicated and depend on the depositional and diagenetic processes. Therefore, it is crucial to evaluate the geomechanical properties of organic-rich shale caprock (ORSC) in the study area for successful CO_2 sequestration.

In this study, we evaluate the rock compositional variation and the subsequent effect on elastic and geomechanical properties of the ORSC of Draupne and Heather formations in the northern North Sea, offshore Norway. The aim is to identify the caprock depositional and compaction processes variations by petrographic, petrophysical, rock physical and geophysical interpretations and find out the possible correlation between properties. The local depositional variation is identified using the differences in gamma-ray responses. Depositional processes are the critical factor for the mineralogy and fabric changes (i.e., grain size, shape, sorting, etc.) within sub-basin, which influence the property of caprocks. The properties are altered just after the deposition by compaction processes (i.e., mechanical and chemical compaction). The depositional variation is validated by petrographic analysis (XRD; SEM and thin section), while the compaction effects are analyzed by three rock physics templates (Vp-Density; E-PR and LambdaRho-MuRho). The influence of TOC on caprock properties is also evaluated by analyzing maturation, type, and distribution of organic matter. Moreover, the geomechanical properties of the caprock are assessed by analyzing the brittleness indices values calculated both from mineralogical composition and elastic properties. Finally, a qualitative evaluation between the inverted acoustic impedance (AI) from seismic data and log-derived elastic, and geomechanical properties are accomplished to assess the possibility of extracting caprock geomechanical properties from the seismic data. The caprocks property (i.e., ductility/brittleness) in the study area is established by integrating all these analyses, which is a crucial parameter to evaluate the caprock's sealing potential.

2. Lithostratigraphy and structural setting

The Late Jurassic Heather Formation shale is a part of the Viking Group that overlying and interfingering with Krossfjord, Fensfjord, and Sognefjornd formation sandstones of the Brent Group (Fig. 2a). Heather

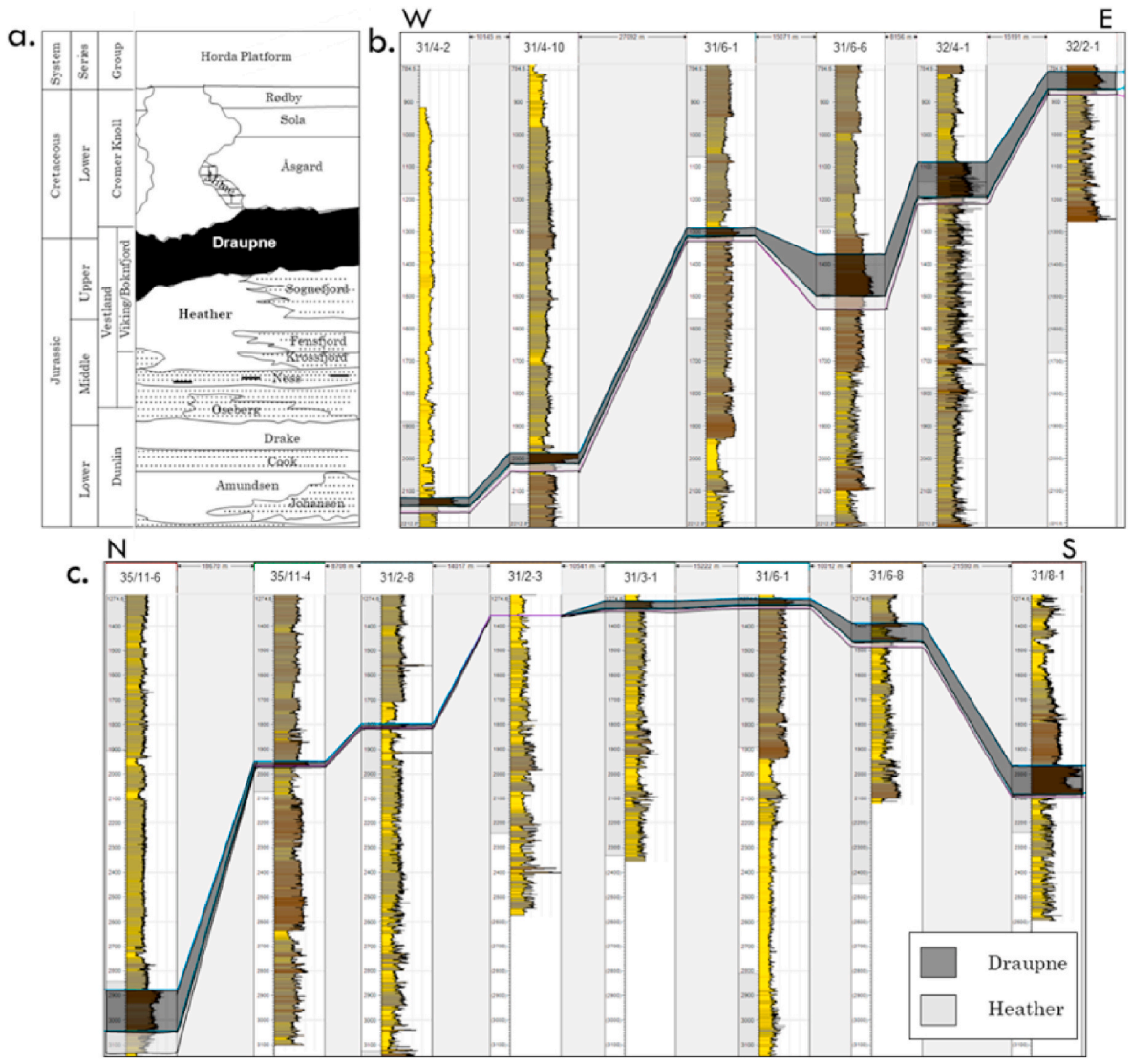

Fig. 2. a) A generalized Jurassic and Cretaceous stratigraphic succession in the study area (modified from NPD CO_2 Atlas, 2014). Well correlations along the b) E-W and c) N–S lines (Fig. 1) show the present-day depth variations of Draupne and Heather formations within the study area. Note that both correlations have vertical scale differences.

Formation consists of mainly grey silty claystone with thin streaks of limestone deposited in an open marine environment (NPD, 2020). On the Horda Platform, this unit interdigitates with the Middle Jurassic sandstones (Krossfjord, Fensfjord, and Sognefjord formations), where it sometimes becomes highly micaceous and may grade into sandy siltstone. Heather Formation also has significant thickness variations within the study area ranging between 0 and 159 m (Table 1). Stewart et al. (1995) divided Heather Formation in the Horda Platform area into three sub-units (A, B, and C). In this study, we evaluate only the Heather C unit, which is sandwiched between the Sognefjord and Draupne formations.

The Draupne Formation shale is also a part of the Viking Group, deposited in the Late Jurassic time within the East Shetland Basin, the Viking Graben, and over the Horda Platform area (NPD CO_2 atlas, 2014). The thickness of Draupne Formation varies significantly within the study area, ranges from 0 to 159 m (Table 1). The Draupne Formation consists of dark grey-brown to black, usually non-calcareous, carbonaceous, occasionally fissile claystone. It acts as the primary seal of the Middle Jurassic Sognefjord Formation sandstone reservoir. The formation was deposited in an open marine environment with restricted bottom circulation and often with anaerobic conditions (NPD, 2020), and characterized by high gamma-ray values (usually above 100 API) because of TOC and high Uranium content. Interbedded sandstone and siltstone, as well as minor limestone streaks and concretions, are also present. In the lower boundary, Draupne Formation generally has a diachronous contact with the Heather Formation. However, on the northern Horda Platform, Late Jurassic sandstones of Sognefjord Formation mark the base of the Draupne Formation. The upper boundary of the Draupne Formation is usually marked by Cretaceous rock (Cromer Knoll Group), which has a higher velocity and lower gamma-ray response than the over and underlying rocks (NPD, 2020).

The two main rifting events occurred in the Horda Platform area during the Permo-Triassic and the Late Jurassic to Mid-Cretaceous times (Whipp et al., 2014). During the 1st rifting event, a wide basin with deep-rooted faults and thick syn-depositional wedges was centered below the Horda Platform. However, Late Jurassic to Mid Cretaceous event shifted westward with major rifting and tilting observed in Lomre Terrace in the Late Jurassic (Stewart et al., 1995) and weak stretching on the Horda Platform itself (Roberts et al., 1993, 2019; Færseth, 1997; Whipp et al., 2014). The study area consists of several N–S trending faults (Fig. 1b), which are believed to be rooted in Caledonian zones of crustal weakness (Whipp et al., 2014). These faults also demarcate the

Table 1
Maximum burial depth, present depth, and thickness of Draupne and Heather formations penetrated by the studied wells. The structural elements as suggested by NPD (2020).

Well name	Structural Elements (NPD)	Draupne Formation top depth (m BSF)		Thickness (m) Draupne	Heather[b] Formation top depth (m BSF)		Thickness (m) Heather
		Present	Max.[c]		Present	Max.[c]	
31/2-1	Bjørgvin Arch	1066	1186	26	1092	1212	0
31/2-2		1126	1256	63	1189	1319	0
31/2-3		1023	1413	0	1023	1413	0
31/2-4		1004	1264	0	1004	1264	0
31/2-5		1171	1411	0	1171	1411	0
31/2-6		1113	1483	11	1124	1494	0
31/2-8		1451	1681	16	1467	1697	0
31/2-15		1147	1417	0	1147	1417	0
31/2-18		1163	1443	0	1163	1443	0
31/3-1		963	1343	32	995	1375	9
31/3-2		1176	1496	26	1202	1522	0
31/3-3		1193	1713	49	1242	1762	10
31/3-4		1247	1577	23	1270	1600	0
31/4-3		1815	1985	8	1823	1993	0
31/4-6		1968	2118	13	1981	2131	14
31/4-8		1936	2076	3	1939	2079	0
31/4-10		1749	1869	20	1769	1889	0
31/5-2		1133	1323	41	1174	1364	6
31/5-5		1224	1444	0	1224	1444	0
31/5-6		1441	1646	3	1444	1649	0
31/7-1		2000	2150	11	2011	2161	0
32/2-1		453	1253	54	508	1308	17
35/11-7		1409	1604	3	1412	1607	0
31/6-1	Stord Basin	986	1316	25	1011	1341	14
31/6-2		996	1456	113	1109	1569	25
31/6-3		1044	1474	125	1169	1599	16
31/6-5		1061	1451	92	1153	1543	38
31/6-6		1056	1526	129	1185	1655	40
31/6-8		1087	1417	73	1160	1490	22
31/8-1		1664	1914	110	1774	2024	14
32/4-1		774	1474	106	880	1580	23
31/1-1	Lomre Terrace	1685	1885	3	1688	1888	0
31/4-4		2061	2181	65	2126	2246	0
35/11-2		2532	2692	115	2647	2807	128
35/11-4		1594	1784	18	1612	1802	0
35/11-5		2298	2478	129	2428	2608	65
35/11-6		2505	2655	159	2664	2814	96
35/11-9		2003	2183	150	2153	2333	17
31-4-2	Brage Host	1979	2139	25	2004	2164	19
35/10-1	Marflo Spur	2714	2854	48	2762	2902	118
35/10-2	Flatfisk Slope	3525	3650	97	3622	3747	131
35/11-1	Reggeteinen Ridge	1633	1963	0	1633	1963	95
35/12-1	Uer Terrace	1984	2464	37	2021	2501	159
35/12-3		1638	1998	14	1652	2012	13

[c] Corrected for exhumation estimated from Vp-Depth trend to represent the maximum burial depth.
[b] Only considered interval between Draupne and top reservoirs section.

structural elements interpreted by NPD (2020). For example, the Horda Platform (Bjørvin Arch and Stord Basin) is separated by the Troll fault complex in the west and Øygarden fault complex in the east. Moreover, the faults Vette, Tusse, and Svart created compartmentalization within the Horda Platform, which separated Troll East and West Fields (Fig. 1b). Other major faults like Kima, Brage, Idunn fault complexes, and minor faults also played an essential role during structural deformation within the study area. Uplifted blocks acted as provenance to fill the accommodation spaces created by rifting and then following the thermal subsidence (Jordt et al., 1995; Anell et al., 2009; Faleide et al., 2015).

The structural well correlations show the present-day depth difference of Draupne and Heather formations within the studied wells (Fig. 2b&c). In the middle of the study area (crossing Troll East), both formations are gradually going deeper from east to west with varying thickness. In contrast, the N–S correlation shows that the Draupne and Heather formations deepen in both north and south direction, with the northern well (Lomre Terrace) being deeper than the southern well (Stord Basin). The wells with the shallowest reservoir lie in the center (Bjørgvin Arch) containing very thin or no Draupne and Heather formations.

The study area became tectonically active during Late Jurassic time when the Draupne and Heather formations were deposited. The major faults rotated as a result of the basement blocks' rotation produced numerous local basins (Faleide et al., 2015), which lead to forming a high energy ribbon trending NNE-SSW along the present Troll West area following the Troll fault zone. This trend is gradually prograding north-westward and crosses the main boundary fault (Troll fault) into the Lomre Terrace. Moreover, the Horda Platform has tilted towards the east during the Late Kimmeridgian time, which resulted in NNE-SSW zero thickness trend, and thin Heather deposited into the Troll East because of sediment bypassed into the Lomre Terrace area (Stewart et al., 1995). This zero thickness bypass or erosional trend is also found in Draupne and Heather formation's thickness maps (Fig. 5), which reveals that during transgression, the erosional/non-depositional structural high on top of Troll West existed and influences the sedimentation in the study area.

Table 2
Summary of the TOC and R_0 from the available well reports (NPD, 2020). The corresponding log derived TOC is also shown for comparison.

Formation	Well name	Structural Elements	TOC (wt%) rock-eval			TOC (wt%) log[c]		R0 (%)	
			Mean	STD	N	Mean	STD	Mean	STD
Draupne	31/3-1	Bjørgvin Arch	3.03	0.47	4	3.12	0.89	0.41	0.06
	31/5-2		2.62	1.21	7	2.57	1.21	–	–
	31/4-3		5.71	1.00	1	5.19	2.24	0.33	–
	31/8-1	Stord Basin	3.35	1.78	12	3.50	1.74	0.36	0.02
	31/6-1		1.63	0.10	3	1.47	1.36	0.42	0.00
	31/6-3		1.47	1.04	9	1.75	2.37	0.55	0.04
	31/4-4	Lomre Terrace	2.71	2.26	3	2.18	1.94	–	–
	35/11-4		0.71	1.05	6	1.01	0.64	0.45	0.05
	35/11-6		3.77	0.55	7	4.18	2.01	–	–
	35/10-1	Marflo Spur	3.93	1.27	4	4.29	2.88	–	–
Heather	31/8-1	Stord Basin	6.18	1.30	2	4.92	0.57	–	–
	31/6-1		2.62	0.25	2	0.93	1.28	–	–
	35/11-6	Lomre Terrace	3.60	0.80	4	3.20	3.14	–	–
	35/10-1	Marflo Spur	3.56	0.50	8	3.82	1.49	–	–

Mean (Harmonic); STD – Standard deviation; n – number of readings.
[c] Predicted using equation 1.

3. Database and methods

The log-derived elastic properties can reveal the compaction history of a caprock. Moreover, the correlation between the present-day caprock properties and the paleo-depositional history can be illustrated by analyzing the petrographical images. However, the compaction processes are too complicated due to the influence of several factors (i.e., tectonics, sea-level fluctuation, initial pore-water chemistry, etc.), which can be very difficult to predict. We utilized the data from 44 exploration wells (Fig. 1) from the study area to evaluate Draupne and Heather formations caprock properties. Table 1 shows the available wells and structural setup; these wells represent the exhumation and thickness of Draupne and Heather formations. The majority of the wells (i.e., 31) are from the Horda Platform area (i.e., Bjørgvin Arch and Stord Basin); however, the remaining wells are the control points for other structural elements such as Lomre Terrace, Uer Terrace, Brage Host, Marflo Spur, Flatfisk Slope, and Reggeteinen Ridge. All the wells were used in the thickness map generation process, while 27 wells were selected based on Draupne Formation thickness (>10 m) and available logs (i.e., gamma-ray, density, p-sonic, resistivity, neutron porosity, etc.) for physical and mechanical property evaluation. Moreover, 10 wells out of 44 have available geochemical data (NPD, 2020), which were used to evaluate TOC maturation in the study area (Table 2). Also, three wells (32/2–1, 32/4–1 & 35/11–4) that have the core and cutting samples within the caprock intervals were selected for petrographic study and grain size analysis.

3.1. Paleo-depositional environment and petrographic analysis

The gamma-ray log signatures help to identify the sea-level fluctuations and paleo-depositional variations within the local sub-basins. These depositional variations affect the rock properties during diagenesis (mechanical and chemical compactions). A funnel-shaped log curve in shallow marine setup reflects an upward increase in depositional energy with shallowing upward and coarsening while a bell shape replicates upward fining with a decrease in energy. However, a block shape curve represents the minimal fluctuation of depositional energy (Emery and Myers, 1995). Moreover, the vertical stacking pattern of the gamma-ray log curve reveals the paleo depositional relation between accommodation spaces and sediment supply rates (Van Wagoner et al., 1988).

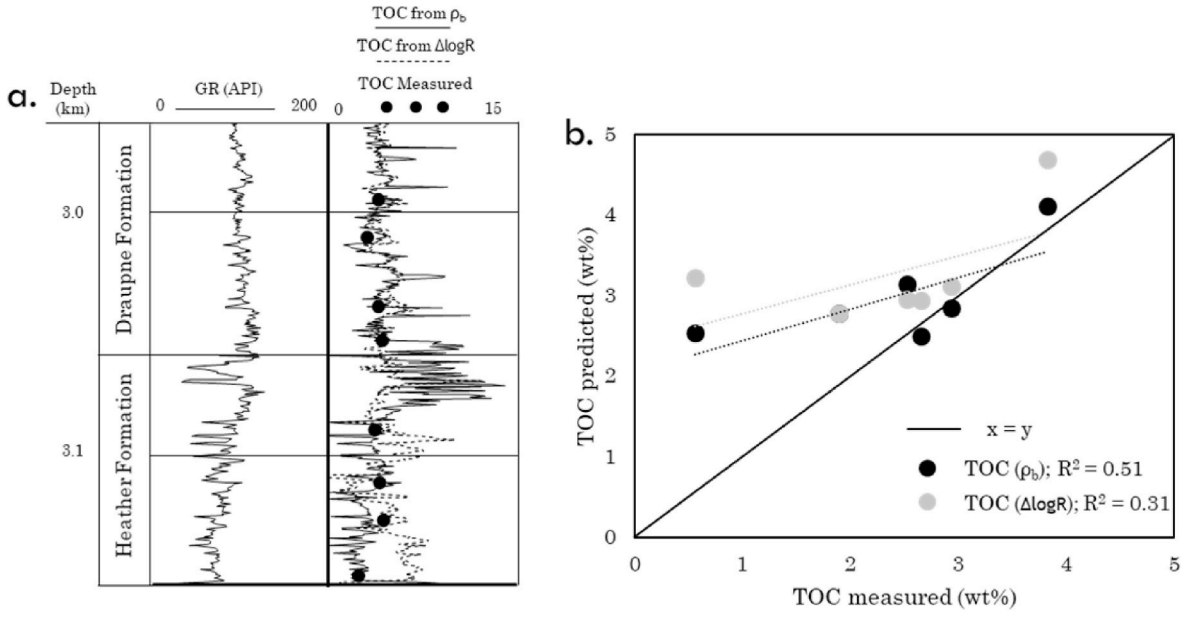

Fig. 3. a) Comparison of predicted TOC with the measured TOC (black dots; NPD, 2020) of Draupne and Heather formations in well 35/11–6. Calculations from ΔlogR method (Passey et al., 1990) are represented by the dotted line and from equation (1) using the bulk density by a solid line. The gamma-ray shows the variation with depth. b) Measured versus predicted TOC of the same data points show the correlation coefficient of two methods.

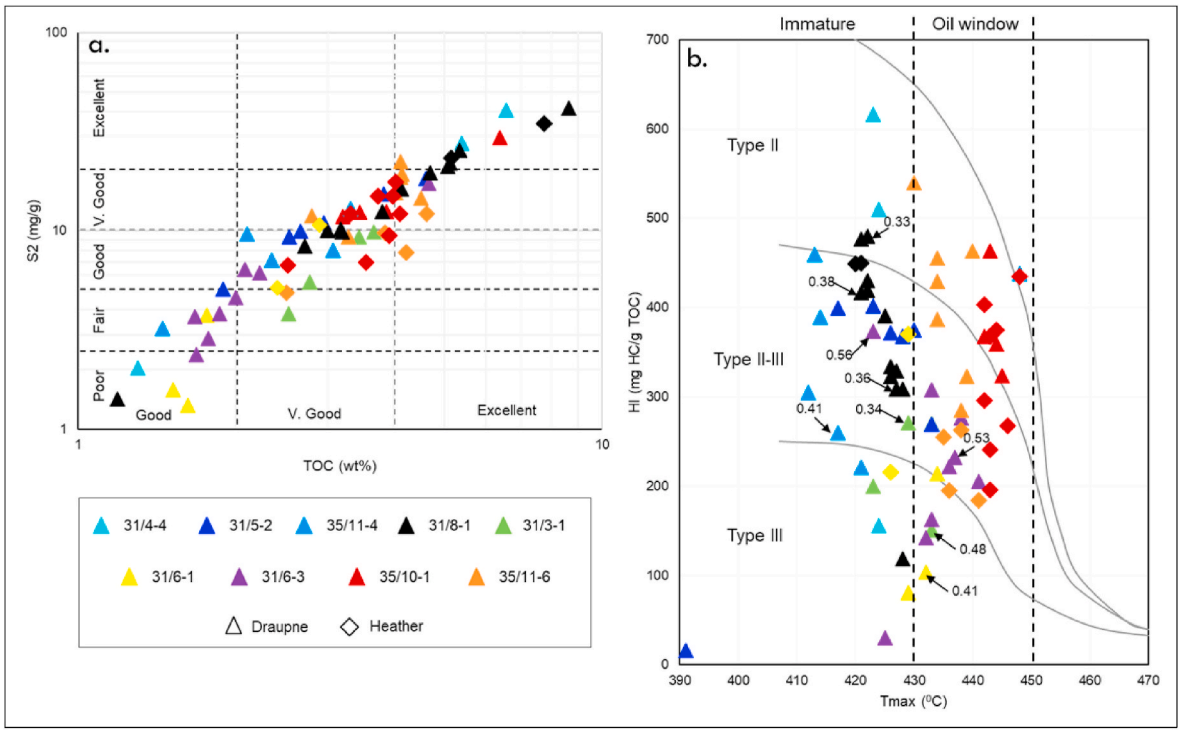

Fig. 4. a) Cross-plot of TOC versus S2 of Draupne and Heather formations showing the quality of the organic matter in the study area. The background template is modified after Peter (1986). (b) Pyrolysis T_{max} versus Hydrogen Index (HI) of Draupne and Heather formations from ten wells in the northern North Sea, showing the kerogen type and thermal maturity, according to Hunt (1996). It also indicates the associated vitrinite reflectance (R_o%) readings from NPD (2020).

Accommodation spaces, however, are a result of sea-level fluctuation and paleo tectonic activity while sediment supply depends on the sediment sources and weathering processes. Therefore, the log shape and variations of the stacking pattern of Draupne and Heather formations within the study area were analyzed to evaluate the depositional differences within the sub-basins. This paleo-depositional analysis is later validated using the petrographic interpretation. The interpretation of mineral fractions, grain sizes, and textural contrast was investigated by X-Ray diffraction (XRD), scanning electron microscope (SEM), and thin section analysis using the available core and cutting samples.

3.2. Geochemical data and TOC prediction

Organic matter types and maturation play vital roles for caprock properties; therefore, geochemical reports consisting of TOC (total organic carbon) data are scouted from the public domain database (NPD, 2020). Only 10 out of 44 wells have measured geochemical data; therefore, TOC for the rest of the wells was calculated using empirical relations (e.g., Passey et al., 1990; Vernik and Landis, 1996). Calculated TOC was calibrated with the laboratory-measured TOC acquired from the NPD (Norwegian Petroleum Directorate) database. Two methods were tested using the well 35/11-6 dataset, where the sonic and resistivity logs were used in the ΔlogR method (Meyer and Nederlof, 1984; Passey et al., 1990) and density log in equation (1) (Vernik and Landis, 1996; Carcione, 2000) to estimate TOC fractions. A comparison of predicted TOC using the two methods is shown in Fig. 3.

Both methods show reasonable estimation; however, density generated TOC fraction has a better match with measured data compared to ΔlogR method (Fig. 3b). Therefore, we calculated density based TOC for all the studied wells using the following equation:

$$TOC\ (wt\%) = a[\rho_k(\rho_m - \rho_b)]/[\rho_b(\rho_m - \rho_k)] \quad (1)$$

Where, ρ_k is the kerogen density that has a range of 1.1–1.6 g/cm^3 (Hansen et al., 2019) and it depends on the maturation of organic matter (Vernik and Landis, 1996; Passey et al., 2010; Vernik and Milovac, 2011; Alfred and Vernik, 2013; Dang et al., 2016); ρ_m is the matrix density which depends on the mineralogy, grain fabric and diagenesis, i.e., clay mineral transformation (Hart et al., 2013; Carcione and Avseth, 2015); ρ_b is the bulk density log, and 'a' is the constant which is related to the fraction of carbon in organic matter and can vary according to the maturation level. For example, Vernik and Landis (1996) assume a = 67, while a = 70–85 is suggested by Vernik and Milovac (2011).

In our calculation, the study area was subdivided into four zones based on the OM volume, type, and maturation. Overall the OM is type-II to type-III with immature in Horda platform area (i.e., Bjørgvin Arch and Stord Basin) and within the oil window in the deeper section in Lomre Terrace and Marflo Spur (Fig. 4). Based on this information, we fixed 'a' and ρ_k value for all the wells located in each sub-sections. Later, the matrix density (ρ_m) in equation (1) was used as the variable to get the best fit with measured TOC (Table 2). When there was a better match between the measured and calculated mean TOC values (Table 2), the same properties (i.e., 'a', ρ_k & ρ_m) used to calculate the TOC percentage for the rest of the wells (used the nearest measured well values).

3.3. Compaction and caprock properties

Caprock properties are varied significantly due to the maximum temperature and pressure it experienced. This whole rock compaction process was divided into zones where mechanical compaction is stress-dependent, and chemical compaction depends on temperature. Therefore, the estimation of maximum burial depth of the zones of interest is necessary. Hence, the exhumation and temperature of each studied wells were calculated. The normal compaction trend-based (NCT-based) exhumation estimation was carried out to evaluate the maximum burial of the caprocks (Table 1). The silt-kaolinite (50:50) normal compaction trend (NCT) suggested by Mondol (2009) was used to estimate the exhumation. The maximum burial depth calculated in this study was calibrated with the published literature (Baig et al., 2019). The temperature, however, estimated using BHT (bottom hole temperature) and TVD (total vertical depth) of the studied wells and denoted as:

Table 3
Present and maximum burial depth with the corresponding temperature of Draupne and Heather formations dividing the wells into three compaction clusters (MC, TZ, and CC).

	Well name	Draupne Formation				Heather Formation			
		Present Depth (m BSF)	P. Temp. (^{0}C)	Max.[a] Depth (m BSF)	M. Temp. (^{0}C)	Present Depth (m BSF)	P. Temp. (^{0}C)	Max.[a] Depth (m BSF)	M. Temp. (^{0}C)
MC	32/2-1	453	15.9	1253	43.9	508	17.8	1308	45.8
	32/4-1	774	27.1	1474	51.6	880	30.8	1580	55.3
	31/3-1	963	33.7	1343	47.0	995	34.8	1375	48.1
	31/6-1	986	34.5	1316	46.1	1011	35.4	1341	46.9
	31/6-2	996	34.9	1456	51.0	1109	38.8	1569	54.9
	31/6-3	1044	36.5	1474	51.6	1169	40.9	1599	56.0
	31/6-6	1056	37.0	1526	53.4	1185	41.5	1655	57.9
	31/6-5	1061	37.1	1451	50.8	1153	40.4	1543	54.0
	31/2-1	1066	37.3	1186	41.5	1092	38.2	1212	42.4
	31/6-8	1087	38.0	1417	49.6	1160	40.6	1490	52.2
	31/2-2	1126	39.4	1256	44.0	1189	41.6	1319	46.2
	31/5-2	1133	39.7	1323	46.3	1174	41.1	1364	47.7
	31/3-2	1176	41.2	1496	52.4	1202	42.1	1522	53.3
	31/3-3	1193	41.8	1713	60.0	1242	43.5	1762	61.7
	31/2-8	1451	50.8	1681	58.8	1467	51.3	1697	59.4
	35/11-4	1594	55.8	1784	62.4	1612	56.4	1802	63.1
	31/8-1	1664	58.2	1914	67.0	1774	62.1	2024	70.8
	31/4-10	1749	61.2	1869	65.4	1769	61.9	1889	66.1
	31/4-3	1815	63.5	1985	69.5	1823	63.8	1993	69.8
TZ	31/4-6	1968	68.9	2118	74.1	1981	69.3	2131	74.6
	31-4-2	1979	69.3	2139	74.9	2004	70.1	2164	75.7
	31/4-4	2061	72.1	2181	76.3	2126	74.4	2246	78.6
CC	35/11-5	2298	80.4	2478	86.7	2428	85.0	2608	91.3
	35/11-6	2505	87.7	2655	92.9	2664	93.2	2814	98.5
	35/11-2	2532	88.6	2692	94.2	2647	92.6	2807	98.2
	35/10-1	2714	95.0	2854	99.9	2762	96.7	2902	101.6

Temperature were calculated using the aveargе temperature gradient (35^{0}C/KM).
[a] Corrected for exhumation estimated from Vp-Depth trend to represent the maximum burial depth.

$$m = \frac{(y - c)}{TD} \quad (2)$$

where m is thermal gradient, y is bottom hole temperature, c is mean annual temperature at the seafloor, and TD is the total depth below the seafloor. We used 5 °C as mean annual temperature for the study area.

Based on the exhumation and corresponding maximum burial/temperature, Draupne and Heather formations were divided into three subgroups: i) MC-mechanically compacted, ii) TZ-transition zone, and iii) CC-chemically compacted. As TZ is a range instead of a single value, we defined 65–75 °C as the TZ for the study area (Table 3). The P-wave velocity (Vp) versus density (ρ) template is a good tool for acoustic property characterization where the background curves (i.e., friable sand model, 20%, 50%, 80% and 100% clay volume curves) were adapted from Avseth et al. (2005). This model called the Dvorkin-Gutierrez silty shale model, where the saturated elastic moduli of shale were estimated by using the Hashin-Shtrikman lower bound as a function of clay content, assuming the adding silt grains consist of 100% quartz (Avseth et al., 2005). Moreover, the effect of the volume of shale within the caprocks was assessed by comparing the volume of clay (Vsh) data points with the background curves. Though the gamma-ray (GR) is the proxy for the volume of clay in any formation, the GR values also depend on many other factors. We calculated the volume of shale (Vsh) from the gamma-ray log using Larionov's (1969) younger (MC zone wells) and older (CC zone wells) rock equations. The elastic properties such as Young's Modulus (E), Poisson's Ratio (ν) and Lame parameters such as LambdaRho (λρ) and MuRho (μρ) was characterized using the templates where the background curves were adapted from Grieser and Bray (2007) and Perez and Marfurt (2014). These properties represent the geomechanical properties of the caprock under stresses, and for their calculations, P-wave velocity (Vp), S-wave velocity (Vs), and density are required. Vp and density are available, but Vs (shear wave velocity) is not recorded in any of the studied wells; therefore, we predict Vs using Random Forest (RF) - a machine learning algorithm. We tested several algorithms, where the RF yielded comparatively better results.

A prestack seismic inversion was also carried out for the 3D seismic volume GN1101 (Fig. 1b) covering the Smeaheia area (East of the study area) penetrated by two exploration wells (32/2–1 & 32/4–1). A set of five available partial stacks were used comprising angles 0–10°, 10–20°, 20–30°, 30–40°, and 40–50° to perform prestack inversion. Before extracting statistical wavelets from all the five partial stacks, a preconditioning alignment of traces using a non-rigid method (NRM) was carried out. Both the wells were correlated with seismic and obtained moderate to good correlation coefficient (0.6–0.7). Finally, the simultaneous inversion was applied to the partial stacks to obtain the acoustic impedance (AI) cube. The geometrical mean of AI value of Draupne and Heather formations was calculated using the surface attribute function.

3.4. Brittleness indices

The brittleness index (BI), which is the qualitative measure of rock behavior, was also estimated. The mineralogical composition of the caprocks significantly influences the geomechanical properties. The fraction of stiff minerals increases the caprock brittleness, while the ductile components decrease it. Several correlations are tested using published equations (Jarvie et al., 2007; Glorioso and Rattia, 2012; Alzahabi et al., 2015) within which Jarvie et al. (2007) equation (Eq. (3)) provide a better estimate of mineralogy-based brittleness index (MBI^1) for the studied caprocks:

$$MBI^1 = \frac{\text{Qtz}}{\text{Qtz} + \text{Carb} + \text{Cly}} \quad (3)$$

where Qtz is Quartz, Carb is Carbonate, and Cly is Clay. $MBI^1 = 1$ indicates brittle behavior, while $MBI^1 = 0$ represents the ductile behavior of the caprocks. It is noteworthy to mention that several authors considered dolomite (Wang and Gale, 2009), carbonate (Glorioso and Rattia, 2012), feldspar (Jin et al., 2014) and pyrite (Alzahabi et al.,

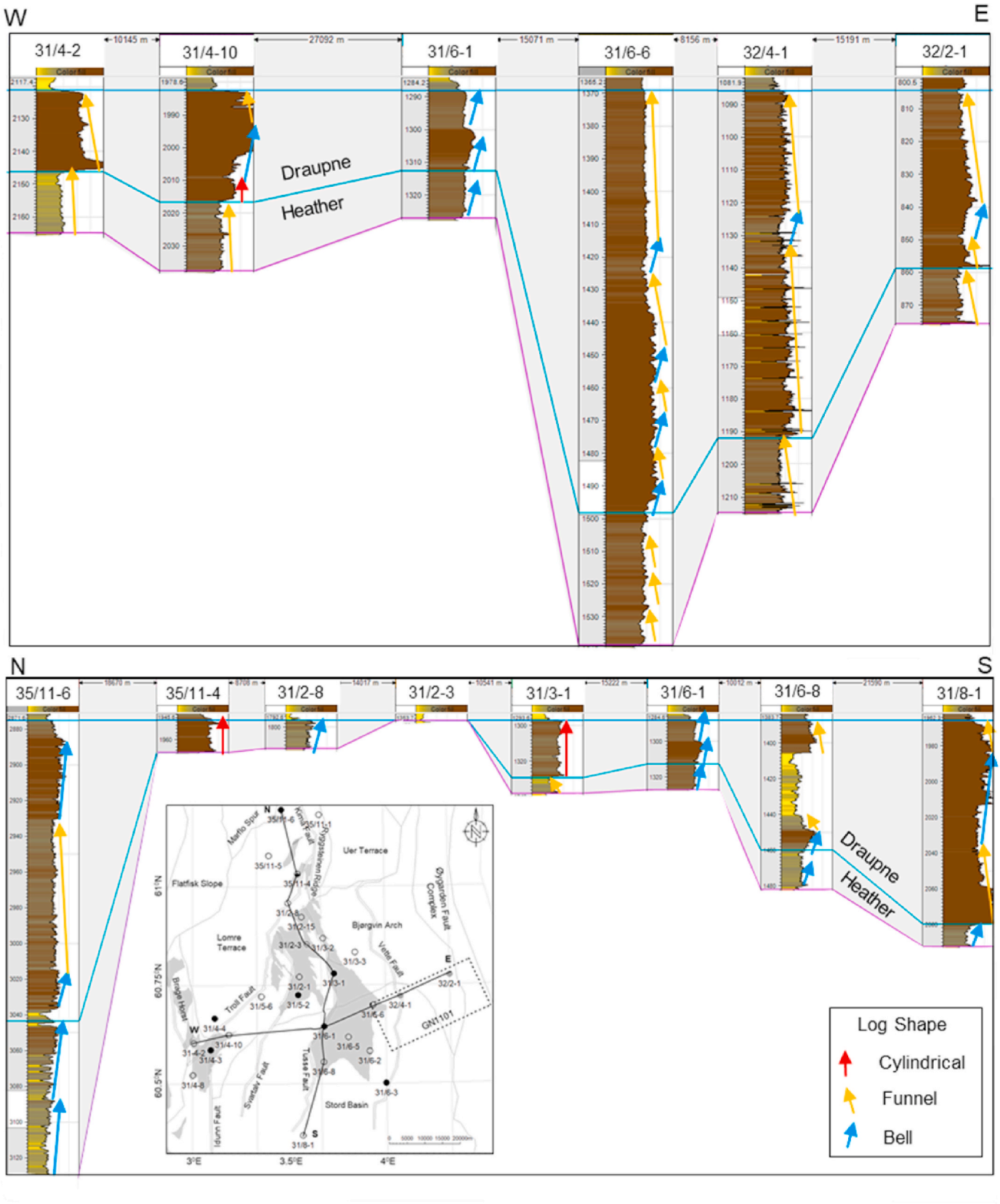

Fig. 5. Stratigraphic correlation along W-E and N–S cross-sections, flattened on top of the Draupne Formation showing the thickness variation with variable gamma-ray log patterns (cylindrical, funnel, and bell) in Draupne and Heather formations, which reveal the paleo-depositional changes. The insert map shows the profile locations and structural elements.

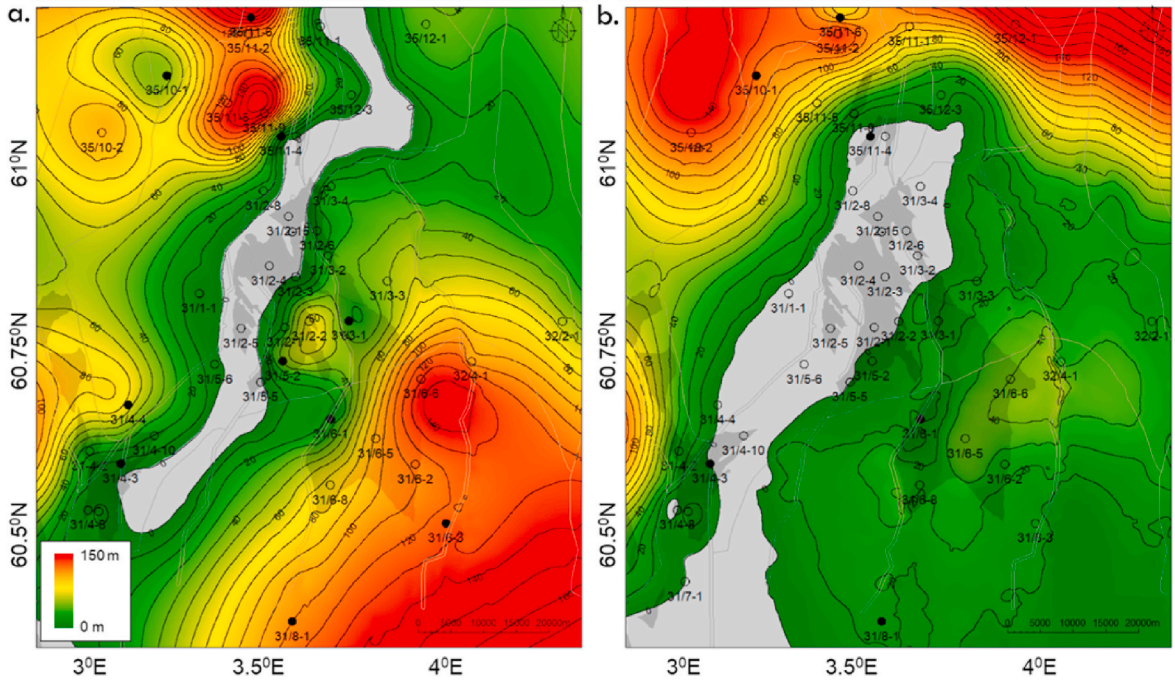

Fig. 6. The thickness maps generated from well log data for a) Draupne Formation and b) Heather Formation. A NNE-SSW zero thickness trend occurs in both formations. The contour intervals are 10 m in both maps.

2015; Rybacki et al., 2016) as stiff minerals while TOC (Wang and Gale, 2009) as a ductile component. Considering this, we modified equation (3) and proposed the following equation for mineralogy-based brittleness index (MBI^2):

$$MBI^2 = \frac{\text{Qtz} + \text{Carb} + \text{Fsp} + \text{Py}}{\text{Qtz} + \text{Carb} + \text{Fsp} + \text{Py} + \text{Cly} + \text{TOC}} \quad (4)$$

where Fsp is Feldspar, Py is Pyrite, and TOC is total organic carbon, and MBI^2 ranges between 0 (ductile) to 1 (brittle). Like MBI, elastic property based brittleness indices (EBI) are also available (i.e., Grieser and Bray, 2007; Rickman et al., 2008; Sharma and Chopra, 2012; Chen et al., 2014; Jin et al., 2014). We estimated the EBI using two elastic property-based empirical equations proposed by Grieser and Bray (2007) and Fawad and Mondol, 2020; unpublished, patent-pending on the procedure). The Grieser and Bray (2007) empirical equation is:

$$EBI^1 = \frac{1}{2}\left[\frac{E - E_{min}}{E_{max} - E_{min}} + \frac{\nu - \nu_{max}}{\nu_{min} - \nu_{max}}\right] \quad (5)$$

where E is static Young's modulus, E_{max} is 69 GPa, E_{min} is 0 GPa, and ν is static Poisson's ratio, ν_{max} is 0.5, ν_{min} is 0. Also, the higher the EBI^1 value is, the more brittle the caprock would be.

The log driven dynamic Young's modulus and Poisson's ratio were converted to log-based static values using Mullen et al. (2007) equation:

$$E_{stat} = \left[\frac{E_{dyn}}{3.3674}\right]^{2.042} \quad (6)$$

$$\nu_{stat} = \nu_{dyn} \quad (7)$$

The equation proposed by Fawad and Mondol (2020; unpublished, patent-pending on the procedure) is:

$$EBI^2 = \frac{0.00044AI - 1.3 - \sqrt{0.62\,\frac{R_W}{R_D}}\,(0.00019AI + 0.25)}{1.35 + 0.00028AI} \quad (8)$$

where AI is the acoustic impedance (g/cm^3×m/s); R_D is true formation resistivity (ohm-m), and R_W is the resistivity of pore water (ohm-m). Here we define the brittleness as an increase in stiffness of a rock due to compaction and addition of stiff mineral content (quartz, carbonate, or dolomite). Equation (8) is based on the physical and elastic properties of the organic matter (kerogen), quartz, and clay/water as end-members of a ternary model.

4. Results

4.1. Paleo depositional variation

The gamma-ray log shape is analyzed to identify the local depositional variations (i.e., facies changes) between the different sub-basins in the study area. The wells used for this analysis are carefully chosen so that all the structural elements (NPD, 2020) are represented, and the whole study area is covered. The N–S and W-E well sections (Fig. 5), consisting of 14 wells representing all the sub-basins, are used for this analysis. The number and type of log shapes vary within the wells and studied formations (i.e., Draupne and Heather). There is a sharp boundary observed between Heather and Draupne formations in wells (31/4–2, 31/4–10 & 31/8–1) in the SW part while more gradual changes observed in the rest of the study area (Fig. 5). The number of log cycles is thickness dependent. Wells, with a considerable thickness of Draupne and Heather formations, have more variety of patterns than the wells (31/2–8, 31/3–1, 31/4–2, and 35/11–4) penetrated thin sections mostly a single shape observed. The gamma-ray log shape patterns, however, do not follow any specific trend in some wells (such as wells 31/6–8 & 35/11-6 drilled in specific structural elements), which rather have a mixture of different patterns within the zones studied.

The gamma-ray values also show a considerable variation within the same formation as well as between Draupne and Heather formations. Generally, Heather Formation has low values of gamma-ray values compared to Draupne Formation, which might be an indication of the variation of depositional energy (i.e., higher energy leading to coarser grains in Heather Formation). However, depending on the locations and thickness, GR value varies significantly. The highest GR value in Draupne Formation is observed in the wells 31/4–2, 31/4–10, and 31/8–1. These wells are located within the south-western part of the study area covering part of the Stord Basin and Lomre Terrace. The lowest GR

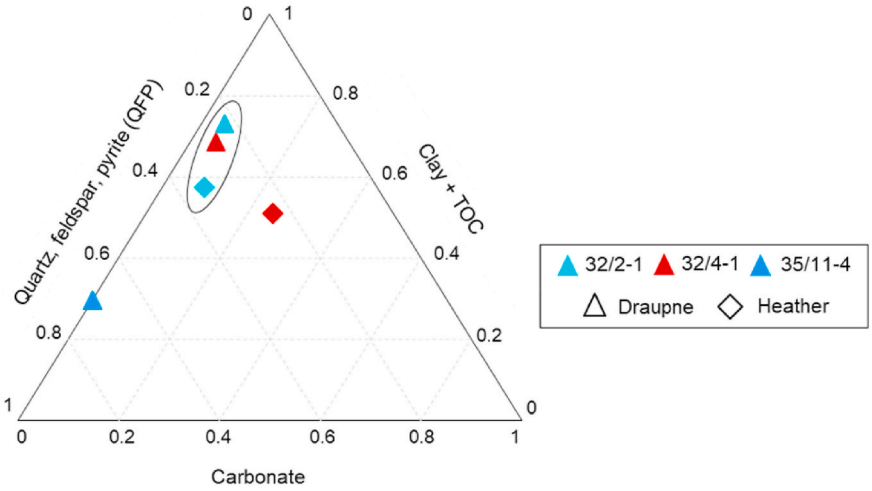

Fig. 7. The Ternary plot represents the compositional variability of Draupne and Heather formations within the three wells 32/2–1, 32/4–1, and 35/11–4. Note that carbonate minerals consist of calcite, dolomite, and siderite.

Table 4
Summary of bulk mineralogy and TOC of Draupne and Heather formations. Log-derived TOC is also shown for comparison.

Formation	Well no.	Mineralogy from XRD (wt%)					TOC[a]	TOC (wt%) log[b]	
		Quartz	Feldspar	Pyrite	Carbonate	Total Clay	(wt%)	Mean	STD
Draupne	32/2-1	18	4	1	5	70	2.81	2.26	1.31
	32/4-1	25	0	2	5	66	2.78	1.72	0.96
	35/11-4	43	6	22	0	28	2.08	1.01	0.64
Heather	32/2-1	24	10	1	8	55	2.64	1.63	0.54
	32/4-1	15	8	1	25	49	2.31	1.08	0.81

[a] TOC estimated from elementary study from the same core and cuttings used in XRD.
[b] Corrected for exhumation estimated from Vp-Depth trend to represent the maximum burial depth.

values are found near the Troll West area in well 31/2–8.

The paleo-depositional environment also affects the thickness of a formation. Along with sea-level fluctuation, thickness reflects the accommodation spaces and sediment supply during deposition. The thickness map reveals the paleo-depocenters within the study area. The thickness map of Draupne and Heather formations shows significant thickness variation with local depocenters within the study area (Fig. 6). Moreover, local highs and lows are following the fault orientation. The thickness of Draupne Formation ranges between 0 and 160 m, while it is 0–159 m in Heather Formation. A NE-SW zero thickness trend find following the Troll fault zone in both formations where the Troll fault is the boundary between the eastern platform area (Horda Platform) and the deep western basin (Viking Graben). The thickness of the Draupne Formation gradually increases in both NW and SE directions from the zero thickness trend. However, few local depocenters are also observed with higher thickness than the surroundings. In contrast, the thickness of Heather Formation increases towards West and NW direction (mainly in the deep basin area) while a blanket like deposition (minimal thickness variation) observed in the platform area (Fig. 6b). However, a moderate increase in thickness is found in the down-thrown block of the Vette fault near well 31/6-6, where a depocenter is also evident in the Draupne thickness map (Fig. 6a).

4.2. Mineral composition and texture

Bulk mineralogical analysis tells us the total percentage of minerals without indicating their origin. However, mineralogical information (i.e., the fraction of stiff and soft minerals) defines the geomechanical properties of the caprock. The bulk mineral fractions of Draupne and Heather formations are divided into three clusters; i) stiff quartz, feldspar, and pyrite (QFP), ii) soft clay and TOC, and iii) carbonate (Fig. 7). In general, the carbonate fractions within the study area are relatively low (<10%) except in the case of Heather Formation in well 32/4–1, which has 25% of carbonate (mainly siderite). The higher percentage of stiffer minerals (~70%) are found in the Draupne sample in well 35/11–4, while other samples have a higher percentage of softer minerals (>55%). The highest and lowest percentage of soft minerals are present in wells 32/2–1 and 35/11–4 in Draupne Formation, respectively. Individual quartz and clay fractions also show significant variations within the studied samples (Table 4). There is no significant variation observed between Draupne and Heather formations. However, within the same well higher percentage of stiff minerals are found in Heather Formation compared to the Draupne Formation.

Bulk mineralogy can be estimated from XRD analysis, but it is not possible to distinguish between the diagenetic or detrital phases. Therefore, petrographic observation is carried out to define the origin and texture of these constituents. Textural heterogeneity within the seal rocks is related to the relative alignment of minerals, mineral aggregates, organic matter or other components, and diagenesis, etc. Texturally caprock shales are often heterogeneous at the micrometer to millimeter scale when examined petrographically. In this study, scanning electron microscope (SEM) images from Draupne and Heather formations are analyzed to evaluate textural variation (Figs. 8 and 9). Draupne Formation in wells 32/2–1 and 32/4–1 is fine-grained with a matrix-supported framework compared to well 35/11–4, which has comparatively coarser grains with a mixed type framework. Both forms of shallow diagenetic pyrite (framboids and euhedral shape) are precipitated in well 35/11–4 (~22%), while wells 32/2–1 and 32/4–1 (1–2%) have only local framboid pyrite. Pyrite precipitation mainly depends on the initial pore fluids geochemical composition, where the pyrite framboids iron monosulfide (spherical aggregates of micrometer-sized pyrite crystals) is associated with organic matter (Figs. 8 and 9)

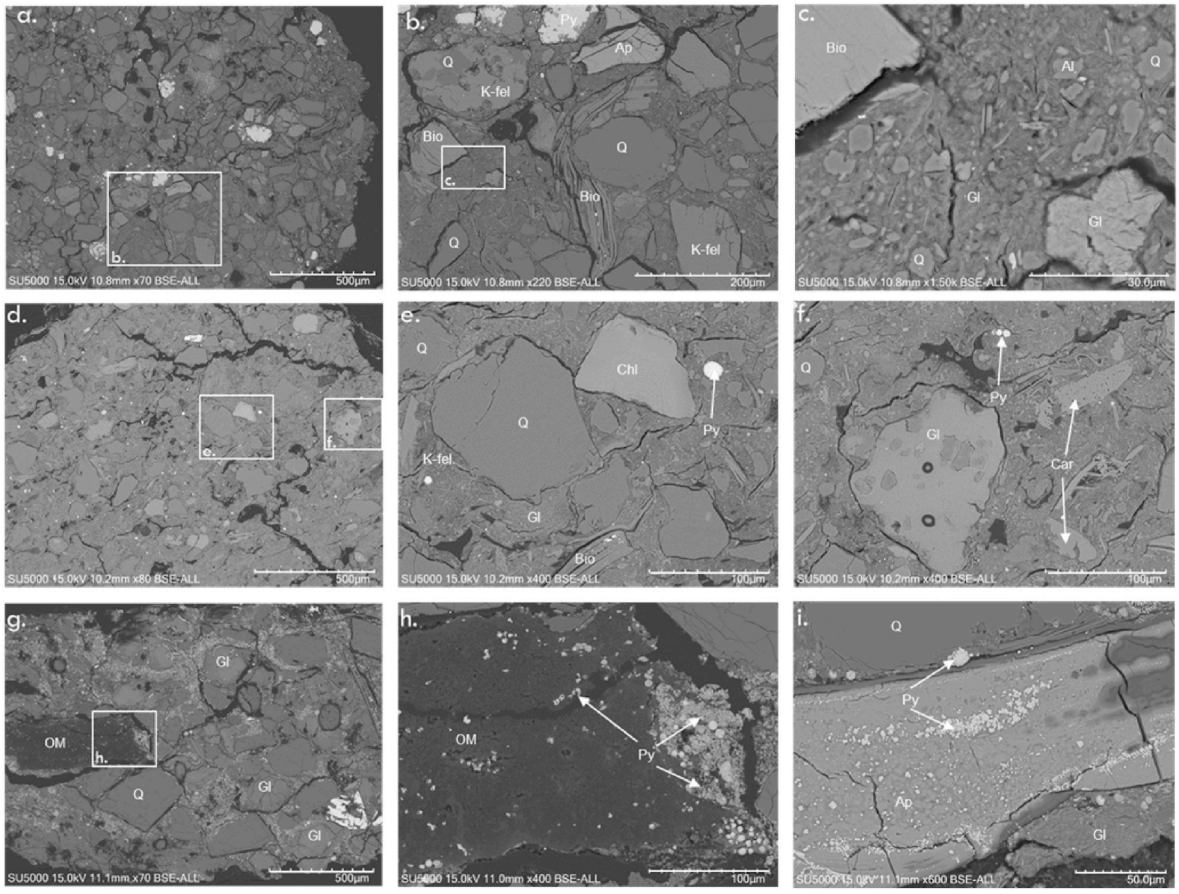

Fig. 8. High-resolution backscatter SEM images of Draupne Formation show the changes in composition and texture in a single caprock unit from wells 32/2–1 (a, b & c), 32/4–1 (d, e & f) and 35/11–4 (g, h & i). All the white dots are the pyrite (Py.) framboids and euhedral shape, which have a significant variation in volume and distribution within the studied wells. The abbreviations of Q.-Quartz, Gl.-Glauconite, Ap.-Apatite, Bio.-Biotite, K-fel.-K-Feldspar, Al.-Albite, Chl.-Chlorite, and Car.-Carbonate are used for simplicity. Note the variability of scale in different images.

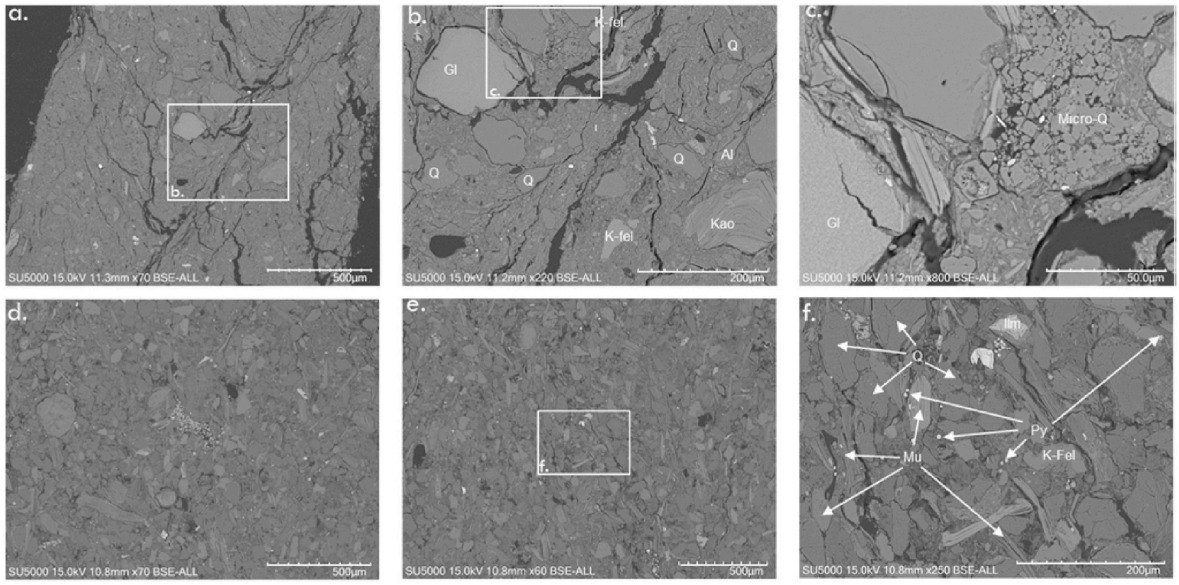

Fig. 9. High-resolution backscatter SEM images of Heather Formation show the changes in composition and texture from wells 32/2–1 (a, b & c) and 32/4–1 (d, e & f). The abbreviations of Q.-Quartz, Gl.-Glauconite, Kao.-Kaolinite, Mu.-Muscovite, K-fel.-K-Feldspar, Al.-Albite, Py.-Pyrite, and Ilm.-Ilmenite are used for simplicity. Note the variability in scale between images.

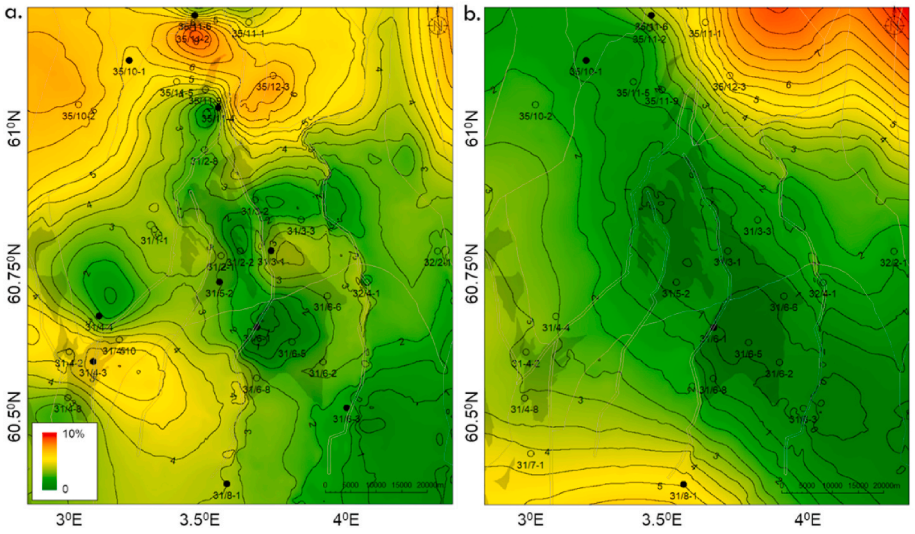

Fig. 10. Maps of TOC distribution based on the log derived well data points (harmonic average) of a) Draupne and b) Heather formations. Note that the contour interval is 0.5%.

and direct precipitation of micrometer-sized euhedral crystals are linked with iron oxide minerals (Fig. 8i) (Taylor and Macquaker, 2011). These observations indicate that there is a variation of initial fluid geochemical components between NW and SE wells. In contrast, Heather Formation has diagenetic quartz in both wells 32/2–1 and 32/4–1. Heather Formation has comparatively coarser grains compared to the Draupne Formation within the same wells except well 35/11–4, where a coarser Draupne Formation is observed. The number of samples is limited, but still, it is possible to identify the sub-zones with varying mineralogy and fabric. Based on our analysis, the NW part of the zero thickness trend is course-grained with low percentage of soft minerals assemblages compare to the south-eastern area where caprocks are fine-grained with a high percentage of soft minerals.

4.3. TOC distribution

Paleo-depositional variations also influence the variation in original TOC content and its preservation during and after deposition. The present-day TOC fraction depends on the anoxic condition of the seafloor during deposition and the preservation processes after deposition. The TOC distribution map based on well data points (calculated using equation (1)) shows significant TOC variation within the study area. Though there is considerable uncertainty in the calculated TOC (equation (1)), the harmonic average (Table 2) and the location of the measured TOC wells (solid black points in Fig. 10) added confidence in the TOC distribution map. Different TOC trends are observed between the Draupne and Heather formations. Lower TOC in Draupne Formation is found in the Troll area, which continued in the SE direction covering the Bjørgvin Arch and Stord Basin (Horda Platform), while the North and

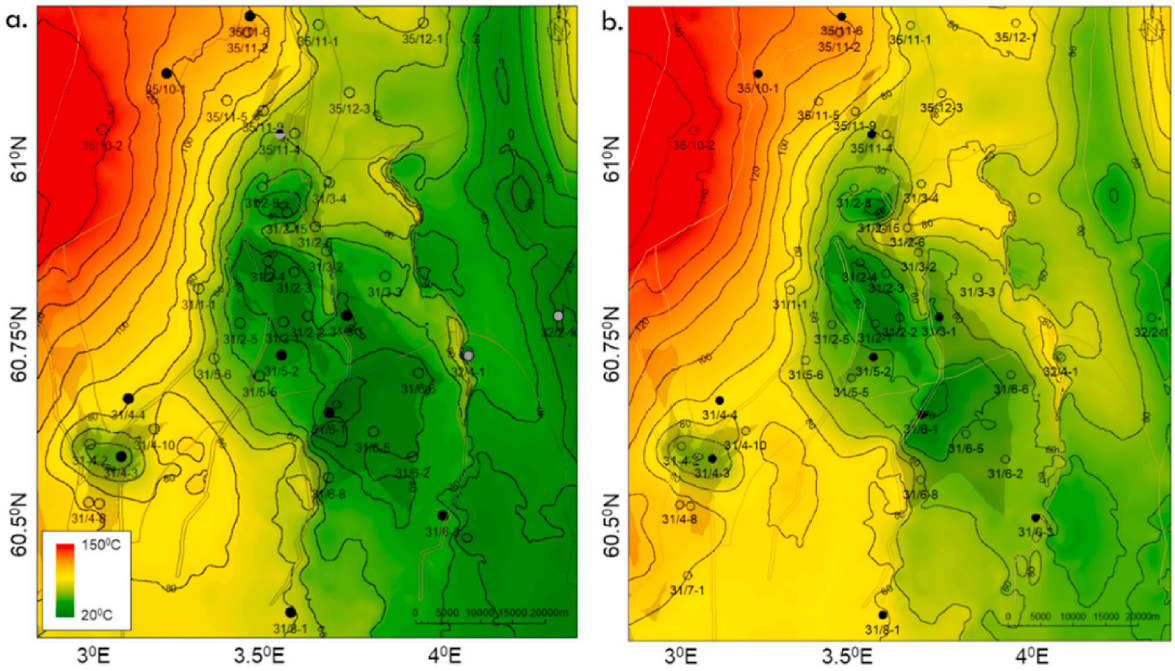

Fig. 11. The temperature map on top of Draupne Formation calculated using a geothermal gradient of 35 °C/Km representing a) present-day temperature and b) the maximum (exhumation corrected) temperature. The contour interval is 10 °C showing a gradual increase in temperature from southeast to northwest.

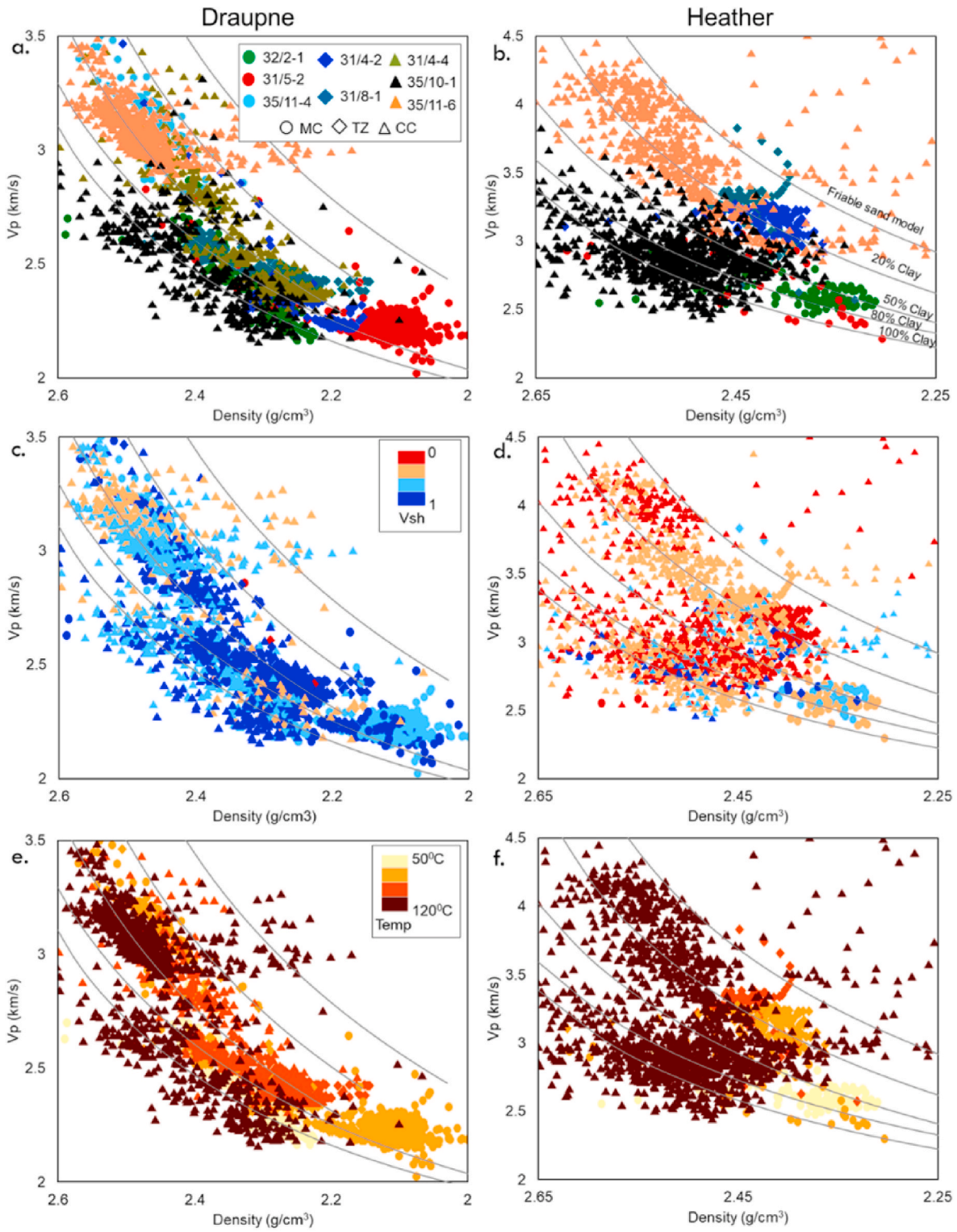

Fig. 12. Crossplots of Density versus Vp of Draupne and Heather formations from the eight selected wells representing MC, TZ, and CC data, color-coded by well names (a & b), Vsh (c & D) and Temperature (e & f) with the reference curves adapted from Avseth et al. (2005). (For interpretation of the references to color in this figure legend, the reader is referred to the Web version of this article.)

SW part of the areas have higher TOC covering the northern part of Lomre Terrace, Marflo Spur, and Brage Host. In contrast, Lower TOC in Heather Formation follows an NW-SE trend in the middle of the study area and increases both NE and SW directions (Fig. 10).

4.4. Compaction and properties of caprocks

The caprock properties are gradually altered due to the compaction processes (MC and CC). The transition between MC and CC in caprocks are mainly dependent on temperature and the mineralogy of the zone. Due to the lack of mineralogical analysis, the transition zone (TZ) of the

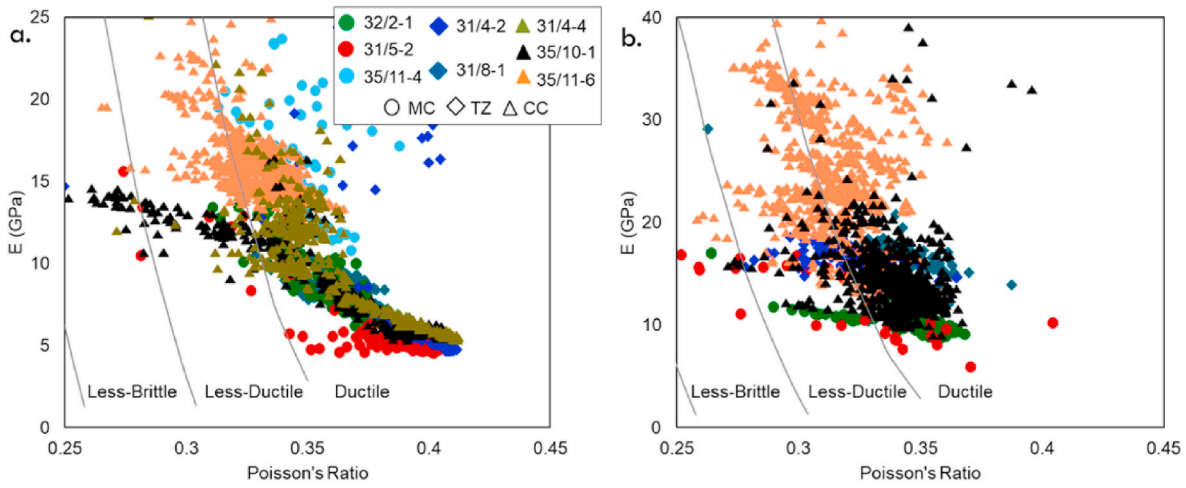

Fig. 13. Cross-plot of Young's modulus versus Poisson's ratio of a) Draupne and b) Heather formations with the reference curves adapted from Perez and Marfurt (2014).

studied area is defined by only the maximum temperature experienced by the caprock formations. The mechanical compaction in sandstone is dominated at temperature 70 °C considering 35 °C/km geothermal gradient; however, the transition for fine-grain particle-like shale depends on many other factors (i.e., mineralogy, type of clay, pore water chemistry, etc.) and ranges between 60^0 to 120 °C (Bjørlykke et al.,

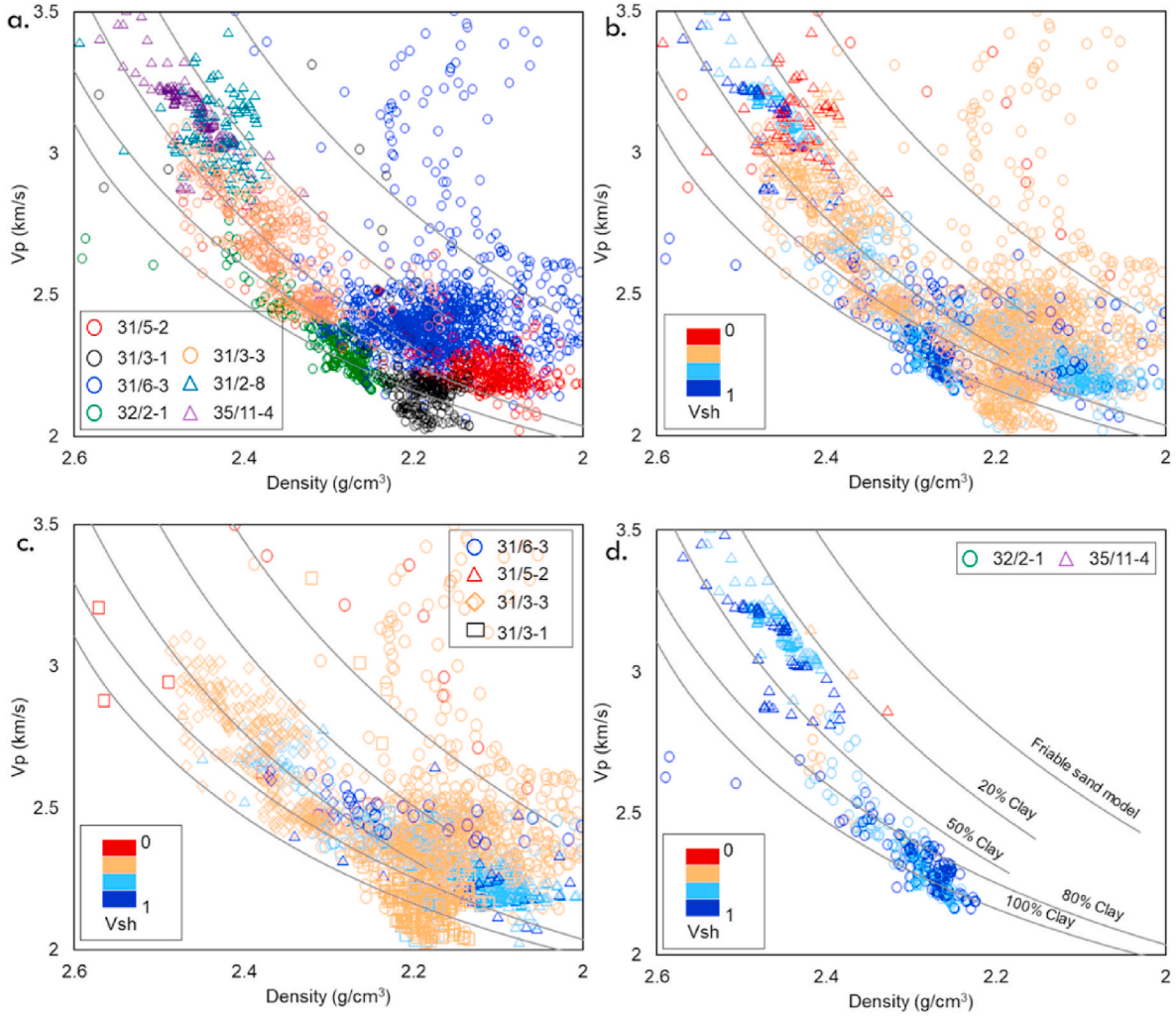

Fig. 14. Crossplots of density versus Vp of Draupne Formation data from the mechanically compacted (MC) wells color-coded by well names (a), and Vsh (b, c & d) with the reference curves adapted from Avseth et al. (2005). The circle represents the wells located in the SE part from zero thickness, while the triangles represent the NW wells. (For interpretation of the references to color in this figure legend, the reader is referred to the Web version of this article.)

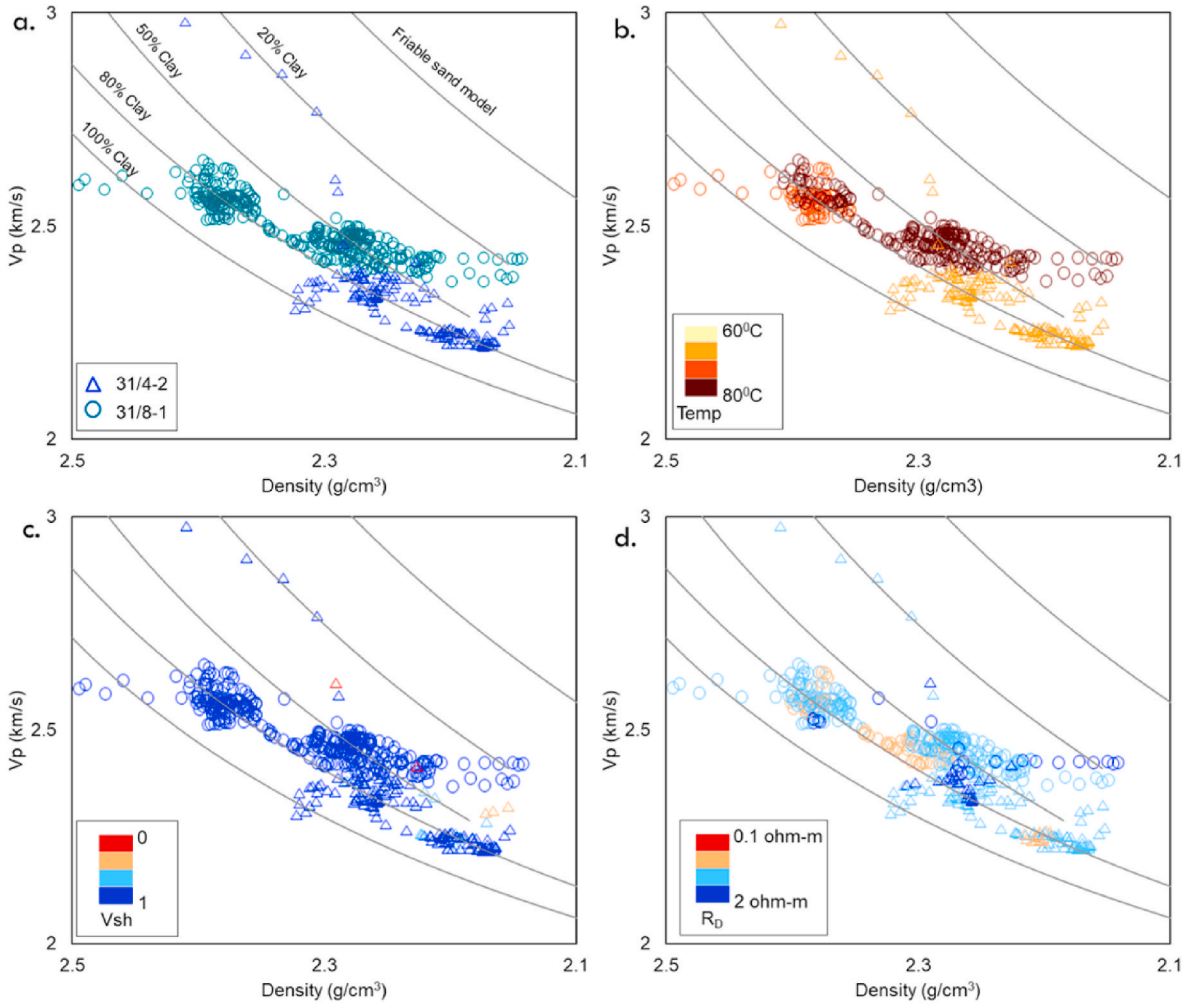

Fig. 15. Density versus Vp cross-plot of Draupne Formation based on data from the transition zone (TZ) wells color-coded by well names (a), temperature (b), Vsh (c), and R_D (d) with the reference curves adapted from Avseth et al. (2005). (For interpretation of the references to color in this figure legend, the reader is referred to the Web version of this article.)

2015). In this study, a range, i.e., 65–75 °C is used as a transition zone considering the uncertainties. According to present-day temperature on top of the Draupne Formation, the majority of the studied wells are within the MC zone compared to TZ and CC. However, after the exhumation correction, the numbers of wells falling in TZ and CC are increased (Table 3). The present and maximum temperature map on top of the Draupne Formation show the spatial distribution within the different sub-groups (Fig. 11). The northwestern part of the studied area is in the realm of chemical compaction, which covered the Lomre terrace and Marflo Spur structural elements. In contrast, the western part of the Stord Basin is within the TZ temperature, and the rest of the platform, including the Troll Gas Field area, is within the MC zone. A similar temperature trend is also observed in the Heather Formation temperature distribution maps.

The Vp and density data of Draupne and Heather formations from eight wells covering all sub-groups (MC, TZ & CC wells) are cross-plotted to evaluate variations of the caprock elastic properties (Fig. 12). We find no specific clusters for different sub-group in Draupne Formation; instead, a mixture of different well clusters is observed. The stiff rock (high Vp & density) data points are from an MC well 35/11–4 and a CC well 35/11–6, while the soft rock (low values of Vp & density) is represented by an MC well 31/5–2 and the TZ well 31/4–2. The rest of the wells, which are from all three sub-groups, show data in the intermediate range. We find no trend in Vsh and temperature as high and low-temperature data is clustered in the same region (Fig. 12e). Heather Formation also shows a similar pattern (no sub-group clustering) of data distribution and temperature variation, but overall the elastic properties have higher values compare to Draupne Formation (Fig. 12b). Moreover, in this formation, all the wells show silty to sandy type shales, which have significant variations of elastic properties compared to the Draupne data points.

Geomechanical properties in the study area show similar trends like acoustic properties. The wells plotted in the Vp-density plain also used in this analysis, which covers wells from MC, TZ, and CC zones. The soft Draupne Formation (low E and high PR) data points are plotted from wells 31/5–2, 31/4–2, 32/2–1, and 31/8–1 while high values of E and comparatively low values of PR observed in wells 35/11–4 and 35/11–6 (Fig. 13). However, the data from wells 31/4-4 and 35/10-1 have a wide-range where data from both wells started in the very soft-clustered area but ended up following the trend with a significant decrease in PR. A gentle increase in E is found in well 35/10–1, and an increase in E with a constant PR observed in well 31/4-4 (Fig. 13a). In contrast, Heather Formation seems to be stiffer than Draupne Formation but follows a similar increasing trend (i.e., increasing E but with a constant range of PR) (Fig. 13b). For further analyses, individual sub-groups are investigated in the successive sections under the different subheadings.

4.4.1. *Caprock properties in shallow depth wells (MC)*

Vp and density data points of seven wells of Draupne Formation located in the MC zone (MCZ) are chosen to evaluate variations of

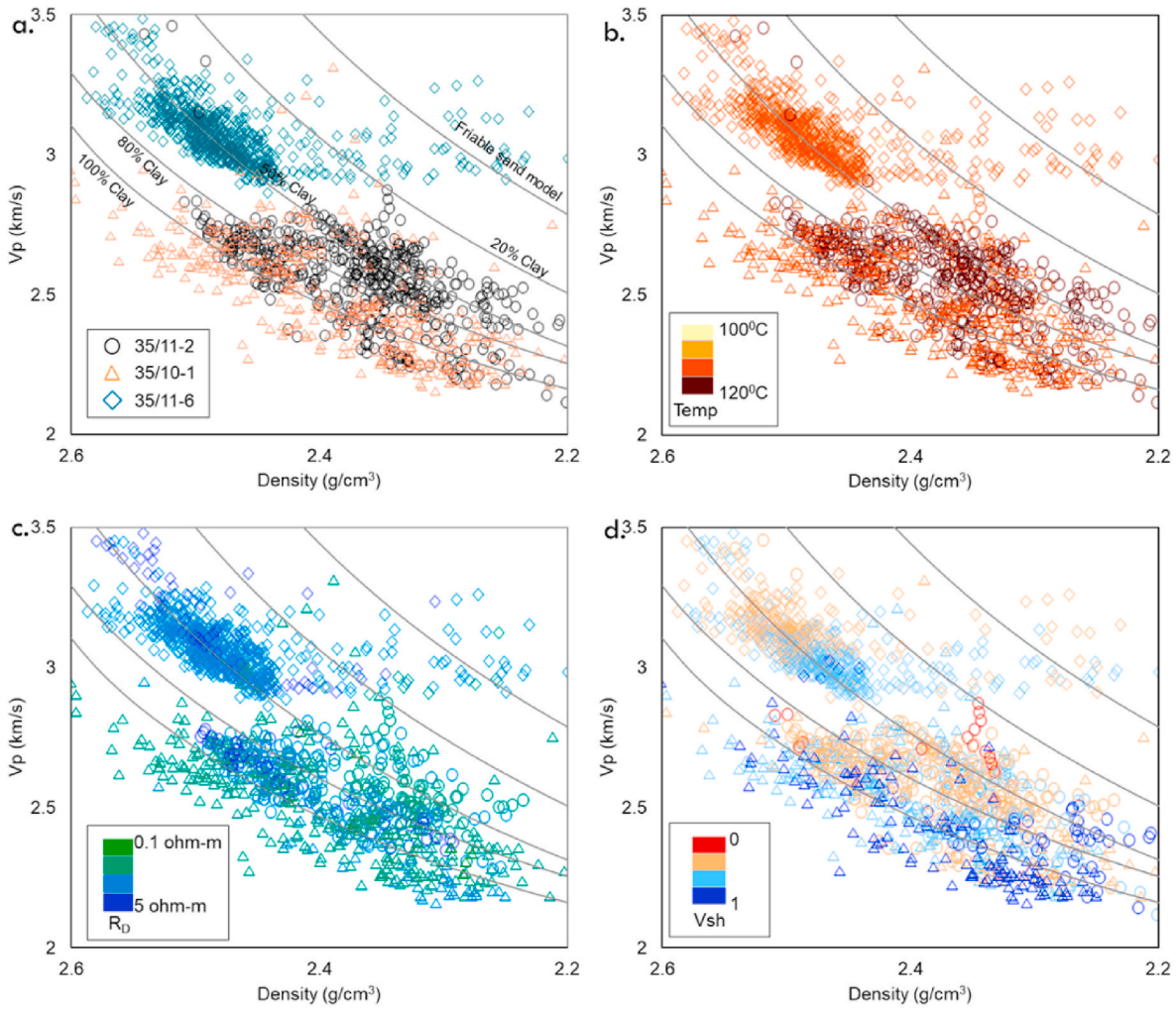

Fig. 16. Cross-plot of density versus Vp of Draupne Formation data retrieved from the chemically compacted zone (CCZ) color-coded by well names (a), temperature (b), deep resistivity (c), and Vsh (d) with the reference curves adapted from Avseth et al. (2005). (For interpretation of the references to color in this figure legend, the reader is referred to the Web version of this article.)

caprock properties. Two different symbols (i.e., circles and triangles) are used to separate the NW, and SE wells, where the circles represent SE, whereas the NW wells are denoted as triangles. The Draupne Formation situated in MCZ shows a significant variation of Vp and density where the NW wells 31/2–8, and 35/11-4 show stiff nature (high Vp & Density) compared to the wells from the SE part (Fig. 14). However, the well 31/3-3, which is located in the SE part, has an intermediate range of properties. Vsh values within the studied MC wells also vary significantly. Wells 31/5–2, 32/2–1, and 35/11–4 are more clayey compared to the other wells, whereas wells 31/3–1, 31/3-3, and 31/6–1 are less clayey with almost 0% clay in well 31/2–8. However, the distribution of caprock properties within the wells is not following the mechanical compaction trend. For example, wells 31/2–8 and 35/11-4 have a significant variation in Vsh but cluster in one location, while wells 31/3–1, 31/5–2, 31/6–1, and 32/2–1 contain soft rock with different depth and Vsh value. Another observation between wells 32/2–1 and 35/11–4 is that both wells have a high percentage of Vsh where well 32/2–1 follows the higher clay reference curve (80–100% clay line), while well 35/11–4 is shifted diagenetically and follows the 50-20% clay curves (Fig. 14d). The high values of Vp and density in well 35/11-4 might be due to a difference in grain size and precipitation of pyrite (Fig. 8h&i). Therefore, the higher Vsh percentage has not much effect on density and velocity in this case. On the contrary, the Draupne zone is silty in well 21/2–8 owing to a low Vsh value with high values of Vp and density. Therefore, the log driven caprock properties need validation with the petrographic analysis before deriving any conclusion.

4.4.2. *Caprock properties in intermediate depth wells (TZ)*

Two wells penetrated the studied caprocks in TZ are analyzed for characterizing the caprock properties. Data points from wells 31/4–2 and 31/8-1 have lower Vp and density values. All the wells have a high percentage of clay content (high Vsh) generally following the 80% clay curve. However, data from wells 31/8–1 and 31/4–2 are scattered within the 80-50% clay range. Overall the data signify the soft nature of the caprock zone though the temperature is quite high (Fig. 15b).

4.4.3. *Caprock properties in deeply buried wells (CC)*

Draupne Formation falling in the CC zone (CCZ) in three wells within the study area is plotted in the Vp-density rock physics template to evaluate variations of rock properties within the CC wells (Fig. 16). There are significant variations of rock properties observed where well 35/11-6 has stiff (high Vp & density) rocks compared to wells 35/10–1 and 35/11–2. Though the difference in temperature and resistivity values are not significant, comparatively lower temperatures and higher deep resistivity are found in well 35/11–6. The Vsh values show considerable variations within the wells and with the reference curves. The soft (low Vp and density) properties well 35/10-1 has high values of Vsh and follow the 100% clay line. However, the data points of well 35/11-2 shift upward, having higher values of velocity and similar density with decreasing Vsh. In contrast, well 35/11-6 has higher Vp and density

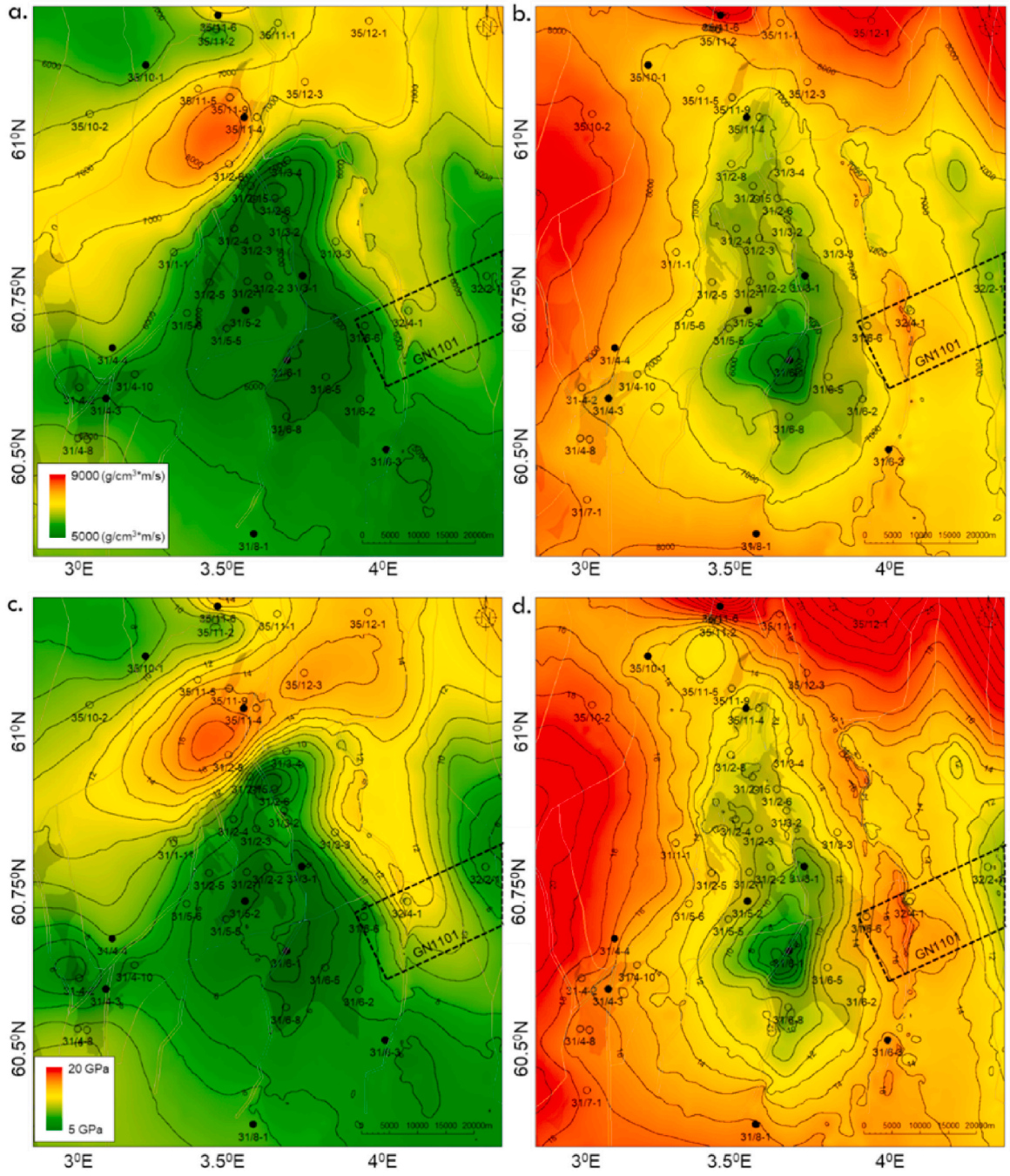

Fig. 17. Caprock property maps generated using the well data points of Draupne and Heather formations showing AI in Draupne (a), AI in Heather (b), E in Draupne (c), and E in Heather (d). The same color scale is used for each property within both formations to show the variability. (For interpretation of the references to color in this figure legend, the reader is referred to the Web version of this article.)

but the same range of Vsh compared to well 35/11–2 (Fig. 16d).

Differences in caprock properties within the studied wells also reflected in the property maps generated from the average values. Acoustic Impedance (AI) and Young's Modulus (E) of Draupne and Heather formations' spatial distribution within the studied area are shown in Fig. 17. The same color scale is used for both formations to compare those properties variations visually. Both formations have lateral change within the study area where the Draupne Formation has higher contrast than the Heather Formation. Moreover, the property variation tends to follow the structural elements, especially the major faults. The softer Draupne caprock (low values of AI and E) found in the Troll area is bounded by Vette fault in the east and Troll fault in the west. There is a stiff rock trend observed in the north of the Troll field, which follows a NE-SW strip. However, following the stiff rock trend, a comparatively softer rock found in the north-western corner of the study area. In contrast, Heather Formation's rock properties follow a different pattern where the relatively soft rock is found in the Troll Field area, which gradually becomes stiff in all directions.

4.5. Brittleness indices

Draupne and Heather formation's brittleness indices values are summaries in Table 5. Four different BI's (EBI[1], EBI[2], MBI[1] & MBI[2]) are estimated to evaluate the geomechanical properties of the caprocks

Table 5
Comparison of average brittleness indices within various structural elements, and brittleness calculated by different equations for Draupne and Heather formations.

Well no.	Structural Elements (NPD)	Draupne Formation				Heather Formation			
		EBI1	EBI2	MBI1	MBI2	EBI1	EBI2	MBI1	MBI2
31/2-1	Bjørgvin Arch	0.14	0.18	–	–	–	–	–	–
31/2-2		0.13	0.07	–	–	–	–	–	–
31/2-6		0.17	0.02	–	–	–	–	–	–
31/2-8		0.36	0.50	–	–	–	–	–	–
31/3-1		0.14	0.17	–	–	0.22	0.38	–	–
31/3-2		0.24	0.15	–	–			–	–
31/3-3		0.25	0.31	–	–	0.29	0.39	–	–
31/4-3		0.18	0.23	–	–	–	–	–	–
31/4-8		0.21	0.33	–	–	–	–	–	–
31/4-10		0.16	0.20	–	–	–	–	–	–
31/5-2		0.13	0.17	–	–	0.27	0.42	–	–
32/2-1		0.14	0.26	0.19	0.27	0.23	0.37	0.27	0.43
35/11-7		0.34	0.49	–	–	–	–	–	–
31/6-1	Stord Baisn	0.13	0.17	–	–	0.17	0.26	–	–
31/6-2		0.18	0.24	–	–	0.30	0.41	–	–
31/6-3		0.15	0.24	–	–	0.33	0.48	–	–
31/6-5		0.14	0.14	–	–	0.28	0.41	–	–
31/6-6		0.17	0.22	–	–	0.32	0.46	–	–
31/6-8		0.14	0.20	–	–	0.23	0.36	–	–
31/8-1		0.18	0.28	–	–	0.34	0.50	–	–
32/4-1		0.26	0.36	0.26	0.31	0.28	0.43	0.17	0.49
31/4-4	Lomre Terrace	0.19	0.32	–	–	–	–	–	–
35/11-2		0.21	0.37	–	–	0.36	0.55	–	–
35/11-4		0.32	0.49	0.61	0.70	–	–	–	–
35/11-6		0.28	0.41	–	–	0.53	0.61	–	–
31-4-2	Brage Host	0.13	0.23	–	–	0.38	0.51	–	–
35/10-1	Marflo Spur	0.20	0.31	–	–	0.29	0.46	–	–

where the EBI's are calculated using elastic properties, and mineralogical fractions are used to estimate the MBI's. Overall the Draupne and Heather formations show the BI values tend to be more ductile with few less ductile readings in Heather Formation. However, there is a significant variation observed within the values estimated by the various BIs. $EBI^{1,}$ which is calculated from Young Modulus (E) and Poisson's ratio (PR), has lower BI values than $EBI^{2,}$ which is estimated using AI and R_D. Similar differences are also found between MBI^1 and MBI^2 where MBI^2 has higher BI value than MBI^1. This is expected as MBI^2 considered all the brittle minerals (i.e., quartz, feldspar, pyrite, and carbonate) to calculate BI compared to only quartz in MBI^1. However, EBI^1 has a good match with MBI^1 and, similarly, EBI^2 with MBI^2. In well 35/11–4, where the percentage of ductile minerals (Clay and TOC) has a meager influence, the estimated MBIs are significantly higher than EBIs. Moreover, this well represents the highest BI value (0.70) within the studied wells.

BI maps of Draupne and Heather formations show a significant lateral variation of the caprock brittleness properties within the study area (Fig. 18). According to the maps, the less ductile zones are found in Heather Formation, which is calculated using equation (8) (Fig. 18d). Overall, as seen in the well average, EBI^2 is stiffer than $EBI^{1,}$ wherein both scenarios, Heather Formation is less ductile, the BI maps also represent a similar trend. Moreover, the maps illustrated that the more ductile caprock located in the center of the study area, mainly covering the Troll Field and gradually increasing in all directions. However, in Draupne Formation, a NE-SW trending brittleness anomaly exists in the NW corner of the study area (Fig. 18a&c).

4.6. Brittleness indices trend

In this analysis, we are evaluating the qualitative brittleness increasing trends based on elastic impedance-based brittleness in Young's modulus (E) versus Poisson's ratio (PR) and LMR (LamdaRho versus MuRho) templates. We choose six wells (31/4–2, 31/8–1, 32/2–1, 35/10–1, 35/11–4 & 35/11–6) with different depth levels to cover the whole vertical compaction ranges and cover the area spatially. There is a significant difference observed in brittleness increment trend when compared with reference curves (Figs. 19 and 20). According to Grieser and Bray (2007) zonation, the studied Draupne and Heather formations data points fall within the brittle area though the brittleness indices values are quite low (Fig. 19). However, the brittleness indices increase with increasing E.

There is also a significant difference observed in the brittleness increment trend between the studied data points and reference curves in the E versus Poisson's ratio cross-plots (Fig. 20). In E versus PR cross-plot, the Draupne and Heather formations data points follow an increased brittleness trend with increasing E and a constant range of PR. Moreover, a zone of very low values of E and high values of PR is found, which does not follow the trend and exhibits very low brittleness hence deemed ductile. Similar different pattern finds in $\lambda\rho$ versus $\mu\rho$ cross-plots where the reference curve brittleness increases with a moderate rise in $\mu\rho$ and decrease in $\lambda\rho$ while brittleness of Draupne and Heather formations increase with increasing $\lambda\rho$ and $\mu\rho$ (Fig. 20c & d).

4.7. Variation of AI in prestack inverted cube

The prestack inverted cube of acoustic impedance (AI) of Draupne and Sognefjord formations shows the lateral amplitude variation in the Smeaheia area (Fig. 21b). An increasing trend of amplitude follows the time structural dipping trend, i.e., increases from NE to SW direction (Fig. 21a). A similar amplitude increasing trend also observed in the cross-section where the AI value of Draupne and Heather formations gradually increases from NE to SW direction (Fig. 21c), which strongly follows the log-derived elastic and geomechanical properties (Fig. 17). The log-based AI and Young's modulus (E) of Draupne and Heather formations within the seismic cube boundary (GN1101) show a similar gradual increase in properties. Moreover, the elastic log-based brittleness indices estimated using empirical equations confirm the same trend (Fig. 18). The relation between inverted seismic volume and geomechanical property (i.e., brittleness) helps for the qualitative characterization of organic-rich caprock from seismic data.

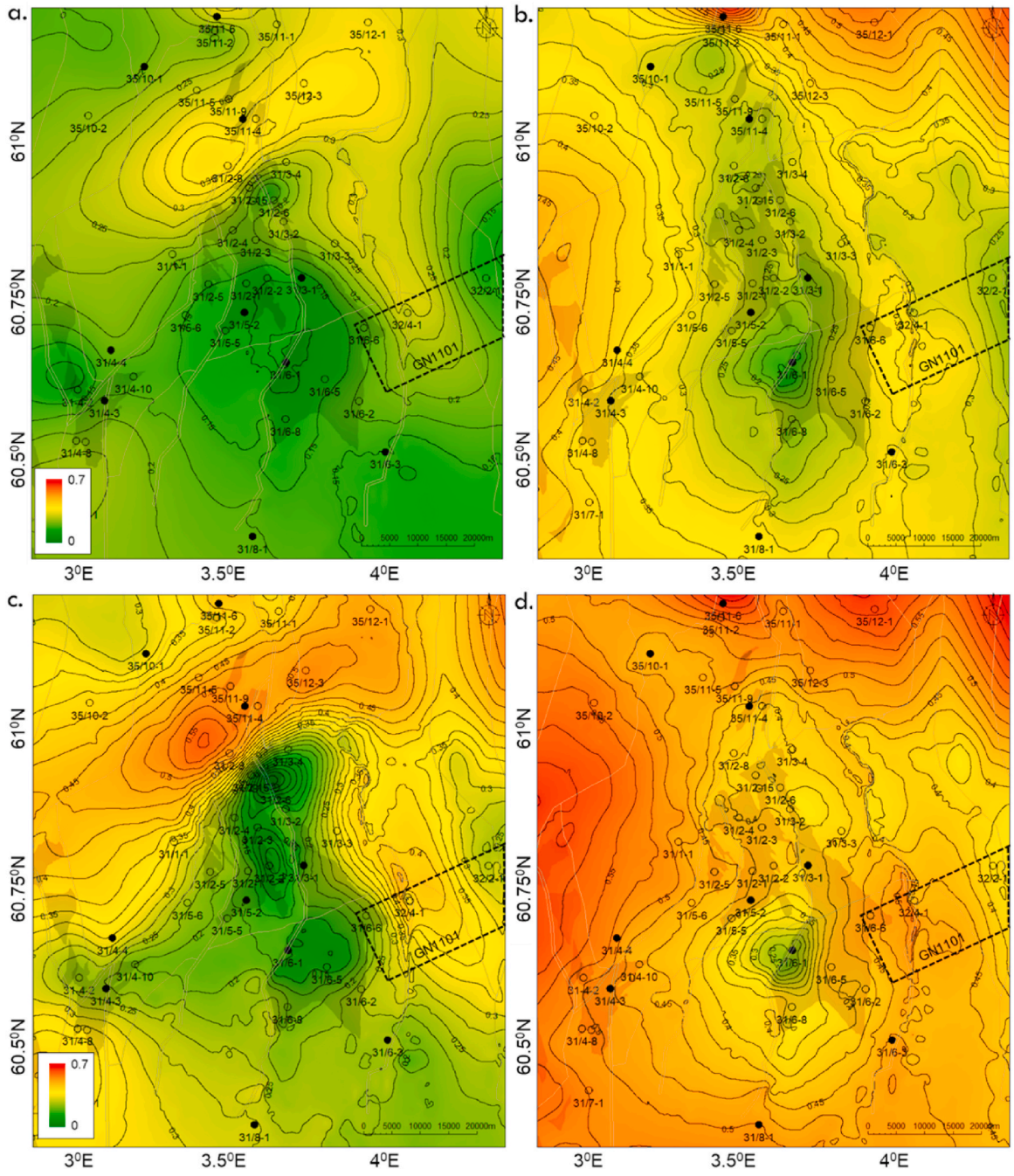

Fig. 18. Brittleness Index maps calculated from average well data points using Grieser and Bray (2009) for a) Draupne and b) Heather formations, and Fawad and Mondol (2020, unpublished, patent-pending on the procedure) for both c) Draupne and d) Heather formations. The contour interval is 0.025, and the same color scale is used for all the maps to show the variability between equations and formations. (For interpretation of the references to color in this figure legend, the reader is referred to the Web version of this article.)

5. Discussion

5.1. Paleo depositional environment

Based on the gamma-ray log pattern, height, and the corresponding values (Emery and Myers, 1996), a significant variation is found in the paleo-depositional environment of Draupne and Heather formations within the study area. This differences might influence the mineralogy, grain size, fabric, initial pore fluids geochemistry, etc. as shales in a basin typically follow a systematic vertical pattern with the fluctuation of relative sea-level changes. However, tectonics, climate, and relative sea-level condition affect the ultimate character of that basin-fill succession (Slatt, 2011). These factors have a direct effect on the caprock integrity, which are observed in log derived elastic and geomechanical properties. However, without a basin-wide analysis of the sediment input and deposition system, it is challenging to identify the factors that influence a small area like this study. Considering these uncertainties, gamma-ray still represents the local variation and proves to be an excellent tool for qualitative interpretation.

According to the gamma-ray log shape and value in the studied area, the possible high energy sediments (mainly silt) within Draupne caprock was deposited in the NW close to the Lomre Terrace area, while in the SE (including the Bjørgvin Arch, and Stord Basin) possessed a proximal shelf depositional environment within a marine embayment. However,

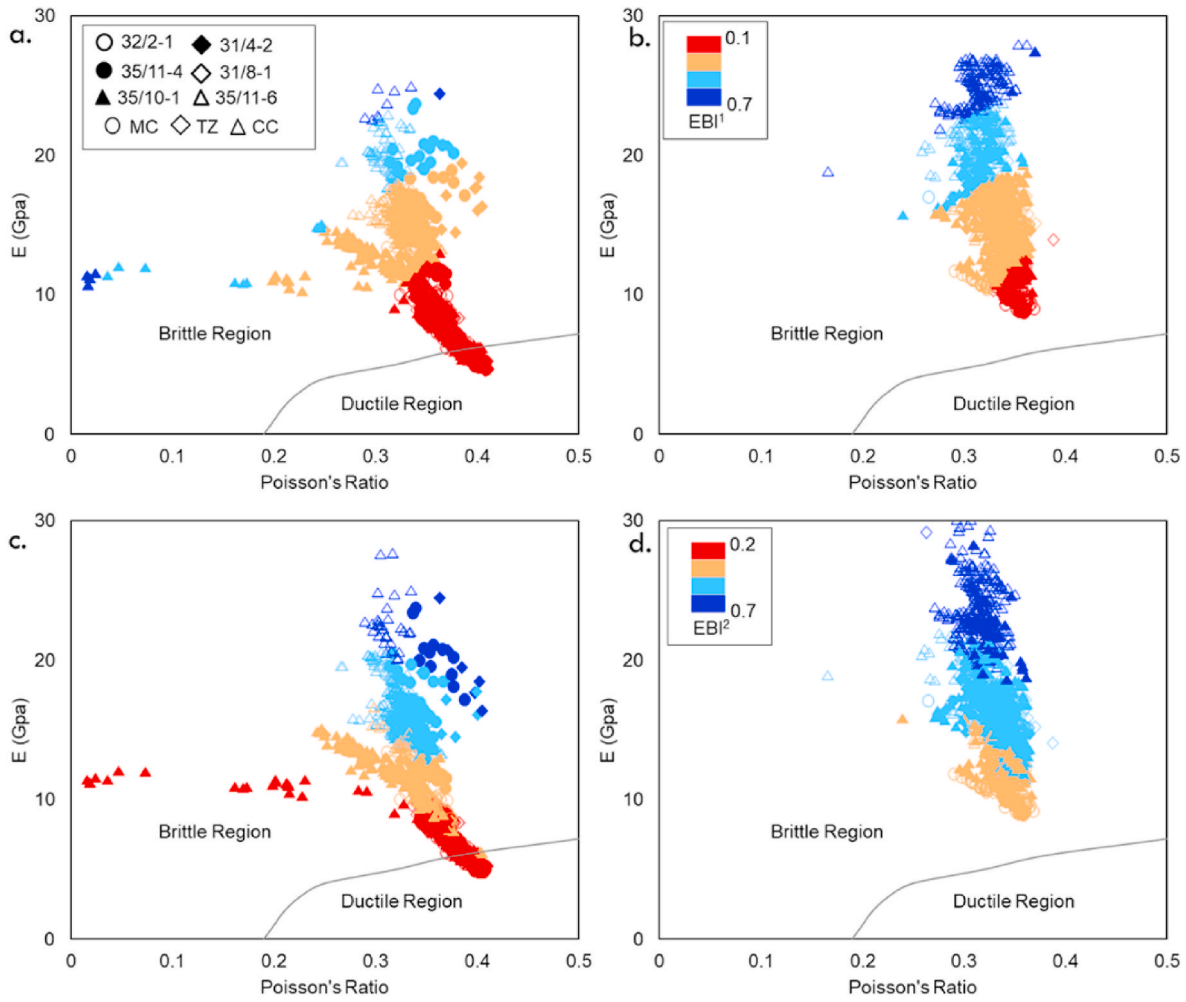

Fig. 19. Young's modulus versus Poisson's ratio cross-plots of Draupne (a) and Heather (b) formations color-coded by EBI^1 and same formations in (c) and (d) color-coded by EBI^2 with the reference curve adapted from Grieser and Bray (2007).

the distal shelf environment in the SW and western areas, which cover the SW part of the Stord Basin and Lomre Terrace, is more clayey with a higher fraction of organic matter. Other major faults (i.e., Vette, Tusse, Svartalv, Idunn, etc.) also influenced the local thickness, which ultimately impacted the mineralogy, grain size and fabric, and initial pore water chemistry. The local depocentres interpreted in the thickness maps explain the effect of the fault-related accommodation spaces variation during deposition, and the consequence of that was also observed in the log shape and vertical stacking pattern differences within the studied wells (Fig. 5). These depositional variations influenced the mineral assemblages within Draupne and Heather formations. Significant changes of stiff (i.e., quartz, pyrite, feldspar, and carbonate) and soft (i.e., clay, organic matter) mineral fractions were found within NW (35/11–4) and SE (32/2–1 & 32/4–1) wells. The well 35/11-4 has courser grains with the abundance of pyrite and a small fraction of clay mineral while wells 32/2–1 and 32/4-1 have fine-grained (clay fractions) with local clustering of pyrite and a small fraction of quartz in Draupne Formation (Figs. 7–9). In Heather Formation, micro-quartz (32/2–1) and abundance of siderite (32/4–1) are found where the ratio of soft and stiff mineral assemblages are 50:50.

5.2. Effect of compaction

The Draupne Formation data point cluster does not separate mechanical and chemical compacted wells; instead, the data overlapped different regions (Figs. 12 and 13). Similar data distribution trends are also found in Heather Formation, but the properties have higher values and different trends compared to Draupne Formation. The wells located in high-energy deposition area (i.e., in the NW close to troll fault, i.e., 31/2–8, 35/11–4 & 35/11–6) have higher values of acoustic and geomechanical properties compared to the SE platform and SW deep basin areas (e.g., wells 31/4–2, 31/4-4, 31/5–2, 32/2–1 & 35/10–1). Grain size and sorting also have a significant impact on caprock properties. Larger grain size with mixed type of rock framework (a mix between matrix and grains) were observed in NW well (35/11–4) compared to the SE wells (32/2–1 & 32/4–1) where grains are finer making a matrix-supported caprock. The grain sizes and their distributions are other possibilities for stiffer zones in NW wells because poorly sorted coarse-grained sediments compacted more than the fine-grained shales (Storvoll et al., 2005; Mondol et al., 2007; Marcussen et al., 2009; Thyberg et al., 2009). Moreover, homogeneous fine-grained rocks can preserve higher stress; hence behave more ductile than heterogeneous coarse-grained rocks. Also, larger grain size makes rocks easier to fracture thus is stiffer (Zhang et al., 2016) because of more inter-granular cracks within small grains, which allow mobilizing more strength, also the larger grains containing larger and longer inter-granular cracks lower stress is required to initiate and propagate cracks (Eberhardt et al., 1999).

The sections of Draupne and Heather formations exposed to chemical compaction (i.e., 35/10–1, 35/11–2 & 35/11–6) also show a significant variation of caprock properties where the stiff data points (high Vp, high density, and high E) fall within the same range with sections that only

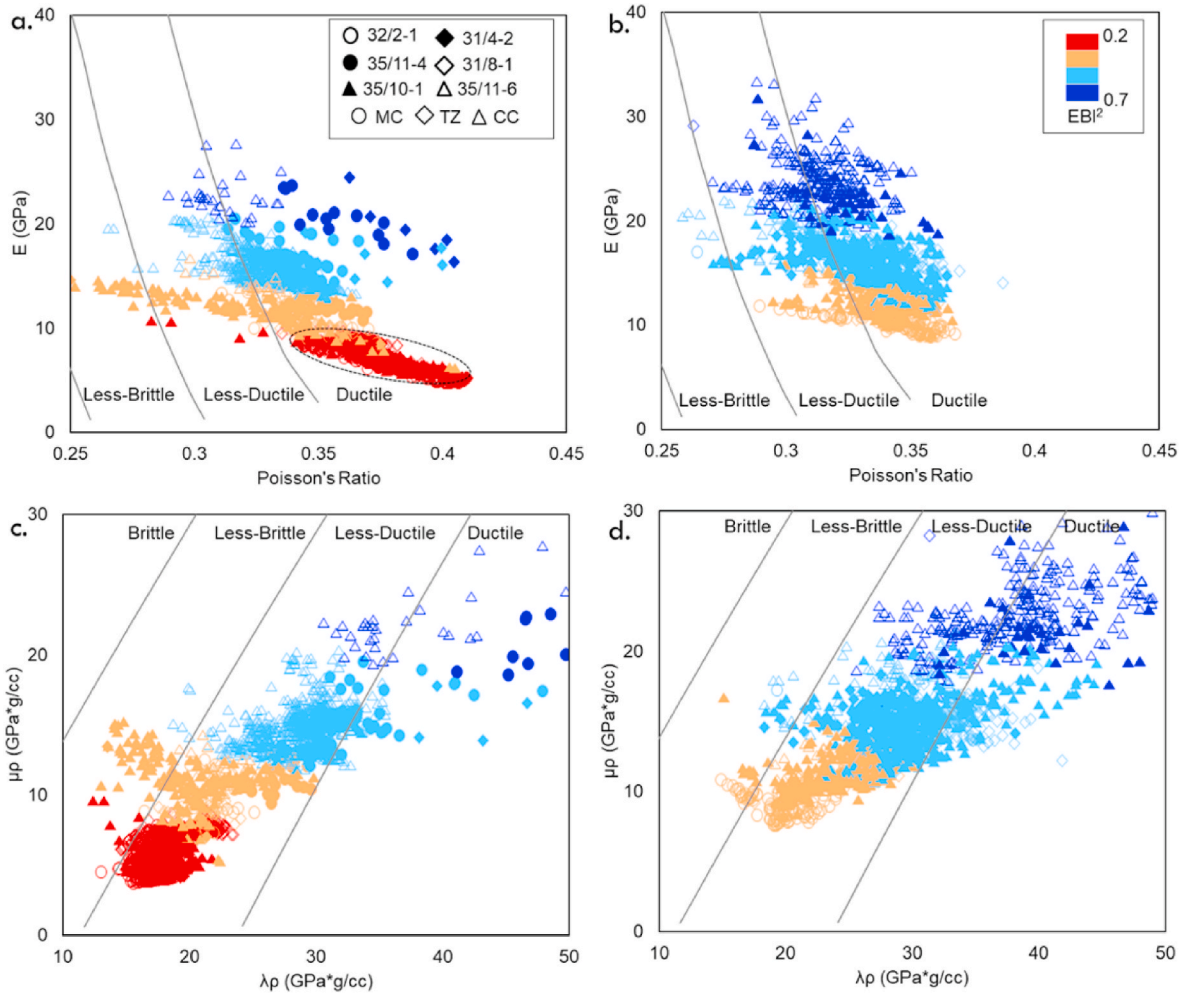

Fig. 20. Cross-plots of data points from six wells show the Young's modulus versus Poisson's ratio of Draupne (a) and Heather (b) formations and the μρ versus λρ of Draupne (c) and Heather (d) formations with the reference curves adapted from Perez and Marfurt. (2014). All the cross plots color-coded with EBI^2 brittleness indices value.

experienced mechanical compaction (i.e., wells 31/2–8, 21/3-3 & 35/11–4). The location of the well 35/10–1 is in the deep basin area, which explains the high Vsh percentage. Moreover, the wells 35/11–2 and 35/11-6 located in its close proximity also manifest a similar range of Vsh values. There might be an effective-stress difference in reservoir-caprock pair between dry hole (35/11–6) and discovery (35/10–1 and 35/11–2) wells as both reservoirs contain different fluids at different reservoir pressure. These might be leading to a different compaction process with variation in caprock properties. The effect of depth (equivalent temperature) on caprock properties might have acted in both ways (decreasing or increasing stiffness) because of the combined impact of pressure, temperature, diagenesis, and TOC as functions of depth. TOC itself has a complex effect on caprock properties. The maturation of TOC increases porosity hence increase rigidity (Rybacki et al., 2016) while during conversion, the heavy residual TOC portion increases the bulk density hence the rock stiffness. However, the effect of TOC on caprock geomechanical properties more depends on fabric (i.e., sparsely or layered distribution) than the TOC volume fraction (Slatt and Abousleiman, 2011). Moreover, in fine-grained, thick shale formations, there might be possibilities of developing overpressure by un-expelled fluid resulting in the reduction of the effective stress, hence decreasing the caprock stiffness. The low values of acoustic and geomechanical properties of chemically compacted wells (NW) within the study area might be the effect of those parameters (Fig. 4). The immature TOC in the SW part of the study area representing low values of elastic properties is possibly a function of weak mineral contents (i.e., clay and TOC), rather than a TOC alteration effect. This indicates the immature TOC behaves like a soft mineral assemblage.

5.3. Brittleness indices

In MBI^1, which is only considered quartz as stiff mineral, underestimated the formation of brittleness and has a poor correlation with caprock properties (Fig. 22a&e). However, considering the total stiff minerals, we found a better correlation compare with only quartz (Fig. 22c&e). Moreover, the mineralogy based brittleness indices are sometimes overestimating because the equations do not consider any diagenetic effects such as compaction related grain fabric or chemical precipitation (i.e., pyrite or quartz cement, etc.). The process does not consider the origin of the mineral assemblages (i.e., detrital or diagenetic), which has a significant impact on rock mechanical behavior too. For example, in well 35/11–4, the mineralogical BI's are significantly higher than the elastic property-based BI's because MBI's only considered bulk mineralogy fractions but did not consider the effective rock framework impact. On the other hand, the estimated elastic properties have embedded consideration of depositional and diagenetic effects, which is reflected in the EBI's assessed values (Table 5). Moreover, EBI's increasing trend is significantly different than the published trends (Figs. 19 and 20). The zones defined in the background curves are estimated from the data points of Barnett shale from the Fort Worth

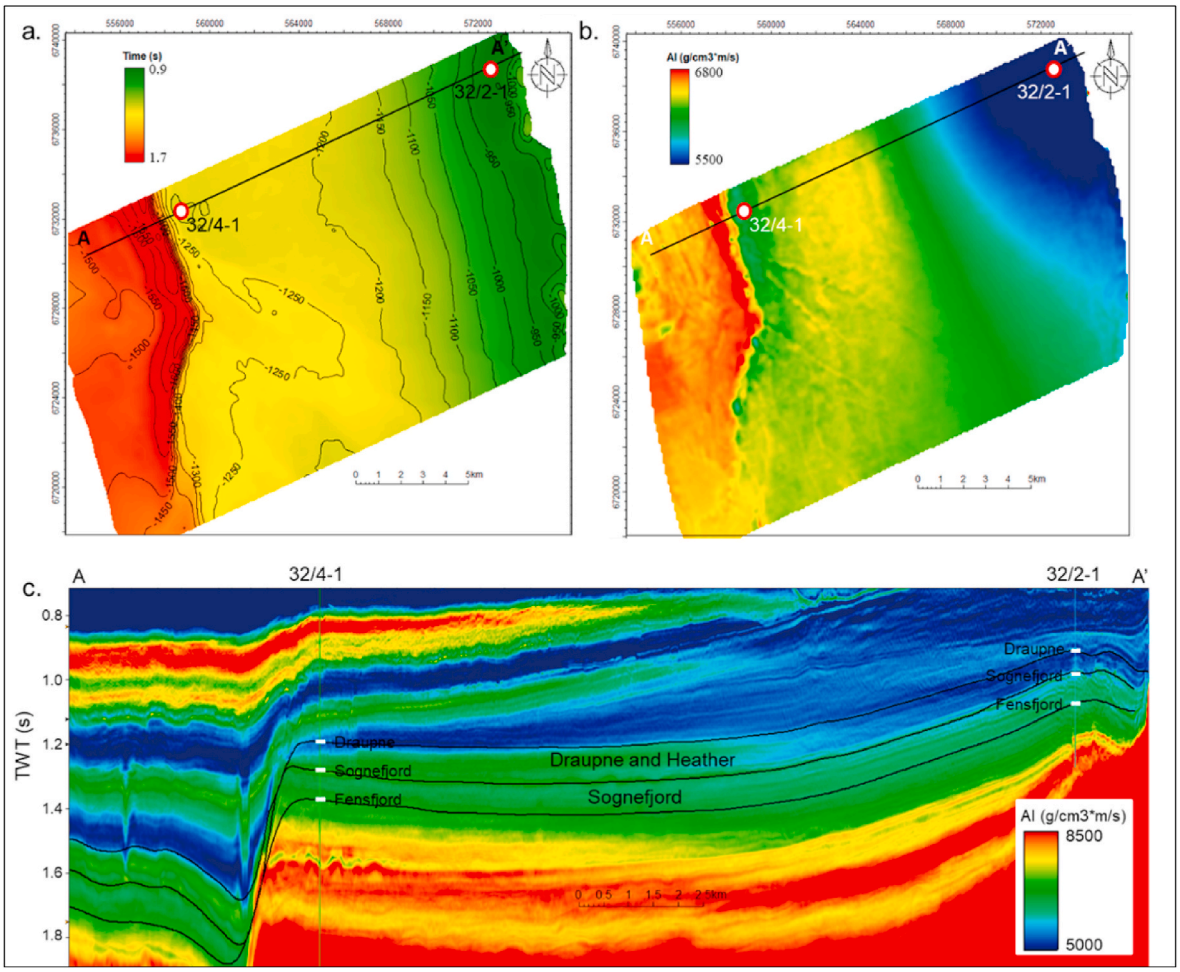

Fig. 21. a) Time structure map of Draupne Formation based on the 3D seismic data outlined in Fig. 1, with the location of random line A-A′ and exploration wells 32/2–1 and 32/4–1. B) Geometrical mean values between Draupne and Sognefjord formations of inverted AI cube showing the lateral impedance variation with the same random line. C) The inverted AI cross-section along the line A-A'. The top Draupne, Sognefjord, and Fensfjord Formation horizons are shown for reference.

Basin, North Texas. There are significant differences in depositional and diagenetic processes between the studied caprocks (Draupne and Heather formations) and the Barnett Shale. Therefore, the range of Young's modulus and Poison's ratio used by Grieser and Bray (2007) to define ductile and brittle regions are working well in their studied basin but are not representative of our study area. Similarly, the mineralogy based brittleness increment trend proposed by Perez and Marfurt (2014) is specific for the Barnett shale and not demonstrated the trend observed in the studied caprocks. This indicates a basin specific brittleness analysis is needed to characterize the geomechanical behavior of the caprocks.

Caprocks with high values of elastic properties (i.e., AI, E, $\mu\rho$, and $\lambda\rho$) tend to be stiffer though PR do not show a significant variation with change in brittleness values. However, the very soft ductile caprock cluster exhibits significantly high PR and low E values. The elastic properties based stiffness might be a tool to evaluate qualitative measures of the ability of the caprock to deform, but the whole procedure is much more complicated. For example, the well 35/11–4, which has stiff (Figs. 12 and 13) caprock (i.e., high values of elastic properties) with low clay fraction and a high percentage of stiff minerals (Table 3), acted as an effective caprock overlying a discovery. Although certain minerals (i.e., stiff mineral fraction) and processes (i.e., depositional and diagenetic) may enhance acoustic and geomechanical properties of the caprock (Fig. 22), the deformation of the rock is controlled by many other factors including clay type, microstructure, and distribution of minerals within the matrix, etc.

The complex nature of geomechanical properties of caprocks defines the sealing efficiency of any reservoir-caprock pairs. Considering all the analyses performed in this study, the Draupne Formation is in the realm of ductile caprock (BI's $< \sim 0.5$), which indicates significant sealing potential in the studied area. However, the thickness variation may raise questions regarding caprock failure, which is already answered by Troll West Field, where the studied caprocks are thin or not present, but overburden rocks acted as a potential cap. In contrast, the Heather Formation tends to be less ductile (higher BI's than Draupne) but can be an effective seal combined with the Draupne Formation (Fig. 18).

5.4. Implication

The relation between mineralogical composition and elastic properties within the organic-rich caprock shales allows us to estimate geomechanical properties from seismic data (Fig. 21). However, the complex nature of the geomechanical properties of caprock makes it challenging to approximate it. For example, the caprock properties (i.e., acoustic and geomechanical) of MC well 35/11–4 and CC well 35/11-6 plot in high Vp-density zone where the former well possesses effective caprock that contains gas in the underlying reservoir. In contrast, the latter well failed to find commercial hydrocarbon (only oil shows) considering minimal stress changes due to exhumation (i.e., ~150 m). The data from the other two wells containing the effective caprock, i.e., 31/5–2 (MC) and 35/10–1 (CC), show soft (low to intermediate Vp & density) ductile (Fig. 23). This type of distribution of acoustic properties

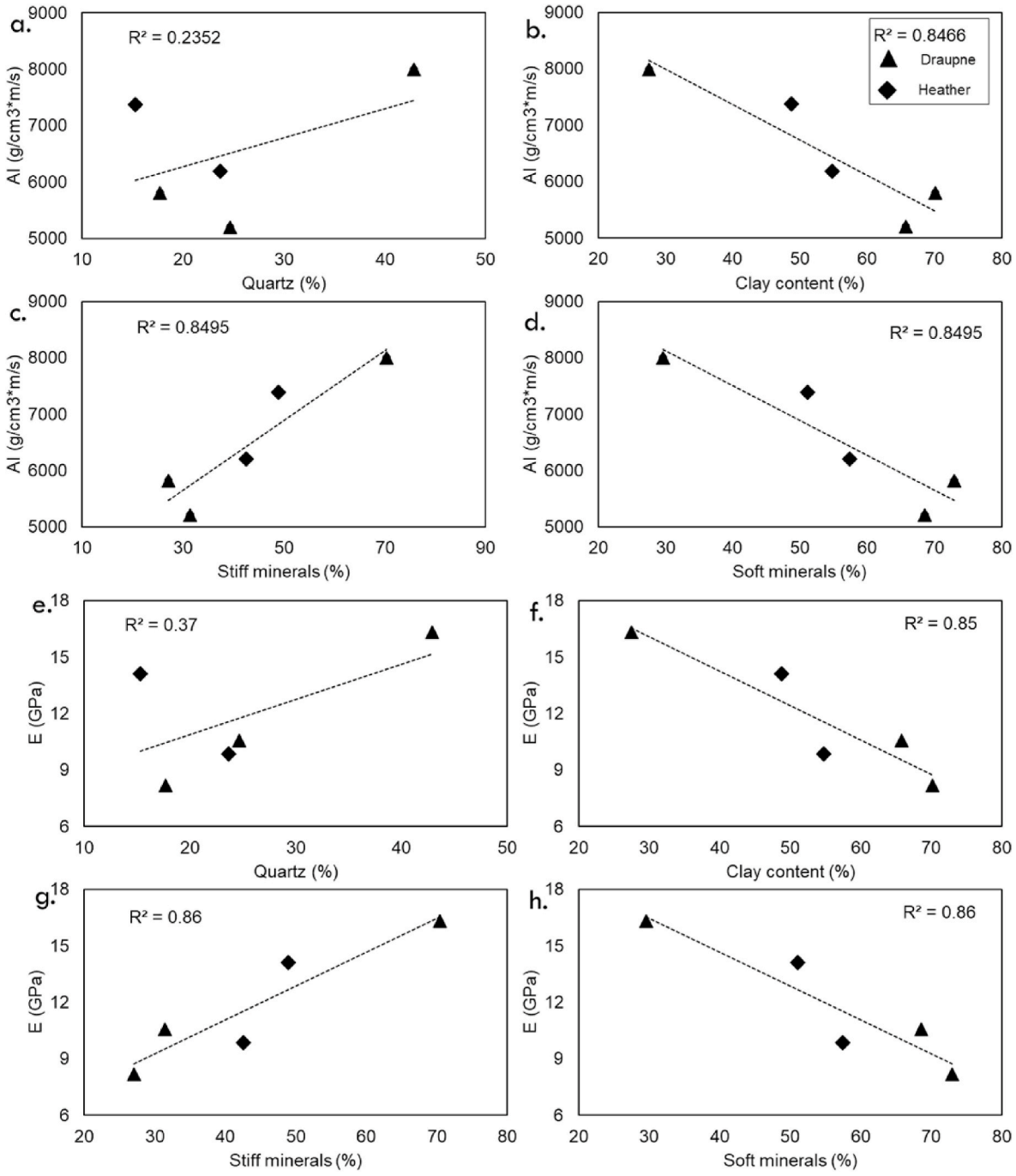

Fig. 22. Cross-plots of Draupne and Heather formations data points from the studied wells show the correlation of a) AI versus quartz, b) clay, c) stiff minerals, d) ductile minerals, e) E versus quartz, f) clay, g) stiff minerals and h) ductile minerals. Stiff mineral assemblages are composed of quartz, feldspar, pyrite, and carbonate, while ductile minerals consist of total clay and total organic content (TOC).

makes it very challenging to identify the effective seal rocks from seismic data. Therefore, an integrated approach (i.e., petrographic, petrophysical, seismic inversion, and laboratory analysis) is needed to get a detailed characterization of caprocks with their sealing effectiveness; otherwise, it might be misleading sometimes. Moreover, the caprock properties are not possible to describe by a single parameter such as stiffness or brittleness; instead, it is controlled by a combination of factors including in situ stress condition, pore-throat size, matrix permeability, capillary pressure, the existence of natural fractures, manner of well completion, as well as rock properties such as elastic moduli and mineralogy (Yang et al., 2013).

6. Conclusions

Depositional and diagenetic processes and their effect on caprock elastic and geomechanical properties were assessed. The critical observation of this study are as follows:

- The high energy NE-SW trend following the Troll fault zone separates the study area into two paleo-depositional regions where the NW part has high energy silts deposited compared to fine-grained clay-bearing zones in the SE part. However, in the NW and SW corners of the study area (far from the coastal plain), soft clay content and a higher percentage of organic matter are found.

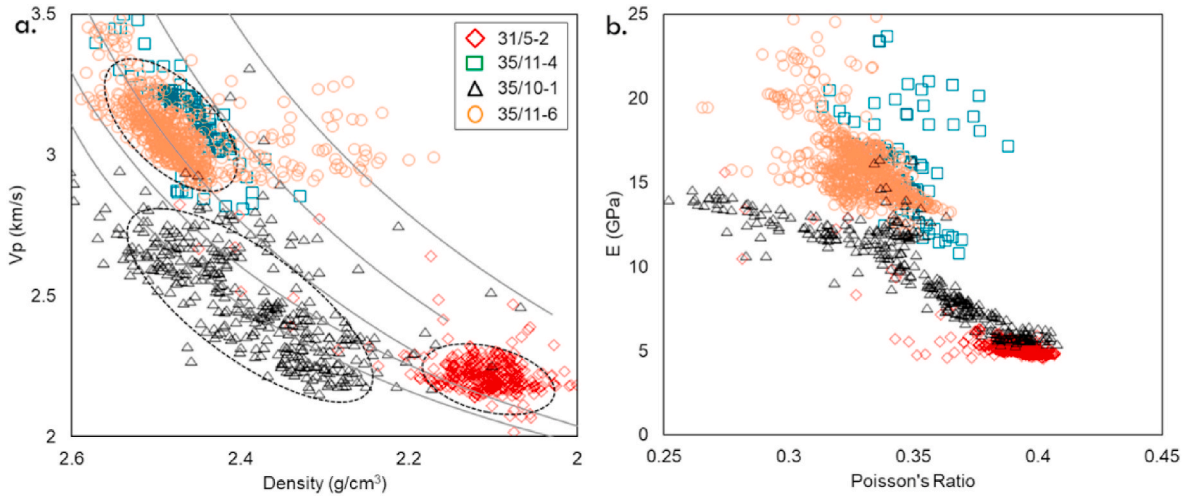

Fig. 23. Draupne Formation data points from wells 31/5–2, 35/10–1, 35/11–4, and 35/11–6 cross-plotted in a) the Vp-density template with reference curve adapted from Avseth et al. (2005) and b) E-PR template showing the increasing brittleness trend.

- Draupne and Heather formations in the study area showed a wide range of elastic and geomechanical properties. The data clustering irrespective of diagenetic variation makes it difficult to assess the properties from surface seismic.
- A stiff relationship is found between the rock mineralogical composition and caprock properties (i.e., elastic and geomechanical parameters).
- The mechanical properties of the studied caprocks appear to be ductile. However, Heather Formation is comparatively less ductile compared to Draupne Formation. The brittleness increment trend showed a significant difference with the previously published reference curves and increased with increasing AI, E, μρ, and λρ.
- There is considerable uncertainty involved in the estimation of TOC. However, the sparsely distributed (mostly immature) TOC within the study area has an insignificant impact on the geomechanical properties. The geomechanical properties of caprocks are complex, and further work is needed to quantify the TOC effect.

CRediT authorship contribution statement

Md Jamilur Rahman: Conceptualization, Methodology, Formal analysis, Investigation, Writing - original draft, Writing - review & editing, Visualization. **Manzar Fawad:** Conceptualization, Writing - review & editing, Supervision. **Nazmul Haque Mondol:** Conceptualization, Writing - review & editing, Supervision, Project administration, Funding acquisition.

Declaration of competing interest

The authors declare that they have no known competing financial interests or personal relationships that could have appeared to influence the work reported in this paper.

Acknowledgments

We are grateful for the financial support provided by the Research Council of Norway for the OASIS (Overburden Analysis and Seal Integrity Study for CO_2 Sequestration in the North Sea) project (NFR-CLIMIT project #280472). We are indebted to the additional funding and data provided by Norwegian Petroleum Directorate (NPD), Gassnova, Equinor, and Total. Academic software licenses have been provided by Lloyd's Register for Interactive Petrophysics and Schlumberger for Petrel.

Appendix A. Supplementary data

Supplementary data to this article can be found online at https://doi.org/10.1016/j.marpetgeo.2020.104665.

References

Alfred, D., Vernik, L., 2013. A new petrophysical model for organic shales. Petrophysics 54 (3), 240–247.
Alzahabi, A., AlQahtani, G., Soliman, M.Y., Bateman, R.M., Asquith, G., Vadapalli, R., 2015. June. Fracturability index is a mineralogical index: a new approach for fracturing decision. In: SPE Saudi Arabia Section Annual Technical Symposium and Exhibition. Society of Petroleum Engineers.
Anell, I., Thybo, H., Artemieva, I.M., 2009. Cenozoic uplift and subsidence in the North Atlantic region: geological evidence revisited. Tectonophysics 474 (1–2), 78–105. https://doi.org/10.1016/j.tecto.2009.04.006.
Aoudia, K., Miskimins, J.L., Harris, N.B., Mnich, C.A., 2010. January. Statistical analysis of the effects of mineralogy on rock mechanical properties of the Woodford shale and the associated impacts for hydraulic fracture treatment design. In: 44th US Rock Mechanics Symposium and 5th US-Canada Rock Mechanics Symposium. American Rock Mechanics Association.
Avseth, P., Mukerji, T., Mavko, G., 2005. Quantitative Seismic Interpretation: Applying Rock Physics Tools to Reduce Interpretation Risk. Cambridge University Press, New York.
Baig, I., Faleide, J.I., Mondol, N.H., Jahren, J., 2019. Burial and exhumation history controls on shale compaction and thermal maturity along the Norwegian North Sea basin margin areas. Mar. Petrol. Geol. 104, 61–85. https://doi.org/10.1016/j.marpetgeo.2019.03.010.
Bjørlykke, K., 2015. Petroleum migration. In: Bjørlykke, K. (Ed.), Petroleum Geoscience. From Sedimentary Environments to Rock Physics, second ed. Springer-Verlag Berlin Heidelberg, pp. 373–384. https://doi.org/10.1007/978-3-642-34132-8.
Carcione, J.M., 2000. A model for seismic velocity and attenuation in petroleum source rocks an Acoustic Model for Petroleum Source Rocks. Geophysics 65 (4), 1080–1092. https://doi.org/10.1190/1.1444801.
Carcione, J.M., Avseth, P., 2015. Rock-physics templates for clay-rich source rocks RPTs for clay-rich source rocks. Geophysics 80 (5), D481–D500. https://doi.org/10.1190/geo2014-0510.1.
Chen, J., Zhang, G., Chen, H., Yin, X., 2014. The Construction of Shale Rock Physics Effective Model and Prediction of Rock Brittleness. *2014*. SEG Technical Program Expanded Abstracts, pp. 2861–2865.
Dang, S.T., Sondergeld, C.H., Rai, C.S., 2016. A new approach to measuring organic density. Petrophysics 57 (2), 112–120.
Davis, D., Reynolds, S.J., 1996. Structural Geology of Rocks and Regions, second ed. Wiley and Sons.
Eberhardt, E., Stead, D., Stimpson, B., 1999. Quantifying progressive pre-peak brittle fracture damage in rock during uniaxial compression. Int. J. Rock Mech. Min. Sci. 36 (3), 361–380. https://doi.org/10.1016/S0148-9062(99)00019-4.
Emery, D., Myers, K., 1996. Sequence Stratigraphy. John Wiley & Sons.
Faerseth, R.B., 1997. Interaction of permo-triassic and jurassic extensional fault-blocks during the development of the northern North sea. Oceanogr. Lit. Rev. 7 (44), 710.
Faleide, J.I., Bjørlykke, K., Gabrielsen, R.H., 2015. Geology of the Norwegian continental shelf. Chapter 25 from the book. "Bjørlykke, K Petrol. Geosci.: From Sedimentary Environments to Rock Physics" 603–637, 2nd edition.
Fawad, M. & Mondol, N. H., 2020. (Proposed unpublished brittleness equation).

Fossen, H., Hurich, C.A., 2005. The hardangerfjord shear zone in SW Norway and The north sea: a large-scale low-angle shear zone in the caledonian crust. J. Geol. Soc. 162 (4), 675–687. https://doi.org/10.1144/0016-764904-136.
Gabrielsen, R.H., Faleide, J.I., Pascal, C., Braathen, A., Nystuen, J.P., Etzelmuller, B., O'Donnell, S., 2010. Latest Caledonian to present tectonomorphological development of southern Norway. Mar. Petrol. Geol. 27 (6), 1290–1295. https://doi.org/10.1016/j.marpetgeo.2009.06.004.
Gale, J.F., Reed, R.M., Holder, J., 2007. Natural fractures in the Barnett Shale and their importance for hydraulic fracture treatments. AAPG Bull. 91 (4), 603–622. https://doi.org/10.1306/11010606061.
Glorioso, J.C., Rattia, A., 2012. March. Unconventional reservoirs: basic petrophysical concepts for shale gas. cp-285. In: SPE/EAGE European Unconventional Resources Conference & Exhibition-From Potential to Production. European Association of Geoscientists & Engineers. https://doi.org/10.3997/2214-4609-pdb.285.spe153004.
Grieser, W.V., Bray, J.M., 2007. January. Identification of production potential in unconventional reservoirs. In: Production and Operations Symposium. Society of Petroleum Engineers.
Handin, J., Hager Jr., R.V., 1957. Experimental deformation of sedimentary rocks under confining pressure: tests at room temperature on dry samples. AAPG (Am. Assoc. Pet. Geol.) Bull. 41 (1), 1–50. https://doi.org/10.1306/5CEAE5FB-16BB-11D7-8645000102C1865D.
Hansen, J.A., Mondol, N.H., Fawad, M., 2019. Organic content and maturation effects on elastic properties of source rock shales in the Central North Sea. Interpretation 7 (2), T477–T497. https://doi.org/10.1190/INT-2018-0105.1.
Hart, B.S., Macquaker, J.H., Taylor, K.G., 2013. Mudstone ("shale") depositional and diagenetic processes: implications for seismic analyses of source-rock reservoirs. Interpretation 1 (1), B7–B26. https://doi.org/10.1190/INT-2013-0003.1.
Hunt, J.M., 1996. Petroleum geology and geochemistry. emanandCompanyt SanFrancisco 26i (5), 273, 197g.
Jarvie, D.M., Hill, R.J., Ruble, T.E., Pollastro, R.M., 2007. Unconventional shale-gas systems: the Mississippian Barnett Shale of north-central Texas as one model for thermogenic shale-gas assessment. AAPG Bull. 91 (4), 475–499. https://doi.org/10.1306/12190606068.
Jin, X., Shah, S.N., Roegiers, J.C., Zhang, B., 2014. February. Fracability evaluation in shale reservoirs-an integrated petrophysics and geomechanics approach. In: SPE Hydraulic Fracturing Technology Conference. Society of Petroleum Engineers.
Johnson, J.W., Nitao, J.J., Morris, J.P., 2004. Reactive transport modeling of cap-rock integrity during natural and engineered CO2 storage. Carbon dioxide capture for storage in deep geologic formations 2, 787.
Jordt, H., Faleide, J.I., Bjørlykke, K., Ibrahim, M.T., 1995. Cenozoic sequence stratigraphy of the central and northern North Sea Basin: tectonic development, sediment distribution and provenance areas. Mar. Petrol. Geol. 12 (8), 845–879. https://doi.org/10.1016/0264-8172(95)98852-V.
Larionov, V.V., 1969. Radiometry of Boreholes. Nedra, Moscow, p. 127.
Marcussen, Ø., Thyberg, B.I., Peltonen, C., Jahren, J., Bjørlykke, K., Faleide, J.I., 2009. Physical properties of Cenozoic mudstones from the northern North Sea: impact of clay mineralogy on compaction trends. AAPG Bull. 93 (1), 127–150. https://doi.org/10.1306/08220808044.
Meyer, B.L., Nederlof, M.H., 1984. Identification of source rocks on wireline logs by density/resistivity and sonic transit time/resistivity crossplots. AAPG Bull. 68 (2), 121–129. https://doi.org/10.1306/AD4609E0-16F7-11D7-8645000102C1865D.
Mondol, N.H., Bjørlykke, K., Jahren, J., Høeg, K., 2007. Experimental mechanical compaction of clay mineral aggregates—changes in physical properties of mudstones during burial. Mar. Petrol. Geol. 24 (5), 289–311. https://doi.org/10.1016/j.marpetgeo.2007.03.006.
Mondol, N.H., 2009. Porosity and Permeability Development in Mechanically Compacted Silt-Kaolinite Mixtures. SEG Technical Program Expanded Abstracts, pp. 2139–2143. *2009*.
Mullen, M.J., Roundtree, R., Turk, G.A., 2007. January. A composite determination of mechanical rock properties for stimulation design (what to do when you don't have a sonic log). In: Rocky Mountain Oil & Gas Technology Symposium. Society of Petroleum Engineers.
Norton, D.L., 1984. Theory of hydrothermal systems. Annu. Rev. Earth Planet Sci. 12 (1), 155–177.
Nygård, R., Gutierrez, M., Bratli, R.K., Høeg, K., 2006. Brittle–ductile transition, shear failure and leakage in shales and mudrocks. Mar. Petrol. Geol. 23 (2), 201–212. https://doi.org/10.1016/j.marpetgeo.2005.10.001.
Passey, Q.R., Creaney, S., Kulla, J.B., Moretti, F.J., Stroud, J.D., 1990. A practical model for organic richness from porosity and resistivity logs. AAPG Bull. 74 (12), 1777–1794.
Peters, K.E., 1986. Guidelines for evaluating petroleum source rock using programmed pyrolysis. AAPG Bull. 70 (3), 318–329.
Perez Altamar, R., Marfurt, K., 2014. Mineralogy-based brittleness prediction from surface seismic data: application to the Barnett Shale. Interpretation 2 (4), T1–T17. https://doi.org/10.1190/INT-2013-0161.1.
Rickman, R., Mullen, M.J., Petre, J.E., Grieser, W.V., Kundert, D., 2008. January. A practical use of shale petrophysics for stimulation design optimization: all shale plays are not clones of the Barnett Shale. In: SPE Annual Technical Conference and Exhibition. Society of Petroleum Engineers.
Roberts, A.M., Yielding, G., Kusznir, N.J., Walker, I., Dorn-Lopez, D., 1993. January. Mesozoic extension in the North Sea: constraints from flexural backstripping, forward modelling and fault populations. In: Geological Society, London, Petroleum Geology Conference Series, vol. 4. Geological Society of London, pp. 1123–1136. https://doi.org/10.1144/0041123. No. 1.
Roberts, A.M., Kusznir, N.J., Yielding, G., Beeley, H., 2019. Mapping the bathymetric evolution of the Northern North Sea: from Jurassic synrift archipelago through Cretaceous-Tertiary post-rift subsidence. Petrol. Geosci. 25 (3), 306–321. https://doi.org/10.1144/petgeo2018-066.
Rybacki, E., Meier, T., Dresen, G., 2016. What controls the mechanical properties of shale rocks?–Part II: Brittleness. J. Petrol. Sci. Eng. 144, 39–58. https://doi.org/10.1016/j.petrol.2016.02.022.
Shell, U.K., 2014. Peterhead CCS project: geomechanics report. Revision-K02, doc. No. PCCS-05-PT-ZP-9025-00004.
Sharma, R.K., Chopra, S., 2012. New attribute for determination of lithology and brittleness. In: SEG Technical Program Expanded Abstracts 2012. Society of Exploration Geophysicists, pp. 1–5.
Slatt, R., 2011. Important geological properties of unconventional resource shales. Open Geosci. 3 (4), 435–448.
Slatt, R.M., Abousleiman, Y., 2011. Merging sequence stratigraphy and geomechanics for unconventional gas shales. Lead. Edge 30 (3), 274–282. https://doi.org/10.1190/1.3567258.
Stewart, D.J., Schwander, M., Bolle, L., 1995. Jurassic Depositional Systems of the Horda Platform, Norwegian North Sea: Practical Consequences of Applying Sequence Stratigraphic Models, vol. 5. Norwegian Petroleum Society Special Publications, pp. 291–323. https://doi.org/10.1016/S0928-8937(06)80073-1.
Storvoll, V., Bjørlykke, K., Mondol, N.H., 2005. Velocity-depth trends in mesozoic and cenozoic sediments from the Norwegian shelf. AAPG Bull. 89 (3), 359–381. https://doi.org/10.1306/10150404033.
Taylor, K.G., Macquaker, J.H., 2011. Iron minerals in marine sediments record chemical environments. Elements 7 (2), 113–118.
Thyberg, B., Jahren, J., Winje, T., Bjørlykke, K., Faleide, J.I., 2009. From mud to shale: rock stiffening by micro-quartz cementation. First Break 27 (2). https://doi.org/10.3997/1365-2397.2009003.
Van Wagoner, J.C., Posamentier, H.W., Mitchum, R.M.J., Vail, P.R., Sarg, J.F., Loutit, T.S., Hardenbol, J., 1988. An overview of the fundamentals of sequence stratigraphy and key definitions.
Verdon, J.P., Kendall, J.M., Stork, A.L., Chadwick, R.A., White, D.J., Bissell, R.C., 2013. Comparison of geomechanical deformation induced by megatonne-scale CO2 storage at Sleipner, Weyburn, and in Salah. Proc. Natl. Acad. Sci. Unit. States Am. 110 (30), E2762–E2771. https://doi.org/10.1073/pnas.1302156110.
Vernik, L., Landis, C., 1996. Elastic anisotropy of source rocks: implications for hydrocarbon generation and primary Migration1. AAPG Bull. 80 (4), 531–544. https://doi.org/10.1306/64ED8836-1724-11D7-8645000102C1865D.
Vernik, L., Milovac, J., 2011. Rock physics of organic shales. Lead. Edge 30 (3), 318–323. https://doi.org/10.1190/1.3567263.
Walles, F., 2004. A new method to help identify unconventional targets for exploration and development through integrative analysis of clastic rock property fields.
Wang, F.P., Gale, J.F., 2009. Screening criteria for shale-gas systems.
Whipp, P.S., Jackson, C.L., Gawthorpe, R.L., Dreyer, T., Quinn, D., 2014. Normal fault array evolution above a reactivated rift fabric; a subsurface example from the northern Horda Platform, Norwegian North Sea. Basin Res. 26 (4), 523–549.
Yang, Y., Sone, H., Hows, A., Zoback, M.D., 2013. January. Comparison of brittleness indices in organic-rich shale formations. In: 47th US Rock Mechanics/geomechanics Symposium. American Rock Mechanics Association.
Zhang, D., Ranjith, P.G., Perera, M.S.A., 2016. The brittleness indices used in rock mechanics and their application in shale hydraulic fracturing: a review. J. Petrol. Sci. Eng. 143, 158–170. https://doi.org/10.1016/j.petrol.2016.02.011.

Paper-2

Probabilistic Analysis of Vette Fault Stability in Potential CO_2 Storage Site Smeaheia, Offshore Norway

Md Jamilur Rahman
Jung Chan Choi
Manzar Fawad
Nazmul Haque Mondol

International Journal of Greenhouse Gas Control, 2021

International Journal of Greenhouse Gas Control 108 (2021) 103315

Contents lists available at ScienceDirect

International Journal of Greenhouse Gas Control

journal homepage: www.elsevier.com/locate/ijggc

Probabilistic analysis of Vette fault stability in potential CO_2 storage site Smeaheia, offshore Norway

Md Jamilur Rahman [a,*], Jung Chan Choi [b], Manzar Fawad [a], Nazmul Haque Mondol [a,b]

[a] Department of Geosciences, University of Oslo (UiO), Sem Sælands vei 1, 0371, Oslo, Norway
[b] Norwegian Geotechnical Institute (NGI), Sognsveien 72, 0806, Oslo, Norway

ARTICLE INFO

Keywords:
Fault stability
Probability of failure
FORM method
Monte-Carlo simulation
System reliability
Uncertainty
Sensitivity

ABSTRACT

Reliable assessment of fault stability is key for safe CO_2 storage in a saline aquifer in fault-bounded structures. The Alpha structure located in the Vette fault's footwall in the Smeaheia area, offshore Norway, is one of the potential CO_2 storage sites with a fault-bounded three-way closure. Assessing fault stability in the Smeaheia area is challenging because of the uncertainties associated with the subsurface fault properties (i.e., fault rock lithologies, strength and geometry of faults, etc.). Besides, CO_2 injection-related pore pressure changes is another critical factor for mechanical deformation and potential failure. We employed a stochastic analytical approach to assess the probability of Vette fault failure using the Monte Carlo Simulation (MCS) and First Order Reliability Method (FORM). The possible fault smear scenarios of the Vette fault zone are evaluated by interpreting the seismic section and the detailed geological understanding. Each scenario's likelihood and the corresponding probability of failure are then integrated stochastically using an event tree method. Overall, Vette fault's system reliability shows a good to average performance range, which has a system probability of failure between 10^{-3} to 10^{-4}. This finding suggests that the Vette fault will likely act as a potential barrier during CO_2 injection into the Alpha structure. Moreover, the sensitivity study reveals that the stresses (both horizontal and vertical) and fault rock strength (i.e., cohesion and friction angle) are the most crucial parameters to characterize uncertainty reduction.

1. Introduction

Capture and geological storage of CO_2 into a saline aquifer is a proven technology to mitigate anthropogenic greenhouse gas emissions into the atmosphere (IPCC, 2005). The CCS technique has already been demonstrated as a safe and reliable solution by several pilot projects worldwide (i.e., Snøhvit, Norway, Chiaramonte et al., 2011; In Salah, Algeria, Mathieson et al., 2010; Sleipner, Norway, Baklid et al., 1996; Ketzin, Germany, Martens et al., 2012; Otway, Australia, Hortle et al., 2013; Quest, Canada, Rock et al., 2017). In partnership with the oil and gas industries, the Norwegian government has evaluated some sites in the Norwegian Continental Shelf (NCS) and developed a strategy for large-scale (Gt storage potential) geological CO_2 sequestration. Smeaheia area is one of the potential sites containing the fault-bounded structural closures Alpha (32/4-1) and Beta (32/2-1), investigated by Equinor and Gassonova (NPD CO_2 Atlas, 2014) (Fig. 1). The area is located east of the Troll East Field, bounded by two major faults; Vette fault (VF) in the west and Øygarden fault complex (ØFC) in the east. The Alpha structure is located in the VF's footwall, whereas the Beta structure is located in the hanging wall of the ØFC (Mulrooney et al., 2018). Fault stability of the Alpha structure could be the critical factor that needs to be evaluated before any CO_2 injection-related activity in the area. However, because of the uncertainties in the subsurface associated with fault properties (i.e., fault rock lithologies, strength, and geometry of fault), it poses a significant challenge to assess the Vette fault's stability.

In addition to the inherent subsurface uncertainties, operational uncertainties associated with pore pressure change during CO_2 injection into a saline aquifer can be another critical factor, which changes the effective stress (i.e., principal stress minus pore pressure) and influences mechanical rock deformation and failure (Verdon et al., 2013). The elastic behavior of pore fluid under the drainage condition is one of the critical factors affecting the mechanical behavior and the stress path of oil field reservoirs, known as a poroelastic effect (Addis, 1997; Grasso, 1992; Hillis, 2001; Segall, 1989). In the case of a supercritical CO_2 (sCO_2) injection, additional processes such as hydraulic aperture

* Corresponding author.
E-mail address: m.j.rahman@geo.uio.no (M.J. Rahman).

https://doi.org/10.1016/j.ijggc.2021.103315
Received 9 November 2020; Received in revised form 15 March 2021; Accepted 20 March 2021
Available online 31 March 2021

evolution, hydrological property changes, effective stress induction, and mechanical strength degradation can influence the effective stresses in fault planes, which can be leading to reactivation and failure of faults (Park et al., 2020; Rutqvist et al., 2007). Although many North Sea faults are proven to have effective sealing properties by supporting considerable hydrocarbon columns (Yielding, 2002), there is still high uncertainty associated with dynamic pressure buildup related to CO_2 injection and wettability of a CO_2-brine-fault rock system (Karolytė et al., 2020; Miocic et al., 2019), also resulting in the potential failure of faults and caprock (Skurtveit et al., 2018). Therefore, a careful investigation of the relation between the fault rock properties, in-situ stresses, and pore pressure perturbation is required to prevent any risk related to CO_2 injection (Chiaramonte et al., 2015).

The potential fault failure can be assessed using either analytical or numerical methods where both approaches have their advantages and disadvantages. This study only considered the analytical techniques, which estimate the fault stability from the theoretical calculations of fault plane stress states and its distance to its nearest shear strength, which generally relies on the Coulomb failure criterion for shear strength calculation (Bohloli et al., 2015; Park et al., 2020). The critical fault slip pressure and fault stability threshold can be determined from the fault's internal properties such as fault orientation, fault material strength, etc. (Vidal-Gilbert et al., 2010; Wiprut and Zoback, 2000) as well as its in-situ stresses. Though analytical methods rely on many assumptions and simplifications for a complicated hydro-mechanical process, these have been proven as useful tools in the preliminary assessment.

The fault zone's structural complexity and the poor seismic resolution along fault make it complicated to predict the fault rock strength (i.e., clay/shale smear, sandstone fragments, mixed lithology, etc.). The fault zone architecture, the distribution of fault rock within the fault zones, and its capacity to seal are still not well-understood, though many research and publications are available (e.g., Faulkner et al., 2010; Færseth, 2006; Færseth et al., 2007, 1984; Gibson, 1994; Jev et al., 1993; Kim et al., 2003; Yielding et al., 1997; Zieglar, 1992). The wettability properties of fault rock and fault rock composition are highly uncertain and significantly different compared with the hydrocarbon system (Miocic et al., 2019). Moreover, most fault zones are beyond seismic resolution and containing several major slip surfaces (Childs et al., 1997; Doughty, 2003; Færseth et al., 2007; Foxford et al., 1998; Gibson, 1994; Walsh et al., 1998). These problems result in inaccuracies in the prediction and quantification of fault rock failure. The shale smearing within the fault zone depends on the relation between fault throw and the amount of clay and shale in the host rock (Bouvier et al., 1989; Fisher and Knipe, 2001; Lindsay et al., 1993; Skerlec, 1996; Yielding et al., 1997). The shalier the host rock is the higher proportion of clay lining that forms in the fault zone, causing a higher capillary entry pressure. The higher the fault throw, the less possibility of having continuous

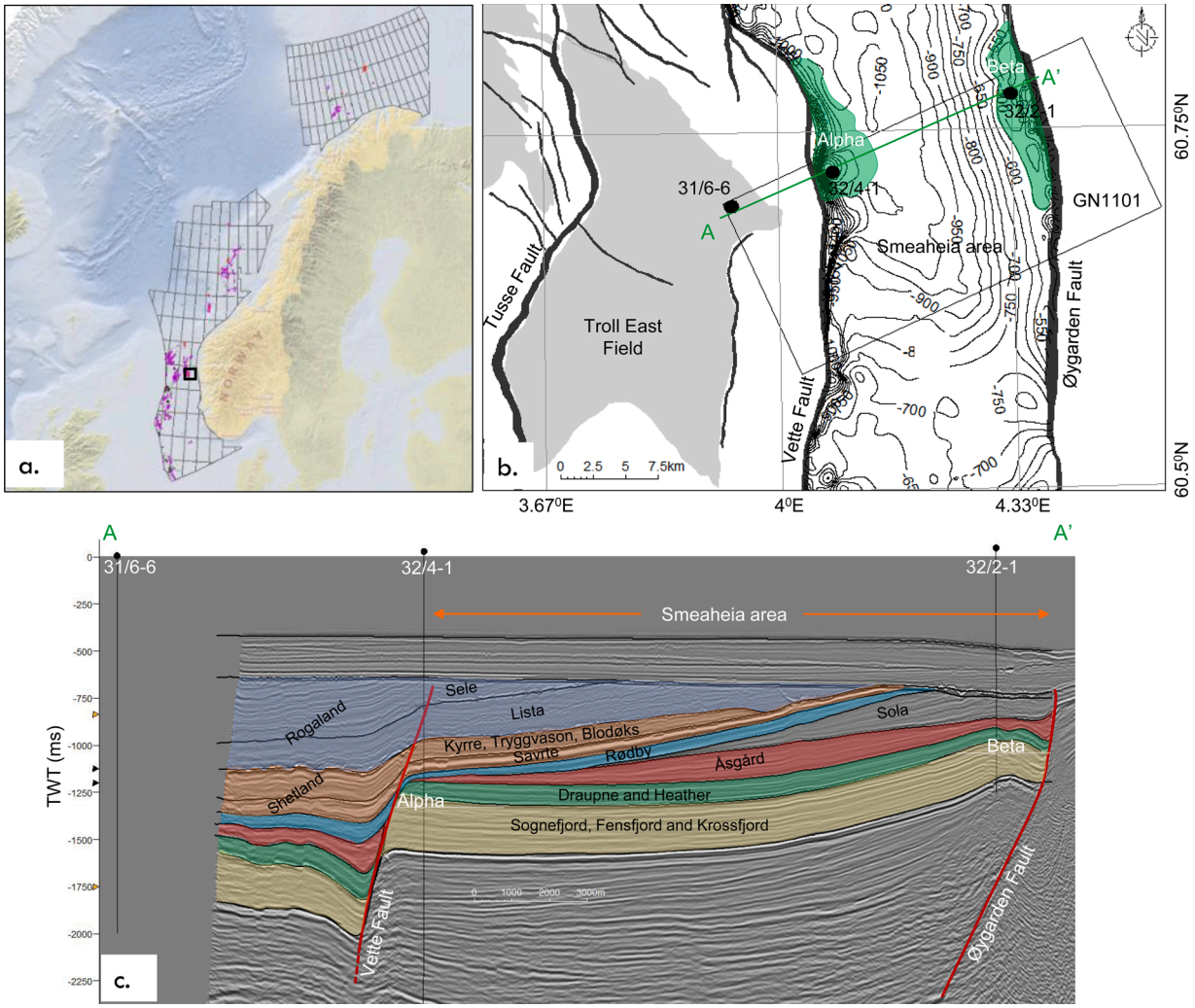

Fig. 1. a) Location (black rectangle) of the study area b) the depth structure map of the top reservoir unit (Sognefjord Formation) is interpreted using the well tops showing the major faults and Troll East Gas Field in the study area, and c) A WSW-ENE seismic profile (AA') crossing three wells shows the faults and critical horizons.

shale smearing throughout the fault zone. However, estimating fault throw using a single fault surface is not representative of the actual scenario because fault zones often contain several major slip surfaces (Childs et al., 1997; Doughty, 2003; Færseth et al., 2007; Foxford et al., 1998; Gibson, 1994; Walsh et al., 1998). Moreover, stress path changes and fault rock strength are not known precisely. Therefore, the deterministic approach assumes that, all the input parameters are well-known with high certainty and that the input consists of only one scenario, which is somewhat questionable when the varying degree of uncertainty exists (Duncan, 2000); instead, obtaining a probability of failure is a more suitable methodology (Christian, 2004; Nadim, 2007).

This study evaluated the stability of Vette fault probabilistically using the Monte-Carlo simulation (MCS) and the First Order Reliability Method (FORM). The fault stability is evaluated using the analytically estimated stress conditions acting on the fault plane and the Mohr-Coulomb failure criteria. The uncertainty of the fault-rock strength properties is handled by interpreting four different fault smearing scenarios and their likelihood based on the study area's geological understanding. The overall VF system reliability is estimated based on the qualitative approximation of all four scenarios using an event tree. The likelihood of each fault rock strength scenario and the corresponding probability of failure is embedded in the system failure number, which could be a reasonable estimation for the future project decision. The pore pressure/stress coupling, also known as the reservoir stress path, is also incorporated to evaluate the complex poroelastic interaction due to the fluid injection in the horizontal stress field. Finally, the relative importance of different parameters (i.e., vertical and horizontal stresses assumptions, pore pressure, stress path, fault rock strength, etc.) on fault stability is evaluated. In the discussion section, we highlighted the potential for a failure probability estimation for subsurface structures. It is a new approach and needs a concrete workflow to implement successfully in the fault stability analysis.

2. Geology of the study area

The Smeaheia area is situated on the northeastern edge of the northern North Sea (i.e., Horda Platform) and bounded by two regional N-S trending normal faults (Fig. 1). The Horda Platform (HP) area experienced two main rifting events during Permo-Triassic and the Late Jurassic to Mid-Cretaceous times (Whipp et al., 2014), where during the 1st rifting event, a wide basin with deep-rooted faults and thick syn-depositional wedges was formed in the center of HP (Stewart et al., 1995). The 2nd rifting event shifted westward but reactivated all the major faults and created a collection of NW-SE trending smaller faults with minor displacement within the proposed reservoir (Sognefjord Formation) and top seal (Heather + Draupne Formations) units throughout the HP (Duffy et al., 2015; Skurtveit et al., 2018; Stewart et al., 1995; Whipp et al., 2014). These events created several N-S trending faults (i.e., Vette, Tusse, Øygarden, etc.), which are believed to be rooted in the Caledonian zones of crustal weakness (Whipp et al., 2014) and tipped out in the overburden stratigraphy into the Rogaland Group (Fig. 1c). The studied Vette fault is one of them which needs to be sealing for safe CO_2 storage in the Alpha structure (Fig. 1b).

The main reservoir rocks in the Alpha structure consist of a succession of three Upper Jurassic sandstone formations (i.e., Sognefjord, Fensfjord & Krossfjord) with good to moderate reservoir quality (Dreyer et al., 2005; Holgate et al., 2015), while organic-rich Heather and Draupne formations act as the primary seal. The reservoir sandstones were deposited in a coastal shallow marine environment and inter-finger with the Heather Formation (Fig. 2a). The Heather Formation shale consists of mainly grey silty claystone with thin streaks of limestone deposited in an open marine environment (NPD, 2020). The organic-rich Draupne Formation shale has an approximate thickness of 106 m in well 32/4-1, which varies laterally and consists of dark grey-brown to black, usually non-calcareous, carbonaceous, occasionally fissile claystone. The Draupne Formation was deposited in an open marine environment with restricted bottom circulation and often anaerobic conditions (NPD, 2020).

The overburden rocks above the Draupne Formation are vital to detect any permeable layer juxtaposition with the reservoirs across the faults. The whole overburden unit is 475–800 m thick, comprising westward-dipping alternating fine- and coarse-grained siliciclastic packages with occasional carbonate-rich deposits (Faleide et al., 2015). The overburden Rødby Formation is crucial as it juxtaposes the top part of the reservoirs. The Rødby Formation consists of red-brown marlstone and deposited in an open marine, oxygenated environment with a

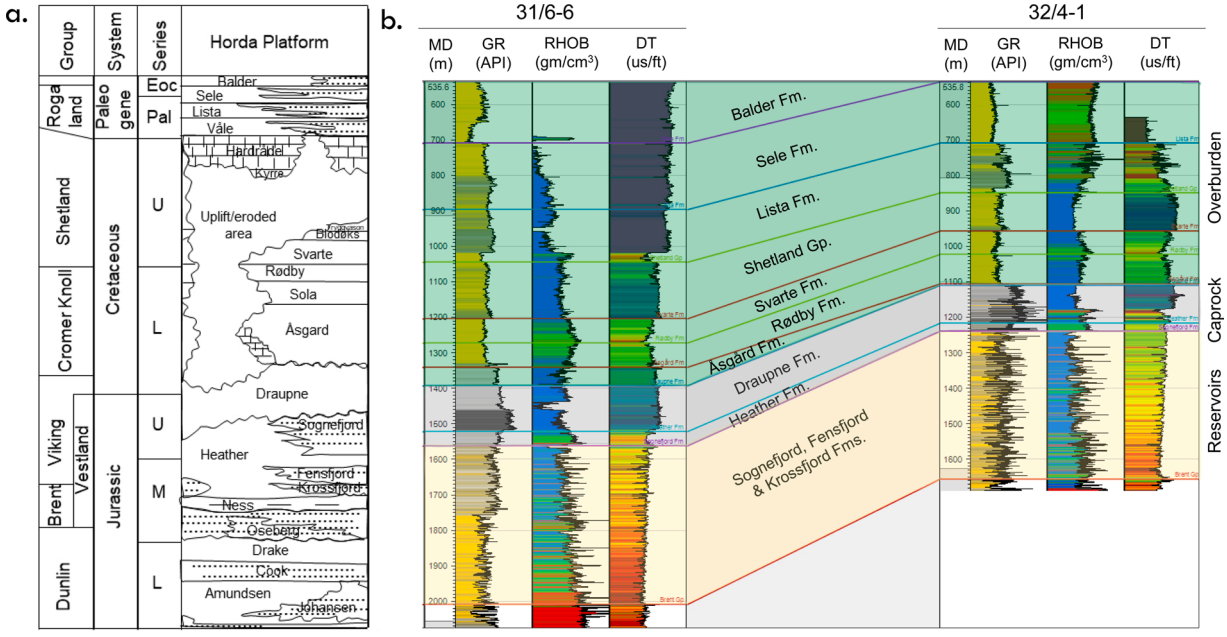

Fig. 2. a) A generalized Jurassic and Cretaceous stratigraphic succession in the study area (modified from NPD CO_2 Atlas, 2014). b) A correlation of footwall (32/4-1) and hanging wall (31/6-6) wells of the Vette Fault flatten on top of Balder Formation. Note the variations in the petrophysical logs (i.e., GR = Gamma-ray; RHOB = Density; DT = Compressional sonic) in both vertical and across the fault direction.

limited supply of clastics (NPD, 2020). In the study area, the Rødby Formation is more calcareous and has a lower gamma-ray response and higher velocity than the overlying units. Wide variations of gamma-ray, density, and P-sonic indicate lithology, acoustic property, and geomechanical changes within the reservoir, cap, and overburden rocks (Fig. 2b).

3. Materials and methods

System reliability of the Vette fault took into account the likelihood of different fault smearing scenarios. The fault stability of each smearing scenario was assessed by an analytically calculated stress acting on the fault plane and the Mohr-Coulomb failure criterion. The workflow used in this study is illustrated in Fig. 3. The input parameters were scouted from the published database (i.e., Gutierrez et al., 2000; Horsrud et al., 1998; Skurtveit et al., 2018, 2015; Zoback, 2010) as well as estimated from the wireline logs from the nearby wells 31/6-6 and 32/4-1. The Mohr-Coulomb failure model that can calculate the Factor of Safety (FoS) was used to define a limit state function of stability. Failure probability was analyzed by the First Order Reliability Method (Hasofer and Lind, 1974) and Monte-Carlo simulation techniques. Finally, the Probability of Failure (P_f) of the Vette fault was estimated for both initial condition and after CO_2 injection scenario for different fault rock strength conditions. The fault system reliability was assessed by combining the likelihood of fault smearing scenarios and the failure probability of each smearing scenario. Moreover, each parameter's sensitivity analysis was investigated by changing one variable at a time while keeping all other input parameters at their initial value (average). In this study, the low and high outcome of the FoS for each uncertain parameter was evaluated.

Most geological processes follow a normal or log-normal law (Christian, 2004). Some geotechnical engineering studies show that changing the probability distribution of the soil parameters from normal to log-normal had a modest effect on the computed probability of failure (Lacasse and Nadim, 1998). Thus, most of the input parameters used for this study were assumed to follow the normal distribution. For the properties that cannot be physically negative within three standard deviations of the average, the distribution is assumed as the log-normal distribution. The standard deviations of the inputs are estimated from the published values.

3.1. Model parameters

3.1.1. Fault smearing scenarios

Fault rock strength is a complicated parameter to describe and highly uncertain; hence it needs a scenario-based approach to deal with the uncertainty. In this study, we evaluated all possible fault zone rock smearing scenarios within the Vette fault employing the interpretation of 3D seismic data of GN1101 (Fig. 4). The major and minor faults with horizons were interpreted from seismic to evaluate the possible fault-rock setup. The reservoir intervals (i.e., Sognefjord, Fensfjord, and Krossfjord formations) in the footwall side juxtapose with the Cromer Knoll Group (i.e., Rødby and Åsgard formations) in the hanging wall side in the Alpha prospect (Fig. 4a). Three possible shale smearing scenarios were interpreted in the studied Vette fault region (Fig. 4b–d). The most likely scenario was the Rødby Formation smearing case. The upper part of the reservoir unit (i.e., Sognefjord Formation) has the best quality reservoir properties (i.e., high porosity and permeability); hence, CO_2 plume is likely to migrate and accumulate within this zone. The Sognefjord Formation is juxtaposed with the Rødby Formation with a minimal fault throw (Færseth et al., 2006), making this formation the best possible smearing candidate (Fig. 4b). Åsgard Formation that pinches out near the fault's footwall side is least likely to be smearing (Fig. 4c); hence we excluded that from the smearing scenario cases. The shale smearing of the primary caprocks (i.e., Draupne and Heather formations) is also very uncertain as the fault throw is significantly large (~1500 m)(Fig. 4d). According to Færseth et al. (2006), the chances of smearing are reduced with increasing fault throw. In this study, the qualitative clay smearing scenarios are evaluated; however, the quantitative SGR values are not estimated. One can not rule out the presence of reservoir rock (i.e., Sognefjord Formation) fragments within the fault zone, which can be considered another fault rock strength scenario (Skurtveit et al., 2018).

Considering the seismic interpreted clay smearing (Fig. 4) and reservoir fragment scenarios with a typical static friction fault without cohesion (Zoback, 2010), we recognized four possible scenarios to analyze for the probability of failure estimation (Table 1). The qualitative probability of each condition was also assigned based on the geological interpretation. Moreover, the probabilistic likelihood values for each scenario were estimated based on the geological understanding of each case, which was later used to quantify the Vette Fault system reliability. Seismic interpretation-related uncertainties (i.e., human error, seismic quality, sub-seismic fault plane, etc.) are always present (Bond et al., 2015), but these are out of the scope of this research. However, the proposed event tree method considered all the uncertainties to estimate the system failure value.

3.1.2. In-situ stress condition

The present-day stress conditions (i.e., vertical and horizontal stresses) on top of the reservoir (i.e., top Sognefjord Formation) were both scouted (i.e., Skurtveit et al., 2018; Statoil Underground report, 2016) and estimated using wireline logs. The vertical stress (σ_v) was calculated using the average density obtained from the density log (Fig. 5) in well 32/4-1. Later the published and estimated vertical stresses were averaged and used for the analysis (Table 2). The initial horizontal stress and pore pressure were both calculated from the XLOT data (Fig. 6) and directly used from the reference data analyzed by Skurtveit et al. (2018). The σ_v was estimated using the following equation:

$$\sigma_v = \rho_f h_w g + \rho_b h_o g \quad (1)$$

where, ρ_f is saline water density (~1025 kg/m^3), h_w is the water depth (~312 m), ρ_b is the bulk density (average) of the overburden formations (~2233 kg/m^3), h_o is the thickness of the overburden (~902 m), and g is the gravitational acceleration. The average bulk density used in this study was obtained by integrating the whole overburden. The estimated point data, using the average density, was later used with scouted vertical stresses to evaluate the range (Table 2).

According to Skurtveit et al. (2018), a normal faulting regime (i.e., vertical stress is greater than horizontal stresses) with isotropic horizontal stress conditions (i.e., maximum horizontal stress = minimum horizontal stress) is a reasonable stress model for the study area. The extended leak-off test (XLOT) data from the nearby Troll area also

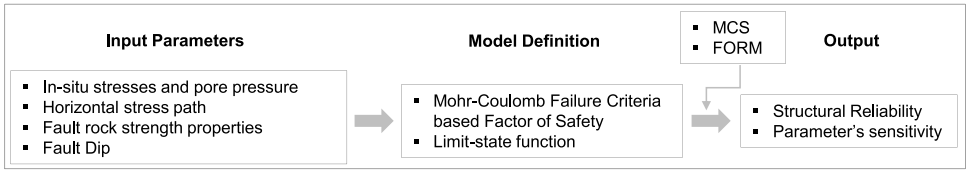

Fig. 3. The workflow to estimate the failure probability of the Vette Fault, used in this study.

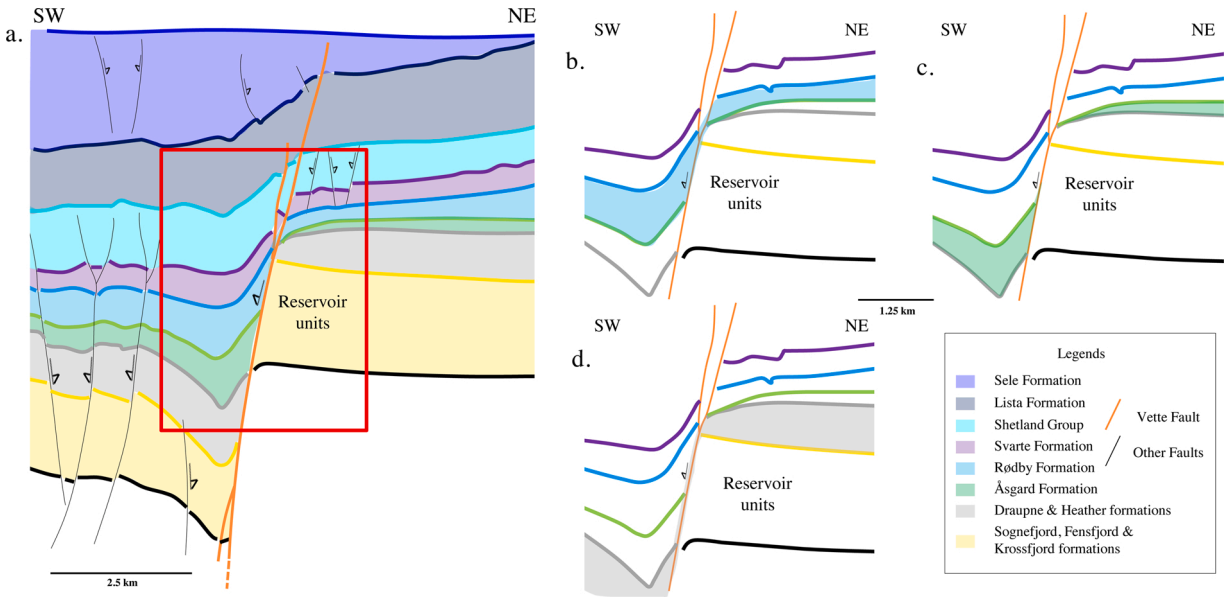

Fig. 4. a) Schematic representation shows the seismic interpretation of horizons and faults. The zone of interest (red rectangle) is further analyzed for possible shale smearing along the Vette fault zone for, b) Rødby Formation, c) Åsgard Formation, and d) Draupne and Heather formations.

Table 1
Possible fault smearing scenarios and likelihoods based on the geological explanation. Note that the likelihood terms are taken from Nadim (2007).

	Fault Smearing Scenario	Likehood	Probability Range[a]	Assign Probability[b]
Case 1	Static frictional fault	Very Unlikely	0 – 0.1	0.01
Case 2	Sognefjord rock fragment	Unlikely	0.1 – 0.25	0.12
Case 3	Draupne smearing	Unlikely	0.1 – 0.25	0.07
Case 4	Rødby smearing	Likely	0.5 – 0.9	0.80

[a] Based on Nadim (2007) and Brændeland et al. (2010).
[b] Based on Geological understanding of Vette fault.

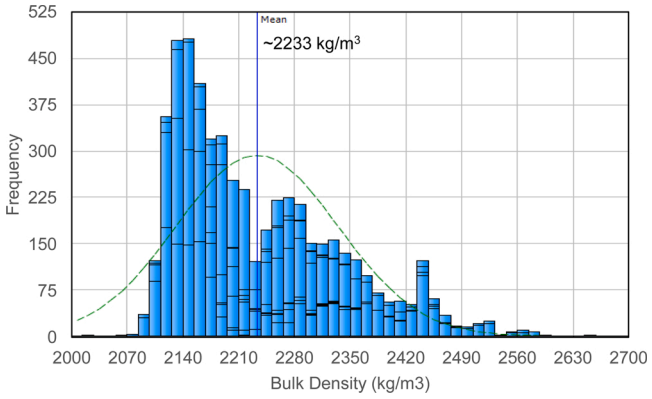

Fig. 5. Distribution of bulk density log of overburden formations of well 32/4-1. The mean density value for the overburden is 2233 kg/m^3.

revealed that the Alpha structure is within the normal faulting regime because the vertical stress gradient is significantly higher than the horizontal stress profile (Fig. 6). The hydrostatic pore pressure gradient was calculated using the depth profile from the well 32/4-1.

The post-injection scenarios assume a pore pressure change of 0.82 MPa by CO_2 injection, which was used from the Statoil dynamic simulation model analyzed for the Smeaheia feasibility study (Gassnova, 2016). The model used an injection rate of 1.3 MT per year over a period of 25 years within an excellent quality (permeability 1.3D, porosity 35 %, and thickness 60 m) reservoir (i.e., Sognefjord Formation). The compaction-induced changes in the total vertical stress were minimal for laterally extensive reservoirs, assuming equal elastic properties for the reservoir and the overburden (Geertsma, 1973). Moreover, the stiffness contrast of factor 10 in a numerical model shows a very negligible effect on the vertical total stress change in a laterally extensive reservoir (Hettema et al., 2000). The main reservoir rock (Sognefjord Formation) in the study area is also laterally extensive, which indicated an insignificant vertical stress change due to pore pressure variation; hence we do not consider any vertical stress changes in our model. The change of the effective vertical stress was thus assumed to be the same as pore pressure. However, the horizontal stress path, which is sensitive to the pore pressure changes, was calculated from the log-based Poisson's ratio using the equation proposed by Hettema et al. (2000):

$$\gamma_h = \frac{\Delta\sigma_h}{\Delta P} = \alpha\left(\frac{1-2\nu}{1-\nu}\right) \tag{2}$$

where σ_h is the total horizontal stress; ΔP is the pore pressure change; α is Biot's coefficient, and ν is the Poisson's ratio.

Moreover, fault can influence the horizontal stress changes during injection if major faults bound the reservoirs, or the injection points are near the fault (Addis et al., 1998, 1994). Therefore, the total horizontal stress in a normal faulting region was also estimated, which can be written as:

$$\gamma_{fault} = \alpha\left(\frac{2\sin\psi}{1-\sin\psi}\right) \tag{3}$$

where $\nu \geq (1-\sin\psi)/2$, with ψ being the fault friction angle. If $\nu < (1-\sin\psi)/2$, the minimum horizontal stress re-orientates parallel to the strike of the fault, and the stress path becomes:

$$\gamma_{fault} = \alpha\left(\frac{\sin\psi + 1 - 2\nu}{1+\sin\psi}\right) \tag{4}$$

3.1.3. *Fault rock geometry and strength*

The fault rock geometry significantly changes with changing horizontal and vertical directions. Therefore, in this study, we estimated the

Table 2
The database used in this study with the type of distribution and data sources.

Parameters	Average	Unit	Standard Deviation	Random Distribution	Sources
Initial vertical stress (σ_v)	22.25	MPa	0.65	Normal	Skurtveit et al., 2018; Wireline log (RHOB; Eq. (1))
Initial horizontal stress (σ_h)	16.85	MPa	0.95	Normal	Skurtveit et al., 2018; XLOT
Initial pore pressure (Pp)	10.48	MPa	1.32	Normal	Skurtveit et al., 2018; XLOT
Horizontal stress path (γ_h)	0.51	–	0.07	Normal	Wireline log (PR; Eq. (2))
Horizontal stress path (γ_{fault})	0.54	–	0.03	Normal	Wireline log (PR; Eq. (4))
Vette fault Dip (θ)	45.25	Degree	4.00	Normal	Fault surface interpreted from 3D seismic in zone of interest
Friction angle, cohesionless (ϕ^1)	31.00	Degree	0.00	–	Standard cohesionless fault angle (Zoback, 2010)
Cohesion, Sognefjord (S_0^2)	5.01	MPa	1.62	Log-Normal	Skurtveit et al., 2018; Wireline log (PHIT; Eq. (5))
Friction angle, Sognefjord (ϕ^2)	19.50	Degree	4.50	Normal	Skurtveit et al., 2018
Cohesion, Draupne (S_0^3)	3.93	MPa	1.05	Log-Normal	Skurtveit et al., 2015; Horsrud et al., 1998; Gutierrez et al., 2000; Wireline log (DT; Eq. (6))
Friction angle, Draupne (ϕ^3)	21.63	Degree	5.14	Normal	Skurtveit et al., 2015; Gutierrez et al., 2000
Cohesion, Rødby (S_0^4)	6.81	MPa	0.60	Log-Normal	Wireline log (DT; Eq. (6))
Friction angle, Rødby (ϕ^4)	21.63	Degree	5.14	Normal	Equivalent to Draupne

MPa – Mega Pascal; The numbers shown as superscript in the friction angle and cohesion are indicated case numbers mentioned in Table 1.

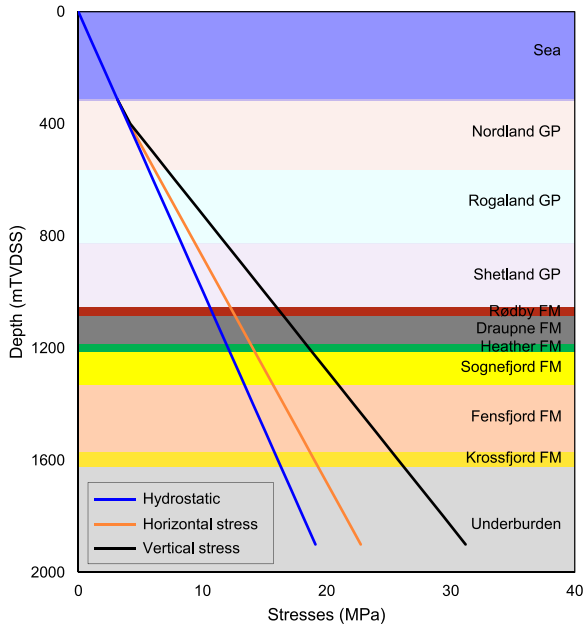

Fig. 6. In-situ stress profile for the Alpha structure assuming normal faulting regime with isotropic horizontal stress condition. Note that the vertical and horizontal stress profiles were calculated using extended leak-off test (XLOT) data from the nearby Troll area. The hydrostatic profile was estimated using water density ~1025 kg/m^3.

fault dip within the zone of interest (from the top of Rødby Formation to the base Viking Group), because the CO_2 injection-related impact will be encountered in this zone. The average dip of the fault in the zone of interest is calculated by the fault interpretation module in the Petrel-2018 software using the available 3D seismic data (i.e., GN1101), where the mean value is estimated at 45.25° from the 3D interpretation of the Vette fault.

Rock strength parameters (i.e., cohesion and friction angle) for case 2 (Sognefjord equivalent) and case 3 (Draupne equivalent) were available from laboratory test results (Gutierrez et al., 2000; Horsrud et al., 1998; Skurtveit et al., 2018, 2015). However, there was no laboratory-measured data for Rødby Formation (Case 4). Therefore, the empirical equations based on porosity (for Sandstone) and P-wave velocity (for shale) were used to estimate the uniaxial compressive strength (C_0) for all different scenarios. In cases 2 and 3, both laboratory test data and empirically estimated data are averaged and used as input parameters, whereas for case 4, the only option is the estimated data.

The empirical equation used for case 2 is taken from Plumb (1994), which stated that:

$$C_0 = 357(1 - 2.8\Phi)^2 \ (\Phi < 0.357) \quad (5)$$

where C_0 is in MPa and Φ as a fraction

And Horsrud (2001) equation was used for cases 3 and 4:

$$C_0 = 0.77V_p^{2.93} \ (\Phi = 30 - 55\%) \quad (6)$$

where C_0 is in MPa and V_p is in km/s

Moreover, the same average friction angle is used for both cases 3 and 4 as there are no measurements for Rødby Formation.

The Mohr-Columb plot of the initial stress state condition on top of the reservoir near the Vette fault is shown in Fig. 7. The Columb failure surfaces for all the fault rock strength scenarios are also representing the relative distance from the Mohr circle. Moreover, the fault plane dipping points (red points) on the Mohr-Columb diagram show that the fault dipping close to 60° is the closest to the classical fault failure surface compared with 45°. In this study, the mean Vette fault dip interpreted in the zone of interest is 45.25°. However, overall, the fault plane dip ranges from 35 to 52°.

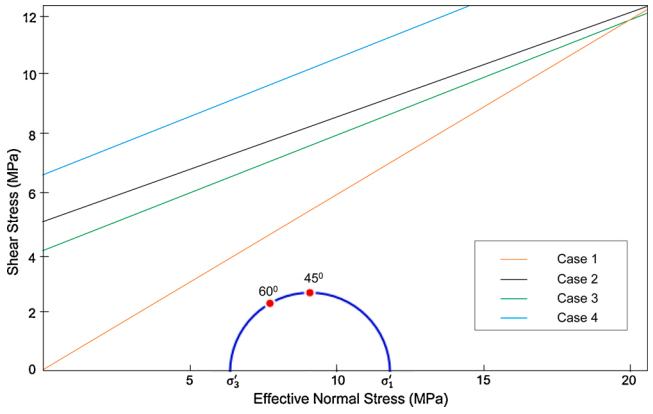

Fig. 7. The Mohr-Columb plot is representing the shear stress and effective normal stresses of the initial reservoir stress state condition. The failure surfaces for all the fault rock strength scenarios (Table 1) are shown for comparison. Note that red points on top of the Mohr circle represent the fault plane location based on the fault dip.

3.2. Model definition

3.2.1. Reliability analysis concept

The reliability analyses provide a rational framework for dealing with the structural uncertainties that assist in making the decision. However, the probability of failure does not necessarily correspond to high safety (deterministic estimation); instead, it depends on the uncertainties in load and resistance (Nadim, 2007). For a structural component with uncertain resistance R and load S and their random variables, probability density functions $f_R(r)$ and $f_S(s)$ respectively, the probability of failure may be determined by:

$$P_f = P(R \le S) = P(R - S \le 0) = \int_{-\infty}^{\infty} f_R(X) f_S(X) dx \tag{7}$$

where X is the random variable, assuming the load and the resistance variables are statistically independent.

However, the probability of failure is not determined by the overlapping of the two curves but by the realization of the random variables R and S. If both the resistance and load variables are normally distributed, the failure probability may be assessed directly by considering the random variable M often referred to as the safety margin:

$$M = R - S \tag{8}$$

where the probability of failure may be assessed through

$$P_f = P(R - S \le 0) = P(M \le 0) \tag{9}$$

where M is also normally distributed with parameters with the mean $\mu_M = \mu_R - \mu_S$ and standard deviation $\sigma_M = \sqrt{\sigma_R^2 + \sigma_S^2}$.

The failure probability may be determined by the use of the standard normal distribution function as:

$$P_f = \Phi\left(\frac{0 - \mu_M}{\sigma_M}\right) = \Phi(-\beta) \tag{10}$$

where $\mu_M/\sigma_M = \beta$ is called the safety/reliability index, which is the standard deviation by which the mean value of the safety margin M exceeds zero or most likely exceeds the failure point (Fig. 8).

However, if the resistance and the load cannot be described by only two random variables but rather by functions of the same random variables and statistically dependent, the safety margin M will be:

$$M = R - S = f_1(X) - f_2(X) = g(X) \tag{11}$$

where X is a vector with n so-called basic random variables, the function g(X) is denoted as the limit state function, which is a boundary between desired (g(X) >0) and undesired (g(X) ≤ 0) performance of any structure and defined within a mathematical model for functionality and performance (Ditlevsen and Madsen, 2007).

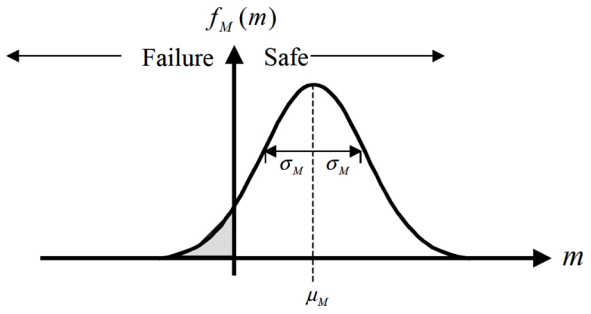

Fig. 8. Normally distributed, the probability distribution function of safety margin M showing the probable failure and safe zones (adapted from Faber, 2009).

3.2.2. Limit state function

In this study, we considered the limit state function is based on the Mohr-Coulomb failure criteria. Considering isotropic horizontal stress condition and normal faulting regime in the study area (Skurtveit et al., 2018), the factor of safety (FoS) is defined as:

$$FoS = \frac{\tau_{MC}}{\tau_{current}} \tag{12}$$

$$\tau_{MC} = S_0 + \sigma_n^{'} \cdot tan\varnothing \tag{13}$$

$$\tau_{current} = \frac{\sigma_1^{'} - \sigma_3^{'}}{2} \cdot sin2\theta \tag{14}$$

$$\sigma_n^{'} = \frac{\sigma_1^{'} + \sigma_3^{'}}{2} + \frac{\sigma_1^{'} - \sigma_3^{'}}{2} \cdot cos2\theta \tag{15}$$

where τ_{MC} is critical shear stress or shear strength, $\sigma_n^{'}$ is effective normal stress, S_0 is cohesion, σ_1 is initial vertical stress, σ_3 is initial horizontal stress, $\sigma_1^{'}$ is effective vertical stress, $\sigma_3^{'}$ is effective horizontal stress, $\varnothing$ is an effective friction angle, and θ is fault dip.

The state of the structure is safe when the factor of safety is greater than 1 and fails when it is less than 1. Therefore, the limit-state function defines as:

$$g(x) = FoS - 1 \tag{16}$$

where g(x) is the limit-state function which is the boundary between safe (g(x) >0) and failure (g(x) ≤ 0) state.

3.3. Reliability method

Several well-established reliability methods are available (i.e., First Order Second Moment, First Order Reliability Method/Second Order Reliability Method, Monte Carlo simulation, etc.). We tested Monte Carlo Simulation (MCS) and First Order Reliability Method (FORM) to estimate Vette fault's probability of failure. The MCS is a procedure where the limit state function is evaluated by randomly selected samples from the input values to determine whether the configuration is desirable or not. The probability of failure (P_f), however, is estimated by the number of unwanted settings (n_f), with respect to the total numbers of samples (n).

$$P_f = \frac{n_f}{n} \tag{17}$$

It is a powerful technique but sometimes impractical when the probability of failure is small and requires many simulations to obtain a reliable distribution. However, sampling techniques (i.e., Latin Hypercube, Orthogonal, etc.) can optimize the number of simulations required for reliable distribution of the response, which we did not consider in this study.

On the contrary, the First Order Reliability Method (FORM) is a basic method for reliability evaluation in structural reliability theory and is widely used in practical engineering problems (Faber, 2009; Nadim, 2007), which is proposed by Hasofer and Lind (1974). According to this method, the reliability index (β_{HL}) is the shortest distance z* from the origin to the failure surface g(z) in a normalized space and denoted as:

$$\beta_{HL} := \beta = \overrightarrow{\alpha^T} z^* \tag{18}$$

where the normalized space is transformed to standardized normally distributed random variables with zero means and unit standard deviations (Fig. 9). $\overrightarrow{\alpha}$ denotes the normal vector to the failure surface g(z) and is given by:

$$\overrightarrow{\alpha} = -\frac{\nabla g(z^*)}{|\nabla g(z^*)|} \tag{19}$$

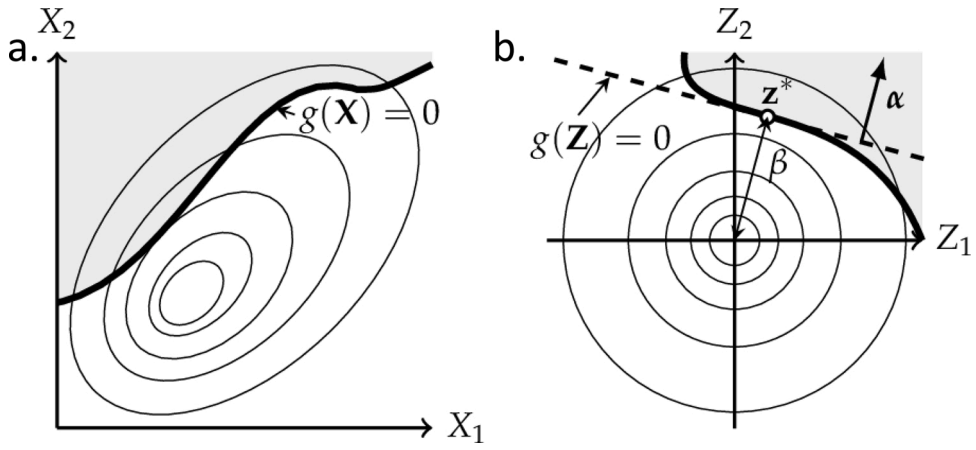

Fig. 9. a) Illustration of a physical space of two random variables (X1 and X2) with the limit state function stated g(X), and b) after normalization of the random variables into standardized normally distributed variables Z with the design point z* and reliability index β. Note that the grey shaded area denoted the failure domain, and g(X)/g(Z) = 0 is the failure surface (modified after Madsen et al., 2006).

where g(z) is the gradient vector, which is assumed to exist:

$$\nabla g(z) = \left(\frac{\partial g}{\partial z_1}(z), \ldots\ldots\ldots, \frac{\partial g}{\partial z_n}(z)\right) \tag{20}$$

Therefore, the reliability index β is an optimization problem and non-linear case; an iterative method must be used (Madsen et al., 2006; Thoft-Christensen and Baker, 1982). Hence the probability of failure is equal to the probability that an undesired performance will occur and determined through the following n-dimensional integral:

$$P_f = \int_{g(x)\leq 0} f_X(X)dx \tag{21}$$

where $f_X(X)$ is the joint probability density function for the vector of basic random variables X, and the integration is performed over the failure domain. This procedure called FORM, and β is the First Order Reliability Index (Madsen et al., 2006). The results of FORM, which uses a linearization of the limit state function, could be inaccurate if the points for the linearization are not properly selected. This study adopted a search algorithm to find the most probable failure points instead of using the mean and the standard deviation as the linearization points.

The Python-based open-source structural reliability analysis module PyRe (Hackl, 2018) was used to initiate and run the MCS and FORM techniques models. PyRe has been created from FERUM (Finite Element Reliability Using Matlab) project started in 1999 at the University of California, Berkeley, for pedagogical purposes. However, only the core function of the FERUM was implemented, which focuses on the reliability analysis and not considered finite element methods. Along with the core reliability functionality and summarizing output, PyRe is also very flexible and extensive, making it applicable to a large suite of problems. Other softwares, such as excel™ 2016 version is used for the cross-plots and sensitivity analysis, while 2018 version of Petrel™is used for seismic and petrophysical interpretation. Moreover, the MohrPlotter™ version-3 is used for the Mohr-Columb failure plot.

4. Results

4.1. Estimated reliability of the Vette fault

The probability of failure of the Vette fault is summarized in Table 3. All four different fault smearing scenarios described in chapter 3.1.1 are considered for this reliability analysis. As outlined in Table 3, the probability of failure (P_f) of the Vette fault varies significantly with the variation of fault rock strength properties (i.e., different cases). When the fault smearing is assumed as cohesionless material (i.e., case 1), this scenario results in the highest probability of failure (i.e., 1.64E-02). However, when the fault smearing scenario is assumed to be from Rødby Formation (i.e., case 4), the calculated probability of failure (i.e., $<10^{-6}$) using the number of trials 10^8. The failure probability of cases 2 and 3 ranges in between at 10^{-4} and 10^{-6}, respectively.

Table 3
Probability of failure of VF in different scenarios estimated using MCS and FORM.

	Monte-Carlo		FORM	
	Initial condition	After injection	Initial condition	After injection
Case 1	1.64E-02	1.24E-02	8.70E-03	1.16E-02
Case 2	1.14E-04	1.15E-04	1.68E-04	1.27E-04
Case 3	7.58E-06	8.60E-06	2.84E-04	2.01E-04
Case 4	$<10^{-6}$	$<10^{-6}$	1.20E-11	2.23E-12

The MCS results are sensitive to the number of trails; hence, the accuracy depends on it. If there are enough trials, the MCS calculates fairly accurate probability. The number of MCS trial sensitivity is shown in Fig. 10, where failure probability is run in different iterations for case 1 initial scenario. The obtained failure probability fluctuated significantly and eventually became insensitive to the number of trials when the number was larger than 10^6. This indicated that the probability of failure estimated using MCS for cases 3 and 4 are within the sensitive zone and need additional trials for more accurate values.

On the contrary, the First Order Reliability Method (FORM) gives

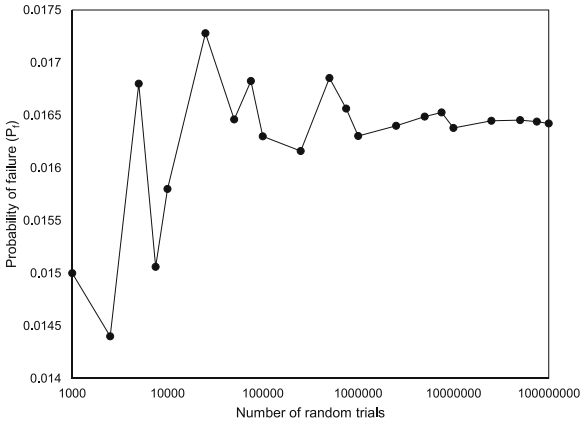

Fig. 10. Failure probabilities were calculated based on the different number of iterations for case 1, showing the sensitivity of the MCS method.

consistent failure results compared with the MCS (i.e., cases 1 and 2) (Table 3). As cases 3 and 4 need more trials in the MCS method, we assume FORM approximated realistic values for these cases. Therefore, FORM results in this study are considered reliable and used for further discussions.

When the FORM results are compared with the initial condition, and after CO_2 injection scenarios, the difference is minimal. Although the pore pressure change due to injection is used as a deterministic number in this study, the after-injection scenarios showed a slightly higher failure value than the initial condition except case 4, where the value is somewhat smaller (Table 4). The reliability index value in the First Order Reliability Method also followed a similar trend (i.e., lower in the after-injection scenarios than the initial condition except case 4).

The differences in fault failure for horizontal stress path calculated using Eqs. (2) and (4) are very minimal. The P_f values using the FORM method in the after-injection scenario are shown in Table 5. Overall, the normal faulting region horizontal stress change option has slightly lower values compared to the case where we ignored the faulting influence.

4.2. Computational efficiency

The concepts of both stochastic Monte-Carlo simulation and the First Order Reliability Method are different and have their advantages and disadvantages. Monte-Carlo simulation is a powerful technique, but analyzing a very low (i.e., case 4) structural probability of failure can sometimes be unrealistic. For example, to estimate the case 4 failure probability, the Monte-Carlo simulation required more than 10^{12} trials (FORM estimated failure value is 2.23E-12), which are very time-consuming and practically impossible. In contrast, the number of iterations needed to approximate the reliability index in the First Order Reliability Method is minimal (Table 6); hence, the time required is insignificant but shown to be quite accurate compared to Monte-Carlo simulation results.

4.3. Sensitivity analysis

Both deterministic and probabilistic sensitivity factors are evaluated where each has its unique advantages. The deterministic sensitivity indicates how much each random variable's mean and standard deviation contributes to the response's variability. In contrast, the probabilistic sensitivity, which results from the probabilistic analyses, indicated each parameter's effect on the reliability function (Easley et al., 2007).

4.3.1. Deterministic sensitivity

Each parameter's weight acted on the Vette fault safety factor is analyzed using 'one variable at a time' (OVAT) sensitivity analysis technique (Campolongo et al., 2000; Rohmer and Seyedi, 2010). The concept is that each input parameter is alternatively assigned its minimum and maximum values, whereas the other input parameters are fixed to their mean values. The input parameter ranges are summarized in Table 7. The factor of safety parameter has been calculated as output using Eq. (12). The case 4 scenarios are illustrated here as equivalent to the Rødby Formation strength case, which is most likely the scenario based on our geological interpretation.

The OVAT analysis illustrated that the initial horizontal and vertical stresses (i.e., initial stress state) have the most significant impact than any other input parameters (Fig. 11). Therefore, these can be the critical parameters related to the fault failure risk. The smallest value of $\sigma_3^{'}$ corresponds to the highest failure tendency and vice versa. On the contrary, the minimum value of $\sigma_v^{'}$ denotes the higher safety state while the higher failure state symbolizes the maximum $\sigma_v^{'}$ values. The fault rock strength properties (i.e., cohesion and friction angle) and pore pressure also have a strong influence on safety measures. On the contrary, the horizontal stress path and fault dip values have minimal effect on assessing fault safety.

4.3.2. Probabilistic sensitivity

The relative design sensitivity factors or the relative importance factors (α) are often referred to as probabilistic sensitivity factors, which are very useful for the relative ranking of random variables. This is obtained by performing several probabilistic analyses and treating every individual parameter as a deterministic variable in each study (NESUS Theoretical Manual, 2011; Pereira et al., 2014). A positive sensitivity indicates a direct relationship between the variable's value and the response, while a negative sensitivity suggests an inverse relationship. Moreover, the square of each sensitivity factor (α_i^2) is a measure of its contribution to the probability, and the sum is equal to unity (i.e., 1). However, this sensitivity factor is not always ideal for the design process as it is only represented by standard normal variates while the mean, standard deviation, and distribution type needed to represent the full picture (Easley et al., 2007).

In this study, the probabilistic sensitivity factors (α) showed that different variables' relative significance is different in other cases (Fig. 12). For example, in case 1, pore pressure (P_p) and horizontal stress (σ_h) contributed most of the variability, while the fault dip (θ) with the null value indicated no contribution. In contrast, horizontal stress (σ_h), fault dip (θ), and cohesion (S_0) represent the most contributor

Table 4
Probability of Failure (P_f) and Reliability Index (β) of different scenarios estimated using FORM in the initial condition and after injection scenarios.

	Initial condition		After injection	
	P_f	β	P_f	β
Case 1	8.70E-03	2.3781	1.16E-02	2.2692
Case 2	1.68E-04	3.5856	1.27E-04	3.6586
Case 3	2.84E-04	3.4465	2.01E-04	3.5384
Case 4	1.20E-11	6.6797	2.23E-12	6.9219

Table 5
Effect of injection-related horizontal stress path on failure probability values estimated using FORM.

	γ_h	γ_{fault}
Case 1	**1.16E-02**	**1.16E-02**
Case 2	**1.27E-04**	**1.20E-04**
Case 3	**2.01E-04**	**2.01E-04**
Case 4	**2.23E-12**	**2.23E-12**

Table 6
The number of iterations to estimate the failure probability represents the time required for each technique.

	FORM[a]	Monte-Carlo
Case 1	**6**	100000000
Case 2	**9**	
Case 3	**10**	
Case 4	**26**	

[a] The number of iteration required to minimize the distance to the design point z in the Eq. (20) from origin.

Table 7
Input parameters with minimum and maximum values used in the deterministic sensitivity analysis.

Parameter	Value Range
Initial vertical stress (σ_v)	**21.60−22.90 (MPa)**
Initial horizontal stress (σ_h)	**15.90−17.80 (MPa)**
Pore pressure (Pp)	**9.16−11.80 (MPa)**
Horizontal stress path (γ_h)	**0.44−0.58**
Vette fault Dip (θ)	**41.25–49.25°**
Cohesion, Rødby (S_0)	**6.21–7.41 (MPa)**
Friction angle, Rødby (ϕ)	**16.49−26.77°**

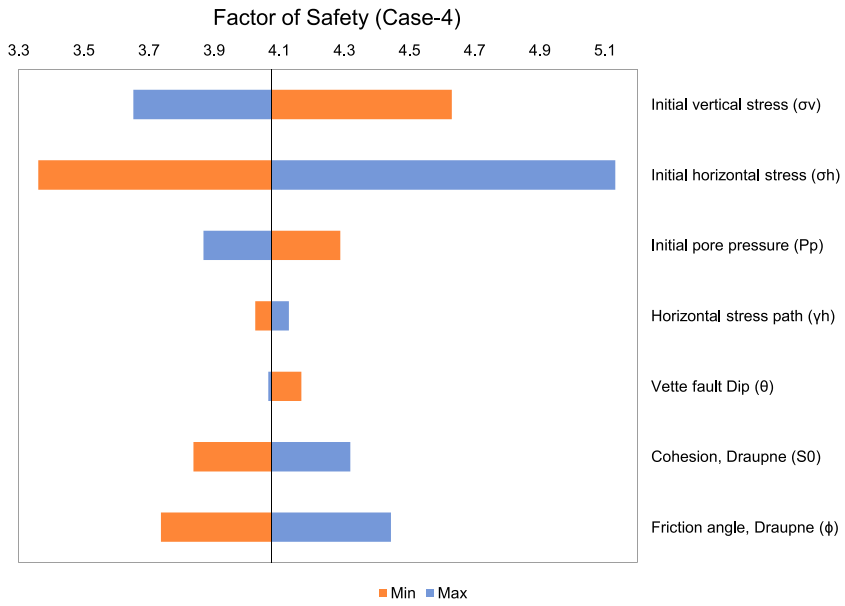

Fig. 11. The tornado diagram of the most likely scenario (case 4) after the injection case shows the relative importance of parameters.

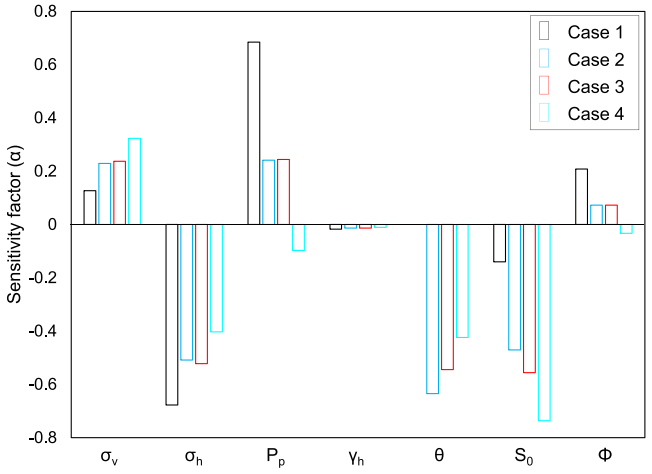

Fig. 12. Sensitivity factors (α) for the probabilistic analysis of Vette fault using FORM showing the relative ranking of the random variables (i.e., σ_v = Vertical stress; σ_h = Horizontal stress; P_p = Pore pressure; γ_h = Horizontal stress path; θ = Fault dip; S_0 = Cohesion and Φ = friction angle).

parameters for the rest of the cases (i.e., cases 2, 3, and 4). The least influential factor for all the cases is the horizontal stress path (γ_h), which is also shown in deterministic sensitivity analysis for case 4 (Fig. 11). Overall, both analyses for case 4 have similarities except fault dip (θ) and friction angle (S_0), where a significant variation was observed between the analyses.

4.4. System reliability analysis of Vette fault

In this study, we estimated the Vette fault system reliability using an event tree. The reliability results of each case show that the most unlikely scenario (i.e., case 1) resulted in a 100 times higher probability of failure than less likely scenarios (i.e., cases 2 and 3) and a million times higher probability than likely scenarios (i.e., case 4). To evaluate the overall stability of faults, the probability of possible fault smearing cases is weighted by scenario likelihoods. The event probability values for each likelihood are assigned based on the Vette fault's geological understanding, while the ranges are validated using the published literature (Brændeland et al., 2010; Nadim, 2007). Subsequently, for each case, the failure and non-failure state are estimated using the probability of failure values calculated by the FORM. We used the FORM estimated P_f values because all the fault rock strength scenarios have approximated values that are quite accurate compared to the Monte-Carlo simulation results in higher P_f scenarios (i.e., case 1 and 2). The total probability of failure and non-failure values for each case are estimated by considering the fault rock strength parameters (i.e., cohesion and friction angles) uncertainties. Finally, by adding all the failure values, the system failure of the Vette fault is calculated.

The calculated system reliability is summarized in Fig. 13. The computed system probability of failure of the Vette fault is around 1.46E-04. The Vette fault system failure values are equivalent to cases 2 and 3 (i.e., 1.27E-04 and 2.01E04, respectively) while significantly higher than case 4 (i.e., 2.23E-12) and lower than case 1 (i.e., 1.16E-02). Although case 1 is a very unlikely scenario, this scenario's weight on system failure's total probability is important (i.e., 1.16E-04 out of 1.46E-04), because the probability of failure of scenario 1 is significantly higher than the other scenarios. On the contrary, the contribution of the most likely scenario (i.e., case 4), which has the probability of failure of 10^{-12}, on the total system failure probability seems to be negligible. If we exclude the unlikely scenarios from the decision making, it can underestimate the system failure. Thus, caution needs to be taken for the low likelihood scenarios; for example, in the worst-case scenario (i.e., case 1), the consequences might be intense. The event tree is used to calculate system failure probability, which considered all the probabilistic incident, hence an excellent approach to represent the system reliability.

The system reliability index (β) is also estimated from the relationship between the probability of failure (P_f) and the reliability index (β). The trend line is drawn using the data points calculated for different cases in the initial condition scenario using the FORM. According to the graph, the Vette fault system reliability is ~3.7 (Fig. 14).

5. Discussion

In the case of Vette fault stability in the Smeaheia area, the failure probability estimation approach is new and essential to understanding the fault seal risks. The riskiest scenario (i.e., case 1) is unlikely to happen as several similar fault-related traps (i.e., Tusse, Svartalv, and Troll faults) in nearby Troll Field contain thick hydrocarbon columns.

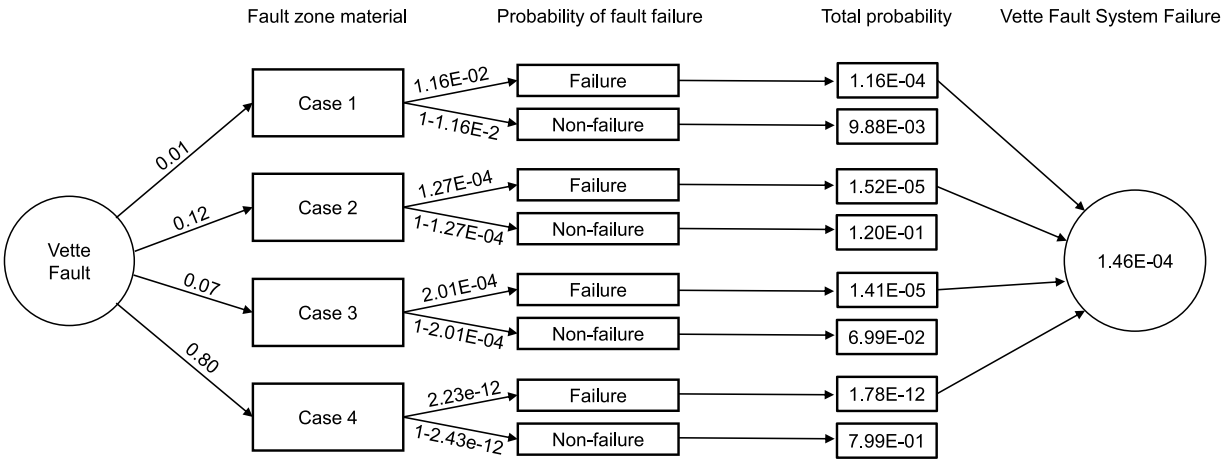

Fig. 13. Event tree of Vette fault system reliability analysis showing the system failure number.

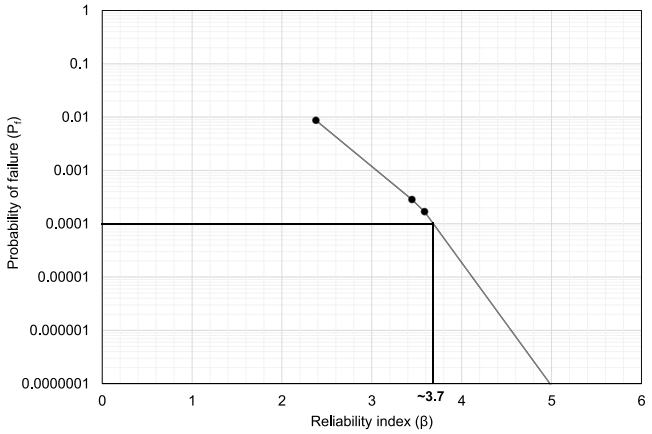

Fig. 14. Relationships between the reliability index and the probability of failure of this study. The trend line is generated by connecting the data points estimated for various scenarios.

Moreover, the evolution and extent of these faults (i.e., Vette, Tusse, Svart, Troll, etc.) are related (Stewart et al., 1995; Whipp et al., 2014), which indicated similar fault geometry and fault zone complexities in Vette fault as well. However, as case 1 is unlikely but a possible scenario, despite a low possibility, there are always chances of this event to happen, and if it occurs, the consequences will be significant. For instance, the probability of unsatisfactory performance for case 1 is 11 out of 1000, which belongs to the poor-to-unsatisfactory zone in the expected performance level (Table 8). To compare the poor and unsatisfactory level illustrated 23 and 70 failure events out of 1000 runs, respectively. On the other hand, the best-case scenario (case 4), where the Rødby Formation juxtaposes with the main reservoir rock (i.e., Sognefjord Formation), has very high fault seal probability (i.e., 0.7–1.0). Based on Færseth et al. (2007), the qualitative fault seal method shows a high uncalibrated shale gauge ratio (SGR). However, towards the south of the primary Vette fault, relay zones are formed, with cross-fault self-juxtaposition of the reservoir interval indicating low fault seal probability value (i.e., 0−0.3) (Mulrooney et al., 2018). There could be a possibility of pressure communication through this reservoir-reservoir juxtaposition. Still, the location is far from the proposed Alpha structure (south tipping point of the Vette fault) and might not be influential considering short post-injection time compare with the geological time frame (Fulljames et al., 1997). However, it is worth testing the scenario in any future numerical fluid flow model.

Table 8
The expected performances are based on the reliability index and the probability of failure values, adapted from U.S. Army Corps of Engineers (1997).

Expected Performance Level	Reliability index (β)	Probability of Unsatisfactory Performance[a]
High	5.0	0.0000003
Good	4.0	0.00003
Above average	3.0	0.001
Below average	2.5	0.006
Poor	2.0	0.023
Unsatisfactory	1.5	0.07
Hazardous	1.0	0.16

[a] Probability of unsatisfactory performance is the probability that the value of performance function will approach the limit state, or that an unsatisfactory event will occur.

The Draupne Formation shales could have been smeared in the early stage of the Vette fault; however, at present, the fault throw is significantly high near the Alpha structure, reducing the chances of smearing of this formation (Færseth, 2006). Fault rock strength equivalent to Sognefjord Formation is also unlikely as the fault interpreted in the 3D seismic (i.e., GN1101) is very sharp and seems to be a single surface. Moreover, there might be a possibility of sub-seismic resolution faults, which might change the likelihood of this case. However, the 3D seismic used for the structural interpretation (i.e., fault dip and definition of different scenarios) has good quality. Still, there are always interpretation-related uncertainties (i.e., human error, seismic quality, sub-seismic fault plane, etc.) present (Bond et al., 2015). The probabilistic approach such as this study incorporated those interpretation related uncertainties by using a probable data range. In contrast, the result of a deterministic method cannot include such a range and cannot cope with the uncertainties. Moreover, there might be the risk of biasness while assigning the probabilistic likelihood values for cases based on the geological understanding of that area. However, system reliability using the event tree method can significantly reduce that risk because the worst-case scenario dictates the final failure probability. For example, the Vette fault system PoF is within the 10^{-4} region, which is also the worst-case total probability of failure. If we change the likelihood number for other cases, the system failure number will be still within the 10^{-4} region. However, caution is needed to assign the worst-case scenario likelihood because if decreased tenfold, the system failure will be responding accordingly.

One of the positive findings is that the Vette fault failure probability decreases significantly with increasing the likelihood of the fault rock strength scenarios (Fig. 15). The higher the likelihood, the higher the possibility of the event to happen, hence increasing the possibility of sealing the Vette fault. Considering the geological interpretation with the failure probability, the Vette fault likely provides a structural trap for

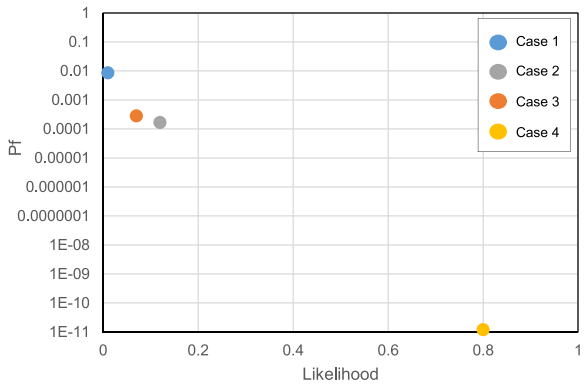

Fig. 15. Probability of failure (P_f) versus the likelihood of various fault rock strength scenarios of Vette fault in the initial condition.

the Alpha prospect; however, numerical modeling is required to evaluate the effect of the southward fault segment changes.

The reliability index (β) and the probability of failure (P_f) in any structure are a relative measurement of the current condition and provide a qualitative estimation of the expected performance (U.S. Army Corps of Engineers, 1997). Table 8 shows the β and P_f values with the corresponding performances to interpret structural safety. According to the chart (U.S. Army Corps of Engineers, 1997), the Vette fault system is in between the good to above-average performance range (i.e., β = ~3.7), which is also recommended by NORSOK standard Report (2010) for offshore installation. The unsatisfactory failure event for the Vette fault estimated is only 14 of 100000 results. Considering these published failure ranges, we can conclude that the Vette fault system's overall probability of failure is within the acceptable range and suggests that this fault may be a barrier in the potential Alpha structure.

The input parameters used to evaluate subsurface fault failure are often highly uncertain and cannot include all the uncertainties in the deterministic approach. However, the probabilistic method such as this study can integrate all the possible uncertain parameters with different ranges and can estimate the reliability; hence indicates the significance of the probabilistic approach in any structural integrity issues (i.e., fault seal analysis). Moreover, this study shows that integrating the likelihood of possible scenarios can result in different results than the case considering the only most likely scenario. In this way, the method considered all the possible worst-case scenario risks within the whole structural system reliability value; hence it was deemed more reliable. Also, the deterministic safety factor does not reflect the corresponding failure probability (Nadim, 2007). For example, Christian et al. (1994) illustrated a significantly different probability of failure for James Bay dikes for three height of dikes, where the factor of safety is similar. The probabilistic analysis can also explicitly show the trade-off between investment and reduction of potential losses, thus facilitating decision-making in the presence of uncertainties (Juang et al., 2019). In connection with the CO_2 storage sites, the structural system reliability value might thus simplify the future project decision.

This study shows that the methods used for system reliability analysis should be convenient and robust that can capture the risk of unlikely scenario. When the low failure probability of the case 4 was calculated, the crude Monte-Carlo simulation needs a significant number of iterations to get a result. It might be expensive and in some cases practically impossible. This study indicates that the FORM technique seems to be one of the appropriate method for this kind of subsurface static problems. When the limit state function is a smooth and monotonic function, which are typical for most of the static system, FORM can estimate the reliability index relatively accurately (Madsen et al., 2016). However, for the highly non-linear and high dimensional problems, which can often be for dynamic systems, FORM can result in a local minimum and consequently lead to an error (Fiessler et al., 1979). Thus, applying FORM for highly non-linear dynamic problems should be prudent. In further studies which calculate the stress conditions coupled with flow simulations using numerical methods (e.g., finite element method), other reliability approaches including optimized Monte Carlo simulations (e.g., importance sampling method) should be taken into account and the accuracy and efficiency should be tested.

The analytical solutions for the factor of random safety variables are usually represented as normal random variables with limited probability distribution options; hence numerical tools are necessary (Nomikos and Sofianos, 2011). However, assessing the possibility of evaluating the sensitivity of various input parameters in the analytical model is very convenient. This analysis will provide guidelines for future investigation. This study finds that the anisotropy of in-situ horizontal stress could be the most sensitive parameter for Smeaheia faults stability analysis; furthermore, the vertical stress and fault rock strength properties also have a significant impact. The in-situ stress field in Smeaheia needs further investigation for a better fault reliability understanding. In this study, we considered only 2D stress conditions by assuming the isotropic horizontal stress condition. The extended leak-off test database from the North Sea shows almost isotropic horizontal stress conditions for most North Sea hydrocarbon reservoirs (Andrews et al., 2016). However, 3D uncertainties along the fault plane could also be important when the probability of failure is near the marginal range. Besides, the pore pressure effect along the vertical section of fault might be critical to evaluate fault safety. Therefore, these parameters need further study before any future modeling work (i.e., analytical or numerical modeling approach).

6. Conclusion

The structural reliability of the Vette fault is the key to a successful Alpha structure CO_2 injection project. However, the parameters needed to evaluate the fault sealing integrity are highly uncertain. Therefore, we proposed this probabilistic reliability technique to estimate the structural failure likelihood of the Vette fault. The critical observations of this study are as follows:

- The cohesionless fault scenario has the highest failure probability, while the fault rock properties equivalent to the Rødby Formation case shows the lowest value. Moreover, the difference between the initial condition and the after-injection scenario is minimal.
- Both deterministic and probabilistic sensitivity analyses revealed that the in-situ stresses (vertical and horizontal) and fault rock strength properties (cohesion and friction angle) are the critical parameters influencing fault stability.
- Integrating the likelihood of possible scenarios using the event tree method can quantify the overall structural failure. The failure value estimated using this approach is the better representation of total failure compared to the case considering only the most likely scenario because the event tree method considered all the possible scenarios. However, caution needs to be taken for the low likelihood scenarios if the low likelihood scenario's failure probability is significantly higher than other likely scenarios.
- The Vette fault system reliability analysis' probabilistic value suggested that the fault seems to be structurally reliable. Hence, it may act as a potential barrier during the injection of CO_2 into the Alpha structure.

We can conclude that the probabilistic scenario-based event tree approach can be useful to quantify the subsurface structural reliability and proved to be a valuable tool in case considerable uncertainties are present.

CRediT authorship contribution statement

Md Jamilur Rahman: Conceptualization, Methodology, Formal

analysis, Investigation, Writing - original draft, Writing - review & editing, Visualization. **Jung Chan Choi:** Conceptualization, Methodology, Writing - review & editing, Supervision. **Manzar Fawad:** Writing - review & editing, Supervision. **Nazmul Haque Mondol:** Writing - review & editing, Supervision, Project administration, Funding acquisition.

Declaration of Competing Interest

The authors declare that they have no known competing financial interests or personal relationships that could have appeared to influence the work reported in this paper.

Acknowledgments

We are thankful for the funding provided by the Research Council of Norway for the OASIS (Overburden Analysis and Seal Integrity Study for CO_2 Sequestration in the North Sea) project (NFR-CLIMIT project #280472) and the FME NCCS Centre (NFR project #257579/E20). We are also grateful to Schlumberger™ for the Petrel-2018 academic software license, Python Software Foundation for Python, and Rick Allmendinger's Stuff for MohrPlotter.

References

Addis, M.A., 1997. The stress-depletion response of reservoirs. In: SPE Annual Technical Conference and Exhibition. Society of Petroleum Engineers. https://doi.org/10.2118/38720-MS.

Addis, M.A., Last, N.C., Yassir, N.A., 1994. The estimation of horizontal stresses at depth in faulted regions and their relationship to pore pressure variations. In: Rock Mechanics in Petroleum Engineering. Society of Petroleum Engineers. https://doi.org/10.2118/47289-MS.

Addis, M.A., Choi, X., Gunning, J., 1998. The influence of the reservoir stress-depletion response on the lifetime considerations of well completion design. In: SPE/ISRM Rock Mechanics in Petroleum Engineering. Society of Petroleum Engineers. https://doi.org/10.2118/28140-MS.

Andrews, J.S., Fintland, T.G., Helstrup, O.A., Horsrud, P., Raaen, A.M., 2016. Use of unique database of good quality stress data to investigate theories of fracture initiation, fracture propagation and the stress state in the subsurface. In: 50th US Rock Mechanics/Geomechanics Symposium. American Rock Mechanics Association.

Baklid, A., Korbol, R., Owren, G., 1996. Sleipner vest CO2 disposal, CO2 injection into a shallow underground aquifer. In: SPE Annual Technical Conference and Exhibition. Society of Petroleum Engineers. https://doi.org/10.2118/36600-MS.

Bohloli, B., Choi, J.C., Skurtveit, E., Grande, L., Park, J., Vannest, M., 2015. Criteria of Fault Geomechanical Stability During a Pressure Buildup. IEAGHG Rep. 4.

Bond, C.E., Johnson, G., Ellis, J.F., 2015. Structural model creation: the impact of data type and creative space on geological reasoning and interpretation. Geol. Soc. London Spec. Publ. 421, 83–97.

Bouvier, J.D., Kaars-Sijpesteijn, C.H., Kluesner, D.F., Onyejekwe, C.C., Van der Pal, R.C., 1989. Three-dimensional seismic interpretation and fault sealing investigations, Nun river Field, Nigeria. Am. Assoc. Pet. Geol. Bull. 73, 1397–1414. https://doi.org/10.1306/44B4AA5A-170A-11D7-8645000102C1865D.

Brændeland, G., Refsdal, A., Stølen, K., 2010. Modular analysis and modelling of risk scenarios with dependencies. J. Syst. Softw. 83, 1995–2013. https://doi.org/10.1016/j.jss.2010.05.069.

Campolongo, F., Kleijnen, J.P.C., Andres, T., 2000. Screening methods. Wiley Ser. Probab. Stat.Chiaramonte, L., White, J.A., Trainor-Guitton, W., 2015. Probabilistic geomechanical analysis of compartmentalization at the Snøhvit CO2 sequestration project. J. Geophys. Res. Solid Earth 120, 1195–1209. https://doi.org/10.1002/2014JB011376.

Chiaramonte, L., Johnson, S., White, J.A., 2011. Preliminary geomechanical analysis of CO2 injection at Snøhvit, Norway. In: 45th US Rock Mechanics/Geomechanics Symposium. American Rock Mechanics Association.

Childs, C., Walsh, J.J., Watterson, J., 1997. Complexity in fault zone structure and implications for fault seal prediction. Norwegian Petroleum Society Special Publications. Elsevier, pp. 61–72. https://doi.org/10.1016/S0928-8937(97)80007-0.

Christian, J.T., 2004. Geotechnical engineering reliability: how well do we know what we are doing? J. Geotech. Geoenviron. Eng. 130, 985–1003. https://doi.org/10.1061/(ASCE)1090-0241(2004)130:10(985).

Christian, J.T., Ladd, C.C., Baecher, G.B., 1994. Reliability applied to slope stability analysis. J. Geotech. Eng. 120, 2180–2207. https://doi.org/10.1061/(ASCE)0733-9410(1994)120:12(2180).

Ditlevsen, O., Madsen, H.O., 2007. Structural Reliability Methods. Internet e. ed.. John Wiley and Sons.

Doughty, P.T., 2003. Clay smear seals and fault sealing potential of an exhumed growth fault, Rio Grande rift, New Mexico. Am. Assoc. Pet. Geol. Bull. 87, 427–444. https://doi.org/10.1306/10010201130.

Dreyer, T., Whitaker, M., Dexter, J., Flesche, H., Larsen, E., 2005. From spit system to tide-dominated delta: integrated reservoir model of the Upper Jurassic Sognefjord Formation on the Troll West Field. Geological Society, London, Petroleum Geology Conference Series. Geological Society of London 423–448. https://doi.org/10.1144/0060423.

Duffy, O.B., Bell, R.E., Jackson, C.A.-L., Gawthorpe, R.L., Whipp, P.S., 2015. Fault growth and interactions in a multiphase rift fault network: horda Platform, Norwegian North Sea. J. Struct. Geol. 80, 99–119. https://doi.org/10.1016/j.jsg.2015.08.015.

Duncan, J.M., 2000. Factors of safety and reliability in geotechnical engineering. J. Geotech. Geoenviron. Eng. 126, 307–316. https://doi.org/10.1061/(ASCE)1090-0241(2000)126:4(307).

Easley, S.K., Pal, S., Tomaszewski, P.R., Petrella, A.J., Rullkoetter, P.J., Laz, P.J., 2007. Finite element-based probabilistic analysis tool for orthopaedic applications. Comput. Methods Programs Biomed. 85, 32–40. https://doi.org/10.1016/j.cmpb.2006.09.013.

Faber, M.H., 2009. Basics of Structural Reliability. Swiss Fed. Inst. Technol. ETH, Zürich, Switz.

Færseth, R.B., 2006. Shale smear along large faults: continuity of smear and the fault seal capacity. J. Geol. Soc. London. 163, 741–751. https://doi.org/10.1144/0016-76492005-162.

Færseth, R.B., Oppenboen, K.A., Saeboe, A., 1984. Trapping styles and associated hydrocarbon potential in norwegian North Sea. Am. Assoc. Pet. Geol. Bull. 68, 1201–1201.

Færseth, R.B., Johnsen, E., Sperrevik, S., 2007. Methodology for risking fault seal capacity: implications of fault zone architecture. Am. Assoc. Pet. Geol. Bull. 91, 1231–1246. https://doi.org/10.1306/03080706051.

Faleide, J.I., Bjørlykke, K., Gabrielsen, R.H., 2015. Geology of the Norwegian Continental Shelf. Petroleum Geosciences: From Sedimentary Environments to Rock Physics, pp. 603–637.

Faulkner, D.R., Jackson, C.A.L., Lunn, R.J., Schlische, R.W., Shipton, Z.K., Wibberley, C.A.J., Withjack, M.O., 2010. A review of recent developments concerning the structure, mechanics and fluid flow properties of fault zones. J. Struct. Geol. 32, 1557–1575.

Fiessler, B., Rackwitz, R., Neumann, H.-J., 1979. Quadratic limit states in structural reliability. J. Eng. Mech. Div. 105, 661–676.

Fisher, Q.J., Knipe, R.J., 2001. The permeability of faults within siliciclastic petroleum reservoirs of the North Sea and Norwegian Continental Shelf. Mar. Pet. Geol. 18, 1063–1081. https://doi.org/10.1016/S0264-8172(01)00042-3.

Foxford, K.A., Walsh, J.J., Watterson, J., Garden, I.R., Guscott, S.C., Burley, S.D., 1998. Structure and content of the Moab Fault Zone, Utah, USA, and its implications for fault seal prediction. Geol. Soc. London Spec. Publ. 147, 87–103. https://doi.org/10.1144/GSL.SP.1998.147.01.06.

Fulljames, J.R., Zijerveld, L.J.J., Franssen, R., 1997. Fault seal processes: systematic analysis of fault seals over geological and production time scales. Norwegian Petroleum Society Special Publications. Elsevier, pp. 51–59. https://doi.org/10.1016/S0928-8937(97)80006-9.

Gassnova, 2016. Feasibility Study for Full-scale CCS in Norway. https://ccsnorway.com/wp-content/uploads/sites/6/2019/09/feasibilitystudy_fullscale_ccs_norway_2016.pdf.

Geertsma, J., 1973. A Basic Theory of Subsidence Due to Reservoir Compaction; the Homogeneous Case.

Gibson, R.G., 1994. Fault-zone seals in siliciclastic strata of the Columbus Basin, offshore Trinidad. Am. Assoc. Pet. Geol. Bull. 78, 1372–1385. https://doi.org/10.1306/A25FECA7-171B-11D7-8645000102C1865D.

Grasso, J.-R., 1992. Mechanics of seismic instabilities induced by the recovery of hydrocarbons. Pure Appl. Geophys. 139, 507–534.

Gutierrez, M., Øino, L.E., Nygaard, R., 2000. Stress-dependent permeability of a demineralised fracture in shale. Mar. Pet. Geol. 17, 895–907. https://doi.org/10.1016/S0264-8172(00)00027-1.

Hackl, J., 2018. PyRe Documentation [WWW Document]. URL. http://github.com/hackl/pyre.

Hasofer, A.M., Lind, N.C., 1974. Exact and invariant second-moment code format. J. Eng. Mech. Div. 100, 111–121.

Hettema, M.H.H., Schutjens, P., Verboom, B.J.M., Gussinklo, H.J., 2000. Production-induced compaction of a sandstone reservoir: the strong influence of stress path. SPE Reserv. Eval. Eng. 3, 342–347. https://doi.org/10.2118/65410-PA.

Hillis, R.R., 2001. Coupled changes in pore pressure and stress in oil fields and sedimentary basins. Pet. Geosci. 7, 419–425. https://doi.org/10.1144/petgeo.7.4.419.

Holgate, N.E., Jackson, C.A.L., Hampson, G.J., Dreyer, T., 2015. Seismic stratigraphic analysis of the Middle Jurassic Krossfjord and Fensfjord formations, Troll oil and gas field, northern North Sea. Mar. Pet. Geol. 68, 352–380. https://doi.org/10.1016/j.marpetgeo.2015.08.036.

Horsrud, P., 2001. Estimating mechanical properties of shale from empirical correlations. SPE Drill. Complet. 16, 68–73. https://doi.org/10.2118/56017-PA.

Horsrud, P., Sønstebø, E.F., Bøe, R., 1998. Mechanical and petrophysical properties of North Sea shales. Int. J. Rock Mech. Min. Sci. 35, 1009–1020. https://doi.org/10.1016/S0148-9062(98)00162-4.

Hortle, A., Xu, J., Dance, T., 2013. Integrating hydrodynamic analysis of flow systems and induced-pressure decline at the Otway CO2 storage site to improve reservoir history matching. Mar. Pet. Geol. 45, 159–170.

IPCC, 2005. Carbon Dioxide Capture and Storage.

Jev, B.I., Kaars-Sijpesteijn, C.H., Peters, M.P.A.M., Watts, N.L., Wilkie, J.T., 1993. Akaso field, Nigeria: use of integrated 3-D seismic, fault slicing, clay smearing, and RFT

pressure data on fault trapping and dynamic leakage. Am. Assoc. Pet. Geol. Bull. 77, 1389–1404. https://doi.org/10.1306/BDFF8EA2-1718-11D7-8645000102C1865D.
Juang, C.H., Zhang, J., Shen, M., Hu, J., 2019. Probabilistic methods for unified treatment of geotechnical and geological uncertainties in a geotechnical analysis. Eng. Geol. 249, 148–161. https://doi.org/10.1016/j.enggeo.2018.12.010.
Karolytė, R., Johnson, G., Yielding, G., Gilfillan, S.M.V., 2020. Fault seal modelling–the influence of fluid properties on fault sealing capacity in hydrocarbon and CO2 systems. Pet. Geosci.
Kim, J., Berg, R.R., Watkins, J.S., Tieh, T.T., 2003. Trapping capacity of faults in the Eocene Yegua Formation, east sour lake field, southeast Texas. Am. Assoc. Pet. Geol. Bull. 87, 415–425. https://doi.org/10.1306/08010201129.
Lacasse, S., Nadim, F., 1998. Risk and Reliability in Geotechnical Engineering.
Lindsay, N.G., Murphy, F.C., Walsh, J.J., Watterson, J., Flint, S., Bryant, I., 1993. Outcrop studies of shale smears on fault surfaces. Geol. Model. Hydrocarb. Reserv. Outcrop Analog. 15, 113–123.
Madsen, H.O., Krenk, S., Lind, N.C., 2006. Methods of Structural Safety. Courier Corporation.
Martens, S., Kempka, T., Liebscher, A., Lüth, S., Möller, F., Myrttinen, A., Norden, B., Schmidt-Hattenberger, C., Zimmer, M., Kühn, M., 2012. Europe's longest-operating on-shore CO2 storage site at Ketzin, Germany: a progress report after three years of injection. Environ. Earth Sci. 67, 323–334. https://doi.org/10.1007/s12665-012-1672-5.
Mathieson, A., Midgley, J., Dodds, K., Wright, I., Ringrose, P., Saoul, N., 2010. CO 2 sequestration monitoring and verification technologies applied at Krechba, Algeria. Lead. Edge 29, 216–222.
Miocic, J., Johnson, G., Bond, C.E., 2019. Uncertainty in fault seal parameters: implications for CO2 column height retention and storage capacity in geological CO2 storage projects. Solid Earth.
Mulrooney, M.J., Osmond, J., Skurtveit, E., Wu, L., Braathen, A., 2018. Smeaheia, a potential northern North Sea co2 storage site: structural description and de-risking strategies, in: fifth CO2 Geological Storage Workshop. Eur. Assoc. Geoscient. Eng. 1–5. https://doi.org/10.3997/2214-4609.201802957.
Nadim, F., 2007. Tools and strategies for dealing with uncertainty in geotechnics. Probabilistic Methods in Geotechnical Engineering. Springer, pp. 71–95.
NESUS Theoretical Manual, 2011. Southwest Research Institute, San Antorio, Texas.
Nomikos, P.P., Sofianos, A.I., 2011. An analytical probability distribution for the factor of safety in underground rock mechanics. Int. J. Rock Mech. Min. Sci. 48, 597–605. https://doi.org/10.1016/j.ijrmms.2011.02.015.
NORSOK standard Report, 2010. Integrity of Offshore Structures.
NPD, 2020. NPD FactPages [WWW Document]. URL. https://factpages.npd.no/en/wellbore/PageView/Exploration/All/2918.
NPD CO2 Atlas, 2014. NPD CO2 Atlas Report.
Park, J.-W., Guglielmi, Y., Graupner, B., Rutqvist, J., Kim, T., Park, E.-S., Lee, C., 2020. Modeling of fluid injection-induced fault reactivation using coupled fluid flow and mechanical interface model. Int. J. Rock Mech. Min. Sci. 132, 104373 https://doi.org/10.1016/j.ijrmms.2020.104373.
Pereira, F.L.G., Roehl, D., Laquini, J.P., Oliveira, M.F.F., Costa, A.M., 2014. Fault reactivation case study for probabilistic assessment of carbon dioxide sequestration. Int. J. Rock Mech. Min. Sci. 71, 310–319. https://doi.org/10.1016/j.ijrmms.2014.08.003.
Plumb, R.A., 1994. Influence of composition and texture on the failure properties of clastic rocks. Rock Mechanics in Petroleum Engineering. Society of Petroleum Engineers.
Rock, L., O'Brien, S., Tessarolo, S., Duer, J., Bacci, V.O., Hirst, B., Randell, D., Helmy, M., Blackmore, J., Duong, C., 2017. The Quest CCS Project: 1st year review post start of injection. Energy Procedia 114, 5320–5328.
Rohmer, J., Seyedi, D.M., 2010. Coupled large scale hydromechanical modelling for caprock failure risk assessment of CO2 storage in deep saline aquifers. Oil Gas Sci. Technol. 65, 503–517. https://doi.org/10.2516/ogst/2009049 l'Institut Français du Pétrole.
Rutqvist, J., Birkholzer, J., Cappa, F., Tsang, C.-F., 2007. Estimating maximum sustainable injection pressure during geological sequestration of CO2 using coupled fluid flow and geomechanical fault-slip analysis. Energy Convers. Manage. 48, 1798–1807. https://doi.org/10.1016/j.enconman.2007.01.021.
Segall, P., 1989. Earthquakes triggered by fluid extraction. Geology 17, 942–946. https://doi.org/10.1130/0091-7613(1989)017<0942:ETBFE>2.3.CO;2.
Skerlec, G.M., 1996. Risking Fault Seal in the Gulf Coast (Abs.): AAPG Annual Convention Program and Abstracts, v. 5, p. A131.
Skurtveit, E., Grande, L., Ogebule, O.Y., Gabrielsen, R.H., Faleide, J.I., Mondol, N.H., Maurer, R., Horsrud, P., 2015. Mechanical testing and sealing capacity of the Upper Jurassic Draupne Formation, North Sea. 49th US Rock Mech. Symp. Am. Rock Mech. Assoc.
Skurtveit, E., Choi, J.C., Osmond, J., Mulrooney, M., Braathen, A., 2018. 3D fault integrity screening for smeaheia CO2 injection site. 14th Greenhouse Gas Control Technologies Conference Melbourne 21–26.
Stewart, D.J., Schwander, M., Bolle, L., 1995. Jurassic depositional systems of the Horda Platform, Norwegian North Sea: practical consequences of applying sequence stratigraphic models. Nor. Pet. Soc. Spec. Publ. 291–323. https://doi.org/10.1016/S0928-8937(06)80073-1.
Thoft-Christensen, P., Baker, M.J., 1982. Reliability of structural systems. Structural Reliability Theory and Its Applications. Springer, Berlin, Heidelberg, pp. 113–127.
U.S. Army Corps of Engineers, 1997. Engineering and Design Introduction to Probability and Reliability Methods for Use in Geotechnical Engineering. Washington, D.C..
Verdon, J.P., Kendall, J.M., Stork, A.L., Chadwick, R.A., White, D.J., Bissell, R.C., 2013. Comparison of geomechanical deformation induced by megatonne-scale CO2 storage at Sleipner,Weyburn, and in Salah. Proc. Natl. Acad. Sci. 110, E2762–E2771. https://doi.org/10.1073/pnas.1302156110.
Vidal-Gilbert, S., Tenthorey, E., Dewhurst, D., Ennis-King, J., Van Ruth, P., Hillis, R., 2010. Geomechanical analysis of the Naylor Field, Otway Basin, Australia: implications for CO2 injection and storage. Int. J. Greenh. Gas Control 4, 827–839. https://doi.org/10.1016/j.ijggc.2010.06.001.
Walsh, J.J., Watterson, J., Heath, A.E., Childs, C., 1998. Representation and scaling of faults in fluid flow models. Pet. Geosci. 4, 241–251. https://doi.org/10.1144/petgeo.4.3.241.
Whipp, P.S., Jackson, C.L., Gawthorpe, R.L., Dreyer, T., Quinn, D., 2014. Normal fault array evolution above a reactivated rift fabric; a subsurface example from the northern Horda Platform, Norwegian North Sea. Basin Res. 26, 523–549. https://doi.org/10.1111/bre.12050.
Wiprut, D., Zoback, M.D., 2000. Fault reactivation and fluid flow along a previously dormant normal fault in the northern North Sea. Geology 28, 595–598. https://doi.org/10.1130/0091-7613(2000)28<595:FRAFFA>2.0.CO;2.
Yielding, G., 2002. Shale gouge ratio—calibration by geohistory. Nor. Pet. Soc. Spec. Publ. 11, 1–15. https://doi.org/10.1016/S0928-8937(02)80003-0.
Yielding, G., Freeman, B., Needham, D.T., 1997. Quantitative fault seal prediction. Am. Assoc. Pet. Geol. Bull. 81, 897–917. https://doi.org/10.1306/522B498D-1727-11D7-8645000102C1865D.
Zieglar, D.L., 1992. Hydrocarbon columns, buoyancy pressures, and seal efficiency: comparisons of oil and gas accumulations in California and the Rocky Mountain area. Am. Assoc. Pet. Geol. Bull. 76, 501–508. https://doi.org/10.1306/BDFF884E-1718-11D7-8645000102C1865D.
Zoback, M.D., 2010. Reservoir Geomechanics. Cambridge University Press. Case.

Paper-3

Effect of overburden spatial variability on field-scale geomechanical modeling of potential CO_2 storage site Smeaheia, offshore Norway

Md Jamilur Rahman
Manzar Fawad
Jung Chan Choi
Nazmul Haque Mondol

Journal of Natural Gas Science and Engineering, 2022

Journal of Natural Gas Science and Engineering 99 (2022) 104453

Contents lists available at ScienceDirect

Journal of Natural Gas Science and Engineering

journal homepage: www.elsevier.com/locate/jngse

Effect of overburden spatial variability on field-scale geomechanical modeling of potential CO_2 storage site Smeaheia, offshore Norway

Md Jamilur Rahman [a,*], Manzar Fawad [a], Jung Chan Choi [b], Nazmul Haque Mondol [a,b]

[a] Department of Geosciences, University of Oslo (UiO), Sem Saelands vei 1, 0371, Oslo, Norway
[b] Norwegian Geotechnical Institute (NGI), Sognsveien 72, 0806, Oslo, Norway

ARTICLE INFO

Keywords:
Smeaheia
3D field-scale geomechanical model
Surface deformation
One-way coupling
Finite element method
Overburden
Spatial variability

ABSTRACT

Although geological CO_2 sequestration is an essential solution for reducing anthropogenic carbon dioxide from the atmosphere, the method needs critical evaluation of injection-induced mechanical risks for safe and reliable CO_2 storage. 3D field-scale geomechanical modeling is a preeminent solution for assessing mechanical risks of subsurface geological CO_2 storage. However, data scarcity of seals and overburden rocks might limit building the 3D field-scale geomechanical model. This study focuses on seismic data-derived 3D field-scale geomechanical modeling of potential CO_2 storage site Smeaheia, offshore Norway. The geomechanical properties inverted from seismic data are resampled in the 3D grid to consider spatial variabilities of seal and overburden rock properties. This method allows us to investigate the effect of overburden rock spatial variability imposed in seismic data on the 3D geomechanical model of Smeaheia. The model was built in Petrel-2019, while the one-way geomechanical simulation is iterated using the finite element method. Simplified constant overburden property models are also constructed to analyze the sensitivity of the overburden rock properties. The results reveal that the seismic data-driven spatially distributed overburden properties model workflow used in this study is a convenient and robust solution for 3D field-scale geomechanical modeling. The maximum vertical estimation of rock deformation is doubled in the simplified (isotropic) overburden rock property model compared to the new spatially variable (anisotropic) overburden rock property model. The Mohr-Coulomb failure envelope reveals that the new modeling approach is less prone to failure than the simplified (isotropic) model, which might influence the project decision. Moreover, our study demonstrates the importance of considering the spatial variability of overburden rock properties in building the 3D field-scale geomechanical model.

1. Introduction

Geological sequestration of anthropogenic CO_2 (CCS) into saline aquifers or depleted hydrocarbon reservoirs is one of the many solutions to achieve the Paris Climate Accords to keep the average global temperature rise well below 2 °C by 2050. According to NPD CO_2 Atlas (2014), the CO_2 storage capacity of the Norwegian Continental Shelf (NCS) is significant, where the Norwegian government and industries already show interest in the gigaton level of CO_2 storage (i.e., Northern lights project under the Longship). The phase 1 plan for this project is to capture, transport, inject and store up to 1.5 MT of CO_2 per year, while in the future, the project will store up to 5 MT of CO_2 per year based on the market demand from the large CO_2 emitters across Europe (Northern Lights project). However, any CCS project needs critical evaluation of injection-related risks (3D field-scale geomechanical modeling) for safe, reliable, and permanent geological storage.

Injecting CO_2 into saline aquifer changes the fluid saturation that results in a local disturbance in pressure and temperature and influences the mechanical behavior of the reservoir, cap, and overburden rocks. The potential geomechanical consequences would be the flexure of the top-seal and overburden, reactivation of existing faults, induced share failure, formation of new fracture and faults, changes in porosity within the reservoir, etc. (Hawkes et al., 2005; Herwanger and Koutsabeloulis, 2011; Rutqvist et al., 2008, 2007; Soltanzadeh and Hawkes, 2008; Streit and Hillis, 2004, Fig. 1). Therefore, evaluating CO_2 injection-related geomechanical risks is essential for reliable and successful CCS projects like Smeaheia and Longship.

The reliability of the CCS project depends on seal integrity, which includes caprock effectiveness and fault sealing potential (Chiaramonte et al., 2015; Park et al., 2020; Rahman et al., 2020, 2021; Rutqvist et al.,

* Corresponding author.
E-mail address: m.j.rahman@geo.uio.no (M.J. Rahman).

https://doi.org/10.1016/j.jngse.2022.104453
Received 18 November 2021; Received in revised form 26 December 2021; Accepted 28 January 2022
Available online 4 February 2022

2007; Skurtveit et al., 2018). Generally, the top seal consists of fine-grained rocks with a significantly small pore throat radius and exceptionally high capillary entry pressure. Watts (1987) introduced the concept as hydraulic seals, i.e., seals where the capillary entry pressure is so high that seal breach only occurs due to fracturing (i.e., shear failure) of the caprock (Ingram et al., 1997). Therefore, assessment of the potential flexure of the top seal and overburden rocks becomes important. The injected CO_2 into the saline aquifer will change the effective stress (i.e., principal stress minus pore pressure) and influence the mechanical deformation of rock and failure (Verdon et al., 2013). This process may lead to enormous rock deformation, such as the seafloor heave illustrated in Fig. 1. The elastic behavior of pore fluid under the drainage condition (i.e., poroelasticity) might influence the mechanical behavior and stress path within the reservoirs (Addis, 1997; Grasso, 1992; Hillis, 2001; Segall, 1989), which also indirectly affect the above cap and overburden rocks. Additional processes such as hydraulic aperture evolution, hydrological property changes, effective stress induction, and mechanical strength degradation can influence the effective stress (Park et al., 2020; Rutqvist et al., 2007), leading to different caprock and overburden deformation.

During drilling a well, there has been good coverage of data (i.e., cores, wireline logs, pressure data, etc.) acquired in the reservoir section. However, the caprock and overburden sections have mostly been ignored to collect data. This data gap is reflected in most geomechanical modeling works, where simple assumptions are used for overburden rock property evaluation (i.e., Fischer and Henk, 2013; Fokker et al., 2011; Grollimund and Zoback, 2003; Mandal et al., 2021; Newell et al., 2017; Olden et al., 2014; Ouellet et al., 2011; Tenthorey et al., 2013; Vidal-Gilbert et al., 2010). However, the effectiveness of 3D field-scale geomechanical modeling in rock deformation and failure is proven and published by several authors to evaluate the influence of CO_2 injections and gas storage projects worldwide. For instance, a 3D geomechanical model building and calibrating workflow proposed by Fischer and Henk (2013) using a gas reservoir in the North German Basin; while Vidal-Gilbert et al. (2010) and Tenthoreya et al. (2013) analyzed the geomechanical consequences using the gas fields (Naylor and Iona) from Australia. Several authors also investigated the surface upliftment at the In Salah CO_2 storage site (Fokker et al., 2011; Newell et al., 2017). However, the simple assumption in the overburden section is used in all the work except Mandal et al. (2021), where they build a gridded overburden static geomechanical model. They used 1D well properties points dataset during interpolating laterally. When limited wells are present, the interpolation method increases the uncertainty significantly. The effect of anisotropic overburden properties in the dynamic simulation is missing in their work. On the contrary, other authors (Olden et al., 2014; Ouellet et al., 2011) did the dynamic simulation but focused on mainly the reservoir and caprock sections and used simple assumptions for the overburden section.

Seismic data have been used for geomechanical models, but only focusing on reservoir and cap rocks sections and not on the whole subsurface (Herwanger and Koutsabeloulis, 2011; Sengupta et al., 2011). The seismic data-driven geomechanical properties of cap and overburden rocks can be a possible solution to fill the data gap because the 3D seismic volume has a full coverage of data from the seafloor to below the reservoir zone. This gap in geomechanical model building motivates us to carry out this research so that we can integrate all the pieces and build a robust geomechanical model to answer the critical questions regarding associated risks during CO_2 injection into the prospective reservoirs. The results from a simple modeling approach might hide possible risks demonstrated in Fig. 1b. Therefore, a high-resolution spatial gridded cap and overburden sections are needed in geomechanical modeling to assess the caprock integrity and realistic overburden rock deformation.This study proposed a workflow to resolve this issue by integrating spatially gridded overburden properties with numerical simulation for stress-strain changes due to CO_2 injection-induced pore pressure change. This research investigates the effect of overburden spatial variability by introducing a seismic properties-based 3D, one-way coupling geomechanical modeling workflow integrating petrophysics, rock physics, and seismic inversion techniques. The main aim is to test the sensitivity of overburden rock properties on rock mechanical failure due to CO_2 injection-related reservoir pressure increase. Moreover, the total vertical displacement of reservoir-caprock interaction is also estimated.

The credibility and practicality of this new modeling approach are

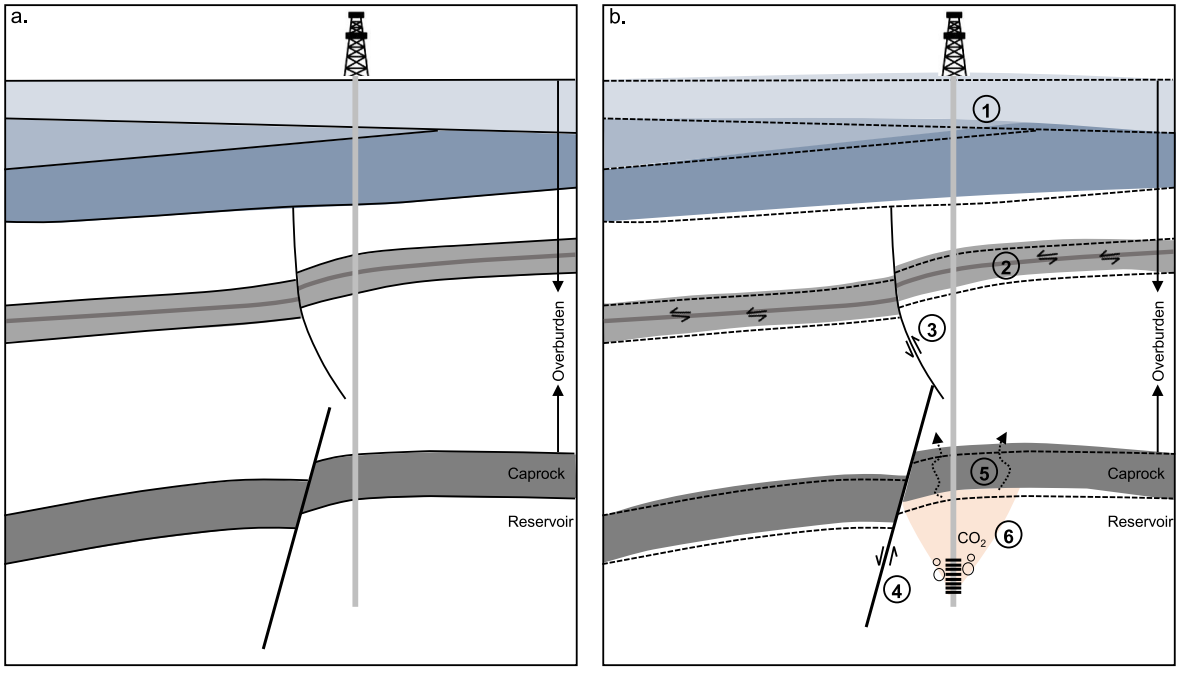

Fig. 1. Schematic representation of CO_2 injection-induced geomechanical effects in a saline storage complex including reservoir, caprock, and overburdens (a) pre-injection state and (b) during/post-injection scenario. Potential consequences include (1) surface heave, (2) bedding parallel slip along with soft layers, (3) & (4) fault reactivation, (5) caprock rock fracturing, and (6) Poro-perm change due to reservoir expansion.

tested using seismic and well log data of the potential CO_2 storage site Smeaheia, offshore Norway. Finally, a field-scale comparative analysis of different models from the Smeaheia injection site is evaluated. To our known reference, the overburden spatial variability on field-scale geomechanical models in CO_2 storage or hydrocarbon production fields is not analyzed before; hence this work is a novel approach in this research arena.

2. Geological setting, cap, and overburden rock properties

The studied Smeaheia area is located in the Horda Platform (HP), northern North Sea, and bounded by two regional N–S trending faults; Vette fault (VF) in the west and Øygarden fault complex (ØFC) in the east (Fig. 2a). The area is positioned east of the giant Troll east gas field and has two structural closures named Alpha (32/4-1) and Beta (32/2-1). Both structures are fault-bounded closures where the Alpha structure is located in the footwall of the Vette Fault, and the Beta structure is located in the hanging wall of the Øygarden Fault Complex (Rahman et al., 2020). These faults are believed to have been formed during the Permo-Triassic 1st rifting event and rooted in the Caledonian zones of crustal weakness (Whipp et al., 2014). During the 1st rifting event, a wide basin with thick syn-depositional wedges is formed in the center of HP, while the 2nd rifting event (Late Jurassic to Mid-Cretaceous times) shifted westward but reactivated all the major faults and formed several smaller faults with minor displacement (Duffy et al., 2015; Skurtveit et al., 2018; Stewart et al., 1995; Whipp et al., 2014). Several small-scale faults/fractures are also created within the overburden section during the post-rift thermal subsidence (Claussen et al., 1999; Mulrooney et al., 2020).

The study area consists of Upper to Middle Jurassic reservoir and caprock pairs where the Sognefjord, Fensfjord, and Krossfjord formation sandstones act as the main reservoir rocks with good to moderate reservoir quality (Dreyer et al., 2005; Fawad et al., 2021a; Holgate et al., 2015) and organic-rich Draupne and Heather formation shales act as the primary seal (Fig. 2b). The reservoir sandstones were deposited in a coastal shallow marine environment and interfingering with Heather Formation. In contrast, the caprock shales (Upper part of the Heather and Draupne Formations) were deposited in an open marine environment with restricted bottom circulation and often anaerobic conditions (NPD, 2021). A thick westward-dipping overburden section (475–800 m) is also present, comprising fine-to coarse-grained siliciclastic packages with occasional carbonate-rich deposits (Faleide et al., 2015).

Overburden rocks play a vital role in vertical surface displacement and sealing effectiveness assessment. Therefore, the overburden rocks properties used in geomechanical modeling work are critical and need to evaluate cautiously. It is crucial to know the complexities of the studied overburden rocks. The complexities varied from basin to basin, but this study tries to assess the effect of simplification of overburden rocks in 3D field-scale geomechanical modeling and the consequences on vertical surface displacement. The overburden rocks in the studied area (i.e., Smeaheia) have complex structural settings. For instance, the Cretaceous and Paleocene rocks are uplifted in the eastern part and eroded by Hordaland unconformity, while thick packages of those units are present in the west (Fig. 3a). Thick Quaternary glacial moraine sediments (Nordland Group) are deposited on top of the Hordaland unconformity. Due to the paleodepositional complexities, lateral depositional and diagenetic variations are observed, leading to various elastic and mechanical properties in the lateral and vertical directions (Fig. 3). Moreover, the inverted seismic cubes showed a good agreement between the rock properties with geophysical data (Fawad et al., 2021a & b).

In geomechanical modeling workflow, constant properties of overburden, sideburden, and underburden geomechanical grids usually added with the spatially gridded reservoir model to mitigate the boundary effects and bending artifacts (Ouellet et al., 2011). However, considering the data range estimated from the seismic inversion (Fawad et al., 2021a & b) in the study area (Table 1), it is evident that a constant value for the whole overburden section might be over-simplification resulting in the omission of the actual mechanical risks. For instance, Young's modulus (E) of overburden rocks ranges between 0.4 and 2.57 GPa with an average value of 1.53 GPa. The difference is considerably large. Other properties also follow a similar trend with a significant difference between the minimum and maximum values. These overburden properties range indicates the urgency to have the spatially distributed overburden grids in 3D geomechanical model risk

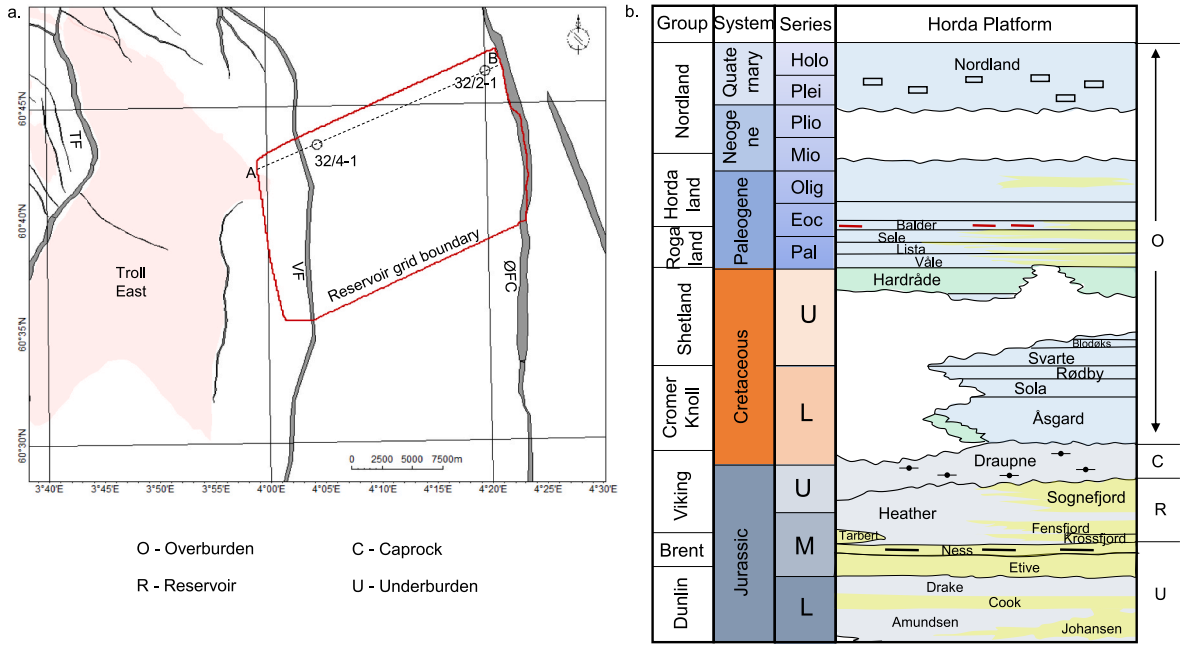

Fig. 2. The red polygon shows the studied model boundary located in the Horda Platform, offshore Norway (a). The area is placed east of the giant Troll east gas field and bounded by two major faults (Vette and Øygarden). The grey shaded lines represent major (*TF – Tusse fault; VF – Vette fault; ØFC – Øygarden fault complex*) and minor faults, and the dotted line indicates the cross-section A to B through the exploration wells 32/4-1 and 32/2-1. This cross-section is used later in the sub-section. (b) A generalized stratigraphic succession of Horda Platform covering the section from Lower Jurassic to the Quaternary (modified after NPD CO_2 Atlas, 2014).

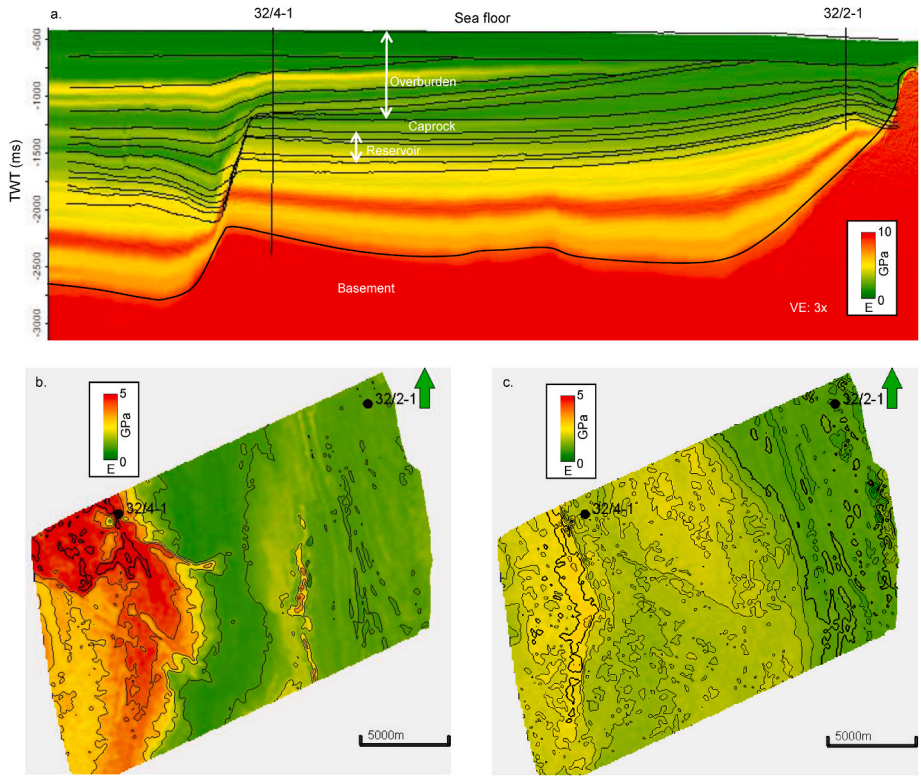

Fig. 3. The spatial and vertical distributions of seismic data-derived Young's modulus (E) shows the W-E cross-section A to B (marked on Fig. 2) view with reservoir, caprock, and overburden horizons and wells (a). The extracted E on top of Lista (b) and Rødby (c) formations demonstrated the lateral variations of rock properties within the overburden.

Table 1
Overburden properties of density, Young's modulus (E), Poisson's ratio (PR), Friction angle (FA), and Unconfined compressional stress (UCS) show the minimum, average and maximum values in the study area.

	Density (gm/cc)	E (GPa)	PR	FA (^{0})	UCS (MPa)
Min	2.14	0.4	0.35	24.51	5.02
Avg	2.24	1.53	0.39	25.92	10.90
Max	2.31	2.57	0.45	26.96	16.46

assessment.

3. Database and workflow

The field-scale reservoir model structural grid is constructed using the seismic interpreted surfaces. The seismic interpretation (i.e., horizons and faults) is carried out using a 3D post-stack seismic volume named GN1101 and two available wells 32/4-1 and 32/2-1 (Fig. 2a). Moreover, pre-stack simultaneous inversion (Fawad et al., 2021a & b) is carried out to invert 3D properties to estimate porosity, Young's Modulus (E), Poisson's Ratio (PR), and Density cubes to populate properties within the structural grids and volume of clay (Vsh), and P-sonic (DT) cubes are used to estimate Friction Angle (FA) and Unconfined Compressional Stress (UCS), respectively.

Fig. 4 illustrates the workflow used in this research to estimate field-scale rocks stress and strain in one-way coupling geomechanical modeling project. The 3D seismic inverted property cubes, which is calibrated with lab measurement and wireline logs during estimation, are directly used in the 3D structural grid. The seismic resampling function in the Petrel-2019 earth modeling module is used to distribute the properties within the model grids. However, the structural grid is constructed earlier, using the seismic interpreted time surfaces. Afterward, the whole reservoir model (i.e., structural grid and properties) is converted into depth using the Smeahiea average velocity cube. Geomechanical grid is introduced in-depth domain by adding sideburden, underburden, overburden, and plate with the reservoir grid. The boundary conditions (i.e., present tectonic stresses and pore pressure) have been defined. The model is now ready for numerical simulation; hence, the VISAGE simulator (Ouellet et al., 2011) is used to run one-way coupling (i.e., changing strain with stress change). After calibration with the observed stresses, the numerically simulated field-scale 3D model is transferred to the Petrel software for interpretation when the estimated value shows a reasonable outcome. This is the workflow we used in this research to run and interpret our models (described in detail later).

4. Model setup

A detailed description of the reservoir and geomechanical modeling structures are described in this section. In each sub-section, the reservoir model describes first, which follows the description of the geomechanical model. Please note that the model time to depth conversion is performed after reservoir model elastic and strength properties distribution.

4.1. Model scenarios

The main focus of this research is to assess the effect of the constant (isotropic) overburden properties versus the spatially distributed true (anisotropic) properties on vertical displacement and changes of strain. Therefore, four models are run to see the overburden sensitivity (Table 2), where model 1 (M-1) has the spatially distributed overburden properties from seismic. In contrast, the rest of the models (M-2, M-3 & M-4) have constant overburden properties with the minimum, mean and maximum values (Table 1), respectively. Please note that the models have the same reservoir and caprock seismic driven properties (Fawad

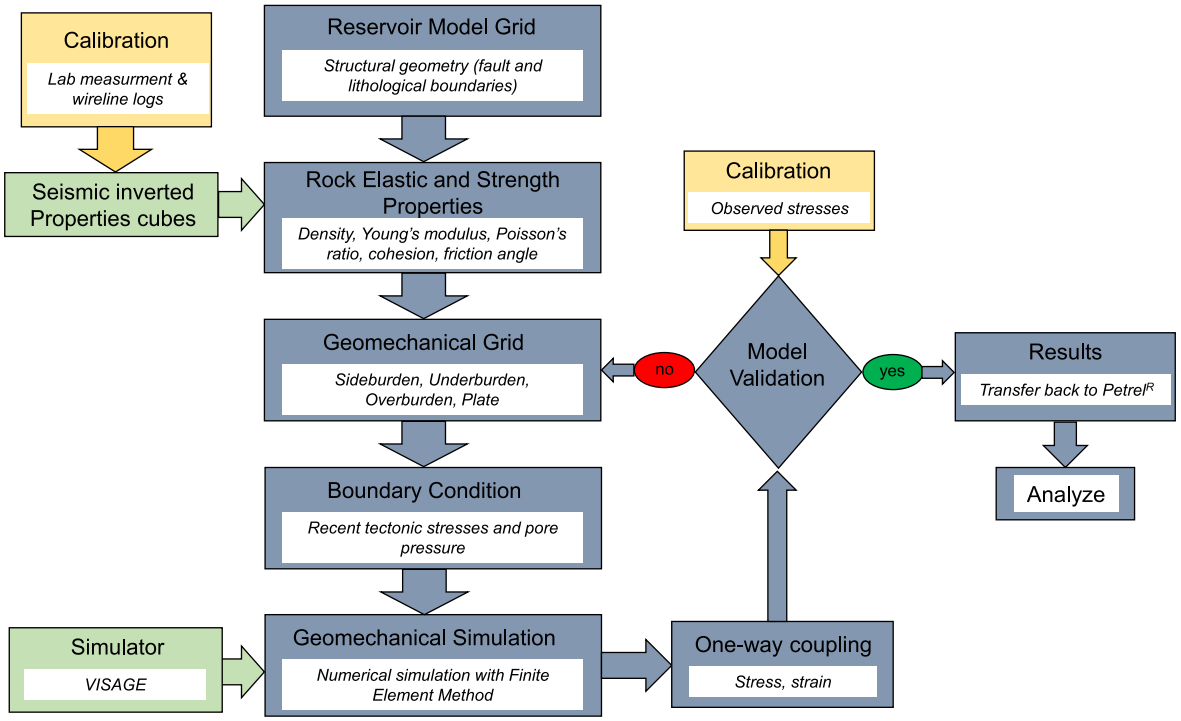

Fig. 4. Seismic properties based one-way coupling field-scale 3D geomechanical modeling workflow used in this research.

Table 2
The criteria used for various models tested in this research.

Model no.	Comments
M-1	Model with overburden reservoir grid and spatially distributed properties
M-2	Model with overburden geomechanical grid and minimal constant properties
M-3	Model with overburden geomechanical grid and average constant properties
M-4	Model with overburden geomechanical grid and maxmimum constant properties

et al., 2021a & b) with the same number of grids.

The reservoir simulation model is out of the scope of this study; hence there is no direct grid by grid pressure increase due to CO_2 injection data being available. Instead, in the one-way coupling, the reservoir simulation result of the Gassnova study is adapted (Gassnova, 2012). However, different model grids require a constant increase in reservoir pressure in different time steps. In the Gassnova model, a total of 160 MT of CO_2 is injected for 50 years with a 3.2 MT/year rate. The average reservoir porosity is 0.26, while the permeability is 690 mD, and the Kv/Kh ratio is equal to 0.1. No solubility of CO_2 into the water function is used because a minor effect has been observed during the sensitivity study (Gassnova, 2012). We assess five (5) different time steps for one-way coupling starting from the initial hydrostatic scenario with every 10-years time step (Fig. 5). Because the main objective of this study is to evaluate the overburden spatial rock sensitivity, we do not consider other time steps such as every 5 years or every year scenario. The hydrostatic initial reservoir pressure is increased constantly throughout the model by multiplying the percentage adapted for each time step from the Gassonova reservoir simulation model. However, in the fluid simulation model, the CO_2 plume will migrate in a specific area and direction based on the poro-perm and structural dip; hence, the reservoir pressure will be varied spatially. Nonetheless, this study has no effect because the same reservoir pressure increase scenarios are used in all the models.

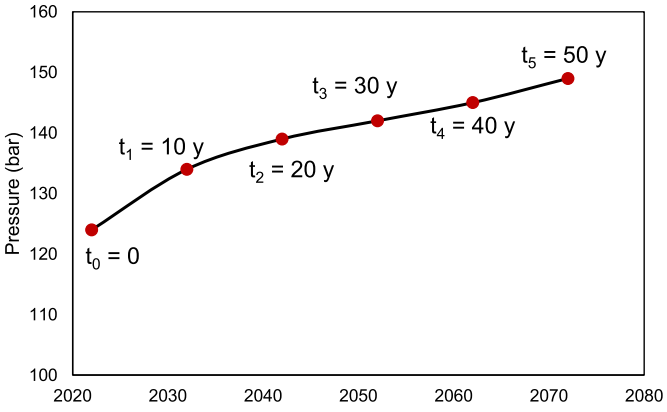

Fig. 5. Reservoir pressures in different time steps adapted from the Gassnova reservoir simulation model (Gassnova, 2012).

4.2. Structural grid

Two sets of reservoir grids are prepared using Petrel structural modeling platform to analyze the overburden rock sensitivity. The first structural grid is for M-1 consists of 14 time surfaces interpreted from the 3D seismic cube (GN1101). This model comprises 13 zones, out of which 7 zones are from the overburden section, and the lowermost zone is underburden rock (Dunlin Group). The total number of vertical layers

Table 3
Statistical comparison of reservoir grids constructed for Model-1 and Models-2/-3/-4.

	Reservoir Grid		Geomechanical Grid	
	M-1	M-2/-3/-4	M-1	M-2/-3/-4
No of horizons	14	6	16	8
No. of zones	13	5	15	7
No. of layers	44	21	48	27
No. of grid cells	340,692	158,928	442,320	243,648

is 44, with more than 340 thousand active grid cells (Table 3). On the contrary, the reservoir grids for M-2/-3/-4 are consist of only caprock and reservoirs with 6 horizons and 5 zones (1 caprock and 4 reservoirs zone). Moreover, the total layers and grid cells are much lower than the first grid with 21 and 158 thousand, respectively. The reservoir grid covers an area of 22 × 13 km^2 (Fig. 5), while each grid covers an area of 250 × 250 m^2. The faults (i.e., Vette, Øygarden, and minor faults) are also considered during seismic horizon interpretation. However, a separate fault grid with different properties is not assigned for model simplicity.

The reservoir grid is expanded laterally and vertically while building the geomechanical grid to mitigate boundary effects and buckling artifacts over the domain of interest. The original reservoir grids with the properties keep unchanged for both grids. The M-1 grid does not need overburden because the overburden section is included within the reservoir grid. Therefore, the sideburden and underburden are added to the reservoir grid for M-1, and sideburden, underburden, and overburden are added to the later grid. Along with the sideburden direction (horizontal), the size of neighboring cells increases by a factor of 1.5 from the edge of the reservoir grid to the edge of the geomechanical grid and covers an area of 68 × 69 km^2 (Fig. 6). The vertical thickness used 5 km; hence the additional depth is adjusted by adding additional underburden in both geomechanical grids.

4.3. Model properties

The seismic inverted rock deformation and rock strength properties are resampling using the geometrical modeling function in Petrel-2019. The interpolate function is used where each cell is a weighted interpolation of 4 seismic cells closest to the center of the grid cell. The prestack seismic inverted property cubes are estimated using an algorithm based on modified Fatti three reflectivity terms (Fatti et al., 1994; Fawad et al., 2020; Hampson et al., 2005). Five partial stacks with angles 0-10^0, 10-20^0, 20-30^0, 30-40^0, and 40-50^0 are used as the input data for the prestack simultaneous inversion (Fawad et al., 2021a). The properties such as porosity, density, Young's modulus (E), Poisson's ratio (PR) are estimated from seismic inversion and directly resampled within the grid, while the other inverted cubes such as volume of shale (Vsh) and P-sonic (DT) are used to calculate friction angle (FA) and unconfined compressive stress (UCS) properties. The FA is estimated using a linear equation based on Vsh and stated that:

$$FA = -12.5Vsh + 32.5 \quad (1)$$

where the sand point (Vsh = 0) and shale point (Vsh = 1), the FA values are used as 32.5 and 20, respectively. The UCS is estimated from P-sonic (DT) using the equation proposed by Horsrud (2001):

$$UCS = 0.77(304.8/DT)^{2.93} \quad (2)$$

where, DT is the P-sonic in μs/ft, and UCS is in MPa.

Fig. 7 illustrates the cross-sectional view (AB marked on Fig. 2) of Young's modulus property distributed within the reservoir grids. The spatially distributed overburden model (M-1) shows property variations within the overburden section (Fig. 7a), while the other model (Fig. 7b) indicated no overburden reservoir grid; hence, no lateral distribution. However, in the geomechanical grid, constant overburden, sideburden,

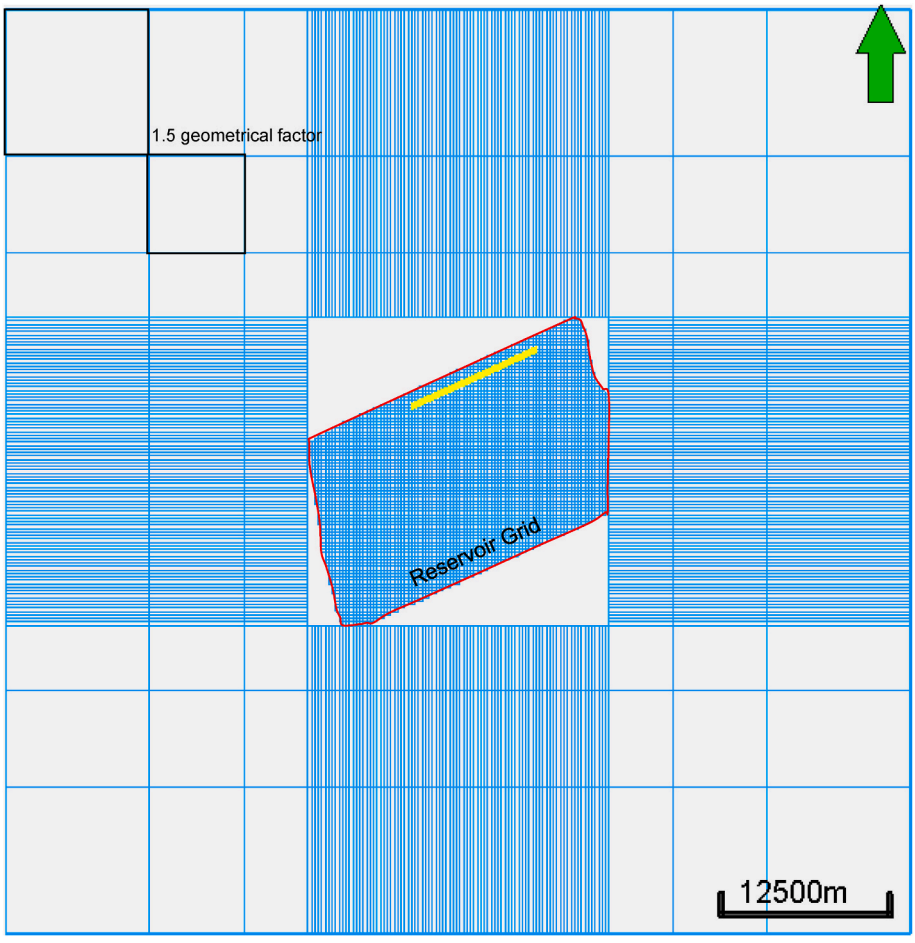

Fig. 6. The model grid shows the reservoir and geomechanical grids distribution. The reservoir grid remains unchanged, while the geomechanical grid used a 1.5 geometrical factor when added.

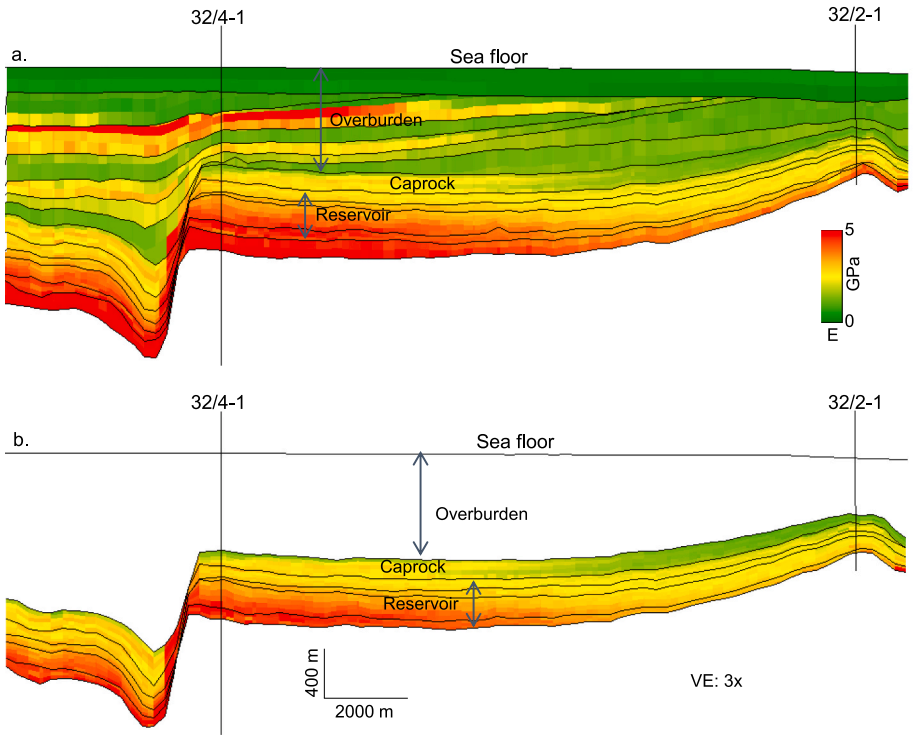

Fig. 7. Cross-section of seismic inverted Young's modulus distributed within the reservoir model grid (a) spatially distributed overburden (M-1) and (b) constant overburden properties (M-2, -3 & −4).

and underburden values are used. Different models are tested using various overburden properties, while the sideburden and underburden properties are the same for all geomechanical grids. Average properties of Dunlin Group are used for underburden, while the caprock properties are used for sideburden grids. A 50 m stiff plate is also added at the edge of the geomechanical grid, which allows us to distribute the pressure within the grids uniformly. In addition, a Mohr-Coulomb failure criteria-based model is assigned. The sensitivity of Biot's coefficient is not tested in this research; instead, it used 1 in all models. Moreover, the thermal effect is out of the scope of this work.

4.4. Pore pressure and in-situ stresses

It is crucial to know the pore pressure to identify the stress field since stress and pore pressure are closely related via poroelastic responses (Grollimund et al., 2001). The large parts of the Norwegian sector show pore pressure close to hydrostatic, including the areas surrounding the Troll and Oseberg fields. Initial hydrostatic reservoir pressure is also applied in this research. Although there is a possibility of depletion due to Troll production, this is not considered in this work.

The in-situ principal stresses in an area depend on many factors and change with time. Moreover, in the study area, very few measurements are available. Based on the present-day seismicity (C-quality data) and leak of test (LOT) data observation, a normal faulting stress regime is assigned in the study area where the vertical stress (lithostatic stress) is the highest principal stress and the minimum horizontal stress is the lowest one (Heidbach et al., 2018; Rahman et al., 2021; Skurtveit et al., 2018). The minimum horizontal stress (SHmin) gradient is used as 0.01245 MPa/m estimated using X-LOT (Rahman et al., 2021), while the maximum horizontal stress (SHmax) assumed 10% more stress than SHmin (Fig. 8). Moreover, based on the seismicity database near Troll field, SHmax azimuthal direction is used as 103^0 (Heidbach et al., 2018).

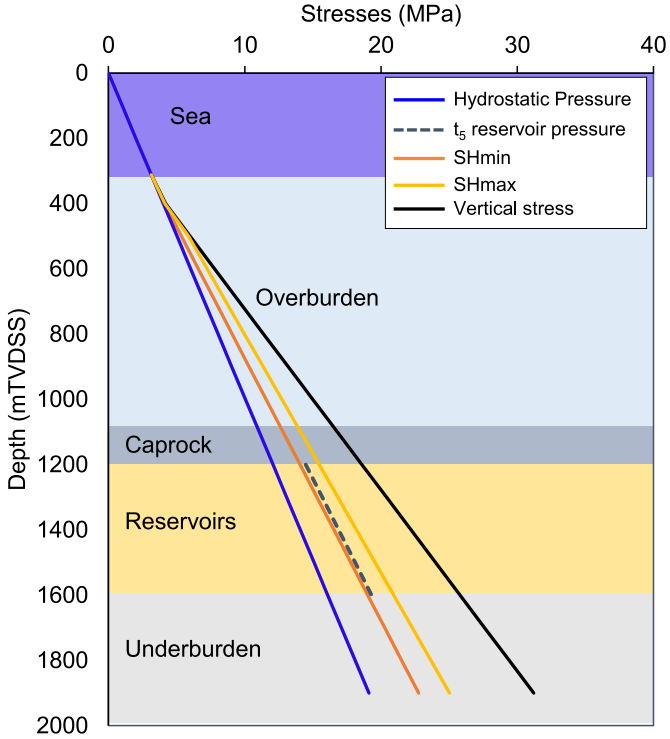

Fig. 8. The pore pressure and in-situ stresses in Alpha well (32/4-1) location assuming a normal faulting regime (modified after Rahman et al., 2021). The reservoir pressure increase after 50 years of injection (t_5) is also illustrated for reference.

4.5. Simulator

In this study, the VISAGE finite element mechanical simulator has been used to conduct one-way coupling (Ouellet et al., 2011). The static model preparation and simulation cases are defined in the Petrel-2019 platform. When the model cases are ready, a VISAGE plug-in is used to iterate the defined models. As we used plug-in, the model results are directly available in the Petrel platform to analyze.

5. Results

The one-way coupling simulation is conducted using 5 different reservoir pressure scenarios illustrated in Fig. 9. The t_0 time represents the initial hydrostatic reservoir pressure which increases with time due to CO_2 injection in every 10-years time step. It is worth mentioning that the pressure increment is only applied within the Vette- Øygarden fault block (Fig. 9). Each pressure grid is assigned a time step mentioned in Fig. 5. As expected, the pressure increases from initial (t_0) to t_1 is significant. After that, the increment is more gentle but has slight lateral variation.

5.1. Ground deformation (seafloor)

The estimation of vertical displacement of the seafloor is crucial to assess the suitability of the CO_2 injection sites. The top view of seafloor deformation due to CO_2 injection in various time steps in M-1 is illustrated in Fig. 10. The grid located west of the Vette fault is excluded because no pressure difference is addressed in this section, hence no deformations. The seafloor experienced a gradual uplift with time; however, spatial variation is also observed. Although the trend of lateral dissimilarity for each step shows similarity, it does not follow the pressure increase trends. Moreover, the maximum uplift estimated in M-1 is 7 cm, located in the middle and southern part of the model.

5.2. Vertical displacement on the reservoir-caprock interface

The base layer of the caprock is also assessed to evaluate the deformation in the reservoir-caprock interface (Fig. 11). The grids west of the Vette fault are also excluded from the map-viewed results. Overall, the caprock is uplifted due to CO_2 injection-related reservoir pressure change. The rock deformation gradually increases with time and reaches maximum uplift of 8 cm (at time t_5). However, the increment of rock deformation followed a patchy trend nucleus at the middle-west part of the VF and continued eastward. Moreover, the deformation is observed minimal in both well locations.

5.3. Comparative analysis

One of the main objective of this research is to evaluate the sensitivity of the overburden rock properties. In this section, we assessed that by comparing the models. In addition, the rock deformation difference between seafloor and base caprock is also evaluated.

5.3.1. M-1 versus M-3

The main difference between M-1 and M-3 models is the value of overburden properties and the distribution within grids. In M-1 seismic driven properties are spatially distributed while M-3 represents average constant properties for the whole overburden section. These variations not only significantly influence the seafloor deformations but also affect caprocks. The rock layer's upliftment doubled while using the average constant value compared with actual spatially distributed seismic driven properties. The maximum seafloor upliftment estimated is 7 cm in M-1, while M-3 assessed 14 cm (Fig. 12). A similar trend is also observed in caprock deformation scenarios (i.e., 8 cm and 15 cm in M-1 and M-3, respectively). However, both models (M-1 & M-3) show smooth deformation in seafloor and a patchy upliftment in the base caprock layer. Moreover, base caprock deformed slightly higher compared to the

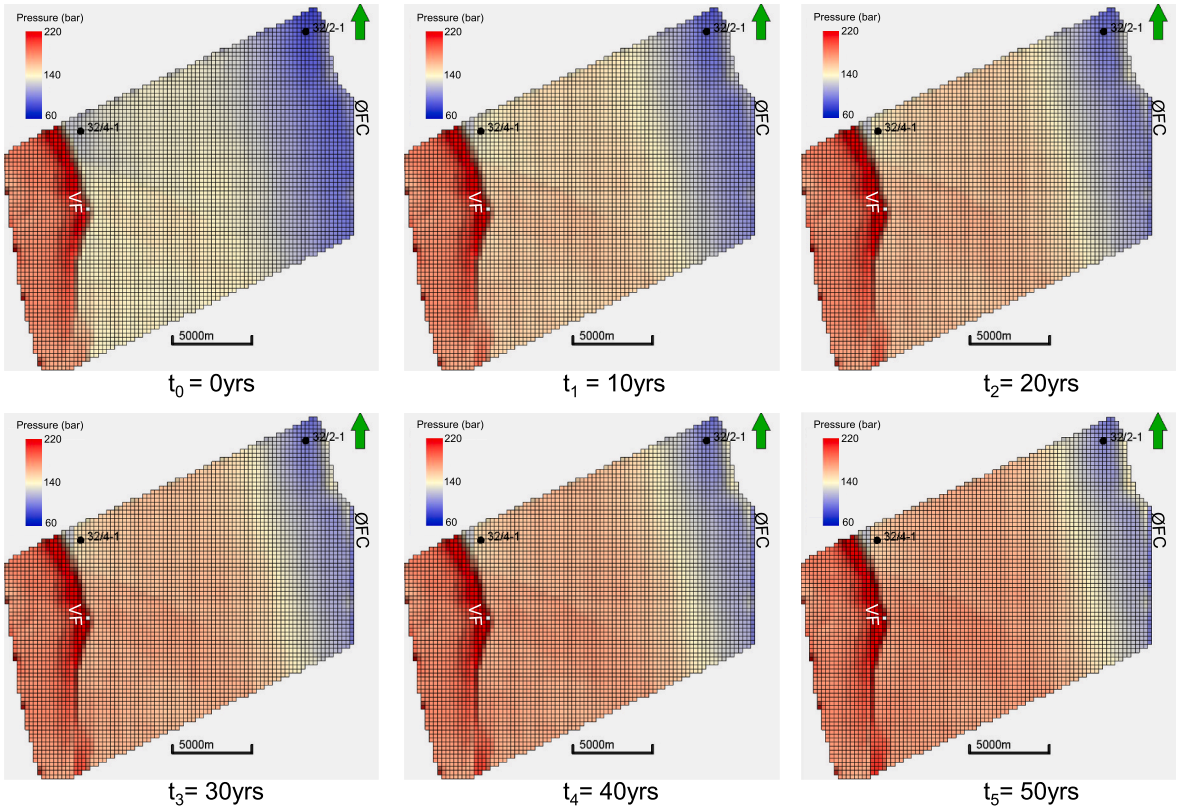

Fig. 9. The top reservoir layer shows the reservoir pressure changes in different time steps. Reservoir pressure increase confined between Øygarden Fault Complex (ØFC) and Vette Fault (VF). Note that there are no pressure changes west of VF.

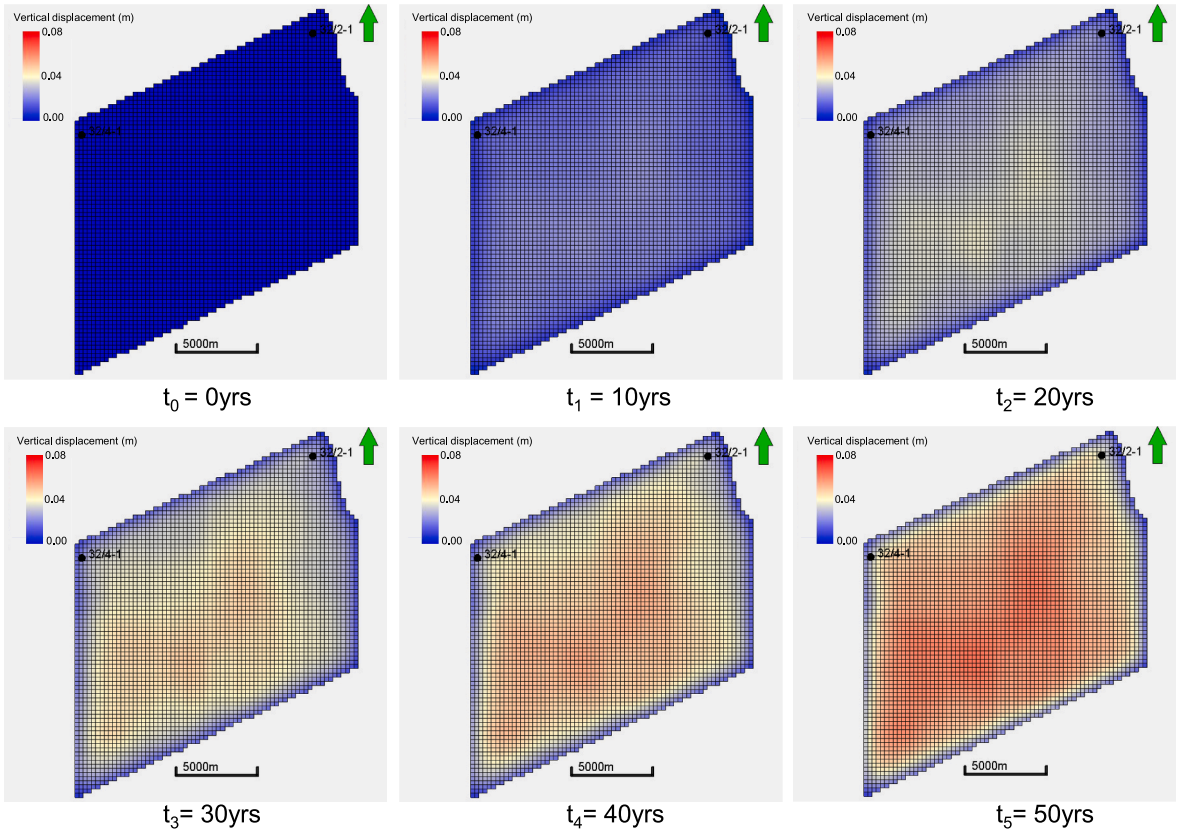

Fig. 10. Vertical displacement in various time steps is estimated in M-1. Seafloor gradually uplifted due to CO_2 injection-related reservoir pressure increase.

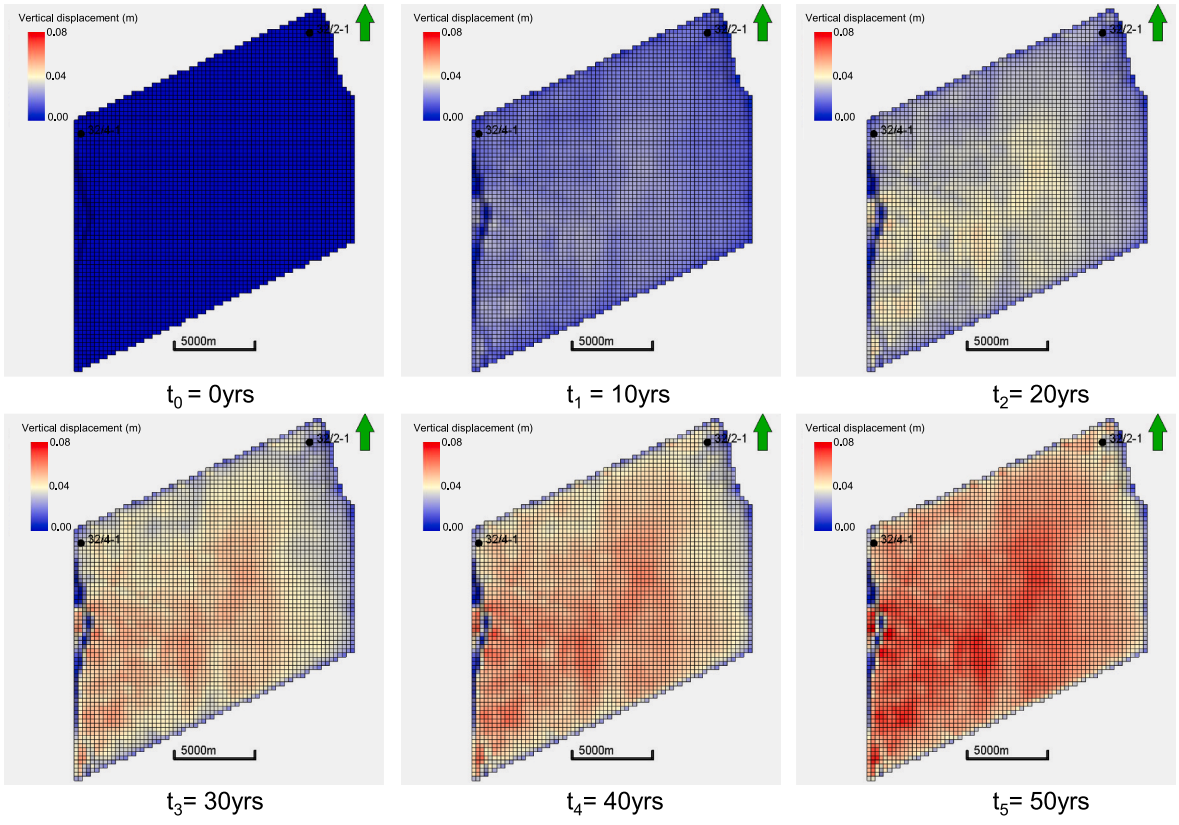

Fig. 11. Estimated vertical displacement of the base layer of caprock in various time steps in M-1. Significant upliftment (~8 cm) is observed just above the reservoir zone.

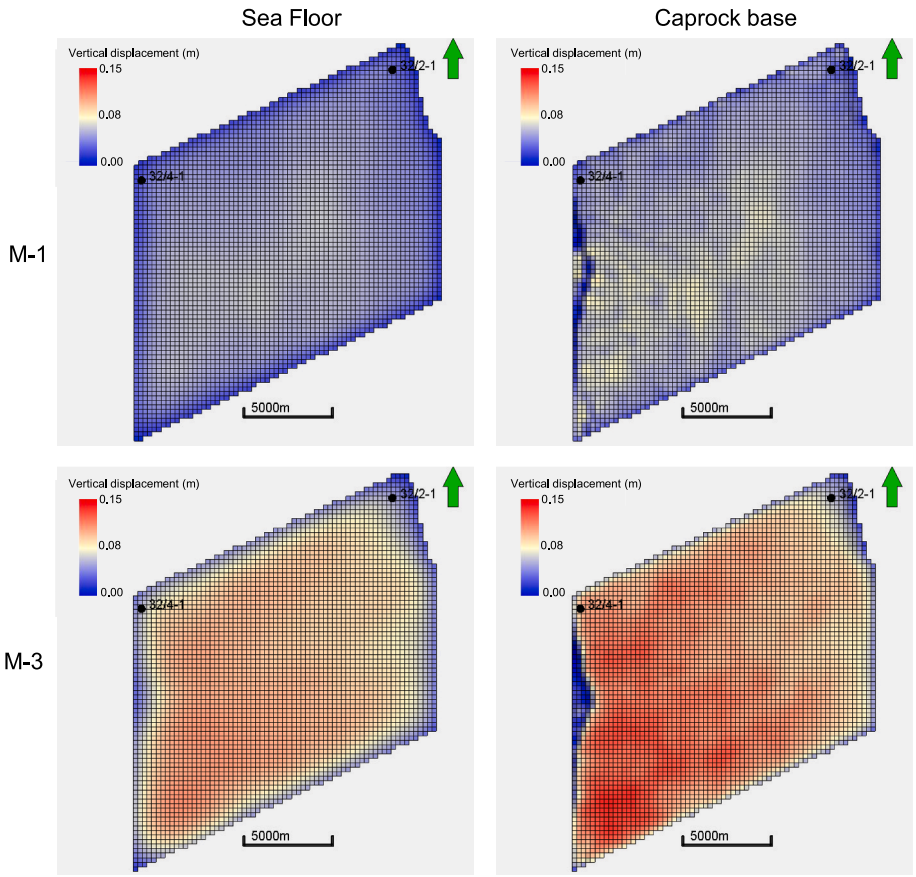

Fig. 12. Vertical displacement of the seafloor and base caprock layers at t_5 time step shows the comparison between M-1 and M-3.

seafloor upliftment.

Similar spatial differences are also observed in the 3-dimensional cross-section of the model M-1 and M-3 (Fig. 13). The cross-section plane shown is in the middle of the model, where the wells (i.e., 32/4-1 and 31/2-1) are displayed for reference. The overburden structural variations are clearly visible, where M-1 followed the actual structural setup (3D seismic interpreted), and in M-3 overburden section is divided into three horizontal layers. The average overburden property model (M-3) significantly changes the vertical upliftment within caprock and overburden sections and influences the upper part of the reservoir (Fig. 13b).

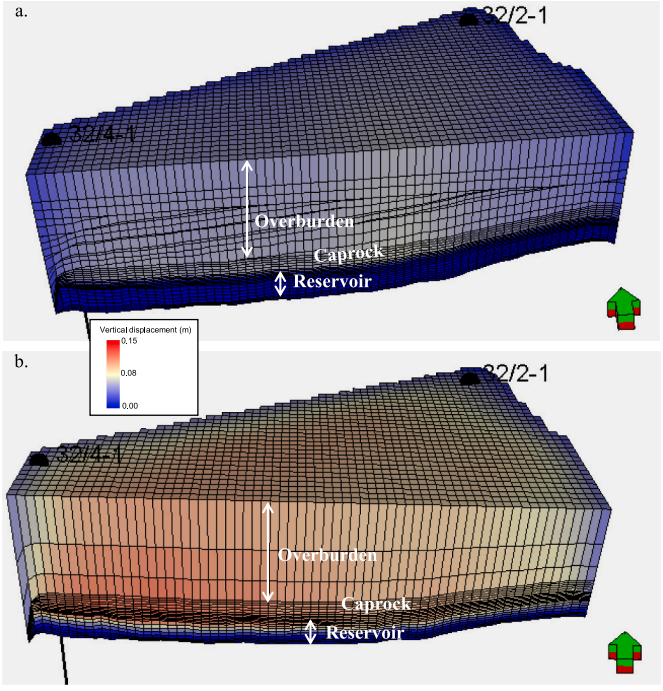

Fig. 13. The difference of vertical displacement between M-1 (a) and M-3 (b) are illustrated three-dimensionally. M-3 model shows significantly higher upliftment compared to M-1.

The differences between M-1 and M-3 are also observed in Mohr-Coulomb failure envelopes. The failure diagrams illustrated in Fig. 14 are located in the middle of the studied grid (i:j; 50:53) where overburden (Fig. 14a&b), caprock (Fig. 14c&d), and reservoir rocks (Fig. 14e and f) are compared. All the stress circles are at the compressive side and below the failure envelope except the M-3 reservoir zone, which indicated that the rock is in shear form with less possibility of matrix deformation. However, in all the scenarios, the chance of shear failure is higher in M-3 compared to M-1. The stress circles are moved to the left due to CO_2 injection within the reservoir. However, in model 3, the t_5 scenario touches the rock compressive strength, which is usually equal to the mean value of maximum principal stress (Ahmed and Al-Jawad, 2020).

5.3.2. *M-2 versus M-3 versus M-4*

Although there is a significant difference observed between M-1 and M-3, the effect of different overburden constant values (Table 2) on 3D model simulation is trivial. The difference between the models in time steps t_1 and t_5 is illustrated in Fig. 15. Due to CO2 injection, the reservoir pressure increases, resulting in a seafloor heave, but that is insignificant. Moreover, the surface deformation trends in all models are similar.

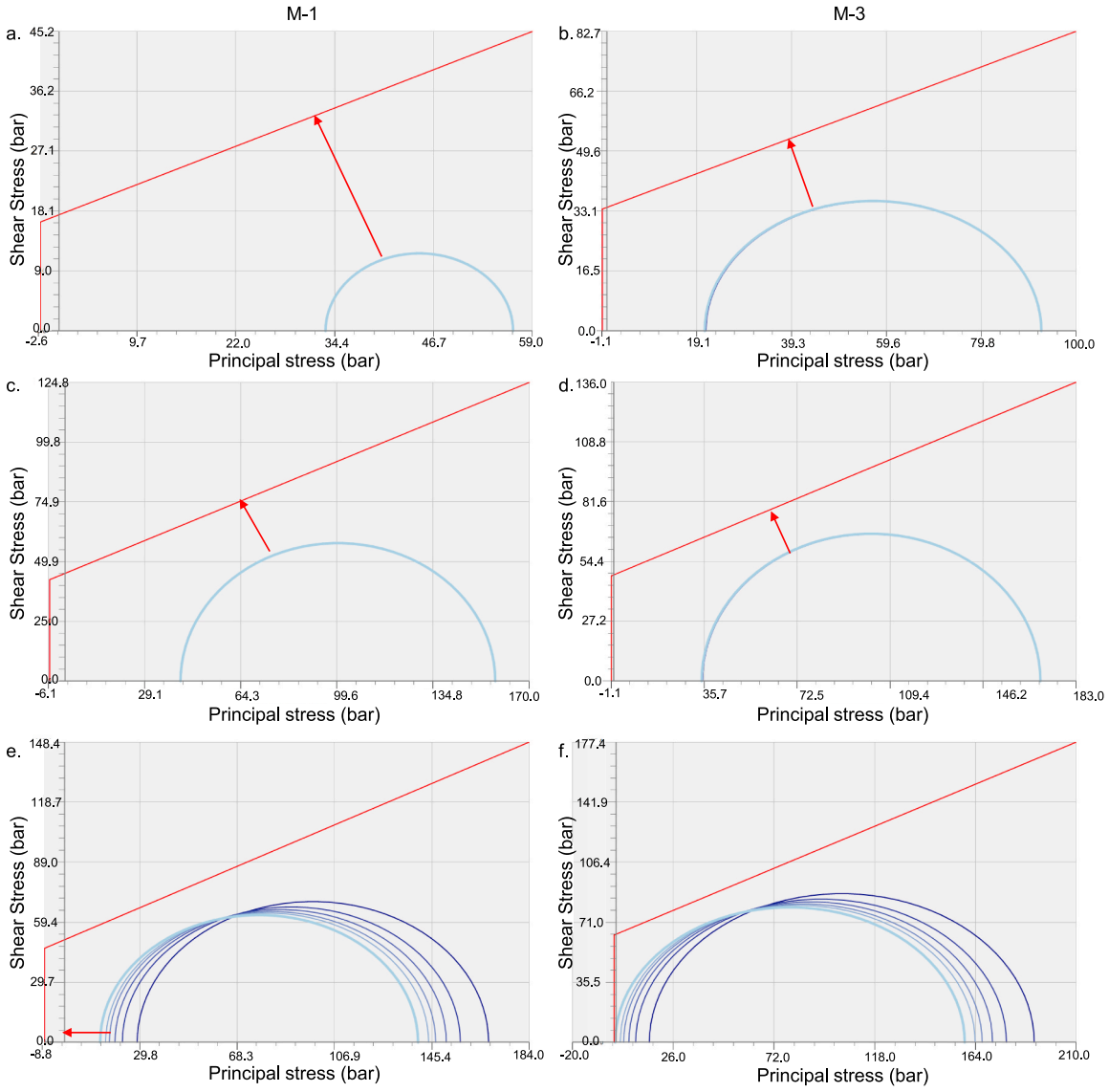

Fig. 14. Mohr-Coulomb diagram of location in the middle of the model (I,j; 50, 53) shows the comparison between the model M-1 and M-3 within overburden (a, b), caprock (c, d), and reservoir (e, f) zones. M-3 represents significantly higher chances of failure compared to M-1. Also, note that both horizontal and vertical scales have differences.

6. Discussion

The geomechanical modeling approach applied in this study shows the practicality. Although the spatially variable overburden properties gridded model (M-1) has a higher number of active cells, the computational time required is not abnormally high (qualitatively, the model required 4 times higher time than the constant properties models). This research also reveals that the seismic inverted properties can be improved to the traditional modeling approach where well data properties are interpolated using different algorithms. Moreover, where the well database is limited, the range of uncertainties are significantly high in 3D space. In this scenario, a seismic-driven approach could be a solution introduced in this study. However, for seismic driven properties modeling workflow explained in this research is dependent on the availability of 3D seismic cube. Moreover, 3D field-scale geomechanical modeling is critical to evaluate injection-related induced mechanical risks in any injection site. Furthermore, this approach allows us to incorporate the complex structural setup.

The fluid simulated reservoir pressure used in this study has a total pore volume model. The base case Gassnova (2012) model included the whole Vette-Øygarden fault block, while the model used in this study covers one-fourth of surface area compared with the Gassnova model. However, the injected reservoir rocks layers are the same; hence, assumed to have similar reservoir quality (i.e., Poro-perm). Although the model area is significantly small in this study, there is no effect on this study's main purpose (i.e., overburden sensitivity). This also indicates the urgency of having a coupled fluid flow – mechanical modeling approach, where we have full control and the ability to evaluate the stress-dependent poro-perm changes.

6.1. *Effect of overburden properties on rock deformation*

Constant overburden model properties might introduce misinterpretation in rock deformation, which leads to poor decisions during site specification. Different overburden rock units have a significant variation in mechanical properties (Fig. 7). A significant difference in vertical rock deformation is also observed (Figs. 12–14). The stress differences between the overburden formations in M-1 have also illustrated the effect of initial mechanical rock properties. Fig. 16 represents the variation of the Mohr-Coulomb failure envelope between different layers

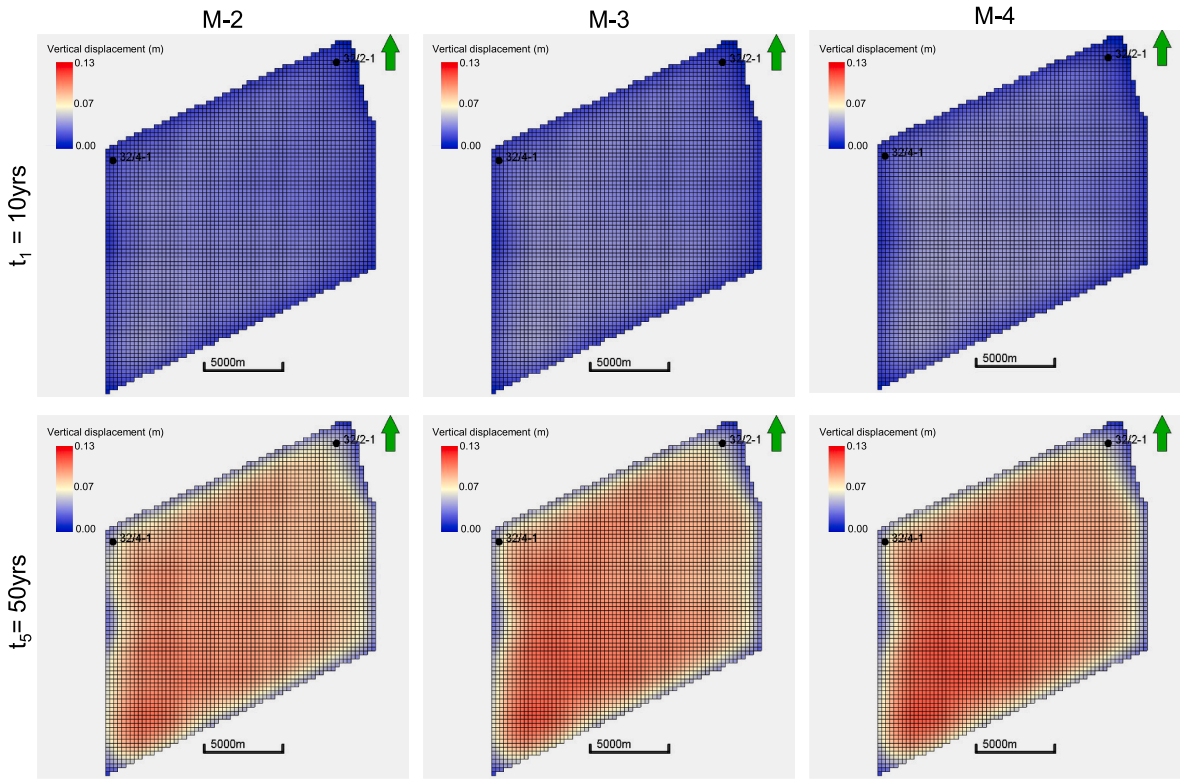

Fig. 15. Seafloor heave in t_1 and t_5 time steps shows the comparison between minimum, average, and maximum constant overburden properties.

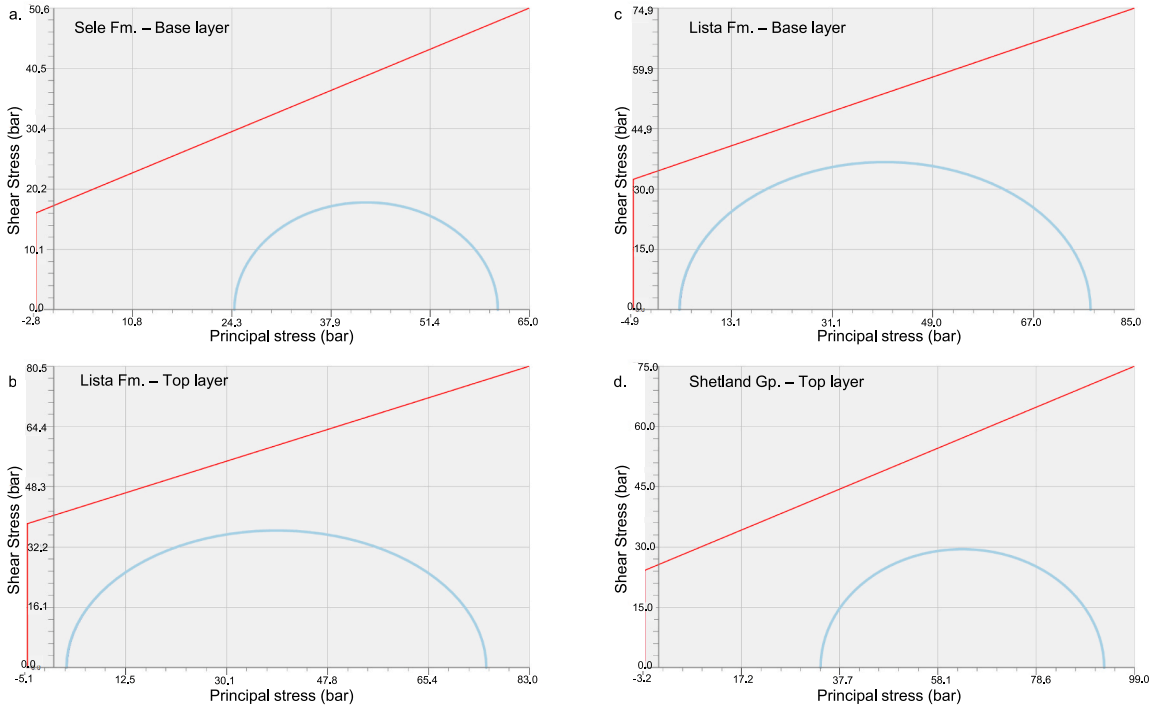

Fig. 16. The variation of failure mode within overburden rocks in M-1 illustrated the Mohr-Coulomb plot of the base layer of Sele Formation (a), the top layer of Lista Formation. (b), base Lista Formation. (c) and top Shetland Group. (d). Please note that both horizontal and vertical scales have differences.

while horizontal location (i & j) remains the same (50 & 53). The Lista Formation shows significantly higher failure possibility (both shear and tensile) compared to the above Sele Formation and below Shetland Group layers. This indicates the importance of using the right overburden properties in geomechanical modeling work. Simplication of model properties might be an over-or underestimation of the rock failure, which leads to a significant issue during real injection scenarios.

6.2. Implication in CCS

The rock deformation due to reservoir pressure change is critical in the subsurface CO_2 storage project. The quantitative assessment of vertical displacement of rocks reveals the failure potential of the cap and overburden rock which determined the seal effectiveness in any injection site. In addition, the mechanical failure threshold of caprock and overburden makes the site non-reliable because of caprock and fault failure. Therefore, vertical rock displacement plays a vital role in decision-making for any injection site evaluation.

The significant influence of caprock properties on rock displacement becomes crucial because the traditional way of including simplified overburden properties in the geomechanical model might lead to inaccurate estimation of the potential of storage and injectivity of any site. The estimate of optimal capacity and injectivity before any failure of any CO_2 injection site is crucial because it defines the safe storage potential of that site. However, to evaluate the total safe storage reservoir capacity, a fluid simulation model needs to couple with the geomechanical model called a two-way coupling model. This study, however, assessed only the stress-strain geomechanical deformations in a specific injection rate and injection time. Although this study cannot estimate the total safe storage capacity and injectivity based on the analysis, the comparative investigation suggested a significant overestimation of potential geomechanical risks might be estimated based on the traditional simple overburden properties model. In this way, we might lose half of our safe storage capacity, which might influence the project decision considerably.

Moreover, this approximate estimation might influence the management to declare the injection site non-economical. Additionally, seafloor installation (i.e., wellhead) might be at risk due to overestimation of seafloor heave, resulting in a possible instability risk that might influence the site-specific decision-making. Although we did not perform the maximum displacement analysis, our rock can hold before failure in this study, 100% increase in seafloor upliftment in M-3 indicated the importance of adding spatially distributed overburden properties in the geomechanical modeling (M-1) approach. However, despite the importance of overburden uncertainties in decision-making, the attempt to quantify overburden uncertainties in decision-making has been discounted in CCS management, especially for geomechanics consideration.

7. Conclusions

The seismic data-driven 3D field-scale geomechanical model workflow shows the value while evaluating the mechanical risks in any CO_2 injection sites. This study proved the efficiency and practicality of such a model. The key findings are as follows:

- The effect of overburden properties on rock deformation is significant. For instance, the simplified average constant overburden properties doubled the seafloor uplift compared to the model using the seismic inverted spatially variable properties. Moreover, the Mohr-Coulomb failure envelopes of overburden rocks indicated the importance of spatial overburden properties within the geomechanical modeling workflow.
- Vertical rock deformation increases with time in both seafloor and interface between the reservoir and caprock. However, the vertical uplift is slightly higher in the reservoir-caprock interface compared to the seafloor.
- Although the induced pressure increase in each time steps used a constant change, the rock deformation spatially varied due to the variation in mechanical properties.
- The simplified assumption of overburden properties in the geomechanical model effect the CO_2 storage project significantly by influencing the capacity and injectivity of any site.

The field-scale 3D geomechanical model workflow proposed in this study is effective and time-efficient to simulate the one-way coupling. However, a two-way coupling with reservoir simulation will reveal the pore volume changes within the reservoir. Therefore, two-way partial or fully coupling methods will be the future study.

Credit author statement

Md Jamilur Rahman: Conceptualization, Methodology, Formal analysis, Investigation, Writing – original draft, Writing – review & editing, Visualization, Software. Manzar Fawad: Writing – review & editing, Supervision. Jung Chan Choi: Writing – review & editing, Supervision. Nazmul Haque Mondol: Writing – review & editing, Supervision, Project administration, Funding acquisition

Declaration of competing interest

The authors declare that they have no known competing financial interests or personal relationships that could have appeared to influence the work reported in this paper.

Acknowledgments

We are grateful for the financial support provided by the Research Council of Norway for the OASIS (Overburden Analysis and Seal Integrity Study for CO_2 Sequestration in the North Sea) project (NFR-CLIMIT project #280472). We are indebted to the additional funding and data provided by Norwegian Petroleum Directorate (NPD), Gassnova, Equinor, and TotalEnergies. Thank you very much for the academic software licenses provided by Schlumberger for Petrel-2019 and the VISAGE simulator.

References

Addis, M.A., 1997. The stress-depletion response of reservoirs. In: SPE Annual Technical Conference and Exhibition. Society of Petroleum Engineers.

Ahmed, B.I., Al-Jawad, M.S., 2020. Geomechanical modelling and two-way coupling simulation for carbonate gas reservoir. J. Pet. Explor. Prod. Technol. 10, 3619–3648.

Chiaramonte, L., White, J.A., Trainor-Guitton, W., 2015. Probabilistic geomechanical analysis of compartmentalization at the Snøhvit CO2 sequestration project. J. Geophys. Res. Solid Earth 120, 1195–1209.

Clausen, J.A., Gabrielsen, R.H., Reksnes, P.A., Nysaether, E., 1999. Development of intraformational (Oligocene-Miocene) faults in the northern North Sea: influence of remote stresses and doming of Fennoscandia. J. Struct. Geol. 21, 1457–1475. https://nam11.safelinks.protection.outlook.com/?url=https%3A%2F%2Fdoi.org%2F10.1016%2FS0191-8141&data=04%7C01%7Cs.venkiteswaran%40elsevier.com%7Cdf73c34b4fd046b2a0c708d9ed509086%7C9274ee3f94254109a27f9fb15c10675d%7C0%7C0%7C637801753841890024%7CUnknown%7CTWFpbGZsb3d8eyJWIjoiMC4wLjAwMDAiLCJQIjoiV2luMzIiLCJBTiI6Ik1haWwiLCJXVCI6Mn0%3D%7C1000&sdata=oagJ1Lmjhs%2FERdAowDUZ2aFm9BaSWMdUXucem6NBI6c%3D&reserved=0(99)00083-8.

Dreyer, T., Whitaker, M., Dexter, J., Flesche, H., Larsen, E., 2005. From spit system to tide-dominated delta: integrated reservoir model of the Upper Jurassic Sognefjord Formation on the Troll West Field. In: Geological Society, London, Petroleum Geology Conference Series. Geological Society of London, pp. 423–448.

Duffy, O.B., Bell, R.E., Jackson, C.A.-L., Gawthorpe, R.L., Whipp, P.S., 2015. Fault growth and interactions in a multiphase rift fault network: Horda Platform, Norwegian North Sea. J. Struct. Geol. 80, 99–119.

Faleide, J.I., Bjørlykke, K., Gabrielsen, R.H., 2015. Geology of the Norwegian continental Shelf. In: Petroleum Geosciences: from Sedimentary Environments to Rock Physics, pp. 603–637.

Fatti, J.L., Smith, G.C., Vail, P.J., Strauss, P.J., Levitt, P.R., 1994. Detection of gas in sandstone reservoirs using AVO analysis: a 3-D seismic case history using the Geostack technique. Geophysics 59, 1362–1376.

Fawad, M., Hansen, J.A., Mondol, N.H., 2020. Seismic-fluid detection-a review. Earth Sci. Rev., 103347

Fawad, M., Rahman, M.J., Mondol, N.H., 2021a. Seismic reservoir characterization of potential CO2 storage reservoir sandstones in Smeaheia area, Northern North Sea. J. Petrol. Sci. Eng. 205, 108812.

Fawad, M., Rahman, M.J., Mondol, N.H., 2021b. Seismic-derived geomechanical properties of potential CO2 storage reservoir and cap rock in Smeaheia area, northern North Sea. Lead. Edge 40, 254–260.

Fischer, K., Henk, A., 2013. A workflow for building and calibrating 3-D geomechanical models &ndash a case study for a gas reservoir in the North German Basin. Solid Earth 4, 347–355.

Fokker, P.A., Orlic, B., Van der Meer, L.G.H., Geel, C.R., 2011. Geomechanical modeling of surface uplift around well KB-502 at the in Salah CO2 storage site. In: 73rd EAGE Conference and Exhibition Incorporating SPE EUROPEC 2011. European Association of Geoscientists & Engineers p. cp-238.

Gassnova, 2012. Troll Kystnær Subsurface Status Report.

Grasso, J.-R., 1992. Mechanics of seismic instabilities induced by the recovery of hydrocarbons. Pure Appl. Geophys. 139, 507–534.

Grollimund, B., Zoback, M.D., 2003. Impact of glacially induced stress changes on fault-seal integrity offshore Norway. Am. Assoc. Petrol. Geol. Bull. 87, 493–506.

Grollimund, B., Zoback, M.D., Wiprut, D.J., Arnesen, L., 2001. Stress orientation, pore pressure and least principal stress in the Norwegian sector of the North Sea. Petrol. Geosci. 7, 173–180.

Hampson, D.P., Russell, B.H., Bankhead, B., 2005. Simultaneous inversion of pre-stack seismic data. In: SEG Technical Program Expanded Abstracts 2005. Society of Exploration Geophysicists, pp. 1633–1637.

Hawkes, C.D., McLellan, P.J., Bachu, S., 2005. Geomechanical factors affecting geological storage of CO2 in depleted oil and gas reservoirs. J. Can. Pet. Technol. 44.

Heidbach, O., Rajabi, M., Cui, X., Fuchs, K., Müller, B., Reinecker, J., Reiter, K., Tingay, M., Wenzel, F., Xie, F., 2018. The World Stress Map database release 2016: crustal stress pattern across scales. Tectonophysics 744, 484–498.

Herwanger, J., Koutsabeloulis, N., 2011. Seismic Geomechanics. How to Build Calibrate Geomech. Model. Using 3D 4D Seism. Data EAGE Publ.

Hillis, R.R., 2001. Coupled changes in pore pressure and stress in oil fields and sedimentary basins. Petrol. Geosci. 7, 419–425.

Holgate, N.E., Jackson, C.A.L., Hampson, G.J., Dreyer, T., 2015. Seismic stratigraphic analysis of the middle jurassic Krossfjord and Fensfjord formations, Troll oil and gas field, northern North Sea. Mar. Petrol. Geol. 68, 352–380.

Horsrud, P., 2001. Estimating mechanical properties of shale from empirical correlations. SPE Drill. Complet. 16, 68–73.

Ingram, G.M., Urai, J.L., Naylor, M.A., 1997. Sealing processes and top seal assessment. In: Norwegian Petroleum Society Special Publications. Elsevier, pp. 165–174.

Mandal, P.P., Essa, I., Saha, S., Rezaee, R., 2021. Multi-purpose Utility of Constructing 3D Static Geomechanical Model in the Ichthys Field, Browse Basin. 3rd AEGC Geosci. Sustain. World.

Mulrooney, M.J., Osmond, J.L., Skurtveit, E., Faleide, J.I., Braathen, A., 2020. Structural analysis of the Smeaheia fault block, a potential CO2 storage site, northern Horda Platform, North Sea. Mar. Pet. Geol. 121, 104598. https://nam11.safelinks.protection.outlook.com/?url=https%3A%2F%2Fdoi.org%2F10.1016%2Fj.marpetgeo.2020.104598&data=04%7C01%7Cs.venkiteswaran%40elsevier.com%7Cdf73c34b4fd046b2a0c708d9ed509086%7C9274ee3f94254109a27f9fb15c10675d%7C0%7C0%7C637801753841890024%7CUnknown%7CTWFpbGZsb3d8eyJWIjoiMC4wLjAwMDAiLCJQIjoiV2luMzIiLCJBTiI6Ik1haWwiLCJXVCI6Mn0%3D%7C1000&sdata=29BBiTDlAheqJEq%2BQtAKR%2BfSxe8OdpCcRlaVi%2Fefar0%3D&reserved=0.

Newell, P., Yoon, H., Martinez, M.J., Bishop, J.E., Bryant, S.L., 2017. Investigation of the influence of geomechanical and hydrogeological properties on surface uplift at in Salah. J. Petrol. Sci. Eng. 155, 34–45.

Northern Lights https://northernlightsccs.com/what-we-do/.

NPD, 2021. NPD FactPages [WWW Document]. URL. https://npdfactpages.npd.no/factpages/Default.aspx?culture=en.

NPD CO2 Atlas, 2014. Report.

Olden, P., Jin, M., Pickup, G., Mackay, E., Hamilton, S., Somerville, J., Todd, A., 2014. Geomechanical modelling of CO2 geological storage with the use of site specific rock mechanics laboratory data. Petrol. Geosci. 20, 323–337.

Ouellet, A., Bérard, T., Desroches, J., Frykman, P., Welsh, P., Minton, J., Pamukcu, Y., Hurter, S., Schmidt-Hattenberger, C., 2011. Reservoir geomechanics for assessing containment in CO2 storage: a case study at Ketzin, Germany. Energy Proc. 4, 3298–3305.

Park, J.-W., Guglielmi, Y., Graupner, B., Rutqvist, J., Kim, T., Park, E.-S., Lee, C., 2020. Modeling of fluid injection-induced fault reactivation using coupled fluid flow and mechanical interface model. Int. J. Rock Mech. Min. Sci. 132, 104373.

Rahman, M.J., Choi, J.C., Fawad, M., Mondol, N.H., 2021. Probabilistic analysis of Vette fault stability in potential CO2 storage site Smeaheia, offshore Norway. Int. J. Greenh. Gas Control 108, 103315. https://doi.org/10.1016/j.ijggc.2021.103315.

Rahman, M.J., Fawad, M., Mondol, N.H., 2020. Organic-rich shale caprock properties of potential CO2 storage sites in the northern North Sea, offshore Norway. Mar. Petrol. Geol. 122, 104665.

Rutqvist, J., Birkholzer, J., Cappa, F., Tsang, C.-F., 2007. Estimating maximum sustainable injection pressure during geological sequestration of CO2 using coupled fluid flow and geomechanical fault-slip analysis. Energy Convers. Manag. 48, 1798–1807.

Rutqvist, J., Birkholzer, J.T., Tsang, C.-F., 2008. Coupled reservoir–geomechanical analysis of the potential for tensile and shear failure associated with CO2 injection in multilayered reservoir–caprock systems. Int. J. Rock Mech. Min. Sci. 45, 132–143.

Segall, P., 1989. Earthquakes triggered by fluid extraction. Geology 17, 942–946.

Sengupta, M., Dai, J., Volterrani, S., Dutta, N., Rao, N.S., Al-Qadeeri, B., Kidambi, V.K., 2011. Building a seismic-driven 3D geomechanical model in a deep carbonate reservoir. In: SEG Technical Program Expanded Abstracts 2011. Society of Exploration Geophysicists, pp. 2069–2073.

Skurtveit, E., Choi, J.C., Osmond, J., Mulrooney, M., Braathen, A., 2018. 3D fault integrity screening for smeaheia CO2 injection site. In: 14th Greenhouse Gas Control Technologies Conference Melbourne, pp. 21–26.

Soltanzadeh, H., Hawkes, C.D., 2008. Semi-analytical models for stress change and fault reactivation induced by reservoir production and injection. J. Petrol. Sci. Eng. 60, 71–85.

Stewart, D.J., Schwander, M., Bolle, L., 1995. Jurassic depositional systems of the Horda Platform, Norwegian North Sea: practical consequences of applying sequence stratigraphic models. Nor. Pet. Soc. Spec. Publ. 291–323.

Streit, J.E., Hillis, R.R., 2004. Estimating fault stability and sustainable fluid pressures for underground storage of CO2 in porous rock. Energy 29, 1445–1456.

Tenthorey, E., Vidal-Gilbert, S., Backe, G., Puspitasari, R., Pallikathekathil, Z.J., Maney, B., Dewhurst, D., 2013. Modelling the geomechanics of gas storage: a case study from the Iona gas field, Australia. Int. J. Greenh. Gas Control 13, 138–148.

Verdon, J.P., Kendall, J.M., Stork, A.L., Chadwick, R.A., White, D.J., Bissell, R.C., 2013. Comparison of geomechanical deformation induced by megatonne-scale CO2 storage at Sleipner,Weyburn, and in Salah. Proc. Natl. Acad. Sci. 110, E2762–E2771.

Vidal-Gilbert, S., Tenthorey, E., Dewhurst, D., Ennis-King, J., Van Ruth, P., Hillis, R., 2010. Geomechanical analysis of the Naylor field, Otway basin, Australia: Implications for CO2 injection and storage. Int. J. Greenh. Gas Control 4, 827–839.

Watts, N.L., 1987. Theoretical aspects of cap-rock and fault seals for single-and two-phase hydrocarbon columns. Mar. Petrol. Geol. 4, 274–307.

Whipp, P.S., Jackson, C.L., Gawthorpe, R.L., Dreyer, T., Quinn, D., 2014. Normal fault array evolution above a reactivated rift fabric; a subsurface example from the northern Horda Platform, Norwegian North Sea. Basin Res. 26, 523–549.

Paper-4

3D field-scale geomechanical modeling of potential CO_2 storage site Smeaheia, offshore Norway

Md Jamilur Rahman
Manzar Fawad
Nazmul Haque Mondol

energies, 2022

energies

MDPI

Article

3D Field-Scale Geomechanical Modeling of Potential CO_2 Storage Site Smeaheia, Offshore Norway

Md Jamilur Rahman [1,*], Manzar Fawad [1] and Nazmul Haque Mondol [1,2]

[1] Department of Geosciences, University of Oslo (UiO), 0371 Oslo, Norway; manzar.fawad@geo.uio.no (M.F.); m.n.h.mondol@geo.uio.no (N.H.M.)
[2] Norwegian Geotechnical Institute (NGI), 0806 Oslo, Norway
* Correspondence: m.j.rahman@geo.uio.no; Tel.: +47-41383196

Abstract: Injection-induced rock mechanical failure risks are critical in CO_2 sequestration, and thus there is a need to evaluate these occurrences to ensure safe and reliable subsurface storage. A stress–strain-based numerical simulation can reveal the potential mechanical risks of any CO_2 sites. This study investigated the hydromechanical effect on geomechanical failure due to injection-induced stress and pore pressure changes in the prospective CO_2 storage site Smeaheia, offshore Norway. An inverted-seismic-property-driven 3D field-scale geomechanical model was carried out in the Smeaheia area to evaluate the rock failure and deformation risks in various pressure-build-up scenarios. A one-way coupling between the before- and after-injection pressure scenarios of nine different models has been iterated using the finite element method. The effect of the sensitivity of total pore volume and pore compressibility on rock mechanical deformation is also evaluated. Although various models illustrated comparative variability on failure potential, no model predicted caprock failure or fracture based on the Mohr–Coulomb failure envelope. Moreover, the lateral mechanical failure variation among different locations indicated the possibility to identify a safer injection point with less chances of leakage. In addition, the pore volume and pore compressibility significantly influence the mechanical behavior of the reservoir and caprock rocks. Although this analysis could predict better injection locations based on geomechanical behavior, a fluid simulation model needs to be simulated for assessing lateral and vertical plume migration before making an injection decision.

Keywords: Smeaheia; 3D geomechanical model; caprock; finite element method; tensile failure

Citation: Rahman, M.J.; Fawad, M.; Mondol, N.H. 3D Field-Scale Geomechanical Modeling of Potential CO_2 Storage Site Smeaheia, Offshore Norway. *Energies* **2022**, *15*, 1407. https://doi.org/10.3390/en15041407

Academic Editors: Pierre Rolf Cerasi and Nikolaos Koukouzas

Received: 10 January 2022
Accepted: 14 February 2022
Published: 15 February 2022

1. Introduction

The subsurface state of stress defines the reliability of a field or basin and depends on the structure of the subsurface (geometry of layers, fault location, orientation, etc.), the spatial distribution of rock properties (strength and elastic properties), and the far-field stresses (pore pressure and tectonic stresses) [1]. A geomechanical model is a numerical representation of the state of stress and rock mechanical properties where all the components are included and assessed dynamically. As the geological sequestration of anthropogenic CO_2 changes the subsurface state of stress by injecting CO_2 into the saline aquifers or depleted reservoirs, a field-scale geomechanical assessment is crucial for safe, reliable, and permanent subsurface CO_2 storage. Changes in the state of stress might influence the rocks' (i.e., reservoir, cap, and overburden) mechanical behavior. There might be several potential geomechanical consequences such as top-seal and overburden flexure, reactivation of existing faults, pressure-induced share failure or fracture, formation of new faults, changes in porosity/permeability within the reservoir, etc. [2–8]. Therefore, a thorough geomechanical assessment is critical to evaluate CO_2 storage sites.

The studied injection site, the Smeaheia area in the Horda Platform (HP), northern North Sea, is one of the potential subsurface CO_2 storage sites. It is bounded by two regional N-S trending faults: the Vette fault in the west and the Øygarden fault complex

in the east (Figure 1a). Two structural closures named Alpha (32/4-1) and Beta (32/2-1) are located in the Smeaheia area, where both structures are three-way closures against the Vette and Øygarden faults, respectively. The area is positioned east of the giant Troll east gas field and has the same reservoir–caprock pairs. The main reservoirs consist of Upper to Middle Jurassic Sognefjord, Fensfjord, and Krossfjord formation sandstones with good to moderate reservoir quality [9–11] and were deposited in a shallow coastal marine environment, interfingering with Heather Formation shales (Figure 1b). The primary caprock of the studied area also consists of Upper Jurassic shale formations such as organic-rich Draupne and Heather formation shales. Both formations are deposited in an open marine environment with restricted bottom circulation and often anaerobic conditions [12]. A thick westward-dipping overburden rock package is also present, mainly consisting of fine- to coarse-grained siliciclastic with occasional carbonate-rich deposits [13].

Effective vertical stress-dependent mechanical compaction deformed the rocks by frictional slippage, rotation, sliding, and reorientation of grains [14,15], which can be obtained by subtracting pore pressure from the total vertical stress. The total vertical stress is carried out by the grain framework (solid phase) and the pore pressure (fluid phase). Therefore, the effective vertical stress is only transmitted through the grain contacts and deforms the rock. Injecting CO_2 into the subsurface would increase the reservoir pore pressure, which influences the normal stresses but not the shear stress because fluid is unable to transfer shear properties. Therefore, the effective normal stress is directly related to the total normal stress and pore pressure, which changes the state of stress and, hence, mechanical properties [16]. Although the pore pressure changes are confined within the reservoir due to the tensor characteristic of the stress, the induced stresses can transfer and deform the overburden and underburden rock layers. To predict the injection-related changes in CO_2 storage, a 3D geomechanical model with spatially gridded overburden and underburden layers is essential.

The tectonic stress regime and failure mechanisms also play a vital role during rock deformation. The magnitude and order of the principal stresses vary from basin to basin with a defined stress regime within that specific area. Three different stress regimes, such as extensional (normal faulting), compressional (reverse faulting), and strike-slip (strike-slip or wrench faulting), are considered, which is called Andersonic fault classification ([17,18]; Figure 2). The failure plane varies based on the stress regime condition. Moreover, the pore pressure and stress coupling significantly change in different stress regimes. The Mohr diagram shift due to pore pressure changes is affected substantially by the stress regime (Figure 2).

A hydromechanical (HM) coupling can describe the geomechanical deformation due to stress and pore pressure changes [19,20]. A fluid-saturated porous rock can be deformed by changing the external load (i.e., overburden stress) or the internal pore fluid pressure change (i.e., injection or production). This poromechanics behavior of a fluid-saturated rock can be defined by introducing a numerical simulated geomechanical modeling approach where the mechanical and hydraulic processes affect each other through changing the material properties. However, building a geomechanical model requires the integration of various parameters. For instance, the caprock and overburden section are mostly ignored during the acquisition of relevant databases compared to the reservoir interval and use simple assumptions in the modeling workflow [21–30]. Irrespective of the data limitation, the effectiveness of 3D field-scale geomechanical modeling in rock deformation and failure has been proven and published by several authors for CO_2 injection and gas storage projects worldwide [21,22,24–29]. However, the conventional 1D well property-point-interpolation method and a simple assumption in the missing interval (mainly caprock and overburden sections) have been considered in most of the models. The interpolation method increases the spatial properties' distribution uncertainty significantly if limited wells are present. Moreover, a simple assumption is missing the anisotropic behavior of the properties. Seismic-data-driven models can resolve the spatial anisotropic issue; however, to date, they have only focused on the reservoir and caprock intervals [3,31]. Considering these

issues, Rahman et al. [32] proposed the seismic-inverted-property-driven 3D field-scale geomechanical model workflow, where an integrated approach has been introduced. This study is the continuation of that modeling work, in which the field-scale geomechanical failure risks for the Smeaheia area in offshore Norway have been assessed to evaluate the mechanical behavior of rocks during CO_2 injection into the sandstone reservoirs of Sognefjord, Fensfjord, and Krossfjord formations.

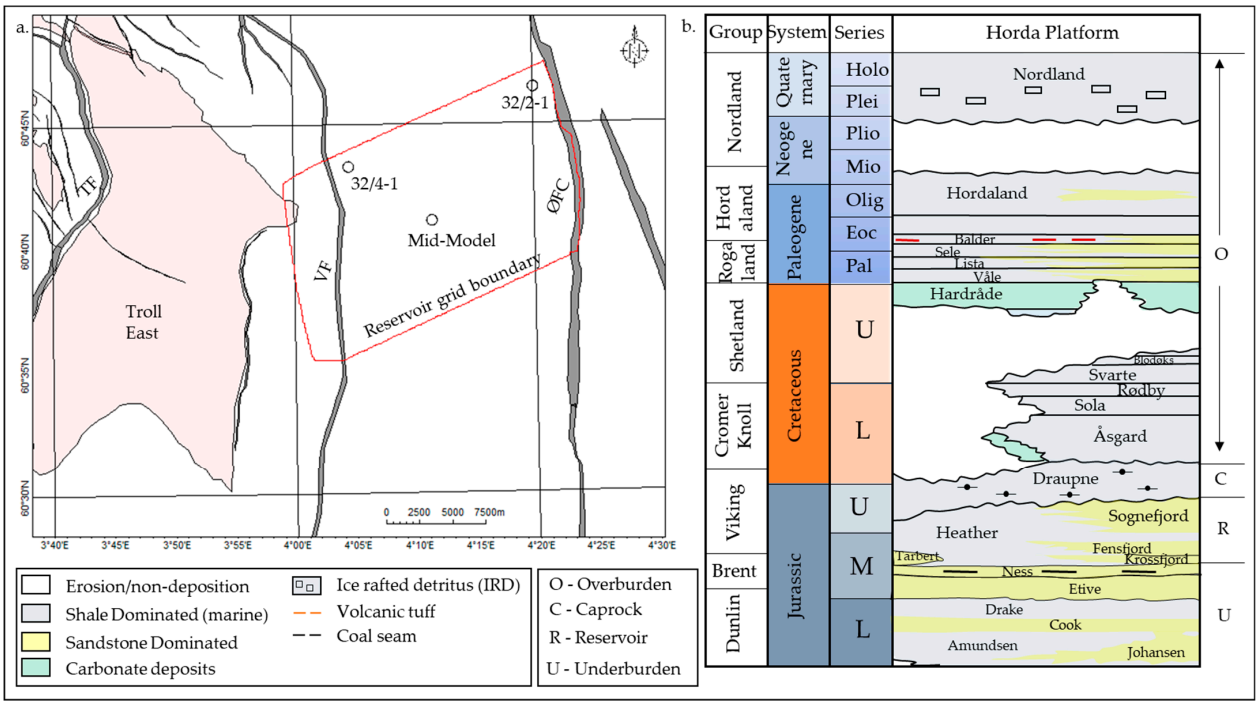

Figure 1. The map of the study area represents the model boundary (red polygon) and the bounding faults (ØFC—Øygarden fault complex; VF—Vette fault) with the studied locations such as 32/4-1, 32/2-1, and Mid-Model (**a**). The area is located east of the Troll east field, which is bounded by VF and TF (Tusse fault). A few minor faults (gray lines) are also illustrated. (**b**) A generalized stratigraphic succession of Horda Platform from Lower Jurassic to Quaternary is presented where the overburden, caprock, reservoir, and underburden sections are also marked (modified after [32]).

Seismic-property-driven field-scale geomechanical modeling was analyzed to investigate the CO_2-injection-induced failure potential and rock deformation in the Smeaheia area. The main objective was to evaluate the sensitivity of rock compressibility and the pore volume effect on the reservoir and caprock failure potential in Alpha (32/4-1), Beta (32/2-1), and Mid-Model (i:j—50:50) locations (Figure 1a). Moreover, the total vertical displacement of the reservoir and caprocks was also estimated and analyzed. Finally, a comparative assessment between the different injection points as well as worst-case and best-case injection scenarios in the Smeaheia site area is discussed. The credibility and practicality of the seismic-property-based modeling approach was tested by Rahman et al. [32]; hence, it is directly used in this research.

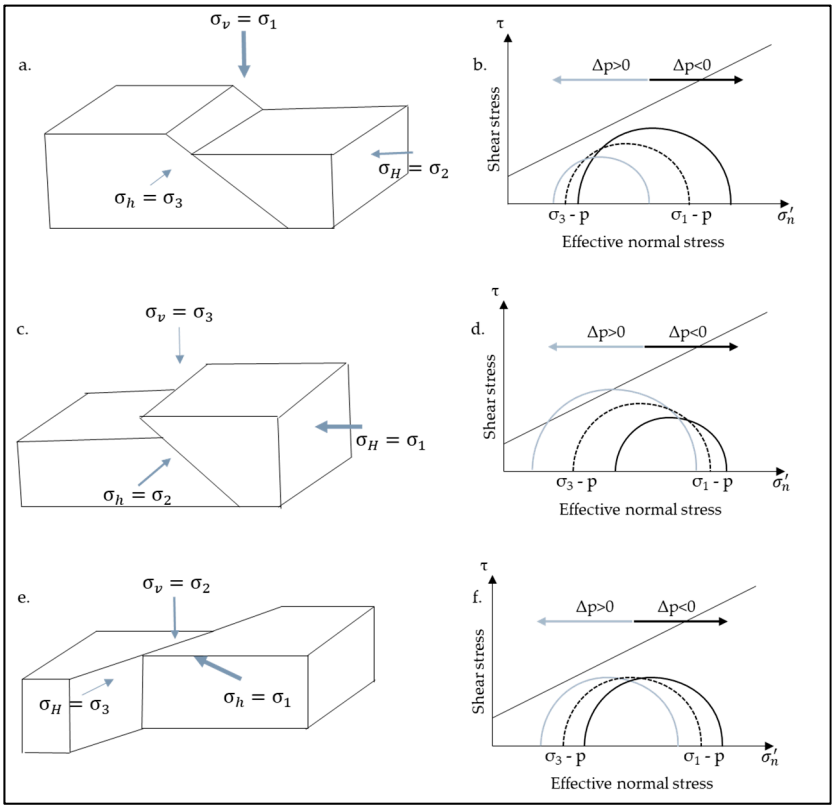

Figure 2. Shows the magnitude and order of principal stresses and the corresponding Mohr–Coulomb diagram effect of pore pressure changes on extensional stress (**a**,**b**), compressional stress (**c**,**d**), and strike-slip (**e**,**f**) regimes (modified after Altmann, [18]).

2. Model Setup

A detailed description of the model-building processes was presented in Rahman et al. [32]; the model with spatially distributed overburden properties was adapted for this study. The overburden rock properties have considerable variation, which influences the mechanical rock failure potential; hence, the model considered both spatial and temporal variations of overburden properties. The model properties (overburden, cap, reservoir, and underburden rocks) were estimated from the prestacked simultaneous inversion using a 3D seismic survey named GN1101 [33]. The properties of 3D cubes allowed us to have better vertical and horizontal control of rock properties than the conventional wireline log-based property-interpolation techniques. However, we needed a proper calibration of these property cubes before using them in the reservoir models. Fourteen (14) seismic interpreted time surfaces (i.e., top Nordland GP., top Rogaland GP., top Lista Fm., top Shetland GP., top Svarte Fm., top Rødby Fm., top Asgård Fm., top Draupne Fm., top Sognefjord Fm., top Heather Fm., top Fensfjord Fm., top Krossfjord Fm., top Dunlin GP. and top Statfjord GP.) were used to build the structural grid. Faults were considered during interpretation but not included in the grid as a separate element. The 3D properties were later distributed within the reservoir grid using the seismic resampling function in the Petrel-2019 geometrical modeling module. However, each of reservoir grids had a unique value estimated from the seismic cube. The average properties of each layer have been given in Table 1 for better clarity. The reservoir model with properties was then converted from time domain to depth domain using the velocity model constructed from the average velocity cube, which was estimated from the 3D stacking velocity. To mitigate the boundary effects and buckling artifacts over the zone of interest (i.e., reservoir model area), the reservoir grid was expanded laterally and vertically to a certain extent. The hydrostatic gradient was used for the initial pore pressure during the boundary condition, while the lithostatic gradient was considered for the vertical stress profile. A normal faulting stress regime was assigned to the study

area. [34–37]. The minimum horizontal stress gradient used was 0.1245 MPa/m, which was estimated from the X-LOT database from the study area [24]. Moreover, the maximum horizontal stress was assumed to be 10% higher than the minimum horizontal stress. In addition, the horizontal stress azimuth was used as 103^0 based on the seismicity database near the Troll field area [34]. The overall workflow for seismic properties based on one-way coupling is illustrated in Figure 3. The model used finite element method-based numerical simulation to evaluate the injection-induced geomechanical risks.

Table 1. Average properties of the model grids show the variations among different model zones.

Zones	Density (g/cm^3)	E (GPa)	PR	FA (^{0})	UCS (Mpa)
Nordaland Gp.	2.14	0.4	0.45	24.51	5.03
Rogaland Gp.	2.18	1.23	0.39	26.96	9.41
Lista Fm.	2.31	2.57	0.35	26.19	16.46
Shetland Gp.	2.24	1.44	0.39	26.19	10.35
Svarte Fm.	2.27	2.03	0.36	26.46	14.01
Rødby Fm.	2.27	1.59	0.38	25.93	11.01
Asgård Fm.	2.25	1.44	0.39	25.20	10.04
Draupne Fm.	2.31	2.15	0.37	25.43	13.96
Sognefjord Fm.	2.23	2.63	0.34	27.97	16.80
Heather Fm.	2.25	2.95	0.33	27.97	17.99
Fensfjord Fm.	2.28	3.46	0.32	28.22	21.03
Krossfjord Fm.	2.34	3.95	0.31	27.44	23.40
Dunlin Gp.	2.44	4.48	0.3	26.78	24.95

The fluid simulation model was out of the scope of this study; however, the pressure build-up due to 50 years of CO_2 injection was directly adapted from the study performed by Gassnova [38]. Based on the Gassnova [38] model, nine different scenarios were simulated and analyzed (Table 2). The reservoir simulation model was built based on the geological structures with an injection rate of 3.2 million tonnes per year for a period of 50 years. The average porosity within the reservoir interval is 0.26, while the permeability is 690 mD (milidarcy), and the K_v/K_h ratio is equal to 0.1. Moreover, the solubility of CO_2 in water was not considered because a study on the sensitivity of solubility revealed a minor effect on the fluid simulation model [38]. Although the amount of total injected CO_2 was the same within the studied model, based on the different pore volumes and pore compressibility, the pressure increase within the reservoir significantly varied (Table 2). Gassnova [38] was defined the total pore volume based on the different criteria. For instance, the low case volume (51 GSm^3) was estimated based on the boundary to the south as defined by the data available within the Øygarden–Vette fault block, while the southern limit of the sandstones defined the base volume (160 GSm^3). The next western fault block (Vette–Tusse) was also considered for the two high cases, High1 (297 GSm^3) and High2 (418 GSm^3), where the High1 was considered up to the southern limit of the Troll east field, and High2 included all the pore volumes within these two fault blocks. Moreover, the pore volume (rock) compressibility in the Smeaheia area was not defined because of the lack of laboratory experiments. Therefore, Gassnova [38] tried three different models based on the pore compressibility database from SINTEF. The reference case value (4.0×10^{-5} bar^{-1}) was adapted from the Johansen study (Aurora) with a good match in the Smeaheia study (i.e., according to Hall's correlation), while one optimistic (1.6×10^{-4} bar^{-1}) and one pessimistic (1.6×10^{-6} bar^{-1}) case were also simulated. Out of these ten (10) models, nine pressure-build-up-at-the-well-location scenarios were adopted in this study except High2. Although injection-induced pore pressure increases varied spatially (decreases away from the well), we considered a constant reservoir pore pressure increase during geomechanical simulation due to model limitation.

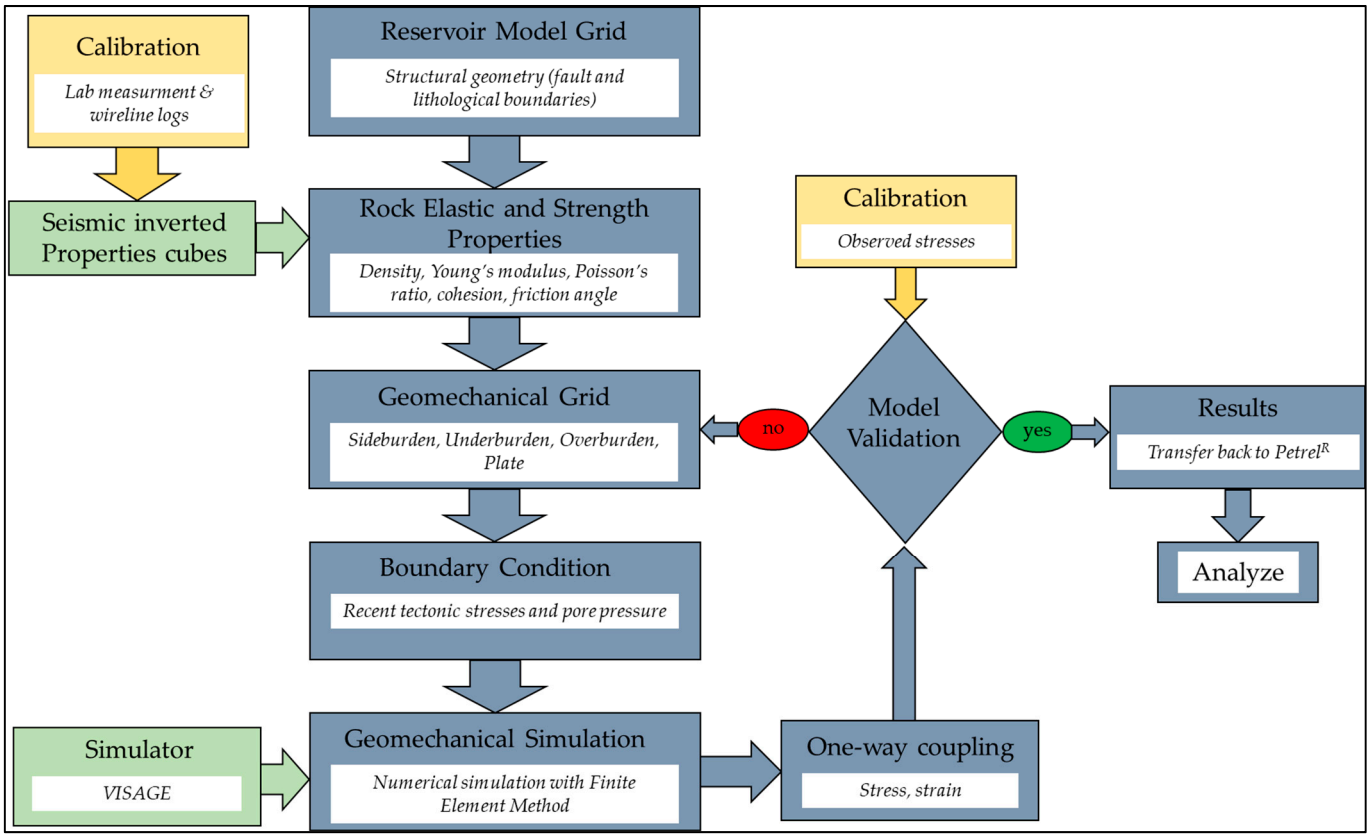

Figure 3. The workflow illustrated the different components of one-way coupling geomechanical model to evaluate the pressure-induced stress and strain change of the studied rocks (adapted from Rahman et al. [32]).

Out of these nine models, three cases were selected for detail analysis where the worst-case (orange) scenario is presented by the 'Pessimistic-Low' scenario, the base case (gray) was combined by the base total pore volume and reference rock compressibility, and the best case (green) was defined by high pore volume with optimistic compressibility (Table 2). The geomechanical failure of these three models (i.e., worst, base, and best cases) are presented in the Results section for comparative analysis. Moreover, three locations, namely Alpha (32/4-1), Beta (32/2-1), and the middle of the model (Mid-Model), were considered for mechanical assessment to find a better location for the optimum injection point (Figure 1a).

Table 2. Pressure increase from hydrostatic in well location after 50 years of injection of 3.2 million tonnes per year (adapted from [38]). The studied worst (orange), base (gray), and best (green) cases are highlighted by different colors.

Rock Compressibility	Total Pore Volume		
	Low	Base	High
Pessimistic	1.94	1.31	1.19
Reference	1.58	1.20	1.12
Optimistic	1.31	1.12	1.07

The pressure build-up (times) is relative to the initial hydrostatic pressure.

3. Pore Pressure and Effective Stress

Effective stress depends on the in situ stresses and pore pressure. The CO_2-injection-induced pore pressure changes change the effective stresses within the reservoirs, which influence the reservoir and the overburden rocks due to the tensor behavior of the stress.

This study used the hydrostatic pore pressure gradient as the initial reservoir pressure (Figure 4a). The in situ pore pressure decreases from west to east due to the structural dipping (reservoirs dipping towards the west). Moreover, the hanging wall side of the Vette fault (VF) shows comparatively high pore pressure because of depth. However, the Troll east gas field is located within this fault block (Tusse–Vette fault block) and has been in production for several years from the same reservoirs, so one can expect a depleted pore pressure. However, the previous analyses [35,36,39] indicated sealed VF in the study area, so we assumed a hydrostatic gradient in the VF footwall block. Moreover, this study focused on the Smeaheia fault block; hence, it did not adjust the depleted pore pressure on the west side of the VF. Therefore, the hanging wall side (west of the Vette Fault) was not included in any analysis but was retained as the grid considered the complete area of the studied 3D cube (GN1101).

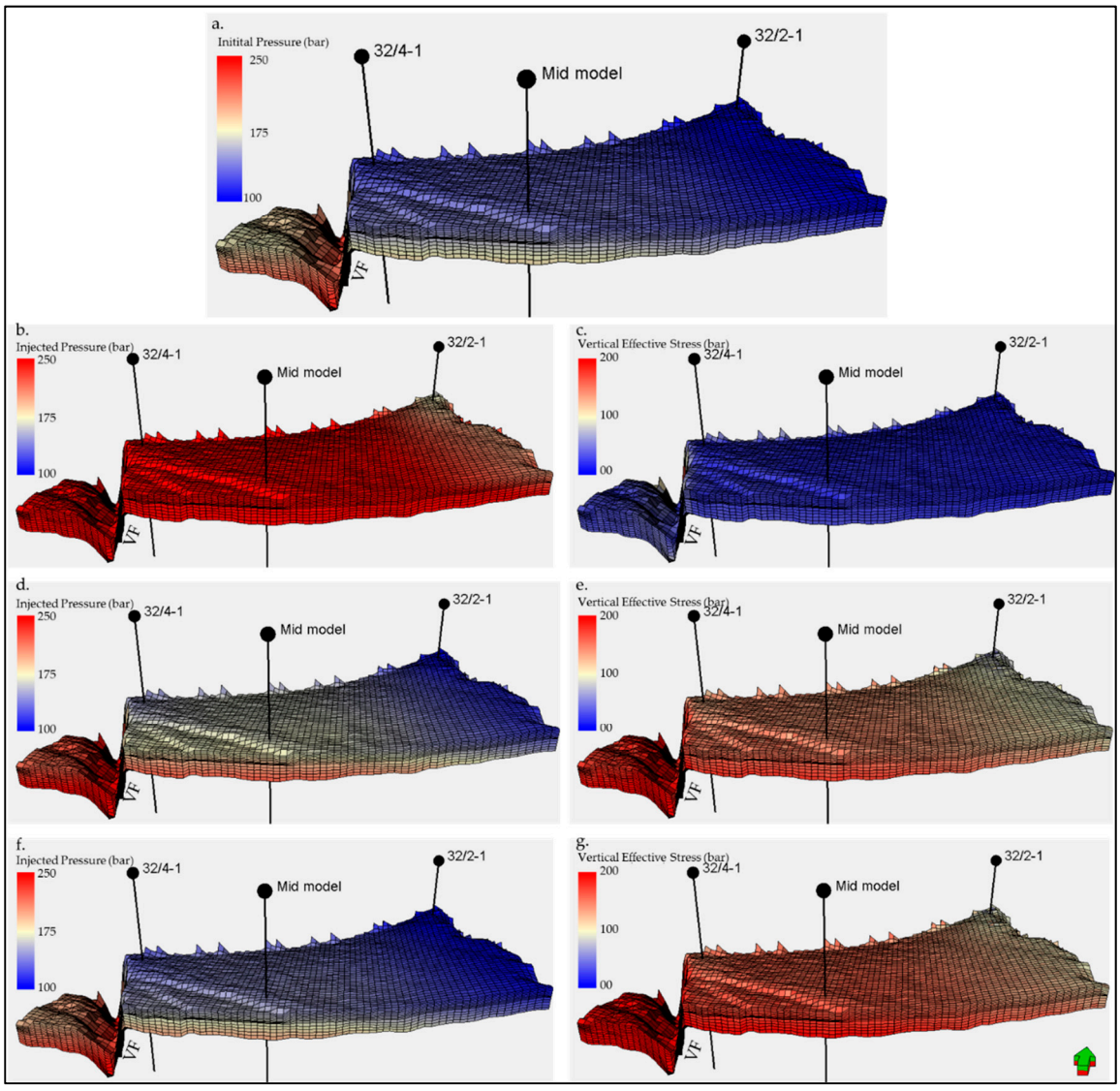

Figure 4. 3D illustration of reservoir grids shows the initial hydrostatic pore pressure (**a**) after-injection pressure and corresponding vertical effective stress in the worst-case model (**b**,**c**), the base-case model (**d**,**e**), and the best-case model (**f**,**g**), respectively. The locations and Vette fault (VF) are shown for reference. Moreover, the green arrow indicated the north direction of the model. Additionally, note that the color scales demonstrate differences between the after-injection pressure and effective vertical stresses.

The CO_2-injection-induced reservoir pressure increase in worst-, base-, and best-case models is illustrated in Figure 4b,d,f, where the worst-case scenario represents a significantly high reservoir pressure increase (~72 bar) compared to base- (~15 bar) and best-case (~6 bar) models. The corresponding vertical effective stresses are also demonstrated in Figure 4c,e,g. The highest reservoir pressure increase model (i.e., worst-case) showed the lowest vertical effective stress and vice versa. The worst case indicated an effective vertical stress of 96 bar, while the base and best cases showed average stresses of 152 and 161 bar, respectively.

4. Results

4.1. Reservoir and Caprock Assessment

The potential geomechanical risks such as failure and deformation were assessed for different rock compressibilities and pore volume scenarios. Four different vertical layers within the studied reservoir (Top Sognefjord and Fensfjord) and caprock (Top and base caprock) were analyzed.

4.1.1. Failure Potential in Different Locations

- Alpha location (well 32/4-1)

Based on the Mohr–Coulomb failure criteria, the model grid penetrated by the well 32/4-1 was evaluated for potential injection-induced failure. All the models showed a similar trend with various intensities; hence, three (i.e., worst-, base-, and best-case models) out of nine models' results are presented here. The potential failure of these models is illustrated in Figure 5. Based on the rock strength and stress-state condition, no caprock failure or fractures were observed in any of the models (Figure 5a,d,g). However, the mobilized shear stress/strength significantly increased at the base of the caprock, which represents the Heather Formation shale (Figure 5b,e,h). The Mohr circles were closer to the Coulomb failure envelope at the base (Heather) compared to the top caprock (Draupne).

Moreover, after 50 years of CO_2 injection, the shear stress/strength increase was negligible within the caprock except for the Heather Formation in the worst-case model, where the Mohr circle shifted to the left, close to the tensile failure line. In the other two models, the caprock Mohr circle was juxtaposed in before- and after-injection scenarios. This indicates a minimal CO_2-injection-induced effect on caprock failure.

On the contrary, the injection-induced reservoir pressure change considerably increased the possibility of tensile fractures within the reservoir (Figure 5c,d,f). There was no fracture observed in the in situ stress-state condition based on the Coulomb failure criteria. However, the worst-case model illustrated significant tensile fracture risks in after-injection scenarios, which decreased in base- and best-case models.

- Beta (well 32/2-1) and Mid-Model locations

The Beta location (32/2-1) is structurally shallower compared to Alpha (32/4-1), while the Mid-Model location is deeper than Alpha. For instance, the top reservoir TVD at Beta is 889 m, while the Mid-Model top reservoir depth is 1359 m compared to the top reservoir of Alpha, which is 1250 m. Therefore, lower in situ stresses and initial pore pressure was expected in the Beta location, and higher value were expected in the Mid-Model, considering the same gradient was used in all the models. Moreover, as the injection-induced reservoir pressure change was directly estimated from the initial pore pressure, the pore pressure change also varied spatially (Figure 4). Furthermore, the elastic properties differed both laterally and vertically, which might have had an influence on the numerical simulations.

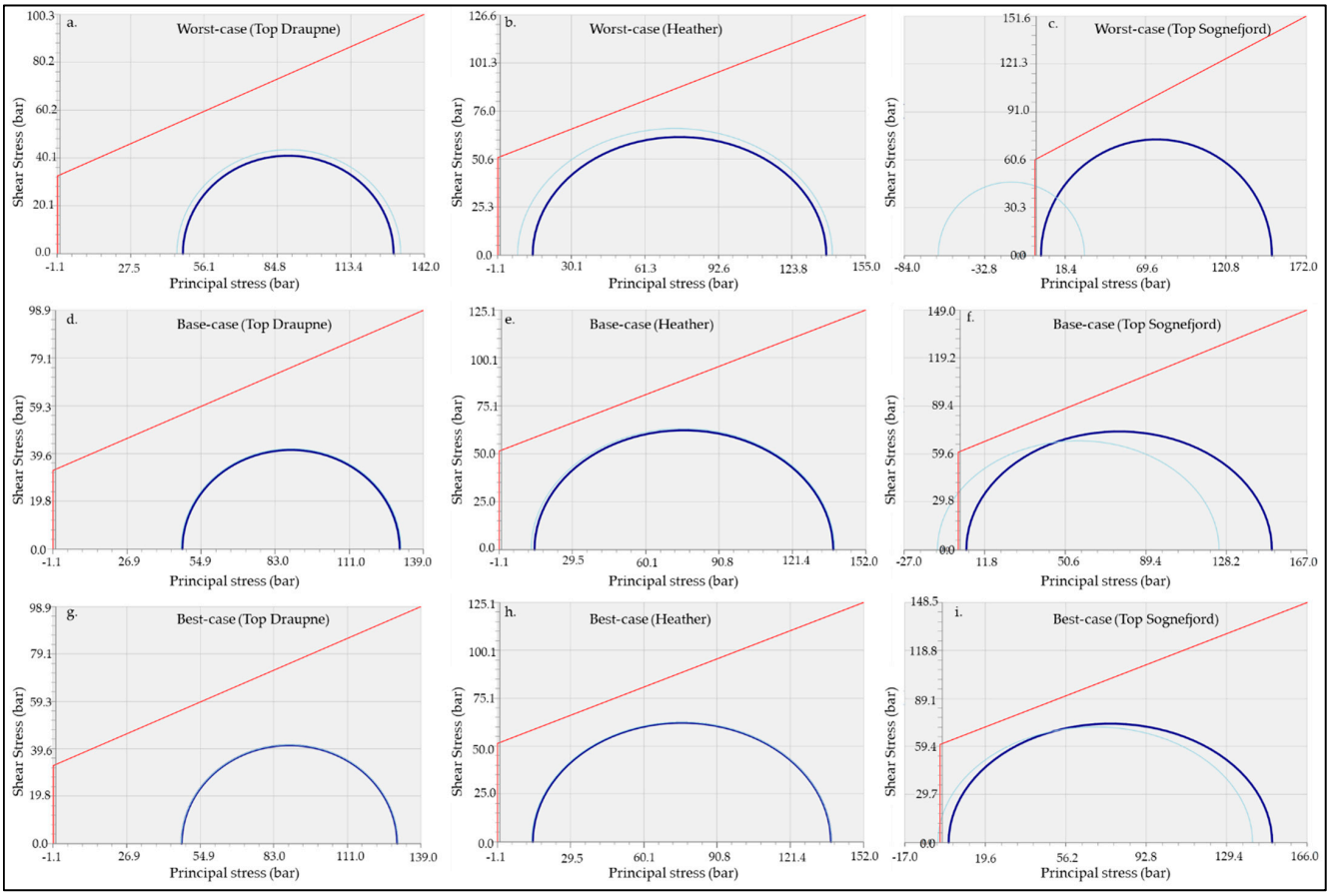

Figure 5. The Mohr–Coulomb failure envelope in Alpha location illustrated the failure potential before- and after-injection periods of top caprock layer (Draupne), base caprock layer (Heather) and top reservoir (Sognefjord) for worst-case model (**a**–**c**), base-case model (**d**–**f**), and best-case model (**g**–**i**), respectively. The dark blue represents the in situ stress state, while the light-blue curve indicates after-injection scenario.

Similar to the Alpha location, there was no caprock failure or fractures observed in either the Beta or Mid-Model locations. However, the shear strength was comparatively high in the Beta structure in contrast with the Mid-Model location. The Mohr–Coulomb failure of the reservoir rock significantly differed in Beta and Mid-Model locations compared to the Alpha location. Although the worst-case models had a tensile failure risk, such as in the Alpha location, the base- and best-case models did not demonstrate any tensile failure (Figure 6). Moreover, based on the tensile failure cut-off (1 bar), the in situ stress-state condition, the failure risk was significantly lower in both Beta and Mid-Model locations than in the Alpha structure. In addition, irrespective of in situ stresses and pore pressure variation between Beta and Mid-Model locations, the reservoir rock strength illustrated a similar trend (i.e., tensile failure in the worst case and no failure in base and best cases), though the Mid-Model case showed slightly lower strength.

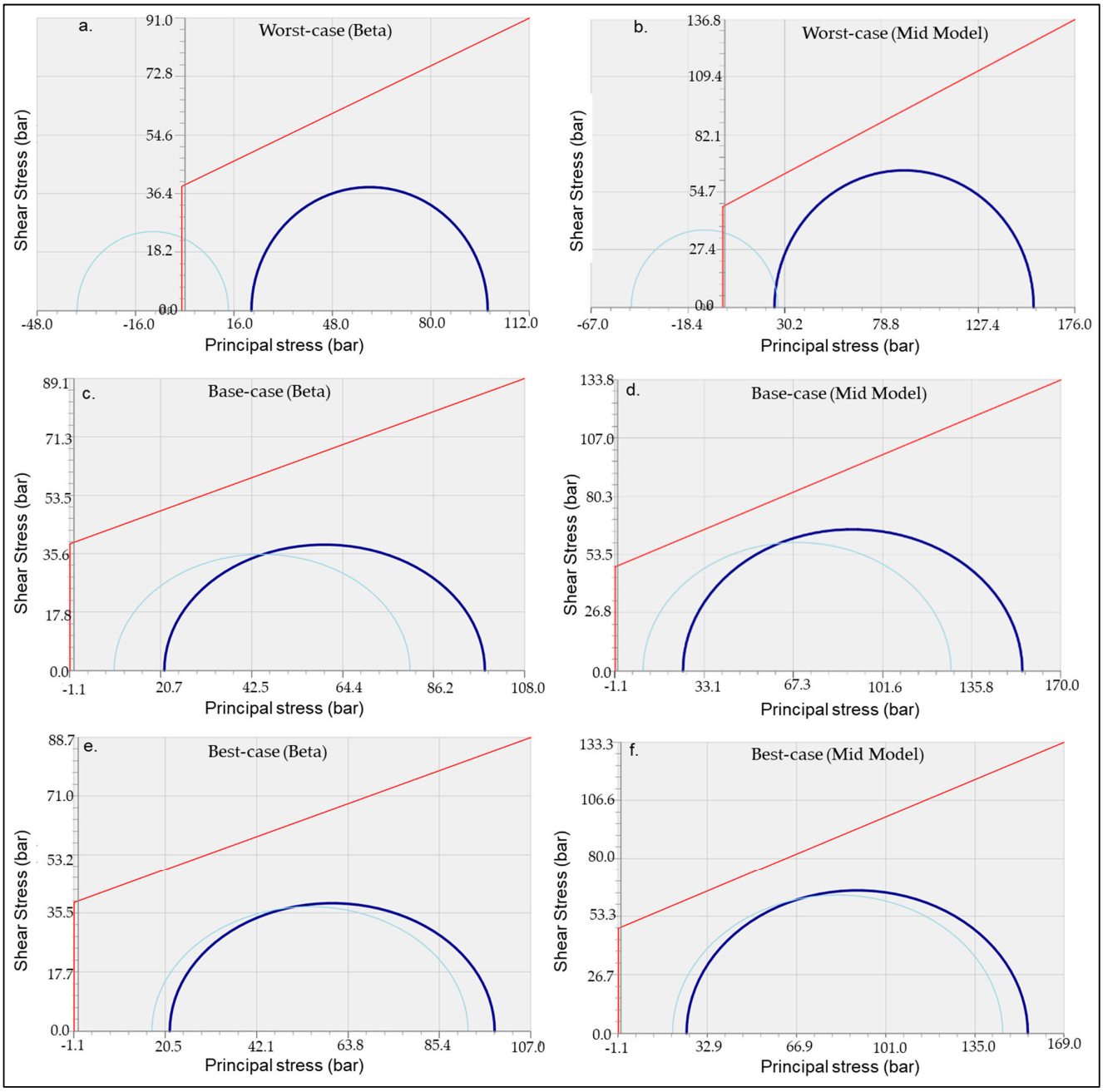

Figure 6. The Mohr–Coulomb failure envelopes of the top reservoir (Sognefjord) are illustrated, along with the failure potential before and after injection periods in Beta (32/2-1) and Mid-Model locations for the worst case (**a**,**b**), base case (**c**,**d**), and best case (**e**,**f**), respectively. The dark blue represents the in situ stress state, while the light-blue curve indicates after-injection scenario.

4.2. Effect of Pore-Volume-Induced Pressure Build-Up

The effect of pore volume sensitivity on rock deformation and failure was analyzed by comparing the three pore volume models (i.e., low, base, and high) in a reference case for rock compressibility (Table 2). The vertical rock displacement of the top Draupne and top Sognefjord formations is illustrated in Figure 8. The same color scale was used for all the model cases for a better visual comparison. It is evident that the pore volume change significantly influenced vertical rock displacement. The low pore volume model estimated a maximum displacement of 74 cm, while the high-pore-volume case indicated only a 15 cm maximum uplift. The intermediate base-case model showed a 26 cm uplift.

Comparing the same models in the Mohr–Coulomb failure envelope, the shear stress/strength decreased with increasing pore volume (Figure 9). Although the pore pressure change influenced rock failure or fracture, the changes were minimal considering the studied failure envelope. Therefore, no caprock failure was observed in any case. On the contrary, injection-induced pressure change shifted the Mohr circle in the left direction with tensile failure considering the tensile cut-off of 1 bar. Irrespective of total-pore-volume-induced pressure build-up, after-injection tensile failure within the reservoir was observed in all three cases. However, the strain rate decreased with increasing pore volume. The above Mohr–Coulomb failure analysis was based on the Alpha location. However, interpretation changes in different studied locations (i.e., Beta and Mid-Model) followed a similar trend as described above in location-based comparative analysis.

4.3. Effect of Rock-Compressibility-Induced Pressure Build-Up

The pore compressibility sensitivity was also evaluated by analyzing the pessimistic, reference, and optimistic rock compressibility models, where base case pore volume was used for all three models (Table 2). Similar to the pore volume study, the same color scale was used for visual comparison to show the vertical deformation (Figure 10). The vertical displacement of the caprock and reservoir decreased with increasing pore compressibility values (i.e., optimistic case). However, the maximum uplift difference was not as significant as the pore volume effect, but considerably high, as the pessimistic model estimated a 40 cm uplift compared to 15 cm in the optimistic case. The reference model's maximum upliftment was 26 cm.

Moreover, the Mohr–Coulomb failure envelope revealed that the rock shear stress/strength decreased with increasing pore compressibility; however, the changes were negligible (Figure 11). There was no caprock failure observed, while reservoir tensile failure was determined to potentially occur after injection-induced pressure changes.

4.3.1. Rock Deformation

The vertical rock deformations of top Draupne, top Sognefjord, and top Fensfjord formations are illustrated in Figure 7. The different color scales were used for different models because of the significant differences in the total vertical deformation. The positive deformation indicates upliftment, while the negative value represents subsidence. The studied models indicated overall upliftment due to CO_2-injection-caused pressure changes in the study area. The upliftment between the formation followed a similar pattern in all three models, where the Draupne and Sognefjord formations were uplifted significantly higher compared to the Fensfjord Formation. Lateral upliftment variation was also observed, but the intensity was minimal. However, a significant difference was estimated when comparing the vertical upliftment among the models (i.e., worst, base, and best cases). As expected, high upliftment was observed in the worst-case scenario with the maximum value of 120 cm, while maximum upliftment in the base case was 26 cm and 9 cm in the best-case model.

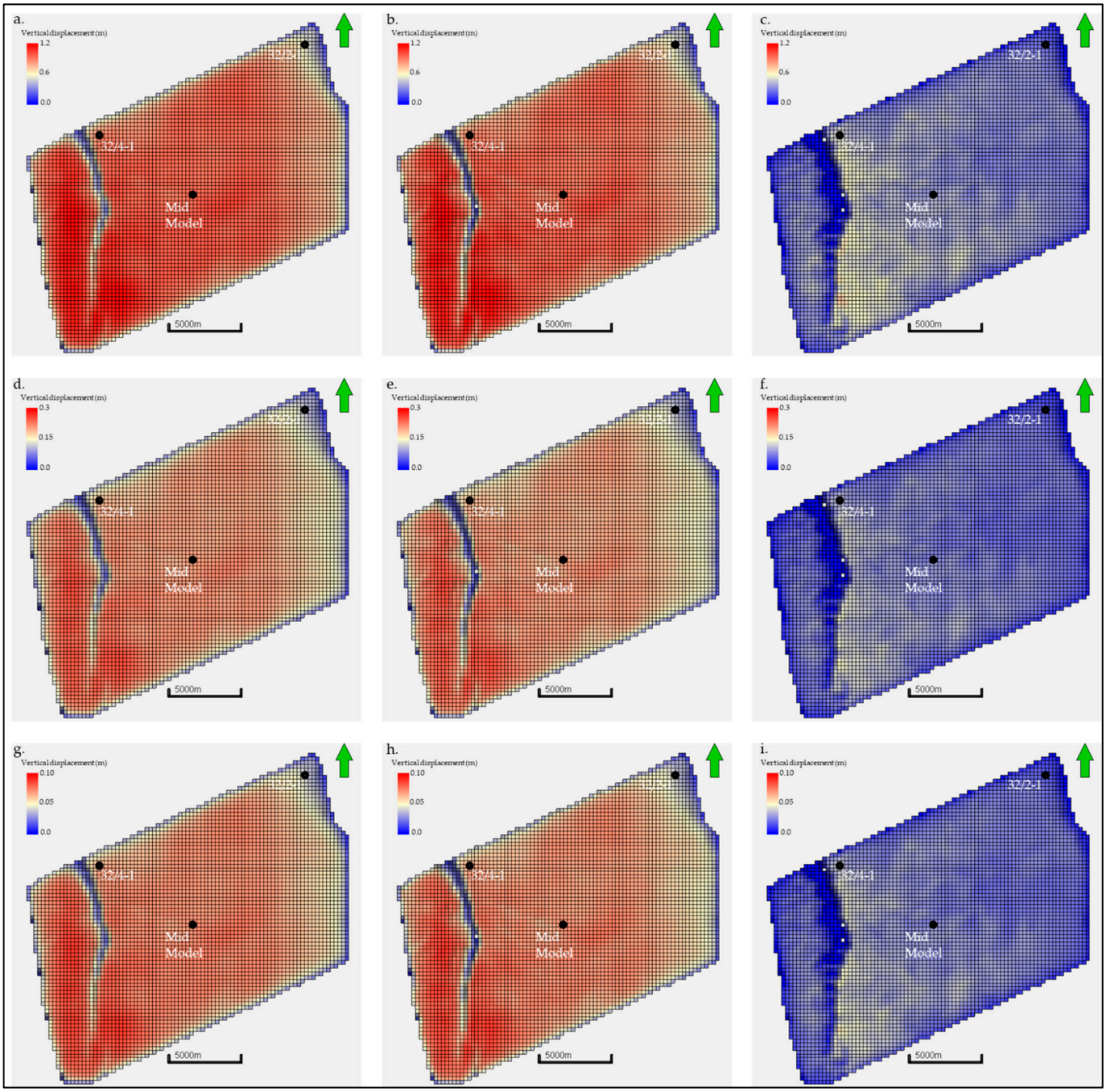

Figure 7. Estimated vertical displacements of the top Draupne, top Sognefjord, and top Fensfjord after injection period show the upliftment for the worst-case model (**a**–**c**), base-case model (**d**–**f**), and best-case model (**g**–**i**), respectively. Note that the color bar varied significantly among models. The Alpha, Beta, and Mid-Model locations are also indicated on the maps for reference. Moreover, the green arrow indicated the north direction of the model.

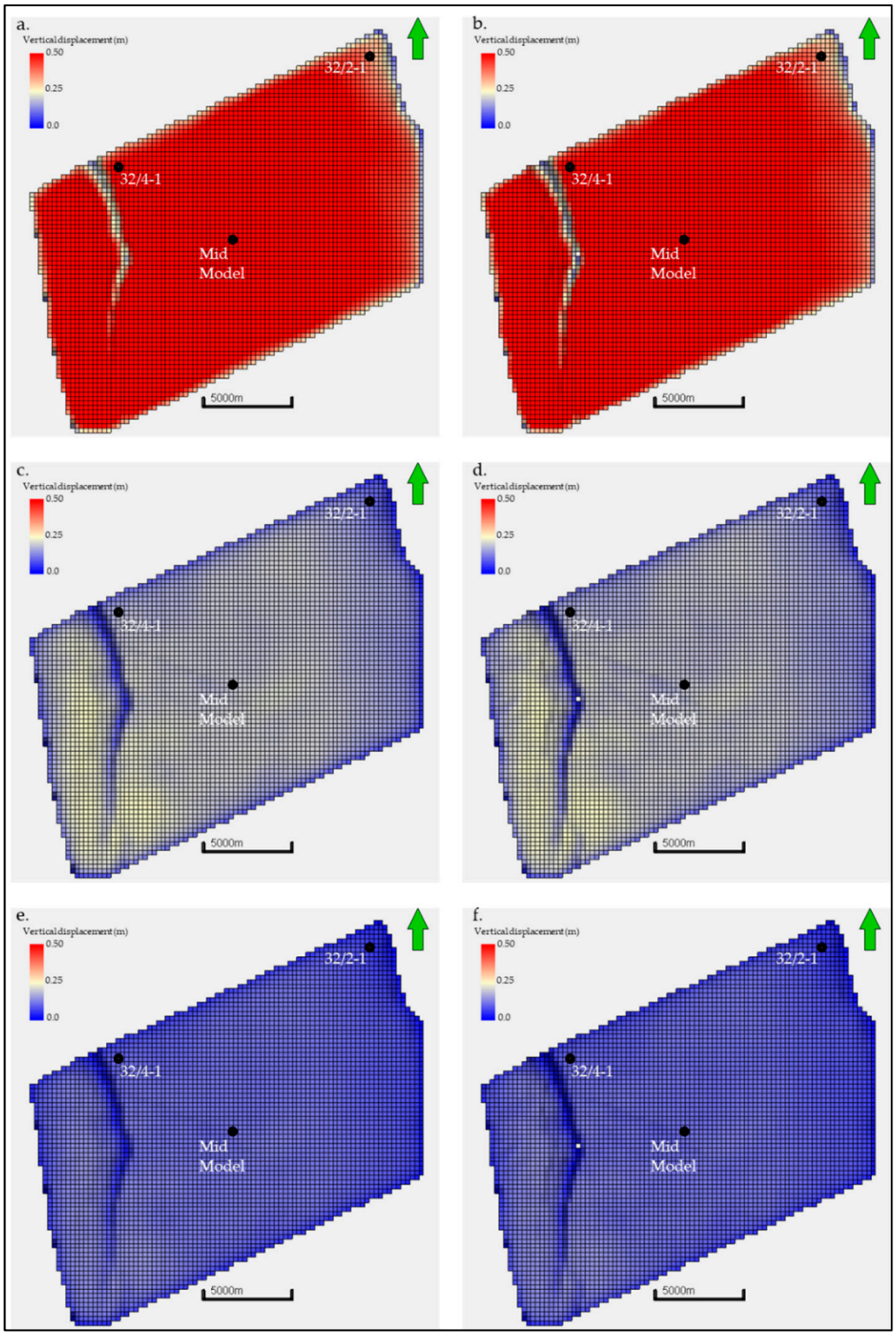

Figure 8. A comparison of vertical displacement of the top Draupne and top Sognefjord after injection period shows the upliftment for model RL (**a**,**b**), model RB (**c**,**d**), and model RH (**e**,**f**), respectively. The Alpha, Beta, and Mid-Model locations are indicated on the maps for reference. Moreover, the green arrow indicated the north direction of the model.

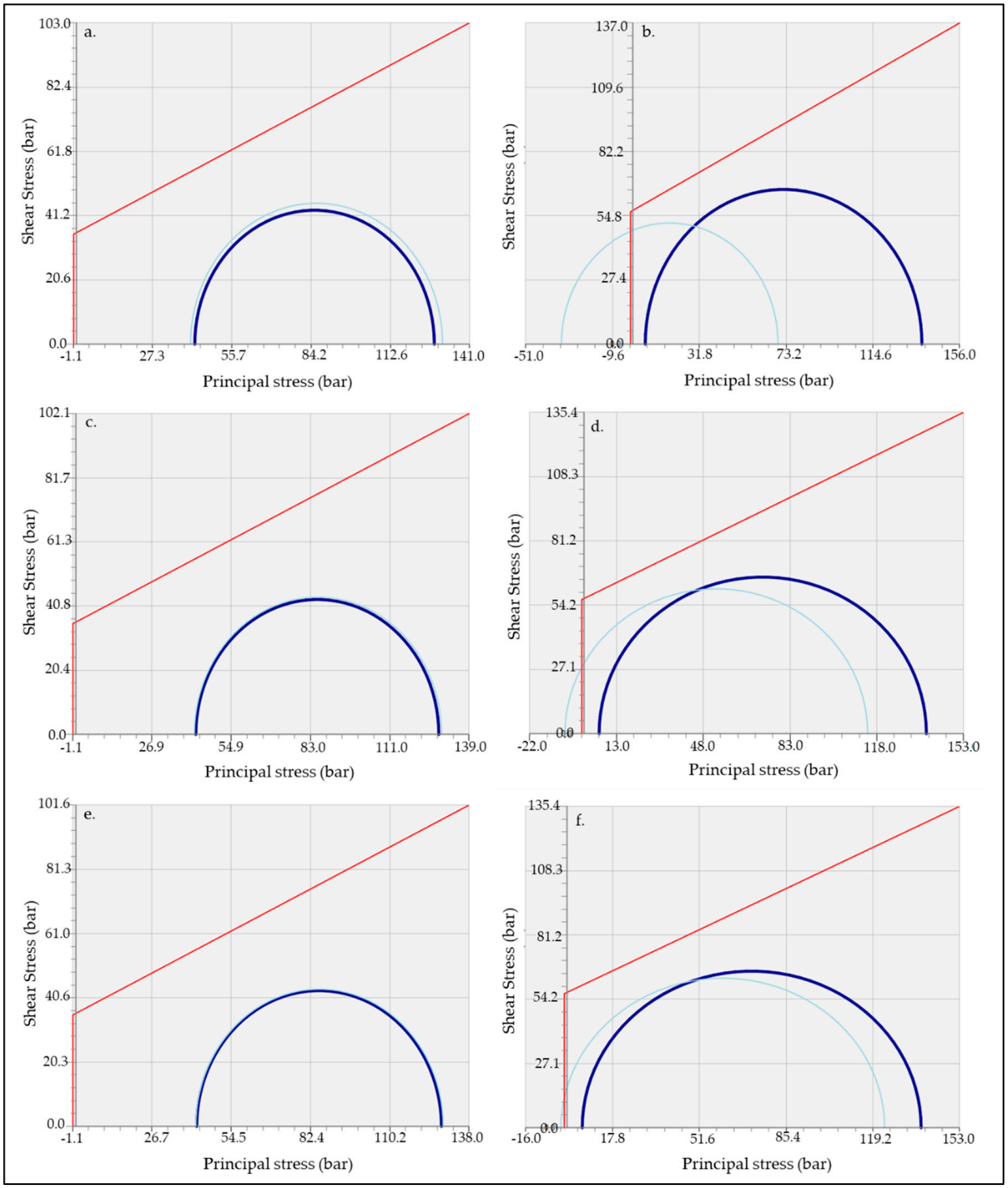

Figure 9. The Mohr–Coulomb failure envelope of top Draupne and top Sognefjord layers in Alpha location illustrated the failure potential of model RL (**a**,**b**), model RB (**c**,**d**), and model RH (**e**,**f**), respectively. Note that the dark blue represents the in situ stress state, while the light-blue curve indicates the post-injection scenario.

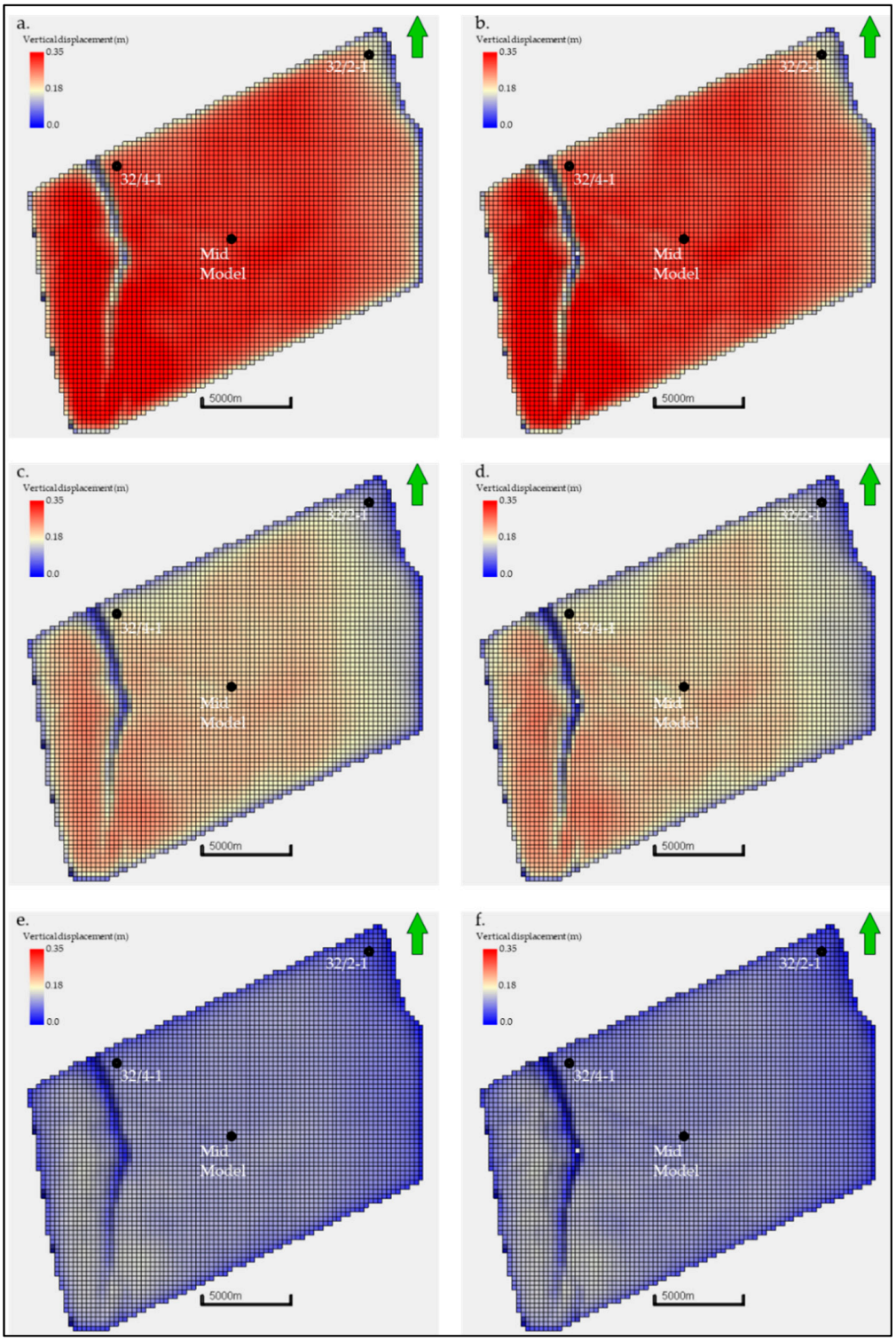

Figure 10. A comparison of vertical displacement of the top Draupne and top Sognefjord formations after injection period show the upliftment for model PB (**a**,**b**), model RB (**c**,**d**), and model OB (**e**,**f**), respectively. The Alpha, Beta, and Mid-Model locations are marked on the maps for reference. Moreover, the green arrow indicated the north direction of the model.

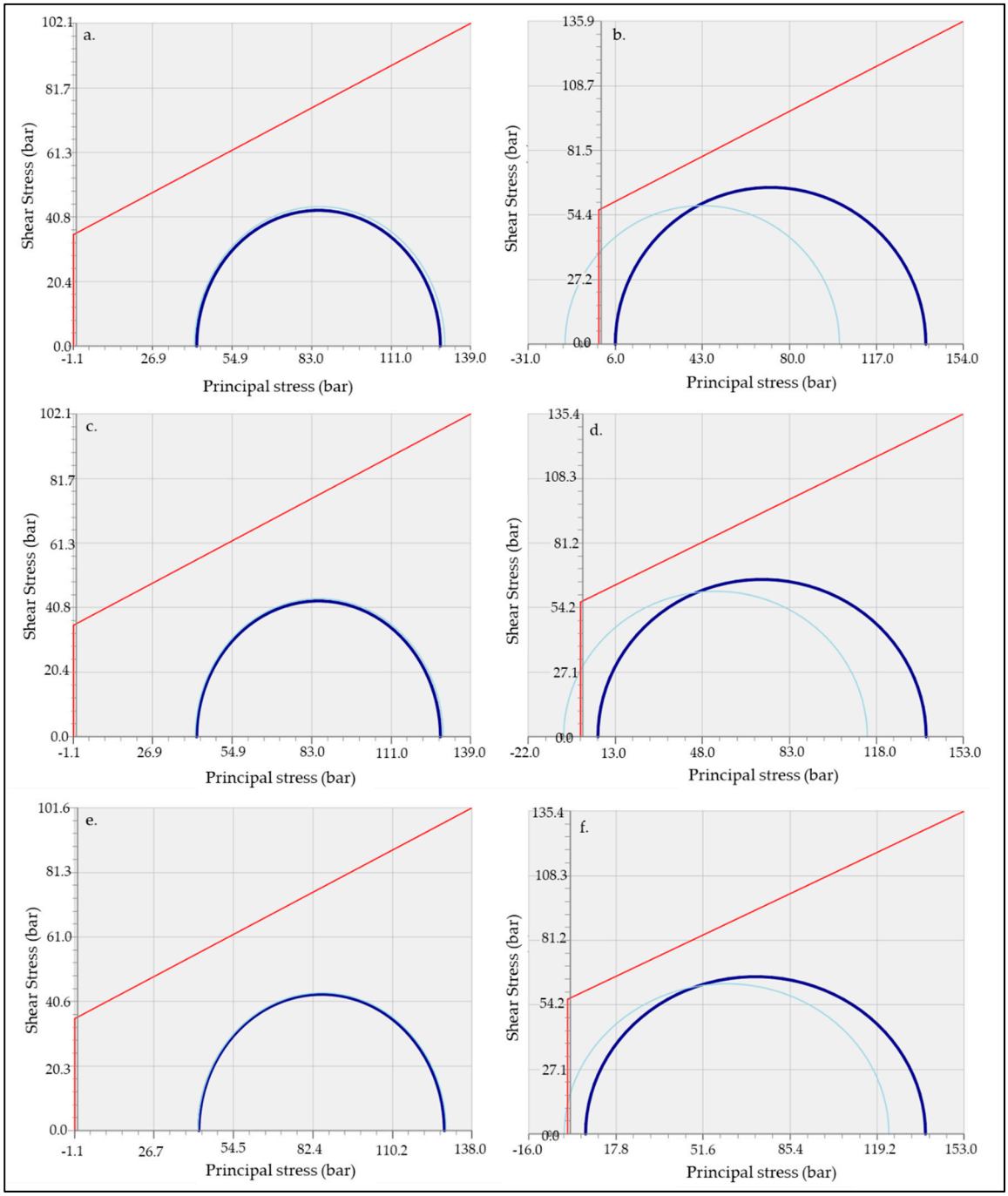

Figure 11. The Mohr–Coulomb failure envelope of top Draupne and top Sognefjord layers in Alpha location illustrated the failure potential of the models PB (**a**,**b**), RB (**c**,**d**), and OB (**e**,**f**), respectively. Note that the dark blue represents the in situ stress state, while the light-blue curve indicates post-injection scenario.

5. Discussions

Although there are many uncertainties about the magnitude and order of principal stresses, this study attempted to evaluate the mechanical rock failure and deformation in the Smeaheia area using the available database. However, although the principal stresses significantly influenced the overall field-scale mechanical risks, there was no failure or fracture risk observed within the caprock and reservoir under the initial stress condition. When the injection-induced reservoir pressure increases were introduced within the models, a significant variation was observed among studied model scenarios (i.e., worst, base, and

best cases) and among the various model locations (i.e., Alpha, Beta, and Mid-Model). The differences observed within the various cases were constrained by the pore pressure build-up within the reservoir because the same elastic properties' geomechanical grid had been used for all the models. However, the variation in Alpha, Beta, and Mid-Model locations within the same model illustrated the spatial variation in the seismic-driven elastic properties. This explains the lower failure risk in the Mid-Model location compared to the Alpha location, though the Mid-Model location is structurally deeper. In the Beta location, these could be a combination of low initial stresses and elastic properties as the Beta location is structurally shallower than both Alpha and Mid-Model locations. Mechanical properties such as cohesion varied among the studied locations. For instance, the Alpha location had a 52-bar cohesion within the top Sognefjord layer compared with 40 and 48 bar in Beta and Mid-Model locations, respectively. Therefore, the Coulomb failure envelope changes various shear failures within the locations. Moreover, due to the difference in effective stresses, the Mohr circle position relative to tensile failure cut-off in in situ and after-injection scenarios were varied and influenced the tensile failure risks.

Although the rock failure risks decreased from the worst-case to best-case model, no caprock failure or fracture risks were observed based on the Mohr–Coulomb failure envelope in any case. However, the base caprock layer, equivalent to the Heather Formation shale, poses higher failure risks than the organic-rich upper Draupne caprock shale (Figures 5 and 6). The Heather Formation shale is more brittle than the Draupne shale [40], which explains the higher mechanical failure risk in the base caprock layer. Moreover, the base layer might have more influence due to the reservoir interval below.

The possibility of tensile fracturing within the reservoir in the worst-case scenario after injection was observed in all three locations (i.e., Alpha, Beta, and Mid-Model). However, in base- and best-case models, the reservoir fracture might have only occured in the Alpha location, while the Beta and Mid-Model locations did not have any potential failure risks. The worst-case model represents a closed aquifer (i.e., confined low pore volume) system, which significantly influences the storage efficiency. However, reservoirs commonly have an open system at their margins with lateral and vertical single-phase flow, allowing waters to escape without any detrimental effect on the storage integrity [41]. This indicates that the worst-case scenario is a hypothetical case and does not exist. Nevertheless, we must keep in mind that all the tensile failure risk assessments illustrated in this study are based on the tensile stress cut-off of 1 bar. There was no sensitivity analysis performed in this research; hence, the tensile failure results might vary depending on the tensile stress cut-off value.

The total pore volume and pore compressibility significantly influenced the pressure build-up within the reservoir interval, considering the same volume of CO_2 injected into the aquifer (Table 2). This study reveals the influence on rock deformation and failure of these different pressure build-up scenario models. As we used the same geomechanical grid for all the models, the rock deformation and failure variations observed were due to the pressure difference related to the pore volume and compressibility of the study area. The total pore volume and compressibility significantly influenced the geomechanical behavior of the studied rocks. The maximum vertical upliftment in the low-pore-volume scenario was considerably high, even using the reference pore compressibility value (Figure 12). However, the confined low pore volume is not common in nature [41]. Moreover, the influence of pore compressibility was also high but not significant, like pore volume (Figure 12). Pore compressibility is an important factor and depends on both rock and pore fluid compressibilities. Therefore, this is a complex property and depends on a combination of parameters such as mineralogy, porosity, type of fluid, etc. However, due to the importance of rock compressibility in geomechanical behavior revealed in this study, further investigation is needed, such as laboratory experiments on the well 32/4-1 (Alpha) to reduce the pore volume compressibility uncertainty.

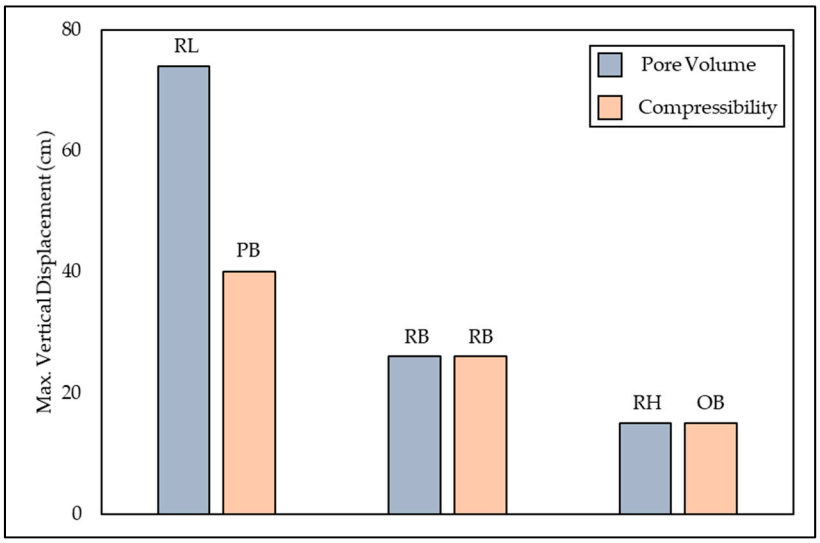

Figure 12. The bar chart illustrates the maximum vertical displacement estimated for different pressure build-up scenarios in various total pore volume and pore compressibility models.

Implication for Geological Storage of CO_2

One of the crucial parameters in subsurface CO_2 storage is the evaluation of the safe volume of injected CO_2. The safe volume of injection-induced pressure build-up describes the amount of CO_2 injection before any leakage happens. Moreover, the optimal injectivity (injection rate) played a vital role in a safe CO_2 storage project. Estimation of optimal capacity and injectivity of any CO_2 injection site is one of the criteria in storage site characterization. A fluid simulation model, which was out of the scope of this work, can assist the studied geomechanical model by providing different pressure changes scenarios as an input. However, the studied scenarios can also reveal the acceptable amount of pressure build-up before any leakage happens. The base-case model we analyzed had a 25-bar reservoir pressure increase. According to Gassnova [38], this is the acceptable amount of pressure build-up in the Smeaheia injection site compared to the base case. The pressure build-up in the worst- and best-case models were 117 bar and 9 bar, respectively. Although Gassnova [38] suggested the base-case model is geomechanically not safe, the caprock failure risk in this study indicated no failure. However, the Vette Fault (for the Alpha structure) and the Øygarden Fault (for the Beta structure) sealing potentials were not investigated here, which may also be critical to assess the overall top seal integrity. The results from this study indicate the practicality of the proposed numerical simulation workflow to evaluate the geomechanical risks in any CO_2 injection site.

The CO_2 injection point in any CCS project is also essential. The spatial variation of rock failure risks in the same model indicates the importance of having a potentially better location for injection. The failure risk assessment shows that the Beta and Mid-Model locations are safe compared to the Alpha structure. However, considering the Øygarden fault failure risk not addressed in this study, the better location would be the Mid-Model case (i:j—50:50). Nevertheless, the lateral and vertical plume migration and their effects must be evaluated using a fluid simulation model.

Moreover, the fluid flow model needs to be integrated into the modeling workflow because the fluid flow model depicts the actual CO_2-injection-induced pressure changes within the reservoir. The pore pressure change varied laterally and vertically based on pore connectivity, injection interval, and locations. Using a constant pressure increase gradient within the whole reservoir (this study) limits the sensitivity analysis to estimate any injection site's optimum capacity and injectivity rate. Nevertheless, this is a future opportunity where fluid flow integrated geomechanical modeling will be executed.

6. Conclusions

The key findings from this study are stated below:

- The pore volume and pore compressibility significantly influenced the mechanical rock failure and deformation. The low pore volume with reference compressibility was estimated at ~74 cm vertical upliftment on the reservoir–caprock interval, while the pessimistic compressibility model has a base pore volume calculated ~40 cm uplift. Irrespective of considerable vertical upliftment, no caprock failure was observed in any models. However, although there was no reservoir rock failure in in situ stress-state conditions, tensile failure occurred after injection-induced pressure change scenarios.
- The Mohr–Coulomb failure risks varied within the studied locations. Based on the assessment, the Alpha structure indicated low mobilized shear stress/strength compared to the Beta and Mid-Model locations. However, a fluid simulation model should be implemented to evaluate the plume migration for building confidence.

Assuming the base-case as the real injection scenario, the caprock might act as an effective top seal. However, the fault sealing analysis should be carried out before any injection decision.

Author Contributions: Conceptualization, M.J.R.; methodology, M.J.R.; software, M.J.R.; validation, M.J.R., M.F. and N.H.M.; formal analysis, M.J.R.; investigation, M.J.R.; resources, M.J.R.; data curation, M.J.R.; writing—original draft preparation, M.J.R.; writing—review and editing, M.J.R., M.F. and N.H.M.; visualization, M.J.R., M.F. and N.H.M.; supervision, M.F. and N.H.M.; project administration, N.H.M.; funding acquisition, N.H.M. All authors have read and agreed to the published version of the manuscript.

Funding: This research was funded by the Research Council of Norway, grant number "280472".

Institutional Review Board Statement: Not applicable.

Informed Consent Statement: Not applicable.

Data Availability Statement: Not applicable.

Acknowledgments: We are grateful for the financial support provided by the Research Council of Norway for the OASIS (Overburden Analysis and Seal Integrity Study for CO_2 Sequestration in the North Sea) project (NFR-CLIMIT project #280472). We are indebted to the additional funding and data provided by Norwegian Petroleum Directorate (NPD), Gassnova, Equinor, and TotalEnergies. We are thankful for the academic software licenses provided by Schlumberger for Petrel-2019 and the VISAGE simulator.

Conflicts of Interest: The authors declare no conflict of interest.

References

1. Al-Zubaidi, N.S.; Al-Neeamy, A.K. 3D mechanical earth model for Zubair oilfield in southern Iraq. *J. Pet. Explor. Prod. Technol.* **2020**, *10*, 1729–1741. [CrossRef]
2. Hawkes, C.D.; McLellan, P.J.; Bachu, S. Geomechanical factors affecting geological storage of CO_2 in depleted oil and gas reservoirs. In Proceedings of the Canadian International Petroleum Conference, Calgary, AB, Canada, 8 June 2004.
3. Herwanger, J.; Koutsabeloulis, N. *Seismic Geomechanics. How to Build Calibrate Geomech Model Using 3D 4D Seism Data*; EAGE: Kuala Lumpur, Malaysia, 2011.
4. Rutqvist, J.; Birkholzer, J.; Cappa, F.; Tsang, C.-F. Estimating maximum sustainable injection pressure during geological sequestration of CO_2 using coupled fluid flow and geomechanical fault-slip analysis. *Energy Convers. Manag.* **2007**, *48*, 1798–1807. [CrossRef]
5. Rutqvist, J.; Birkholzer, J.T.; Tsang, C.-F. Coupled reservoir–geomechanical analysis of the potential for tensile and shear failure associated with CO_2 injection in multilayered reservoir–caprock systems. *Int. J. Rock Mech. Min. Sci.* **2008**, *45*, 132–143. [CrossRef]
6. Soltanzadeh, H.; Hawkes, C.D. Semi-analytical models for stress change and fault reactivation induced by reservoir production and injection. *J. Pet. Sci. Eng.* **2008**, *60*, 71–85. [CrossRef]
7. Streit, J.E.; Hillis, R.R. Estimating fault stability and sustainable fluid pressures for underground storage of CO_2 in porous rock. *Energy* **2004**, *29*, 1445–1456. [CrossRef]
8. Ganguli, S.S.; Sen, S. Investigation of present-day in-situ stresses and pore pressure in the south Cambay Basin, western India: Implications for drilling, reservoir development and fault reactivation. *Mar. Pet. Geol.* **2020**, *118*, 104422. [CrossRef]

9. Fawad, M.; Rahman, M.D.J.; Mondol, N.H. Seismic reservoir characterization of potential CO_2 storage reservoir sandstones in Smeaheia area, Northern North Sea. *J. Pet. Sci. Eng.* **2021**, *205*, 108812. [CrossRef]
10. Dreyer, T.; Whitaker, M.; Dexter, J.; Flesche, H.; Larsen, E. From spit system to tide-dominated delta: Integrated reservoir model of the Upper Jurassic Sognefjord Formation on the Troll West Field. *Geol. Soc. Lond. Pet. Geol. Conf. Ser.* **2005**, *6*, 423–448. [CrossRef]
11. Holgate, N.E.; Jackson, C.A.L.; Hampson, G.J.; Dreyer, T. Seismic stratigraphic analysis of the Middle Jurassic Krossfjord and Fensfjord formations, Troll oil and gas field, northern North Sea. *Mar. Pet. Geol.* **2015**, *68*, 352–380. [CrossRef]
12. NPD. NPD FactPages. 2021. Available online: https://npdfactpages.npd.no/factpages/Default.aspx?culture=en (accessed on 20 December 2021).
13. Faleide, J.I.; Bjørlykke, K.; Gabrielsen, R.H. Geology of the Norwegian Continental Shelf. In *Petroleum Geoscience*; Springer: Berlin/Heidelberg, Germany, 2015; pp. 603–637.
14. Chuhan, F.A.; Kjeldstad, A.; Bjørlykke, K.; Høeg, K. Porosity loss in sand by grain crushing—Experimental evidence and relevance to reservoir quality. *Mar. Pet. Geol.* **2002**, *19*, 39–53. [CrossRef]
15. Bjørlykke, K. Compaction of Sedimentary Rocks: Shales, Sandstones and Carbonates. In *Petroleum Geoscience*; Springer: Berlin/Heidelberg, Germany, 2015; pp. 351–360.
16. Terzaghi, K. *Theoretical Soil Mechanics*; John Wiley & Sons: New York, NY, USA, 1943; pp. 11–15.
17. Anderson, E.M. The dynamics of faulting. *Trans. Edinburgh Geol. Soc.* **1905**, *8*, 387–402. [CrossRef]
18. Altmann, J.B. Poroelastic Effects in Reservoir Modelling. Ph.D. Dissertation, Karlsruher Institut für Technologie, Karlsruhe, Germany, 2010.
19. Kümpel, H.J. *Theory of Linear Poroelasticity—With Applications to Geomechanics and Hydrogeology*; Wang, H.F., Ed.; Princeton University Press: Princeton, NJ, USA, 2000; p. 287.
20. Rutqvist, J.; Stephansson, O. The role of hydromechanical coupling in fractured rock engineering. *HydroGeol. J.* **2003**, *11*, 7–40. [CrossRef]
21. Fischer, K.; Henk, A. A workflow for building and calibrating 3-D geomechanical models &ndash a case study for a gas reservoir in the North German Basin. *Solid Earth* **2013**, *4*, 347–355.
22. Fokker, P.A.; Orlic, B.; Van der Meer, L.G.H.; Geel, C.R. Geomechanical modeling of surface uplift around well KB-502 at the In Salah CO_2 storage site. In Proceedings of the 73rd EAGE Conference and Exhibition Incorporating SPE EUROPEC 2011, Vienna, Austria, 23–27 May 2011.
23. Grollimund, B.; Zoback, M.D. Impact of glacially induced stress changes on fault-seal integrity offshore Norway. *Am. Assoc. Pet. Geol. Bull.* **2003**, *87*, 493–506. [CrossRef]
24. Mandal, P.P.; Essa, I.; Saha, S.; Rezaee, R. *Multi-Purpose Utility of Constructing 3D Static Geomechanical Model in the Ichthys Field, Browse Basin*; AEGC: Brisbane, Australia, 2021.
25. Newell, P.; Yoon, H.; Martinez, M.J.; Bishop, J.E.; Bryant, S.L. Investigation of the influence of geomechanical and hydrogeological properties on surface uplift at In Salah. *J. Pet. Sci. Eng.* **2017**, *155*, 34–45. [CrossRef]
26. Olden, P.; Jin, M.; Pickup, G.; Mackay, E.; Hamilton, S.; Somerville, J.; Todd, A. Geomechanical modelling of CO_2 geological storage with the use of site specific rock mechanics laboratory data. *Pet. Geosci.* **2014**, *20*, 323–337. [CrossRef]
27. Ouellet, A.; Bérard, T.; Desroches, J.; Frykman, P.; Welsh, P.; Minton, J.; Pamukcu, Y.; Hurter, S.; Schmidt-Hattenberger, C. Reservoir geomechanics for assessing containment in CO_2 storage: A case study at Ketzin, Germany. *Energy Procedia* **2011**, *4*, 3298–3305. [CrossRef]
28. Tenthorey, E.; Vidal-Gilbert, S.; Backe, G.; Puspitasari, R.; Pallikathekathil, Z.J.; Maney, B.; Dewhurst, D. Modelling the geomechanics of gas storage: A case study from the Iona gas field, Australia. *Int. J. Greenh. Gas Control* **2013**, *13*, 138–148. [CrossRef]
29. Vidal-Gilbert, S.; Tenthorey, E.; Dewhurst, D.; Ennis-King, J.; Van Ruth, P.; Hillis, R. Geomechanical analysis of the Naylor Field, Otway Basin, Australia: Implications for CO_2 injection and storage. *Int. J. Greenh. Gas Control* **2010**, *4*, 827–839. [CrossRef]
30. Ganguli, S.S.; Vedanti, N.; Akervoll, I.; Dimri, V.P. Assessing the feasibility of CO_2-enhanced oil recovery and storage in mature oil field: A case study from Cambay Basin. *J. Geol. Soc. India* **2016**, *88*, 273–280. [CrossRef]
31. Sengupta, M.; Dai, J.; Volterrani, S.; Dutta, N.; Rao, N.S.; Al-Qadeeri, B.; Kidambi, V.K. Building a Seismic-Driven 3D Geomechanical Model in a Deep Carbonate Reservoir. In *SEG Technical Program Expanded Abstracts 2011*; Society of Exploration Geophysicists: Tulsa, OK, USA, 2011; pp. 2069–2073.
32. Rahman, M.J.; Fawad, M.; Choi, J.C.; Mondol, N.H. Effect of overburden spatial variability on field-scale geomechanical modeling of potential CO_2 storage site Smeaheia, offshore Norway. *J. Nat. Gas Sci. Eng.* **2022**, *99*, 104453. [CrossRef]
33. Fawad, M.; Rahman, M.J.; Mondol, N.H. Seismic-derived geomechanical properties of potential CO_2 storage reservoir and cap rock in Smeaheia area, northern North Sea. *Lead. Edge* **2021**, *40*, 254–260. [CrossRef]
34. Heidbach, O.; Rajabi, M.; Cui, X.; Fuchs, K.; Müller, B.; Reinecker, J.; Reiter, K.; Tingay, M.; Wenzel, F.; Xie, F.; et al. The World Stress Map database release 2016: Crustal stress pattern across scales. *Tectonophysics* **2018**, *744*, 484–498. [CrossRef]
35. Rahman, M.J.; Choi, J.C.; Fawad, M.; Mondol, N.H. Probabilistic analysis of Vette fault stability in potential CO_2 storage site Smeaheia, offshore Norway. *Int. J. Greenh. Gas Control* **2021**, *108*, 103315. [CrossRef]
36. Skurtveit, E.; Choi, J.C.; Osmond, J.; Mulrooney, M.; Braathen, A. 3D fault integrity screening for smeaheia CO_2 injection site. In Proceedings of the 14th Greenhouse Gas Control Technologies Conference, Melbourne, Australia, 21–26 October 2018; pp. 21–26.

37. Thompson, N.; Andrews, J.S.; Wu, L.; Meneguolo, R. Characterization of the in-situ stress on the Horda platform–A study from the Northern Lights Eos well. *Int. J. Greenh. Gas Control* **2022**, *114*, 103580. [CrossRef]
38. Gassnova. Troll Kystnær Subsurface Status Report. Report no. TL02-ROS-Z-RA-005, Rev. 3. 2012. Available online: https://ccsnorway.com/app/uploads/sites/6/2019/09/tl02-ros-z-ra-0005-troll-kystnaer-subsurface-status-report-rev03.pdf (accessed on 2 January 2022).
39. Michie, E.A.H.; Mulrooney, M.J.; Braathen, A. Fault interpretation uncertainties using seismic data, and the effects on fault seal analysis: A case study from the Horda Platform, with implications for CO_2 storage. *Solid Earth* **2021**, *12*, 1259–1286. [CrossRef]
40. Rahman, M.J.; Fawad, M.; Mondol, N.H. Organic-rich shale caprock properties of potential CO_2 storage sites in the northern North Sea, offshore Norway. *Mar. Pet. Geol.* **2020**, *122*, 104665. [CrossRef]
41. Chadwick, A.; Smith, D.; Hodrien, C.; Hovorka, S.; Mackay, E.; Mathias, S.; Lovell, B.; Kalaydjian, F.; Sweeney, G.; Benson, S.; et al. The realities of storing carbon dioxide—A response to CO_2 storage capacity issues raised by Ehlig-Economides & Economides. *Nat. Preced* **2010**. [CrossRef]

SECTION-3

(APPENDICES)

APPENDIX-1

RP-1

Reservoir Fluid Effect on Caprock Properties in the Horda Platform Area, Northern North Sea.

Md Jamilur Rahman
Manzar Fawad
Nazmul Haque Mondol

GHGT-15, 2021

15th International Conference on Greenhouse Gas Control Technologies, GHGT-15

15th - 18th March 2021 Abu Dhabi, UAE

Reservoir fluid effect on caprock properties in the Horda Platform area, northern North Sea

Md Jamilur Rahman[a*], Manzar Fawad[a], Nazmul Haque Mondol[a,b]

[a]*Department of Geosciences, University of Oslo (UiO), Oslo-0371, Norway*
[b]*Norwegian Geotechnical Institute (NGI), Oslo-0855, Norway*

Abstract

Upper Jurassic organic-rich shales' caprock properties in the Horda Platform area are crucial due to their importance as primary seals for the Middle Jurassic reservoir sandstones. The reservoir sandstones are Sognefjord, Fensfjord, and Krossfjord formations. These reservoir sandstones are overlain by the Upper Jurassic Draupne and Heather Formation Shales. Caprock failure due to injection-related pore pressure change is one of the critical risks for CO_2 storage. The thick gas column in Troll East Field, located in the Horda Platform area, can consider an analog for a CO_2 post-injection scenario in the area. Evaluating the caprock properties above the thick gas column in the Troll Field helps to understand the area's caprock integrity qualitatively. This study assesses Draupne and Heather Formation Shales' caprock properties using petrophysical and rock physical analyses. Four exploration wells from the Troll East area consider in this study where wells 31/3-1 and 31/6-1 have gas columns of approximately 224 and 222 m, respectively, and two other wells (31/3-3 and 31/6-3) are water wet. The exhumation correction suggests that Draupne and Heather Formations of four studied wells' maximum burial depth experienced only the mechanical compaction. Two rock physics templates, such as Vp versus density and Young's modulus versus Poisson's ratio, are used to evaluate the caprock behavior due to HC accumulation-related overpressure. The caprock shales in wells with gas column show a significantly soft nature compared to the shale in the dry well 31/3-3. However, a dry well (31/6-3) also shows remarkably low stiffness. The pressure changes due to the HC accumulation might change the pressure above the reservoir. The caprocks may behave more ductile due to the generation of non-connected micro-fractures. However, fracture connectivity might initiate the caprock's mechanical failure, which poses a significant risk in CO_2 post-injection scenario. Moreover, a significantly thick caprock in well 31/6-3 may have influenced the caprock properties differently compared to the other dry well. The caprock mechanical behavior is complex and influenced by several factors.

Keywords: Caprock properties characterization; CO_2 storage risk; mechanical compaction; seal rock Ductility

1. Introduction

Characterization of caprock properties becomes crucial for safe CO_2 storage into saline aquifers. Horda Platform (HP) is one of the areas in the Norwegian Continental Shelf (NCS), where several potential large-scale CO_2 storage sites (i.e., Alpha, Beta, Longship, etc.) are under evaluation. This research characterizes the Upper Jurassic caprock

*Corresponding author. Tel.: +4741383196
E-mail address: m.j.rahman@geo.uio.no

(i.e., Draupne and Heather formations) in the HP area, overlying the Middle Jurassic sandstones (i.e., Sognefjord, Fensfjord, and Krossfjord formations). The success of CO_2 injection projects primarily depends on sealing effectiveness, mainly caprock integrity. There might be possibilities of shear failure or fracture in caprock shale during injection and post-operation, also generating micro-seismicity. These phenomena depend on the caprock mechanical behaviors (i.e., brittleness) and in-situ stress conditions. Therefore, careful investigations of caprock mechanical properties are necessary to evaluate any CO_2 leakage risk.

Caprock properties vary significantly because caprock shales deposited in a wide range of environments (i.e., floodplains, lakes, shorefaces, prodelta areas, abyssal plains, etc.), owing to different origin (i.e., weathering products, biogenic remains), and exposure to post-depositional processes (e.g., bioturbation, compaction, cementation, recrystallization, dissolution, organic maturation, etc.) [1]. These processes lead to significant changes in grain size distribution and mineralogy within the shale, which control the compaction (i.e., Mechanical and Chemical) after deposition. Mechanical compaction (MC) governs by the effective vertical stress, which is the difference between the total vertical stress and pore pressure [2]. If the pore pressure increases (due to HC accumulation in sandstone or fluid expulsion in shale), the overall vertical stress is reduced, resulting in less mechanical compaction. The rock properties change in the MC domain via frictional slippage, rotation, sliding [3], and reorientation [4] of the grains under perpetual vertical stress (i.e., in the extensional basin). However, MC's intensity is different in sandstones and shales. It depends on the geological parameters such as grain size, sorting, and fluid expulsion rate from the compacting sediments. For example, coarse grain shale (Kaolinite) compact readily compared to the fine-grained shale (Smectite), which compacts less due to the increase in fluid pressure because of low permeability [5-8].

The mechanical behavior of caprock, often classified as brittleness or fracability [9-14], is a complex function of rock strength, lithology, texture, effective stress, temperature, fluid type [15-18], diagenesis, TOC [19], natural fractures and other planes of weakness [20, 21]. The effect of depth on brittleness can work in both directions because an increase in depth increases diagenesis, increasing brittleness, while the higher temperature and pressure augment the ductile behavior [9]. Moreover, the exhumation and overpressure make the whole process more complicated.

The caprock shale geomechanical properties (i.e., Young's modulus and Poisson's ratio) can be evaluated using rock physics templates. Young's modulus is a proxy for caprock stiffness, while Poisson's ratio describes lateral expansion to axial contraction [22]. This study evaluated Draupne and Heather Formations' geomechanical properties' variation using rock physics templates in the Horda Platform area, northern North Sea. The focus is to assess the influence of reservoir pore pressure changes on caprock properties by petrophysical and rock physical analysis.

2. Geology of the Horda Platform (HP)

The study area experienced two main rifting events that occurred in the Permo-Triassic and the Upper Jurassic to Mid-Cretaceous times [23] and formed several N-S trending faults (i.e., Vette, Tusse, Svartarv, Troll, etc.) (Fig. 1). These faults are created in the 1st rifting event and reactivated during the 2nd event and are believed to be rooted in Caledonian zones of crustal weakness [23]. These faults also demarcate the structural elements and create compartmentalization within the Horda Platform (Fig. 1b). The 1st rifting event was centered below the Horda Platform, and thick syn-depositional wedges were deposited. However, during the 2nd event, major rifting took place, and the tilting shifted westward, while a weak stretching held on the Horda Platform itself [23-25]. The primary caprocks (Draupne and Heather formations) in HP were deposited during the 2nd rifting event with minimal tectonic influence because of the rifting's westward shift episode (Fig. 2a).

The structural well correlations show the present-day depth difference of Draupne and Heather formations within the studied wells (Fig. 2c). Wells close to the footwall of the Tusse fault (i.e., 31/3-1 and 31/6-1) are shallower compare to the wells on the hanging wall (i.e., 31/3-3 and 31/6-3). Similarly, footwall wells 31/3-1 and 31/6-1 contain hydrocarbon columns with height 224 and 222 m, respectively, whereas the other two wells are dry. Caprocks (i.e., Draupne and Heather formation) thickness also varies significantly and depends on well location respective to faults (thickness increases away from the footwall).

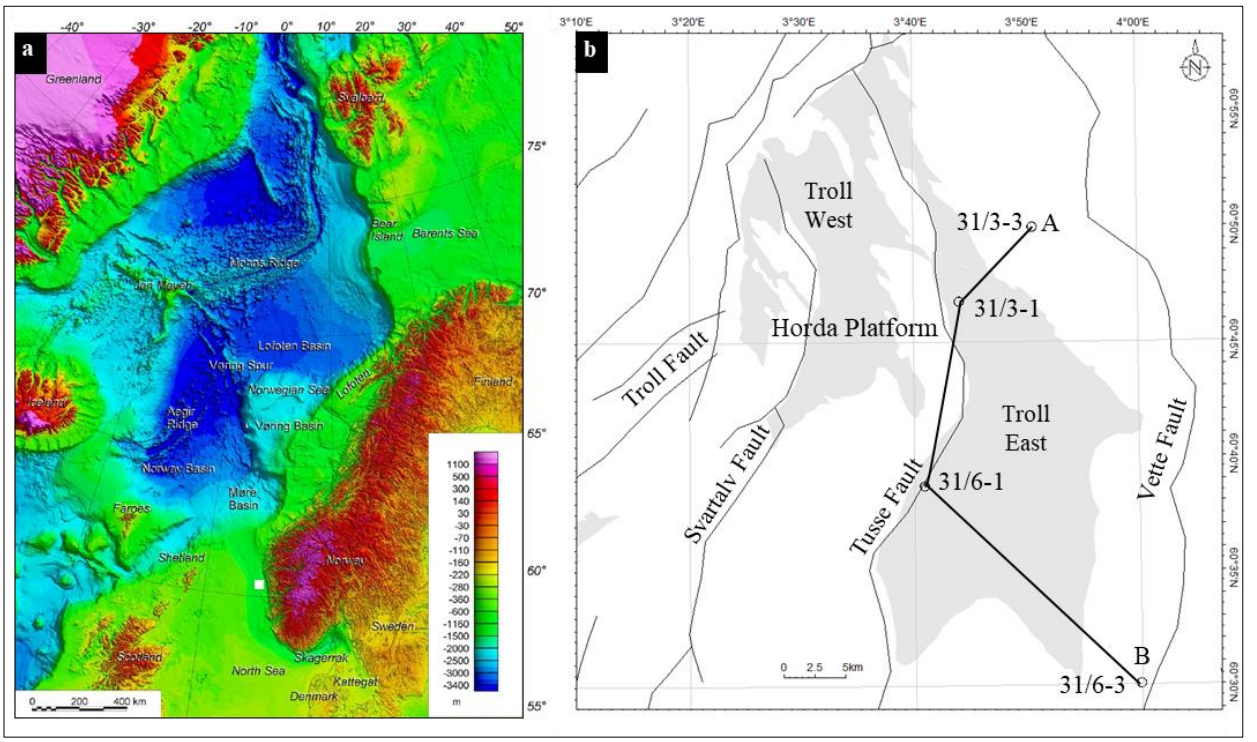

Fig. 1. (a) The white square shows the study area on the Norwegian Continental Shelf (modified after Olesen et al. [26]), (b) The locations of the studied wells correspond to the structural element and major faults. The grey shaded areas are the hydrocarbon fields within the study area. The black line A-B represents the correlation presented in Figure 2.

The Upper Jurassic Heather Formation shale consists mainly of grey silty claystone with thin streaks of limestone deposited in an open marine environment. It overlies and interfingers with the main reservoir rocks Krossfjord, Fensfjord, and Sognefjornd formation sandstones of the Viking Group (Fig. 2a) [27]. Stewart et al. [28] divided Heather Formation in the Horda Platform area into three sub-units (A, B, and C). This study evaluates only the Heather C unit, which is sandwiched between the Sognefjord and Draupne Formations. The primary caprock Draupne Formation shale is part of the Viking Group and consists of dark grey-brown to black, usually non-calcareous, carbonaceous, occasionally fissile claystone. The formation was deposited in an open marine environment with restricted bottom circulation and often with anaerobic conditions [27]. Interbedded sandstone and siltstone, as well as minor limestone streaks and concretions, are also present. Draupne Formation generally has a diachronous contact with the Heather Formation in the lower boundary. In contrast, the upper boundary of the Draupne Formation is usually characterized by Cretaceous rocks (Cromer Knoll Group), which have a higher velocity and lower gamma-ray response than the over and underlying rocks [27].

3. Database and Methods

The caprock's mechanical behavior was evaluated using the wireline log data from four exploration wells located between the Vette and Tusse faults (Fig. 1b). Table 1 shows the exhumation and thickness of caprocks (i.e., Draupne and Heather Formations) and reservoir rocks (i.e., Sognefjord, Fensfjord, and Krossfjord formations) within the studied wells. Draupne Formation thickness varies significantly (32 to 125 m), while the reservoir units' thickness variations are minimal. The wells are located in Bjørgvin Arch (31/3-1 and 31/3-3), Stord Basin (31/6-1 and 31/6-3) [27], and are within the mechanical compaction zones (considering before exhumation depth) [30]. In this research, the available wireline logs (i.e., Gamma-ray, density, P-sonic, resistivity, etc.) from the studied wells were analyzed.

Moreover, the SEM images were analyzed by using the cutting samples from well 31/3-1. The Vs (shear wave velocity) is not acquired in any of the studied wells; therefore, a machine learning technique (i.e., Random Forest) was used to predict Vs. We tested several machine learning techniques, where the Random Forest yielded comparatively better results. The dynamic mechanical properties such as Young's Modulus (E), and Poisson's Ratio (ν) were calculated using the following equations:

$$E = \frac{\rho V_s^2 (3V_p^2 - 4V_s^2)}{V_p^2 - V_s^2} \quad (1)$$

$$\nu = \frac{V_p^2 - 2V_s^2}{2(V_p^2 - V_s^2)} \quad (2)$$

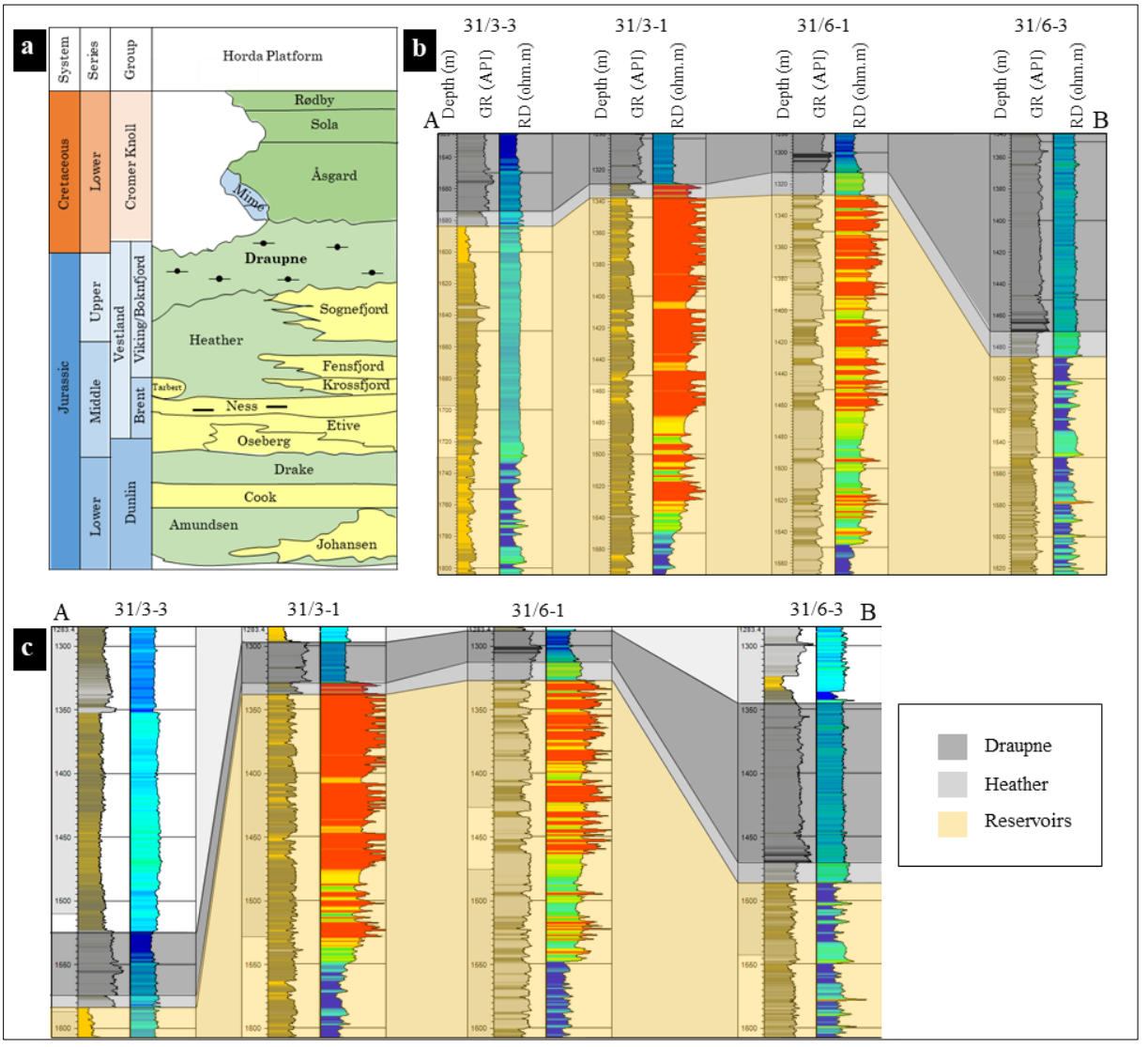

Fig. 2. (a) A generalized Jurassic and Cretaceous stratigraphic succession in the study area (modified from NPD CO2 Atlas, [29]). Well correlations flatten on Draupne Formation (b) and flatten on 0 m SSTVD (c). The structural correlation (c) shows the present-day depth variations of Draupne and Heather formations within the studied wells. The deep resistivity value shows the mineralogy, compaction, and fluid variations within wells.

The log driven dynamic Young's modulus was converted to log-based static values using Mullen et al. [31] equation:

$$E_{stat} = [\frac{E_{dyn}}{3.3674}]^{2.042} \quad (3)$$

The P-wave velocity (Vp) versus density (ρ) cross-plot is a useful tool for acoustic property characterization used in this research. The background template (i.e., friable sand model, 50% and 100% clay volume curves) was adapted from Avseth et al. [32]. This model is called the Dvorkin-Gutierrez silty shale model, where the saturated elastic moduli of shale were estimated using the Hashin-Shtrikman lower bound as a function of clay content, assuming the added silt grains consist of 100% quartz [32]. The mechanical properties such as Young's Modulus (E), and Poisson's Ratio (ν) were characterized using the templates where the background curve was adapted from Grieser and Bray [33]. This template represents the ductile to brittle region transition of the seal rock used to evaluate the studied well caprocks.

Table 1. Maximum burial depth, present depth, and thickness of Draupne and Heather formations penetrated by the studied wells. The structural elements, as suggested by NPD [27].

Wells	Structural Element	Draupne Formation top depth (m BSF)		Thickness (m) Draupne	Heather Formation[b] top depth (m BSF)		Thickness (m) Heather	Sognefjord Formation top depth (m BSF)		Thickness (m) Sognefjord[c]
		Present	Max[a]		Present	Max[a]		Present	Max[a]	
31/3-1	Bjørgvin Arch	963	1343	32	995	1375	9	1004	1384	418
31/3-3		1193	1713	49	1242	1762	10	1252	1771	524
31/6-1	Stord Basin	986	1316	25	1011	1341	14	1025	1355	424
31/6-3		1044	1474	125	1169	1599	16	1185	1615	421

[a]Corrected for exhumation estimated from Vp-Depth trend; [b]Only considered interval between Draupne and top reservoir section; [c]Whole reservoir units (Sognefjord, Fensfjord & Krossfjord formations)

Elastic impedance-based brittleness index (BI) was also estimated, which is the qualitative measure of rock behavior. There are many empirical equations [13, 33-37], out of which the two methods tested were proposed by Grieser and Bray [33] and Fawad and Mondol [37]. The Grieser and Bray [33] empirical equation is based on the normalization of Young's modulus and Poisson's ratio and stated that:

$$BI^1 = \frac{1}{2}[\frac{E-E_{min}}{E_{max}-E_{min}} + \frac{\nu-\nu_{max}}{\nu_{min}-\nu_{max}}], \quad (4)$$

where E is static Young's modulus, E_{max} is 69 GPa, E_{min} is 0 GPa, and ν is static Poisson's ratio, ν_{max} is 0.5, ν_{min} is 0. Also, the higher the BI^1 value is, the more brittle the caprock would be.

The other equation proposed by Fawad and Mondol [37] is:

$$BI^2 = \frac{0.00044AI-1.3-\sqrt{0.62\frac{R_W}{R_D}}(0.00019AI+0.25)}{1.35+0.00028AI}, \quad (5)$$

where AI is the acoustic impedance (gm/cm^3 x m/s); R_D is true formation resistivity (ohm-m), and R_W is the resistivity of pore water (ohm-m). Equation 5 is based on the physical and elastic properties of the organic matter (kerogen), quartz, and clay/water as end-members of a ternary model, and here the brittleness is defined as an increase in stiffness of a rock due to compaction and addition of stiff mineral content (quartz, carbonate, or dolomite).

4. Results

4.1. Elastic properties of the caprock

The velocity (Vp) and density (ρ) data points from Draupne and Heather formations are evaluated using the wireline logs from wells 31/3-1 and 31/3-3 (Fig. 3). The caprock with a thick hydrocarbon column in well 31/3-1 shows significantly low density and velocity compared with the dry well 31/3-3. Considering gamma-ray (GR) value as a proxy of grain size (assuming higher GR values represent fine grains), the wells do not follow the compositional trend (Fig. 3b). The various gamma-ray data points are clustered in low Vp and ρ zone in well 31/3-1, while in well 31/3-3, the data points follow an increasing trend irrespective of GR values. Moreover, the wells do not follow the background curves, which are estimated based on the composition variations. Although the Heather Formation has lower gamma-ray values than Draupne (larger grain size), the data points' distribution does not follow any trend.

Compare the properties with other wells in the same fault block (between Vette and Tusse fault), 31/6-1, and 31/6-6 wells plotted in Vp versus density cross-plot, 31/6-1 has a thick gas column like 31/3-1 and 31/6-3 is a dry well (Fig. 3c). Both wells are clustered in low velocity and density zone except few data points from Draupne and the Heather Formations in well 31/6-3. The gamma-ray value represents a similar range with 31/3-1 except the Heather Formation data points from 31/6-3, which compacted more (high Vp and ρ) than the other data (Fig. 3d).

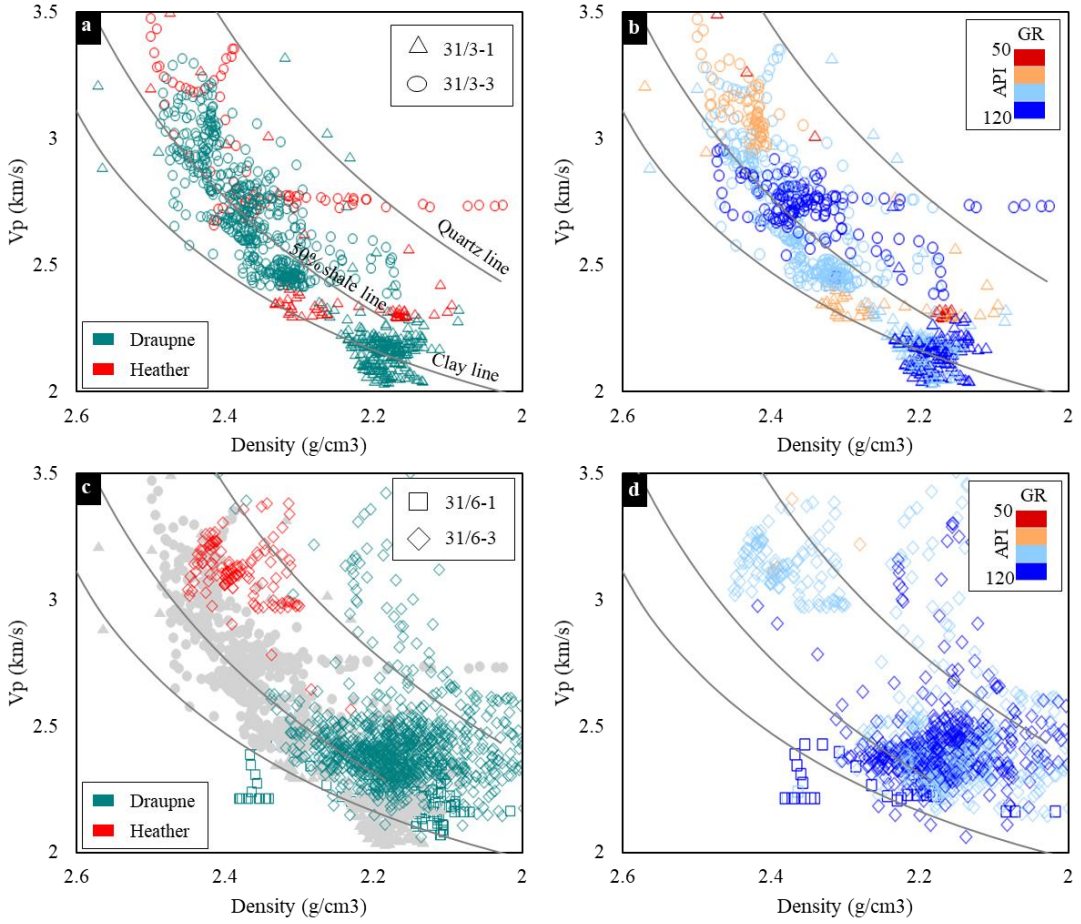

Fig. 3. Vp versus density cross-plot of Draupne and Heather Formation data points from well 31/3-1 and 31/3-3 color-coded with formation names (a), Gamma-ray (b). Wells 31/6-1 and 31/6-3 color-coded with formation names (c) and Gamma-ray (d). The grey background data points in (c) are from wells 31/3-1 and 31/3-3. The reference curves are adapted from Avseth et al. [32].

4.2. Geomechanical properties and brittleness

Mechanical properties of studied wells are evaluated using the Young's modulus (E) versus poisson's ratio (PR) cross-plots, where the converted static E was used (Fig. 4). There is no separation between the Draupne and Heather Formation data points like the elastic properties.

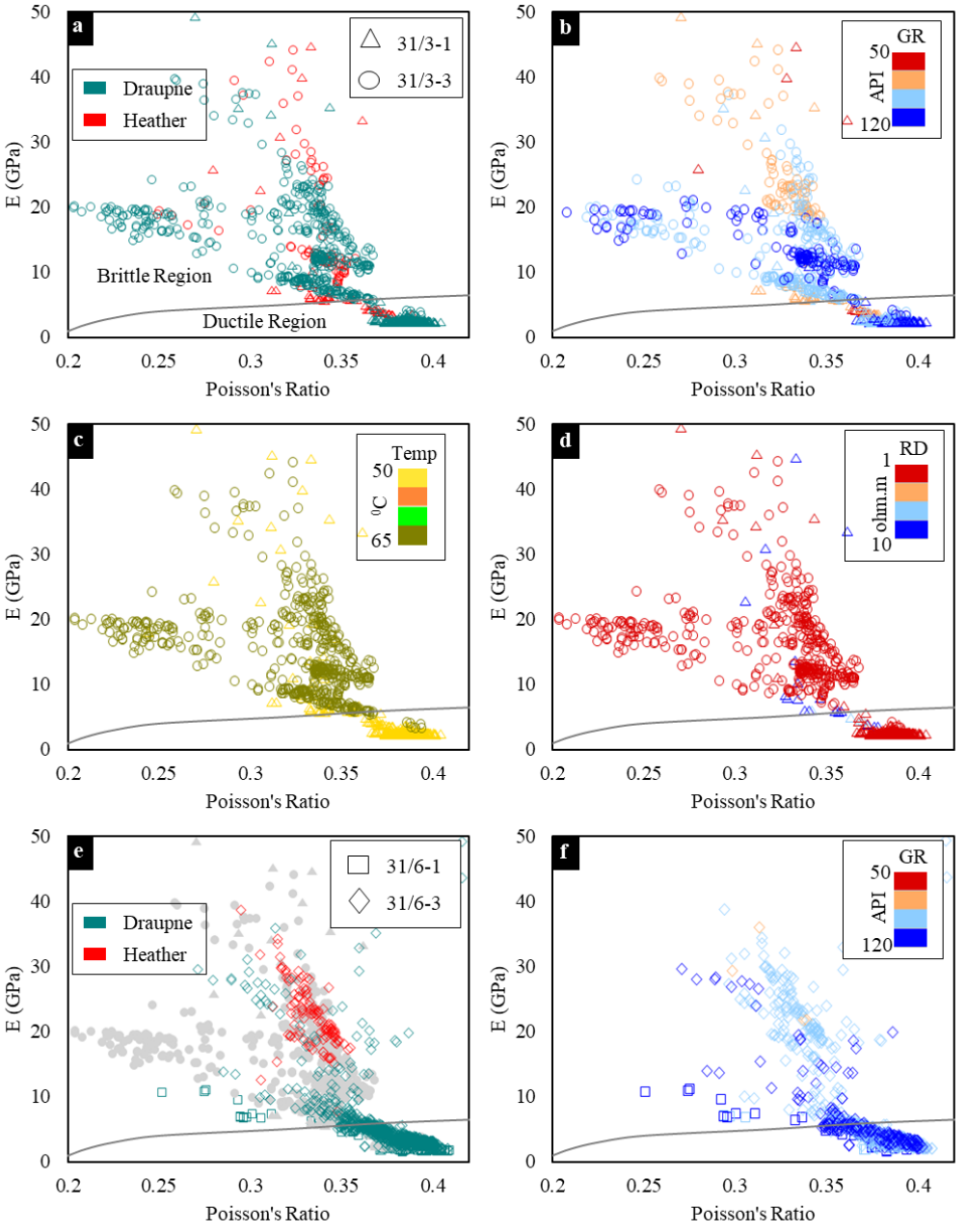

Fig. 4. Cross-plots of Young's modulus (E) and Poisson's ratio of Draupne and Heather Formation data points from well 31/3-1 and 31/3-3 color-coded with formation names (a), Gamma-ray (b), temperature (c), and deep resistivity (d). Well 31/6-1 and 31/6-3 color-coded with formation names (e), with grey background data points from well 31/3-1 and 31/3-3 and GR (f). The reference curves are adapted from Greiser and Bray [33].

The well with a thick gas column has very high PR with very low E values, while the other well (31/3-3) data points are widely distributed with a large range of E and PR. There is no compositional influence observed; however, the high GR data from well 31/3-3 shows a significant decrease in PR with a gentle increase in E compared to a significant increase in E with a gentle PR decrease containing low GR values (Fig. 4b). Moreover, the exhumed temperature shows two values following the depth difference, though the variation is not significant (Fig. 4c). The low deep resistivity values also reveal that the caprocks are immature, and no gas leaking took place through fractures in well 31/3-1 (Fig. 4d). Compared with the background curves, most data from well 31/3-1 fall within the ductile region, while the dry well data points are displayed within the brittle zone.

The Draupne Formation in wells 31/6-1 and 31/6-3 plot generally within the ductile region with high PR and low E values, whereas the Heather Formation data fall in the brittle zone with few data points from Draupne (Fig. 4e). Moreover, comparing the Draupne Formation within the dry wells, the formation in well 31/3-3 shows higher stiffness (high E and low PR) than Draupne in well 31/6-3.

The brittleness indices (BI) values range between 0.1 to 0.5, where BI^2 illustrates a comparatively higher value than the corresponding BI^1 value. Moreover, the brittleness increasing trend in both methods has significant differences. The BI^1, which is calculated using E and PR, increases with increasing E and PR (Fig. 5a). However, the increasing brittleness trend in BI^2 depends on the changes in E while the PR has a long-spread within the same BI values (Fig. 5b). According to the template, the data points from wells 31/3-1, 31/6-1, and 31/6-3 fall within the ductile region, while the data points from 31/3-3 and few data from 31/6-3 (i.e., few data from Draupne and Heather formations) fall within the brittle zone. However, the ductile zone data show significantly low BI values in both methods (~0.1 to 0.2).

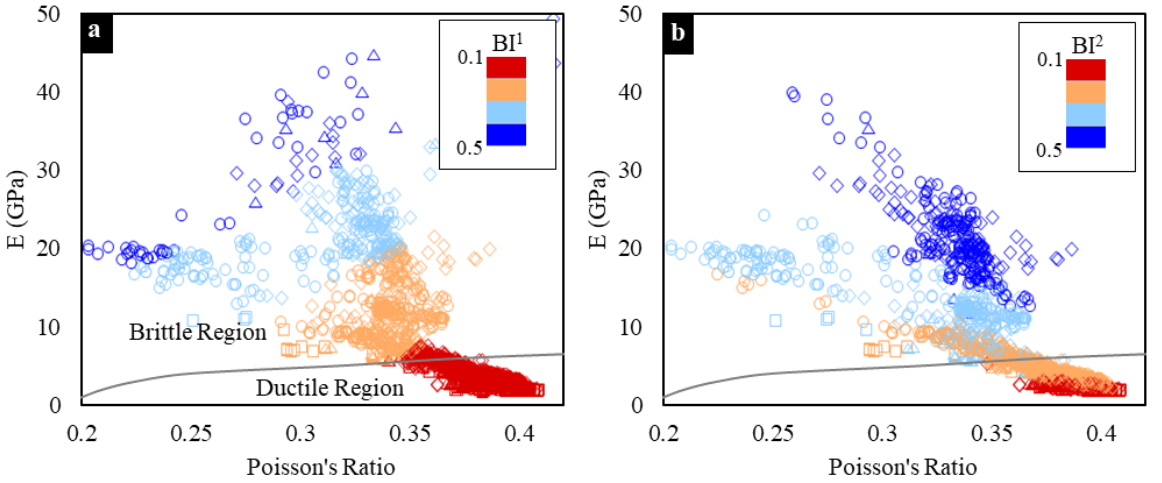

Fig. 5. Young's modulus versus Poisson's ratio cross-plots of Draupne and Heather formations color-coded by BI^1 (a), and BI^2 (b) with the reference curve adapted from Grieser and Bray [33].

5. Discussion

Caprock behavior under stress is a function of mechanical properties of the rock, effective pressure, and shear zone geometry [18, 38]. For example, a brittle rock is more likely to dilate at a given effective pressure than a ductile one. Moreover, Pore pressure becomes an important parameter when the pressure in the underlying reservoir is significantly high. The risk of vertical natural hydraulic fractures through the seal rock increases dramatically in such a scenario. The pore pressure increase within reservoirs in wells 31/3-1 and 31/6-1 due to gas accumulation, hence decrease the vertical effective stress and mechanical compaction [4]. These overpressure phenomena within the reservoir might

increase the caprock's pressure, hence generating micro-fractures (Fig. 6). However, the deep resistivity log indicated no HC migration upward into the caprock, demonstrating that the caprock did not fail, but the pressure increased the ductility [9]. We observed this effect in mechanical properties with low E and high PR values. In contrast, the normal pore pressure within the reservoir showed a high modulus with higher brittleness. However, a significant increase in caprock thickness might influence the seal behavior.

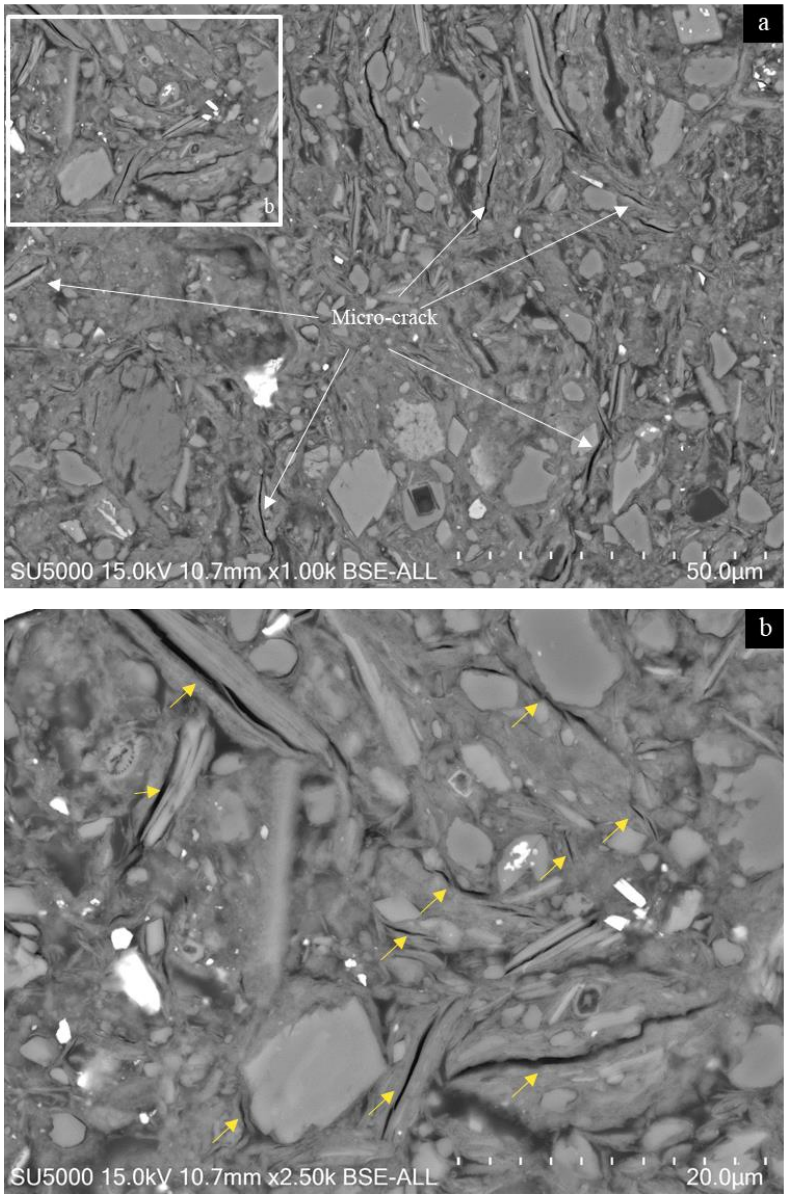

Fig. 6. SEM images of cutting samples from the well 31/3-1 show disconnected small micro-cracks within the clay matrix. Note that the images have scale differences.

Although well 31/6-3 is dry, the ductile nature of caprock compares with other dry well (31/3-3) might be the influence of the caprock thickness and the depositional variations. Therefore, caprock's soft nature due to the thick column of HC within the below reservoir might be another parameter along with increasing TOC explained by Hansen

et al. [39] (Fig. 7). Many other parameters, such as grain size [5-8], clay mineralogy [6], fabric [1], etc., also play a significant role in controlling rock properties during mechanical compaction.

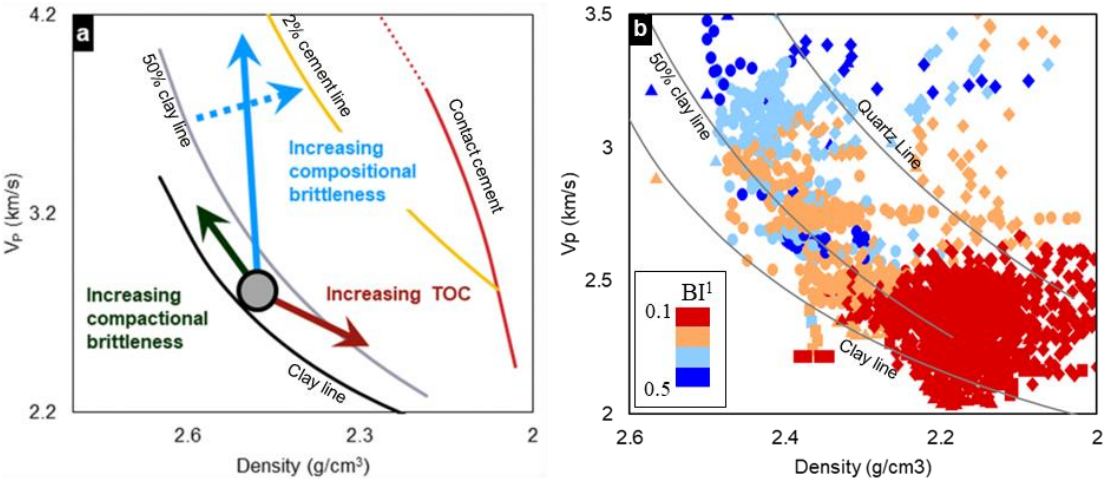

Fig. 7. (a) Influence of different processes on shale properties with the rock physics template summarized by Hansen et al. [39], (b) Draupne and Heather shale data points color-coded with BI[1].

6. Conclusions

The effect of a thick HC column on caprock mechanical behavior is evaluated. The critical observations of this study are as follow:

- A thick gas column below the caprock significantly changes the mechanical properties resulting in a more ductile behavior.
- The caprock behaves more ductile with non-connected micro-fracture generated within the caprocks due to the thick hydrocarbon column within the underlying reservoir. However, if the fracture connectivity increases, the top seal's mechanical failure may increase.
- Thick caprock has softer behavior irrespective of fluid within the underlying reservoir.

Acknowledgments

We are grateful for the Research Council of Norway's financial support for the OASIS (Overburden Analysis and Seal Integrity Study for CO_2 Sequestration in the North Sea) project (NFR-CLIMIT project #280472). We are indebted to the additional funding and data provided by Norwegian Petroleum Directorate (NPD), Gassnova, Equinor, and Total. Academic software licenses have been provided by Lloyd's Register for Interactive Petrophysics and Schlumberger for Petrel.

References

[1] B. S. Hart, J. H. S. Macquaker, and K. G. Taylor, “Mudstone (‘shale’) depositional and diagenetic processes: Implications for seismic analyses of source-rock reservoirs,” Interpretation, vol. 1, no. 1, pp. B7–B26, 2013.

[2] K. Bjørlykke, K. Høeg, and N. H. Mondol, “Introduction to Geomechanics: stress and strain in sedimentary basins,” in Petroleum geoscience, Springer, 2015, pp. 301–318.

[3] F. A. Chuhan, A. Kjeldstad, K. Bjørlykke, and K. Høeg, “Porosity loss in sand by grain crushing—Experimental evidence and relevance to

reservoir quality," Mar. Pet. Geol., vol. 19, no. 1, pp. 39–53, 2002.
[4] K. Bjørlykke and J. Jahren, "Sandstones and sandstone reservoirs," in Petroleum Geoscience, Springer, 2015, pp. 119–149.
[5] V. Storvoll, K. Bjørlykke, and N. H. Mondol, "Velocity-depth trends in Mesozoic and Cenozoic sediments from the Norwegian Shelf," Am. Assoc. Pet. Geol. Bull., vol. 89, no. 3, pp. 359–381, 2005.
[6] N. H. Mondol, K. Bjørlykke, J. Jahren, and K. Høeg, "Experimental mechanical compaction of clay mineral aggregates—Changes in physical properties of mudstones during burial," Mar. Pet. Geol., vol. 24, no. 5, pp. 289–311, 2007.
[7] Ø. Marcussen, B. I. Thyberg, C. Peltonen, J. Jahren, K. Bjørlykke, and J. I. Faleide, "Physical properties of Cenozoic mudstones from the northern North Sea: Impact of clay mineralogy on compaction trends," Am. Assoc. Pet. Geol. Bull., vol. 93, no. 1, pp. 127–150, 2009.
[8] B. Thyberg, J. Jahren, T. Winje, K. Bjørlykke, and J. I. Faleide, "From mud to shale: Rock stiffening by micro-quartz cementation," First Break, vol. 27, no. 2, 2009.
[9] F. P. Wang and J. F. W. Gale, "Screening criteria for shale-gas systems," 2009.
[10] R. M. Holt, E. Fjaer, O. M. Nes, and H. T. Alassi, "A shaly look at brittleness," 2011.
[11] R. M. Holt, E. Fjær, J. F. Stenebråten, and O.-M. Nes, "Brittleness of shales: relevance to borehole collapse and hydraulic fracturing," J. Pet. Sci. Eng., vol. 131, pp. 200–209, 2015.
[12] Y. Yang, H. Sone, A. Hows, and M. D. Zoback, "Comparison of brittleness indices in organic-rich shale formations," 2013.
[13] X. Jin, S. N. Shah, J.-C. Roegiers, and B. Zhang, "Fracability evaluation in shale reservoirs-an integrated petrophysics and geomechanics approach," 2014.
[14] E. Rybacki, T. Meier, and G. Dresen, "What controls the mechanical properties of shale rocks?–Part II: Brittleness," J. Pet. Sci. Eng., vol. 144, pp. 39–58, 2016.
[15] J. Handin and R. V Hager Jr, "Experimental deformation of sedimentary rocks under confining pressure: Tests at room temperature on dry samples," Am. Assoc. Pet. Geol. Bull., vol. 41, no. 1, pp. 1–50, 1957.
[16] J. Handin, R. V Hager Jr, M. Friedman, and J. N. Feather, "Experimental deformation of sedimentary rocks under confining pressure: pore pressure tests," Am. Assoc. Pet. Geol. Bull., vol. 47, no. 5, pp. 717–755, 1963.
[17] D. G. H. R. SJ, "Structural Geology of Rocks and Regions: Colorado." New York John Wiley and Sons, Inc, 1996.
[18] R. Nygård, M. Gutierrez, R. K. Bratli, and K. Høeg, "Brittle–ductile transition, shear failure and leakage in shales and mudrocks," Mar. Pet. Geol., vol. 23, no. 2, pp. 201–212, 2006.
[19] F. Walles, "A new method to help identify unconventional targets for exploration and development through integrative analysis of clastic rock property fields," 2004.
[20] D. Zhang, P. G. Ranjith, and M. S. A. Perera, "The brittleness indices used in rock mechanics and their application in shale hydraulic fracturing: A review," J. Pet. Sci. Eng., vol. 143, pp. 158–170, 2016.
[21] J. F. W. Gale, R. M. Reed, and J. Holder, "Natural fractures in the Barnett Shale and their importance for hydraulic fracture treatments," Am. Assoc. Pet. Geol. Bull., vol. 91, no. 4, pp. 603–622, 2007.
[22] E. Fjar, R. M. Holt, A. M. Raaen, and P. Horsrud, Petroleum related rock mechanics. Elsevier, 2008.
[23] P. S. Whipp, C. L. Jackson, R. L. Gawthorpe, T. Dreyer, and D. Quinn, "Normal fault array evolution above a reactivated rift fabric; a subsurface example from the northern Horda Platform, Norwegian North Sea," Basin Res., vol. 26, no. 4, pp. 523–549, 2014.
[24] A. M. Roberts, G. Yielding, N. J. Kusznir, I. Walker, and D. Dorn-Lopez, "Mesozoic extension in the North Sea: constraints from flexural backstripping, forward modelling and fault populations," in Geological Society, London, Petroleum Geology Conference series, 1993, vol. 4, no. 1, pp. 1123–1136.
[25] A. M. Roberts, N. J. Kusznir, G. Yielding, and H. Beeley, "Mapping the bathymetric evolution of the Northern North Sea: from Jurassic synrift archipelago through Cretaceous–Tertiary post-rift subsidence," Pet. Geosci., vol. 25, no. 3, pp. 306–321, 2019.
[26] O. Olesen et al., "New aeromagnetic and gravity compilations from Norway and adjacent areas: methods and applications," in Geological Society, London, Petroleum Geology Conference series, 2010, vol. 7, no. 1, pp. 559–586.
[27] NPD, "NPD FactPages," 2020. https://npdfactpages.npd.no/factpages/Default.aspx?culture=en.
[28] D. J. Stewart, M. Schwander, and L. Bolle, "Jurassic depositional systems of the Horda Platform, Norwegian North Sea: Practical consequences of applying sequence stratigraphic models," Nor. Pet. Soc. Spec. Publ., no. 5, pp. 291–323, 1995.
[29] "NPD CO2 Atlas Report," 2014.
[30] M. J. Rahman, M. Fawad, and N. H. Mondol, "Organic-rich shale caprock properties of potential CO2 storage sites in the northern North Sea, offshore Norway," Mar. Pet. Geol., vol. 122, p. 104665, 2020.
[31] M. J. Mullen, R. Roundtree, and G. A. Turk, "A composite determination of mechanical rock properties for stimulation design (what to do when you don't have a sonic log)," 2007.
[32] P. Avseth, T. Mukerji, and G. Mavko, "Quantitative seismic interpretation: Applying rock physics tools to reduce interpretation risk: Cambridge," 2005.
[33] W. V. Grieser and J. M. Bray, "Identification of production potential in unconventional reservoirs," 2007.
[34] R. Rickman, M. J. Mullen, J. E. Petre, W. V. Grieser, and D. Kundert, "A practical use of shale petrophysics for stimulation design optimization: All shale plays are not clones of the Barnett Shale," 2008.
[35] R. K. Sharma and S. Chopra, "New attribute for determination of lithology and brittleness," in SEG Technical Program Expanded Abstracts 2012, Society of Exploration Geophysicists, 2012, pp. 1–5.
[36] J. Chen*, G. Zhang, H. Chen, and X. Yin, "The construction of shale rock physics effective model and prediction of rock brittleness," in SEG Technical Program Expanded Abstracts 2014, Society of Exploration Geophysicists, 2014, pp. 2861–2865.
[37] M. Fawad and N. H. Mondol, "Proposed unpublished brittleness equation," 2020.
[38] G. M. Ingram, J. L. Urai, and M. A. Naylor, "Sealing processes and top seal assessment," in Norwegian Petroleum Society Special Publications,

vol. 7, Elsevier, 1997, pp. 165–174.

[39] J. A. Hansen, N. H. Mondol, F. Tsikalas, and J. I. Faleide, “Caprock characterization of Upper Jurassic organic-rich shales using acoustic properties, Norwegian Continental Shelf,” Mar. Pet. Geol., vol. 121, p. 104603, Nov. 2020, doi: 10.1016/j.marpetgeo.2020.104603.

RP-2

Seismic Reservoir Characterization of Potential CO_2 Storage Reservoir Sandstones in Smeaheia Area, Northern North Sea.

Manzar Fawad
Md Jamilur Rahman
Nazmul Haque Mondol

Journal of Petroleum Science and Engineering, 2021

Journal of Petroleum Science and Engineering 205 (2021) 108812

Contents lists available at ScienceDirect

Journal of Petroleum Science and Engineering

journal homepage: http://www.elsevier.com/locate/petrol

Seismic reservoir characterization of potential CO_2 storage reservoir sandstones in Smeaheia area, Northern North Sea

Manzar Fawad [a,*], MD Jamilur Rahman [a], Nazmul Haque Mondol [a,b]

[a] University of Oslo, Norway
[b] Norwegian Geotechnical Institute, Norway

ARTICLE INFO

Keywords:
CO_2 storage
Sognefjord formation
Fensfjord formation
Krossfjord formation
Porosity
Shaliness
Permeability
Prestack seismic inversion

ABSTRACT

Evaluating any subsurface CO_2 storage site comprises the reservoir, seal, and overburden investigation to mitigate injection and storage-related complications. The Upper-Middle Jurassic Sognefjord, Fensfjord, and Krossfjord formation sandstones are potential CO_2 storage reservoirs at the Smeaheia area, northern North Sea. The Smeaheia area is located east of the Troll oil and gas field. The Upper Jurassic organic-rich Heather and Draupne Formation shales are the main seals for the sandstone reservoirs. In this study, we carried out a prestack seismic inversion to obtain elastic property cubes of acoustic impedance (*AI*), velocity ratio (*Vp/Vs*), and bulk density (*RhoB*). From these elastic cubes, we obtained the reservoir properties such as porosity (*Phi*), shaliness (V_{sh}), and permeability (k) of Sognefjord, Fensfjord, and Krossfjord formations. We introduced two new equations to extract the shale volume and porosity cubes from the inverted elastic cubes in the present study. These equations are nonlinear based on the *AI* versus *Vp/Vs* rock physics template. Both equations are correlated first with the well log data and then applied on the elastic property cubes (*AI* versus *Vp/Vs*) to obtain the V_{sh} and *Phi* property cubes. An additional porosity cube (*PhiD*) was generated from the inverted *RhoB* for comparison. Finally, using an empirical equation, permeability was extracted from the porosity cube. The reservoir properties we derived from 3D seismic, in addition to the well log, revealed the vertical and lateral variations of porosity, shaliness, and permeability in the Smeaheia area. We used these reservoir properties to infer the depositional environment and the viability of reservoirs for CO_2 storage. The depositional environments identified were shoreface and deltaic from the extracted sand-body geometries. We found the Sognefjord Formation possessing the best reservoir properties, followed by the Fensfjord Formation as the secondary storage potential. In contrast, the Krossfjord Formation owed the lowest reservoir quality in the Smeaheia area.

1. Introduction

Subsurface CO_2 storage is one of the many solutions proposed for reducing greenhouse gas emissions in the atmosphere. A hydrocarbon trap is a demonstration of a working reservoir, seal, and overburden system; however, in a subsurface geological CO_2 sequestration, the storage and capping elements viability requires proper investigation. This study focuses on a prestack seismic inversion to obtain the reservoir properties (e.g., porosity, shaliness, and permeability) of Sognefjord, Fensfjord, and Krossfjord formations in a potential CO_2 storage site "Smeaheia" offshore Norway (Fig. 1a). The Smeaheia area is located east of the Troll field in the Bjørgvin Arch and Stord Basin in the northern North Sea. The area is bounded by an array of faults separating the Troll Field in the west by the Vette Fault (VF) and the Caledonian Basement Complex in the east by the Øygarden Fault Complex (ØFC). There are two structural closures in the Smeaheia area 'Alpha-32/4-1' in the east and the 'Beta-32/2-1' in the west, possessing dry wells (Fig. 1b). The area is among the few potential CO_2 storage sites under consideration in the northern North Sea.

Fig. 2a shows a stratigraphic succession (Jurassic and younger rocks) at the exploration well 32/4-1 (Alpha prospect) in the Smeaheia area. The primary reservoir sandstone is the Sognefjord Formation, which consists of coastal-shallow marine sands, overlain by the Heather and Draupne Formation shales, the main caprocks in the area. The Sognefjord Formation is medium to coarse-grained, well-sorted, friable, locally micaceous, and minor argillaceous sandstone. The Fensfjord Formation is fine to medium-grained, well-sorted, and moderately friable to consolidated sandstones with shale intercalations. The

* Corresponding author.
E-mail address: manzar.fawad@geo.uio.no (M. Fawad).

https://doi.org/10.1016/j.petrol.2021.108812
Received 19 October 2020; Received in revised form 26 March 2021; Accepted 11 April 2021
Available online 20 April 2021

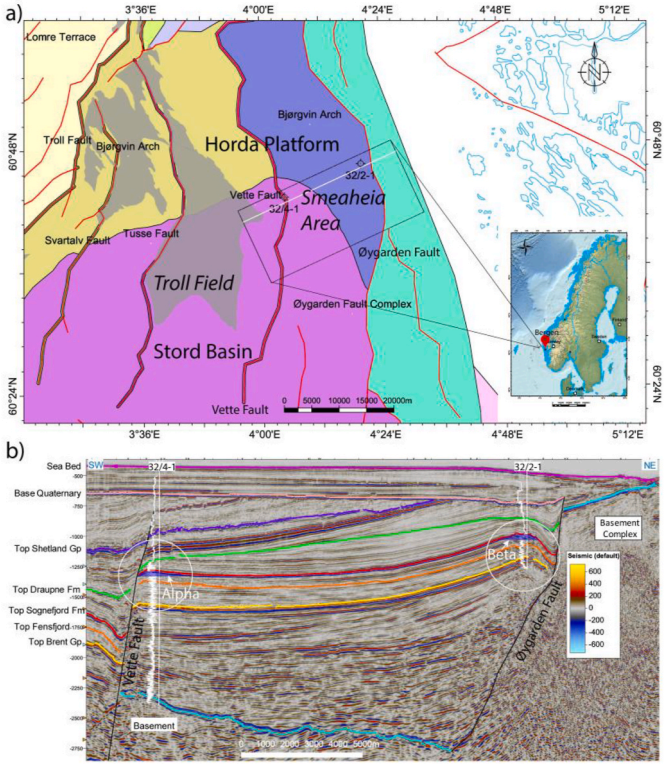

Fig. 1. (a) Location of the CO_2 storage site Smeaheia, offshore Norway. (b) A SW-NE running inline-1066 of 3D survey GN1101 over the Smeaheia area showing the Alpha and Beta prospects and other regional structures delineated by the key surfaces. Two dry wells are present in the area with trajectories highlighted on the seismic section by gamma-ray (GR) curves.

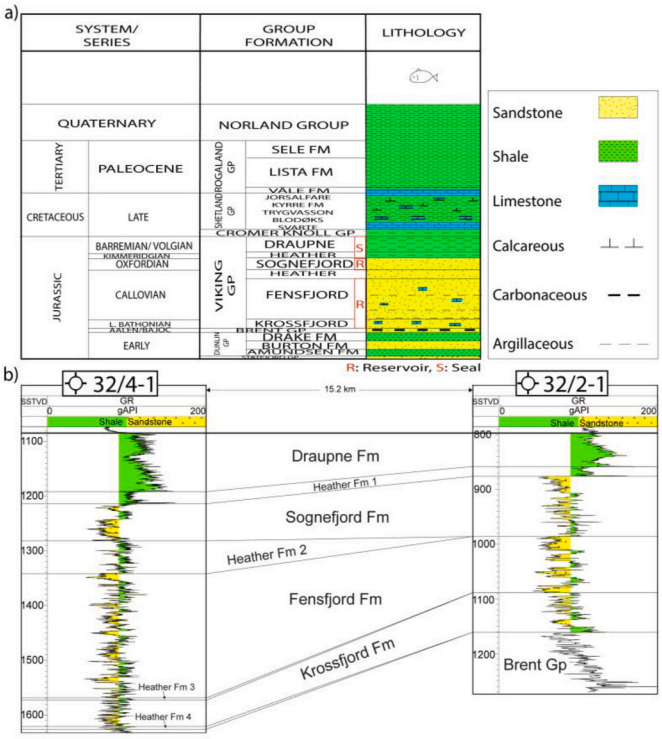

Fig. 2. (a) A generalized Jurassic to Quaternary stratigraphic succession in the study area (modified from Kinn et al., 1997). (b) A west to east stratigraphic cross-section between the wells 32/4-1 and 32/2-1 flattened on top Draupne Formation (primary seal). The potential reservoir sandstones of Sognefjord, Fensfjord, and Krossfjord formations show several prograding cycles.

Krossfjord Formation is medium to coarse-grained, well-sorted, and loose to friable sandstone. Bioclastic material and occasional cemented bands occur in all the three potential reservoir sandstones of Sognefjord, Fensfjord, and Krossfjord formations. The Heather Formation shale interfingers with sandstones of the Krossfjord, Fensfjord, and Sognefjord formations (Fig. 2b). It consists mainly of silty claystone with thin streaks of limestone, occasionally becoming highly micaceous grading into sandy siltstone (NPD, 2020). The Draupne Formation comprises dark grey-brown to black, usually non-calcareous, carbonaceous, and fissile claystones. It is characterized by high gamma-ray radioactivity (often above 100 API units) because of the elements associated with organic matter. The Draupne Formation deposited in a marine environment had restricted bottom circulation, mostly under anaerobic conditions (NPD, 2020). The Heather and Draupne Formations combined are the primary seals for the CO_2 storage reservoir sandstones of the Sognefjord and the underlying formations.

Considering only the Sognefjord Formation having good reservoir quality, a CO_2 storage reservoir, Alpha and Beta structures have a potential storage capacity of roughly 100 Mt each (Statoil, 2016). The main risks of leakage of injected CO_2 in the Smeaheia area are sideways migration along the ØFC and fractures towards the east, where the reservoir juxtaposes the fractured basement rocks and the VF in the west (Fig. 1b). Other risks are associated with numerous faults/fractures of sub-seismic resolution and fluid pathways related to palaeo- and seafloor pockmarks (Mulrooney et al., 2018). The topmost layer (Fig. 2a, Quaternary sediments) of the overburden is glacial sediments comprising of claystone and till, and their thickness ranges from about 50 m and up to more than 200 m (Halland et al., 2014). There is also a concern of pressure communication with the Troll field that produces oil and gas from the same reservoir sandstones. The Troll field lies about 8 km west of the Smeaheia area on the VF hanging wall.

For evaluating a potential GCS, the storage and capping integrity are critical, which need proper investigation. The target Jurassic sandstones in the Smeaheia area from the well log data seem suitable for CO_2 geological storage for having the required physical properties, i.e., porosity, permeability, and water salinity. However, it is essential to know the subtle horizontal variations in addition to the vertical changes in reservoir properties (for instance, porosity and permeability) to predict the behavior of an injected CO_2 plume and its migration updip, or vertically upward to the base of the reservoir seal (Chadwick et al., 2004; Riley, 2010). A 3D reservoir simulation model constructed by stochastically distributing various properties from well log data cannot predict the CO_2 plume movement and associated risks. Therefore, it is crucial to extract reservoir properties using 3D seismic data volume to extend and complement the well log data.

A seismic profile is an array of processed seismic traces, with each trace being considered to be the convolution of a source wavelet with an input reflectivity sequence with each reflectivity spike representative of the contrast in acoustic impedance (AI = P- wave velocity x bulk density) across the geological contact. The magnitude of AI and other elastic parameters in a formation depends upon many factors such as rock mineralogy, texture, pore fluid type, saturation, effective pressure, and compaction level that provide the relationship between rock physics, litho-fluid facies, and depositional environments (Avseth et al., 2005; Chuhan et al., 2003; Fawad et al, 2010, 2011; Giles, 1997; Hart et al., 2013; Mondol et al., 2008a; Schmitt, 2015; Thyberg et al., 2000). The mineralogy and texture depend upon the depositional environments, whereas the degree of compaction is a function of the depth of burial and temperature (Bjørkum et al., 1998). The compaction trend of both shale and sand behave differently with the depth influencing the seismic signatures (Brown, 2010; Fawad et al., 2010; Mondol et al., 2007). The properties of rocks gradually change from the time of deposition, through burial at the greater depth and convert the loose sands to

sandstones (Bernabé et al., 1992; Bjørlykke and Egeberg, 1993), and the soft clay particles into brittle mudstones (Aplin and Macquaker, 2011; Thyberg et al., 2009). The main diagenetic processes are stress-dependent mechanical compaction (MC) and temperature plus time-dependent chemical compaction (CC), which converts the reservoir and caprock properties into the present state (Bjørlykke and Jahren, 2015).

Extracting reservoir properties and fluid detection from seismic has always been an objective of geophysicists since active source reflection seismic has been used for hydrocarbon exploration (Fawad et al., 2020; Sheriff and Geldart, 1995). Standard reservoir characterization workflows comprise seismic inversion and amplitude-variation-with-offset (AVO) or amplitude-variation-with-angle (AVA) analyses. The change in amplitude with angle has long been developed by Zoeppritz in 1919 (Zoeppritz, 1919). Since the Zoeppritz equations were not intuitive, many approximations to solve AVO/AVA have been presented over the years (e.g., Aki and Richards, 1980; Fatti et al., 1994; Goodway et al., 1997; Shuey, 1985; Smith and Gidlow, 1987; Verm and Hilterman, 1995).

The *AI,* which is a real physical material property, is a zero-offset reflection function. On the contrary, an elastic impedance (*EI*) is not a physical property but a derived attribute of the seismic data, which can be computed for non-normal incident angles (Connolly, 1999). The *EI* contains fluid information. The *EI* method is further improved by Whitcombe et al. (2002), calling it Extended Elastic Impedance (*EEI*) with the option of a theoretical rotation angle (*chi*) from -90° to $+90^{\circ}$ in the intercept-gradient crossplot space. Particular rotation angles are related to elastic parameters, such as Lambda-Mu-Rho (*LMR*) (Goodway et al., 1997) and the compressional-to-shear wave velocity ratio (*Vp/Vs*). The *LMR* parameters are useful lithology and fluid discriminators.

Seismic inversion is a well-established technique since 1972 when Lindseth (1972) put forward a new method of processing, displaying, and interpreting seismic data that was mainly the inverse of producing seismograms from borehole sonic logs. The basic procedure uses the reflectivity at an interface between two successive layers to derive the layers' effective elastic properties. At present various types of seismic inversion algorithms exist, e.g., colored impedance inversion (Lancaster and Whitcombe, 2000), simultaneous AVO inversion (Hampson et al., 2005; Ma, 2001), and joint facies-based impedance inversion (Kemper and Gunning, 2014). The inversion may utilize either post-stack or prestack seismic data, employing deterministic or stochastic procedures, with or without a background low-frequency model.

Geostatistical methods consider the uncertainties of spatial correlation, conditioning to different kinds of data, and incorporating sub seismic heterogeneities (Bosch et al., 2010; Buland and Omre, 2003; Zhao et al., 2014). The stochastic inversion methods using a general Bayesian formulation are implemented in two different workflows (Bosch et al., 2010). In the sequential approach, first seismic data are inverted, deterministically or stochastically, into elastic properties. The inversion-derived elastic properties are then converted to the rock properties using a rock physics model (Dvorkin and Nur, 1996; Ødegaard and Avseth, 2004). The joint or simultaneous workflow accounts for the elastic parameters and the reservoir properties, often in a Bayesian formulation, assuring stability between the elastic and reservoir properties. Rock physics models link elastic parameters such as impedances and velocities to the reservoir properties such as lithologies, porosity, and fluids. Generally, the inversion is based on ray-tracing modeling on a single interface assumption, which introduces errors and requires substantial pre-processing for stratified models. To overcome those problems, a joint PP and PS Pre-stack Seismic Inversion for Stratified Models Based on the Propagator Matrix Forward Engine has been proposed (Luo et al., 2020). The authors demonstrated the algorithm to be better than the single PP inversion in terms of consistency and accuracy, especially for S-wave velocity and density.

In terms of layer properties, the *EEI* represents a straight line rotation in a crossplot of *AI* versus *Vp/Vs* (Avseth et al., 2014; Avseth and Veggeland, 2015). Since the background trend in the *AI, Vp/Vs* domain is highly nonlinear due to the complex relationship between compaction and rock-physics properties, Avseth et al. (2014) proposed new equations "*CPEI*- Curved Pseudo Elastic Impedance" and "*PEIL*-Pseudo Elastic Impedance" as fluid and rock stiffness indicators respectively. The authors extracted these attributes consistent with a rock physics template (RPT), taking into account compaction and cementation (Avseth and Veggeland, 2015). Recently, Lehocki et al. (2020) suggested an inversion of the Zoeppritz equation (Zoeppritz, 1919) to obtain the ratio of the density of two layers at the layers' interface. The distinction seemed possible employing the density ratio technique even in (initially) cemented rocks as the diagenetic cement dampens the fluid effect on elastic properties. This technique is in a developing stage and needs testing in other fluid-lithology environments.

The reservoir properties such as porosity, shaliness, and saturation obtained from inverted seismic data (Yenwongfai et al, 2017, 2018) can further be used as input and subsequent calibrations to a 3D reservoir simulation or geomechanical model (e.g., (Herwanger and Koutsabeloulis, 2011). The present study's objective is to deterministically extract the reservoir properties (e.g., porosity, shaliness, permeability) from seismic data using new rock physics equations correlatable with the well log data. The results from work can be used to develop and calibrate a 3D field scale reservoir, and subsequently a geomechanical model for the potential CO_2 storage site Smeaheia in the northern North Sea.

2. Dataset and methodology

A 3D seismic volume GN1101 covering the Smeaheia area, wireline log data from two exploration wells 32/4-1 (Alpha) and 32/2-1 (Beta), and petrographic analysis of Sognefjord Formation sandstone were available for the study. Seismic interpretation carried out by GASSNOVA was also available with the database. We selected the key surfaces (Fig. 1b) for the low-frequency model building before the prestack simultaneous inversion. The complete logs in both wells were gamma-ray curves, whereas, at shallower depths, the sonic and density log data were not recorded. To fill the information against those missing lengths of logs (ranging from 250 m to 800 m), an inversion (Lindseth, 1972) was carried out along the well trajectories starting from the seafloor obtaining the acoustic impedance curves. Using Gardner's equation ($\rho = aV_p^{0.25}$, Gardner et al., 1974), the acoustic impedance data was split in P-wave velocity (*Vp*, in m/s) and bulk density (*RhoB*, in g/cm3), iterating the coefficient *'a'* at which the curves splice best with the deeper available *Vp* and density logs. Since the shear wave (*Vs*) logs were not acquired in both the wells, synthetic *Vs* were generated using Greenberg and Castagna (1992) method employing the volume of shale from gamma-ray ($V_{sh}GR$) as input for mineral constrain.

We carried out the prestack inversion using commercial software. The inversion algorithm was based on a modified Fatti et al. (1994) three reflectivity terms (Hampson et al., 2005; Fawad et al., 2020). The available seismic data comprised a set of five partial stacks with angles 0–10°, 10–20°, 20–30°, 30–40°, and 40–50° (Fig. 3a). A preconditioning alignment of traces using a non-rigid method (NRM) was carried out before using these stacks for inversion. After extracting statistical wavelets from all the five partial stacks, both the wells were correlated with the seismic (Fig. 3b). Moderate to good correlation coefficients (0.6–0.7) were obtained. The linear regressions between the acoustic impedance and shear impedance, and acoustic impedance and density were taken as default. The inversion analysis along the wellbore was, however, reasonable within the zone of interest (Fig. 3c).

Finally, the simultaneous inversion was applied on the partial stacks to obtain the acoustic impedance (*AI*), P- to S-wave ratio (*Vp/Vs*), and Density (*RhoB*) cubes (Fig. 4a–c).

A standard petrophysical evaluation was carried out on the logs from both wells 32/4-1 and 32/2-1. The volume of shale (V_{sh}) was calculated by the Clavier method (Asquith et al., 2004) using the gamma-ray log:

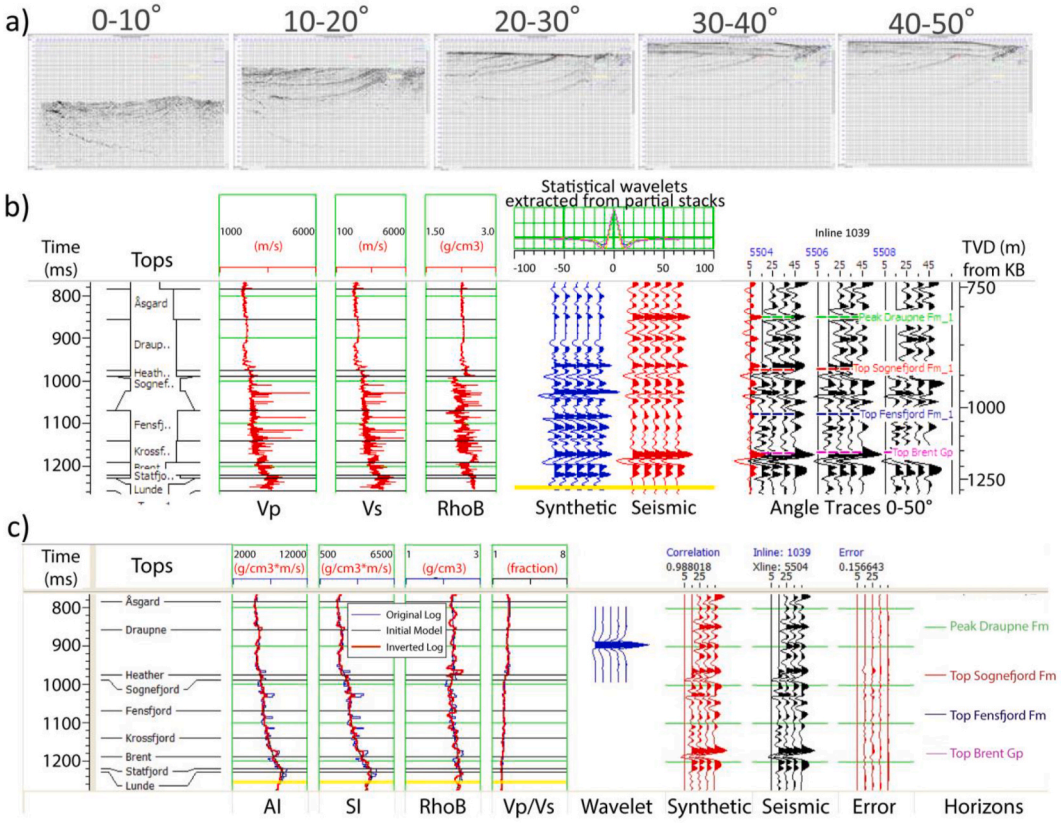

Fig. 3. (a) Angle stacks after preconditioning-alignment of traces using a non-rigid method (NRM). (b) Seismic to well correlation in case of well 32/2-1 showing a moderate to good correlation between the well-synthetic and seismic. (c) Inversion analysis at well (32/2-1) location highlighting the difference of the original elastic properties with the corresponding inverted values.

$$V_{shGR} = 1.7 - \sqrt{3.38 - (I_{GR} + 0.7)^2} \quad (1)$$

where I_{GR} is the gamma ray index that normalizes the GR curve from 0 to 1 based on the selection of sand and shale lines, respectively.

Effective porosity (φ_e) was calculated using the density (*RhoB*) log with the V_{sh} input. The grain and brine densities were considered 2.65 g/cm3 and 1.02 g/cm3, respectively. Only one core segment in well 32/4-1 was acquired within the Sognefjord Formation (Kinn et al., 1997). The porosity values from the core analysis are slightly higher than the effective porosity (φ_e) estimated from the *RhoB* log (Fig. 5a&b). The permeability was calculated using the φ_e (in fraction) from logs employing a logarithmic-linear form of the equation (PetroWiki, 2021; Timur, 1968):

$$log_{10}k = Clog_{10}\varnothing_e + D, \quad (2)$$

where k is absolute permeability in millidarcies, coefficients C and D were adjusted to 8.4 and 7.6, respectively, to obtain the permeability comparable to that of the core.

The net reservoir thickness, net-to-gross thickness ratio (N/G) were obtained using cut-off $V_{sh} \leq 0.3$, $\varphi_e \geq 0.1$, and permeability (k) > 20mD (Fig. 5). The arithmetic average for each reservoir parameter for both wells (32/4-1 & 32/2-1) is documented in Table 1. Using a nonlinear approach (Avseth et al., 2014; Avseth and Veggeland, 2015), employing a relation between the S-wave velocity and the P-wave velocity (Lee, 2003), we came up with an equation to calculate shale volume (V_{sh}) based on the *AI, Vp/Vs* ratio domain.

$$V_{sh} = \frac{\left\{\rho_{ma} - \frac{AI}{V_{Pma}} - \left[1 - \left(\frac{V_S}{V_P G\alpha}\right)^{\frac{1}{n}}\right]\left[AI\left(\frac{1}{V_{Pw}} - \frac{1}{V_{Pma}}\right) - (\rho_w - \rho_{ma})\right]\right\}}{\left[(\rho_{sh} - \rho_{ma}) - AI\left(\frac{1}{V_{Psh}} - \frac{1}{V_{Pma}}\right)\right]}, \quad (3)$$

where V_{sh} is the volume of shale in fraction, *Phi* is porosity in fraction, *AI* is acoustic impedance in g/cm^3*m/s, V_P is P-wave velocity in m/s, V_S is S-wave velocity in m/s, G is mineralogy/shaliness coefficient, α is *Vs/Vp* ratio of the mineral/rock matrix, n is stress/cementation coefficient, V_{Pma}, V_{Psh} and V_{Pw} are the P-wave velocities (in m/s) of the mineral matrix (e.g., quartz), shale and water respectively, ρ_{ma} is the density of mineral grains, ρ_{sh} is the density of shale, ρ_w is the density of water (all in g/cm3). Equation (3) is based on a three component system, defined by a matrix pole (e.g., quartz), shale pole and a water pole (Fig. 6). Changing the mineralogy/shaliness coefficient 'G' results in a vertical static shift in the iso-V_{sh} contours (Fig. 6), that we selected 1.02 for well 32/4-1, and 0.99 for 32/2-1. The stress/cementation coefficient 'n' controls the slope of the iso-V_{sh} contour lines and is selected (n = 0.55 in our case) such that the line with $V_{sh} = 0$ calibrates with the brine saturated sandstone trend from the well data. The matrix and fluid-related constants may be taken from Mavko et al. (2009) and vendors' logging chart books. The values of V_{Psh} and ρ_{sh} define the shale pole constraining the $V_{sh} = 1$ contour on the *AI, Vp/Vs* plane.

A variant of Equation (3), modified empirically to calculate porosity using *AI, Vp/Vs* information, is:

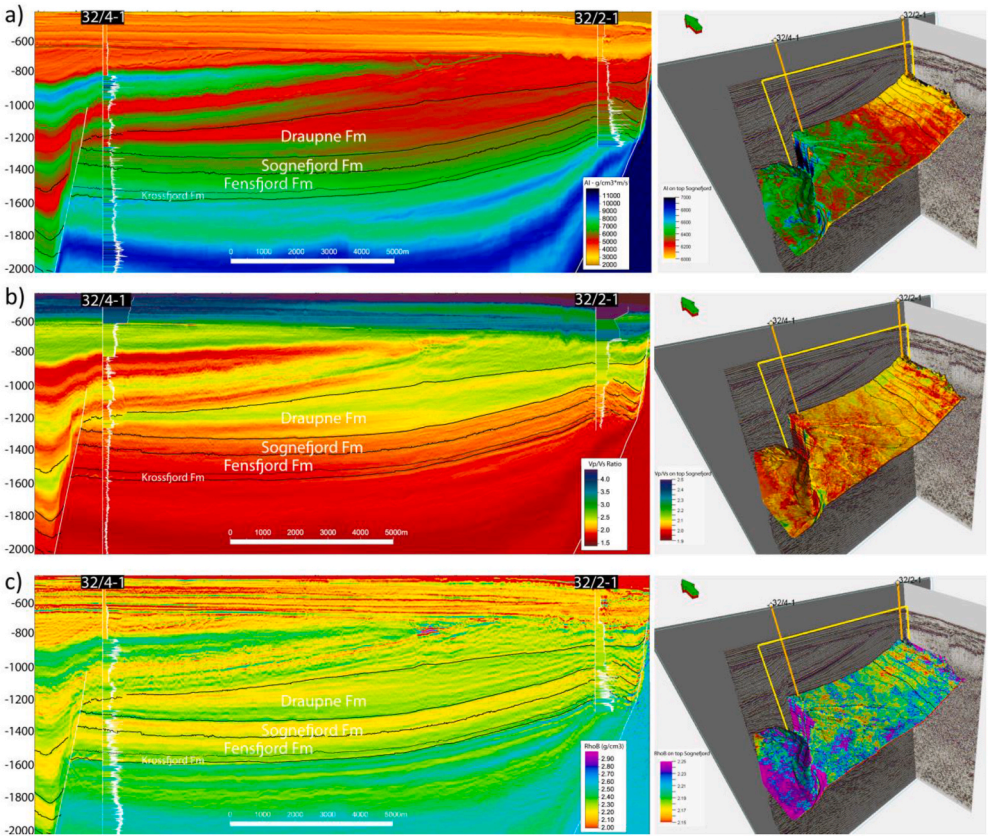

Fig. 4. Profiles from the prestack inverted cubes (a) *AI*, (b) *Vp/Vs* Ratio, and (c) *RhoB*. The corresponding properties displayed on the top Sognefjord TWT surface are placed on the right, with the profile locations highlighted by yellow rectangles. (For interpretation of the references to color in this figure legend, the reader is referred to the Web version of this article.)

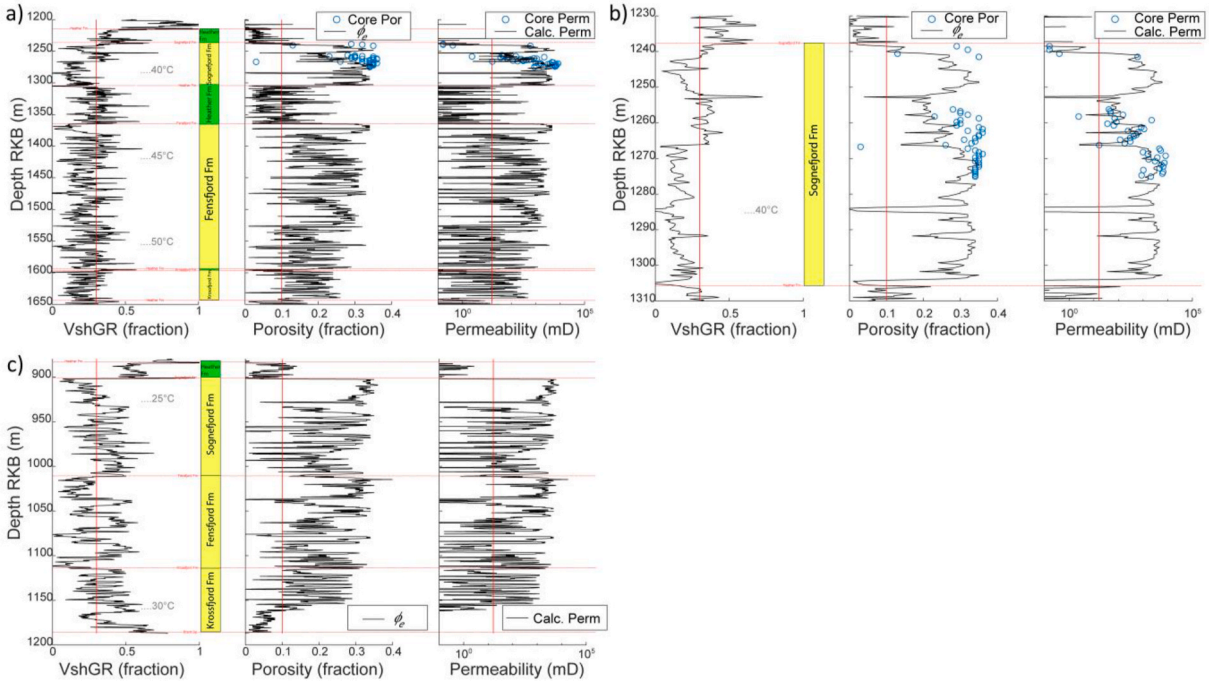

Fig. 5. Reservoir parameters plotted against depth with corresponding cut-off lines (red), (a) Shale volume (Vsh_{GR}), effective porosity (φ_e), and permeability (k) calculated using petrophysical methods from logs in well 32/4-1 with the porosity and permeability data measured in the core (Kinn et al., 1997, blue circles). (b) Same plot showing Sognefjord Formation only, (c) $V_{sh}GR$, φ_e, and k calculated using petrophysical methods from logs in well 32/2-1. (For interpretation of the references to color in this figure legend, the reader is referred to the Web version of this article.)

Table 1
Reservoir zones and the corresponding average parameters obtained from the petrophysics analysis.

Zone Name	Top	Bottom	Gross	Net	N/G	Av Phi	Av Sw	Av Vsh	Av Perm	Phi*H	Vsh*H
	m MDRKB	m MDRKB	m	m	fraction	fraction	fraction	fraction	mD	m	m
Well 32/4-1											
SOGNEFJORD FM	1238	1306	68	48.88	0.72	0.30	1.0	0.16	2039	14.5	8.0
FENSFJORD FM	1366	1595	229	135.11	0.59	0.26	1.0	0.19	921	35.2	25.3
KROSSFJORD FM	1598	1645	47	23.77	0.51	0.21	1.0	0.18	130	5.1	4.4
All Zones	1238	1645	344	207.77	0.60	0.26	1.0	0.18	1094	54.7	37.6
Well 32/2-1											
SOGNEFJORD FM	902	1012	110	39.11	0.36	0.31	1.0	0.23	2989	12.2	8.9
FENSFJORD FM	1012	1115	103	53.25	0.52	0.28	1.0	0.18	1729	15.1	9.5
KROSSFJORD FM	1115	1187	72	11.89	0.17	0.25	1.0	0.24	511	2.9	2.8
All Zones	902	1187	285	104.24	0.37	0.29	1.0	0.20	2063	30.3	21.2

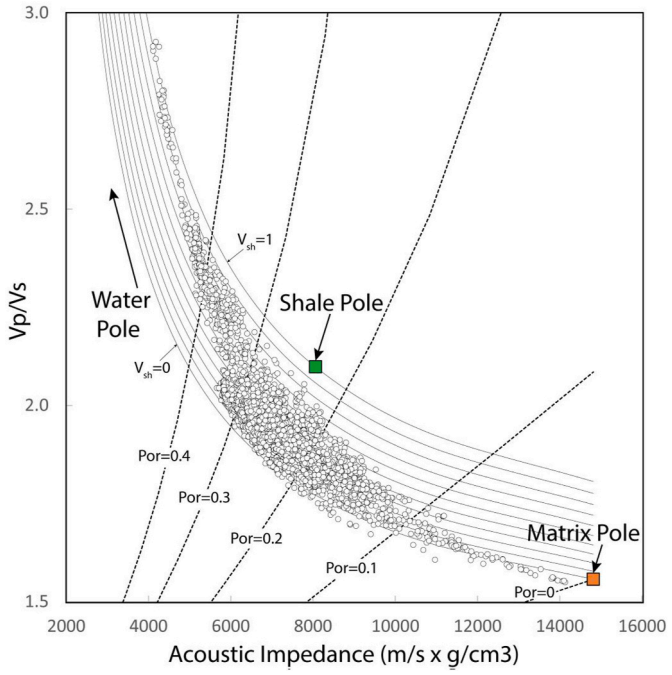

Fig. 6. Well 32/4-1 data plotted on an *AI, Vp/Vs* plane with iso-V_{sh} and iso-porosity contours computed using Equations (3) and (4) respectively. Positions of the three components (Matrix, Shale, and Water) are indicated accordingly.

$$Phi = 1 - \frac{0.001429AI - J - \left[1 - \left(\frac{V_s}{V_p G\alpha}\right)^{\frac{1}{n}}\right][0.00024AI + J - 1]}{\left[(\rho_{ma} - J) - AI\left(\frac{1}{V_{Pma}} - 0.001429\right)\right]}, \quad (4)$$

where *Phi* is porosity in fraction, and J is calibration coefficient (with values 1 to 4) that laterally moves the iso-porosity contours, with zero porosity contour anchored on the matrix pole (Fig. 6). There is a patent-pending on the quantification procedure related to Equation (3). Derivations and other related details of these equations will be presented in a subsequent publication. We generated *G* cube with a transition of values from well 32/4-1 to 32/2-1 and subsequently using Equation (3) and Equation (4) by putting the *AI* and *Vp/Vs* cubes, obtained the V_{sh} and *Phi* cubes, respectively. The porosity was calculated using Equation (4) only in zones with V_{sh} below 0.3. Permeability (*k*) cube from porosity (*Phi*) cube was extracted using Equation (2). Finally, using the V_{sh} cube, we extracted sand depositional geometries to get an insight into the depositional environments.

We performed exhumation estimates on wells 32/4-1 and 32/2-1, comparing the *Vp* data with experimental compaction trends of 50:50 silt-kaolinite mixture (Hansen et al., 2017; Marcussen et al., 2010) and reconstituted Etive Sandstone (Marcussen et al., 2010).

Furthermore, a rock physics evaluation was carried out to relate the reservoir properties with the depositional environment and diagenesis, employing well log data on the *RhoB-Vp* plane (Avseth et al., 2005). The critical porosity was assumed according to the data distribution at low density/high porosity. In a transitional depositional environment, the water density was considered to be 1.02 g/cm^3.

3. Results and discussion

3.1. Comparison between seismic-derived and well log-based reservoir parameters

The Sognefjord Formation in well 32/2-1 has a gross thickness of 110 m with an average porosity of 0.31. The thickness and porosity within the Sognefjord Formation decrease towards the west in well 32/4-1 (thickness 68 m and porosity 0.30 respectively); however, the net-to-gross thickness ratio (*N/G*) 0.36 is low in well 32/2-1 compared to 0.72 in well 32/4-1 (Table 1). The Fensfjord Formation in well 32/2-1 has a gross thickness of 103 m and *N/G* 0.52 lower than in well 32-4-1 (i.e., thickness 229 m and *N/G* 0.59 respectively). The Fensfjord Formation average porosity is 0.28 in well 32/2-1, which is slightly better than in well 32/4-1 (0.26). The Krossfjord Formation generally exhibits poor reservoir properties in both wells. In well 32/2-1 the Krossfjord is comparatively thin (gross thickness 72 m), with a high average porosity (0.25) compared to a lower gross thickness of 47 m and porosity 0.21 in well 32/4-1. The Krossfjord Formation *N/G*, however, is a lot better (*N/G* 0.51) in well 32/4-1 compared to that of in well 32/2-1 (0.17). The average permeability is generally higher in the Sognefjord, Fensfjord, and Krossfjord formations in well 32/2-1.

The V_{sh} values calculated using the *AI* and *Vp/Vs* logs matched well with the V_{sh} extracted from the gamma-ray log (i.e., $V_{sh}GR$) except for some over-prediction within the Draupne Formation in well 32/4-1 (Fig. 7a). The porosity values calculated from the *AI, Vp/Vs* showed a good fit with the effective porosity (φ_e) derived from the density log. There is some porosity over prediction within the lower part of the Krossfjord Formation in well 32/2-1 (Fig. 7b). Both the V_{sh} and φ_e calculations from traditional petrophysics generally show a good correlation with the respective properties calculated using rock physics models (i.e., Eqs. (3) and (4)), except in the case of low porosity, which the rock physics method slightly overpredicts (Fig. 7c and d).

Extracting the inverted cubes within a 25 m distance around both wells (32/4-1 & 32/2-1) show that the *AI* and *Vp/Vs* have restricted distribution compared to the same data from well logs on the *AI, Vp/Vs* plane (Fig. 8a–e). This is due to the difference in the resolution of the well logs and seismic data. The V_{sh} value distribution is similar to that from the well logs in the *AI, Vp/Vs* plane (Fig. 8a–b). The porosity cube extracted using Equation (4) shows a better match with the well log porosity than that calculated from the *RhoB* cube (Fig. 8c–e).

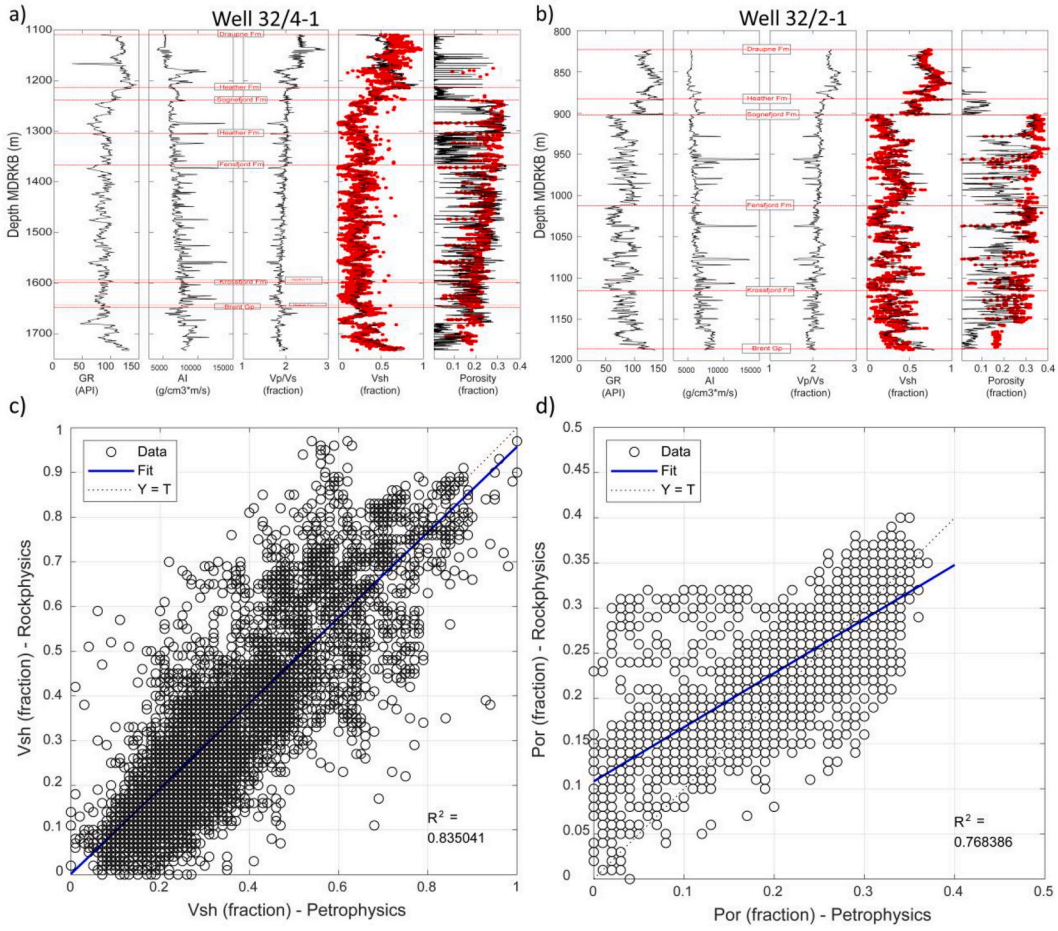

Fig. 7. Comparison between V_{sh} extracted using Equation (3) (red points), V_{sh} from gamma ray log (black line), *Phi* extracted from Equation (4) (red points), and φ_e from density log (black line) in (a) well 32/4-1 and (b) well 32/2-1. (c) Comparison between V_{sh} computed from *GR* log using a petrophysical method and the V_{sh} from the rock physics-based Equation 3, (d) φ_e calculated from the *RhoB* log using petrophysics versus *Phi* from the rock physics based Equation (4). (For interpretation of the references to color in this figure legend, the reader is referred to the Web version of this article.)

3.2. Rock physics analysis of the potential reservoir sands

We carried out a rock physics analysis to further investigate the relationship between elastic properties (i.e., velocity and density) and reservoir properties such as porosity, cementation, and shale volume. The objective was to infer the degree of influence of these reservoir properties on the seismic-derived attributes. Considering the section from top Draupne Formation to top Brent Group in both wells (32/4-1 and 32/2-1) that comprises the Sognefjord, Fensfjord, and Krossfjord formations, there are numerous spikes in the *Vp* and *RhoB* logs (Fig. 9a and c). These are a possible manifestation of carbonate laminations, as the carbonate minerals owe high P- wave velocity and density. The reservoir sands are at a present-day temperature ranging from 40 to 50 °C in well 32/4-1 (Fig. 9a); however, the data plotting above the constant cement line on the *RhoB-Vp* plane indicates a higher paleo-temperature regime (Fig. 9b). Some missing data points within the Draupne Formation were infilled using Gardner's equation that is manifested as a linear trend on the *RhoB-Vp* plane, signifying the limitations of using synthetic data. In well 32/2-1, the zone of interest lies between present-day temperature 25–30 °C (Fig. 9c), while the absence of cementation on the *RhoB-Vp* plane confirms that the sands stayed within the mechanical compaction zone since deposition (Fig. 9d).

The Sognefjord Formation sandstone is possibly well sorted when deposited as the data plots on a high porosity against low Vp values. To include the high porosity data under the contact cement line, a high critical porosity (φ_c = 0.44) was selected for the contact cement line calculation on the *RhoB-Vp* plane (Fig. 10a). The well 32/2-1 data falls below the constant cement line indicating the zone falling within the mechanical compaction zone. Several of the cleanest sand data points in well 32/4-1 generally plot above the constant cement line showing the formation has been exposed to a temperature (~70 °C), higher than the present-day temperature. Assuming the present-day North Sea temperature gradient (i.e., 35 °C/km), it can be inferred that the maximum burial depth of the area around well 32/4-1 was more than the present depth of 700 m. This assertion is confirmed by the uplift analysis that reveals 1100 m uplift for the well 32/4-l (Fig. 11a). The uplift increases towards the east in well 32/2-1, i.e., 1300 m (Fig. 11b). In both the wells, no overpressure has been reported; furthermore, there is a scatter of high density, high-velocity points indicating the presence of thin carbonate cemented intervals (Fig. 10a).

The Fensfjord Formation sandstones are similar to the Sognefjord Formation sandstones in terms of sorting. Most of the cleanest sandstone data in well 32/4-1 fall above the constant cement line indicating exposure to temperatures higher than 70 °C (Fig. 10b). The high density, high velocity scattered points indicate carbonate-bearing intervals in both the wells (32/4-1 & 32/2-1). The Fensfjord Formation data in well 32/2-1 plots below the constant cement line signifying that the formation in the study area possibly remained within the mechanical compaction zone since deposition.

The Krossfjord Formation, in contrast to the type section (NPD, 2020), is possibly poorly sorted in this area. Therefore, to constrain the data, the critical porosity is assumed to be lower (φ_c = 0.4) than the

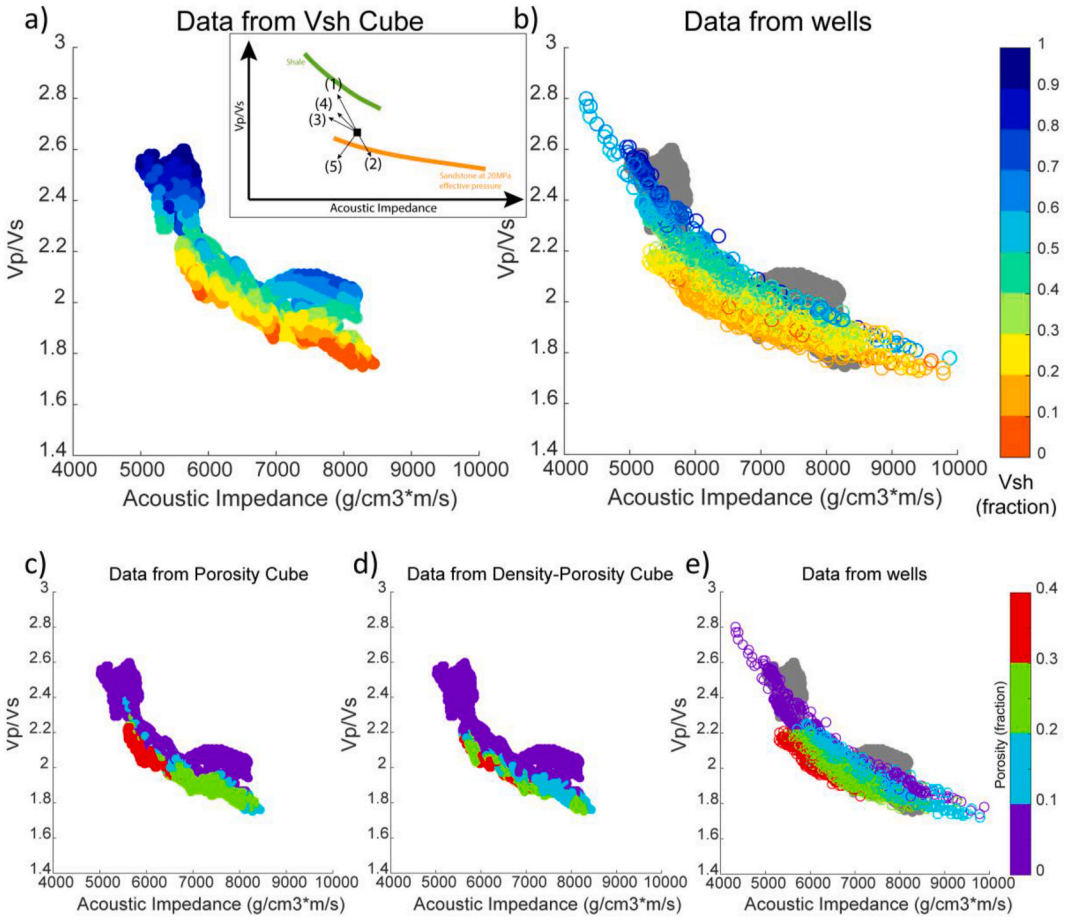

Fig. 8. (a) Comparison between the inverted cube data extracted within a distance of 25 m around the two wells (32/4-1 and 32/2-1) with the properties obtained from well logs onto the *AI, Vp/Vs* plane (a) V_{sh} extracted from the prestack inversion, (b) $V_{sh}GR$ points overlapping the inverted data points (gray), (c) *Phi* extracted from the inverted data using Equation 4, (d) *Phi* calculated from the inverted density cube, and (e) φ_e obtained using *RhoB* logs overlapping the inverted data points (gray). The inset in (a) does also show how the brine saturated sandstone will plot as the (1) shale content increase, (2) the amount of cement increase, (3) the porosity in the sandstone increase, (4) the effective pressure in the formation decrease and (5) the saturation of gas increasing relatively to the saturation of hydrocarbon within the sandstone (Avseth et al., 2005).

shallower formations (Fig. 10c). The formation in well 32/2-1 is unclean with shale intercalations; however, as the zone becomes deeper towards the well 32/4-1, the sands are cleaner with a high level of cementation. Few high density, high-velocity points indicate thin carbonate laminations. As expected, the formation possesses overall low porosity compared to the shallower Fensfjord and Sognefjord Formations.

3.3. Seismic-derived reservoir properties

The maximum magnitude of reservoir parameters extracted from the inverted seismic data within the respective interval of Sognefjord, Fensfjord, and Krossfjord formations showed that the best sand (V_{sand}>0.9 or V_{sh}<0.1) is present in the east with a north-south strike (Fig. 12a–c). This feature is very prominent in the Sognefjord Formation (Fig. 12a), which seems to shift southwards in the deeper Fensfjord and Krossfjord Formations (Fig. 12b–c). The porosity calculated using Equation (4) shows a systematic decrease from east to west in all the three Sognefjord, Fensfjord, and Krossfjord formations (Fig. 12a–c). Also, there is an overall porosity decrease from Sognefjord Formation to the deeper Fensfjord and Krossfjord Formations. The porosity estimated using the *RhoB* cube also shows a similar decrease of porosity in deeper formations, with Sognefjord Formation sandstone exhibiting the best overall porosity. The lateral change in porosity with depth within a formation is not so prominent in the *PhiD* attribute compared to *Phi* (Fig. 12a–c).

The average magnitude of the reservoir properties has limitations owing to the low seismic resolution compared to the wireline logs; however, it may yield useful information. The Sognefjord Formation shows an average V_{sh} of ~0.3 that decreases in the northeast towards the well 32/2-1 (Fig. 13a). The sands are generally homogenous over the area. The average porosity in both *Phi* and *PhiD* calculations seems to be high (~0.28) in the middle of the area, which is somehow influenced by the NW-SE running faults. The average V_{sh} range within the Fensfjord Formation is similar to the Sognefjord Formation except for some high sand anomalies (V_{sh}~0.2) in the middle and southeast of the area (Fig. 13b). Both *Phi* and *PhiD* show higher porosity values (~0.28) in the middle of the area. The average V_{sh} in Krossfjord Formation is low (~0.20) in some patches, which possibly represent various sand bodies deposited in the area (Fig. 13c). The *Phi* calculations show a relatively better porosity in the northeast (~0.27), whereas the overall porosity in the *PhiD* map is low and patchy.

The highest permeability (~2000 mD) in Sognefjord Formation lies in the east; however, the average permeability anomaly (<1000 mD) is exhibited in the middle and southeast of the area (Fig. 14a). Since permeability is derived from the porosity (*Phi*), there is a permeability distribution controlled by faults as in the case with porosity (Fig. 13a). The Fensfjord Formation permeability increases towards the east, manifested by both the maximum and average magnitude maps. The overall permeability values are, however, lower than the Sognefjord Formation permeability (Fig. 14b). The Krossfjord Formation

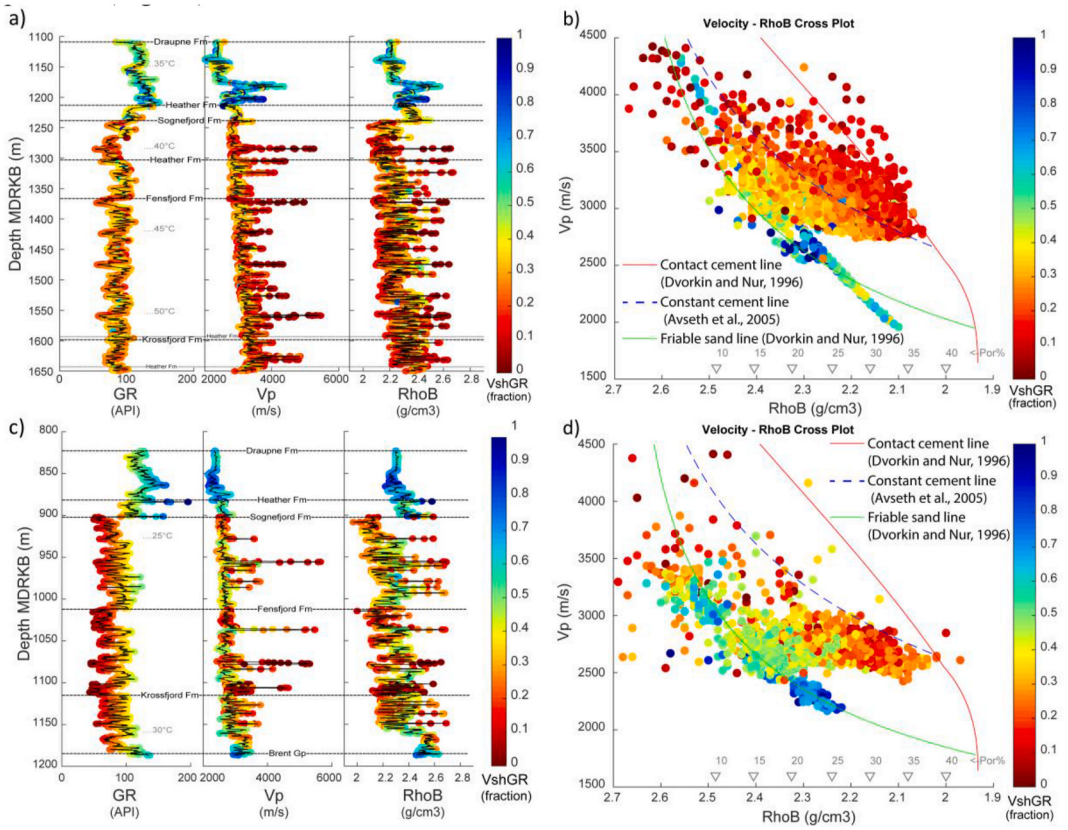

Fig. 9. Well log data from Top Draupne Formation to Top Brent Group color-coded with $V_{sh}GR$ (a) *GR*, *Vp*, and *RhoB* values in well 32/4-1 plotted against depth. (b) *RhoB-Vp* crossplot (in well 32/4-1) with (red) contact cement line (Dvorkin and Nur, 1996), (blue stippled) constant cement line (Avseth et al., 2005), and (green) friable sand line (Dvorkin and Nur, 1996). The linear trend represents the data within Draupne Formation generated using Gardner's equation. (c) Well 32/2-1 GR, *Vp*, and *RhoB* values plotted against depth. (d) *RhoB-Vp* crossplot (in well 32/2-1) with contact cement line (Dvorkin and Nur, 1996), constant cement line (Avseth et al., 2005), and friable sand line (Dvorkin and Nur, 1996). The spikes in *Vp* and *RhoB* (a and c) are possible carbonate cemented zones. (For interpretation of the references to color in this figure legend, the reader is referred to the Web version of this article.)

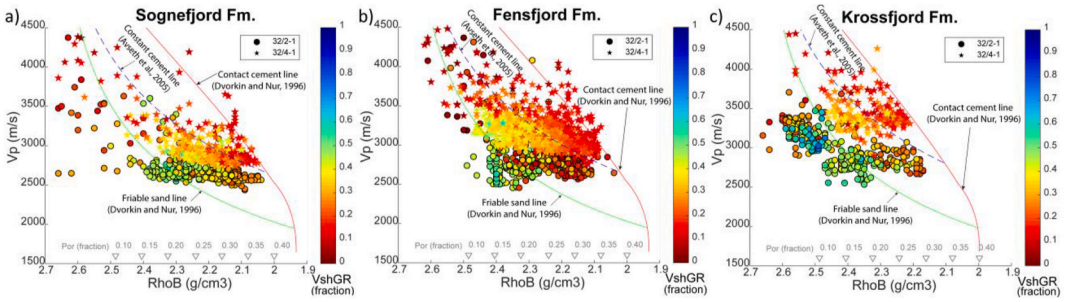

Fig. 10. *RhoB-Vp* crossplots with contact cement line (Dvorkin and Nur, 1996), constant cement line (Avseth et al., 2005), and unconsolidated sand line (Dvorkin and Nur, 1996) for (a) Sognefjord Formation, (b) Fensfjord Formation and (c) Krossfjord Formation.

permeability in the maps show maximum and average magnitude permeability increasing towards the east; however, the overall values are lower than that of the Sognefjord and Fensfjord Formations (Fig. 14c).

On a profile (inline-1266) from the V_{sand} (1-V_{sh}) cube, the cleanest sands (V_{sh}<0.1) are present on the easternmost part within the Sognefjord Formation, whereas there are some lens-shaped bodies interpreted to be possible point bars within the lower part of the Krossfjord Formation (Fig. 15a). Occasional point bars are also present in the lower part of the Fensfjord Formation. Using the clean sand data points (with cutoff V_{sh}<0.1), 3D litho-bodies were generated (Fig. 15b). The bodies connecting the point bars assumed a shape interpreted to be deltaic. The north-south striking sand body, also exhibited in Fig. 12, is interpreted to be deposited in a shoreface/beach setting. A northward shift of the strike of the sand body from deep to shallow formations is evident here. These findings support previous studies where spit to the deltaic depositional environment was reported in Troll area for the Sognefjord, Fensfjord and Krossfjord formations (Dreyer et al., 2005; Holgate et al., 2015). The *Phi* profile shows the highest overall porosity within the Sognefjord Formation (Fig. 16a), whereas the *PhiD* profile shows overall high porosity within both the Sognefjord and Fensfjord Formations and relatively low porosity within the Krossfjord Formation (Fig. 16b). One interesting feature in both *Phi* and *PhiD* attributes is that the porosity within the possible delta-related deposits/point bars is comparatively low.

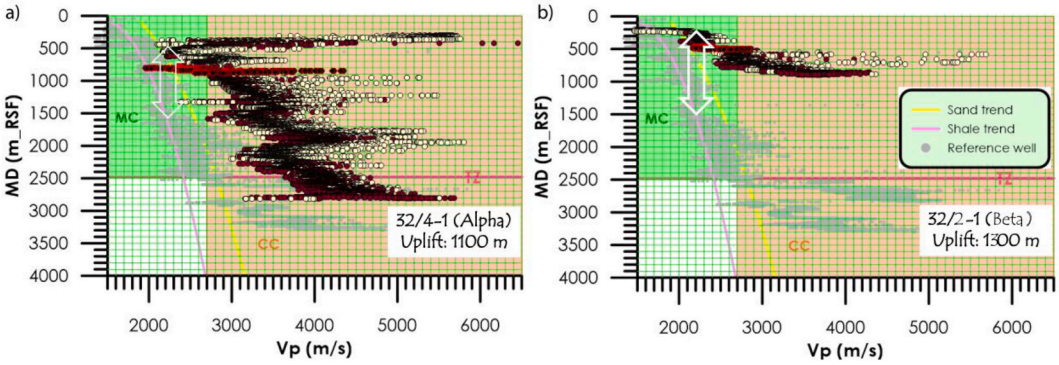

Fig. 11. Uplift estimation by comparing the well log *Vp* data with that of reference sand and shale trends (Hansen et al., 2017; Marcussen et al., 2010; Mondol et al., 2008b). A reference North Sea well with normal compaction and zero-uplift is also plotted (grey points). (a) The well 32/4-1 shows an uplift ~1100 m, (b) the well 32/2-1 shows an uplift ~1300 m. RSF: Reference from the Seafloor, MC: Mechanical Compaction, CC: Chemical Compaction, TZ: Transition Zone.

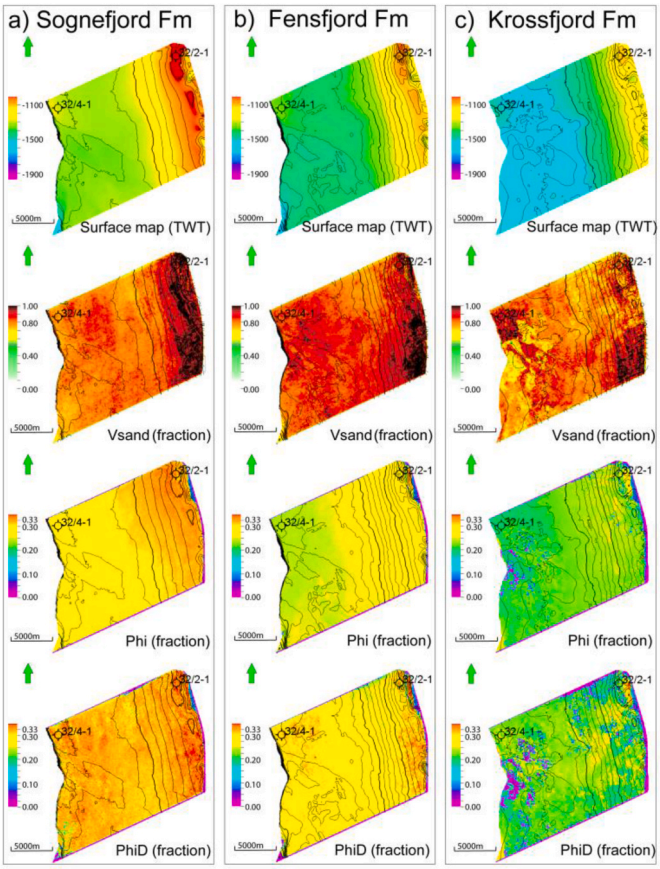

Fig. 12. TWT surface maps and maximum magnitude of reservoir properties extracted from the inverted cubes within (a) Sognefjord Formation, (b) Fensfjord Formation, and (c) Krossfjord Formation.

3.4. Smeaheia sandstone reservoirs as potential CO_2 storage candidates

The buoyancy trapping is the main process for CO_2 storage during the injection and the subsequent early stage of storage (Riley, 2010). Therefore, CO_2 injection is carried out at the base of the reservoir, and the plume moves laterally within the most permeable layers until it finds a vertical conduit to move vertically upwards. The plume behavior depends on the subtle horizontal and vertical heterogeneities within the reservoir, which are adequately reflected in the physical properties. The lateral continuation of thin clay and silt layers or carbonate laminations may help lateral distribution of CO_2 in the storage, until the plume finds a vertical permeable zone to move and accumulate below the caprock base. One example is the Sleipner GCS project, where the time-lapse seismic enables one to identify and delineate the migration path and subsequent accumulation of the CO_2 plume (Chadwick et al., 2004). Therefore, predicting the CO_2 plume behavior from seismic-derived properties in addition to the wireline log information is essential, keeping in mind the issues of the low resolution of seismic.

The reservoir sandstones in the Smeaheia area appear to be sheet-like in the *Vsand* profile extending from the well 32/4-1 to 32/2-1 (Fig. 15a); however, looking at the logs, the sandstones exhibit coarsening upward cycles indicating progradation (Fig. 2b). The shoreface/beach depositional system prograded westwards, forming continuous sand sheets, can be potentially excellent reservoirs for geological CO_2 sequestration. The shoreface sands seem to be shifting along the strike gradually northwards from the older Krossfjord to the younger Sognefjord Formations (Fig. 12a–c). Towards the west, there are possible deltaic sands, mainly in the Krossfjord Formation and partially in the Fensfjord Formation with the source possibly from the north. These sands are very clean but possess comparatively low porosity that could be attributed to a moderate level of cementation for being deep in stratigraphic succession, possibly with not enough chlorite coatings on the quartz grains (Ehrenberg, 1993). A further analysis focussing on the three reservoir sandstones is given below:

3.4.1. Sognefjord Formation

Minor shale beds separate the Sognefjord sandstones in both wells 32/4-1 and 32/2-1 (Fig. 2b). The shales are somehow identifiable, especially in the east, towards well 32/2-1 in the V_{sand} cube, where the shale thickness is more than the seismic resolution (Fig. 15a). Our rock physics analysis indicates that while deposition, the sands were well sorted with high initial porosity. Since the eastern part of the area, towards well 32/2-1, has always been within the mechanically compacted zone (Fig. 11b), the porosity and permeability are excellent, as evident in Figs. 12 and 14. The eastern side uplifted about 1300 m for being closer to the continental mass. The average porosity (both *Phi* and *PhiD*) is misrepresented as the interval average takes into account the effective shale porosity (φ_{sh}~0), which results in a reduction of the porosity where the shale thickness is above the seismic resolution. In the west, towards well 32/4-1, the formation experienced quartz cementation, especially the clean sandstones show a higher level of cementation (Fig. 10a). This implies that the western side has been exposed to a minimum temperature of 70 °C at maximum burial depth, indicating a subsequent uplift of around 1100 m (Fig. 11a). The porosity in the western part is also good, as recorded in well 32/4-1 (Table 1) and also from the seismically derived porosities, i.e., *Phi* and *PhiD* (Figs. 12a and 13a).

The 32/4-1 well core analysis (Martin and Lowrey 1997) shows fine to very fine-grained, well-sorted with moderate to good quality Sognefjord sandstone (Fig. 17). The intermediate permeability (~602mD)

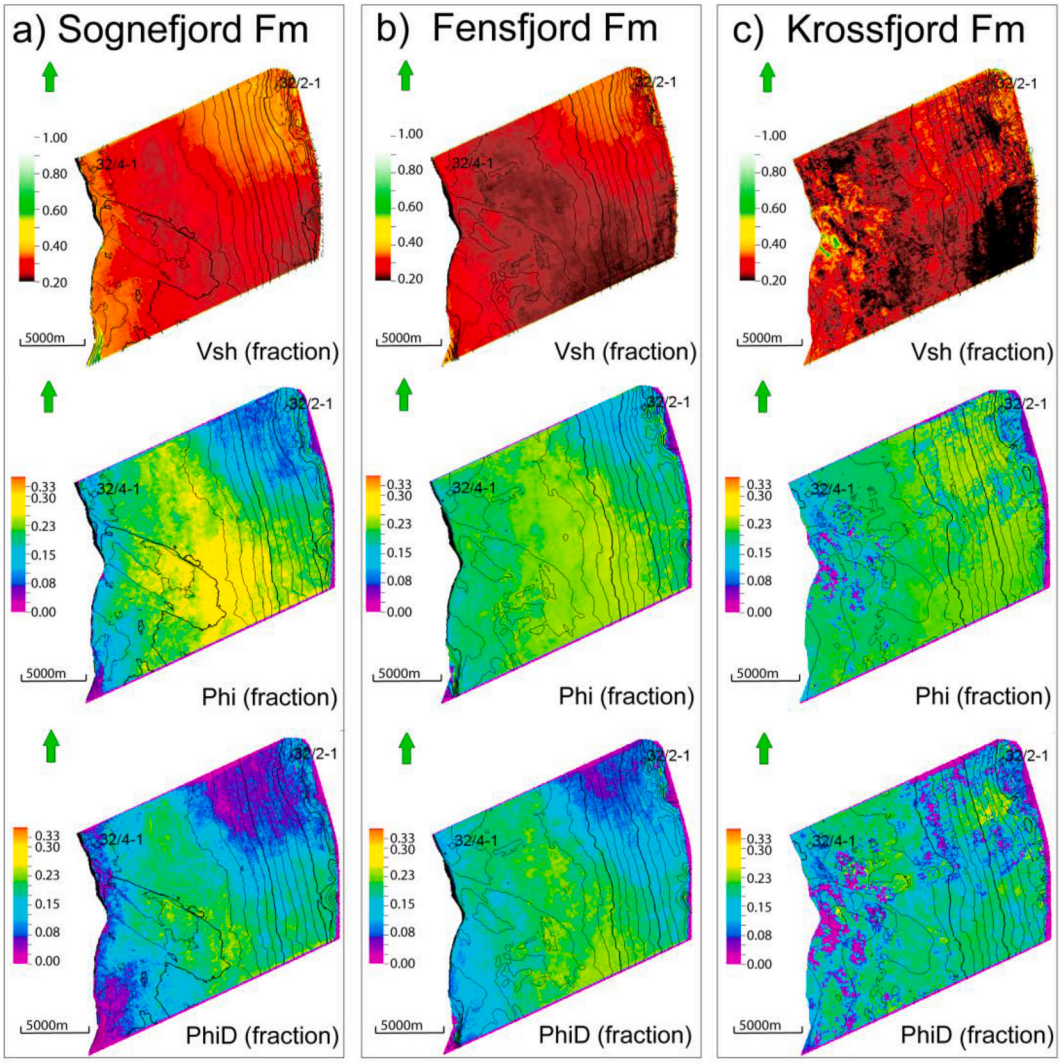

Fig. 13. The average magnitude of reservoir properties extracted from the inverted cubes within (a) Sognefjord Formation, (b) Fensfjord Formation, and (c) Krossfjord Formation.

sandstone contains an open porosity network and good pore connectivity (Fig. 17a). The undeformed muscovite mica flakes (Fig. 17a) indicate a low compaction level. The comparatively low permeability (~70mD) can be attributed to small pore sizes and associated narrow pore throats, although the sandstone owes abundant and well-connected porosity (Fig. 17b). The preferred orientation of elongated grains indicates a comparatively higher compaction level. The high permeability sandstone (~4600 mD) contains slightly larger pores (up to 100 μm diameter) with excellent connectivity through widespread clean and open pore throats (Fig. 17c). A zoomed view of this high permeability sandstone reveals the presence of some pore-filling Kaolinite occasionally located within a grain dissolution pore (Fig. 17d). The secondary porosity is generated through the dissolution of K-Feldspar grains and overgrowths (Fig. 17d). These samples are at the present depth of 1241–1268 m (MDRKB), and the thin section images confirm that these sandstones lie mainly within the mechanical compaction zone with no significant influence of chemical compaction. Kaolinite clays do not swell as much as Smectites in the presence of water to reduce porosity and permeability. However, migration of clay grains could plug the pore-throats while a CO_2 injection, potentially reducing permeability in a high amount of kaolinite-bearing sandstone (Aksu et al., 2015).

The permeability barriers due to the presence of carbonate stringers (Fig. 9a and c) are too thin to detect on seismic-derived data, which may provide resistance in a vertical CO_2 flow; however, these features can also help regulate the injected CO_2 for better lateral distribution (Sundal et al, 2013, 2016).

3.4.2. Fensfjord Formation

The Fensfjord Formation sandstones also exhibit a sheet-like deposition by the prograding shoreface; however, there are few sand bodies possibly of deltaic origin in the middle of the Smeaheia area (Fig. 12b), likely in the lower part (Fig. 15a). The overall porosity (>0.25) and permeability (~1000 mD) are good, generally increasing in the east towards well 32/2-1 (Table 1, Figs. 12b and 14b) for being within the mechanically compacted zone (Figs. 10b and 11b). However, the average porosity maps show high porosity in the middle due to the presence of low V_{sh} in that area (Fig. 13b). Similar to the Sognefjord Formation, there are carbonate related permeability barriers within the Fensfjord Formation (Fig. 9a and c), which could be helpful in a lateral CO_2 distribution (Sundal et al, 2013, 2016).

3.4.3. Krossfjord Formation

The Krossfjord Formation sandstones are discontinuous, separated by several sand bodies (Figs. 12c and 13c). The southeastern corner of the area contains a prominent sand anomaly that is deposited possibly in a shoreface environment. In the west, the deposition is possibly delta related (Fig. 15a–b); however, these clean sands are quartz cemented, exhibiting a moderate porosity (Fig. 10c and 16a-b). The low gross

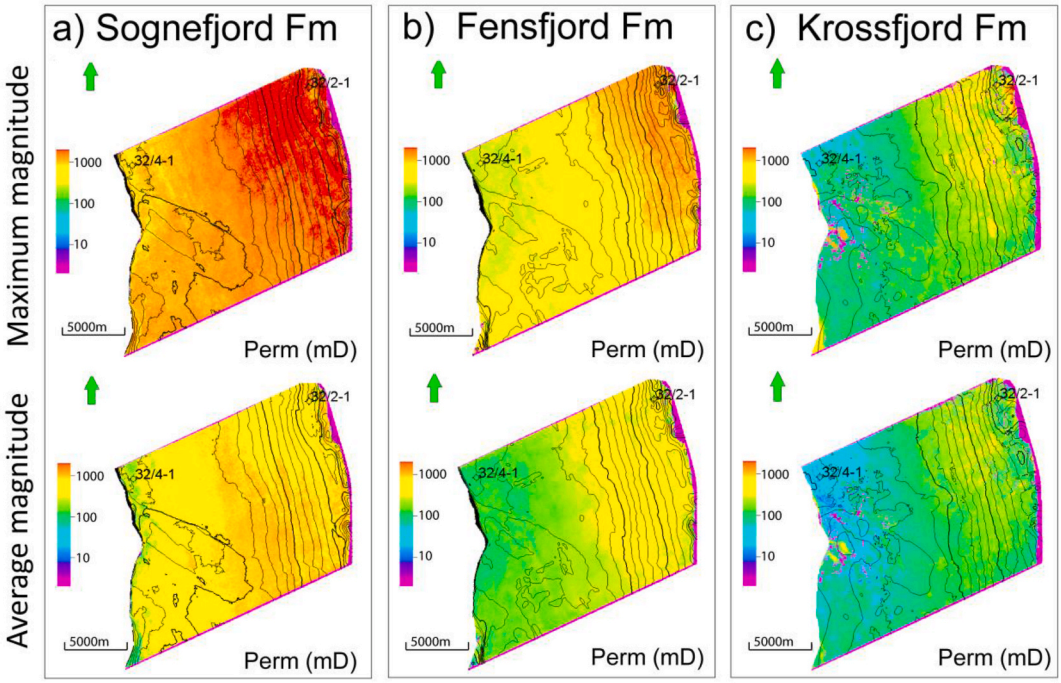

Fig. 14. The maximum and average magnitude of reservoir permeability extracted from the Phi cubes within (a) Sognefjord Formation, (b) Fensfjord Formation, and (c) Krossfjord Formation.

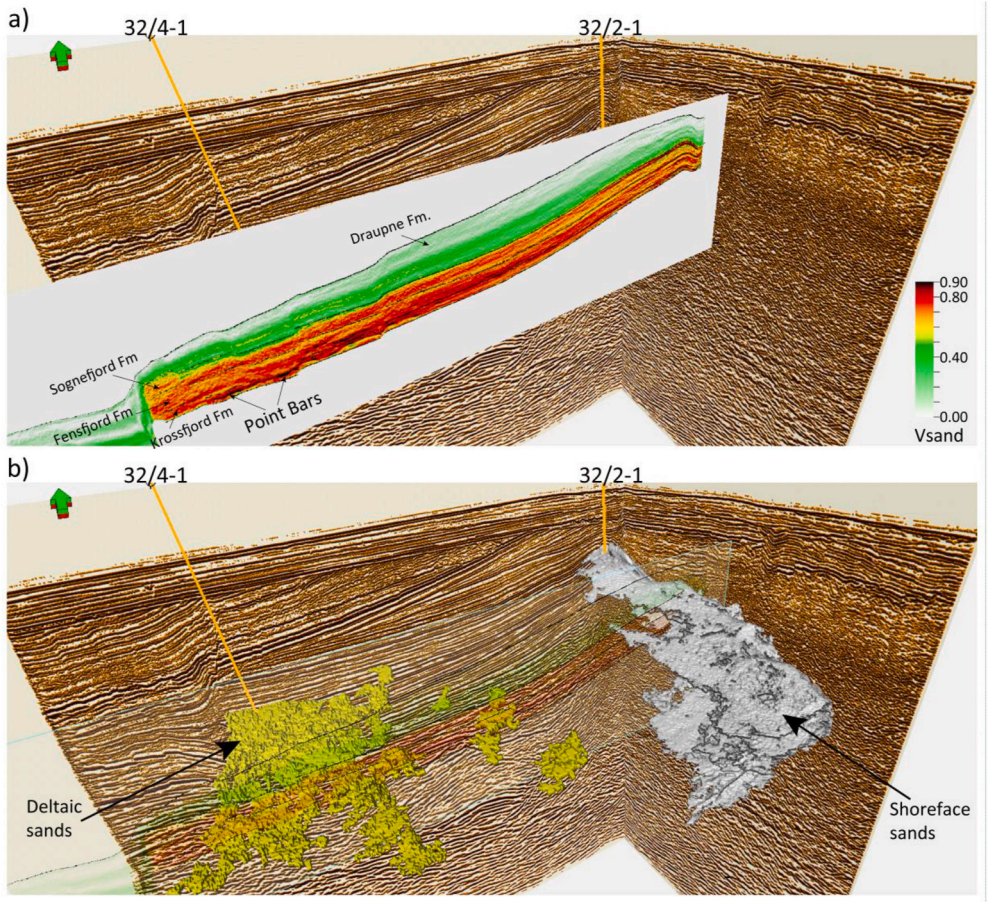

Fig. 15. (a) V_{sand} profile (inline-1266) showing possible point bars where the sand is very clean (V_{sh}<0.1). (b) Sand bodies extracted using the clean sand data reveal two main depositional geometries, i.e., possible shoreface/beach and deltaic depositional environments. The shoreface/beach sands prograded westwards, forming continuous sand layers within all the three Sognefjord, Fensfjord, and Krossfjord formations accordingly (a).

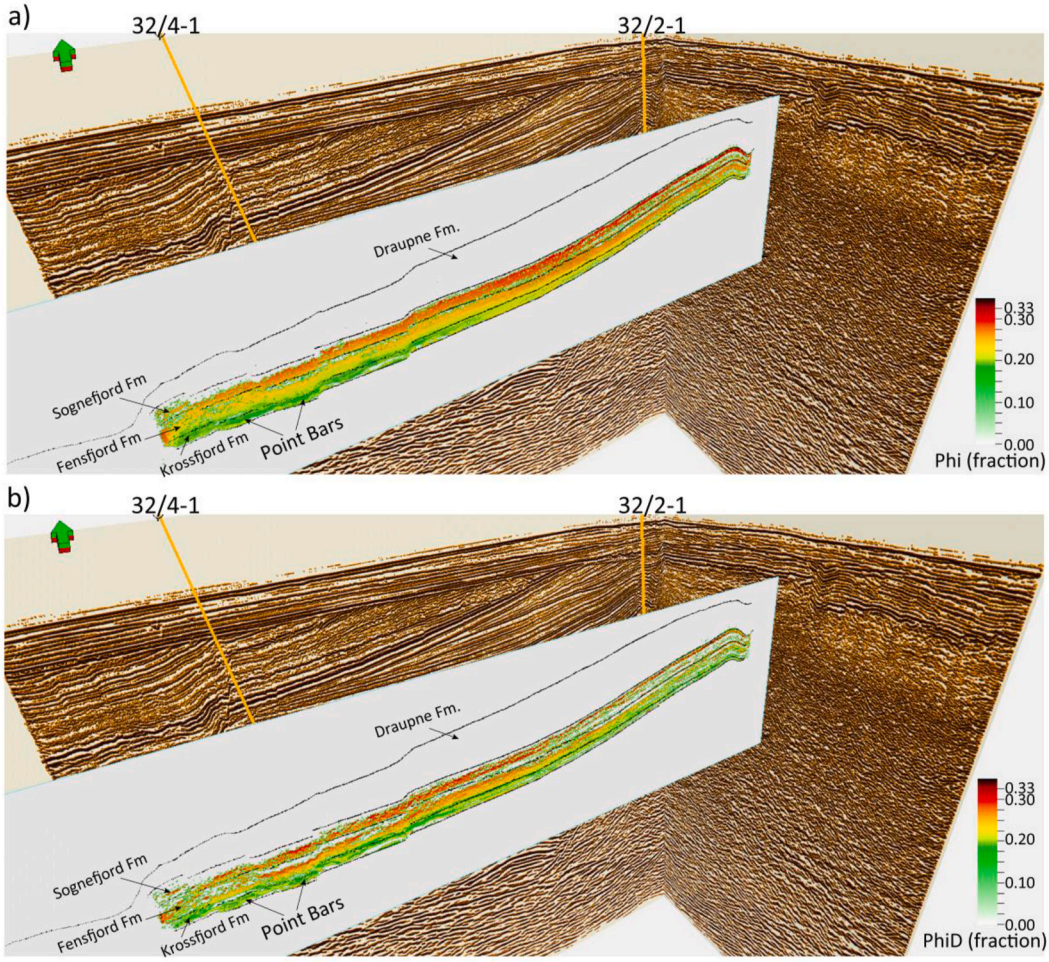

Fig. 16. (a) Inline-1266 showing porosity (a) calculated from the inverted seismic data using Equation (4) and (b) calculated from the inverted *RhoB* cube. The delta-related sands (point bars) exhibit relatively low porosity in the profiles from both the porosity extraction methods.

thickness and *N/G*, high shaliness, moderate porosity, and permeability, uncertainties in the sand body connectivity make the Krossfjord Formation a less likely candidate for CO_2 storage.

3.5. Limitations and pitfalls

Assuming a frequency of 40 Hz with an average seismic velocity of 2600 m/s, the vertical seismic resolution around this depth is approximately 16 m in the Smeaheia area. Therefore, extracting meaningful reservoir properties in sandstones with thickness below the seismic resolution is challenging. The other limitation in our case was the absence of *Vs* logs in the zones of interest. Only ~40 m length of Vs was acquired in well 32/2-1 within the deeper Brent Group and Lunde Formation. A machine learning model trained on a Central North Sea database (Rahman et al., 2020) was used to extract *Vs* employing Random Forest (RF), neural network (NN), and K-Nearest Neighbors (kNN) against the available *Vs* log depths. We compared the synthetic logs generated from the Greenberg and Castagna (1992) and machine learning methods with the acquired *Vs* log within the same zone (Fig. 18). On the *Lambda-Rho, Mu-Rho* plane (Goodway et al., 1997), the synthetic trend from Greenberg and Castagna (1992) drifts towards the quartz pole with an increase in Lambda-Rho compared to the acquired *Vs* that leans towards the carbonate pole. This has implications on lithology inversion from seismic, as minerals, especially carbonate would have lumped in the quartz domain. However, the thickness of carbonate stringers within our zone of study in the Smeaheia area is generally below seismic resolution that provides confidence in our inversion results. It is evident here that the *Vs* generated using machine learning methods, particularly the neural network (NN) and K-Nearest Neighbors (kNN) yield better results compared to the Random Forest (RF) method. However, in our previous work (Rahman et al., 2020) the RF method showed better correlations within the Heather and Draupne Formation zones. Although in the present study, uncertainty related to the usage of right machine learning method exists, however, in other cases, the machine learning methods can be useful to generate synthetic *Vs* as input for seismic inversion.

Our proposed equation (Eq. (3)) for calculating shale volume is meant only for low TOC shales. The maximum TOC in Draupne Formation in well 32/4-1 is 3% (NPD, 2020) that yields reasonable results with Equation (3). High TOC contents tend to pull the data point towards "southwest" in an *AI, Vp/Vs* ratio plane, which in the presence of acquired *Vs* may require a different quantification approach. As the fluid and lithology extraction solutions are not unique, the rock physics-based deterministic methods have limitations. We are working to mitigate the data holes in extracted cubes (e.g., Fig. 16) and the inherent uncertainties, using a stochastic approach.

4. Conclusions

We found Sognefjord Formation the best candidate due to a sheet-like continuous deposition and optimum reservoir properties for CO_2 storage in the Smeaheia area, with carbonate-related permeability barriers considered helpful in the lateral distribution of injected CO_2. The Fensfjord Formation was identified as the second-best quality reservoir

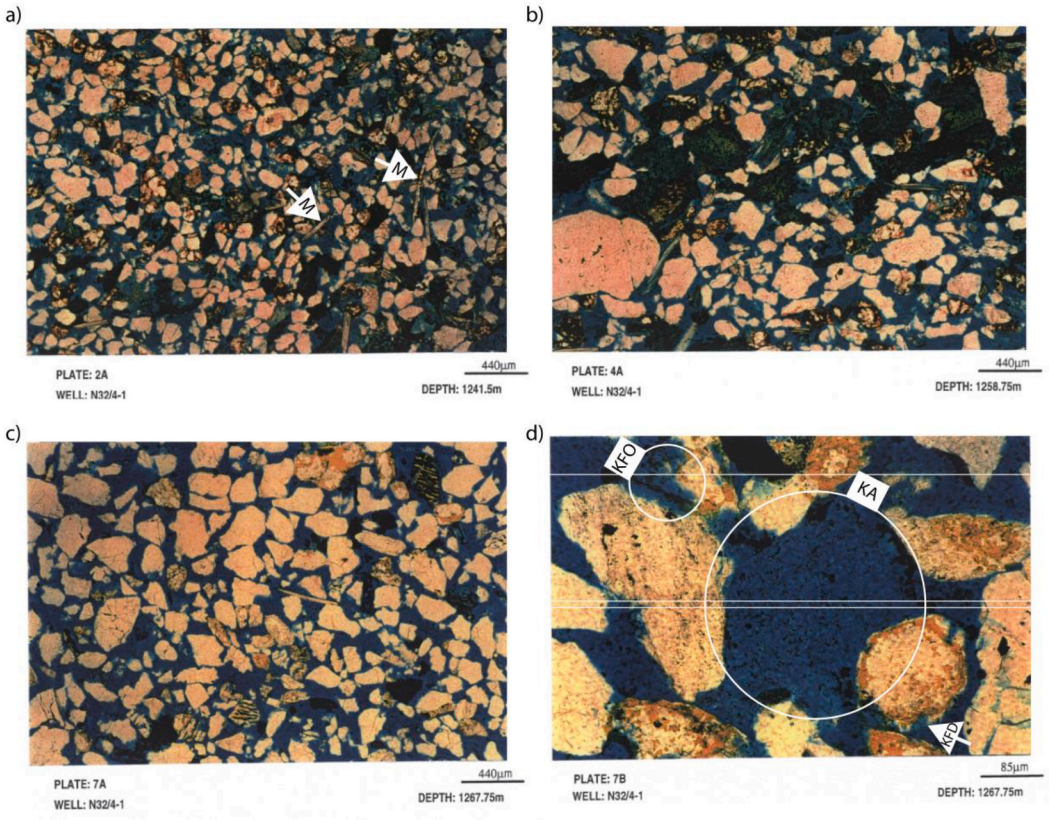

Fig. 17. Thin section images of sandstone at various depths (m MDRKB) of Sognefjord Formation core in well 32/4-1. (a) Intermediate permeability (~602mD) sandstone, (b) low permeability (70mD) sandstone, (c) high permeability (4600mD) sandstone. (d) A zoomed view of the high permeability sandstone (Modified after Martin and Lowrey, 1997). KA: Kaolinite, KFD: K-Feldspar Dissolution, KFO: K-Feldspar Overgrowth, and M: Muscovite.

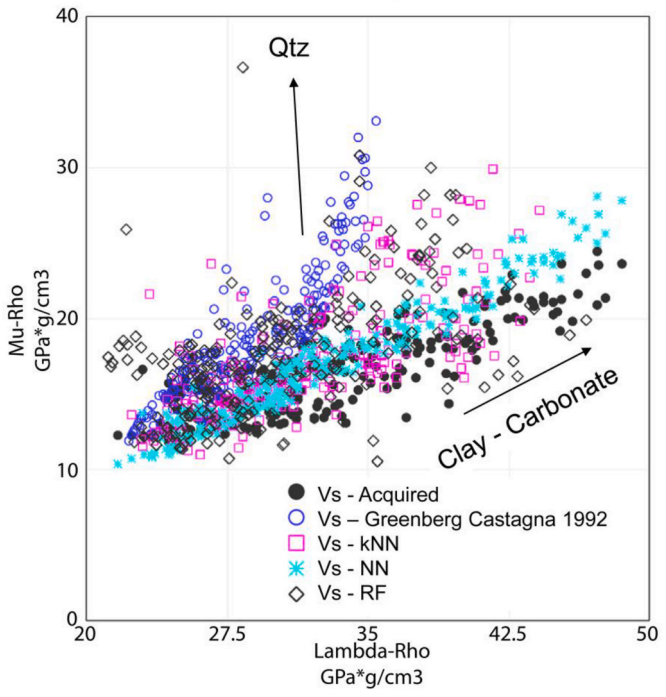

Fig. 18. Comparison of the acquired *Vs* with synthetic *Vs* generated using the Greenberg and Castagna (1992), and other selected machine learning methods, i.e., K-Nearest Neighbors (kNN), Neural Network (NN), and Random Forest (RF).

with the sand layers having suitable reservoir properties for CO_2 storage. The lower part of Fensfjord Formation comprises occasional deltaic sand deposition with possible lateral constrictions, which may pose a barrier for the injected CO_2.

A prograding shoreface possibly deposited the sands of Sognefjord, Fensfjord, and Krossfjord Formations. There is a prominent sheet-like sand distribution in the Sognefjord and Fensfjord Formations. The shoreface sand body also migrated along the strike towards the north gradually, from older Krossfjord to the younger Sognefjord Formations. The presence of various deltaic related sand bodies with uncertain lateral restrictions, low gross thickness, and moderate reservoir properties make the Krossfjord Formation the least suitable for CO_2 storage. For all the three sandstone formations (Sognefjord, Fensfjord, and Krossfjord), the porosity and permeability are increasing in the east towards the well 32/2-1 for always being present within the mechanically compacted zone.

We infer the uplift in the west (towards the well 32/4-1) to be approximately 1100 m, whereas the uplift is 1300 m in the east (towards well 32/2-1). At maximum burial depth, the reservoir sandstones have been exposed to a temperature higher than 70 °C in well 32/4-1. Therefore, the Sognefjord Formation in well 32/4-1 exhibits partial quartz cementation for being exposed to such temperature. The level of cementation increases in the deeper Fensfjord, and Krossfjord Formations, deteriorating the porosity.

The newly conceived equations for calculating V_{sh} and *Phi* from inverted seismic data yielded meaningful results despite the absence of acquired *Vs* logs. The resulted cubes were helpful in delineating the lateral changes in the reservoir sandstones; the vertical visibility was, however, dependent on the seismic resolution limitations.

Our study signifies the usage of nonlinear equations to calculate the reservoir properties from the inverted seismic readily; however, we

recommend future work on a similar line using a stochastic approach to take into account the inherent uncertainties of the input parameters.

CRediT author statement

Manzar Fawad: Conceptualization, Methodology, Formal analysis, Writing – original draft preparation. MD Jamilur Rahman: Data curation, Software, Validation, Writing- Reviewing,and Editing. Nazmul Haque Mondol: Project administration, Supervision, Validation, Writing- Reviewing, and Editing.

Declaration of competing interest

The authors declare the following financial interests/personal relationships which may be considered as potential competing interests: A patent applications "Rock physics model for shale volume estimation in subsurface reservoirs" was filed in Norwegian Industrial Property Office (NIPO), Ref no. AR412254832 on 23.01.2021. A Provisional patent application was also filed with the same title in the U.S. Patent and Trademark Office (USPTO), No. 63140896 on 24.01.2021.

Acknowledgments

We are thankful for the support and funding provided by the Research Council of Norway and industry partners Equinor and Total for the OASIS (Overburden Analysis and Seal Integrity Study for CO_2 Sequestration in the North Sea) project (RCN-CLIMIT Research Project #280472). We are obliged for the support and data provided by Gassnova, NPD, and Equinor and appreciate the fruitful discussion and valuable input from all the OASIS partners. We appreciate CGG for providing Hampson-Russell academic software licenses, dGB Earth Sciences for OpendTect, and Schlumberger for Petrel.

References

Aki, K., Richards, P.G., 1980. Quantitative Seismology: Theory and Methods. Freeman.
Aksu, I., Bazilevskaya, E., Karpyn, Z.T., 2015. Swelling of clay minerals in unconsolidated porous media and its impact on permeability. GeoResJ 7, 1–13.
Aplin, A.C., Macquaker, J.H., 2011. Mudstone diversity: origin and implications for source, seal, and reservoir properties in petroleum systems. AAPG Bull. 95, 2031–2059.
Asquith, G.B., Krygowski, D., Gibson, C.R., 2004. Basic well log analysis. American Association of Petroleum Geologists Tulsa, vol. 16.
Avseth, P., Mukerji, T., Mavko, G., 2005. Quantitative Seismic Interpretation: Applying Rock Physics Tools to Reduce Interpretation Risk. Cambridge university press.
Avseth, P., Veggeland, T., 2015. Seismic screening of rock stiffness and fluid softening using rock-physics attributes. Interpretation 3. SAE85–SAE93.
Avseth, P., Veggeland, T., Horn, F., 2014. Seismic screening for hydrocarbon prospects using rock-physics attributes. Lead. Edge 33, 266–274.
Bernabé, Y., Fryer, D.T., Hayes, J.A., 1992. The effect of cement on the strength of granular rocks. Geophys. Res. Lett. 19, 1511–1514.
Bjørkum, P.A., Oelkers, E.H., Nadeau, P.H., Walderhaug, O., Murphy, W.M., 1998. Porosity prediction in quartzose sandstones as a function of time, temperature, depth, stylolite frequency, and hydrocarbon saturation. AAPG Bull. 82, 637–648.
Bjørlykke, K., Egeberg, P.K., 1993. Quartz cementation in sedimentary basins. AAPG Bull. 77, 1538–1548.
Bjørlykke, K., Jahren, J., 2015. Sandstones and sandstone reservoirs. In: Petroleum Geoscience. Springer, pp. 119–149.
Bosch, M., Mukerji, T., Gonzalez, E.F., 2010. Seismic inversion for reservoir properties combining statistical rock physics and geostatistics: a review. Geophysics 75, 75A165–75A176.
Brown, A.R., 2010. GC Dim Spots in Seismic Images as Hydrocarbon Indicators. Search and Discovery.
Buland, A., Omre, H., 2003. Bayesian linearized AVO inversion. Geophysics 68, 185–198.
Chadwick, R.A., Zweigel, P., Gregersen, U., Kirby, G.A., Holloway, S., Johannessen, P.N., 2004. Geological reservoir characterization of a CO2 storage site: the utsira sand, sleipner, northern North Sea. Energy 29, 1371–1381.
Chuhan, F.A., Kjeldstad, A., Bjørlykke, K., Høeg, K., 2003. Experimental compression of loose sands: relevance to porosity reduction during burial in sedimentary basins. Can. Geotech. J. 40, 995–1011.
Connolly, P., 1999. Elastic impedance. Lead. Edge 18, 438–452.
Dreyer, T., Whitaker, M., Dexter, J., Flesche, H., Larsen, E., 2005. From spit system to tide-dominated delta: integrated reservoir model of the Upper Jurassic Sognefjord Formation on the Troll West Field. In: Geological Society, London, Petroleum Geology Conference Series. Geological Society of London, pp. 423–448.
Dvorkin, J., Nur, A., 1996. Elasticity of high-porosity sandstones: theory for two North Sea data sets. Geophysics 61, 1363–1370.
Ehrenberg, S.N., 1993. Preservation of anomalously high porosity in deeply buried sandstones by grain-coating chlorite: examples from the Norwegian continental shelf. AAPG (Am. Assoc. Pet. Geol.) Bull. 77, 1260–1286.
Fatti, J.L., Smith, G.C., Vail, P.J., Strauss, P.J., Levitt, P.R., 1994. Detection of gas in sandstone reservoirs using AVO analysis: a 3-D seismic case history using the Geostack technique. Geophysics 59, 1362–1376.
Fawad, M., Hansen, J.A., Mondol, N.H., 2020. Seismic-fluid detection-a review. Earth Sci. Rev. 103347.
Fawad, M., Mondol, N.H., Jahren, J., Bjørlykke, K., 2011. Mechanical compaction and ultrasonic velocity of sands with different texture and mineralogical composition. Geophys. Prospect. 59, 697–720.
Fawad, M., Mondol, N.H., Jahren, J., Bjørlykke, K., 2010. Microfabric and rock properties of experimentally compressed silt-clay mixtures. Mar. Petrol. Geol. 27, 1698–1712.
Gardner, G.H.F., Gardner, L.W., Gregory, A.R., 1974. Formation velocity and density—the diagnostic basics for stratigraphic traps. Geophysics 39, 770–780.
Giles, M.R., 1997. Diagenesis: A Quantitative Perspective: Implications for Basin Modelling and Rock Property Prediction. Springer.
Goodway, B., Chen, T., Downton, J., 1997. Improved AVO fluid detection and lithology discrimination using Lamé petrophysical parameters;"λρ","μρ", & "λ/μ fluid stack", from P and S inversions. In: SEG Technical Program Expanded Abstracts 1997. Society of Exploration Geophysicists, pp. 183–186.
Greenberg, M.L., Castagna, J.P., 1992. Shear-wave velocity estimation in porous rocks: theoretical formulation, preliminary verification and applications. Geophys. Prospect. 40, 195–209.
Halland, E.K., Mujezinovic, J., Riis, F., Bjørnestad, A., Meling, I.M., Gjeldvik, I.T., Tappel, I.M., Bjørheim, M., RØD, R., PHAM, V., 2014. CO2 Storage Atlas: Norwegian Continental Shelf. Norwegian Petroleum Directorate.
Hampson, D.P., Russell, B.H., Bankhead, B., 2005. Simultaneous inversion of prestack seismic data. In: SEG Technical Program Expanded Abstracts 2005. Society of Exploration Geophysicists, pp. 1633–1637.
Hansen, J.A., Yenwongfai, H., Fawad, M., Mondol, N., 2017. Estimating exhumation using experimental compaction trends and rock physics relations, with continuation into analysis of source and reservoir rocks: Central North Sea, offshore Norway. In: SEG Technical Program Expanded Abstracts 2017. Society of Exploration Geophysicists, pp. 3971–3975.
Hart, B.S., Macquaker, J.H., Taylor, K.G., 2013. Mudstone ("shale") depositional and diagenetic processes: implications for seismic analyses of source-rock reservoirs. Interpretation 1. B7–B26.
Herwanger, J., Koutsabeloulis, N., 2011. Seismic geomechanics: how to build and calibrate geomechanical models using 3D and 4D seismic data. EAGE.
Holgate, N.E., Jackson, C.A., Hampson, G.J., Dreyer, T., 2015. Seismic stratigraphic analysis of the middle jurassic Krossfjord and Fensfjord formations, Troll oil and gas field, northern North Sea. Mar. Petrol. Geol. 68, 352–380.
Kemper, M., Gunning, J., 2014. Joint Impedance and Facies Inversion–Seismic Inversion Redefined. First Break 32.
Kinn, S., Foldøy, P., Pettersen, K., Ramstad, F., Rasmussen, H., Hansen, T.H., Goldsmith, P.J., 1997. Final Well Report 32/4-1. Phillips Petroleum Company Norway, NPD Factpages.
Lancaster, S., Whitcombe, D., 2000. Fast-track 'coloured'inversion. In: SEG Expanded Abstracts, pp. 1298–1301.
Lee, M.W., 2003. Velocity Ratio and its Application to Predicting Velocities. US Department of the Interior, US Geological Survey.
Lehocki, I., Avseth, P., Mondol, N.H., 2020. Seismic methods for fluid discrimination in areas with complex geologic history—A case example from the Barents Sea. Interpretation 8, SA35–SA47.
Lindseth, R.O., 1972. Approximation of acoustic logs from seismic traces. J. - Can. Well Logging Soc. 5, 13–26.
Luo, C., Ba, J., Carcione, J.M., Huang, G., Guo, Q., 2020. Joint PP and PS prestack seismic inversion for stratified models based on the propagator matrix forward engine. Surv. Geophys. 41, 987–1028.
Ma, X.-Q., 2001. Global joint inversion for the estimation of acoustic and shear impedances from AVO derived P-and S-wave reflectivity data. First Break 19, 557–566.
Marcussen, Ø., Maast, T.E., Mondol, N.H., Jahren, J., Bjørlykke, K., 2010. Changes in physical properties of a reservoir sandstone as a function of burial depth–The Etive Formation, northern North Sea. Mar. Petrol. Geol. 27, 1725–1735.
Martin, M.A., Lowrey, C.J., 1997. Sedimentology and Petrography of the Upper Jurassic Cored Interval from Well 32/4-1 (No. 7944/Id). Robertson Research International Limited.
Mavko, G., Mukerji, T., Dvorkin, J., 2009. The Rock Physics Handbook: Tools for Seismic Analysis of Porous Media. Cambridge University Press.
Mondol, N.H., Bjørlykke, K., Jahren, J., 2008a. Experimental compaction of kaolinite aggregates-effects of grain size on mudrock properties. In: 70th EAGE Conference and Exhibition Incorporating SPE EUROPEC 2008. European Association of Geoscientists & Engineers, p. 40.
Mondol, N.H., Bjørlykke, K., Jahren, J., Høeg, K., 2007. Experimental mechanical compaction of clay mineral aggregates—changes in physical properties of mudstones during burial. Mar. Petrol. Geol. 24, 289–311.
Mondol, N.H., Fawad, M., Jahren, J., Bjørlykke, K., 2008b. Synthetic mudstone compaction trends and their use in pore pressure prediction. First Break 26, 43–51.
Mulrooney, M.J., Osmond, J., Skurtveit, E., Wu, L., Braathen, A., 2018. Smeaheia, a potential northern North Sea CO2 storage site: structural description and de-risking

strategies. In: Fifth CO2 Geological Storage Workshop. European Association of Geoscientists & Engineers, pp. 1–5.
NPD, 2020. Norwegian Petroleum Directorate Fact-Pages. [WWW Document]. URL accessed 8.3.20. https://factpages.npd.no.
Ødegaard, E., Avseth, P., 2004. Well Log and Seismic Data Analysis Using Rock Physics Templates. First Break (October).
PetroWiki, 2021. Permeability Determination [WWW Document]. URL accessed 3.24.21. https://petrowiki.spe.org/Permeability_determination.
Rahman, M.J., Fawad, M., Mondol, N.H., 2020. Organic-rich shale caprock properties of potential CO2 storage sites in the northern North Sea, offshore Norway. Mar. Petrol. Geol. 122, 104665.
Riley, N., 2010. Geological storage of carbon dioxide. Issues Environ. Sci. Technol. 29, 155.
Schmitt, D.R., 2015. Geophysical properties of the near surface earth: seismic properties. In: Treatise on Geophysics. Elsevier, pp. 43–87.
Sheriff, R.E., Geldart, L.P., 1995. Exploration Seismology. Cambridge university press.
Shuey, R.T., 1985. A simplification of the Zoeppritz equations. Geophysics 50, 609–614.
Smith, G.C., Gidlow, P.M., 1987. Weighted stacking for rock property estimation and detection of gas. Geophys. Prospect. 35, 993–1014.
Statoil, A.S., 2016. Mulighetsstudie - Planlegging og prosjektering av et CO2-lager på norsk kontinentalsokkel (No. OED 15/1785. Undergrunnsrapport Smeaheia.
Sundal, A., Nystuen, J.P., Dypvik, H., Miri, R., Aagaard, P., 2013. Effects of geological heterogeneity on CO2 distribution and migration–a case study from the Johansen Formation, Norway. Energy Procedia 37, 5046–5054.
Sundal, A., Nystuen, J.P., Rørvik, K.-L., Dypvik, H., Aagaard, P., 2016. The lower jurassic johansen formation, northern North sea–depositional model and reservoir characterization for CO2 storage. Mar. Petrol. Geol. 77, 1376–1401.
Thyberg, B., Jahren, J., Winje, T., Bjørlykke, K., Faleide, J.I., 2009. From mud to shale: rock stiffening by micro-quartz cementation. First Break 27, 53–59.
Thyberg, B.I., Jordt, H., Bjørlykke, K., Faleide, J.I., 2000. Relationships between sequence stratigraphy, mineralogy and geochemistry in Cenozoic sediments of the northern North Sea. Geological Society, London, Special Publications 167, 245–272.
Timur, A., 1968. An investigation of permeability, porosity, and residual water saturation relationships. In: SPWLA 9th Annual Logging Symposium. Society of Petrophysicists and Well-Log Analysts.
Verm, R., Hilterman, F., 1995. Lithology color-coded seismic sections: the calibration of AVO crossplotting to rock properties. Lead. Edge 14, 847–853.
Whitcombe, D.N., Connolly, P.A., Reagan, R.L., Redshaw, T.C., 2002. Extended elastic impedance for fluid and lithology prediction. Geophysics 67, 63–67.
Yenwongfai, H., Mondol, N.H., Lecomte, I., Faleide, J.I., Leutscher, J., 2018. Integrating facies-based Bayesian inversion and supervised machine learning for petro-facies characterization in the Snadd Formation of the Goliat Field, south-western Barents Sea. Geophys. Prospect. 67, 1020–1039.
Yenwongfai, H.D., Mondol, N.H., Faleide, J.I., Lecomte, I., 2017. Prestack simultaneous inversion to predict lithology and pore fluid in the Realgrunnen Subgroup of the Goliat Field, southwestern Barents Sea. Interpretation 5, SE75–SE96.
Zhao, L., Geng, J., Cheng, J., Han, D., Guo, T., 2014. Probabilistic lithofacies prediction from prestack seismic data in a heterogeneous carbonate reservoir. Geophysics 79, M25–M34.
Zoeppritz, K., 1919. VII b. Über Reflexion und Durchgang seismischer Wellen durch Unstetigkeitsflächen. Nachrichten von der Gesellschaft der Wissenschaften zu Göttingen. Mathematisch-Physikalische Klasse 1919 66–84.

RP-3

Probabilistic Analysis of Draupne Shale Caprock Reliability of the Alpha Prospect-A Potential CO_2 Storage Site in the Smeaheia Area, Northern North Sea

Md Jamilur Rahman
Jung Chan Choi
Manzar Fawad
Nazmul Haque Mondol

TCCS-11, 2021

PROBABILISTIC ANALYSIS OF DRAUPNE SHALE CAPROCK RELIABILITY OF THE ALPHA PROSPECT- A POTENTIAL CO_2 STORAGE SITE IN THE SMEAHEIA AREA, NORTHERN NORTH SEA

Md Jamilur Rahman[1*], Jung Chan Choi[2], Manzar Fawad[1], Nazmul Haque Mondol[1,2]

[1] University of Oslo (UiO), Oslo, Norway
[2] Norwegian Geotechnical Institute (NGI), Oslo, Norway

* Corresponding author e-mail: m.j.rahman@geo.uio.no

Abstract

CO_2 injection into a saline aquifer requires a viable caprock to arrest the vertical movement of the CO_2 plume. Quantitative assessment of caprock integrity is often challenging because of uncertainties involved in the model input parameters. In this study, Draupne Formation's reliability as caprock is evaluated before CO_2 injection by introducing a stochastic approach. We estimated both deterministic factors of safety and probabilistic failure values of different scenarios, and the results are compared. The probabilistic failure values are calculated using the First Order Reliability Method (FORM). Draupne formation shows a considerably low probability of failure with a high-reliability index in the initial stress condition. The sensitivity study reveals that the pore pressure and horizontal stress are the most crucial parameters and contribute two-thirds to failure probability. When the change of effective horizontal stresses in the reservoir is assumed considering the pore pressure change in the Troll field, this study shows that the field production may decrease the probability of shear failure. Moreover, the study indicates that the suggested probabilistic approach is critical in the presence of various uncertainties. However, the assumptions used in this study, especially the change in effective horizontal stresses within the reservoir, can be affected by other factors (e.g., stiffness contrast between reservoir and surroundings, geometrical effects, stress paths, etc.) and should be investigated further.

Keywords: *Caprock integrity; Caprock Reliability; Probability of failure; Draupne Formation; Smeaheia*

1. Introduction

Caprock assessment is a critical parameter in a CO_2 storage project because it prevents the vertical migration of fluids out of traps. The top seal commonly consists of fine-grained rocks, which have significantly small pore throat radii compared to the reservoir below and act as an impermeable layer due to exceptionally high capillary entry pressure. However, leakage occurs when the buoyancy pressure exceeds the capillary entry pressure. The capillary breakthrough is highly unlikely when the caprock consists of fine grain particles; instead, mechanical fracturing becomes the primary failure mood while the reservoir's pore pressure approaches the formation fracture strength [1]. The caprock failure risk significantly increases in the CO_2 storage project because injecting CO_2 into the saline aquifer will increase the reservoir pore pressure and affect the caprock's stress and strength. Therefore, seal strength characterization is necessary to prevent any CO_2 leakage risk.

The studied Alpha prospect is located in the Smeaheia area, northern North Sea, and investigated as a potential storage site by Equinor and Gassonova [2]. The main reservoir rocks comprise Upper Jurassic Sognefjord, Fensfjord, and Krossfjord formation sandstones, where the organic-rich Draupne and Heather Formation shales act as a caprock. Because of the significant amount of fine-grained sediments (i.e., clay minerals) in the caprock [3], the capillary breakthrough is very unlikely; hence, the injection-related top seal fracture is one of the main caprock failure risks in the Alpha prospect. However, estimation of caprock mechanical properties (i.e., brittleness) is very complex and uncertain. Moreover, the stress path changes due to injection are mostly unknown in a saline aquifer. In the presence of many uncertainties, the deterministic method of caprock analysis is somewhat questionable [4]; instead, a probabilistic approach is more suitable [5], [6]. Therefore, we conducted a probabilistic analysis to evaluate the Draupne Formation reliability as a caprock using the First Order Reliability Method (FORM). Comparison analysis between deterministic value and probabilistic assessment is also carried out. Moreover, the relative importance of different uncertain parameters is also evaluated. This probabilistic analysis technique for the subsurface structure is a new approach that was recently introduced by Rahman et al. [7] for fault reliability analysis. The hypothetical failure cases are evaluated to identify the reliability failure values to compare them with the in-situ probability of failure values.

2. Geologic framework of the study area

The study area experienced two rifting events, possibly during the Permo-Triassic and the Late Jurassic to Mid-Cretaceous times [8]–[10]. A wide basin with deep-rooted faults and thick syn-depositional wedges was centered on the Horda Platform during the 1st rifting event. Several N-S trending faults were formed, which were believed to be rooted in Caledonian zones of crustal weakness [10], demarcating the area's structural elements. The Smeaheia area is bounded by two faults, where the Øygarden Fault Complex (ØFC) delineates the east, and the Vette fault outlines the western boundary shown in Figure 1a. In the Late Jurassic to Mid

Cretaceous time during the 2nd event, rifting and tilting activities shifted westward and assumed that weak stretching with the reactivation of major Permo-Triassic faults on the Horda Platform [8]–[13].

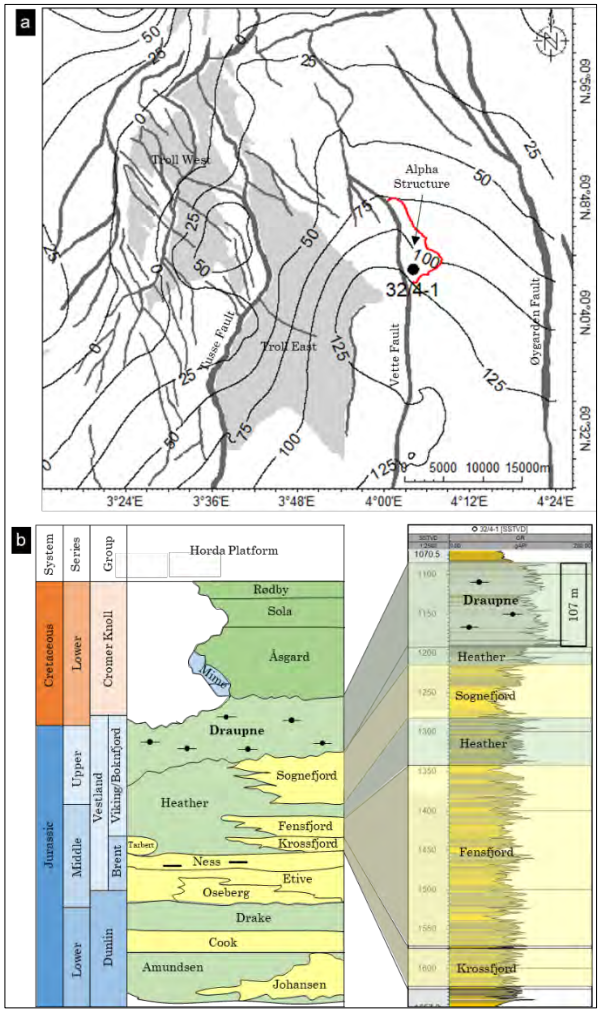

Figure 1: Location map of the Horda Platform showing the major and minor faults with Troll Fields as reference. The contour lines represent the Draupne Formation thickness adapted from [3]. The red polygon against the Vette fault is the Alpha prospect (a). A generalized stratigraphic succession of the Horda Platform showing the Jurassic and Lower Cretaceous formations and the vertical distribution of the Upper Jurassic reservoir-caprock configuration is shown in well 32/4-1 (b).

The primary caprock Draupne Formation shale is part of the Viking Group, deposited in the Late Jurassic syn-rift time within the East Shetland Basin, the Viking Graben, and over the Horda Platform area [2]. The thickness of this formation varies significantly [3], which varies between 75 to 125 m within the Alpha prospect (Fig. 1a), while the well 32/4-1 (Alpha) penetrates 107 m thick Draupne shale. The formation consists of dark grey-brown to black, non-calcareous, carbonaceous, occasionally fissile claystone deposited in an open marine environment with restricted bottom circulation and often with anaerobic conditions [14]. It is also characterized by high gamma-ray values (usually above 100 API) due to high Uranium and TOC content. Interbedded sandstone and siltstone, as well as minor limestone streaks and concretions, are also present. Draupne Formation generally has a diachronous contact with the Heather Formation in the lower boundary. However, on the northern Horda Platform, Late Jurassic sandstones of the Sognefjord Formation mark the base of the Draupne Formation. The upper boundary of the Draupne Formation is usually characterized by Cretaceous rock (Cromer Knoll Group), which has a higher velocity and lower gamma-ray response than the over and underlying rocks [15] (Fig. 1b).

3. Material and Method

Caprock structural reliability depends on the mechanical properties of that layer and the stress state of the area. Mohr-Coulomb failure criterion approach can evaluate caprock stability. This study assesses the Draupne caprock probability of failure by an analytical model defined by the Mohr-Coulomb failure criterion. The corresponding deterministic factor of safety values is also estimated for comparison.

3.1 Model parameters

The recent study suggested that a normal faulting regime with isotropic horizontal stress conditions is a reasonable stress model for the Alpha prospect [16]. Moreover, the extended leak-off test data in the studied area reveal that the vertical stress gradient is significantly higher than the horizontal stress, reflecting a normal faulting regime (Fig. 2). Therefore, the normal faulting with isotropic horizontal stress conditions was used in this study. The hydrostatic pressure gradient shown in Figure 2 was calculated using the depth profile from well 32/4-1 drilled in the Alpha prospect. However, the vertical and horizontal stress profiles were estimated using the extended leak-off test (XLOT) data scouted from the Statoil Underground report [17].

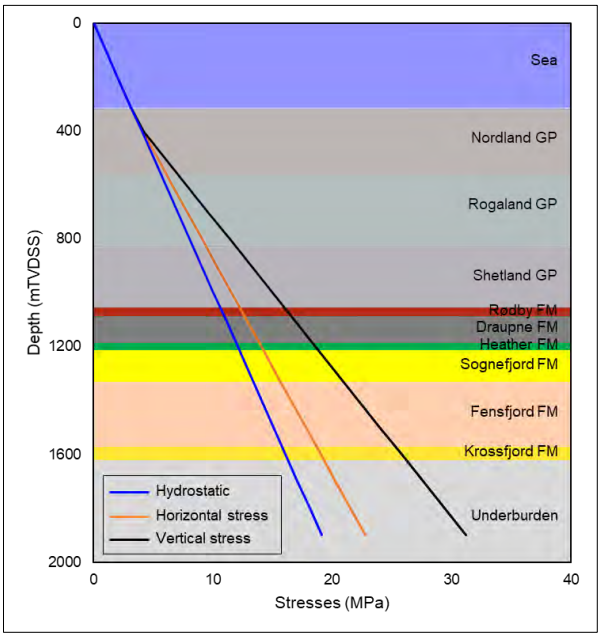

Figure 2: In-situ stress profile for the Alpha structure calculated using extended leak-off test (XLOT) data [17] indicating normal faulting regime with isotropic horizontal stress condition (adapted from [7]).

This study only focuses on the in-situ stress condition, and the dynamic CO_2 injection effect is not considered. However, the pore pressure depletion scenario due to the possible communication with the hydrocarbon production in the Troll Field was analyzed. Maximum 4 MPa depletion estimated by the Statoil studies was used as a case in this modeling work. However, we did not consider any stress path changes while running that scenario.

Moreover, the theoretical failure scenario was analyzed to get a quantitative estimation of probability failure values compared to real cases. The caprock failure scenario was estimated by decreasing horizontal stress while the other parameters (i.e., vertical stress and pore pressure) remain in the initial condition. A summary of all cases is shown in Table 1, which were evaluated to estimate the Draupne caprock probability of failure.

Table 1: Various caprock scenarios tested in this study.

	Assumptions
Case-1	Initial stress condition
Case-2	Depletion due oil/gas production from Troll
Case-3	Caprock failure due to decreasing σ_3

The Mohr-Coulomb plots of the Draupne Formation for three cases are shown in Figure 3. The initial state stress condition (case-1) represents a relatively large distance between the Mohr circle, and Coulomb failure (Fig. 3a). The pore pressure depletion scenario (case-2) further shifts the circle away from the envelope by increasing the effective stresses (Fig. 3b). Moreover, the theoretical caprock failure plots show that the case-3 shear failure occurs at 55^0 σ_1 plane (Fig. 3c). The theoretical caprock failure value for case-3 (σ_h^3) is estimated using the MohrPlotter software by selecting 'failure by horizontal stress' mode, and the horizontal stress value estimated was 10.57 MPa when the shear failure occurs.

The laboratory test result of rock strength parameters (i.e., cohesion and friction angle) of the Draupne Formation were scouted [16]–[20] and also estimated from the wireline log. The compressional velocity (V_p) based empirical equation proposed by Horsrud [19] was used, which stated that:

$$C_0 = 0.77V_p^{2.93} \quad (\Phi = 30 - 55\%), \qquad (1)$$

where C_0 is compressional strength in MPa and V_p is in km/s.

In the model, the input parameters used are shown in Table 2. It should be noted that statistical information in the table is from a limited database and should only be used to test the methodology. It may represent the field condition. Five random variables such as vertical stress (σ_v), horizontal stress (σ_h), pore pressure (P_p), cohesion (S_0), and friction angle (ϕ) are used to run the stochastic model where arithmetic average with standard deviation was used to define the ranges. However, for additional properties of case-2 and case-3 (i.e., P_p^2 & σ_h^3), the same standard deviation (i.e., like case-1) value was used (Table 2).

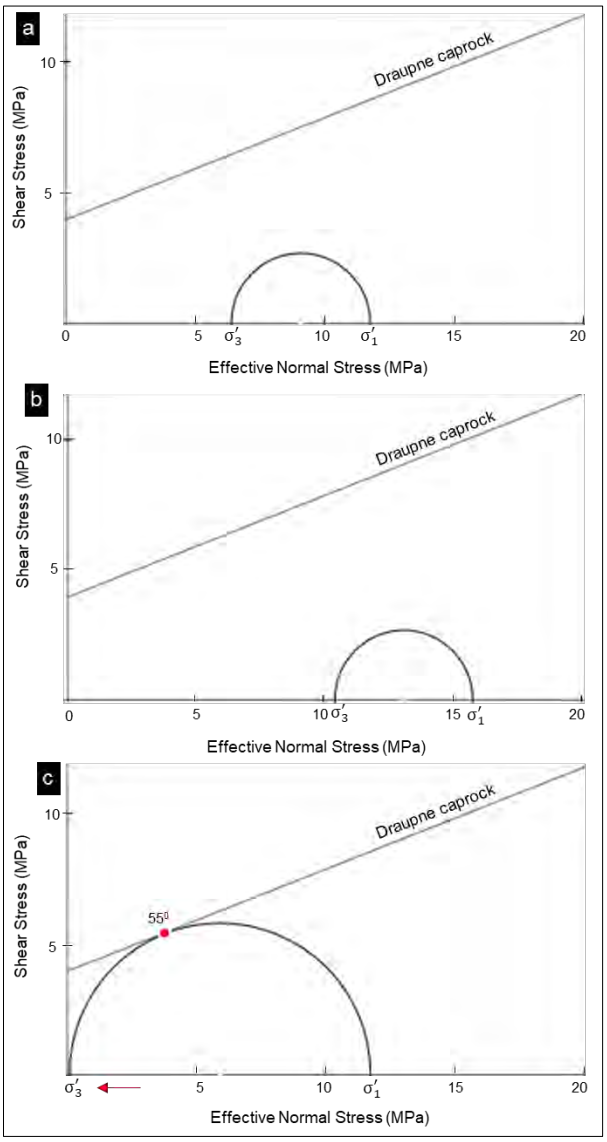

Figure 3: Mohr-Columb plots with Draupne Formation failure surface: (a) initial reservoir stress state condition (case-1), (b) depleted scenario due to oil/gas production from Troll (case-2), and (c) shear failure scenario due to decreasing σ_3 (case-3).

Table 2: Input parameters for the model with the type of distribution and data sources. The superscript numbers in the parameters name represent as case numbers. Note the statistical information in this table is based on a limited database and should be used only to test the methodology. It may not represent the field conditions.

Parameters	Average	Unit	Standard Deviation	Distribution
σ_v	22.25	MPa	0.65	Normal
$\sigma_h^{1,2}$	16.85	MPa	0.95	Normal
σ_h^3	10.57	MPa	0.95	Normal
$P_p^{1,3}$	10.48	MPa	1.32	Normal
P_p^2	6.48	MPa	1.32	Normal
S_0	3.93	MPa	1.05	Log-Normal
ϕ	21.63	Degree	5.14	Normal

Standard deviation can indicate the data spread and might serve as a measure of uncertainty. For example, a small standard deviation value indicates clustered closely around the mean with more precision and vice versa. Moreover, most geological processes follow a normal or log-normal law [5]; thus, we assumed normal distribution for most of the properties except caprock cohesion in this study. A log-normal distribution was used for caprock cohesion assuming the parameter cannot be physically negative within three standard deviations of average.

3.2 Model definition

The reliability of a structural component depends on the uncertainties in load (S) and resistance (R), and if both are normally distributed, the failure probability might be assessed directly by the safety margin M and denoted as:

$$M = R - S, \tag{2}$$

and the probability of failure may be assessed through:

$$P_f = P(R - S \leq 0) = P(M \leq 0), \tag{3}$$

where M is normally distributed with parameters with the mean $\mu_M = \mu_R - \mu_S$ and standard deviation $\sigma_M = \sqrt{\sigma_R^2 + \sigma_S^2}$. The failure probability may be determined by the use of the standard normal distribution function as:

$$P_f = \Phi\left(\frac{0-\mu_M}{\sigma_M}\right) = \Phi(-\beta), \tag{4}$$

where $\mu_M/\sigma_M = \beta$ is called the safety/reliability index, which is the standard deviation by which the mean value of the safety margin M exceeds zero or most likely exceeds the failure point (Fig. 4a). However, if the resistance and the load cannot be described by only two random variables but rather by functions of the same random variables and statistically dependent, the safety margin M will be:

$$M = R - S = f_1(X) - f_2(X) = g(X), \tag{5}$$

where X is a vector with n so-called basic random variables, the function g(X) is denoted as the limit state function, which is a boundary between desired (g(X) >0) and undesired (g(X) ≤ 0) performance of any structure and defined within a mathematical model for functionality and performance [21]. In this study, the Mohr-Coulomb failure criteria-based limit state function was considered. Assuming isotropic horizontal stress condition within a normal faulting regime, the factor of safety (FoS) is defined as:

$$FoS = \frac{[\left(\frac{\sigma_1' + \sigma_3'}{2}\right) + \frac{S_0}{tan\phi}]sin\phi}{\frac{\sigma_1' - \sigma_3'}{2}}, \tag{6}$$

$$\sigma_1' = \sigma_1 - p_p, \tag{7}$$

$$\sigma_3' = \sigma_3 - p_p, \tag{8}$$

where, σ_1' is effective vertical stress, σ_1 is vertical stress, σ_3' is effective horizontal stress, σ_3 is horizontal stress, p_p is pore pressure, S_0 is cohesion, and ϕ is friction angle.

The state of the structure is safe when the factor of safety is greater than 1 and fails when it is less than 1. Therefore, the limit-state function defines as:

$$g(x) = FoS - 1, \tag{9}$$

where, g(x) is the limit-state function which is the boundary between safe (g(x) >0) and failure (g(x) ≤ 0) state.

The First Order Reliability Model (FORM) was used to estimate the failure probability of Draupne caprock. This method was proposed by Hasofer and Lind [22] and widely used in practical engineering problems [6], [23]. This method linearizes the failure surface (g(z)) at a design point z* where the shortest distance is called the reliability index (β) and normal vector direction to the failure surface denoted as α (Fig. 4c). However, the inaccurate result could be estimated if the linearization design points are not correctly selected. Moreover, the reliability index value is also used as a performance indicator and directional vector to describe the random variables' relative importance. We analyzed this sensitivity factor to identify the significance of each parameter used in the model.

The Python-based open-source structural reliability analysis module PyRe [24] was used to initiate and run the FORM models. PyRe has been created using the core function of the Finite Element Reliability Using Matlab (FERUM) project, which is very flexible and extensive, making it applicable to a large number of problems. Other software such as MohrPlotter version-3 and Excel 2016 were also used for the Mohr-Coulomb plot and sensitivity plots, respectively.

The probabilistic reliability analyses deal with the structural uncertainties, provide a rational framework, and have a different approach than the deterministic estimation [6]. Although the failure probability approach is widely used for engineering purposes, it is new for caprock characterization. Therefore, a comparison between deterministic safety factors with the probability of failure was also analyzed. Such a comparison will help to understand caprock failure probability values.

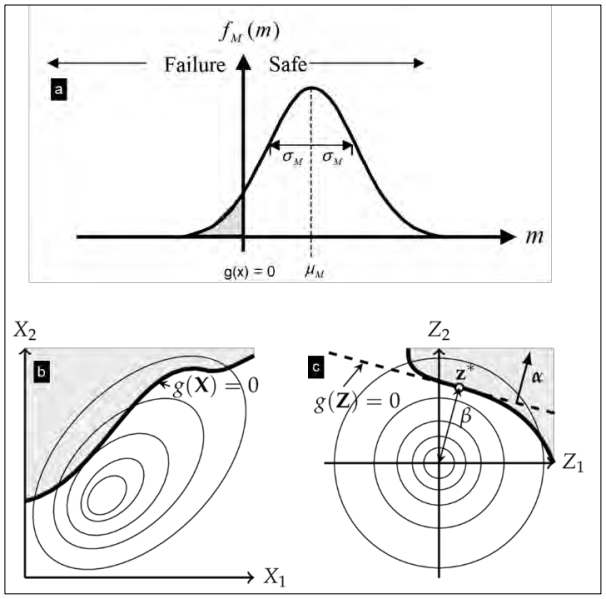

Figure 4: Structural reliability concept and model definition: (a) Gaussian distribution of the probability distribution function of safety margin M showing the failure and safe events modified after Faber [23], (b) limit state function g(X) stated in the physical space using two random variables (X_1 and X_2), and (c) after normalizing the random variables into standardized normally distributed variable (Z_1 and Z_2) with the design point z* and reliability index β. Note that the grey shaded area denoted the failure domain (modified after Madsen et al., [25]).

4. Results

The deterministic and probabilistic failure values with corresponding reliability index (β) are summarized in Table 3. In the in-situ stress condition (case-1), the Draupne Formation probability of failure (PoF) is 1.38E-08, while the factor of safety (FoS) shows a value of 2.60. However, the depleted scenario (case-2) due to Troll Field production decreases the failure probability number (<3.0E-08). The safety factor also increases from 2.60 to 3.16. Although the FoS increases from case-1 to case-2, the increase is not significant compared to PoF. Moreover, the reliability index value also increases from case-1 to case-2. The FoS for theoretical shear failure scenario (case-3) shows caprock failure by representing a value=1. The corresponding PoF and β value showed 2.42E-02 and 1.97, respectively.

Table 3: Deterministic factor of safety (FoS) and the probability of failure (PoF) of different cases. Corresponding reliability index (β) values are also shown.

	FoS	PoF	β
Case-1	2.60	1.38E-08	5.56
Case-2	3.16	<3.0E-08	<5.0
Case-3	1.00	2.42E-02	1.97

The comparative analysis between deterministic and probabilistic sensitivity gives a unique opportunity to explain the reliability of the proposed method (i.e., FORM). The deterministic sensitivity was estimated using the 'one variable at a time' (OVAT) technique [26], [27], where each input parameter is alternatively assigned its minimum and maximum values when the other parameters are fixed to their mean values. The parameters ranges used are summarized in Table 4.

The tornado diagram of case-1 (Fig. 5) illustrated that the initial horizontal stress (σ_h^1) has the most significant impact on the factor of safety than the rest of the input parameters. Moreover, initial vertical stress (σ_v) and Cohesion (S_0) have significant influences.

Table 4: Minimum and maximum values used in the deterministic sensitivity analysis.

Parameter	Value Range
Initial vertical stress (σ_v)	21.60 - 22.90 (MPa)
Initial horizontal stress (σ_h^1)	15.90 - 17.80 (MPa)
Pore Pressure (P_p^1)	9.16 - 11.80 (MPa)
Cohesion (S_0)	2.88 - 4.98 (MPa)
Friction angle (ϕ)	16.49 - 26.77^0

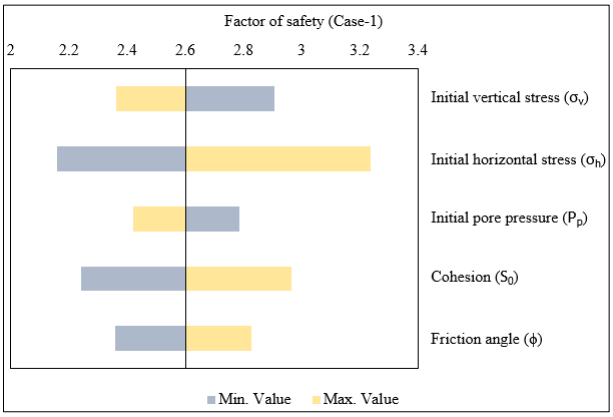

Figure 5: The tornado diagram of the case-1 scenario illustrated the relative importance of the input parameters.

The relative design sensitivity factor or the relative importance factors (α) are often referred to as probabilistic sensitivity and indicate the effect of each parameter on the reliability function [28]. This is very useful for the ranking of random variables and obtained by performing several probabilistic analyses and treating every individual parameter as a deterministic variable in each study [29], [30]. A positive value indicates a direct relationship between the variable's value and the response, while a negative sensitivity suggests an inverse relation. However, the square of each sensitivity factor (α_i^2) is a measure of its contribution to the probability, and the sum is equal to 1. The relation between the input parameters with the probabilistic response is illustrated in Figure 6, where pore pressure and friction angle show a direct connection with the result, and horizontal stress and cohesion suggested an inverse relation. However, the vertical stress showed a significantly low positive value (approximately zero) and indicated insignificance contribution during the calculating probability of failure.

Figure 7 display the relative contribution of each input parameter within different cases. The failure probability using the FORM technique mainly depends on the horizontal stress, pore pressure, and cohesion, in which pore pressure is the most significant. A substantial pore

pressure influence was observed in case-2 (i.e., 60%), which is a depleted scenario due to Troll Field production. A gentle contribution of friction angle is illustrated in case-1; however, there is very little impact in the rest of the cases.

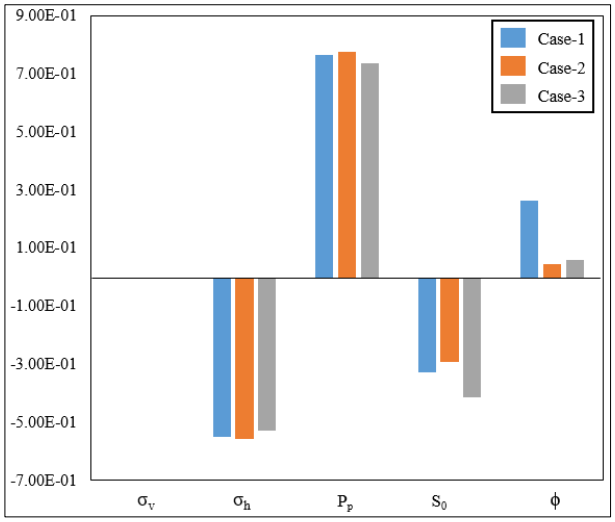

Figure 6: Sensitivity factor (α) in the probabilistic analysis of Draupne Caprock shale using FORM showing the relations between random input variables and the responses.

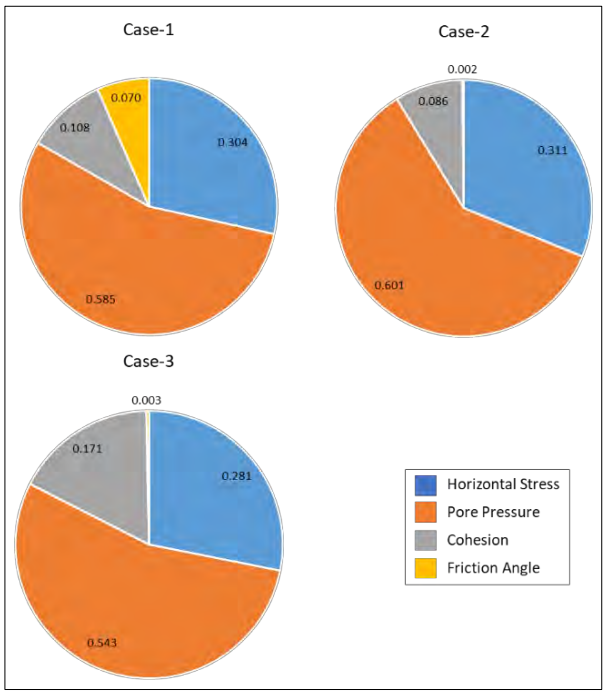

Figure 7: Square of each factor (α^2) showing the contribution variation to the probability failure analysis within different cases.

5. Discussion

The input parameters used for caprock failure analysis are often highly uncertain, and the deterministic safety factor does not reflect the corresponding failure probability [6]. The approach used in this study can integrate all the possible uncertainties by adding the ranges and probabilistically estimating the structural reliability. For example, case-2 failure probability significantly decreases the chances of failure compared to case-1, while the increase of safety factor is insignificant (i.e., from 2.6 to 3.16). Therefore, the probabilistic reliability analysis for subsurface structures could be a useful tool to incorporate the parameter uncertainties and quantify the failure risks. However, the probabilistic method is susceptible to the input parameter ranges and should be defined very carefully. For instance, in this analysis, the standard deviation value defined for σ_v and σ_h is only 3% and 6% of the average value, indicating these properties are not very sensitive and lead to a significantly low PoF, and β value (Table 3). Moreover, the insignificance relative contribution of σ_v might be the effect of the uncertainty range. Therefore, the emphasis is needed to define the uncertain parameters range before use as an input parameter in the failure probability model.

The reliability index and probability of failure in any structure are a relative measurement of the current condition and provide a qualitative estimation of the expected performance [31]. However, integrity analysis of caprocks presents under certain pressure, and temperature conditions are very complex. Although our modeling approach considers various pressure conditions, the temperature effect on caprock mechanical behavior is beyond the scope. Moreover, the variation between the deterministic and probabilistic sensitivity indicates that further analysis is needed to examine the method's reliability. The model used in this study is a novel approach for caprock failure characterization; hence, there are no published charts for standard. However, this method is widely used in geotechnical engineering, and we compare our result with the expected performance range for embankment shown in Table 5 [31]. According to the chart, the in-situ condition (case-1) and depleted scenarios (case-2) are above the highest performance level (High). However, the theoretical failure case does not represent the same reliability index value and is classified as Poor (case-3). The probability of unsatisfactory performance illustrated that for case-3, 24 of every 1000 would result in a failure event. The failure events are significantly different from the theoretical failure due to decreased horizontal stress and pore pressure changes. However, the unsatisfactory performance number of the in-situ stress scenario (case-1) is only 13 out of 10^9 runs, making this case safer.

Table 5: The defined performance level with corresponding unsatisfactory events and reliability index values adapted from U.S. Army Corps of Engineers [31].

Expected Performance Level	Probability of Unsatisfactory Performance	Reliability Index (β)
High	0.0000003	5.0
Good	0.00003	4.0
Above average	0.001	3.0
Below average	0.006	2.5
Poor	0.023	2.0
Unsatisfactory	0.07	1.5
Hazardous	0.16	1.0

6. Conclusion

The probabilistic estimation of the Draupne Formation caprock's reliability is the critical condition for a successful Alpha prospect CO_2 injection site. This study's outcomes proved to be a valuable approach when several uncertainties are present. However, it needs a careful investigation to define the parameter ranges before using them as model input. The main observations of this study are as follows:

- In the initial condition, the reliability of Draupne caprock shales is excellent, with a very low chance of mechanical failure. Moreover, considering the Troll Field depletion scenarios, the failure probability decreases significantly.
- Pore pressure and friction angle directly relate to the probabilistic response, while horizontal stress and cohesion have an inverse relation. Overall, pore pressure and horizontal stress are the main contributors to the probability of failure value.
- Although there is a similar increasing or decreasing trend between deterministic and probabilistic values of different cases, the variations are significant in the probabilistic approach.

This study indicates that the Draupne Formation can be a safety barrier during CO_2 injection into the Alpha prospect. Nevertheless, it should be perceived that this study has focused on the feasibility of the methodology rather than the field evaluation. The injection-related potential risks can be affected by other factors (e.g., stiffness contrast between reservoir and surroundings, geometrical effects, drainage condition, stress paths, etc.) and need to be evaluated further with a better assessment of the statistical input and the numerical simulation.

Acknowledgments

We are thankful for the funding provided by the Research Council of Norway for the OASIS (Overburden Analysis and Seal Integrity Study for CO2 Sequestration in the North Sea) project (NFR-CLIMIT project #280472) and the FME NCCS Centre (NFR project #257579/E20). We are also grateful to Schlumberger for the Petrel academic software license, Python Software Foundation for Python, and Rick Allmendinger's Stuff for MohrPlotter.

References

[1] G. M. Ingram, J. L. Urai, and M. A. Naylor, "Sealing processes and top seal assessment," in *Norwegian Petroleum Society Special Publications*, vol. 7, Elsevier, 1997, pp. 165–174.

[2] NPD CO2 Atlas, "NPD CO2 Atlas Report," 2014.

[3] M. J. Rahman, M. Fawad, and N. H. Mondol, "Organic-rich shale caprock properties of potential CO_2 storage sites in the northern North Sea-offshore Norway," *Mar. Pet. Geol.*, vol. 122, p. 104665, 2020.

[4] J. M. Duncan, "Factors of safety and reliability in geotechnical engineering," *J. Geotech. geoenvironmental Eng.*, vol. 126, no. 4, pp. 307–316, 2000.

[5] J. T. Christian, "Geotechnical engineering reliability: How well do we know what we are doing?," *J. Geotech. geoenvironmental Eng.*, vol. 130, no. 10, pp. 985–1003, 2004.

[6] F. Nadim, "Tools and strategies for dealing with uncertainty in geotechnics," in *Probabilistic methods in geotechnical engineering*, Springer, 2007, pp. 71–95.

[7] M. J. Rahman, J. C. Choi, M. Fawad, and N. H. Mondol, "Probabilistic analysis of Vette fault stability in potential CO_2 storage site Smeaheia, offshore Norway" *Int. J. Greenh. Gas Control*, vol. 108, p. 103315, 2021.

[8] R. B. Færseth, "Interaction of Permo-Triassic and Jurassic extensional fault-blocks during the development of the northern North Sea," *J. Geol. Soc. London.*, vol. 153, no. 6, pp. 931–944, 1996.

[9] R. Steel and A. Ryseth, "The Triassic—Early Jurassic succession in the northern North Sea: megasequence stratigraphy and intra-Triassic tectonics," *Geol. Soc. London, Spec. Publ.*, vol. 55, no. 1, pp. 139–168, 1990.

[10] P. S. Whipp, C. L. Jackson, R. L. Gawthorpe, T. Dreyer, and D. Quinn, "Normal fault array evolution above a reactivated rift fabric; a subsurface example from the northern Horda Platform, Norwegian North Sea," *Basin Res.*, vol. 26, no. 4, pp. 523–549, 2014.

[11] A. M. Roberts, G. Yielding, N. J. Kusznir, I. Walker, and D. Dorn-Lopez, "Mesozoic extension in the North Sea: constraints from flexural backstripping, forward modelling and fault populations," in *Geological Society, London, Petroleum Geology Conference series*, 1993, vol. 4, no. 1, pp. 1123–1136.

[12] A. M. Roberts, N. J. Kusznir, G. Yielding, and H. Beeley, "Mapping the bathymetric evolution of the Northern North Sea: from Jurassic synrift archipelago through Cretaceous–Tertiary post-rift subsidence," *Pet. Geosci.*, vol. 25, no. 3, pp. 306–321, 2019.

[13] R. J. Steel, "Triassic–Jurassic megasequence stratigraphy in the Northern North Sea: rift to post-rift evolution," in *Geological Society, London, Petroleum Geology Conference series*, 1993, vol. 4, no. 1, pp. 299–315.

[14] J. Vollset and A. G. Doré, *A revised Triassic and Jurassic lithostratigraphic nomenclature for the Norwegian North Sea*. Oljedirektoratet, 1984.

[15] NPD, "NPD FactPages," 2021. https://npdfactpages.npd.no/factpages/Default.aspx?culture=en.

[16] E. Skurtveit, J. C. Choi, J. Osmond, M. Mulrooney, and A. Braathen, "3D fault integrity screening for smeaheia CO2 injection site," in *14th Greenhouse Gas Control Technologies Conference Melbourne*, 2018, pp. 21–26.

[17] Statoil Underground report, "Feasibility study of planning and design of a CO2 storage facility on the Norwegian Continental Shelf – Smeaheia," 2016.

[18] M. Gutierrez, L. E. Øino, and R. Nygaard, "Stress-dependent permeability of a de-mineralised fracture in shale," *Mar. Pet. Geol.*, vol. 17, no. 8, pp. 895–907, 2000.

[19] P. Horsrud, E. F. Sønstebø, and R. Bøe, "Mechanical and petrophysical properties of North Sea shales," *Int. J. Rock Mech. Min. Sci.*, vol. 35, no. 8, pp. 1009–1020, 1998.

[20] E. Skurtveit *et al.*, "Mechanical testing and sealing capacity of the Upper Jurassic Draupne Formation, North Sea," *49th US Rock Mech. Symp. Am. Rock Mech. Assoc.*, 2015.

[21] O. Ditlevsen and H. O. Madsen, *Structural Reliability Methods*, Internet e. John Wiley and Sons, 2007.

[22] A. M. Hasofer and N. C. Lind, "Exact and invariant second-moment code format," *J. Eng. Mech. Div.*, vol. 100, no. 1, pp. 111–121, 1974.

[23] M. H. Faber, "Basics of structural reliability," *Swiss Fed. Inst. Technol. ETH, Zürich, Switz.*, 2009.

[24] J. Hackl, "PyRe documentation," 2018. http://github.com/hackl/pyre.

[25] H. O. Madsen, S. Krenk, and N. C. Lind, *Methods of structural safety*. Courier Corporation, 2006.

[26] Campolongo, F., Kleijnen, J.P.C., Andres, T., 2000. Screening methods. Wiley Ser. Probab. Stat.

[27] Rohmer, J., Seyedi, D.M., 2010. Coupled large scale hydromechanical modelling for caprock failure risk assessment of CO2 storage in deep saline aquifers. Oil Gas Sci. Technol. l'Institut Français du Pétrole 65, 503–517.

[28] S. K. Easley, S. Pal, P. R. Tomaszewski, A. J. Petrella, P. J. Rullkoetter, and P. J. Laz, "Finite element-based probabilistic analysis tool for orthopaedic applications," *Comput. Methods Programs Biomed.*, vol. 85, no. 1, pp. 32–40, 2007.

[29] NESUS Theoretical Manual, "Southwest Research Institute," San Antorio, Texas, 2011.

[30] F. L. G. Pereira, D. Roehl, J. P. Laquini, M. F. F. Oliveira, and A. M. Costa, "Fault reactivation case study for probabilistic assessment of carbon dioxide sequestration," *Int. J. Rock Mech. Min. Sci.*, vol. 71, pp. 310–319, 2014.

[31] USA Army Corps of Engineers, "Engineering and design introduction to probability and reliability methods for use in geotechnical engineering," Washington, D.C., 1997. [Online]. Available: www.usace.army.mil/usace-docs.

RP-4

Seismic-derived geomechanical properties of potential CO_2 storage reservoir and cap rock in Smeaheia area, northern North Sea

Manzar Fawad
Md Jamilur Rahman
Nazmul Haque Mondol

The Leading Edge, 2021

Seismic-derived geomechanical properties of potential CO_2 storage reservoir and cap rock in Smeaheia area, northern North Sea

Manzar Fawad[1], Md Jamilur Rahman[1], and Nazmul Haque Mondol[1,2]

https://doi.org/10.1190/tle40040254.1

Abstract

Geologic CO_2 storage site selection requires reservoir, seal, and overburden investigation to prevent injection- and storage-related risks. Three-dimensional geomechanical modeling and flow simulation are crucial to evaluate these mechanical-failure-related consequences; however, the model input parameters are limited and challenging to estimate. This study focuses on geomechanical properties extracted from seismic-derived elastic property cubes. The studied reservoirs (Middle Jurassic Sognefjord, Fensfjord, and Krossfjord formation sandstones) and cap rocks (Heather and Draupne formation shales) are located in the Smeaheia area, northern North Sea, and are evaluated for a potential CO_2 storage site. From the elastic property cubes, i.e., acoustic impedance, P- to S-wave velocity ratio, and bulk density, we obtained geomechanical property cubes of Young's modulus, Poisson's ratio, shear modulus, lambda-rho, and mu-rho. Petrophysical property cubes such as porosity and shale volume were also available and were extracted from the elastic property cubes using deterministic methods. We evaluated the geomechanical properties to observe their relationship with depth, compaction/cementation, and petrophysical properties to characterize the cap and reservoir rocks. We found good coherence between the geomechanical and petrophysical properties and their relationship with compaction as a function of depth. The brittleness analyses using elastic property crossplots reveal that both the cap and reservoir rocks are mainly ductile to less ductile, posing lower fracturing risk during CO_2 injection. This also indicates lower risks of associated microseismic and possible CO_2 leakage.

Introduction

Geologic CO_2 storage (GCS) into a saline aquifer is one of the many solutions for reducing anthropogenic greenhouse gas emissions into the atmosphere (IPCC, 2014). This method has been demonstrated as a safe and reliable solution and is well documented by the Intergovernmental Panel on Climate Change (IPCC) and the International Energy Agency. In partnership with the industry, the Norwegian government has developed a strategy to evaluate potential large-scale (gigatonne storage potential) storage sites for CO_2 sequestration in the Norwegian Continental Shelf. The Smeaheia area is one of the potential sites, where Sognefjord, Fensfjord, and Krossfjord formation sandstones are the main reservoir rocks, and Draupne and Heather formation shales are the primary cap rocks (Figure 1). For evaluating a potential GCS, the storage and capping viability are critical and require proper investigation. It is essential to know the vertical and horizontal variations in reservoir properties (for instance, porosity and permeability) to predict the behavior of an injected CO_2 plume and its migration upward to the base of the reservoir seal (Chadwick et al., 2004; Riley, 2010). A simulation in a 3D geomechanical model can be a possible way to assess the plume behavior, changes in rock mechanical properties, and the associated potential risks. However, making a simulation model by stochastically distributing various properties from well-log data will not reflect the reservoir's heterogeneities. Therefore, it is crucial to obtain reservoir properties using 3D seismic in addition to well-log data.

Extracting reservoir properties from seismic data has always been an objective of geophysicists since commercial seismic has been used for hydrocarbon exploration (Yenwongfai et al., 2017a; Fawad et al., 2020a). Lindseth (1972) put forward a new processing method, displaying and interpreting seismic data that were mainly the inverse of producing seismograms from borehole sonic logs. Following Lindseth's steps presently, various types of seismic inversion algorithms exist, including colored impedance inversion (Lancaster and Whitcombe, 2000), simultaneous amplitude

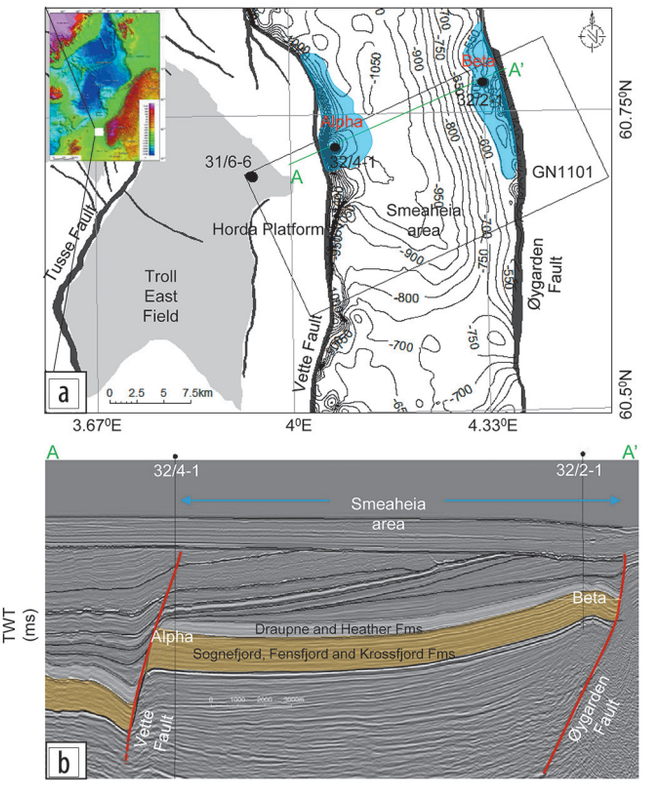

Figure 1. (a) Location of the CO_2 storage site Smeaheia, offshore Norway. Inset map is modified after Olesen et al. (2010). (b) A southwest–northeast-running inline 1066 of 3D survey GN1101 over the Smeaheia area showing the Alpha and Beta prospects and other regional structures delineated by the key surfaces. Both the dry wells (32/4-1 and 32/2-1) are shown on the seismic section.

[1]University of Oslo, Oslo, Norway. E-mail: manzar.fawad@geo.uio.no; m.j.rahman@geo.uio.no; m.n.h.mondol@geo.uio.no.
[2]Norwegian Geotechnical Institute, Oslo, Norway.

variation with offset inversion (Ma, 2001; Hampson et al., 2005), and joint facies-based impedance inversion (Kemper and Gunning, 2014). This process can run in both poststack and prestack seismic data, employing deterministic or stochastic methods and with or without a background low-frequency model. The rock properties generally are extracted from inverted elastic properties using rock-physics models (e.g., Dvorkin and Nur, 1996; Avseth and Ødegaard, 2004).

The reservoir properties obtained from seismic inversion are an amicable solution, and after well calibration, they can be used as an input for the geomechanical model (Herwanger and Koutsabeloulis, 2011; Yenwongfai et al., 2017b, 2018). The CO_2 storage in geologic formation has geomechanical implications, including reservoir stress-strain and microseismicity, borehole stability, cap-rock sealing integrity, and the potential for fault reactivation and related seismic events (Rutqvist, 2012). The geomechanical properties obtained from seismic can be evaluated further using crossplots (Goodway et al., 1997; Perez Altamar and Marfurt, 2014) in addition to the geomechanical simulation.

This research focuses on extracting and analyzing the reservoir and cap-rock geomechanical properties (e.g., Young's modulus, Poisson's ratio, shear modulus, lambda-rho, and mu-rho) from seismic and well-log data. The results will be used to develop and calibrate the field-scale 3D geomechanical model for the potential CO_2 storage site Smeaheia in the northern North Sea.

Geology of the study area

The Smeaheia area is located at the northeastern edge of the northern North Sea on the Horda Platform (Figure 1). Two structural closures, Alpha (32/4-1) and Beta (32/2-1), for potential CO_2 storage are bounded by major faults — Vette fault (VF) in the west and Øygarden fault complex (ØFC) in the east. The Alpha structure is located in the footwall of the VF, whereas the Beta structure is located in the hanging wall of the ØFC (Rahman et al., 2020). Considering only the Sognefjord Formation sandstone (i.e., good quality reservoir unit), both structures have a significant storage capacity potential of roughly 100 Mt each (Statoil, 2016). The reservoir and cap rock belong to the Viking Group that deposited in the Middle to Upper Jurassic time (Figure 2a). The Sognefjord, Fensfjord, and Krossfjord formations comprise reservoir sandstone units. The Sognefjord Formation is overlain by the Heather and Draupne formation shales, the potential cap rocks in the area, with combined thickness ranging from 79 to 129 m. The Sognefjord Formation thickness ranges from 68 to 110 m based on wells 32/4-1 and 32/2-1, respectively (Figure 2b). The formation comprises coastal-shallow marine, medium- to coarse-grained, well-sorted, friable, locally micaceous, and minor argillaceous sandstone. The middle reservoir unit (i.e., Fensfjord Formation) is 103 to 229 m thick; the sandstones are fine to medium grained, well sorted, and moderately friable to consolidated containing shale intercalations. The lowest unit (i.e., Krossfjord Formation) is 47 to 72 m thick, with medium- to coarse-grained, well-sorted, and loose to friable sandstone. The bioclastic material and occasional carbonate cemented bands occur in all three reservoir sandstones.

The Heather Formation shale interfingers with sandstones of the Krossfjord, Fensfjord, and Sognefjord formations (Figure 2b) and consists mainly of silty claystone with thin streaks of limestone, occasionally becoming highly micaceous grading into sandy siltstone (NPD, 2020). The Draupne Formation shale (the main cap rock) is deposited in a marine environment with restricted bottom circulation, mostly under anaerobic conditions (NPD, 2020). It comprises dark gray-brown to black, usually noncalcareous, carbonaceous, and fissile claystone and is characterized by high gamma ray radioactivity (often above 100 API units).

Method

A 3D seismic volume GN1101 (full and angle stacks) covering the Smeaheia area, wireline log data from two exploration wells 32/4-1 (Alpha) and 32/2-1 (Beta), and the elastic property cubes inverted from the 3D seismic GN1101 were available for the study. These cubes were generated using a simultaneous inversion on the partial seismic stacks to obtain the acoustic impedance, P- to S-wave velocity ratio (V_P/V_S), and density (RHOB) in our complementary work, followed by reservoir property cubes extraction (M. Fawad et al., personal communication, 2020). These reservoir properties were the volume of shale (Vsh) and porosity (Phi) cubes. In the present study, we generated Young's modulus (E), Poisson's ratio (ν), shear modulus (mu), lambda-rho, and mu-rho cubes using well-established relations documented in the literature (Goodway et al., 1997; Smidt, 2009; Perez Altamar and Marfurt, 2014; Simm and Bacon, 2014) to evaluate the reservoir viability.

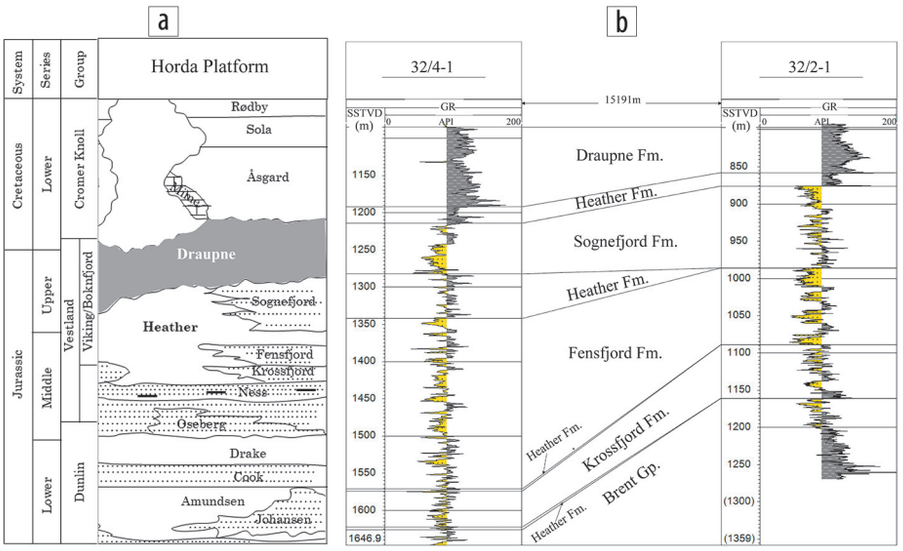

Figure 2. (a) A generalized Early Jurassic to Early Cretaceous stratigraphic succession in the study area (modified from Halland et al., 2014). (b) A west to east stratigraphic correlation between the wells 32/4-1 and 32/2-1 is flattened on Top Draupne Formation (primary seal). The potential reservoir Sognefjord, Fensfjord, and Krossfjord formation sandstones show several prograding cycles.

Comparing the seismic-derived geomechanical properties with the same parameters obtained from well-log data showed a good agreement, confirming the process's adequacy (Figure 3).

We generated a function to convert the dynamic to the static Young's modulus such that in the near surface, $E_{static} \approx 1/5E_{dynamic}$, and at depth, $E_{static} \approx 1/3E_{dynamic}$ (Herwanger and Koutsabeloulis, 2011). Static Poisson's ratio was assumed to be equal to dynamic Poisson's ratio ($\nu_{static} \approx \nu_{dynamic}$).

Results

Seal and reservoir rock comparison. Using the template proposed by Perez Altamar and Marfurt (2014), we generated Poisson's ratio and Young's modulus crossplots. We used the geomechanical and petrophysical data extracted from the seismic-derived elastic properties corresponding to the seal (Heather and Draupne formations) and the reservoir units (Sognefjord, Fensfjord, and Krossfjord formations). The seal or cap-rock points fall within the high Poisson's ratio, low Young's modulus domain, whereas the reservoir sands plot at the low Poisson's ratio and high Young's modulus area (Figure 4a). The data show a strong trend of increasing Young's modulus values with decreasing Poisson's ratio. This trend demonstrates the limitation of using a synthetic shear-wave velocity (V_S) log for prestack inversion (M. Fawad et al., personal communication, 2020).

The rise in shear modulus indicates increasing rock strength due to compaction and possible quartz cementation (Figure 4b). The highest mu values in Figure 4b are evident in the reservoir sandstone points (Figure 4c) with the highest Young's modulus values. The porosity decreases with an increase in Young's modulus and a decrease in the Poisson's ratio (Figure 4d). Overall, the cap-rock shale points plot within the "ductile" zone, whereas the reservoir sands spread from ductile to "less-brittle" regions depending on porosity and the volume of shale and compaction/cementation level (Figure 4).

Perez Altamar and Marfurt (2014) demonstrate the utility of lambda-rho–mu-rho rock-physics templates for lithology characterization and brittleness correlation with rock properties. Using this template, lambda-rho–mu-rho were crossplotted corresponding to the seal (Draupne and Heather formations) and reservoir (Sognefjord, Fensfjord, and Krossfjord formations) units (Figure 5). The plot shows two distinct seal and reservoir clusters merging at the lambda-rho values between 20 and 25 (GPa × g/cm^3) (Figure 5a). Generally, both of the clusters fall within the "less-ductile" area, except for few points plotting within the less-brittle domain with relatively high shear modulus values (Figure 5b). These less-brittle points are clean sands (Figure 5c) with low porosities (Figure 5d).

Reservoir rock formations. Now we focus on the reservoir formation zones, first using the Perez Altamar and Marfurt (2014) Poisson's ratio versus Young's modulus crossplot corresponding to the reservoir sandstones of Sognefjord, Fensfjord, and Krossfjord formations. The shallowest reservoir, i.e., the Sognefjord Formation, mostly plots within the "ductile" area, whereas the deepest Krossfjord Formation reservoir generally falls within the less-ductile zone (Figure 6a). Few Krossfjord Formation points plot within the ductile and less-brittle zones. The Krossfjord data that plot in

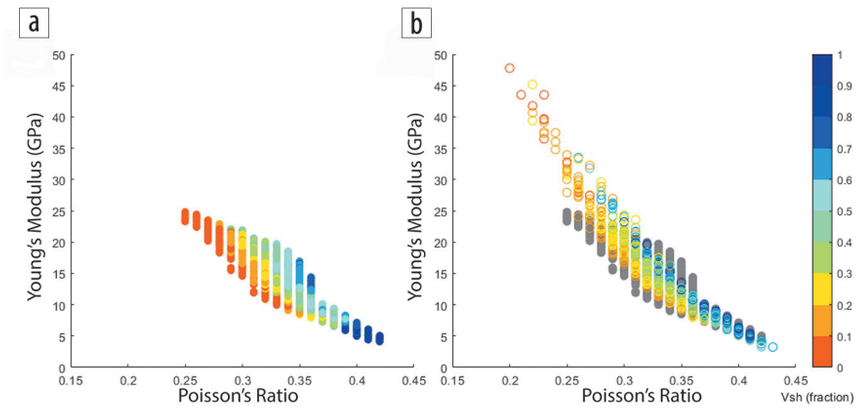

Figure 3. Comparison between the inverted cube data extracted within a distance of 100 m around the two wells (32/4-1 and 32/2-1) and the properties obtained from well logs onto the Poisson's ratio–Young's modulus plane. (a) Data from seismic color-coded with Vsh extracted from the prestack inversion. (b) Data from well log overlapping the seismic-derived data points (gray).

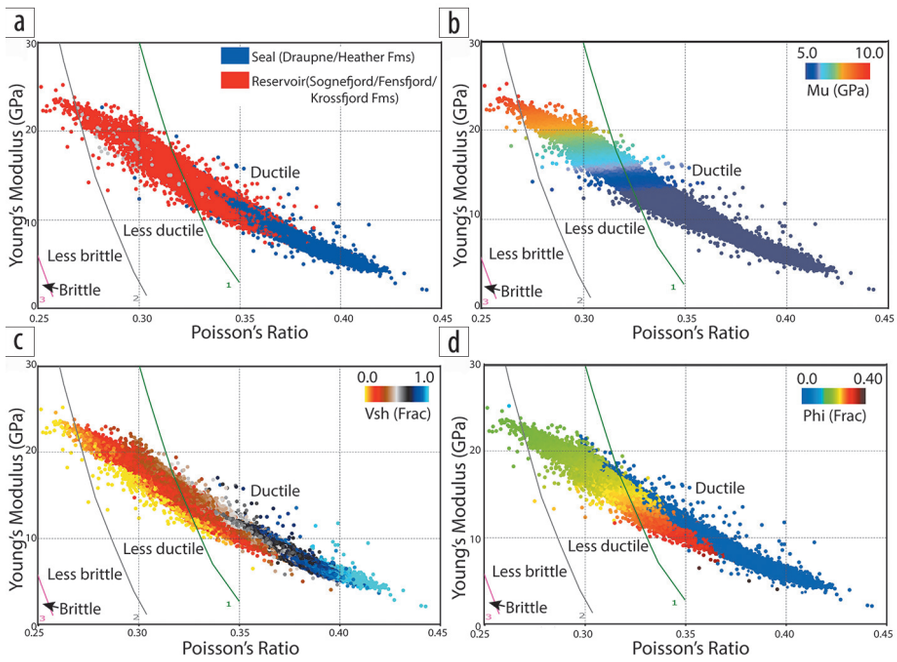

Figure 4. Poisson's ratio versus Young's modulus crossplot color-coded with (a) seal/reservoir classification, (b) shear modulus (mu), (c) volume of shale (Vsh), and (d) porosity (phi).

the less-brittle zone represent compacted or possibly quartz-cemented sandstones having high shear modulus (Figure 6b). The Heather Formation shales that interfinger the reservoir sandstones (Figure 2a) plot within the "ductile" zone (Figure 6c), with the clean sands showing a decrease in porosity with a decrease in Poisson's ratio and an increase in Young's modulus (Figure 6d).

The lambda-rho–mu-rho crossplot with Perez and Marfurt (2014) classification corresponding to the Sognefjord, Fensfjord, and Krossfjord formation sandstones gives an insight into the elastic property limits of these zones (Figure 7a). Almost all of the data plot within the less-ductile zone, except for some points falling within the less-brittle zone close to the less-ductile–less-brittle boundary. The points with the highest shear modulus plotting within the less-brittle region show higher compaction and possible quartz cementation; however, the points with low mu values are possible data picked close to the Øygarden fault (Figure 7b). Some points with high Vsh values, possibly of interfingering Heather Formation, tend to plot closer to the ductile zone (Figure 7c). The porosity trend shows a decrease in porosity with increasing lambda-rho and mu-rho (Figure 7d).

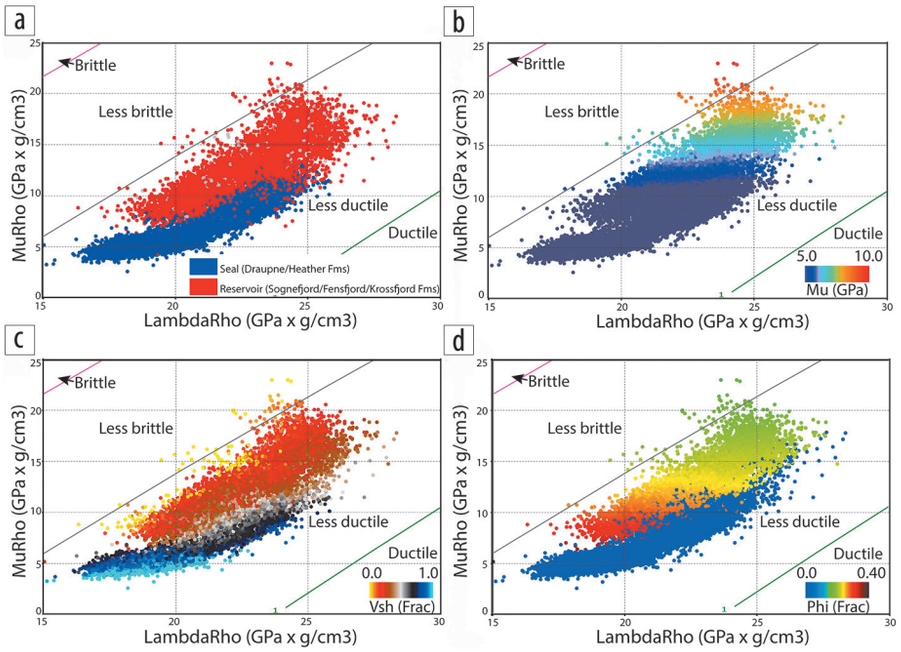

Figure 5. The lambda-rho versus mu-rho crossplot color-coded with (a) seal/reservoir classification, (b) shear modulus (mu), (c) volume of shale (Vsh), and (d) porosity (phi).

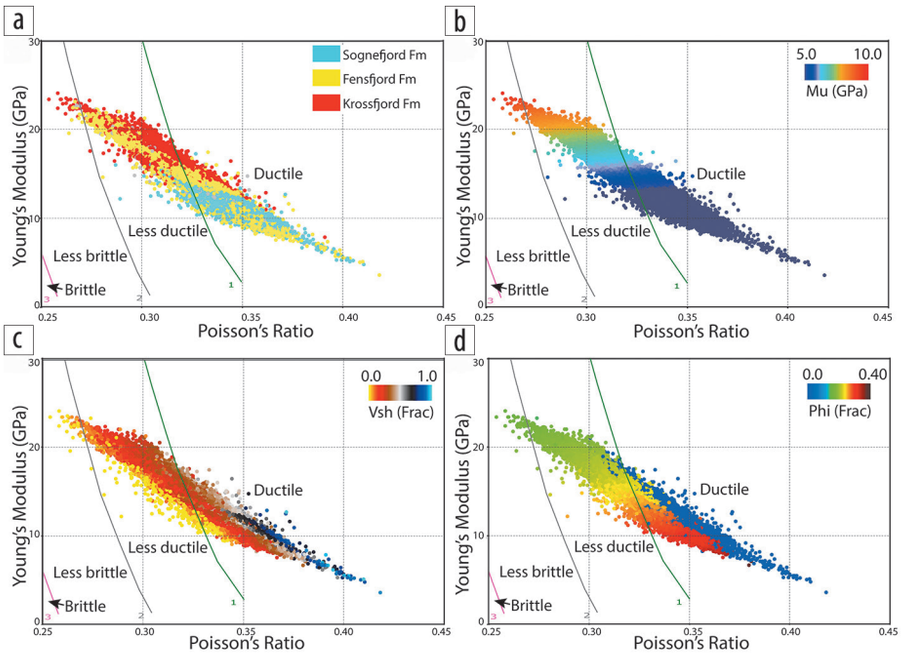

Figure 6. Poisson's ratio versus Young's modulus crossplot color-coded with (a) reservoir formation classification, (b) shear modulus (mu), (c) volume of shale (Vsh), and (d) porosity (phi).

One can directly incorporate the seismic-derived petrophysical and geomechanical properties in a geologic model for reservoir or geomechanical modeling (Figure 8). The model comprises the three sandstone reservoirs of Sognefjord, Fensfjord, and Krossford formations. There are clean sands with Vsh of approximately 20% in the eastern part of the area on the top around the well 32/2-1 and the lower part of the grid around the well 32/4-1 in the west (Figure 8a). There is a decrease in porosity on the top surface (i.e., Top Sognefjord) from east to west as the upper part of sandstone (approximately 4 m) becomes tight and silty toward well 32/4-1. In contrast, the lower layers contain good porosities (Figure 8b). The seismic resolution at this depth (1200–1300 m) is approximately 16 m. The seismic was able to delineate this thin approximately 4 m upper zone by cumulating the overlying Heather Formation response. The vertical and lateral variations in static geomechanical properties (Young's modulus and Poisson's ratio) reflect changes in lithology, porosity, compaction, and cementation (Figures 8c and 8d).

Discussion

The amount of strain a material can endure before a brittle failure depends on its ductility (Ingram and Urai, 1999). Ductility is a function of various factors such as lithology, confining pressure, pore pressure, temperature, and differential stress/strain ratio (Davis et al., 2011). In sedimentary basins, the confining pressure increases with increasing burial

depth. Furthermore, temperatures above approximately 70°C lead to the onset and development of the chemical compaction (quartz cementation), resulting in stiffening and embrittlement of the rock.

Our complementary work (M. Fawad et al., personal communication, 2020) suggests that the quartz cementation is not severe in the area as the major part of the reservoir zones is present above the chemical compaction domain. The Heather and Draupne formation seal rocks are likely within the mechanical compaction zone in the area falling in the ductile zone in the Perez Altamar and Marfurt (2014) classification on the Poisson's ratio–Young's modulus crossplot. The Perez Altamar and Marfurt (2014) classification on the lambda-rho–mu-rho crossplot showed a less-ductile grouping for the seal rocks. This implies that the Heather and Draupne formation cap rocks have a potentially lower risk of fracturing during CO_2 injection, provided the pressure is lower than the fracture pressure of the cap rock.

In the case of the reservoir zones, a minor effect of cementation can be seen increasing from Sognefjord to the deeper Fensfjord and the deepest Krossfjord Formation (M. Fawad et al., personal communication, 2020). The Poisson's ratio–Young's modulus crossplot analysis with Perez Altamar and Marfurt (2014) classification shows that the high-porosity sands fall within the ductile zone, and with a decrease in porosity, the sandstone trend gradually moves from the less-ductile to less-brittle zone. On the lambda-rho–mu-rho crossplot with Perez Altamar and Marfurt (2014) classification, all three reservoir sandstone units plot mainly within the less-ductile zone with a few points falling in the less-brittle region. This implies that the reservoir sandstones in the area are not brittle, reducing fracturing risk during the injection. This also reduces the possibility of microseismic event generation. One should keep in mind that the stress state of a rock, the existence of planes of weakness, and pore pressure must be considered to predict fracturing in addition to the brittleness index (Herwanger et al., 2015). The Perez Altamar and Marfurt (2014) method, though, is region-specific; however, in our area, there are carbonates laminations only with thickness under seismic resolution; therefore, the classification we assume is useful.

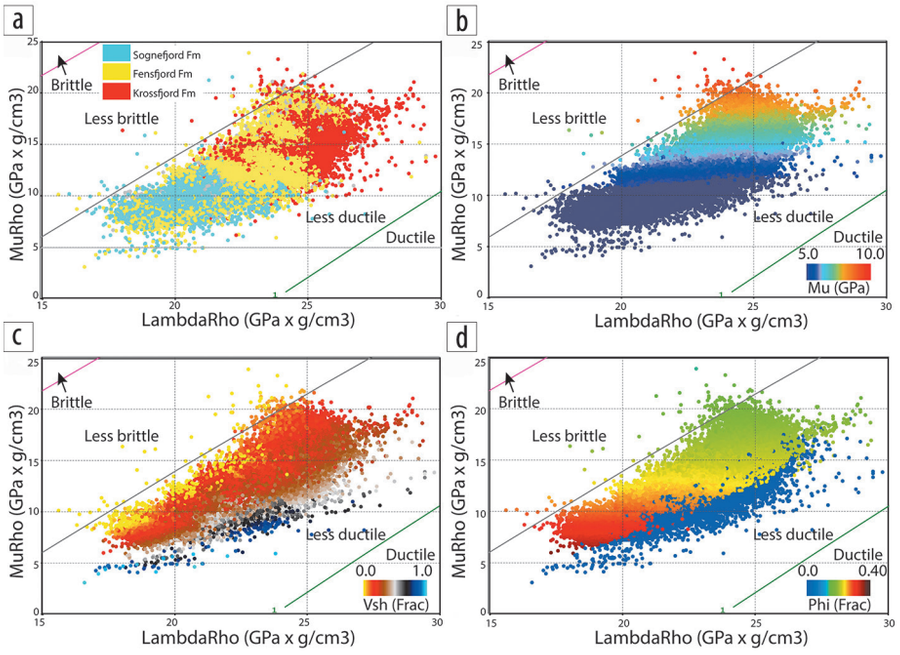

Figure 7. The lambda-rho versus mu-rho crossplot data color-coded with (a) reservoir formation classification, (b) shear modulus (mu), (c) volume of shale (Vsh), and (d) porosity (phi).

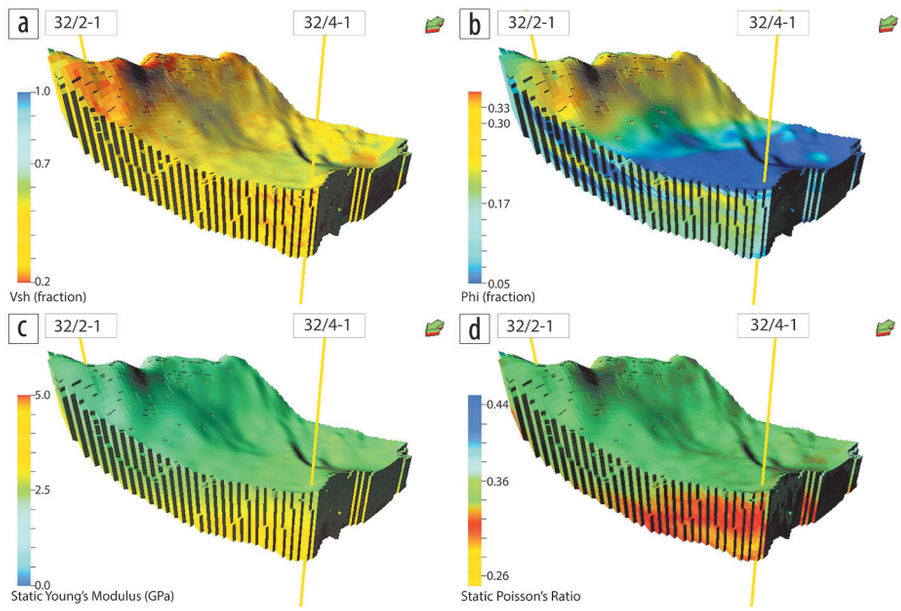

Figure 8. (a) Seismic-derived petrophysical and geomechanical properties incorporated in a geologic model grid. (a) Volume of shale (Vsh), (b) porosity (phi), (c) static Young's modulus, and (d) static Poisson's ratio. The model grid is vertically exaggerated, and the cells' axes directions are different from the seismic cube orientation.

We found a good agreement between the reservoir petrophysical properties and the geomechanical parameters. Young's modulus increases (Figure 9) and Poisson's ratio decreases with formation depth resulting in higher compaction and possible quartz cementation. A high volume of shale and high porosity exhibit high Poisson's ratio and low Young's modulus. The plume behavior mainly depends on the horizontal and vertical heterogeneities within the reservoir. These variations in the reservoir rocks are adequately reflected in

the petrophysical and geomechanical properties. In the Sleipner GCS project, for example, the time-lapse seismic enables us to identify and delineate the migration path and subsequent accumulation of the CO_2 plume with reasonable accuracy (Chadwick et al., 2004). Therefore, predicting the CO_2 plume behavior in a model using seismic-derived properties likely will yield better results, signifying the utility of geophysical methods.

Conclusions

Both the reservoir sandstones (Sognefjord, Fensfjord, and Krossfjord formations) and the seal/cap-rock shales (Heather and Draupne formations) are ductile to less ductile, lowering the potential risk of fracturing and induced seismicity during CO_2 injection. The geomechanical properties extracted using the seismic-derived elastic properties showed good agreement with depth, lithology, porosity, and compaction/cementation. The information from seismic data reduces the uncertainties regarding large-scale geomechanical properties and their distributions. We expect the geomechanical model built using these properties will predict any critically stressed fault movement with expanding reservoir pressure and associated CO_2 leakage. Further work is in progress using the geomechanical and petrophysical property cubes to make and calibrate a geomechanical model. TLE

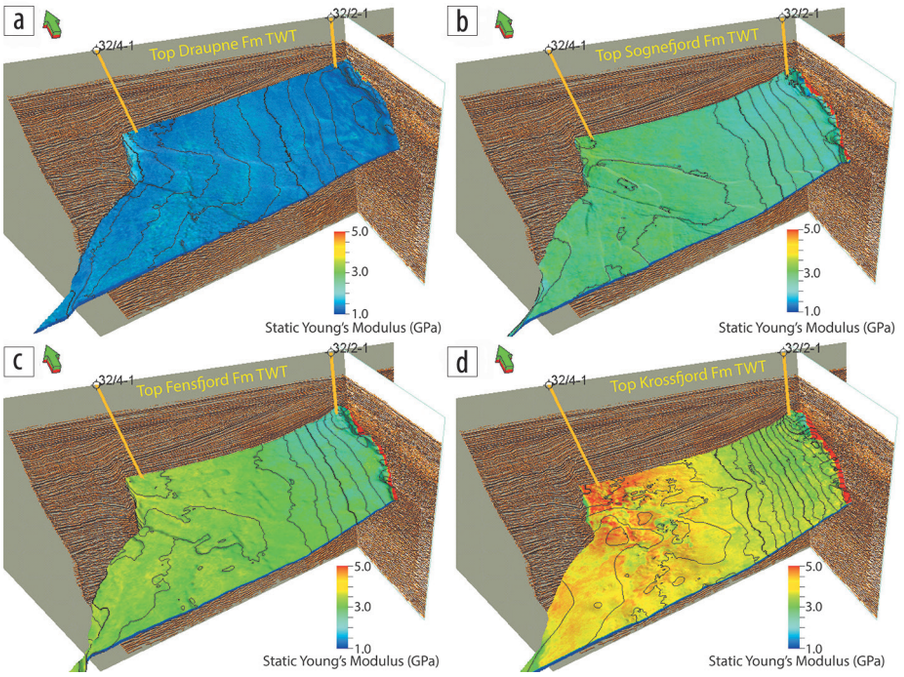

Figure 9. Static Young's modulus values extracted below two-way time (TWT) surfaces of (a) Top Draupne Formation, (b) Top Sognefjord Formation, (c) Top Fensfjord Formation, and (d) Top Krossfjord Formation. The search window was kept 16 ms below each surface. Both lateral and vertical increase in the static Young's modulus is evident as the formations get deeper.

Acknowledgments

The authors thank the University of Oslo for providing the material, financial support, and facilitation to publish this paper. We are grateful for the financial support provided by the Research Council of Norway, Equinor, and Total for the OASIS (Overburden Analysis and Seal Integrity Study for CO_2 Sequestration in the North Sea) project. Academic licenses have been provided by CGG for Hampson and Russell software, Schlumberger for Petrel, and dGB Earth Sciences for OpendTect. The authors would like to thank the editor and the reviewers for their time and valuable input.

Data and materials availability

Data associated with this research are confidential and cannot be released.

Corresponding author: manzar.fawad@geo.uio.no

References

Avseth, P. A., and E. Ødegaard, 2004, Well log and seismic data analysis using rock physics templates: First Break, **22**, no. 10, https://doi.org/10.3997/1365-2397.2004017.

Chadwick, R. A., P. Zweigel, U. Gregersen, G. A. Kirby, S. Holloway, and P. N. Johannessen, 2004, Geological reservoir characterization of a CO_2 storage site: The Utsira Sand, Sleipner, northern North Sea: Energy, **29**, no. 9–10, 1371–1381, https://doi.org/10.1016/j.energy.2004.03.071.

Davis, G. H., S. J. Reynolds, and C. F. Kluth, 2011, Structural geology of rocks and regions: John Wiley & Sons.

Dvorkin, J., and A. Nur, 1996, Elasticity of high-porosity sandstones: Theory for two North Sea data sets: Geophysics, **61**, no. 5, 1363–1370, https://doi.org/10.1190/1.1444059.

Fawad, M., J. A. Hansen, and N. H. Mondol, 2020a, Seismic-fluid detection — A review: Earth-Science Reviews, **210**, https://doi.org/10.1016/j.earscirev.2020.103347.

Goodway, B., T. Chen, and J. Downton, 1997, Improved AVO fluid detection and lithology discrimination using Lamé petrophysical parameters; "$\lambda\rho$","$\mu\rho$", & "λ/μ fluid stack", from P and S inversions: 67th Annual International Meeting, SEG, Expanded Abstracts, 183–186, https://doi.org/10.1190/1.1885795.

Halland, E. K., J. Mujezinovic, F. Riis, A. Bjørnestad, I. M. Meling, I. T. Gjeldvik, I. M. Tappel, M. Bjørheim, R. Rød, and V. Pham, 2014, CO_2 Storage Atlas: Norwegian Continental Shelf: Norwegian Petroleum Directorate.

Hampson, D. P., B. H. Russell, and B. Bankhead, 2005, Simultaneous inversion of pre-stack seismic data: 75th Annual International Meeting, SEG, Expanded Abstracts, 1633–1637, https://doi.org/10.1190/1.2148008.

Herwanger, J. V., A. D. Bottrill, and S. D. Mildren, 2015, Uses and abuses of the brittleness index with applications to hydraulic stimulation: Unconventional Resources Technology Conference Proceedings, 1215–1223, https://doi.org/10.15530/urtec-2015-2172545.

Herwanger, J., and N. Koutsabeloulis, 2011, Seismic geomechanics: How to build and calibrate geomechanical models using 3D and 4D seismic data: EAGE.

Ingram, G. M., and J. L. Urai, 1999, Top-seal leakage through faults and fractures: The role of mudrock properties: Geological Society,

London, Special Publications, **158**, 125–135, https://doi.org/10.1144/GSL.SP.1999.158.01.10.
IPCC, 2014, Climate change 2014: Synthesis report — Summary chapter for policymakers. Contribution of Working Groups I, II and III to the fifth assessment report of the Intergovernmental Panel on Climate Change: IPCC, Geneva.
Kemper, M., and J. Gunning, 2014, Joint impedance and facies inversion — Seismic inversion redefined: First Break, **32**, no. 9, https://doi.org/10.3997/1365-2397.32.9.77968.
Lancaster, S., and D. Whitcombe, 2000, Fast-track 'coloured' inversion: 70th Annual International Meeting, SEG, Expanded Abstracts, 1572–1575, https://doi.org/10.1190/1.1815711.
Lindseth, R. O., 1972, Approximation of acoustic logs from seismic traces: Canadian Well Logging Society Journal, **5**, 13–26.
Ma, X.-Q., 2001, Global joint inversion for the estimation of acoustic and shear impedances from AVO derived P-and S-wave reflectivity data: First Break, **19**, no. 10, 557–566, https://doi.org/10.1046/j.1365-2397.2001.00211.x.
NPD, 2020, Norwegian Petroleum Directorate fact pages, http://www.npd.no/engelsk/cwi/pbl/en/index.htm, accessed 3 August 2020.
Olesen, O., M. Brönner, J. Ebbing, J. Gellein, L. Gernigon, J. Koziel, T. Lauritsen, et al., 2010, New aeromagnetic and gravity compilations from Norway and adjacent areas: Methods and applications: Geological Society, London, Petroleum Geology Conference Series, **7**, 559–586, https://doi.org/10.1144/0070559.
Perez Altamar, R., and K. Marfurt, 2014, Mineralogy-based brittleness prediction from surface seismic data: Application to the Barnett Shale: Interpretation, **2**, no. 4, T255–T271, https://doi.org/10.1190/INT-2013-0161.1.
Rahman, M. J., M. Fawad, and N. H. Mondol, 2020, Organic-rich shale caprock properties of potential CO_2 storage sites in the northern North Sea, offshore Norway: Marine and Petroleum Geology, **122**, https://doi.org/10.1016/j.marpetgeo.2020.104665.
Riley, N., 2010, Geological storage of carbon dioxide, *in* R. E. Hester and R. M. Harrison, eds., Carbon capture: Sequestration and storage: Royal Society of Chemistry, Issues in environmental science and technology, **29**, 155–178, https://doi.org/10.1039/9781847559715-00155.
Rutqvist, J., 2012, The geomechanics of CO_2 storage in deep sedimentary formations: Geotechnical and Geological Engineering, **30**, 525–551, https://doi.org/10.1007/s10706-011-9491-0.
Simm, R., and M. Bacon, 2014, Seismic amplitude: An interpreter's handbook: Cambridge University Press, https://doi.org/10.1017/CBO9780511984501.
Smidt, J. M., 2009, Table of elastic constants for isotropic media: The Leading Edge, **28**, no. 1, 116–117, https://doi.org/10.1190/1.3064156.
Statoil, 2016, Mulighetsstudie — Planlegging Og Prosjektering Av et CO_2-Lager På Norsk Kontinentalsokkel: Statoil AS Norway.
Yenwongfai, H. D., N. H. Mondol, J. I. Faleide, and I. Lecomte, 2017a, Prestack simultaneous inversion to predict lithology and pore fluid in the Realgrunnen Subgroup of the Goliat Field, southwestern Barents Sea: Interpretation, **5**, no. 2, SE75–SE96, https://doi.org/10.1190/INT-2016-0109.1.
Yenwongfai, H. D., N. H. Mondol, J. I. Faleide, I. Lecomte, and J. Leutscher, 2017b, Prestack inversion and multi-attribute analysis for porosity, shale volume, and sand probability in the Havert Formation of the Goliat Field, SW Barents Sea: Interpretation, **5**, no. 3, SL69–SL87, https://doi.org/10.1190/INT-2016-0169.1.
Yenwongfai, H., N. H. Mondol, I. Lecomte, J. I. Faleide, and J. Leutscher, 2018, Integrating facies-based Bayesian inversion and supervised machine learning for petro-facies characterization in the Snadd Formation of the Goliat Field, south-western Barents Sea: Geophysical Prospecting, **67**, no. 4, 1020–1039, https://doi.org/10.1111/1365-2478.12654.

APPENDIX-2

CP-1

Mineralogy Based Geomechanical Behavior of Draupne Caprock Shales in the Northern North Sea, Offshore Norway

Md Jamilur Rahman
Manzar Fawad
Nazmul Haque Mondol

82nd EAGE annual Conference & Exhibition

18-21 October 2021

2021 EAGE ANNUAL
82ND CONFERENCE & EXHIBITION
AMSTERDAM | THE NETHERLANDS

MINERALOGY BASED GEOMECHANICAL BEHAVIOR OF DRAUPNE CAPROCK SHALES IN THE NORTHERN NORTH SEA, OFFSHORE NORWAY

M.J. Rahman[1], M. Fawad[1], N.H. Mondol[1,2]

[1] University of Oslo; [2] Norwegian Geotechnical Institute

Summary

The geomechanical behavior of shale caprock demonstrates the seal effectiveness, which is an essential part of any reservoir-seal system and equally important in both CO_2 injection and hydrocarbon explorations. Mineralogical compositions have a direct impact on the mechanical behavior of caprock though the whole process is very complex and depends on many other factors. In this study, we evaluate the caprock geomechanical properties of organic-rich Draupne Formation shale using core and cutting samples from six exploration wells (32/2-1, 32/4-1, 35/11-4, 15/3-8, 15/12-21 & 34/4-3) in the northern North Sea, offshore Norway. Bulk mineral fractions are estimated using XRD, SEM and thin section analyses to calculate mineralogy based brittleness indices (MBI) using empirical equations. For comparison, an elastic property-based BI also estimated. Results show that the strong and soft mineral fractions varied significantly within the Draupne Formation which leading to different brittleness values within the studied wells. Moreover, significantly different brittleness values observed when compared to MBI and EBI. The well (15/3-8) penetrated the Draupne Formation at higher depth has comparatively low brittleness values due to maturation and generated hydrocarbon from the formation. Brittleness indices can be very useful but have to use carefully because of many other factors contribute combinedly.

Introduction

Caprock shales consist mainly of clay and silt-sized particles (i.e., particles <62.5µm) in addition to other mineral constituents. Mineralogical composition and grain size of shales vary significantly (both vertically and laterally) within a basin due to the difference in depositional processes and diagenetic pathways (Hart et al., 2013). However, clay minerals are not always the dominant constituents in shales. Other minerals such as quartz, calcite, feldspar, pyrite, etc. can be present as fine-grained detrital grains or diagenetic minerals. Based on the mechanical strength, the mineral volume percentage can divide into stiff/brittle minerals (i.e., quartz, feldspar, carbonate, mica, and pyrite) and soft/ductile minerals (i.e., clay and TOC) (Jarvie et al., 2007, Wang and Gale, 2009, Jin et al., 2014 and Rybacki et al., 2016). These variations of relative mineralogical proportions within shales significantly affect the caprock properties. The increase in stiff/brittle minerals increases brittle behavior that could result in a sudden failure/fracture of the caprock, while soft/ductile components have gradual deformation. Therefore, it is crucial to estimate mineralogical composition to evaluate mineral-based caprock geomechanical behaviors.

Draupne Formation act as the primary caprock in the Upper Jurassic sandstone reservoir and consists of dark grey-brown to black, usually non-calcareous, carbonaceous, occasionally fissile claystone. The Draupne Formation deposited within the East Shetland Basin, the Viking Graben, and over the Horda Platform area (Fig. 1). The formation was deposited in an open marine environment with restricted bottom circulation and often with anaerobic conditions (NPD, 2019) and characterized by very high gamma-ray values (often above 100 API) because of its high Uranium content. Interbedded sandstone and siltstone, as well as minor limestone streaks and concretions, are also present throughout the formation. In the lower boundary, Draupne Formation generally has a diachronous contact with the Heather Formation. However, on the northern Horda Platform, Upper Jurassic sandstones of Sognefjord Formation mark the base of the Draupne Formation. The upper boundary usually marked by Cretaceous sediments, which have a higher velocity and lower gamma-ray response than the Draupne Formation (NPD, 2019).

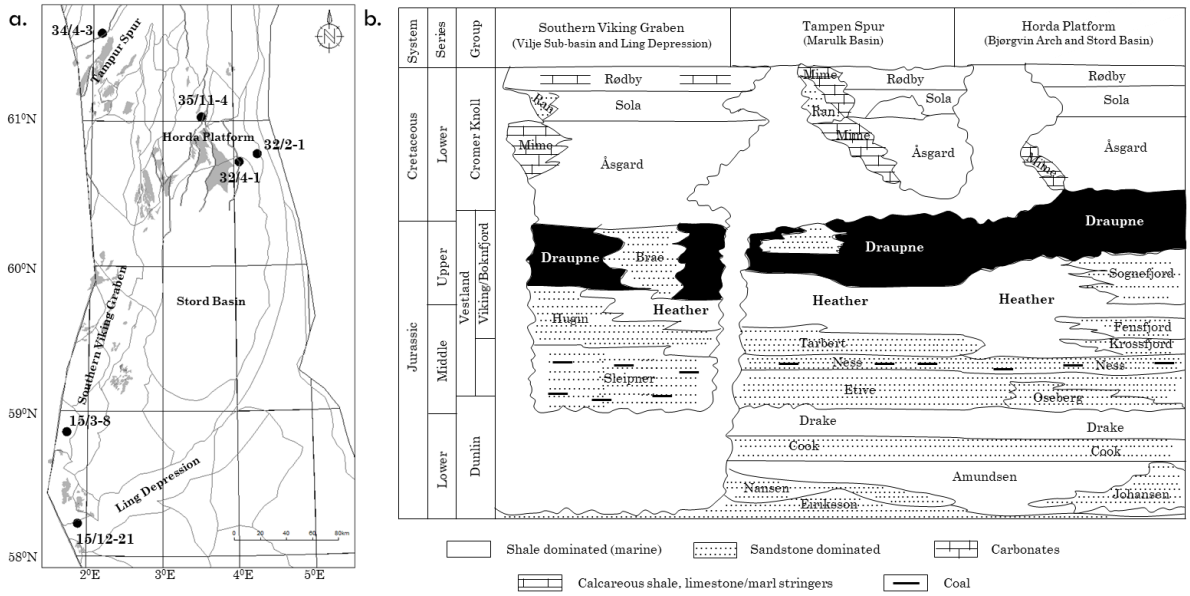

Figure 1 *(a) Location map of the studied wells 15/3-8, 15/12-21, 32/2-1, 32/4-1, 34/4-3, and 35/11-4 with structural elements and marked by oil/gas discoveries. (b) Jurassic and Lower Cretaceous stratigraphic succession in the Norwegian North Sea (modified from CO_2 Atlas, 2014). The studied Upper Jurassic caprock section is marked by black color.*

Six wells covering Southern Viking Graben (SVG), Tampen Spur (TS) and Horda Platform (HP) are chosen for this study where the Draupne Formation in HP wells (32/2-1, 32/4-1 & 35/11-4) are within the mechanical compaction (MC) domain. The three other wells from SVG (15/3-8 & 15/12-21) and

TS (34/4-3) are in the chemical compaction (CC) domain. Furthermore, well 15/3-8 is divided into two subgroups named 15/3-8U and 15/3-8L due to the thick Intra-Draupne Formation sandstone in the middle. The thickness variations within the studied wells are significant and ranges between 18 m in well 35/11-4 and 258 m in well 34/4-3.

Methods

The lithologic variation of shales has a significant impact on the geomechanical behavior of the caprock. Based on the mineral fractions, caprocks behave differently. The addition of strong/brittle minerals increases brittleness, while weak/ductile components decrease brittleness. In this study, core and cutting samples of Draupne Formation from the studied wells are analyzed for mineralogy-based brittleness classification. The bulk fractions of brittle and ductile minerals are estimated from XRD, SEM and thin section analyses. Mineralogy-based Brittleness Indices (MBI) are the qualitative measurements of the rock ductility or the ability of the rock to crack or fracture known as fracability (Wang and Gale, 2009; Yang et al., 2013; Jin et al., 2014; Rybacki et al., 2016). Two MBIs are calculated using the empirical relations proposed by Jarvie et al. (2007) and a modified equation (suggested in this study). Jarvie et al. (2007) proposed quartz as the brittle mineral while carbonate and clay considered less-/non-brittle (MBI-1). However, considering available data and all the proposed MBI equations, the modified equation used quartz, feldspar, carbonate, and pyrite as brittle mineral while clay and TOC fractions are considered as ductile mineral (MBI-2). Moreover, to compare mineralogical and elastic property based brittleness indices, one brittleness index (EBI-1) based on elastic property is estimated using a new empirical equation (Fawad & Mondol, 2020, unpublished, personal communication). The input elastic properties for this equation are taken from the wireline logs (averaged one meter against a sample location).

Results and discussion

Mineral assemblages in a rock build the main framework which may be detrital or biogenic in origin. However, bulk mineralogical analysis tells us the total percentage of minerals without having any indication of origins. Fractions of ductile/soft and brittle/strong minerals define the geomechanical behavior of the caprock. In this study the bulk mineral fractions of Draupne Formation are divided into three clusters; i) strong quartz, feldspar, and pyrite (QFP), ii) soft clay and TOC and iii) carbonate (Fig. 2). The carbonate (calcite and dolomite) fractions within the study area are very low (<10%) compared to other mineral fractions which have a wide range of distribution. The higher percentage of soft minerals (>50%) found in wells 32/2-1, 32/4-1, 15/12-21, and 15/3-8L while strong minerals (>50%) found in wells 15/3-8U, 34/4-3 and 35/11-4. The highest and lowest soft minerals found in wells 32/2-1 and 35/11-4, respectively. The soft and hard mineral assemblages present in studied samples experienced both mechanical (MC) and chemical (CC) compaction (Fig. 2). Mineralogy-based brittleness indices follow the mineral assemblages. The lower MBI values correspond to higher soft minerals present in wells 32/2-1, 32/4-1, 15/12-21 & 15/3-8L and vice versa (Fig. 3). The variations observed within MBI's are due to the difference in hard/strong mineral fractions. The MBI-1 is the representation of quartz while MBI-2 is representing the total strong minerals including carbonate. A very negligible difference observe between MBI-1 and MBI-2 in well 15/3-8 upper and lower samples while significant differences found in wells 34/4-3, 35/11-4, 15/12-21 and 32/2-1. However, comparing with elastic properties based brittleness indices (EBI-1) over- and under-estimating samples are found in wells 15/3-8L, 34/4-3 and 35/11-4 (Fig. 3). For instance, the EBI-1 is significantly higher compared to MBI's in wells 34/4-3 and 15/3-8L while markedly lower in well 35/11-4.

Caprock geomechanical behavior is a complex function of rock strength, lithology, texture, effective stress, temperature, fluid type (Handin and Hagar, 1957; Davis and Reynolds, 1996; Nygård et al., 2006), diagenesis, and TOC (Wells, 2004). The effect of depth on brittleness is compounded and can work in both ways (decreasing or increasing) because pressures, temperature, diagenesis, and TOC are functions of depth. However, the hydrocarbon within caprock reduces the brittleness by increasing pore pressure (Bjørlykke and Jahren, 2015). These are the possible causes behind the comparatively soft nature of chemically compacted Draupne shales in wells 15/3-8, 15/12-21 and 34/4-3. In contrast,

mechanically compacted caprocks are mainly dependent on the rock composition and texture which heavily influence the compaction and hence the brittleness.

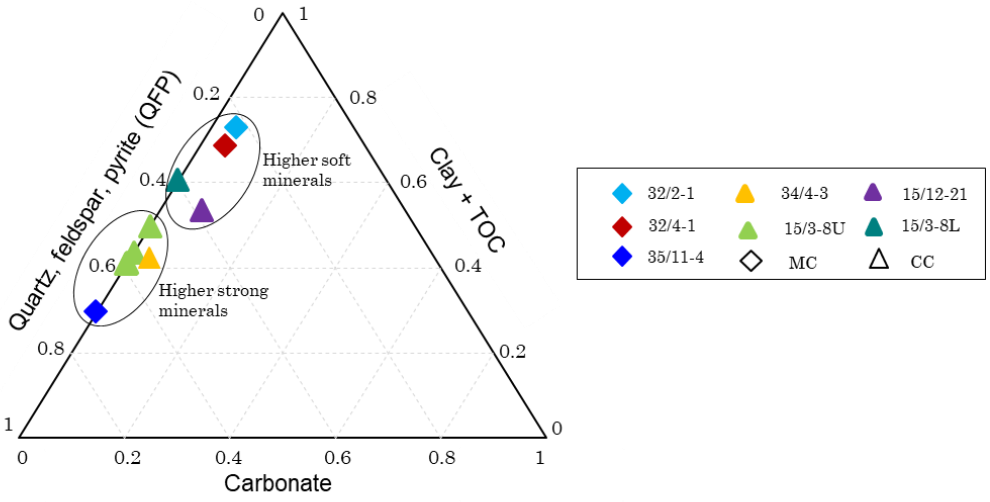

Figure 2: *Ternary plot of brittle (quartz, feldspar, and pyrite), ductile (clay and TOC) and carbonate minerals found in Draupne Formation. Carbonate minerals are absent or very small fraction present in most of the samples. Brittle and ductile minerals fractions are distributed in a wide range within the studied wells.*

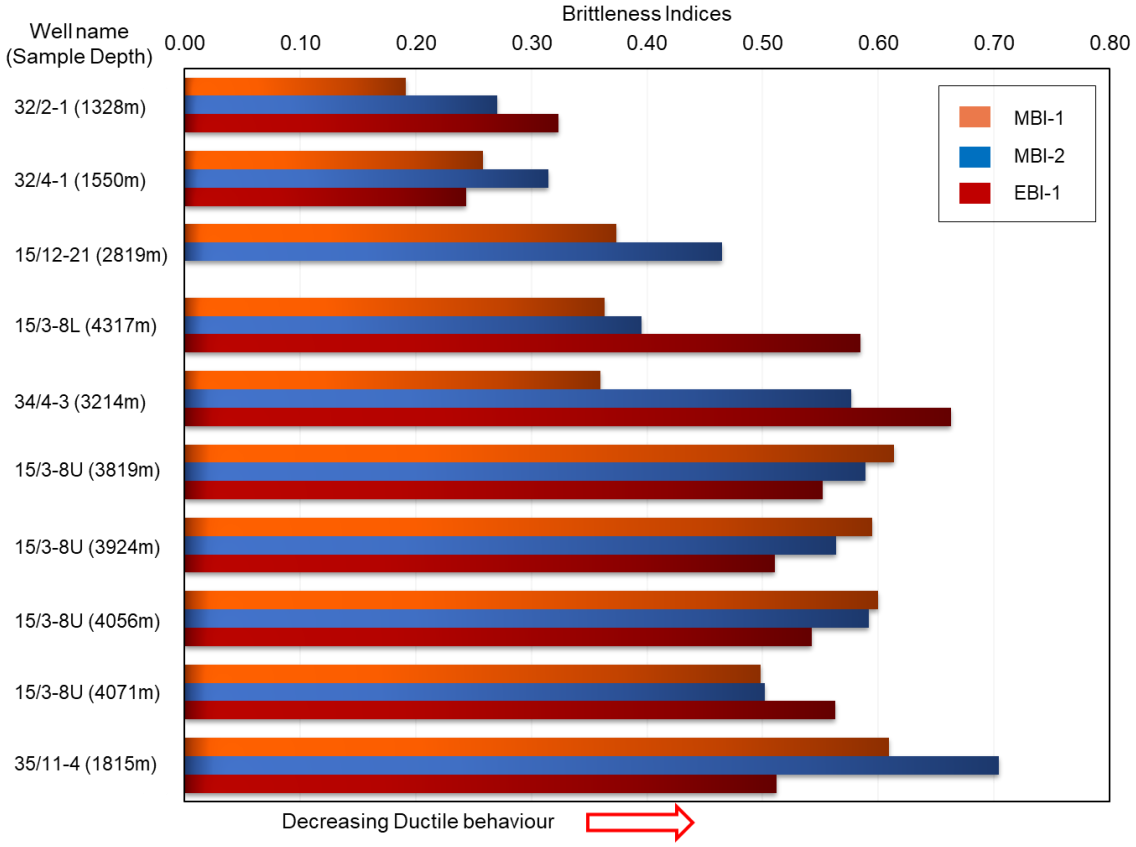

Figure 3: *Calculated brittleness Indices (BI's) of the studied samples using the mineralogy and elastic property based empirical equations. Note that the sample depth presented here is measured from the sea level (BSF), and exhumations in well locations are corrected (Hansen et al., 2019).*

Conclusions

A wide range of soft and hard mineral assemblages are found within the Draupne Formation, which reflects significant differences of mineralogical brittleness values within the studied wells. However, the elastic properties do not directly correlate with mineralogy due to the effect of chemical compaction/cementation, hydrocarbon generation, increase in pore pressure, etc. Overall, the geomechanical behavior of caprock is very complex when the rock is within the chemically compacted zone with TOC maturation while comparatively simpler when the rock experienced only mechanical compaction.

Acknowledgments

We are thankful for the funding provided by the Research Council of Norway for the **OASIS** (Overburden Analysis and Seal Integrity Study for CO2 Sequestration in the North Sea) project (NFR-CLIMIT project #280472). We are indebted to the support and data provided by Gassnova and the Northern Light consortium. Academic software licenses have been provided by Lloyd's Register for Interactive Petrophysics and Schlumberger for Petrel.

References

Bjorlykke, K. and Jahren, J. [2015]. Sandstones and Sandstone reservoirs in Bjorlykke K. (2015), Petroleum Geoscience: From Sedimentary Environments to Rock Physics, Berlin, Heidelberg, Springer-Verlag Berlin Heidelberg, p. 113 – 140.

Davis, D. and Reynolds, S. J. [1996]. Structural geology of rocks and regions, 2nd ed.: Wiley. Glørstad-Clark, E., Faleide, J.I., Lundschien, B.A. and Nystuen, J.P. 2010. Triassic seismic sequence stratigraphy and paleogeography of the western Barents Sea area. Marine and Petroleum Geology, 27, 1448-1475.

Fawad, M. & Mondol, N. H. [2020]. (Proposed unpublished brittleness equation)

Handin, J., and Hager, R. V. [1957]. Experimental deformation of sedimentary rocks under confining pressure: Tests at room temperature on dry samples: AAPG Bulletin, 41, 1–50.

Hansen, J.A., Mondol, N.H. and Fawad, M. [2019]. Organic content and maturation effects on elastic properties of source rock shales in the Central North Sea. Interpretation, Vol. 7, No. 2, p. T477-T497.

Hart, B.S., Macquaker, J.H.S. and Taylor, K.G. [2013]. Mudstone (''shale'') depositional and diagenetic processes: Implications for seismic analyses of source-rock reservoirs. Interpretation, v-1, pp B7-B26.

Jarvie, D.M.; Hill, R.J.; Ruble, T.E.; Pollastro, R.M. [2007]. Unconventional Shale-Gas Systems: The Mississippian Barnett Shale of North-Central Texas As One Model for Thermogenic Shale-Gas Assessment; American Association of Petroleum Geologists: Tulsa, OK, USA; Volume 91, pp. 475–499.

Jin, X.; Shah, S.; Truax, J.; Roegiers, J.C. [2014]. A practical petrophysical approach for brittleness prediction from porosity and sonic logging in shale reservoirs; In Proceedings of the SPE Annual Technical Conference and Exhibition, Amsterdam, The Netherlands.

Nygård, R., Gutierrez, M., Bratli, R.K., Hoeg, K., [2006]. Brittle-ductile transition, shear failure and leakage in shales and mudrocks. Marine and Petroleum Geol. 23, 201-212

NPD CO2 Atlas report, [2014]

NPD Factpages [2019]: https://npdfactpages.npd.no/factpages/Default.aspx?culture=en

Rybacki, E.; Meier, T.; Dresen, G. [2016]. What controls the mechanical properties of shale rocks?—Part II: Brittleness. J. Pet. Sci. Eng., 144, 39–58.

Wang, F.P., Gale, J.F.W., [2009]. Screening criteria for shale-gas systems. Gulf Coast Assoc. Geol. Soc. Trans. 59, 779–793.

Wells, F. [2004]. A new method to help identify unconventional targets for exploration and development through integrative analysis of clastic rock properties. Houston Geological Society Bulletin, 47, 34–49.

Yang, Y.; Sone, H.; Hows, A.; Zoback, M.D. [2013]. Comparison of Brittleness Indices in Organic-rich Shale Formations; American Rock Mechanics Association: Alexandria, VA, USA.

CP-2

Depositional Processes and Shallow Diagenesis Effect on Caprock Elastic Properties in Horda Platform Area, Northern North Sea.

Md Jamilur Rahman
Manzar Fawad
Nazmul Haque Mondol

GeoConvention

21-23 September 2020

geoconvention
Virtual Event
September 21-23
2020
CSPG • CSEG • CWLS • GAC • MAC • IAH

Depositional processes and shallow diagenesis effect on caprock elastic properties in Horda Platform area, northern North Sea

Md Jamilur Rahman[1], Manzar Fawad[1] & Nazmul Haque Mondol[1,2]
[1]University of Oslo (UiO), [2]Norwegian Geotechnical Institute (NGI)

Summary

Mineralogical composition and initial pore water chemistry affect the caprock properties significantly, which are critical factors to evaluate caprock quality. In this study, five exploration wells (31/3-1, 31/2-8, 32/2-1, 32/4-1, and 35/11-4) from the Horda Platform, northern North Sea, are analyzed to assess the Late Jurassic Draupne Formation organic-rich shale caprock properties. The Draupne Formation caprock is in the mechanical compaction zone with a varying thickness within the studied wells. We evaluated elastic properties using a rock physics template (Vp-density) while log shape pattern, mineralogical and petrographical analyses (XRD, SEM & thin section) were used to assess the depositional variations that controlled changes in rock compositions and grain size distributions. The difference in log pattern with different grain size and mineralogy reflected the depositional environment changes and shallow diagenesis (pyrite framboids abundance and distribution) confirmed the variations of initial pore water chemistry within the studied wells. These factors affect the elastic parameters analyzed in the rock physics cross-plots. The results show that the Draupne Formation shales, which have higher clay content and experienced low-intensity shallow diagenesis, are soft and more ductile compared to the zones with higher brittle mineral contents exposed to relatively severe shallow diagenesis.

Introduction

Mechanical and chemical compaction/cementation convert the clay particles into shales (Taylor and Macquaker, 2011), which are strongly influenced by the mineral composition and the sediment pore water chemistry (Hart et al., 2013). The mineralogical composition of shales (caprocks) vary significantly (both vertically and laterally) within a basin because of the changes of sediment sources (e.g., weathering intensity, climate, particle size) and depositional processes (e.g., seal level changes, tectonic subsidence, oceanic circulation patterns) throughout the geological time (Hart et al., 2013). These processes are leading to significant changes in mineralogy and texture of caprocks, which affect the elastic properties. The study area (Horda Platform) is located in the northern North Sea and bounded by Øygarden Fault Complex (ØFC) in the east, Lomre Terrace (LT) in the west, Uer Terrace (UT) in the north and Stord Basin (SB) in the south (Fig. 1). Several major deep-seated north-south trending normal faults (Vette, Tusse, Svartalv & Troll) and many other minor faults are present in the area. The Horda Platform area is tectonically complex, which influences the overall rock composition and fabric and affects the caprock effectiveness, which is essential for a successful and reliable CO_2 storage project as well as hydrocarbon exploration. Therefore, a careful investigation of caprock elastic properties is necessary to prevent any CO_2 leakage, or for a better understanding of the petroleum system in the area. In this study, we characterize the effect of mineralogical variation due to depositional changes and shallow diagenetic processes on the caprock elastic properties in the Horda Platform, northern North Sea.

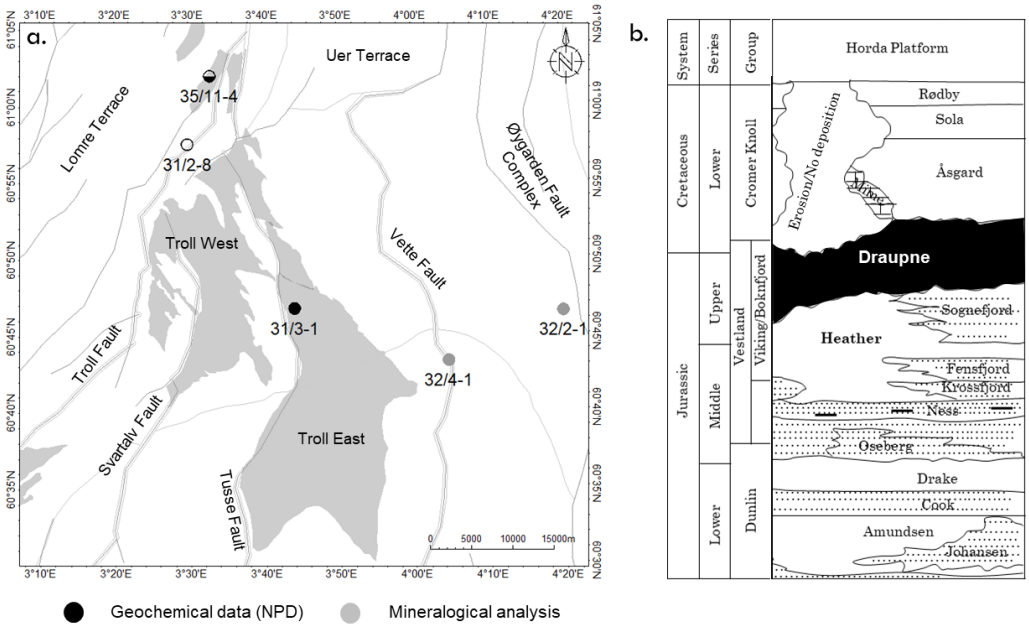

Figure 1: a) The study area showing the structural elements, major faults, and oil/gas discoveries within the studied wells, b) Jurassic and Cretaceous stratigraphic succession in the Horda Platform (modified from NPD CO_2 Atlas, 2014).

The Draupne Formation (the main caprock in the area) is a part of the Viking Group, deposited in Late Jurassic time within the Horda Platform area (Fig. 1b). This formation consists of dark grey-brown to black, usually non-calcareous, carbonaceous, occasionally fissile claystone, which was deposited in an open marine environment with restricted bottom circulation and often with anaerobic conditions (NPD, 2019). It is characterized by high gamma-ray values (usually above 100 API units) because of its Uranium content. Interbedded sandstone and siltstone, as well as minor limestone streaks and concretions, are also present throughout the formation.

Based on the well location, geochemical data and availability of rock samples (both cores and cuttings), five wells from the Horda Platform area are selected for this study (Fig. 1a), out of which wells 31/3-1 and 35/11-4 have geochemical data (retrieved from NPD database, 2020). The Draupne Formation in wells 32/2-1, 32/4-1, and 35/11-4 are sampled and analyzed in this study. The reservoir sandstone (Sognefjord Formation) contains a thick gas column in well 31/3-1 (Troll East), and gas and oil columns in well 35/11-4 (Fram). Oil shows were recorded in well 31/2-8, whereas the other wells are dry (water wet). The caprock thickness varied significantly within the studied wells, ranging from 16 to 106 m in the wells 31/2-8 and 32/4-1, respectively. The Draupne Formation experienced a maximum temperature (exhumation corrected) ranging from 38^0C to 53^0C (assuming a 30^0C/Km geothermal/temperature gradient). The temperature ranges indicate that the studied Draupne Formation in all five wells is within the mechanical compaction zone with various levels of compaction. Moreover, geochemical data from wells 31/3-1 and 35/11-4 (NPD, 2019) suggests that the average TOC content in Draupne Formation is only 2-3%, reflecting an immature (average R_0 = 0.43 and Tmax = 425^0C) source rocks. The deep resistivity (R_D) logs also support the immature Draupne Formation (< 2.5 ohm-m) in all wells except well 31/2-8, which has comparatively high deep resistivity values (~4 ohm-m).

Theory and Method

The log-derived elastic properties can be linked to the compaction history of a caprock. However, the compaction processes are too complicated, and many different factors are involved. In this

study, we attempt to relate elastic properties with the depositional and diagenetic processes using bore-hole log data in addition to the petrographic analysis of cutting samples. The gamma-ray log shape helped identify the sea-level fluctuations and paleo-depositional variations within the local sub-basins (Emery and Myers, 1996). All the studied wells have standard wireline log measurements (i.e., gamma-ray, density, P-sonic, resistivity, neutron porosity and caliper etc.) out of which three of them have sampled for petrographic analysis. The volume of shale (Vsh) was calculated from the gamma-ray log using Larionov's (1969) younger rock equation. A rock physics template (e.g., Vp-Density) is employed to evaluate the elastic properties of the Draupne shale caprock. Mineralogy and petrographic analyses (i.e., XRD, SEM, and thin section study) are carried out to interpret the bulk mineral fractions, grain size differences and textural variations.

Results and discussion

The gamma-ray pattern has varied within the studied wells (Fig. 2). The wells 32/2-1 and 32/4-1 of thick Draupne Formation exhibit multiple funnel and bell-shaped cycles, while other wells have a common trend where wells 31/3-1 and 35/11-4 have cylindrical trend and well 32/2-8 has a bell-shaped pattern. Scanning Electron Microscope (SEM) images also show differences in mineralogy and texture. The northernmost well 35/11-4 has coarser detrital grains with kaolinitic clay mineral, while wells 32/2-1 and 32/4-1 have Illite dominated clays. The pyrite framboids are abundant and observed throughout the studied samples in well 35/11-4; in contrast, these are less plentiful, somewhat localized in wells 32/2-1 and 32/4-1. The Vp-density cross-plots of Draupne Formation also show a presence of stiff caprock (higher Vp and density) in the northern wells (35/11-4 & 31/2-8). The soft caprocks (exhibiting low Vp and density) found in wells 31/3-1 and 32/2-1. The data points from well 32/4-1 and few points from well 32/2-1 fall in intermediate-range (Fig. 3). Comparing with the reference curves and Vsh, wells 32/2-1 and 31/2-8 have a better match and follow the reference trend (higher Vsh well follow the higher clay percentage line and vice versa). The well 31/3-1 is roughly following the 100% clay line; however, the Vsh values range between 40% and 60% while wells 32/4-1 and 35/11-4 are following 40% line with measured Vsh values from 80 to 100% (Fig. 3b).

Shales in a basin typically follow systematic vertical stacking patterns with the relative sea-level changes. However, tectonic, climate, and relative factors affect the ultimate character of that basin fill (Slatt, 2011). During Late Jurassic time, the major faults in the study area rotated as a result of the basement blocks rotation, producing numerous local basins (Faleide et al., 2015), which leads to forming a high energy ribbon trending NNE-SSW along the present Troll West area following the main fault trend (Stewart et al., 1995). The Draupne Formation zero thickness trend also follows the existing NNE-SSW pattern, which reveals that during transgression, the erosional/non-depositional structural high still existed. Therefore, the paleo-depositional setup on both sides of the zero thickness has variation, which is explained by the stacking pattern, mineralogy, and grain size differences within the studied wells. Moreover, the variation of pyrite framboids abundance and distribution within the wells indicate changes in pore water chemistry (Taylor and Macquaker, 2011). These depositional variations also affect the elastic properties. The less ductile caprock in the northern depositional setup compared to the southern wells. The high values of Vp and density in well 35/11-4 are explained by shallow diagenesis (where bacterial iron reduction formed pyrite framboids) while a higher level of compaction occurred due to a higher percentage of silt within the clays in well 31/2-8. On the contrary, the presence of a higher percentage of clay content in well 32/2-1 is reflected by soft, ductile nature (low magnitude elastic properties). However, the elastic properties of well 31/3-1 are softer than well 32/2-1 despite exhibiting high Vsh due to the presence of a thick gas column. The gas column within Sognefjord Formation possibly increased pore pressure hence decreased the effective vertical stress and mechanical compaction (Bjørlykke and Jahren, 2015) within the reservoir, which may also affect the above caprock. Moreover, a slight increase in velocity in well 32/4-1 is explained by the

presence of carbonate in the Draupne Formation (Fig. 2). Therefore, the differences in caprock properties within the studied wells are dependent on the composition and shallow diagenetic variations, which are functions of the depositional processes.

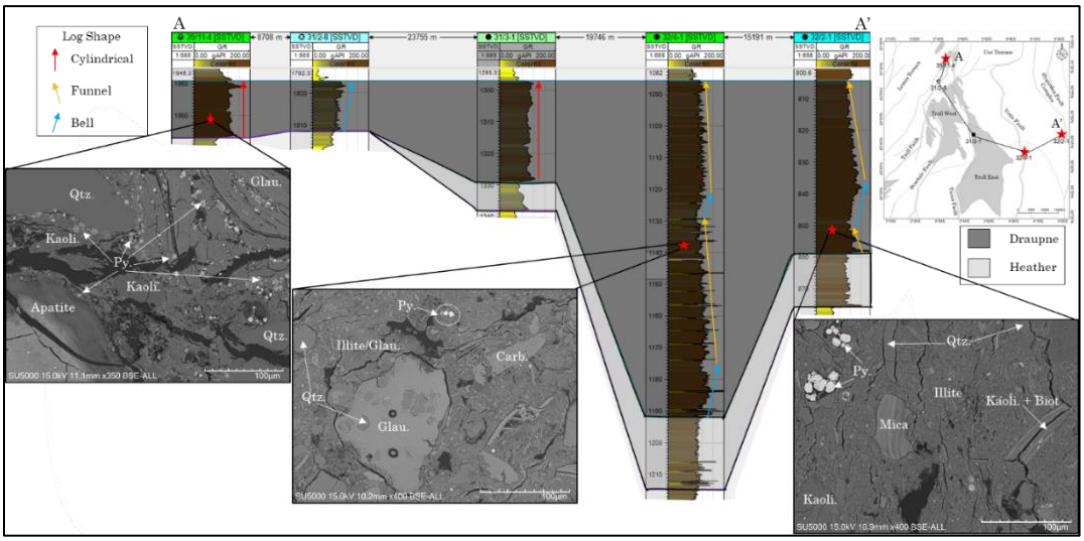

Figure 2: Stratigraphic correlation along AA', flattened on top Draupne Formation showing the thickness variation with variable gamma-ray log patterns (cylindrical, funnel, and bell), which reveal the paleo-depositional differences. Also, the SEM images from the corresponding depth show the changes in composition and texture in a single caprock unit. All the white dots are the pyrite (Py.) framboids, which have a significant variation in volume and distribution within the studied wells. The abbreviations of Qtz. (Quartz), Glau. (Glauconite), Kaoli. (Kaolinite), Biot. (Biotite) and Carb. (Carbonate) are used for simplicity.

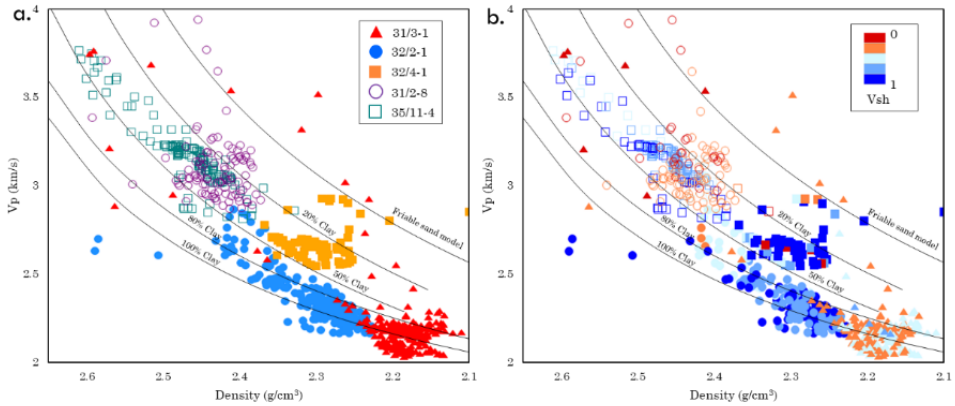

Figure 3: Density vs. Vp cross-plot of Draupne Formation data from the studied wells color-coded by well names (a), and Vsh (b), with reference curves adapted from Avseth et al., 2005.

Two northern wells show similar elastic properties even though well 35/11-4 is a gas/oil discovery, and well 31/2-8 has oil shows. The oil shows possibly indicate that the hydrocarbon migrated into the trap but escaped due to a possible caprock or fault-seal failures. Moreover, the higher deep resistivity (R_D) within the Draupne Formation in well 31/2-8 indicates fluid migration through it (TOC immature in that area). If we assume the bounding fault to be sealed, then mineralogy (mainly clay particles) possibly played a vital role in the caprock breach. In that case, the seal integrity may be difficult to predict only from elastic properties. Caprock properties also depend on many other factors i.e. temperature, stress regime, and diagenesis, etc. (Sone and Zoback, 2014) but heavily depend on the ductile minerals (i.e., clay). Therefore, an integrated approach is needed for a better understanding of caprock effectiveness.

Conclusions

Caprock geomechanical behaviors are the most critical parameters for successful CO_2 storage, and hydrocarbon exploration, which depends on various factors. This study assesses the effect of mineralogical composition and shallow diagenesis of Draupne shale caprock properties in the Horda Platform in the northern North Sea. The changes of the paleo-depositional setup can control the grain size distribution, mineralogy, and pore water chemistry that ultimately influence the compaction processes and caprock properties. However, the elastic property based ductility measurements can be misleading as zones showing similar elastic properties have good sealing potential (oil discovery in well 35/11-4) and a failure (oil shows in well 31/2-8).

Acknowledgments

We are thankful for the support and funding provided by the Research Council of Norway for the OASIS-Overburden Analysis and Seal Integrity Study for CO_2 Sequestration in the North Sea-project (NFR-CLIMIT project #280472). We are indebted to the support and data provided by Gassnova and the Northern Light consortium. Academic software licenses have been provided by Lloyd's Register for Interactive Petrophysics and Schlumberger for Petrel.

References

Avseth, P., Mukerji, T. and Mavko, G. 2005. Quantitative seismic interpretation: applying rock physics tools to reduce interpretation risk. Cambridge University Press, New York.

Bjorlykke, K. and Jahren, J. 2015. Sandstones and Sandstone reservoirs in Bjorlykke K. 2015. Petroleum Geoscience: from Sedimentary Environments to Rock Physics, Berlin, Heidelberg, Springer-Verlag Berlin Heidelberg, p. 113 – 140.

Emery, D. & Myers, KJ. (eds) 1996. sequence stratigraphy. Blackwell Science Limited, 297pp.

Faleide, J.I., Bjørlykke, K., & Gabrielsen, R.H. 2015. Geology of the Norwegian Continental Shelf. Chapter 25 from the book “Bjørlykke, K. (2nd edition): Petroleum Geosciences: From Sedimentary Environments to Rock Physics”, 603-637.

Hart, B.S., Macquaker, J.H.S., and Taylor, K.G. 2013. Mudstone (‘’shale’’) depositional and diagenetic processes: Implications for seismic analyses of source-rock reservoirs. Interpretation, v-1, pp B7-B26.

Larionov, V.V. 1969. Radiometry of Boreholes, NEDRA, Moscow (in Russian).

NPD CO_2 Atlas Report 2014

NPD Factpages 2019: https://npdfactpages.npd.no/factpages/Default.aspx?culture=en

Slatt, R. 2011. Important geological properties of unconventional resource shales. Open Geosciences, 3(4), p. 435-448

Sone, H., and Zoback, M.D. 2014. Viscous relaxation model for predicting least principal stress magnitudes in sedimentary rocks. Journal of Petroleum Science and Engineering, 124, 416-431.Storvoll V., Bjørlykke K. and Mondol N. H. (2005). Velocity-depth trends in Mesozoic and Cenozoic sediments from the Norwegian shelf. AAPG Bulletin, v. 89, p. 359-381.

Stewart, D.J., Schwander, M., and Bolle, L. 1995. Jurassic depositional systems of the HordaPlatform, Norwegian North Sea: practical consequences of applying sequence stratigraphic models. NPF Special Publication 5, p. 291-323

Taylor, K.G. and Macquaker, J.H.S. 2011. Iron Minerals in Marine Sediments Record Chemical Environments. Elements, Vol. 7, p. 113-118

CP-3

Mineralogy Analysis of Jurassic Reservoir Sandstones Using Wireline Log Data in the Northen North Sea

Manzar Fawad
Md Jamilur Rahman
Nazmul Haque Mondol

GeoConvention

21-23 September 2020

geoconvention
Virtual Event
September 21-23
2020
CSPG • CSEG • CWLS • GAC • MAC • IAH

Mineralogy analysis of Jurassic reservoir sandstones using wireline log data in the northern North Sea

Manzar Fawad[1], Md Jamilur Rahman[1]& Nazmul Haque Mondol[1,2]
[1]University of Oslo (UiO), [2]Norwegian Geotechnical Institute (NGI)

Summary

In a hydrocarbon accumulation, the viability of the reservoir and the caprock is well established; however, a subsurface CO_2 storage requires preliminary studies to reduce the risk of poor reservoir quality and the overlying seal integrity. While evaluating a potential reservoir for geological CO_2 sequestration, studying the influence of mineralogy, diagenesis, porosity, permeability, and reservoir fluids is essential. The thin section studies, scanning electron microscopy (SEM) and X-Ray Diffraction (XRD) are valuable tools to investigate the mineralogy of reservoir rocks. However, the well-log data with the application of specific crossplots also help to determine various lithologic reservoir characteristics. The Upper Jurassic Sognefjord Formation sandstone is the main oil and gas reservoir in the Troll Field. Besides, the Middle Jurassic Fensfjord and occasionally Krossfjord Formation sandstones are hydrocarbon-bearing in this area. The Heather Formation mudstone exhibits an interfingering stratigraphic relationship with the Krossfjord, Fensfjord, and the Sognefjord Formations, finally overlain by the Draupne Formation organic-rich shales. The Sognefjord, Fensfjord, and Krossfjord Formations are the potential CO_2 storage reservoirs in the proposed CO_2 storage site Smeaheia (east of the Troll field). We evaluated wireline log data from four exploration wells where the spectral gamma-ray was acquired. Based on this data, we investigated the Sognefjord, Fensfjord, and Krossfjord Formation sandstones in terms of the mineralogy, type of clays, and additional detrital components. We will integrate these findings with the existing data, and our ongoing laboratory studies to understand the reservoir quality of the Krossfjord, Fensfjord and the Sognefjord Formations for CO_2 storage.

Introduction

This study deals with the petrophysical evaluation of the Middle Jurassic Krossfjord, Fensfjord, and Upper Jurassic Sognefjord Formations for their suitability as possible CO_2 storage reservoirs in the Smeaheia area (east of Troll field) in the northern North Sea (Fig. 1a). The Norwegian government is working to establish a large-scale (Gt storage potential) CO_2 subsurface storage site on the Norwegian Continental Shelf (NCS). This research is one of several multidisciplinary studies to evaluate the viability of such CO_2 storage sites (Fawad and Mondol, 2018). The study area covers the Troll field and its satellites on the Horda Platform. The Troll field is located approximately 80 km WNW of Bergen, Norway. The Smeaheia area is among the few of the potential CO_2 storage candidates under consideration. Fig. 1b shows a Jurassic and Lower Cretaceous stratigraphic succession in the study area. The main prospective reservoir is the Sognefjord Formation, which consists of coastal-shallow marine sands, overlain by the Heather and Draupne Formation shales, the main caprocks in the area. The Sognefjord sands are medium to coarse-grained, well-sorted, and friable to unconsolidated, locally weakly micaceous, and minor argillaceous. The Heather Formation interfingers with sandstones of the Krossfjord, Fensfjord, and Sognefjord Formations. It consists mainly of silty claystone with thin streaks of limestone,

occasionally becoming highly micaceous grading into sandy siltstone (NPD, 2020). The Krossfjord Formation is medium to coarse-grained, well-sorted, and loose to very friable sandstone. The Fensfjord Formation is fine to medium-grained, well-sorted, and moderately friable to consolidated sandstones with minor shale intercalations. Bioclastic material and occasional cemented bands occur in all the three Krossfjord, Fensfjord, and Sognefjord Formations. The Draupne formation comprises of dark grey-brown to black, usually non-calcareous, carbonaceous, at places fissile claystone. It is characterized by very high Gamma-ray radioactivity (often above 100 API units), because of organic carbon content. The Draupne Formation deposited in a marine environment had restricted bottom circulation, mostly under anaerobic conditions (NPD, 2020). The Gamma Ray and Spectral Gamma Ray (Potassium, Thorium, and Uranium content) logs from well 31/6-1 are presented in Fig. 1c.

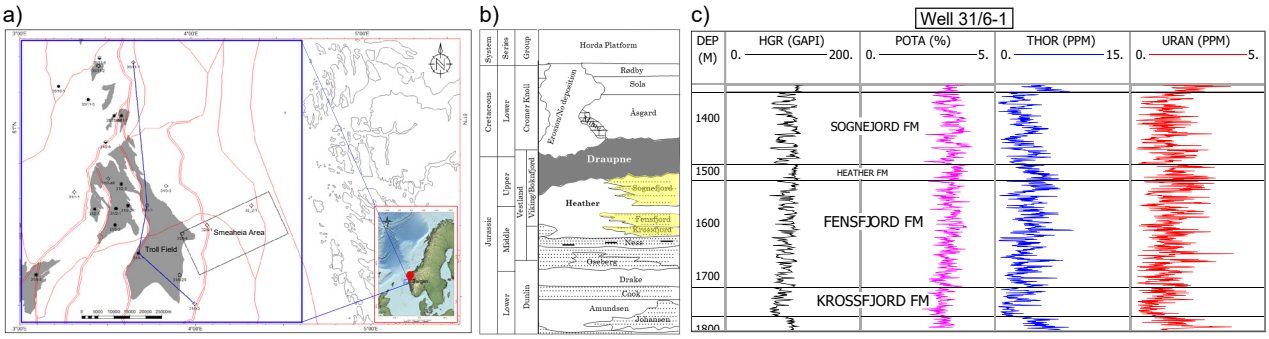

Figure 1: a) The study area lies within the blue rectangle; a SSE-NNW line (A-A') connects the wells selected for this study within, and around the Troll field. (b) A generalized Jurassic and Lower Cretaceous stratigraphic succession in the study area (modified from NPD CO_2 Atlas, 2014). The potential reservoir sandstones are highlighted in yellow color. (c) Gamma Ray and Spectral Gamma Ray (Potassium, Thorium, and Uranium content) curves from well 31/6-1.

The available well log data represents only sporadic information; however, the CO_2 storage covers a large area. Therefore, it is essential to consider all factors that can affect the reservoir quality both laterally and vertically. This study aims to evaluate the reservoir rock composition, with possible detrital and diagenetic mineral assemblages using petrophysics crossplot techniques. This information will help find the factors, which could influence the quality of a CO_2 storage reservoir.

Theory and Method

We selected four wells (31/6-3, 31/6-1, 31/3-1, and 35/11-1) based on the presence of Spectral Gamma Ray (SGR) logs from the available data. The Spectral Gamma Ray log is commonly used for recognizing clay mineral types and clay mineral volume estimation. We made potassium-thorium crossplots, which are handy for the identification of clay minerals and the separation of micas and K-feldspars. In the crossplot, the lines radiating from the origin possess gradients matched with values (Doveton, 1994). Another crossplot of *N* versus *M* is used for lithology determination, lithology trends, gas detection, and clay mineral classification (Fertl, 1981). The *N* and *M* are the mineralogy indicators. The 'Rho matrix apparent' and 'DT matrix apparent', were obtained using Interactive Petrophysics (IP™) software, which we also employed to generate the crossplots (Fig. 2). For matrix calculations, we selected the neutron tool 'CNL', and 'Wyllie' method. The cross-section and map generation was carried out using Petrel™.

Results and discussion

The well 31/3-1 has low potassium content (~2-2.5%) for all the three Sognefjord, Fensfjord, and Krossfjord Formations. On the other hand, the well 35/11-1 has the highest Potassium content (~4-5%) for the Fensfjord and Krossfjord Formations (Fig. 2a). Sognefjord Formation is not present in well 35/11-1. The mineralogy from the Potassium-Thorium crossplot of the Sognefjord, Fensfjord, and Krossfjord Formations in the respective well is approximately the same with a minor difference. Only in well 35/11-1 the Krossfjord Formation is micaceous, whereas the Fensfjord sands are glauconitic to Felspathic. In well 31/3-1, there is minor Chlorite in the Fensfjord Formation; however, the Illite, Mica, Glauconite, and Feldspar are present in all the three, Sognefjord, Fensfjord and Krossfjord Formations.

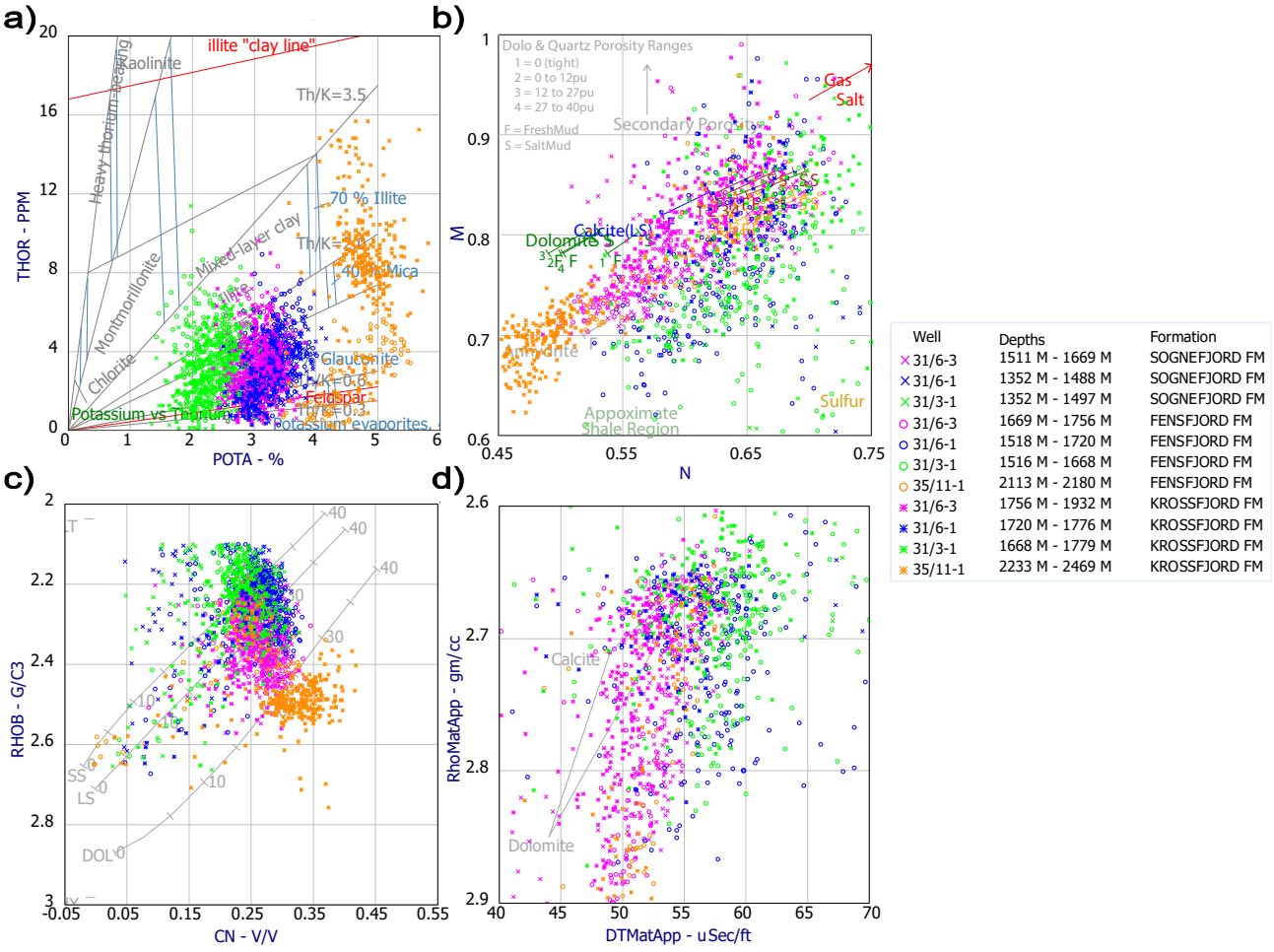

Figure 2: Data points of Sognefjord, Fensfjord, and Krossfjord Formations from the wells 31/6-3, 31/6-1, 31/3-1, and 35/11-1 on (a) Potassium vs. Thorium crossplot with (Schlumberger™) mineral classification overlay, (b) N vs. M crossplot with (Schlumberger™) mineral classification overlay, (c) Neutron porosity vs. bulk density (RHOB) crossplot with a typical mineral-trend overlay, and (d) A 'DT matrix apparent' vs. 'RHOB matrix apparent' crossplot with three-mineral (ternary) overlay.

In the N-M crossplot (Fig. 2b), data from all three wells show a wide scatter falling within Quartz to the Calcite trend. The three sandstones (Sognefjord, Fensfjord, and Krossfjord Formations) in well 31/6-3 show a range from Sandstone to Calcite. In well 35/11-1, both Fensfjord and

Krossfjord data points pull towards Anhydrite zone, whereas in wells 31/3-1 and 31/6-1, mainly the Fensfjord Formation data points pull towards Shale region in the crossplot.

The neutron-density crossplot (Fig. 2c) shows that in wells 31/3-1 and 31/6-1, all the three Formations (Sognefjord, Fensfjord, and Krossfjord) exhibit high porosities (~30%). Porosities drop down in the sandstones approximately to 25% in well 31/6-3. In wells 31/3-1 and 31/6-1, the data points pulling the cluster towards the Limestone trend indicate some calcite cementation or lamination. The deepest well (35/11-1) show comparatively low porosities (average ~20%), and a wide range of data scatter from the Quartz sand trend to the Dolomite trend. This scatter could be because of the presence of high-density Glauconite in addition to Calcite.

Most of the sandstones are within the mechanical compaction zone owing to their present shallow depth (less than 2000m). Only the Fensfjord and Krossfjord Formations in the deepest well (35/11-1) could have been exposed to the early stages of chemical compaction (quartz cementation). There is no Chlorite content in these formations in this well (Fig. 2a); therefore, we do not expect any inhibition of quartz cement precipitation due to the presence of Chlorite (Ehrenberg, 1993). In the “DT apparent matrix” versus “RHOB apparent matrix” crossplot (Fig. 2d), a part of the data plots along the Quartz-Calcite leg of the triangle indicating calcite cementation or laminations. The points plotting to the south of the three-mineral triangle could be due to the presence of Glauconite, and to some extent, Mica.

Conclusions

The petrophysical analysis of four selected wells reveals that mostly the Sognefjord, Fensfjord, and Krossfjord Formation sandstones are at shallow depths (mechanically compacted zone) and therefore retaining high porosities. Only the deeper Fensfjord and Krossfjord Formations have exposed to the early stages of quartz cementation. We expect no quartz cement inhibition in the deeper zones because of the absence of Chlorite content. Mica and Feldspar contents are dominant in the deeper zones (in well 35/11-1). Calcite cementation or laminations are evident from all the well data. We will correlate these results with the existing laboratory data, and our ongoing mineralogical and geochemical analyses.

Acknowledgments

We are thankful for the support and funding provided by the Research Council of Norway for the OASIS (Overburden Analysis and Seal Integrity Study for CO2 Sequestration in the North Sea) project (NFR-CLIMIT project #280472). We appreciate the support and data provided by Gassnova and the Northern Light consortium. Academic software licenses have been provided by Lloyd’s Register for Interactive Petrophysics and Schlumberger for Petrel.

References

Doveton, J.H. 1994. Geological Log Interpretation. SEPM (Society for Sedimentary Geology).

Ehrenberg, S.N. 1993. Preservation of anomalously high porosity in deeply buried sandstones by grain-coating chlorite: examples from the Norwegian continental shelf. AAPG Bulletin, 77, 1260–1286.

Fawad, M. & Mondol, N.H. 2018. Reservoir Characterisation of Johansen Formation as Potential CO2 Storage Reservoir in the Northern North Sea. In: Fifth CO2 Geological Storage Workshop.

Fertl, W.H. 1981. Openhole Crossplot Concepts A Powerful Technique in Well Log Analysis. Journal of Petroleum Technology, 33, 535–549.

NPD CO2 Atlas report. 2014.

NPD. 2020. Norwegian Petroleum Directorate Fact pages of exploration wellbores. Available from http://factpages.npd.no/factpages/.

CP-4

Nanoscale mechanical properties of organic-rich Draupne shale caprock, offshore Norway

Md Jamilur Rahman
Maxim Lebedev
Nazmul Haque Mondol

SEG Annual Meeting (IMAGE)

26 September – 1 October 2021

Nanoscale mechanical properties of organic-rich Draupne shale caprock, offshore Norway

Md Jamilur Rahman (UiO), Maxim Lebedev (CU), Nazmul Haque Mondol (UiO & NGI)*

Summary

Assessment of the geomechanical properties such as hardness and Young's modulus is crucial for evaluating the caprock integrity. This study investigated the nanoscale mechanical properties of two core samples of organic-rich Draupne shale caprock in the North Sea. The samples are taken from wells 35/11-4 (S-1) and 15/3-8 (S-2), located in Horda Platform and South Viking Graben, respectively. The maximum burial depth and temperature data reveal that the S-1 is within the mechanical compaction zone, while the S-2 sample is chemically compacted. The caprock properties are characterized using the nano-indentation techniques combined with quantitative observation of X-ray diffraction (XRD) and scanning electron microscopy (SEM) image analyses. The mineralogical influences on mechanical properties are observed in nanoscale hardness and indentation modulus results. Although the number of samples is limited, the correlation between these properties is in good agreement with literature data, which indicated a strong relation between rock mineralogy and mechanical properties. Moreover, the comparison of Young's modulus between nano-indentation and the Triaxial test reveals that the nanoscale methods effectively evaluate mechanical properties. This may reduce the mechanical properties estimation limitation for caprock and overburden using small cuttings in nano-indentation analysis. Additionally, the studied samples indicated that the caprock shale behaves ductile irrespective of diagenetic influences. However, a large number of samples with different burial conditions are needed to get a robust result.

Introduction

Caprock shale act as a top seal has exceptionally high capillary entry pressure because shales mainly consist of fine-grained clay and silt-sized particles with low pore connectivity, hence extremely low permeability (Du et al., 2020; Mondol et al., 2011, 2008; Storvoll et al., 2005). Because of this phenomenon, it is highly unlikely that the capillary breakthrough will occur. However, caprock mechanical failure due to reservoir pore pressure change might be a risk for top seal integrity (Ingram et al., 1997). The failure risk increases significantly in CO_2 injection into saline aquifer scenarios due to increased injection-related reservoir pressure. Therefore, the characterization of caprock shale is essential for seal integrity evaluation.

Caprocks mechanical property (i.e., stiffness) is a complex function of many factors (i.e., rock strength, lithology, texture, effective stress, temperature, fluid type, diagenesis, TOC, etc.) and usually estimated from a conventional laboratory experiment, for example, unconfined and confined triaxial compression and shear tests (Lama and Vutukuri, 1978), true triaxial shear test (Colmenares and Zoback, 2002; Minaeian et al., 2014), ultrasonic techniques (Wang, 2002), etc. However, most of the conventional experiments need core samples with considerable size, which is very limited for caprock and overburden sections. On the contrary, the nano-indentation technique used comparatively small cuttings or core samples which was proposed by Oliver and Pharr (2004, 1992) to study the local mechanical properties of composite materials, such as ceramics, polymers, and geomaterials. The mechanical properties (i.e., Hardness and indentation modulus) are determined from the indentation depth generated by applying load on top of the materials. Although this method can estimate several mechanical properties of caprock, there is no standardize indentation benchmark available for materials such as shale to date (Du et al., 2020). Therefore, a comparative analysis was also carried out to assess the differences between nanoscale results with the triaxial lab test based static properties.

In this research, we evaluated the nanoscale mechanical properties (i.e., Hardness and indentation modulus) of two core samples of Draupne shale caprock from the North Sea. However, the influence of different test loads called 'scale-effect' does not analyze in this study. Draupne Formation shale is part of the Viking Group, deposited in the Late Jurassic time, and consists of dark grey-brown to black, usually non-calcareous, carbonaceous, occasionally fissile claystone (NPD, 2021). The formation was deposited in an open marine environment with restricted bottom circulation and often with an anaerobic condition, which was characterized often by high gamma-ray values (usually above 100 API) because of high TOC and Uranium content. Moreover, Draupne Formation was deposited within the East Shetland Basin (ESB), the Viking Graben (VG), and over the Horda Platform (HP) area, where the studied core samples S-1 (35/11-4) and S-2 (15/3-8) were taken from the wells located in HP and south VG; respectively. The sample depth and the temperature have significant differences, which indicated the S-1 is within the mechanical compaction zone while S-2 is chemically compacted (Table 1).

Table 1: Core samples used in this study show the depth and temperature experienced by the caprocks.

Sample No.	Well Name	Basin	Present depth (m)	Paleo depth (m)	Present temp. (^{0}C)	Paleo temp. (^{0}C)
S-1	35/11-4	HP	1608.5	1798.5	56.64	63.33
S-2	15/3-8	SVG	4070.8	4070.8	127.78	127.78

Depths are from the Sea floor (BSF)

Experimental Methods

The test was carried out using a Berkovich intender (Fig. 1a), which follows a series of evenly distributed square lattices referred to as '*grid indentation*'. The intender can apply load ranges between 1mN to 500 mN with a load and depth resolution of 0.07 μN and 0.003 nm, respectively. In this study, small pieces of core samples are glued to a rigid substrate, then are polished to make a flat surface with an average roughness of 0.01 μm and placed inside the nanoindenter. The samples are subjected to loading-unloading with a maximum load of 10 mN. The measured area is a square 0.3mm x 0.3 mm, the distance between measurement points is 20 μm.

The properties (hardness and Young's modulus) of Draupne shale were analyzed assuming homogeneous material by extracted information from load-displacement curves (Fig. 1b). The hardness (H) is defined as the ratio of maximum indentation load to the projected area of contact stated as:

$$H = \frac{P_{max}}{A_c}, \quad (1)$$

where, P_{max} is the maximum load (i.e., 10 mN for this study) and A_c is the area of contact, which for a Berkovich indenter, a simple function of the contact depth, h_c:

$$A_c = 24.5h_c^2, \quad (2)$$

where the parameter h_c is the elastic displacement during unloading (Fig. 1b) and can be determined by the following relationship:

$$h_c/h_{max} = 1 - \varepsilon F_{max}/(Sh_{max}), \quad (3)$$

where h_{max} is the maximum indentation depth, ε is a constant related to the geometry of the indenter (for a Berkovich indenter, ε = 0.75), and S is the contact stiffness, which can be calculated by differentiating the fitting F-h function of the upper part of the unloading curve and evaluating the derivative at the maximum load:

$$S = \frac{\delta F}{\delta h}|_{h_{max}} \quad (4)$$

Assuming a purely elastic unloading behavior, a straightforward dimensional analysis of the involved quantities yields the Bulychev-Alekhin-Shoroshorov (BASh) equation (Bulychev et al., 1975):

$$\frac{S}{M_0\sqrt{A_c}} = \frac{2}{\sqrt{\pi}}, \quad (5)$$

where M_0 is the reduced or indentation modulus reflects the comprehensive elastic response of the indenter and sample. For rigid indentation of anisotropic material, M_0 coincides with the plane stress modulus and stated as:

$$\frac{1}{M_0} = \frac{1-\nu^2}{E} + \frac{1-\nu_i^2}{E_i}, \quad (6)$$

where ν is the Poisson's ratio of the sample (0.28 used in this study estimated from S-2 wireline log), ν_i is the Poisson's ratio of the diamond indenter ($\nu_i = 0.07$), and E_i is Young's modulus of the diamond indenter (E_i = 1140 GPa). Rearranging the equation, Young's modulus was estimated for the samples analyzed in this study:

$$E = (1-\nu^2)/(\frac{1}{M_0} - \frac{1-\nu_i^2}{E_i}) \quad (7)$$

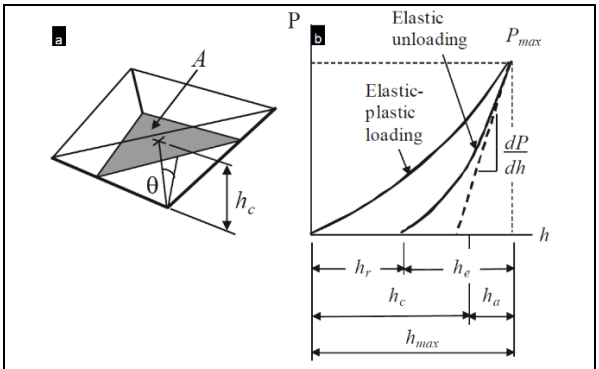

Figure 1: Berkovich Indenter shape (not to scale) and parameters (a), and load versus displacement for elastic-plastic loading followed by elastic unloading (b). h_r is the depth of the residual impression, h_{max} is the depth from the original specimen surface at load P_{max}, h_c is the elstic displacement during unloading, and h_a is the distance from the edge of the contact to the specimen surface at full load. Upon elastic reloading, the tip of the indenter moves through a distance h_e, and the eventual point of contact with the specimen moves through a distance h_a (adapted after Fischer-Cripps, 2007).

Results and Discussion

The hardness (H) and indentation modulus (M_0) with corresponding indentation depth for S-1 and S-2 samples are illustrated in Figure 2. Moreover, the histogram of M_0 for both samples represent the distribution with the corresponding frequencies. The results reveal that the properties are in a nonlinear negative correlation between properties and the indentation depth. However, the behavior and intensity of the curves between the two samples indicated variations. For instance, S-1 at the begging represents high hardness and modulus, which sharply decreases at only 0.5 μm penetration depth. From that point forward, there are very negligible changes with changing the indentation depth (Fig. 2a). On the contrary, hardness and modulus of S-2 have lower initial values than S-1, but the transition between the sharp decreases to gentle trend changes at 0.8 μm (Fig. 2b). Generally, in the initial stage of

the test, the properties depend on the sample surface stiffness. However, when the load reaches a certain value, the cracks are generated, and hardness and modulus decrease due to energy loss (Ping et al., 2015). The histogram of M_0 also reveal the difference by graphically represented the distribution ranges (Fig. 2c). The S-2 represents a normal distribution with a peak at 15 GPa and an average of 16.5 GPa. However, the distribution of the S-1 sample is significantly different, where several peaks were observed with an average of 38 GPa. Several peaks in S-1 indicated that the indenter could measure the mineral scale properties.

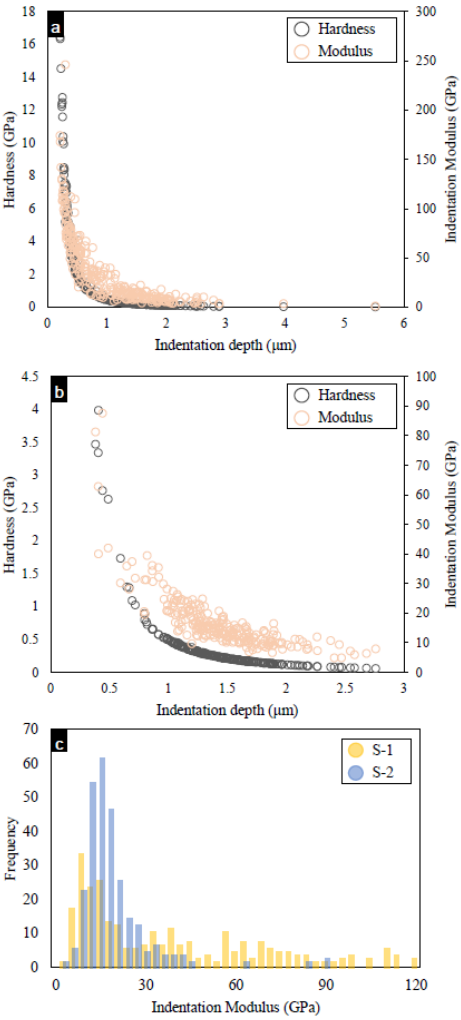

Figure 2: Hardness and indentation modulus versus indentation depth estimated in S-1 (a) and S-2 (b). The distribution of indentation modulus also show the range and distribution type (c).

Estimating microscopic minerals within the studied samples is crucial because the nanoscale technique evaluates mineral level stiffness. The bulk X-ray diffraction (XRD) mineralogy of both samples are shown in Table 2. The percentage of major minerals shows variation between the samples. Although the quartz percentage is low in S-1, another brittle mineral such as pyrite has abundances (i.e., 18.17%), increasing the overall brittle minerals assemblages (i.e., quartz, feldspar, and pyrite) up to 60%. Moreover, the low percentage of clay and TOC (i.e., 25.97%) indicated very low ductile mineral percentage in this sample. On the contrary, the brittle and ductile mineral assemblages in S-2 illustrated an equal percentage (50-50), where the clay and TOC percentage is significantly high (i.e., 50.08%). The mineralogical estimation was also verified using the Scanning Electron Microscopic (SEM) analysis shown in Figure 3. The abundance of pyrite (all the grey dots in figure 3a) in S-1 was also identified in SEM investigation. Moreover, the larger grain size was observed in S-1 compare to S-2. However, in S-2, the thin layers of TOC were observed, which is not present in S-1 (Fig. 3b). The coarse grain size with several M_0 peak in S-1 explains the relation between grain size and mineral level properties estimation in nano-indentation technique.

Table 2: Bulk X-RD mineralogy of the studied samples.

Minerals	**S-1**	**S-2**
Quartz	35.92	42.90
Feldspar	4.88	0
Pyrite	18.17	7.34
Total Clay Minerals	24.01	43.22
TOC	1.96	6.86
Others	15.06	0

Generally, within the shale, different categories of micro-fractures are generated (Kalani et al., 2015). However, the level of fracturing is controlled by a number of factors and processes (i.e., tectonics, TOC content and maturation, mineralogical composition, diagenesis, etc.). Considering the temperature and TOC percentage, the intensity of possible micro-fracture should be higher in S-2 compare to S-1. The high percentage of matured TOC in S-2 indicated an abundance of micro-fracture (Fig. 3b). Moreover, the high percentage of ductile clay mineral make this sample softer (i.e., less stiff). On the contrary, low ductile mineral assemblages with a significant amount of pyrite and coarser grains make the S-1 stiffer. The higher initial hardness and elastic modulus in S-1 are indicating the high surface stiffness, while the high failure depth (i.e., high penetration depth before cracking) in S-2 represents that the TOC-generated micro-fracture within the shale creates the rock more ductile, hence absorbed more energy before crack.

Figure 4 illustrated the correlation between the hardness (H) and indentation modulus (M_o) estimated from grid indentation on the studied samples. A similar relation between H and M_o based on clay/kerogen-rich and carbonate-rich samples were proposed by Abedi et al. (2016)

and Du et al. (2020), respectively. In the current studied samples, the best-fit equation with the high number of the correlation coefficient (i.e., $R^2 = 0.84$) is proposed (Fig. 4), where the power exponent (i.e., 0.57) equivalent to Du et al. (2020). However, the S-2, which has a high percentage of ductile mineral, has a better match with clay/kerogen-rich curves. Moreover, in S-1, pyrite represents similar stiffness to the carbonate-rich published trend. Although there are only two samples used in this study, the relation with published curves indicated the strong relationship between mineralogy and mechanical properties within the Draupne shale, which is also explained by Rahman et al. (2020).

Besides the limitation, Young's modulus (E) shows a good match between the nano-indentation result (S-2) and the Triaxial test (similar clay content and temperature sample) shown in Table 3, where nanoscale estimated 15.82 GPa and 12.2 GPa observed in Triaxial result. However, a significantly higher E value (i.e., 40.66 GPa) was estimated in wireline log-based static property (Mullen et al. (2007) equation was used during dymanic to static conversion) from the same well. This is expected because many uncertainties are involved in log-based static properties. Moreover, comparing the E between S-1 and S-2, the S-1 represents stiffer caprock than S-2, though the S-2 sample experienced significantly high diagenetic processes (both mechanical and chemical compaction) (Table 1). This indicates that the ductile mineral assembalges within shale influences more than the diagenesis processes.

Table 3: Comparison of static Young's modulus between the nanoscale, wireline-log based, and Triaxial test estimation.

	Mean (GPa)
S-1	37.62
S-2	15.82
Wireline-log based[a]	40.66
Triaxial test[b]	12.2

[a]S-2 well (15/3-8); [b]Horsrud et al. (1998)

Conclusions

The effect of mineral composition on caprock nanoscale mechanical properties is evaluated. The critical observations of this study are as follow:

- The shallow caprock sample S-1 is stiffer than the deep sample S-2, though S-2 experienced both mechanical and chemical compaction.
- Nano-indentation is a practical laboratory method to evaluate mechanical properties either from a small core or cutting samples; hence possible to estimate mechanical properties for cap and overburden rocks with limited or no core samples.
- There is a strong relationship between mineralogy and mechanical properties observed. A considerable amount of ductile minerals can create the caprock shale softer. However, further analyses needed to quantify the ductile mineral percentage range

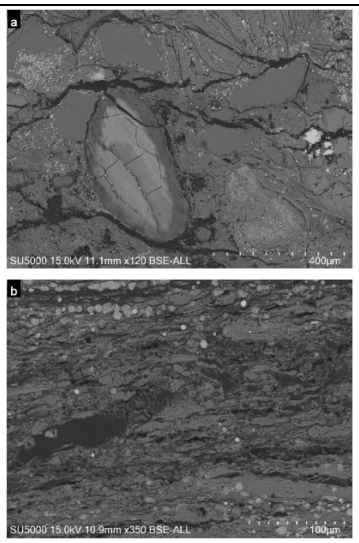

Figure 3: The SEM images of S-1 (a) and S-2 (b) represent compositional variations between wells. Note that images have scale differences.

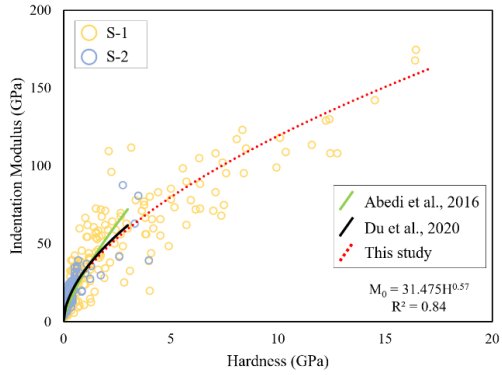

Figure 4: Indentation modulus versus hardness plot of studied samples show the variation between S-1 and S-2. A best-fit equation was also estimated using both samples with a high correlation coefficient. The published curves also represent for comparison

Acknowledgments

We are grateful for the financial support provided by the Research Council of Norway for the OASIS (Overburden Analysis and Seal Integrity Study for CO2 Sequestration in the North Sea) project (NFR-CLIMIT project #280472). We are indebted to the additional funding and data provided by Norwegian Petroleum Directorate (NPD), Gassnova, Equinor, and Total.

REFERENCES

Abedi, S., M. Slim, R. Hofmann, T. Bryndzia, and F.-J. Ulm, 2016, Nanochemo-mechanical signature of organic-rich shales: A coupled indentation–EDX analysis: Acta Geotechnica, **11**, 559–572, doi: https://doi.org/10.1007/s11440-015-0426-4.

Bulychev, S. I., V. P. Alekhin, M. K. Shorshorov, A. P. Ternovskij, and G. D. Shnyrev, 1975, Determination of Young modulus by the hardness indentation diagram: Zavodskaya Laboratoriya, **41**, 1137–1140.

Colmenares, L. B., and M. D. Zoback, 2002, A statistical evaluation of intact rock failure criteria constrained by polyaxial test data for five different rocks: International Journal of Rock Mechanics and Mining Sciences, **39**, 695–729, doi: https://doi.org/10.1016/S1365-1609(02)00048-5.

Du, J., A. J. Whittle, L. Hu, T. Divoux, and J. N. Meegoda, 2020, Characterization of meso-scale mechanical properties of Longmaxi shale using grid microindentation experiments: Journal of Rock Mechanics and Geotechnical Engineering, **13**, 555–567, doi: https://doi.org/10.1016/j.jrmge.2020.09.009.

Fischer-Cripps, A. C., 2007, Introduction to contact mechanics, 2nd ed.: Springer-Verlag, New York.

Horsrud, P., E. F. Sønstebø, and R. Bøe, 1998, Mechanical and petrophysical properties of North Sea shales: International Journal of Rock Mechanics and Mining Sciences, **35**, 1009–1020, doi: https://doi.org/10.1016/S0148-9062(98)00162-4.

Ingram, G. M., J. L. Urai, and M. A. Naylor, 1997, Sealing processes and top seal assessment: Norwegian Petroleum Society Special Publications, **7**, 165–174, doi: https://doi.org/10.1016/S0928-8937(97)80014-8.

Kalani, M., J. Jahren, N. H. Mondol, and J. I. Faleide, 2015, Petrophysical implications of source rock microfracturing: International Journal of Coal Geology, **143**, 43–67, doi: https://doi.org/10.1016/j.coal.2015.03.009.

Lama, R. D., and V. S. Vutukuri, 1978, Handbook on mechanical properties of rocks-testing techniques and results-volume iii.

Minaeian, V., V. Rasouli, and D. Dewhurst, 2014, A laboratory procedure proposed for mechanical testing of shales: APPEA Journal, **54**, 337–344, doi: https://doi.org/10.1071/AJ13034.

Mondol, N. H., J. Jahren, T. Berre, L. Grande, and K. Bjørlykke, 2011, Permeability anisotropy in synthetic mudstones– An experimental study: 73rd EAGE Conference and Exhibition Incorporating SPE EUROPEC 2011, European Association of Geoscientists & Engineers, cp-238, doi: https://doi.org/10.3997/2214-4609.20149090.

Mondol, N. H., K. Bjørlykke, and J. Jahren, 2008, Experimental compaction of clays: relationship between permeability and petrophysical properties in mudstones: Petroleum Geoscience, **14**, 319–337, doi: https://doi.org/10.1144/1354-079308-773.

Mullen, M. J., R. Roundtree, and G. A. Turk, 2007, A composite determination of mechanical rock properties for stimulation design (what to do when you don't have a sonic log): Rocky Mountain Oil & Gas Technology Symposium, Society of Petroleum Engineers, doi: https://doi.org/10.2118/108139-MS.

NPD, 2021, NPD FactPages [WWW Document]: https://npdfactpages.npd.no/factpages/Default.aspx?culture=en

Oliver, W. C., and G. M. Pharr, 1992, An improved technique for determining hardness and elastic modulus using load and displacement sensing indentation experiments. Journal of Materials Research, **7**, 1564–1583, doi: https://doi.org/10.1557/JMR.1992.1564.

Oliver, W. C., and G. M. Pharr, 2004, Measurement of hardness and elastic modulus by instrumented indentation: Advances in understanding and refinements to methodology: Journal of Materials Research, **19**, 3–20, doi: https://doi.org/10.1557/jmr.2004.19.1.3.

Ping, C., H. A. N. Qiang, M. A. Tianshou, and L. I. N. Dong, 2015, The mechanical properties of shale based on micro-indentation test: Petroleum Exploration and Development, **42**, 723–732, doi: https://doi.org/10.1016/S1876-3804(15)30069-0.

Rahman, M. J., M. Fawad, and N. H. Mondol, 2020, Organic-rich shale caprock properties of potential CO_2 storage sites in the northern North Sea, offshore Norway: Marine and Petroleum Geology, **122**, 104665, doi: https://doi.org/10.1016/j.marpetgeo.2020.104665.

Storvoll, V., K. Bjørlykke, and N. H. Mondol, 2005, Velocity-depth trends in Mesozoic and Cenozoic sediments from the Norwegian Shelf: American Association of Petroleum Geologists Bulletin, **89**, 359–381, doi: https://doi.org/10.1306/10150404033.

Wang, Z., 2002, Seismic anisotropy in sedimentary rocks, part 2: Laboratory data: Geophysics, **67**, no. 5, 1423–1440, doi: https://doi.org/10.1190/1.1512743.